

# THIS WEEK



## EDITORIALS

**TELESCOPES** Split decision gives astronomers double vision **p.548**

**WORLD VIEW** Asteroid mining in space is set to be the new Klondike **p.549**

**FRAMED** Danish Greenland photos give a feeling for snow **p.551**

## You say tomato

*Genome studies of food crops offer a powerful way for plant breeders to create products with the most advantageous attributes.*

**T**he average Italian eats 16.5 kilograms of fresh tomatoes a year — the average American consumes even more.

Many of these people will no doubt fondly remember tomatoes as being tastier in years gone by — but nostalgia plays tricks. Over the past five years a European Union collaboration has grown and analysed 7,000 heirloom and modern varieties of tomato and shown that modern tomatoes actually taste better. That is not just a question of subjective perception, either — they contain more of the sugar and acids that make up flavour than the ancestral strains do. And that is all thanks to conventional plant breeders.

The scientists have analysed many more traits in these variants than just taste. They have built up a phenotypic resource that details all the desirable (and undesirable) properties you might want to see in a tomato — from pest-resistance to speed of ripening. The resource will be extremely valuable for those who want to exploit the tomato genome, the sequence of which we publish this week (see page 635). The paper reports the sequences of both the inbred tomato strain Heinz 1706 — generated by the company whose founder Henry Heinz changed the world of tomato ketchup — and its wild ancestor *Solanum pimpinellifolium*. (Among the many aphorisms ascribed to Heinz is this fitting one: to improve the product in glass or can, you must improve it while it is still in the ground.)

Plant genomes are more challenging to sequence than those of animals because they tend to be larger and more complicated. But at around 900 megabases — just over one-quarter of the size of the human genome — the tomato genome proved manageable. Still, more than 300 scientists from 90 institutes across 14 countries have been slaving away at the task since 2003. It is a fabulous effort that has the potential to radically advance plant science. First, however, the biology behind the genome needs to be understood.

Understanding the basis of tomato genomics is important for three reasons. First, it will help scientists to unravel the extraordinary diversity of the tomato plant, and of the natural world in general. The tomato belongs to one of the planet's most diverse plant genera — *Solanum*, which includes more than 1,000 species ranging from the potato (*Solanum tuberosum*) to woody nightshade (*Solanum dulcamara*). Comparing sequences may help researchers to understand evolutionary processes.

Second, the tomato genome will teach scientists more about some basic plant mechanisms. It has already revealed, for example, previously unknown genes involved in the molecular pathways that make some tomatoes red. Deep-red tomatoes may be in high demand, but the colour is actually quite unusual in nature, even among tomatoes.

Third, the genome will help scientists and growers to improve the quality of tomatoes. Tomatoes destined for sauces, for example, need to be viscous. Fresh tomatoes must be able to travel distances without bruising or rotting. Farmers would like all tomatoes to be resistant to disease and pests, and to ripen at the same time for convenient

harvesting. Attempts in the 1990s to market genetically modified tomatoes with a single improved trait failed, in large part because of the public's fear of 'Frankenfoods'.

It is not necessary to go down the genetic-modification path again, at least for tomatoes. The genome should help plant breeders to make clever crosses between variants with desirable traits. In this way, they should be able to create products that can be firm and disease-resistant without compromising on taste. It is a question of knowing which genes sitting on what part of the genome control which traits — because this helps to avoid undesirable knock-on effects of interbreeding for a particular characteristic. The tomato community has a real start on this with its well-planned phenotype resource.

This means, of course, that the skills of traditional plant breeders — who have a feel for the whole organism — will have to come back into fashion in the world of science. In the past, breeders were the vanguard of plant sciences, just as physiologists — also masters of the whole organism — led work on mammalian biology. But the failure of both fields to understand the molecular elements of the systems they were studying limited their scientific progress. Molecular biology and genomics ousted them from their thrones, but molecular tools now give them an opportunity to make triumphant returns. ■

***"The skills of traditional plant breeders will have to come back into fashion in the world of science."***

## A war not yet won

*The eradication of polio is within reach, but it is too early for self-congratulation.*

**J**ust 25 years ago, some 350,000 people contracted polio every year. So far this year, just 60 cases have been reported across four countries worldwide. No wonder, then, that some can foresee world leaders slapping one another on the back for ending polio's scourge on humanity in a few years' time, much as their predecessors did in 1980 when the world was declared smallpox-free.

The Global Polio Eradication Initiative started in 1988 to target poliomyelitis, a paralysing viral disease that mostly affects children. Some US\$9 billion later, the result is the lowest number of cases ever tallied, as well as the fewest countries affected.

But it is too early for self-congratulation and complacency. The polio-eradication campaign faces a US\$1-billion budget shortfall over the next two years that threatens to erase this year's hard-won successes. Despite a long history of mismanagement and missed deadlines

(goals of ending viral spread by 2000 and 2005 passed the programme by, and the same is likely to be true of 2012), the world has come too close to vanquishing this ancient disease to fail to see the task through.

If aggressive vaccination campaigns stop, the virus is likely to rebound more viciously than ever in Nigeria, Afghanistan and Pakistan — the three countries never to end its spread — and in the countries they border. China, which was declared polio-free in 2000, is now battling an outbreak in its northwestern Xinjiang province, imported from neighbouring Pakistan. Bruce Aylward, an assistant director-general at the World Health Organization who is leading the eradication campaign, warns against the “false premise” that polio can be safely contained as a rare threat in a few endemic countries.

The world’s wealthier countries must meet their financial commitments to polio eradication, even in these lean economic times, and countries that have not yet chipped in ought to. Nigeria, Pakistan and Afghanistan have much more pressing public-health concerns than polio, such as high infant mortality. They are battling the virus for the world’s sake and not their own.

Western countries, fast-developing nations and oil-rich Middle Eastern nations such as Saudi Arabia could all do more to help end polio. Rotary International, the Bill & Melinda Gates Foundation and other philanthropic donors need to keep up their already substantial support.

If donors need a reason to think their money will be well spent, they should look no further than India, which has not reported a case of poliomyelitis since January 2011. The country of 1.2 billion was considered one of the hardest in which to eliminate the disease.

India’s success may not offer specific lessons to Nigeria, Pakistan or Afghanistan. Each country — and, indeed, each region where polio still circulates — has its own set of challenges that range from religion-inspired vaccine refusal to domestic terrorism to local government corruption.

An emergency action plan announced by the polio-eradication initiative in Geneva last week is a good start (see page 563). It is right to emphasize local solutions and accountability at all levels. But health officials need to remain flexible if the current plan fails, particularly in Nigeria, which is facing its high-transmission season and is battling outbreaks of three different viral serotypes.

Officials involved in the eradication effort are considering introducing injected vaccines, in conjunction with the oral vaccines in use in endemic countries. Injected vaccines could boost immunity in children who do not receive the multiple doses of oral vaccine needed to ensure protection. Such a move could also accelerate the transition from a live oral vaccine, which carries the rare side effect of triggering the disease it is supposed to fight, to inactivated injected vaccines.

It is tempting to think even further ahead, beyond polio eradication. The World Health Assembly, for example, is already considering a measles-eradication initiative. It should proceed cautiously. The polio initiative, which emphasized vaccination campaigns, may have come at the expense of routine child immunization programmes in some countries.

Measles could offer a distraction from this vital work. Some countries would be unwise to focus on this goal before achieving a high level of routine immunization against diseases such as diphtheria and tetanus.

While the polio-eradication effort was setting out its proposals last week, the World Health Assembly quietly endorsed a separate plan, which sets routine vaccination coverage targets of 90%, and aims for steep reductions in child mortality from vaccine-preventable diseases by 2020. If these goals can be achieved, there may be less political backslapping than for vanquishing polio, but the people of the world should be just as grateful. ■

**“If aggressive vaccination campaigns stop, the virus is likely to rebound more viciously than ever.”**

## Split decision

*The two-location solution for siting the Square Kilometre Array should not surprise us.*

Sharing major international events is the fashion this year. Next week, the finals of the UEFA European Football Championship will kick off in two host countries: Poland and Ukraine. Meanwhile, scientists are digesting another split decision, on where to build the world’s most powerful radio telescope.

The battle to host the Square Kilometre Array (SKA) was between South Africa and a joint Australian/New Zealand bid. Both sides fervently wanted the title, and rhetoric ran high in the weeks before the negotiation. But like many highly anticipated matches, it fell short and ended as a draw. Under the deal, half of the SKA will end up in Australia and the other half in South Africa (see page 555).

Despite some weak justifications from the political leadership of the project, there is no compelling scientific reason to build the SKA in two places. Indeed, the law of parsimony should lead any scientist to conclude that putting the SKA in a single location would be much better than putting it in two locations six time zones apart.

Scientists aren’t protesting too much, yet. They understand that large-scale experiments follow rules other than those of reason. Take, for example, ITER, the massive fusion experiment now under construction near Cadarache in the south of France. In a logical world, that complex machine would be designed, commissioned and assembled by a single directorate near the site, but instead it is being run through a baffling system of contracting and subcontracting. And the world’s most powerful particle accelerator, the Large Hadron Collider (LHC) at CERN near Geneva, has expensive data-analysis centres all over the world.

This added complexity reflects the human side to these large projects. In the case of ITER, the procurement system means that governments can ensure there is work for domestic labs and companies. Distributed computing at the LHC lets researchers who have contributed to its construction participate from their home countries.

But adding another layer of complication to an already sophisticated project adds risk and cost. ITER’s costs have doubled, largely due to its inefficient structure, and procurement is running behind schedule. The International Space Station (ISS), is currently looking at ways to make cuts — perhaps by trimming its four, redundant operations centres.

For the SKA, administering two remote locations will be more difficult than one, and the extra roads, networking, computing and power requirements will surely raise the price. The split site might also threaten the cohesion of the project: it now looks much more like two telescopes than one.

But splitting the site does have potential benefits. For one thing, the redundancy created by international collaboration can come in handy. The ISS, for example, continues to be serviced by a slew of vehicles from its different partners, even though the US space shuttle no longer flies there. There is also a perverse financial advantage — multiple partners are less likely to cancel an over-budget project than is a single government. But the greatest benefit is human: a more complex project draws in more people from more places and gives them an opportunity to participate.

It is easy to view fights over projects such as the SKA as sport. Participants instinctively seek winners and losers, and want to walk away with a trophy. But an international project is far more complicated. In the case of the SKA, both bidders can walk away with their egos intact, and the project has held together.

**➤ NATURE.COM**  
To comment online,  
click on Editorials at:  
[go.nature.com/xhqnqv](http://go.nature.com/xhqnqv)

However unsatisfying the result might seem, it was probably the best way to see that the telescope got built. It is, as the football pundits will say next week, a game of two halves. ■



## Let's mine asteroids — for science and profit

*The commercial dream of trawling space for valuable minerals could bring enormous benefits to a wide range of sciences, argues Martin Elvis.*

Two events in quick succession have transformed the prospects for commercial space activities: the successful rendezvous last week of California-based SpaceX's privately developed Dragon capsule with the International Space Station; and the bold announcement last month of a new asteroid-mining company, Planetary Resources in Bellevue, Washington, backed by deep-pocketed billionaires.

Trawling space for valuable resources may seem an unlikely concept, especially when discussed in the pages of this serious journal, but suspend your disbelief for a moment. We scientists should take the idea seriously, for it could offer two benefits: a burgeoning of planetary sciences, including the discovery of exotic new cosmic materials, and much cheaper space missions to explore the Solar System and the distant Universe. And government agencies, not least NASA, should pay attention too. Asteroid mining could give them a renewed purpose.

It is often overlooked that one of the formal goals of the US space programme, in addition to its scientific and strategic goals, is to advance the country's economic interests. The economic appeal of asteroid mining is clear: precious metals such as gold and platinum sell for around US\$50,000 per kilogram. A smallish asteroid, about 200 metres across and rich in platinum, could be worth \$30 billion.

There is, of course, more to it than just identifying such an asteroid, not least digging the material out with the help of robots and bringing it back to Earth (it is worth nothing in space). But greed is a powerful motivator to get things done.

Asteroids are directly useful in a wide variety of sciences. The least-altered asteroids, the 'carbonaceous' ones, carry 4.5-billion-year-old messages from the period, lasting just a few million years, during which the pre-solar nebula condensed into planets.

Asteroid material can tell us about this process, and why there are ores in Earth's crust, given that gold and other heavy metals should have sunk to the core when Earth was molten. And it can show us whether the water in our oceans came from asteroids and comets that hit Earth soon after the crust had formed.

Some meteorites — pieces of asteroids that reach Earth's surface — contain scores of different amino acids. Did these seed the early Earth and enable life to develop? And are exotic materials such as quasicrystals, with new and perhaps useful properties, to be found in asteroids? An extreme possibility is that a few 'quark nuggets', left over from the Big Bang, are masquerading as small asteroids but have the density of atomic nuclei.

Samples from meteorites are useful, but asteroid material with known provenance in the Solar System is limited to the few milligrams of dust retrieved from the surface of the stony asteroid Itokawa, and the lucky retrieval of 4 kilograms of

meteorites from the small asteroid 2008 TC3, which was detected and hurriedly tracked just 19 hours before it crashed into the Sahara desert. This meagre hoard will not increase quickly. NASA's OSIRIS-REx mission will bring back the first sample from a carbonaceous asteroid, 1999 RQ36, in 2023 — but this will be only 60 grams. Commercial asteroid mining would return not grams of material, but tonnes. Just a fraction of this would expand planetary science immeasurably.

Most importantly, the pressure to make a profit should drive down launch and mission costs by a factor of ten or more. Powerful new observatories and planetary probes that are not now affordable will become so. When seeking profit, time is money, and spending a year bringing back valuable ores is expensive. Known technologies will be developed to speed delivery times. That will accelerate outer Solar System exploration, and get people safely to Mars.

Scientists can help to make this dream a reality. Asteroid mining is a capitalist exercise, but the financial and technical barriers to entry are high. Just as the US government encouraged the development of the American West in the nineteenth century, so NASA and space scientists can help to tame the frontier of space, and make it ripe for harnessing, to the mutual benefit of all involved. The mining companies could gain from surveys by scientist-explorers, just as both the American pioneers and science gained from government-sponsored expeditions. In that era, for example, valuable sources of ores were discovered, as well as abundant dinosaur fossils.

Astronomers will have to map out the new territory — finding easy-to-reach asteroids in the vastness of space is not easy. The carbonaceous asteroids, in particular, are dim and easily missed. And even when they are found, it is hard to determine their size and composition accurately, which directly affects the likely profit. Just 13 meteorites out of the 1,200 or so that have been analysed in detail contain high levels of platinum, for example.

Mining engineers will have to work out ways to anchor, drill into and recover material from what in the trade is known as an 'uncooperative body'. The rocks and dust of 'rubble pile' asteroids are held together almost entirely by their own microgravity, so a mining robot would have nothing to anchor itself to. Cracking this problem will need input from materials scientists and physicists.

To promote such research, NASA's new goal should not be exploration, but enablement of the commercial development of space resources. Exploration will follow naturally. And once profits from asteroid mining start to flow, scientific exploration will be the winner. ■

Martin Elvis is at the Harvard-Smithsonian Center for Astrophysics, Cambridge, Massachusetts, USA.  
e-mail: martinsevelis2@gmail.com

**GREED IS  
A POWERFUL  
MOTIVATOR TO  
GET THINGS  
DONE.**

➔ **NATURE.COM**  
Discuss this article  
online at:  
[go.nature.com/h1gkcu](http://go.nature.com/h1gkcu)



# RESEARCH HIGHLIGHTS

Selections from the  
scientific literature

## CANCER

### Switching p53 back on

Mutations in the gene encoding the tumour-suppressor protein p53 often underlie cancer, but a compound can reverse the effects of a common p53 mutation in mice.

Darren Carpizo and his team at the University of Medicine and Dentistry of New Jersey in New Brunswick identified the compound in a cancer drug database. The authors found that it induced programmed cell death in cancer cells carrying the R175 mutant form of the p53 protein, while leaving non-tumour cell lines relatively intact. The compound slowed down the growth of human tumours bearing this mutation that were implanted in mice, but had little to no effect on tumours carrying other p53 mutations or a non-mutant form of p53. The chemical seems to restore the conformation of the mutated protein, enabling it to function normally.

The compound could be a candidate for drug development, the authors say. *Cancer Cell* 21, 614–625 (2012)

## CHEMICAL SENSING

### A nose for explosives

Explosives such as trinitrotoluene (TNT) are difficult to detect because of

their low volatilities under everyday conditions. Denis Spitzer of the French–German Institute of Saint-Louis, France, and his colleagues have created a device that they estimate can sniff out less than one part per trillion of TNT.

The team coated a tiny, vibrating cantilever with vertically aligned titanium dioxide (TiO<sub>2</sub>) nanotubes (pictured). TNT binds to the nanotubes, altering the frequency of the vibration. The device's sensitivity is due to the nanotubes' structure and large surface area, and to the strong affinity of TiO<sub>2</sub> for TNT. The detector is much less sensitive to other compounds, which reduces the likelihood of false

positives.

The researchers are now adapting their sensor to detect additional chemicals, including other types of explosive.

*Angew. Chem. Int. Ed.*  
<http://dx.doi.org/10.1002/anie.201108251> (2012)

## CANCER DETECTION

### Sequencing spots tumour cells

Patients with cancer can relapse if a few malignant cells survive treatment. Researchers show that high-throughput gene sequencing can detect this minimal residual disease (MRD) with greater sensitivity than conventional methods.

Harlan Robins of the Fred Hutchinson Cancer Research Center in Seattle, Washington, studied 43 children with T-lineage acute lymphoblastic leukaemia/lymphoma, which affects white blood cells called T cells. The team sequenced a region of two genes encoding T-cell receptors before treatment and then looked for the cancer-specific sequences in cells sampled after chemotherapy. When the researchers compared sequencing with the conventional method, which looks for cells with particular surface molecules, they found that both techniques detected cancer cells in 12 patients after treatment. However, only



## PHYLOGENETICS

### Arachnids crossed the Pacific

A family of harvestmen that inhabits tropical forests on both sides of the Pacific Ocean originated in Mesoamerica roughly 82 million years ago. The arachnids' migration is a rare example of a trans-Pacific dispersal.

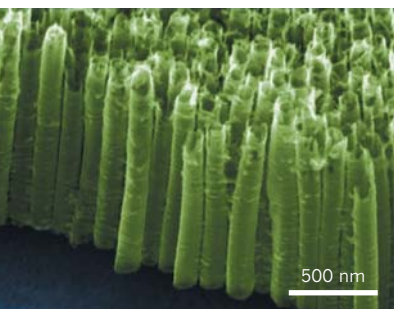
Prashant Sharma and Gonzalo Giribet at Harvard University in Cambridge, Massachusetts, sequenced and analysed DNA from 147 specimens from the sister superfamilies of Zalmoxoidea (a member pictured) and

Samooidea. The authors conclude that the species spread from the Amazon Basin across the Pacific and settled on islands of the Indo-Pacific.

The creatures probably did not disperse through the break-up of the supercontinent Gondwana, so the authors speculate that they made their way across the Pacific on floating vegetation carried by ocean currents.

*Proc. R. Soc. B* <http://dx.doi.org/10.1098/rspb.2012.0675> (2012)

G. GIRIBET





sequencing, which can find one cancerous cell in 100,000, identified MRD in a further 10 patients.

The test could potentially be adapted to monitor other blood cancers.

*Sci. Transl. Med.* 4, 134ra63 (2012)

## INFLUENZA

## Towards a single flu vaccine

Vaccines against the pandemic H1N1 influenza strain of 2009 also generated immunity to other diverse flu viruses.

A team including Rafi Ahmed at Emory University in Atlanta, Georgia, and Patrick Wilson at the University of Chicago in Illinois previously showed that people infected with pandemic H1N1 flu made antibodies that neutralized both H1N1 and other flu strains. Now the researchers have analysed immune cells from 24 people who received an H1N1 vaccine, and found that these cells also produce these broadly neutralizing antibodies. The antibodies recognize conserved molecular features of both seasonal and pandemic flu strains — including the strain responsible for the 1918 pandemic.

The findings could aid the design of flu vaccines that recognize all flu viruses.

*Proc. Natl Acad. Sci. USA* <http://dx.doi.org/10.1073/pnas.1118979109> (2012)

## PALAEOLOGY

## Dating with rare earth elements

The discovery of human remains in the same layer as fossil mammals, including mammoths and mastodons, at a site in Florida has generated debate about whether the species were contemporaneous. An analysis of rare earth elements suggests that they were.

Carbon dating of the fossils, found at Vero Beach, has not yielded conclusive answers, so Bruce MacFadden

at the University of Florida in Gainesville and his team analysed levels of rare earth elements such as cerium to date the remains. The authors show that the levels of these elements are similar in both sets of remains, but are different from those in modern mammals. Assuming that the uptake of rare earth elements by fossils from surrounding groundwater is time-dependent, then the two sets of remains must have been laid down at the same time, probably around 12,000 years ago.

*J. Verteb. Paleontol.* 32, 708–716 (2012)

## IMMUNOLOGY

## Partners for the sunshine vitamin

Whether vitamin D protects the body from infection is controversial. Researchers in California provide a possible explanation for why some studies have failed to link vitamin D to immune response: the vitamin does not work alone to boost immunity.

Richard Gallo at the University of California, San Diego, in La Jolla, and his colleagues found that, in human skin cells, one of two hormones — parathyroid hormone (PTH) and a related peptide, PTHrP — needs to team up with vitamin D's active form to increase the production of the antimicrobial peptide, cathelicidin. Mice injected with PTH fended off a *Streptococcus* infection more successfully than control animals, but only if they could produce the active form of vitamin D. The hormones can compensate for insufficient vitamin D and may participate in a positive feedback system with vitamin D and cathelicidin.

*Sci. Transl. Med.* 4, 135ra66 (2012)

## MOLECULAR BIOLOGY

## Cancer gene shifts chromatin

A cancer gene alters the three-dimensional structure of chromosomes, which could

## COMMUNITY CHOICE

The most viewed papers in science

## GEOLOGY

## Explosions created big sandpit

**HIGHLY READ**  
on [geology.gsa-pubs.org](http://geology.gsa-pubs.org) in April

At the start of the most recent ice age, pressurized sand exploded through cracks in the sea floor at the bottom of the North Sea, producing a body of sand large enough to bury Manhattan under 160-metre-high dunes.

Helge Løseth at the Statoil Research Centre in Trondheim, Norway, and his colleagues created a seismic map of the sand in Norwegian waters, which they combined with data from wells drilled into the sea bed. The authors conclude that after the sand erupted from sea bed cracks, water currents spread it over several kilometres. At 10 cubic kilometres, the sand body is the largest created in this way to be found so far.

The sand sits on top of an oil field and could harbour oil, which can emerge from fractures in the sea floor and seep through porous sand, the authors say.

*Geology* 40, 467–470 (2012)

in turn affect the expression of other genes in ways that promote cancer development.

Mark Rubin at Weill Cornell Medical College in New York and his team mapped chromosomal interactions and changes in gene expression in healthy prostate cells that overexpress a cancer gene called *ERG*. The researchers found that *ERG* overexpression correlated with remodelling of the structure of chromatin — the protein–DNA package that constitutes chromosomes. *ERG* overexpression was linked with an exchange of material between chromosomes 13 and 15. This suggests that *ERG* overactivation might lead to secondary changes in genomic structure.

*Proc. Natl Acad. Sci. USA* <http://dx.doi.org/10.1073/pnas.1112570109> (2012)

## GLACIOLOGY

## Lost photos reveal glacier shifts

Aerial photographs of Greenland from the 1930s — rediscovered in a castle outside Copenhagen — could provide a deeper understanding of the impact of climate change on the island's glaciers than the use of



satellite data alone.

Most studies of Greenland's glaciers have used satellite imagery collected since the 1960s. Anders Björk at the University of Copenhagen and his colleagues found the historical images of 132 Greenlandic glaciers (pictured) and compared them with more recent satellite data. The comparison shows that, overall, glacier retreat over the past decade has been as vigorous as in a similar period of warming in the 1930s. However, glaciers with edges that reach the ocean tended to retreat more rapidly in the 2000s than in the 1930s, whereas those terminating on land regressed faster 80 years ago than in the 2000s.

*Nature Geosci.* <http://dx.doi.org/10.1038/ngeo1481> (2012)

### ► NATURE.COM

For the latest research published by Nature visit:

[www.nature.com/latestresearch](http://www.nature.com/latestresearch)

# SEVEN DAYS

The news in brief

## POLICY

### Amazon forest loss

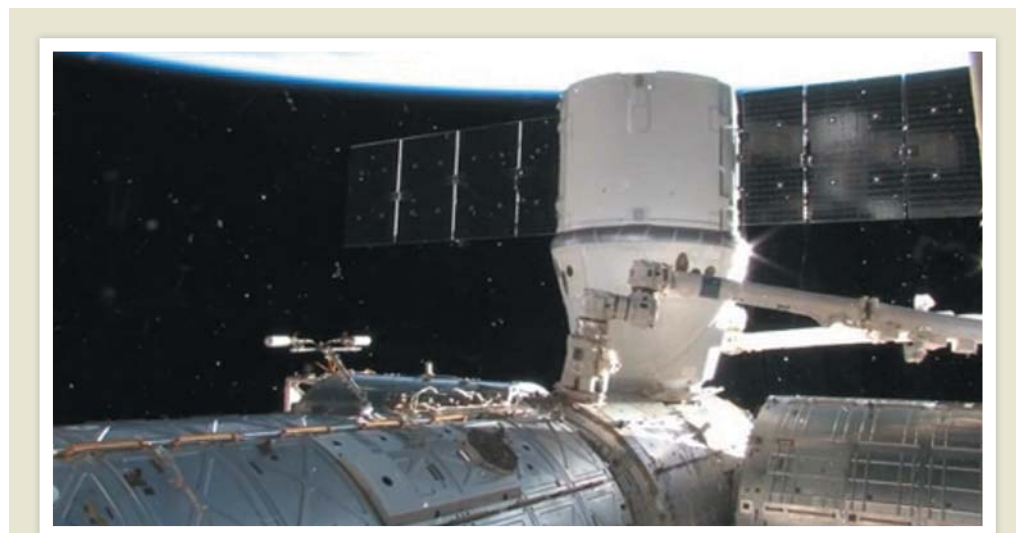
Brazil's president, Dilma Rousseff, has vetoed some controversial provisions of landmark legislation to relax forest protections in the Brazilian Amazon. But in signing the bill into law on 25 May, she stopped short of the outright veto that many environmentalists had called for. Deforestation has plummeted in the Amazon rainforest, but the new laws may reverse that trend. See [go.nature.com/ceoqex](http://go.nature.com/ceoqex) for more.

### Carbon high

In 2011, anthropogenic carbon dioxide emissions reached a record 31.6 gigatonnes, according to estimates released by the International Energy Agency (IEA) in Paris on 24 May. That was 1 gigatonne (3.2%) more than the previous year, the agency said. China's emissions alone rose by 0.7 gigatonnes (9.3%) to 8.5 gigatonnes, mostly because of an increase in coal consumption. Even so, the IEA added, China has reduced its carbon intensity (CO<sub>2</sub> emissions per unit of gross domestic product) by 15% since 2005. See [go.nature.com/qiuyiz](http://go.nature.com/qiuyiz) for more.

### Open access

An online petition urging journal articles from US taxpayer-funded research to be made freely available had gained around 19,000 signatures by 28 May. The White House will have to officially respond if the petition gains 25,000 signatures. On 23 May, the University of California, San Francisco, became the latest institution to require its researchers to make their articles freely available in an online repository (although researchers can



NASA TV

## Space station catches Dragon

Dragon has become the first private spacecraft to reach the International Space Station. The cargo capsule, built by SpaceX of Hawthorne, California, and launched on a Falcon rocket on 22 May, docked with the station (pictured)

on 25 May. It carried 460 kilograms of supplies and will spend 18 days attached to the station. Its return cargo includes a science experiment: aluminium alloy rods melted and solidified in microgravity. See [go.nature.com/7a7dh8](http://go.nature.com/7a7dh8) for more.

opt out if this conflicts with publishers' contracts). On the same day, Argentina's lower house approved a bill requiring nationally funded research to be freely available. See [go.nature.com/prgkit](http://go.nature.com/prgkit) and [go.nature.com/6esof1](http://go.nature.com/6esof1) for more.

### Telescope split

The battle to host the world's largest radio telescope, the US\$1.9-billion Square Kilometre Array, has ended in a draw. Sites in South Africa and Australia will split the project, it was announced on 25 May. See page 555 for more.

### Disease target

The World Health Organization has approved a target to cut premature deaths from non-communicable diseases (NCDs) such as heart attack, cancer, diabetes and chronic respiratory diseases by 25% by 2025. The 26 May agreement at this year's

World Health Assembly in Geneva, Switzerland, followed a high-level United Nations summit on NCDs last September (see *Nature* 477, 260–261; 2011). It came with resolutions to develop a global monitoring framework to prevent and control NCDs, and to strengthen policies promoting more active lifestyles as people age.

### Italian earthquakes

Two fatal earthquakes in the space of nine days have struck Italy's Emilia region. A magnitude-5.8 quake on 29 May had caused at least eight deaths as *Nature* went to press, and a magnitude-5.9 earthquake killed seven people on 20 May. In the aftermath of that quake, seismologists warned that little progress has been made on improving building codes since the magnitude-6.3 earthquake which struck L'Aquila, killing

309 people, three years ago. "It is unacceptable that modern constructions such as warehouses and industrial sheds have collapsed in an earthquake that was strong, but not exceptional," said Stefano Gresta, president of Italy's National Institute for Geophysics and Vulcanology. See [go.nature.com/uujbk1](http://go.nature.com/uujbk1) for more.

### Polio push

The World Health Organization rolled out plans on 24 May to tackle the world's final pockets of polio, calling for more focus on regions in Nigeria, Pakistan and Afghanistan with the lowest vaccination rates against the disease. But the Global Polio Eradication Initiative, which coordinates much of the work, is US\$945 million short of reaching its roughly \$2.2-billion budget for 2012–13. See page 563 for more.

## BUSINESS

**Butanol biofuel**

Gevo, a synthetic-biology firm based in Englewood, Colorado, announced on 24 May that production had begun at the first commercial plant for bio-isobutanol — a potential biofuel that stores more energy per litre than ethanol and is less corrosive to fuel pipelines. The factory, in Luverne, Minnesota, uses genetically modified yeast to ferment corn (maize) starch, and will be making 3.8 million litres of isobutanol per month by the end of the year. Like many other synthetic-biology firms, Gevo will at first sell its product to the chemicals industry, rather than marketing it as an expensive substitute for cheap fossil fuels. See [go.nature.com/x8k3tz](http://go.nature.com/x8k3tz) for more.

## PEOPLE

**Alien-hunter retires**

Astronomer Jill Tarter (pictured), who has pioneered and popularized the search for extraterrestrial intelligence (SETI), is retiring as director of research at the SETI Institute in Mountain View, California. Tarter says that she will instead focus her efforts on what she calls “the search for intelligent funding” — referring to the institute’s troubles raising cash to run the Allen Telescope Array in northern California



(see *Nature* 475, 442–444; 2011). See [go.nature.com/e1pvlc](http://go.nature.com/e1pvlc) for more.

**US nuclear chief**

US President Barack Obama has nominated Allison Macfarlane, a nuclear-policy professor at George Mason University in Fairfax, Virginia, to head the Nuclear Regulatory Commission. The choice was announced on 24 May, three days after the current chairman, Gregory Jaczko, said he would resign. See [go.nature.com/uci4f4](http://go.nature.com/uci4f4) for more.

## RESEARCH

**Clinical stem cells**

California’s state stem-cell agency is focusing more of its funds on clinical development, and shrinking support for basic research, facilities and training. The California Institute for Regenerative Medicine in San Francisco voted for the new strategic plan on 24 May; by

July 2013, it hopes to have two programmes approved for US clinical trials. Translation of stem cells from research tools to therapies had been a major selling point for the agency when it was funded nine years ago. See [go.nature.com/8wckrp](http://go.nature.com/8wckrp) for more.

**Antibiotics search**

The European Union (EU) has launched a seven-year effort to bring academic and industry researchers together to find and develop antibiotics. On 24 May, the EU’s Innovative Medicines Initiative (IMI) in Brussels put out a call for proposals supported by a budget of €224 million (US\$281 million): half from the IMI and half from major pharmaceutical companies. Company contributions will include experimental drugs and expertise. The programme, part of a wider strategy announced late last year to fight the rise of drug-resistant microbes, will focus at first on improving clinical-trial design. See [go.nature.com/c8s9jb](http://go.nature.com/c8s9jb) for more.

**German grants**

Academic scientists in Germany are increasingly relying on project-based grant money for their research. A funding atlas released on 24 May by Germany’s main research agency, the DFG, shows that universities

## COMING UP

**4–11 JUNE**

Disputed claims to own the sea bed are discussed by states that are party to the United Nations Convention on the Law of the Sea. They meet in New York, marking the 30th anniversary of the convention’s adoption. [go.nature.com/m2duzm](http://go.nature.com/m2duzm)

**5–6 JUNE**

The planet Venus passes across the face of the Sun — the last chance to see such a transit until 2117.

[transitofvenus.org](http://transitofvenus.org)

attracted €5.3 billion (US\$6.6 billion) in grants in 2009, more than twice what they got in 1998. The funding that universities receive from the state has not kept pace, increasing by just 23%. Because some external grants don’t include overhead costs, gaining project funding can make it harder for host institutions to provide reliable career paths for young scientists, experts warn. See [go.nature.com/izevp1](http://go.nature.com/izevp1) for more.

**GM crop protest**

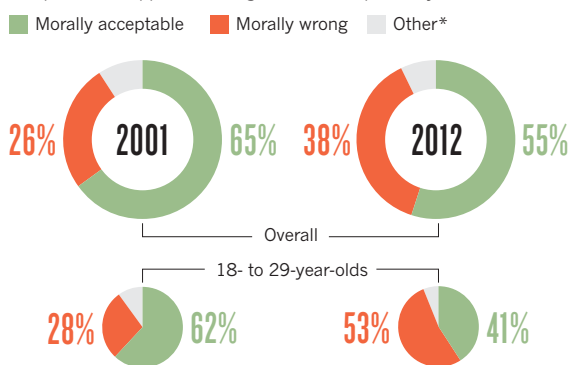
A heavy police presence prevented a protest group of about 200 people from tearing up a trial crop of genetically modified (GM) wheat at Britain’s leading agricultural research centre on 27 May. The ‘Take the Flour Back’ campaign had earlier publicized its intention to destroy the crop at Rothamsted Research in Harpenden; scientists had reacted with public pleas about the importance of their work. With their plans thwarted, protesters instead held a picnic, with speeches focusing largely on corporate malfeasance by agribusinesses. See [go.nature.com/if1d5e](http://go.nature.com/if1d5e) for more.

## TREND WATCH

The proportion of Americans who believe that medical testing on animals is ‘morally wrong’ grew by 12%, to 38%, between 2001 and 2012, according to the Gallup organization’s annual *Values and Beliefs* survey of around 1,000 respondents, released on 22 May. During the same period, the number of people judging the practice ‘morally acceptable’ dropped by 10%, to 55%. The largest jump in opposition has been in 18- to 29-year-olds (see chart).

**GROWING DOUBTS ON ANIMAL TESTING**

More than half of Americans feel medical testing on animals is morally acceptable, but opposition has grown over the past 11 years.



\*No opinion/not a moral issue/depends on situation

➔ **NATURE.COM**

For daily news updates see:  
[www.nature.com/news](http://www.nature.com/news)



# NEWS IN FOCUS

**FOOD SAFETY** US adds six *E. coli* subtypes to the rogues' gallery **p.558**

**SOCIETY** With bullets and bombs, anarchists target science **p.561**

**PUBLIC HEALTH** The polio endgame is on — but \$1 billion short **p.563**



**CONSERVATION** First-class fertility treatment for endangered rhino **p.566**

M. HUTCHINGS/REUTERS



South Africa plans to build 3,000 radio dishes, with about half of them in eight other African nations.

## ASTRONOMY

# Winners all round in telescope bid

*Based in both Australia and South Africa, the Square Kilometre Array will face technical and financial challenges.*

BY GEOFF BRUMFIEL

After months of intense political negotiation, the world's largest radio telescope has found not one home, but two. The decision has satisfied local politicians vying for the project, but has left some scientists worrying that logistical problems and cost increases could jeopardize the telescope's long-term future.

In a plan announced on 25 May, South Africa and Australia will share the Square Kilometre Array (SKA), a €1.5-billion (US\$1.9-billion) project made up of 3,000

15-metre-wide dishes and an even larger number of simple antennas. Under the deal, South Africa will host the dishes, and Australia will get the antennas. The split followed a straw poll of the voting members of the SKA board: Italy, Canada, the United Kingdom, China and the Netherlands. The nations have so far contributed a total of €90 million to the project's pre-construction phase; following the site decision, further commitments are expected to follow by 2014.

The SKA will be dozens of times more powerful than any previous radio telescope. When completed around 2024, it will be able

to image the Universe at the time when the first stars and galaxies began to form, just a few hundred million years after the Big Bang. Its sensitivity makes it capable of spotting a television signal from a planet orbiting a nearby star (if, that is, any aliens are broadcasting).

South Africa has fought hard for the project against a joint bid by Australia and New Zealand. In March, the nation narrowly won out in a scientific assessment of the two sites (see *Nature* <http://doi.org/hst;2012>). But many observers had expected the project to be split. Three different types of antenna technology are used to cover a wide range of frequencies between 70 megahertz and 10 gigahertz, and although the original designers envisaged that all three types would be near one another, there was no technical reason to put them together (see *Nature* 484, 154; 2012).

Officials from both bids welcomed the plan. "I think it's an excellent decision," says Philip Diamond, head of astronomy and space science at Australia's Commonwealth Scientific and Industrial Research Organisation in Marsfield. "We're really extremely delighted about this," adds Phil Mjwara, director general of South Africa's Department of Science and Technology.

But the division will almost certainly mean significant cost increases in the telescope's second phase of construction, scheduled for around 2018, says Heino Falcke, a radio astronomer at Radboud University in Nijmegen, the Netherlands. "The main question is: can the excess cost be offset by the fact that we have two major contributors?"

The project's sheer scale necessitates two phases of building work. In the first phase, due to begin as early as 2016, South Africa will add 190 steerable dishes to its existing MeerKAT array, according to Diamond. Australia will add 60 dishes to its SKA Pathfinder facility, and will also build half a million omnidirectional dipole antennas — cheap, stubby devices that capture radio signals across the sky and assemble them into an image. The result will be an Australian telescope with a wide-angle view of the sky, and a South African telescope with a narrower view and higher sensitivity. The two will be complementary, Diamond says: the Australian telescope might pick up signals that can later be studied in detail by ▶

## ➔ NATURE.COM

What will SKA success mean for South Africa?

[go.nature.com/mcgsbp](http://go.nature.com/mcgsbp)

► the South African array, for example.

"This may be politically expedient, but it is also scientifically driven," says SKA board chairman John Womersley. By building on existing pilot projects in both countries, he says, the SKA's first phase will be even more powerful than originally planned. Operating across two sites will add no more than 10% to the projected €350-million cost of phase one, according to Womersley. South Africa and Australia have already each invested around US\$150 million in their respective pilot projects, and the board concluded that this added capability makes the additional investment worthwhile. First observations from these phase-one facilities could come by the end of the decade.

#### TOUGH SELL

In phase two, the rest of the dishes will be assembled in South Africa and eight other African countries, along with mid-frequency aperture arrays that fill an observing gap between the antennas and the dishes. Meanwhile, Australia will build the remaining dipole antennas. As the SKA grows, it will require an ever-increasing amount of electricity, dedicated fibre-optic networking and supercomputing resources to channel and crunch its data. "Because we don't have a detailed design yet for phase two, it was next to impossible to estimate the costs," says Diamond. But Brian Schmidt, a Nobel-prizewinning astronomer at the Australian National University in Canberra, says that the figures he has seen suggest that the cost increase from running the project at both sites "is likely to be 30%".

"In the current environment that's a tough sell," Schmidt warns. He hopes that if budget shortfalls or other problems make the split site impossible, the SKA's planners would reconsider the arrangement.

Albert Zijlstra, director of the Jodrell Bank Centre for Astrophysics near Manchester, UK, notes that as well as requiring coordination across six time zones, the project will essentially be creating two separate telescopes at two separate locations. With limited international funding, "they may end up competing with each other", he says.

Despite their concerns, Zijlstra, Schmidt and others generally support the decision to split the site. "When I heard the announcement, I actually suddenly decided that it's a good thing," says Andrew Lawrence, an astronomer at the University of Edinburgh, UK. Lawrence and others think that the compromise is crucial to making the project's first phase possible, by settling the long-running site dispute in a way that allows both bids to claim victory. "At this stage, I wouldn't be totally certain that phase two would ever be built," he cautions. "It's a fantastic idea, but it's still a long way from reality." ■ **SEE EDITORIAL P.548**



A gas flare burns at a fracking site in Bradford County, Pennsylvania.

#### ENVIRONMENT

## Fracking boom spurs environmental audit

*As hydraulic fracturing unlocks new gas reserves, researchers struggle to understand its health implications.*

BY HELEN THOMPSON

For Ohio, a Midwestern state hit hard by recession, the promise of an energy boom driven by hydraulic fracturing, or 'fracking', would seem to be a sure route to financial health. Far less certain is whether the technique has an impact on human health. Fracking uses high-pressure fluids to fracture shale formations deep below ground, releasing the natural gas trapped within. With the number of gas wells in Ohio that use fracking set to mushroom from 77 to more than 2,300 in the next three years, the state is the latest to try to regulate a rapidly growing industry while grappling with a serious knowledge gap. No one knows what substances — and at what levels — people near the gas fields are exposed to in the air and water, and what, if any, health threat they might pose.

In a nod to those concerns, Ohio's legislature passed a bill on 24 May, awaiting signing by the state governor as *Nature* went to press, that requires companies to disclose the chemicals they use during the fracking process and during

the construction and servicing of the wells. However, the bill does not compel companies to divulge a complete list of the ingredients in their fracking fluid before it is pumped underground. Some of those ingredients are deemed trade secrets, a position that troubles environmental groups and increases the problem for researchers trying to understand the risks.

"There is a real lack of data," says John Balbus, senior adviser on public health at the National Institute of Environmental Health Sciences in Bethesda, Maryland, who spoke at a workshop organized by the Institute of Medicine in Washington DC last month to discuss research strategies for studying the health impacts of gas extraction. "There's a lot of variability from region to region, in the kinds of mixtures that need to be used for the specific geology."

Fracking fluids are primarily water and sand, but they also contain chemical additives that aid the horizontal fracturing of shale and the release of natural gas. Some components,

➔ **NATURE.COM**

For more on the fracking debate, see: [go.nature.com/ongx2b](http://go.nature.com/ongx2b)

L. STONE/REUTERS



such as citric acid and coffee grounds, are benign, whereas others, such as benzene or toluene, could cause chronic health problems at certain doses. Waste water — fracking fluid mixed with groundwater containing high levels of brine and traces of natural radioactive elements — comes back to the surface during the drilling process.

“The big threats to public health are in wastewater pits and storage and also during transportation when you are trucking around contaminated water,” says Deborah Swackhamer, an environmental chemist at the University of Minnesota in St Paul. “You can have spills or leaks or flooding.”

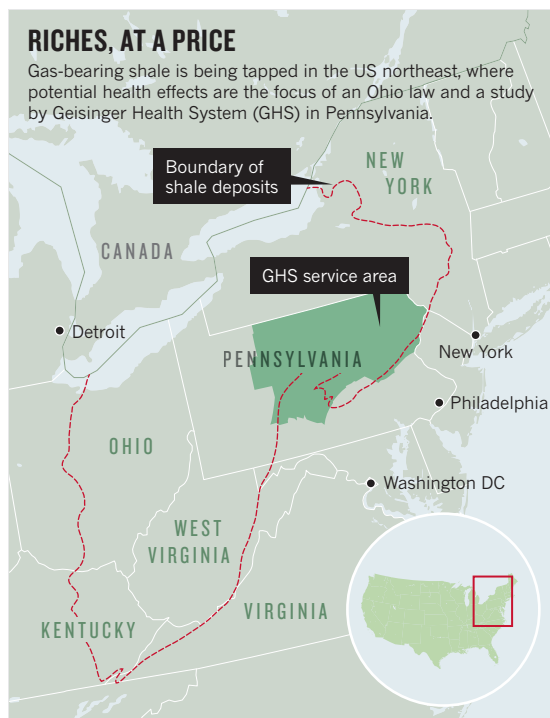
With uneasiness growing about the increasing scale of fracking in the United States, the pressure on companies to be more forthcoming is growing. The Ohio bill would allow a doctor to request proprietary information about fracking fluid when treating a patient who shows signs of exposure to a toxic chemical that might have come from a gas well — but doctors must keep what they learn confidential. An amendment to the bill supported by the Ohio State Medical Association would allow doctors to break the confidentiality rule when professional ethics demands it.

“The end result of any legislation should not impact a physician’s ability to care for his/her patients,” wrote Timothy Maglione, senior director of government relations for the medical association, in a letter to the legislature dated 22 May.

A tougher national disclosure requirement is in the works. Earlier this month the US Bureau of Land Management released a draft version of its rules for fracking operations on federal and Indian lands. Like the Ohio bill, the rules allow companies to withhold trade secrets, but they also put the burden on the firms to convince the bureau that a trade-secret claim is valid. Environmental groups say that even these rules don’t go far enough.

“There is no one chemical-disclosure provision out there that gives the public enough information to know if they’re being exposed to something through natural-gas drilling,” says Thom Cmar, a Chicago-based attorney with the Natural Resources Defense Council in New York City.

Testing the air and water near fracking operations could give a clearer indication of human exposures (see ‘Riches, at a price’). A survey by the US Environmental Protection Agency (EPA) will include case studies in five states where fracking occurs. The studies will



draw from existing water, air and soil data; test waste water; analyse well design and construction; and conduct toxicity tests. At two sites, the agency will compare pre-drilling testing to post-drilling testing. The study, now a year old, will run into 2014, but initial results are expected by the end of this year.

But even after the environmental data from the EPA roll in, there will still be a dearth of information on effects on human health. “There really is nothing out there in terms of well designed epidemiological studies,” says Madelon Finkel, an epidemiologist at the Weill Cornell Medical College in New York City.

At last month’s meeting in Washington, researchers from the Geisinger Health System, which includes hospitals, clinics and community practices in central and northeastern Pennsylvania, announced a plan to use their own 10-year database of electronic health

records to map health trends before and during drilling. The database includes more than 2.6 million residents in a region that has some of the highest concentrations of fracking wells in the United States. “We can at least get a surveillance-level snapshot of what some of the health trends might be,” says David Carey, director of Geisinger’s Weis Center for Research in Danville, Pennsylvania.

Other researchers hope to tap Geisinger’s records for joint projects. Brian Schwartz, an epidemiologist at Johns Hopkins University in Baltimore, Maryland, wants to mine them for multiple health indicators, including trends in asthma cases, which can serve as a bellwether for air quality. His team will overlay these data with computer models for environmental air quality based on EPA monitoring data, which will provide a picture of whether air quality around wells has changed as fracking in the region has intensified and how, where and when pollutants could be affecting asthma patients.

Robert Oswald, a pharmacologist at Cornell’s College of Veterinary Medicine in Ithaca, New York, is taking a different tack: using animal-health reports as proxies for humans. When farmers split their herds between pastures close to and distant from fracking activity, they create inadvertent experimental and control groups. “They’re sentinels for human health,” says Oswald. “If you want to look

at reproductive problems, you might be hard pressed to find 100 pregnant women living near a wastewater impoundment pond, but we can probably find 100 pregnant cows.”

His case survey, published in January (R. Oswald and M. Bamberger *New Solutions* 22, 51–77; 2012), finds two instances of correlation between gas-drilling activity and mortality rates in livestock, but there are several caveats, including small sample size, the fact that the individual cases were all reported by different people, and the fact that toxic sources unrelated to fracking could explain the pattern.

Conducting controlled studies among people will be slow and costly. But Finkel warns that questions about the long-term effects of the fracking boom are too urgent to ignore. “We don’t know the impact on human health,” she says, “and living in blissful ignorance isn’t a solution.” ■



**MORE  
ONLINE**

#### TOP STORY



Ageing eyes hinder biometric scans  
[go.nature.com/cckvgd](http://go.nature.com/cckvgd)

#### MORE NEWS

- Stem cells take root in drug development [go.nature.com/q71tm8](http://go.nature.com/q71tm8)
- Chemists image the Olympic rings on a molecular scale [go.nature.com/lotrfn](http://go.nature.com/lotrfn)
- Mission to drill into Japan’s earthquake zone half a success [go.nature.com/wjsmik](http://go.nature.com/wjsmik)

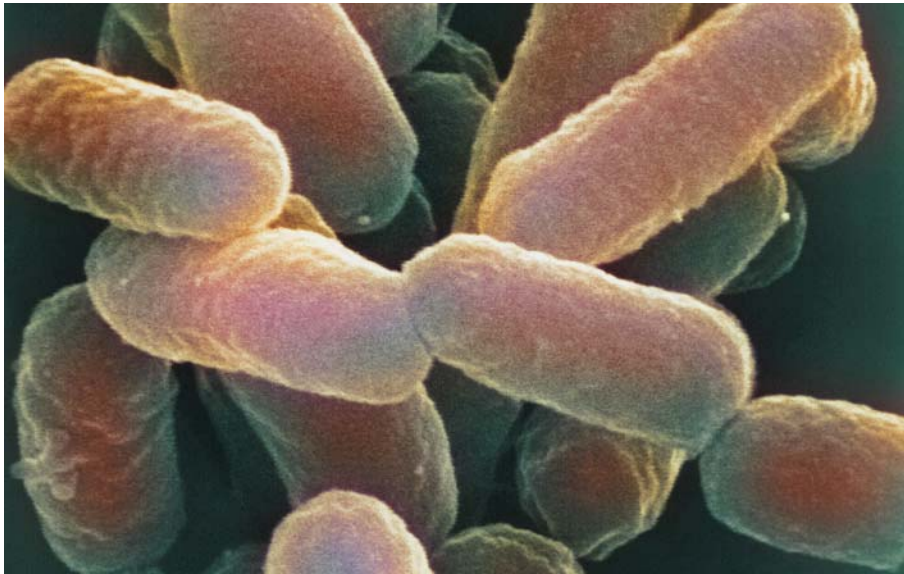
#### SLIDESHOW



Rediscovered photos reveal Greenland’s glacier history  
[go.nature.com/winveh](http://go.nature.com/winveh)

ARCTIC INST. DENMARK





The bacterium *Escherichia coli* O157:H7 can cause serious cases of food poisoning.

## FOOD SAFETY

# US beef tests cook up a storm

Critics question benefits of broader *E. coli* screening.

BY HELEN SHEN

Every week, dozens of kilograms of raw beef from meat-processing plants across the United States are rushed to one of three federal laboratories to be picked apart, pulverized, incubated and analysed. Working for the US Department of Agriculture (USDA), technicians in these labs are searching for *Escherichia coli* O157:H7, a toxic variety of the bacterium that has been monitored in US beef since 1994. But beginning on 4 June, the search will expand to include six more *E. coli* subtypes or 'serogroups'.

US agriculture secretary Tom Vilsack announced the change last September, saying it would "stop problems before they start". The USDA portrays the measure as a way to reduce risk, but it has not quantified the number of people that would be spared illness by the change. With the new screening protocol now imminent, meat producers are questioning the rationale behind the move and at least one outspoken expert agrees.

"I think it's a fundamentally flawed policy, and it's not based on the best science," says Michael Doyle, a microbiologist and director of the Center for Food Safety at the University of Georgia in Griffin. He says that the USDA risks wasting limited resources chasing

bacteria whose effects on human health are still unclear.

Most types of *E. coli* are harmless or even beneficial, such as those that colonize the healthy human gut. But some, such as O157:H7, can produce Shiga toxin, which can be harmful. The USDA began screening raw beef for this microbe after it was linked to the deaths of four children who ate contaminated hamburgers in 1993. Readily identifiable through rapid screening, O157:H7 can sometimes trigger haemolytic uraemic syndrome, which can

cause life-threatening kidney damage.

Over the past decade, improved diagnostic tests have linked a growing number of food-borne illnesses to other Shiga-toxin-producing *E. coli* (STEC) serogroups, including the latest additions to the USDA's testing regimen, dubbed the Big Six (see 'Emerging threat'). Last year, an STEC subtype traced to contaminated fenugreek sprouts made thousands of people across Europe ill, and killed at least 53 (see page 559).

The Centers for Disease Control and Prevention (CDC) in Atlanta, Georgia, estimates that 173,000 STEC infections occur annually across the United States, with O157:H7 responsible for roughly 36% and the Big Six accounting for most of the remainder. By targeting these, the USDA is bringing food regulation in line with public-health data, says Robert Tauxe, deputy director of the division of food-borne, waterborne and environmental diseases at the CDC. "We think this is an important step forward in preventing human disease," he says.

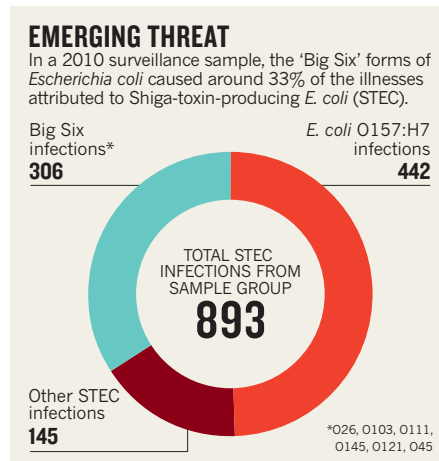
Industry representatives counter that the expanded testing will be redundant, because existing O157:H7 testing is an indicator of overall cleanliness and food safety. "We have done extensive research over the past several years that shows that the preventative controls in our facilities today work equally well for the non-O157:H7 as they do for O157," says James Hodges, executive vice-president of the American Meat Institute (AMI), a trade association in Washington DC.

The AMI estimates that the new tests will cost the industry between US\$172 million and \$324 million a year, because it contends the extra sample analysis will force processors to hold onto meat longer before distributing it. More tests will also mean more false positives that require investigation, says Doyle, delaying release of the meat and lowering its market value.

The USDA acknowledges that most infections linked to the Big Six do not stem from contaminated beef but from other sources, such as vegetables. The tests will not eliminate risk of *E. coli* infection, says David Goldman, assistant administrator for the Office of Public Health Science at the USDA's Food Safety and Inspection Service. Nonetheless, he says, "we expect that this is a truly preventative measure".

The pay-offs of such a precaution are far from certain. Although the Big Six are increasingly seen as sources of illness, their toxic effects are often less severe than those of O157:H7. The serogroups are also divided into strains, not all of which produce toxins. Shiga toxins themselves occur in types that vary in toxicity by up to a factor of 1,000. Scientists are still trying to determine which strains are likely to produce the most harmful Shiga toxins, and to identify auxiliary molecules that predict a given STEC's virulence in humans.

"We're learning more and more, but it's very



K. LOUNATMAA/SPL

SOURCE: CDC FOODNET

complex,” says Phillip Tarr, a microbiologist at Washington University in St Louis, Missouri. Tauxe concedes that more research is needed to better understand STEC pathology. “This is an area that we expect to evolve,” he says. But

if the meat-packing industry challenges the rule in court, as it has done for some previous USDA measures, the science of *E. coli* toxicity could soon find itself again under the microscope — this time, a legal one. ■

## HEALTH

# Reform falters after Europe's *E. coli* scare

*Political debate leaves German surveillance law in limbo.*

BY MARIAN TURNER

One year on from Europe's worst recorded outbreak of *Escherichia coli* infection, governments have made little progress towards improving the monitoring and reporting systems that allowed the crisis to drag on for weeks. The disease, which was spread by contaminated fenugreek sprouts, swept across northern Germany in May and June 2011, infecting thousands and killing 53 people (see *Nature* 474, 137; 2011). Yet although the panic has sparked some proposed policy changes, these have become mired in political debate at both German and European levels.

Under Germany's current system, it can take up to 18 days for local and state health departments to relay case reports to the Berlin-based Robert Koch Institute (RKI), the German federal agency for disease surveillance. Legislators have proposed a law to bring the country's disease-reporting schedule into line with the World Health Organization's International Health Regulations. The law would require local health authorities to report cases of notifiable diseases to state authorities on the next working day; the states would then have another day to relay the information to the RKI. “We've been waiting almost a decade for this,” says Alexander Kekulé, a microbiologist at the Martin Luther University of Halle-Wittenberg in Halle, Germany.

The draft law has been passed by Germany's federal parliament but is stuck in negotiations at the legislative council that represents Germany's 16 states. For scientists, though, this change would still not be enough. “What really delayed the detection of this outbreak was the irregularity with which patients were referred for microbiological follow-up,” says Gérard Krause, an epidemiologist at the RKI. Like many European countries, Germany does not require that a patient with bloody diarrhoea or haemolytic uraemic syndrome (a life-threatening complication of some *E. coli* infections) be tested for the causative bacterial strain. The

same is true of the United States.

After the outbreak, German diagnostic laboratories were provided with kits to test samples for genes belonging to certain pathogenic strains of bacteria, such as those expressing particular toxins, or proteins involved in adhesion or invasion. But physicians are responsible for requesting the tests, and the cost is not covered by German health-insurance companies. “The problem is mostly getting the money to use these kits,” says Angelika Fruth, a microbiologist at the RKI, “and that situation is just the same as before the outbreak.”

It is not only people who need to be tested — the source of most human infection is contaminated food. In the wake of the outbreak, the European Food Safety Authority concluded that sprouted seeds pose a particular food-safety concern (*EFSA J.* 9, 2424–2525; 2011), and recommended that a standardized test for sprouts be developed and adopted across the European Union (EU). But EU member countries are still discussing the proposal, and scientists have yet to develop reliable methods to isolate pathogenic bacteria from seeds or sprouts. Meat can also carry *E. coli*, but whereas the United States screens meat for disease-causing strains (see page 558), EU countries do not routinely do so, relying instead on farm and slaughterhouse hygiene.

There is room for optimism, however. Flemming Scheutz, head of the World Health Organization Collaborative Centre for Reference and Research on *Escherichia* and *Klebsiella* in Copenhagen, believes that after last year's outbreak, physicians are at least more likely to recognize and report food-borne infections. The crisis also coincided with the advent of inexpensive whole-genome sequencing technology, resulting in a glut of new bacterial sequences. Genomics and public-health research groups are now studying how these might help to tackle future outbreaks.

“The push for novelty among testing and surveillance systems will come from scientists rather than politics,” says Scheutz. ■



## ACTIVISM

# Anarchists attack science

*Armed extremists are targeting nuclear and nanotechnology workers.*

BY LEIGH PHILLIPS

A loose coalition of eco-anarchist groups is increasingly launching violent attacks on scientists.

A group calling itself the Olga Cell of the Informal Anarchist Federation International Revolutionary Front has claimed responsibility for the non-fatal shooting of a nuclear-engineering executive on 7 May in Genoa, Italy. The same group sent a letter bomb to a Swiss pro-nuclear lobby group in 2011; attempted to bomb IBM's nanotechnology laboratory in Switzerland in 2010; and has ties with a group responsible for at least four bomb attacks on nanotechnology facilities in Mexico. Security authorities say that such eco-anarchist groups are forging stronger links.

On 11 May, the cell sent a four-page letter to the Italian newspaper *Corriere della Sera* claiming responsibility for the shooting of Roberto Adinolfi, the chief executive of Ansaldo Nucleare, the nuclear-engineering subsidiary of aerospace and defence giant Finmeccanica. Believed by authorities to be genuine, the letter is riddled with anti-science rhetoric. The group targeted Adinolfi because he is a "sorcerer of the atom", it wrote. "Adinolfi knows well that it is only a matter of time before a European Fukushima kills on our continent."

"Science in centuries past promised us a golden age, but it is pushing us towards self-destruction and total slavery," the letter continues. "With this action of ours, we return to you a tiny part of the suffering that you, man of science, are pouring into this world." The group also threatened to carry out further attacks.

The Italian Ministry of the Interior has subsequently beefed up security at thousands of potential political, industrial and scientific targets. The measures include assigning bodyguards to 550 individuals.

The Olga Cell, named after an imprisoned Greek anarchist, is part of the Informal Anarchist Federation, which, in April 2011, claimed responsibility for sending a parcel bomb that exploded at the offices of the Swiss nuclear lobby group, Swissnuclear, in Olten. A letter found in the remains of the bomb demanded the release of three individuals who had been detained for plotting an attack on IBM's flagship

nanotechnology facility in Zurich earlier that year. In a situation report published this month, the Swiss Federal Intelligence Service explicitly linked the federation to the IBM attack.

The Informal Anarchist Federation argues that technology, and indeed civilization, is responsible for the world's ills, and that scien-

"direct support" for each other's activities and talk of a "blossoming" of a more organized eco-anarchist movement.

In the wake of the Mexican bombings, the Monterrey Institute installed metal detectors, began to use police sniffer dogs and started random inspections of vehicles and packages.

After a letter bomb addressed to a nanotechnology researcher at the Polytechnic University of Pachuca in Hidalgo exploded in December last year, the institute installed a perimeter fence and scanners, and campuses across the state heightened security measures.

Italian police investigating the shooting say that they are concerned about the rise in violent action by anarchist groups amid Europe's economic crisis. On 23 May, for example, members of the Informal Anarchist Federation attacked railway signals in Bristol, UK, causing severe transport delays. An online message from the group said that the targets had been chosen to disrupt employees of the Ministry of Defence and defence-technology businesses

in the area, including Raytheon and QinetiQ.

The Swiss report also noted signs of "an increasing degree of international networking between perpetrators". The level of risk to scientists depends on their field of work, says Simon Johner, a spokesman for the Swiss Federal Intelligence Service. "We are not able to tell them what to do. We can only make them aware of the dangers. It's up to institutions to take preventative actions." The agency is working with police forces, businesses and research communities to assess and tackle the threat.

"These people do not represent mainstream opinion. But I am still pretty frightened by this violence," says Michael Haggmann, a biochemist and head of corporate communications for the Swiss Federal Laboratories for Materials Science and Technology near Zurich, a public-sector partner of the IBM facility that also does nanotechnology research.

"Just a few weeks after the attempted bombing, we were due to have a large conference on nanotechnology and we were really quite nervous" about going ahead with it, Haggmann says. "But we concluded that the public discussion was more important and didn't want to scare people by having 20 police guarding us. It would have sent the wrong message." ■



Investigations of the shooting of nuclear-engineering head Roberto Adinolfi have confirmed the involvement of an eco-anarchist group.

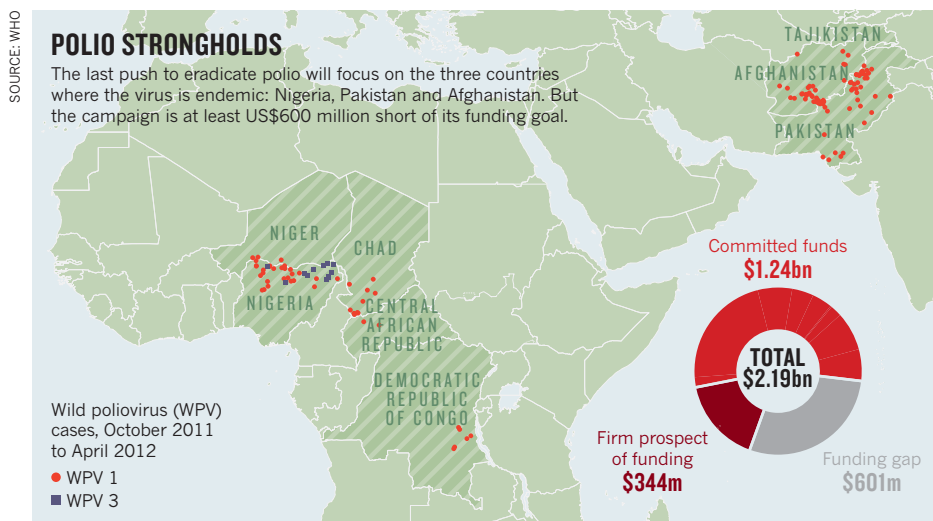
tists are the handmaidens of capitalism. "Finmeccanica means bio- and nanotechnology. Finmeccanica means death and suffering, new frontiers of Italian capitalism," the letter reads.

## GATHERING MOMENTUM

The cell says that it is uniting with eco-anarchist groups in other countries, including Mexico, Chile, Greece and the United Kingdom. Mexico has already seen similar attacks: in August 2011, a group called Individuals Tending Towards Savagery sent a parcel bomb that wounded two nanotechnology researchers at the Monterrey Institute of Technology. One received burns to his legs and a perforated eardrum and the other had his lung pierced by shrapnel (G. Herrera Corral *Nature* 476, 373; 2011). The package contained enough explosive to collapse part of the building, according to police, but failed to detonate properly.

Earlier that year, the same group sent two bombs to the nanotechnology facility at the Polytechnic University of the Valley of Mexico. One was intercepted before anyone could be harmed, but the second detonated, injuring a security guard. It is not clear how closely the group is tied to the Informal Anarchist Federation, but in online forums the two bodies offer





## HEALTH

# Polio's last stand

*As the global eradication effort ramps up, funding shortfalls threaten the programme's gains in Africa and Asia.*

BY EWEN CALLAWAY

A hard-fought battle against the polio virus may be approaching its endgame. Last week, health officials laid out plans to eradicate the virus from its last redoubts, but warned that the effort may founder owing to a US\$1-billion funding gap.

"We are truly at a tipping point in the programme right now," says Bruce Aylward, an assistant director-general at the World Health Organization, who is leading the eradication effort. Speaking at the 65th World Health Assembly in Geneva, Switzerland, he announced an Emergency Action Plan to step up vaccination efforts in the three countries that have never been able to stop the virus from spreading: Nigeria, Afghanistan and Pakistan.

The plan, which would boost global spending to \$2.2 billion over the next two years, aims to stamp out new polio cases by the end of this year. Some experts believe it will take longer, but they agree that the push will eventually deliver victory to the Global Polio Eradication Initiative (GPEI), a \$9-billion campaign that began in 1988, a time when an estimated 350,000 people succumbed to polio each year. The initiative, based in Geneva, made rapid gains in the Americas, Europe and parts of Asia, but since 2001, incidence rates have plateaued, with 1,000–2,000 people developing poliomyelitis each year worldwide.

To eliminate those cases, the GPEI must ensure the vaccination of a majority of children in hard-to-reach and war-torn areas such

as Kandahar province in Afghanistan. But the global economic crisis has created a \$945-million gap of unfulfilled commitments in the initiative's budget for 2012–13, which is already forcing the campaign to limit vaccination in neighbouring countries such as Niger and Tajikistan (see 'Polio strongholds'). Although about one-third of that funding gap looks set to be filled, Aylward warned that shortfalls in the second half of this year could compel the GPEI to pull back in Afghanistan and Pakistan, too.

"If the money doesn't come and they can't build these walls of immunity, there is a risk that polio will implant itself and start circulating" in neighbouring countries, says David Heymann, director of the Centre on Global Health Security at Chatham House in London, and former head of the WHO polio-eradication effort. China's western province of Xinjiang, for example, is fending off an outbreak that originated in Pakistan. The GPEI estimates that if polio is not eradicated and mass vaccination ceases, the number of children paralysed each year will rise to 200,000 within a decade, and unvaccinated adults will be vulnerable to a more aggressive form of the disease, as they are in Xinjiang.

On 25 May the World Health Assembly passed a mostly symbolic measure declaring polio a "programmatic emergency for global public health", but progress in some countries has persuaded GPEI officials that eradication

is within reach. India has not recorded a case of polio in 16 months: an unmitigated victory given that the country's high population density and poor hygiene has in the past made it ripe for the spread of the virus. A wide roll-out of new vaccines that effectively target the strains in circulation seems to have won the battle, says Nicholas Grassly, an epidemiologist at Imperial College London. India's success also shows that "the barriers are not technical, they are about management, implementation, oversight and commitment to eradicating polio", he adds.

Last year, Pakistan seemed to pose a major obstacle to eradication, not least because flooding in 2010 displaced millions of people, many of whom missed scheduled vaccinations. The programme was also hampered by widespread suspicion after the revelation last July that the US Central Intelligence Agency may have used a vaccination campaign to obtain DNA from children living in Osama bin Laden's compound in Abbottabad (see *Nature* 475, 265; 2011). A doctor involved in that effort, Shakil Afridi, was last week sentenced to 33 years in prison.

The incident caused support for vaccination to plummet temporarily in Balochistan province and the Federally Administered Tribal Areas, where most of Pakistan's polio cases occurred last year, says Heidi Larson, an anthropologist at the London School of Hygiene and Tropical Medicine, who maintains a Vaccine Confidence Index for Pakistan and other developing countries.

## GETTING BETTER

But the country now seems to be making progress, recording just 16 cases of polio so far in 2012 — half as many as this time last year, with none in Balochistan. In Afghanistan, worsening security led to a threefold increase in polio cases between 2010 and 2011, but the country has recorded just six cases so far this year. Nigeria, which registered 62 cases due to wild poliovirus strains in 2011 (as well as 33 cases caused by the spread of a strain used in the live vaccine), has had 35 cases so far this year.

The WHO's Emergency Action Plan includes measures tailored to individual areas, such as winning the support of Islamic scholars in Pakistan, and improving tracking of migrant populations in northern Nigeria. "It's a very ambitious programme," says Zulfiqar Bhutta, an immunization expert at Aga Khan University in Karachi, Pakistan. But with a history of poor oversight and a lack of local accountability in the three remaining endemic countries, "the devil is in the detail of implementation".

However, India's success in staunching the spread of polio has shifted the discussion from whether polio will be fully eradicated, to when, says Aylward. The tentative deadline of the end of 2012 is likely to be the initiative's third missed goal, after deadlines in 2000 and 2005 passed the campaign by. "What's changed is that nobody is thinking, 'Maybe we call it off,'" says Aylward. ■ **SEE EDITORIAL P.547**

➔ **NATURE.COM**  
For more see  
*Nature's vaccines*  
special:  
[go.nature.com/a3nzqx](http://go.nature.com/a3nzqx)

## SCIENTOMETRICS

# Scientists: your number is up

ORCID scheme will give researchers unique identifiers to improve tracking of publications.

BY DECLAN BUTLER

In 2011, Y. Wang was the world's most prolific author of scientific publications, with 3,926 to their name — a rate of more than 10 per day. Never heard of them? That's because they are a mixture of many different Y. Wangs, each indistinguishable in the scholarly record.

The list of the world's top 100 authors, all of whom show similarly impressive production rates, is a who's who of conflated Zhangs, Lis, Chens, Lees and other Wangs. But this confusing problem could be solved following the launch later this year of the Open Researcher and Contributor ID (ORCID), an identifier system that will distinguish between authors who share the same name.

Just as barcodes at the supermarket allow the till to distinguish a tomato from a turnip, ORCID aims to reliably attribute research outputs to their true author by assigning every scientist on the planet a machine-readable, 16-digit unique digital identifier. If ORCID takes off, it could revolutionize research management, vastly increase the precision and breadth of scientific metrics and help in developing new analyses of, for example, social networks. "I'm excited," says biologist and bibliometrics researcher Carl Bergstrom of the University of Washington in Seattle, who notes that resolving ambiguities over author names is a major challenge. "Solving this problem broadly is a big deal in the science of science."

Instead of filling out personal details on countless electronic forms associated with submitting papers or applying for grants, a researcher could also simply type in his or her ORCID number. Various fields would be completed automatically by pulling in data from other authorized sources, such as databases of papers, citations, grants and contact details. ORCID does not intend to offer such services itself; the idea is that other organizations will use the open-access ORCID database to build their own services.

So far, some 280 organizations, including major research bodies, funding agencies and publishers, have become members of the ORCID committee, which was set up in 2010 as an independent non-profit organization in Wilmington, Delaware. (Nature Publishing Group is a member, and has a seat on ORCID's board of directors.) US federal research agencies, such as the National Institutes of Health and the National Science Foundation, are in



Don't worry, the tattoo is optional.

discussions to integrate ORCID with a planned identifier scheme called the Science Experts Network Curriculum Vitae (SciENCv), which will automatically create CV-like profiles of agency scientists. These would be used to populate and update staff directories and websites, and to generate science metrics. They could, for example, track the publications or patents that have resulted from grants, or check for duplicate funding.

Experts in data-mining and bibliometrics say that they are most excited by ORCID's potential to link together multiple systems for tracking research, creating a researcher-centric view of science that should enable analysis of scientists' networks and information associated with them. "In my line of work, proper author identification is a *conditio sine qua non*," says Johan Bollen of Indiana University in Bloomington. Bergstrom, too, says that he is particularly enthusiastic about the options it would open up for studying the research trajectories of individual scholars "at a big-data scale" — exploring how their research interests, collaboration patterns and publication trends change over time.

Herbert Van de Sompel at the Research Library of the Los Alamos National Laboratory in New Mexico, who is a long-standing proponent of author identifiers, hopes that the system might be used to generate alternative metrics by linking authors to their outputs in "less

traditional venues of scholarly communication, such as tweets, blog posts, presentations on Slideshare and videos on SciTV."

For ORCID's promise to be realized, however, it must become the accepted standard for all players in research, from funding agencies and universities to publishers and database operators. Expanding membership will require better community outreach, according to a report that ORCID commissioned from Deanna Marcum, managing director of Ithaka S&R, a non-profit research consultancy in New York. At an ORCID outreach meeting in Cambridge, Massachusetts, last week, Marcum presented survey data suggesting that many research institutions do not understand the practical applications of ORCID, and that many academics have never heard of it.

"We need to do a better job of communicating to universities and research agencies why ORCID is important to them," says Laure Haak, who was appointed executive director of ORCID in April. When the scheme opens for business in the coming months, it will at first rely on large publishers and research agencies to build a critical mass of registrants, because they can require researchers to provide or register for an ORCID number in order to publish a paper or submit a grant proposal.

Individual researchers will be able to get an ORCID number for free as of later this year, whereas universities, companies and other organizations will pay tiered-subscription charges. So far, the scheme has been sustained by members working in kind, as well as by donations of US\$574,000 and loans of \$1.2 million. Once membership fees begin flowing, they are expected to raise \$2.5 million each year.

Haak is convinced that when scientists and their patrons see the practical benefits of ORCID, it will become the de facto standard author identifier in research, much as the digital object identifier (DOI) has become for papers and data. ■

## CORRECTION

The News story 'Cancelled project spurs debate over geoengineering patents' (*Nature* **485**, 429; 2012) implied that the Oxford Principles were produced in 2011. In fact, they were drawn up in 2009 before the Asilomar climate conference. The Editorial 'A charter for geoengineering' (*Nature* **485**, 415; 2012) wrongly gave the date for the Asilomar meeting as 2009 instead of 2010.

F. SKOLD/GETTY

➔ **NATURE.COM**  
Read more at  
Nature's metrics  
special:  
[go.nature.com/nj2xqk](http://go.nature.com/nj2xqk)





STEPHEN HOGG WILDTACK PHOTOGRAPHY

# Sex and the single RHINOCEROS

*Conservationists are taking heroic measures to restore the fertility of a three-footed Sumatran rhino. But some ask whether this is the right way to save an endangered species.*

BY HENRY NICHOLLS

First, the vet inserts his arm in a shoulder-length plastic glove. Next, he grips an ultrasound probe and slides both arm and probe deep into the rectum of a 500-kilogram rhinoceros. All eyes of those present, including his, are on the ultrasound image on the laptop monitor nearby. As the vet moves the probe over the animal's intestinal wall, her uterus comes into view on the screen. Even to the untrained eye, it is clear that there is something seriously wrong: marble-sized cysts fill the space where there should be a smooth uterine lining. As if in acknowledgement of the fact, the rhino lets out a doleful moan.

This is Puntung, a Sumatran rhinoceros that is missing a foot as well as a working uterus. Yet the future of this species in Malaysian Borneo may rest on the hairy shoulders of this singular beast. If she is ever to reproduce, she will need Thomas Hildebrandt and his veterinary team from the Leibniz Institute for Zoo and Wildlife Research (IZW) in Berlin to rescue her womb — and then push the boundaries of rhino assisted-reproduction to new extremes.

According to the latest best guess, only 200–300 Sumatran rhinos (*Dicerorhinus sumatrensis*) may be left in the wild, split between three territories in southeast Asia: the Indonesian

**Puntung, a female Sumatran rhino, is part of captive breeding efforts in Malaysia.**



island of Sumatra, Peninsular Malaysia and the state of Sabah in Malaysian Borneo (see “The remaining rhinos”). This perilous situation is a result of a devastating combination of habitat loss (mainly to create lucrative oil-palm plantations) and poaching (to feed the black market for rhino horn). Conservationists say that the species’ small, fragmented population is now the biggest threat to its survival<sup>1</sup>, with animals so sparsely distributed that they are simply unable to meet each other to mate. Because females that haven’t mated when they are in oestrus can develop problems with their uterus, the rare encounters that do take place often come to naught. At best, rhino mothers take several years between pregnancies — meaning that the birth rate in the wild is unlikely to keep up with poaching and natural deaths.

### DRASTIC MEASURES

This desperate situation has led conservationists in Sabah to a desperate conclusion: that the only way to maintain the rhino population here is to capture as many as possible of the remaining animals — which may number as few as 30 — and subject them to assisted reproductive technology. That includes scrubbing out the uterus of Puntung, and possibly techniques such as *in vitro* fertilization (IVF) and cloning, the likes of which have rarely been wielded in the name of conservation. “Either we give up or we try to make every fertile rhino contribute to the future of this species,” says John Payne, executive director of the Borneo Rhino Alliance (BORA) in Kota Kinabalu, Sabah. “The best way to do that is to bring them into fenced, managed facilities.”

Such a drastic attempt to rescue a highly endangered species has precedents. Conservationists have, through heroic efforts, wrestled species such as the Arabian oryx (*Oryx leucoryx*), the black-footed ferret (*Mustela nigripes*) and the California condor (*Gymnogyps californianus*) back from the brink of extinction by bringing all the remaining animals together, using artificial insemination to spread sperm and maximize genetic diversity, and keeping offspring alive through round-the-clock husbandry.

In the case of the Sumatran rhino, however, some conservationists worry that without a long-term strategy for reversing the environmental pressures that are killing them off, captive breeding alone can never restore the wild population. “It’s not a plan unless you’ve mitigated the threats that wiped them out in the first place,” says Alan Rabinowitz, chief executive of the wild-cat conservation group Panthera in New York city. Others are uncomfortable with throwing so much money and effort at a single species — a single animal, in Puntung’s case — when the chances of success are so slim. “One of the biggest challenges facing conservation today is our inability to step back and admit that there are animals that would take a little bit less work and a little bit

less money but have the potential to survive for their genetic diversity into the future,” says John Fraser, chief executive of the New Knowledge Organization in New York city, a think tank and advocate of a triage response to species conservation. “They may not be as charismatic, but quite frankly we have to admit that some species are not going to make it and it’s really, really sad.”

Puntung got her name, which translates roughly as ‘Stumpy’, in 2007, when a ranger in the Tabin Wildlife Reserve in eastern Sabah came across her distinctive three-footed tracks. It is thought that she must have lost her foot to a poacher’s snare as a calf, and that her mother nursed her back to hobbling fitness. “If she had been even two years of age, the wound that she has would not have healed over,” says Zainal Zahari Zainuddin, BORA’s field manager, on-site vet and the person closest to Puntung.

In April 2010, the Sabah Wildlife Department and BORA began a joint operation to catch her. It was the first push in an effort to bring as many as possible of Sabah’s remaining rhinos into captivity. But it was only after 20 frustrating months that she finally walked into a trap. On Christmas Day 2011, a helicopter airlifted Puntung to her current home in a temporary captive facility within the reserve. Payne estimates that the entire operation, including the cost of hiring the helicopter and constructing her enclosure, set BORA back more than US\$250,000.

With Puntung apparently in her reproductive prime, and with a lone male called Tam in residence since 2008, there was hope that the pitter-patter of tiny rhino feet might soon follow. It was something of a setback, then, when ultrasound scans carried out by Hildebrandt

and his team in February showed that Puntung’s uterus was riddled with cysts that would make any full-term pregnancy near impossible. Her ruptured hymen suggests an explanation. “We think she must have mated in the wild, got pregnant, but with her handicap was unable to sustain the fetus and it died *in utero*,” says Hildebrandt, who specializes in the assisted reproduction of endangered mammals and has been involved with Sabah’s rhinos since 2004. The failed pregnancy led to the cysts. “Such pathology is not uncommon in rhinos,” Hildebrandt says, “but is rarely this bad.”

A decade ago, this might have been the moment to give up. But reproductive medicine has advanced at such a pace that there are still options for Puntung, particularly as she seems to be relatively young — with as many as 10 years of reproductive life ahead of her — and her ovulatory cycle seems to be normal.

At the end of March, Hildebrandt and two of his IZW colleagues flew back to Sabah on a uterine-rescue mission, accompanied by huge suitcases filled with veterinary paraphernalia: green scrubs, anaesthetics, antibiotics, drips, probes, a carbon-fibre catheter patented by Hildebrandt and his colleagues for the insemination of rhinos, and a gun case containing a 2-metre-long video endoscope tailor-made to fit Puntung’s reproductive tract.

Once in the Tabin reserve, the IZW vets, BORA staff, including Payne and Zahari, and the Sabah Wildlife Department’s chief field vet assemble in a hut beneath the glare of fluorescent strip lighting to be briefed on the impending procedure. If all goes to plan, explains Hildebrandt, he will insert the endoscope into Puntung’s uterus and attempt to lance some of the cysts, particularly ones that are preventing

## THE REMAINING RHINOS

Roughly 200–300 Sumatran rhinos are thought to be left in the wild, split between three territories in southeast Asia.



SOURCE: REF. 1

sperm from entering the oviducts. That might smooth the way for insemination — either artificially or by Tam — followed quickly by the collection of fertilized embryos before they implant. By repeating the procedure every month for the rest of her reproductive life, it might be possible to harvest as many as 100 embryos, freezing them in liquid nitrogen to be implanted into surrogate females in years to come.

With everyone's questions answered, Hildebrandt and his team wheel their equipment out into the rain. The croak of thousands of invisible amphibians falls suddenly silent as the vets pass by on the way to Puntung's enclosure.

#### RARE BREED

Past efforts to breed Sumatran rhinos in captivity have been spectacularly unsuccessful.

## “WE HAVE TO ADMIT THAT SOME SPECIES ARE NOT GOING TO MAKE IT AND IT’S REALLY, REALLY SAD.”

Between 1984 and 1993, at least 35 wild rhinos were taken into captivity across the region without the birth of a single calf. Zoologists knew little about the reproductive rhythms of rhinos, breeding facilities rarely housed a good mix of males and females, and disagreements over whether the Sabah rhino was a subspecies of the Sumatran rhino meant that there was little cooperation between Indonesia and Malaysia and even between Peninsular Malaysia and Malaysian Borneo. The fruitless attempts frustrated some conservationists, including Rabinowitz. In a frank essay<sup>2</sup> published in 1995, he accused the conservation community of “helping a species go extinct” by placing too much emphasis on captive breeding of the Sumatran rhino at the expense of “the more difficult job of protection and management in the field”.

The case for captive breeding may be stronger now. “In Peninsular Malaysia, the species is either extinct or about to go extinct,” Payne says. And in Sabah “the numbers are so low, that no method exists to find out how many are now left”. In the 1980s, when he was working in what is now the Tabin Wildlife Reserve, he recalls coming across rhino footprints within a matter of days in the field. “At best we can now find old rhino footprints perhaps once or twice per year,” he says.

Meanwhile, captive breeding has scored some successes. In 2001, Cincinnati Zoo announced<sup>3</sup> the first Sumatran rhino to be born in captivity since 1889. The same star breeding pair, on loan from Indonesia, went on to produce two more calves. “We had to learn how to feed this species, we had to learn about its reproductive physiology, and thank goodness we started as early as we did because now

it looks like [captive breeding] is a serious need for the species,” says Terri Roth, director of the zoo’s Center for Conservation and Research of Endangered Wildlife, which works closely with Indonesia’s Sumatran Rhino Sanctuary in Way Kambas National Park.

There are also signs of greater cooperation between captive facilities. At a March meeting of the Sumatran Rhinoceros Global Management and Propagation Board in Jakarta, all parties put their signature to a “Letter of Intent for Collaboration”. This puts aside past taxonomic differences, and acknowledges that all captive animals should be part of a single, globally managed breeding programme and that captive facilities will share sperm and embryos “based on availability and need”. Testifying to this new *entente cordiale*, the Sabah Wildlife Department has agreed to send semen col-

lected from Tam to Cincinnati Zoo to attempt artificial insemination of a young female when she reaches sexual maturity. But with just ten animals in captivity worldwide — three at Cincinnati Zoo, four at the Sumatran Rhino Sanctuary and three in the Tabin reserve — more animals will need to be caught in Sumatra to establish a viable captive population, says Roth. “We need to pull them in and manage them intensively and make sure as many of them breed as possible,” she says.

Rabinowitz acknowledges the greater urgency for captive breeding, but disputes whether the data on population size, sex ratio

and breeding success in the wild are good enough to say that wild populations are in terminal decline or that captive breeding — “an absolute last resort”, he says — is the only option. “When you lack information and just say there’s no hope, then you’re really writing the end of the book.”

#### OPERATION UTERUS

Before her ultrasound scan, the unsuspecting Puntung is lured into a small pen by a bucketful of diced bananas. Hildebrandt’s colleague Frank Göritz loads a syringe with a dose of sedative calculated to send her into a standing anaesthesia, then reaches through the bars to plunge the needle through her sparsely haired hide. Within seconds, she has relaxed into a sling, which supports her bulk and makes it easier to insert an endoscope into her uterus than if she were lying down.

When Robert Hermes, the third member of the team, slides his gloved arm into Puntung’s rectum she barely flinches. She has undergone a period of intensive coaching to tolerate medical procedures. Now, it is impossible to tell that she’s undergoing a transrectal ultrasound scan, were it not for the vet squatting at her rear.

Almost an hour later, however, the first signs of stress are showing — though not from Puntung. The ultrasound is over and Hildebrandt is struggling to insert the carbon-fibre catheter into her uterus. On his knees, with his right arm deep in her vagina and his cheek brushing up against her buttocks, his face is a picture of concentration and his scrubs are darkening with sweat. Puntung’s cervix, tightly constricted owing to the phase of her menstrual cycle, is proving a serious obstacle to the catheter.

Eventually, Hildebrandt triumphs and is able to flush out the uterus with a sterile cell medium, which will be tested for any underlying infection. With the cervix so narrow, there is no hope of moving on to the bigger-bored endoscope, but before Hildebrandt removes the catheter he injects a highly concentrated penicillin solution. This will destroy any pathogenic bacteria, and is so concentrated that it may actually strip away some of the lining and cysts, possibly making it easier to attempt fertilization and embryo collection. Hildebrandt has successfully used this approach to boost the fertility of two tigers and a leopard<sup>4</sup>. If it doesn’t work, the favoured next step is to carry out a similar procedure at a future date, but to inject a more caustic chemical such as kerosene to attack the cysts. This carries a risk. The team has to make sure that the treatment “is not so aggressive that it destroys the uterus”, Hildebrandt says.

Before the vets call it a wrap, there is still time to take a cast of Puntung’s stump, which will be used to fashion a prosthetic foot. This will allow her to move around with greater comfort. If she ever gets a chance to mate with Tam, the foot will also be handy for supporting his weight on her back during the half-hour encounter.



Thomas Hildebrandt (front) and his team carry out an ultrasound examination on Puntung.

H. NICHOLLS





At Cincinnati Zoo, Emi lies back with her calf, one of only three Sumatran rhinos born in captivity since 1889.

Even if embryo collection proves unsuccessful, it might not be the end of the road for Puntung. It should be possible to collect immature eggs, by inserting a fine needle through the wall of her rectum and into her ovaries. The challenge is getting them to mature and fertilize *in vitro*. The IZW vets have attempted this with white and black rhinos<sup>5</sup>. They obtained 29 eggs and managed to fertilize one, but the embryo did not progress beyond the four-cell stage. The only attempt to harvest eggs in Sumatran rhinos — from Cincinnati Zoo's star female just after her death in 2009 — was unsuccessful<sup>6</sup>.

There are other, more futuristic options. In theory, Puntung could be cloned, taking a nucleus from one of her cells and injecting it into an egg stripped of its own DNA. That rhino eggs are in short supply needn't be a problem, says Pasqualino Loi, a reproductive biologist at the University of Teramo in Italy, who, more than a decade ago, used domestic sheep as a source of eggs and surrogates to clone an endangered sheep relative, the mouflon<sup>7</sup>. "Play around," he suggests. "Inject some rhino mitochondria and a nucleus into a horse egg." It's just possible, says Loi, that it could result in a viable embryo that could be successfully

nurtured to term by a surrogate mare.

Pursuing another strategy, scientists at San Diego Zoo in California last year showed that banked tissue from the almost extinct northern white rhino (*Ceratotherium simum cottoni*) could be induced to form a line of pluripotent stem cells, capable of forming many tissues<sup>8</sup>. It's possible that these cells could be used to generate working gametes, using the same techniques that have produced sperm in mice<sup>9</sup>.

Hildebrandt advocates natural mating before attempting IVF or other reproductive technologies, but he is already starting to bank rhino tissue. With part of a €500,000 (US\$640,000) grant from the German Federal Ministry of Education and Research awarded in December 2010, he established a cryo-bank facility in Kota Kinabalu. In it are fibroblasts from Tam and Gelogob, a blind and elderly female rhino in captivity at the Tabin Wildlife Reserve. Cells from Puntung will join them shortly. "If we

➔ **NATURE.COM**  
Watch a video  
of Puntung's  
operation at:  
[go.nature.com/bezucu](http://go.nature.com/bezucu)

can't find the solutions, then people after us can," Hildebrandt says. "We have the responsibility to make it available to the next generation."

Yet the chance that such technologies will succeed in a species like the Sumatran rhino, whose basic biology is still poorly understood, seems remote. Roth says that tissue banking "is not a priority compared with some of the other issues we're up against". And the Indonesian government's action plan for rhino conservation, spanning 2007–17, contains no mention of tissue banking<sup>10</sup>.

Money, too, is in short supply. It is a stinging irony that by far the biggest donor to BORA is the Sime Darby Foundation, the philanthropic arm of the Sime Darby Group, based in Kuala Lumpur, one of the world's biggest producers of palm oil, the crop that led to the destruction of much of the rhino's rainforest home. It has committed a further \$2 million to fund BORA's operations up to 2015 and after that the charity is on its own. "This is a bit of a worry," admits Payne. Hildebrandt says that his grant from the German government has expired. He knows that he needs some demonstrable success with Puntung to get more. "If we are not successful in the next few months, then I think the programme is over," he says.

Other conservation biologists argue that it already is. Even if assisted reproductive technologies do prove possible, Fraser asks how long the new animals would survive. "My concern is that [the Sumatran rhino's] future viability as a species on this planet and the future viability of any offspring is really in question because the habitat just isn't there. So I question the priority setting, although I can certainly understand the emotional state of those invested in saving the animal."

Puntung, of course, is oblivious to the emotions and the debate. The operation over, Göritz injects her again to reverse the effect of the anaesthesia and within minutes she is out of the sling. Zahari enters the enclosure and unfurls a hose to spray her down. It's a ritual she clearly enjoys, raising her neck to meet the droplets of water as they rain down.

Puntung can savour a few weeks of rest and bananas, before science's next assault on her infertility. ■

**Henry Nicholls** is a freelance journalist based in London. His most recent book is *The Way of the Panda*.

1. Ahmad Zafir, A. W. *et al.* *Oryx* **45**, 225–233 (2011).
2. Rabinowitz, A. *Conserv. Biol.* **9**, 482–488 (1995).
3. Roth, T. L., Bateman, H. L., Kroll, J. L., Steinetz, B. G. & Reinhart, P. R. *Zoo Biol.* **23**, 219–238 (2004).
4. Hildebrandt, T. B. *et al.* *Theriogenology* **66**, 1783–1786 (2006).
5. Hermes, R. *et al.* *Theriogenology* **72**, 959–968 (2009).
6. Stoops, M. A., Bateman, H. L., Campbell, M. K. & Roth, T. L. *J. Zoo Wildl. Med.* **42**, 723–726 (2011).
7. Loi, P. *et al.* *Nature Biotechnol.* **19**, 962–964 (2001).
8. Ben-Nun, I. F. *et al.* *Nature Methods* **8**, 829–831 (2011).
9. Hayashi, K., Ohta, H., Kurimoto, K., Aramaki, S. & Saitou, M. *Cell* **146**, 519–532 (2011).
10. Ministry of Forestry of the Republic of Indonesia *Strategy and Action Plan for the Conservation of Rhinos in Indonesia* (Jakarta, 2007); available at [go.nature.com/ssdt2t](http://go.nature.com/ssdt2t).

# THE CONSTANT GARDENERS

ONCE THOUGHT TO BE PASSIVE SENTINELS, MICROGLIA NOW SEEM TO BE CRUCIAL FOR PRUNING BACK NEURONS DURING DEVELOPMENT.

BY VIRGINIA HUGHES

T

he work required the mind of an engineer and the hands of a surgeon. Axel Nimmerjahn had both.

It was 2002 when Nimmerjahn, then a graduate student at the Max Planck Institute for Medical Research in Heidelberg, Germany, began trying to spy on the everyday activity of the mysterious brain cells known as microglia.

Others had caught glimpses of the cells in their spider-like resting state, but only in slices of dead tissue. No one had been able to see them in a live brain. That's because microglia — which, unlike other cells in the brain, are part of the immune system — are extremely sensitive. Cut a nerve, or release infectious bacteria into brain tissue, and microglia spring into action, retracting their many appendages and morphing into big, round blobs that gobble up pathogens and clear away cellular wreckage.

R. CASSIANI/INGONI/SPL

**Microglia (yellow), the brain's immune cells, take on a blob-like shape when active.**



To see the cells without disturbing them, Nimmerjahn used a newly published approach for imaging a live mouse brain<sup>1</sup>. After anaesthetizing the animal and peeling back its scalp, he removed the top two-thirds of the skull's thickness and shaved the bone down to just 20 micrometres — thin enough for light to penetrate, but thick enough to avoid setting off the microglia. The work progressed slowly — Nimmerjahn had to douse the surgical site with cooling fluid after realizing that even the heat from scraping could aggravate the cells. But within a few months at the bench, he was able to record some time-lapse movies<sup>2</sup>.

He was floored by what he saw: 'resting' microglia are anything but. Their delicate branches snake through densely packed brain tissue, constantly extending and shrinking and re-growing. "They're very dynamic, much more than any other cell in the adult brain," says Nimmerjahn, now a biophysicist at the Salk Institute in La Jolla, California. He calculated that the cells' concerted movements could survey the entire brain every couple of hours. But it was unclear why the microglia were moving so much, Nimmerjahn says. "Why does the brain invest so much energy?"

### CODED SIGNALS

Nimmerjahn is not the only researcher intrigued by this question. A flurry of studies during the past two years — the latest published last week in *Neuron*<sup>3</sup> — have investigated microglia's influence in adult and developing brains. The results are overturning the idea that microglia are passive immune sentinels. Several groups have proposed that these shape-shifting cells not only eat up invaders and damaged tissue, but also trim away weak connections, or synapses, between neurons. This pruning process occurs on a large scale in the developing brain, and it is known to be important in learning and memory. Neurodevelopmental disorders such as autism and schizophrenia are often associated with faulty pruning. Two provocative studies have suggested that mouse models of obsessive-compulsive disorder<sup>4</sup> and Rett syndrome<sup>5</sup>, an autism spectrum disorder, show marked improvements after their microglia are replaced.

But many questions remain. No one knows how microglia 'talk' to neurons or other cells, or whether their functions are limited to certain brain regions, notes Richard Ransohoff, a neurologist at the Cleveland Clinic in Ohio and a co-author of the latest *Neuron* report. But, he adds, that makes the field ripe for discovery. "The possible ramifications of these observations, for both developmental diseases like autism and degenerative diseases like Alzheimer's, are virtually endless."

For more than a century, neurons have been the stars of neuroscience. But they account for only about 10% of the cells in the human brain. The balance is made up by different types of glia, which surround and support neurons and influence neuronal signalling. Oligodendrocytes, for example, create fatty sheaths that encase long neuronal branches and help to speed up electrical impulses. Astrocytes surround synapses and have been shown to affect neuronal signalling by controlling the mix of chemical messengers at neuronal junctions.

Microglia are quite different from their neighbours. Unlike neurons and other glial cells, they begin in the embryonic yolk sac as immune-cell progenitors, just as the macrophages that patrol the bloodstream for foreign invaders do. During prenatal development — within eight embryonic days in a mouse — microglia migrate to the brain, where they become its dedicated immune cells. Researchers assume that the brain needs microglia because the blood-brain barrier seals it off not only from toxins, pathogens and some drugs in the bloodstream, but also from the immune cells circulating there.

Microglia spring into action in most brain diseases, engulfing pathogens, dead cells and misfolded proteins. They also clear away synapses that have been damaged by injury. It is not a big intellectual

leap, then, to suppose that microglia have similar roles in the healthy brain, says Helmut Kettenmann, a neurobiologist at the Max Delbrück Center for Molecular Medicine in Berlin, Germany, who has studied glia for the past 30 years. Given the spate of new imaging studies, he says, "I think microglia cells are probably extremely important for synapse remodelling and plasticity in development."

The idea is gaining traction. At the annual meeting of the Society for Neuroscience last November, when some 30,000 neuroscientists convened in Washington DC, the organizers held a session on microglia for the first time. It was packed. The society later circulated a list of the ten most-searched terms on the meeting's website. 'Microglia' was number six, just behind dopamine, optogenetics and schizophrenia.

The momentum has been building since April 2005, when Nimmerjahn published his movies<sup>2</sup>. A month later, a team led by Wen-Biao Gan — a

neuroscientist at New York University, who first developed the skull-thinning method — published similar results<sup>6</sup>. "This was a major breakthrough and inspired a lot of people," says Marie-Ève Tremblay, a postdoctoral researcher at the University of Wisconsin–Madison who studies the role of microglia in sleep and wakefulness.

In 2010, Tremblay and her colleagues published a report on the activity of microglia in the visual cortex of young mice. In rodents and in people, this region is known for its plasticity: the animal begins life with a large number of synapses, and then the ones that are not activated by light input from the eyes are gradually pruned away. Tremblay's study showed that microglia seem to interact with small synapses that disappear within a couple of days. Moreover, when she housed the animals temporarily in darkness — effectively dampening neural activity in the visual cortex — microglia changed into their active, blobby form and seemed to hug synapses more snugly<sup>7</sup>.

Around the same time, other scientists were watching microglia in another highly plastic region of the developing mouse brain — the hippocampus, which is important for learning and memory. They examined young mice lacking the fractalkine receptor protein, which is expressed only by microglia and which binds fractalkine, a protein present on neurons. The mutant mice have an abundance of weak and immature synapses in the hippocampus, according to a study<sup>8</sup> published last September. By the time the mutant mice are adults, the number of synapses normalizes, but the researchers have unpublished data showing that some other synaptic problems remain.

"My guess is that there's probably a very close signalling going on between neurons and microglia, back and forth, that coordinates which synapses they prune," says Cornelius Gross, a neuroscientist at the European Molecular Biology Laboratory in Monterotondo, Italy, who led the study. The trouble is that none of these studies indicate what that signal is. "What you'd like to find is some sort of an 'eat-me' marker, like in *Alice in Wonderland*, displayed on synapses that are to be pruned," Gross says. The latest report in *Neuron* claims to have identified such a tag<sup>3</sup>.

"My guess is that there's probably a very close signalling going on between neurons and microglia, back and forth, that coordinates which synapses they prune," says Cornelius Gross, a neuroscientist at the European Molecular Biology Laboratory in Monterotondo, Italy, who led the study. The trouble is that none of these studies indicate what that signal is. "What you'd like to find is some sort of an 'eat-me' marker, like in *Alice in Wonderland*, displayed on synapses that are to be pruned," Gross says. The latest report in *Neuron* claims to have identified such a tag<sup>3</sup>.

### FULL COMPLEMENT

The study's roots date back to 2007, when Ben Barres, a neurobiologist at Stanford University in California, together with postdoc Beth Stevens and their colleagues, showed that pruning in a deep area of the visual system — part of the thalamus called the lateral geniculate nucleus, or LGN — depends on certain proteins in the complement cascade, part of the innate immune system that helps to clear out pathogens and unwanted cells. The researchers reported that complement proteins are expressed by immature neuronal cells and are more likely to show up around immature synapses than elsewhere during key periods of brain development. Mice that lack complement proteins show a mess of unrefined neural connections<sup>9</sup>.

**"THE POSSIBLE  
RAMIFICATIONS  
OF THESE  
OBSERVATIONS  
FOR AUTISM AND  
ALZHEIMER'S  
ARE VIRTUALLY  
ENDLESS."**

According to Barres, all of this suggested that the complement system was responsible for tagging weak synapses for pruning. But how could this tagging lead to synapse removal? “Our obvious hypothesis was that it might work exactly the same way as it works in the immune system,” Barres says. In the bloodstream, complement proteins tag harmful bacteria, signalling for macrophage cells to come along and eat them. Microglia are both the brain’s resident macrophages and the only brain cells that express the complement receptor. Nimmerjahn, who happened to be starting a postdoc with Barres at the time, had already shown that microglia were interacting with synapses in the mature brain. But nobody knew anything about what microglia were doing in the young brain.

Stevens focused on that question beginning in late 2008, when she launched her own lab at Boston Children’s Hospital in Massachusetts. The *Neuron* paper is her team’s first publication. Dori Schafer, a postdoc in Stevens’s lab, designed an assay for imaging the LGN using a previously developed mutant mouse whose microglia glow bright green under ultraviolet light.

Schafer further altered the mice so that the synapses connected to one eye would appear red, and those linked to the other eye, blue. She then used chemicals to increase the firing of neurons in one eye and decrease it in the other eye. Because neuronal activity is known to make synapses stronger, this manipulation is thought to weaken the synapses for one eye and strengthen those for the other.

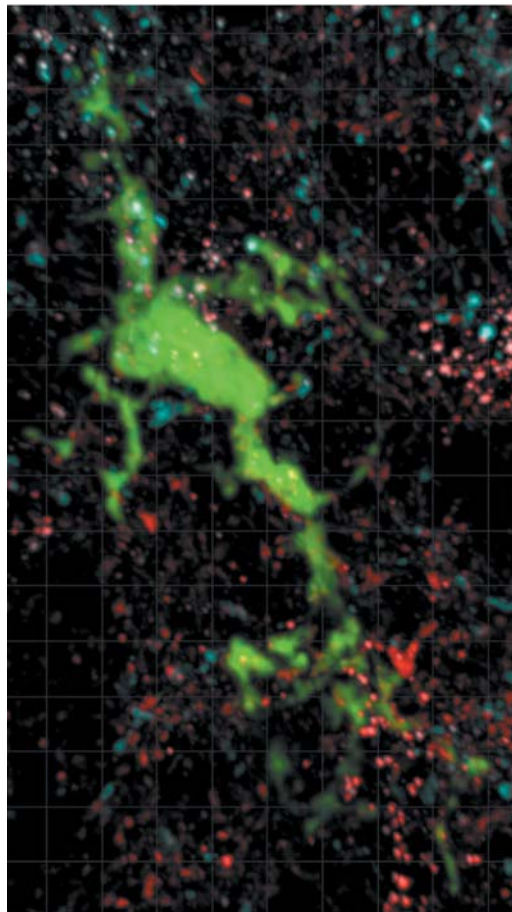
### RIGHT TIME, RIGHT PLACE

The researchers’ colourful pictures, showing fragments of red and blue synapses in the bellies of the microglia, suggested that the cells selectively engulf the weakest synapses (see picture). “This was really exciting because it showed for the first time that, OK, the microglia are actually sensing, in some way, activity changes in the neuron,” Schafer says.

The researchers then repeated the experiments using mice that lacked the complement receptor. Their theory predicted that getting rid of the receptor would thwart microglia’s ability to eat up complement-tagged synapses. Sure enough, these mutant animals had microglia with significantly less-full bellies.

Despite such findings, neuroscientists are still debating whether microglia have an active role in synaptic pruning. The pretty pictures put the cells at the right time and place, but no one has caught them in the act. “We can’t see microglia picking off a synapse in real time,” Schafer says. The cells could be initiating the operation, or they may simply swoop in to clear up the carnage after the synapse has been destroyed.

It is also unclear whether neuronal activity influences the complement-tagging process, notes Carla Shatz, a neurobiologist at Stanford. Her work has shown that other immune-system players — the molecules of the major histocompatibility complex — are necessary for synaptic pruning, influenced by neuronal activity and likely to show up near complement proteins<sup>10</sup>. “I think there’s a way to connect all of these observations, and to really test the idea that they’re all part of a signalling system for synapse elimination,” Shatz says. But current microscopy



**Full belly:** a microglial cell (green) has engulfed bits of synapses (red and blue) in a mouse brain.

tools are a limiting factor. “We just don’t have the resolution to see which cells are making the molecules versus which ones are receiving the signals.”

Meanwhile, microglia studies continue to yield unexpected results. A 2010 study of mouse models of trichotillomania — a psychiatric disorder characterized by compulsive hair-pulling — showed that

disruption of the *Hoxb8* gene, which in the brain is expressed only by certain types of microglia, caused mice to groom the fur right off their bodies<sup>4</sup>. The behaviour stopped after the mice received whole-body irradiation followed by a bone-marrow transplant. The researchers speculate that radiation wipes out defective microglia (and the blood–brain barrier) and allows them to be replaced with new ones from the transplanted bone marrow.

Similarly, a study published in March showed that a bone-marrow transplant greatly increased the lifespan of mouse models of Rett syndrome<sup>5</sup>.

### SINGULAR POWER

These studies have raised the alluring idea that microglial manipulations could be used to treat neurodevelopmental disorders. “This is the only population in the brain that could be very easily replaced,” says Jonathan Kipnis, a neuroscientist at the University of Virginia in Charlottesville and lead investigator of the Rett study. “If we learn how to harness microglia for the benefit of the brain, I think clinically that would be a powerful tool.”

The transplant papers have many critics. It is not known, for one thing, how many microglia repopulate the brain after the procedure. And wiping out an animal’s immune system is bound to cause a host of changes. But Stevens, Gross, Tremblay and others are all forging ahead, beginning to investigate the role of microglia in

various mouse models of autism.

Researchers are also eager to get their hands on a much-anticipated tool: mutant mice that have genes knocked out of microglia but not other cells. Such ‘conditional-knockout’ mice can be used to investigate a gene’s function specifically in microglia, as opposed to in astrocytes or other cells.

Gan says that he and his team have already created conditional-knockout mice for two genes — *MECP2*, which is mutated in human cases of Rett syndrome, and *GRN*, which has mutations associated with a heritable form of frontotemporal dementia. The results are not yet published.

“Right now, the excitement is good about microglia,” Gan says. “We still need to do the hard work to figure out what exactly they do.” ■

**Virginia Hughes** is a freelance science writer in New York City.

1. Grutzendler, J., Kasthuri, N. & Gan, W. B. *Nature* **420**, 812–816 (2002).
2. Nimmerjahn, A., Kirchhoff, F. & Helmchen, F. *Science* **308**, 1314–1318 (2005).
3. Schafer, D. P. et al. *Neuron* **74**, 691–705 (2012).
4. Chen, S.-K. et al. *Cell* **141**, 775–785 (2010).
5. Derecki, N. C. et al. *Nature* **484**, 105–109 (2012).
6. Davalos, D. et al. *Nature Neurosci.* **8**, 752–758 (2005).
7. Tremblay, M.-É., Lowery, R. L. & Majewska, A. K. *PLoS Biol.* **8**, e1000527 (2010).
8. Paolicelli, R. C. et al. *Science* **333**, 1456–1458 (2011).
9. Stevens, B. et al. *Cell* **131**, 1164–1178 (2007).
10. Datwani, A. et al. *Neuron* **64**, 463–470 (2009).

**NATURE.COM**  
For videos of  
microglia in  
action, see:  
[go.nature.com/bpdd1t](http://go.nature.com/bpdd1t)



# COMMENT

**PUBLIC HEALTH** The alarming rise of HIV/AIDS in homosexual men in China **p.576**

**ENVIRONMENT** Rachel Carson's *Silent Spring* still resonates, 50 years on **p.578**



**TECHNOLOGY** Improving the way digital devices talk to one another **p.580**

**EXHIBITION** A look at the collections of Italian geologist and spy Luigi Marsili **p.581**

J. MARSHALL/FORT WORTH STAR-TELEGRAM/MCT/GETTY



The US government's helium reserve near Amarillo, Texas, meets around one-third of world demand for the gas.

## Stop squandering helium

Establish a global agency to build a sustainable market for this precious commodity, say **William J. Nuttall, Richard H. Clarke and Bartek A. Glowacki.**

In recent months, researchers have struggled to obtain supplies of liquid helium for running and cooling their equipment. A UK newspaper reported in March how the shortage had led one scientist to waste £90,000 (US\$142,000) because he could not run experiments on his neutron beamline for three days<sup>1</sup>. The scientist criticized buyers of party balloons for frittering away the gas. But the blame does not lie there.

Helium is an extraordinary commodity. Its use in advanced technologies — from cryogenics and arc welding to space rockets and silicon-wafer manufacture — means that worldwide demand for this inert gas is growing rapidly. But we are not conserving this resource well. Natural gas remains the

richest and most accessible source of helium; extracting it in industrial quantities from the air would be extremely costly. But too often, natural-gas plants treat helium as a valueless gas and vent it to the atmosphere. One large-scale plant producing liquefied natural gas can waste more helium than all the party balloons in the world.

The helium that is extracted is in the hands of a few players. This, combined with the fact that there is little spare capacity, leads to intermittent supply shortages. The US government's decisions to stockpile helium in the 1960s and sell it off in the 1990s have constrained prices artificially. Economic incentives for the natural-gas industry to invest in the separation of helium have

been insufficient, and although advances in fossil-fuel production methods should be making helium separation easier, this opportunity is not being seized.

As demand for helium grows in Asia and new separation plants come online in other countries, the US domination of the helium market will wane. An international body is now needed to oversee global plans for helium. We must extract and geologically stockpile the helium from gas reserves now, and postpone the use of air-extraction methods for as long as possible.

Helium was first liquefied by Dutch physicist Heike Kamerlingh Onnes in 1908, aiding his 1911 discovery of superconductivity in mercury cooled by helium to very ▶

► low temperatures. (Superconducting magnets remain a major component of today's demand.) In 1906, US chemists Hamilton Cady and David McFarland had discovered that helium was associated geologically with natural gas<sup>2</sup>, and along with chemical engineer Clifford Seibel, they handed expertise and leadership in helium production to the United States (see 'Supply and demand').

### A NOBLE STRATEGY

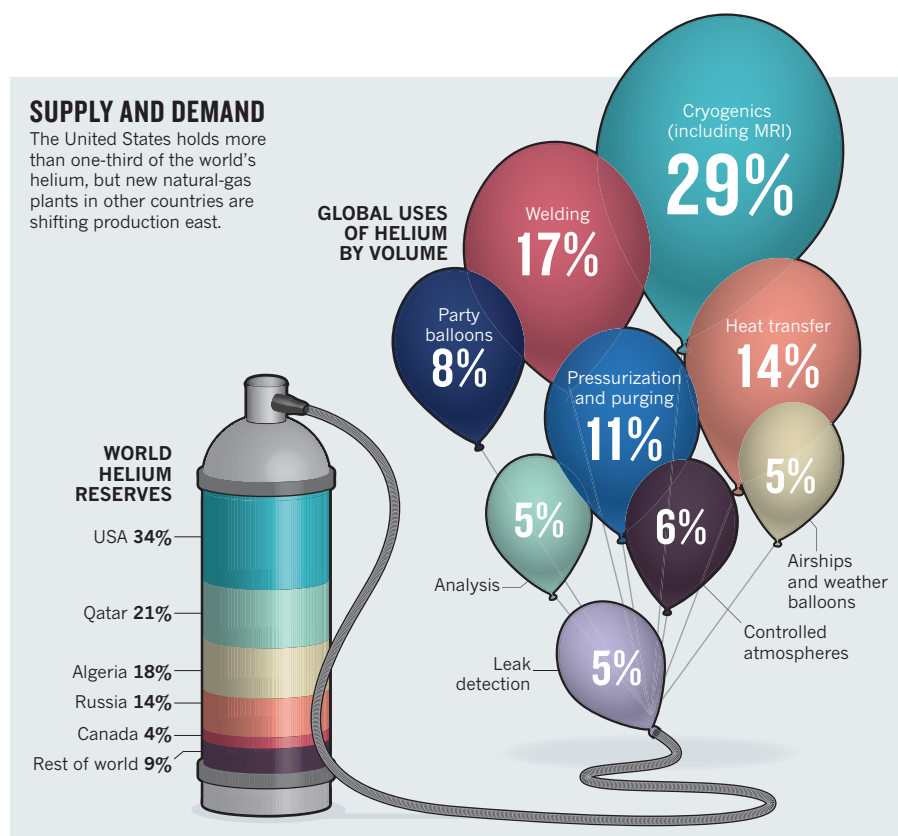
Realizing helium's potential as a lifting gas, the US government was the first to extract and store it for strategic purposes — such as airships, rocket-fuel propellant and electronics manufacture. A vast helium store was instigated at the Bush Dome reservoir in the Cliffside gas field near Amarillo, Texas. After passing the US Helium Act Amendments of 1960, the government purchased large amounts of the gas from private companies and stored it. By the early 1970s, the helium stockpile amounted to more than 20,000 tonnes (see 'Helium sales on the rise'). This remained one of the few sources of commercial helium until 1977, when plants opened in Odolanow, Poland, and Orenburg, Russia.

By the 1990s, however, both the stockpile and the associated federal debt were seen as excessive. In the Helium Privatization Act of 1996, the US Congress resolved to retain a small, strategic reserve of around 2,800 tonnes; since 1998, more than half of the remainder has been sold off by the US Bureau of Land Management. Today, roughly one-third of global helium demand is met by the Amarillo reserve.

Market modelling suggests that, by 2030, demand for helium in technological uses may double<sup>3</sup>. Yet there is sufficient helium in the ground to meet our long-term needs. Global geological reserves are estimated at approximately 8 million tonnes. Released by

### SUPPLY AND DEMAND

The United States holds more than one-third of the world's helium, but new natural-gas plants in other countries are shifting production east.



radioactive minerals at a rate of thousands of tonnes each year, helium is trapped by rock in natural-gas fields at levels ranging from a few parts per million to as much as 7% by volume. Annual production runs at approximately 30,000 tonnes; in 2011, 77% of all helium came from the United States (down from 84% in 2004)<sup>4</sup>.

Yet the natural-gas industry pays scant attention to helium. The global wholesale helium market turns over roughly \$1 billion annually, a tiny sum in comparison with the \$1 trillion generated by natural gas every year. All too frequently, helium remains blended throughout the gas supply chain until it is vented when natural gas

is burnt. Unlike fossil fuels, where unused supplies remain in the ground for later use, any helium that is not separated is lost.

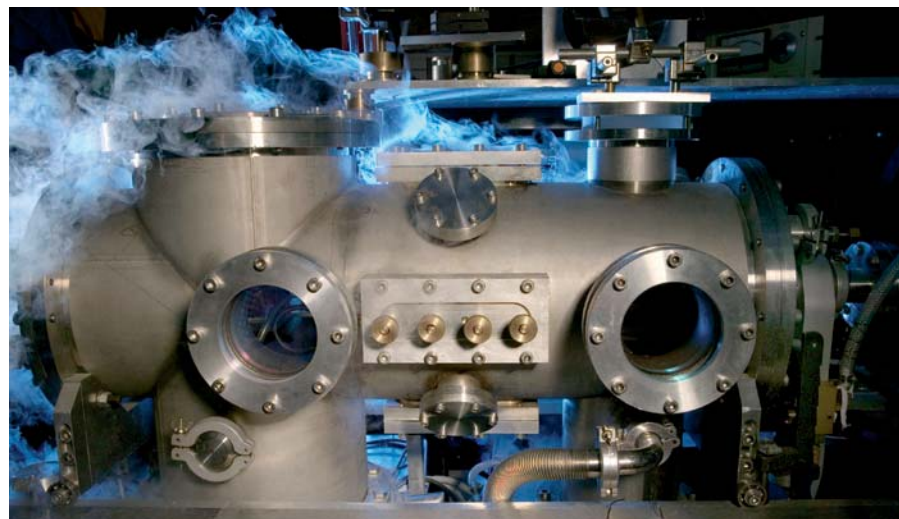
### RIISING PRICES

Helium prices are a function of supply and demand. In addition to the US government, the market is dominated by six companies: Paris-based Air Liquide, Air Products in Pennsylvania, Linde Group and Messer (both in Germany), Matheson in New Jersey and Connecticut-based Praxair. Although this number is sufficient for global competition, some firms effectively have a monopoly in certain regions. US government intervention creates uncertainty for all these companies, who also have to respond to rapid changes and trends in natural-gas extraction.

There is also a wide variety of helium consumers with their own perceptions of need and of how much they are willing to pay. For some, such as operators of magnetic resonance imaging (MRI) equipment for medical diagnosis, helium is an essential business requirement. For others, it is merely a discretionary spend.

These factors combine to create market anxiety. A sense of crisis can descend quickly when upstream supply problems occur — as happened in 2004 after an accidental explosion at a helium-producing facility in Skikda, Algeria, which killed 27 people. Algeria has only recently finished rebuilding the Skikda facilities, and is just about to return to the helium business.

All these reasons have led to an increase in average helium prices. They would



Helium is used in cryogenic systems, such as in the study of large-scale quantum effects.



be even higher in a normal competitive market, but under US law, the Bureau of Land Management increased helium prices by only as much as the (inappropriately low) consumer price index. Suppressed prices deter upstream investment.

As each crisis hits, helium users face a trilemma — to pay high prices, to shut down facilities temporarily or to find a substitute for helium. But managing demand will not fix the real tragedy of helium venting. In the longer term, helium production and storage need to be expanded and embedded within the natural-gas industry.

## ENERGY TRENDS

Transformations that are under way in the natural-gas industry offer opportunities and challenges for the helium market. The increasing use of natural gas for electricity generation means that energy companies are investing billions of dollars in new facilities. This growth could be a boon for helium production, if separation technology were routinely fitted to new plants. Cryogenic processing of liquefied natural gas (at around 112 K) greatly improves the extraction of helium, even when source concentrations of helium are as low as 0.015%, but it is not always done. Because most other by-products condense at these cold temperatures, helium can comprise up to half the waste gas purged from a natural-gas plant<sup>5</sup>.

Other trends in the industry hold less promise for helium production. Most shale gas — produced by hydraulic fracturing (or fracking) of impermeable rocks to extract trapped natural gas — contains almost no helium because its molecules are small enough to diffuse through shale rocks. Greater US production of shale gas means that the country can produce enough gas to exceed its national demand, which has shifted thoughts towards exporting liquefied

natural gas rather than importing it<sup>6</sup>. If such export plants are built, extra helium can be recovered from helium-rich source gas.

Energy decisions that are being made now by the United States will affect the global helium market. The future of the federal helium reserve is currently being considered by Congress: the Helium Stewardship Act proposes the retention of the Amarillo reserve beyond 2015 (when the 1996 act expires) by decreasing sales and improving management of the reserve.

An influential 2010 report<sup>7</sup> by the US National Academy of Sciences concluded that the helium sell-off was not in the national interest: if it continued, the United States would have to import helium from the Middle East and Russia in 10–15 years. The committee recommended that researchers should be given priority access to helium reserves, as well as funds for technology upgrades to reduce their helium usage. But these are short-term measures that centre on the United States.

Helium is a global and long-term issue. Both its demand and its supply bases are shifting east. Although US helium use has long been static, use is growing significantly in countries such as China and South Korea, and production facilities are coming online in the Middle East. In 2013, the world's largest helium-refining unit will open in Qatar, capable of producing more than 20% of global helium<sup>8</sup>. The long-term role of the United States in the helium business is far from certain, but decline seems likely. US policy towards both helium and natural gas will be important in determining the pace of shifts in global markets.

## GLOBAL REACH

The time has come for the world to establish an international oversight body for helium that will set up new strategic reserves and

expand helium production by recovering the noble gas at all major sources.

An international helium agency, operating along similar lines to the International Energy Agency, could draw on multiple strategic stocks around the world to attenuate market shocks and their accompanying price rises. Should unforeseen crises arise, the agency could develop best practices for preserving supply, such as prioritizing customers or rationing. A global agency is urgently needed to address the long-term issues facing the supply and demand of this precious element. In particular, many helium-bearing gas fields have a low energy content, so incentives to develop these fields may be needed.

Helium extraction should become the norm for existing liquefied natural-gas plants and for all new ones, particularly where the source gas is rich in the element. We propose a competitive market for helium in a global economy, with supply largely in private hands. The role of the private sector enhances helium security through free trade and market efficiency in allocating resources. The US model that existed before privatization in 1996 — a combination of private companies and an administered strategic reserve — offers a useful template.

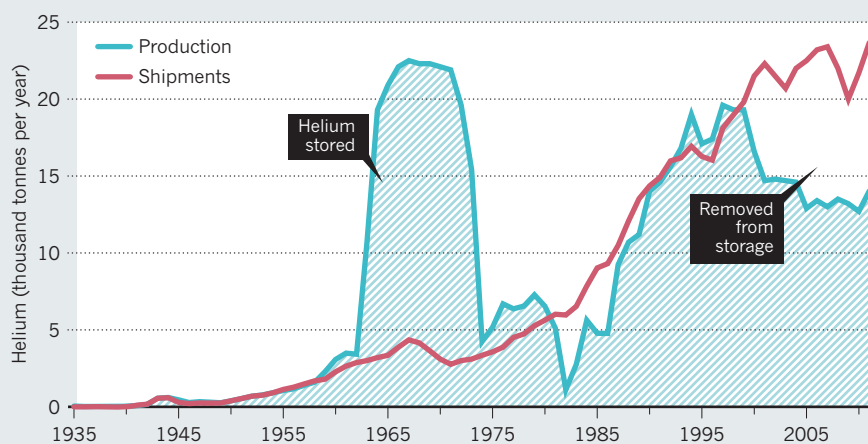
The near-term future of helium will be one of expanded demand coupled with ongoing uncertainty in supply. Whether this growth in demand will be sufficient to motivate investments in upstream supply is far from clear. For this reason, we recommend that global attention is devoted to these issues before we squander this exceptional element through neglect. ■

**William J. Nuttall** is a senior lecturer in technology policy at Judge Business School, University of Cambridge, Cambridge CB2 1AG, UK. **Richard H. Clarke** is a cryogenics and helium specialist at the Culham Centre for Fusion Energy, Abingdon, Oxfordshire OX14 3DB, UK. **Bartek A. Glowacki** is a reader in the Department of Materials Science and Metallurgy, University of Cambridge, Cambridge CB2 3QZ, UK. They are the editors of *The Future of Helium as a Natural Resource* (Routledge, 2012). e-mail: [wjn21@cam.ac.uk](mailto:wjn21@cam.ac.uk)

1. McKie, R. *The Observer* (18 March 2012).
2. Sears, B. in *The Future of Helium as a Natural Resource* (eds Nuttall, W. J. Clarke, R. & Glowacki, B. A.) 15–47 (Routledge, 2012).
3. Cai, Z., Clarke, R., Glowacki, B. A., Nuttall, W. J. & Ward, N. *Resour. Policy* **35**, 77–89 (2010).
4. Peterson, J. B. in *The Future of Helium as a Natural Resource* (eds Nuttall, W. J. Clarke, R. & Glowacki, B. A.) 48–54 (Routledge, 2012).
5. Andrieu, F. et al. *The Ras Laffan Helium Purification Unit* (Air Liquide, 2006); available at <http://go.nature.com/e9fsy1>
6. Rascoe, A. *Reuters* (16 February 2012).
7. National Research Council *Selling the Nation's Helium Reserve* (National Academies Press, 2010).
8. 'Noble gas' *RasGas Magazine* **30**, 10–11 (2010).

## HELIUM SALES ON THE RISE

Annual production and sales of helium from the US federal reserve in Amarillo, Texas. After building up the reserve in the 1960s, legislation in 1996 required the nation to sell off its helium stockpile.



SOURCE: US BUREAU OF LAND MANAGEMENT/S. J. MAIONE



HIV testing is free in China, but many people fear having their HIV status exposed.

# Bring safe sex to China

China's discomfort over discussing sex, and especially homosexuality, is a major problem when it comes to HIV, says a **consortium of researchers** in China.

An estimated 18 million men engage in homosexual sex in China, and they face growing risks to their health. Transmission between homosexuals has continued to gain ground among all reported HIV cases since surveillance of HIV among this group began a decade ago, rising from 0.3% before 2005 to more than 13.7% by 2011 (see 'On the rise').

The alarming spread of HIV among gay men is not seen in other high-risk groups, such as intravenous drug users and former commercial blood donors, and is fuelled by a stigma against homosexuality in China. In many ways, attitudes towards sexuality today in China resemble those of Western countries a quarter of a century ago. For instance, homosexuality was declassified as a mental illness in the United States in the early-1970s; this was not done in China until 2001. The main pressure for homosexuals to conceal their identity comes from friends and family, who place large emphasis on traditional obligations to uphold the family reputation and lineage. Many gay men say that they fear 'losing face', or having their social integrity damaged, if their orientation were to be revealed. Indeed, surveys of Chinese men who have sex with men have reported that up to 31.2% are married<sup>1</sup>.

Chinese people aren't uncomfortable

just in discussing homosexuality — sex in general is still considered extremely personal and is rarely addressed openly or directly, irrespective of orientation. This discomfort has resulted in a pervasive stigma against people with HIV, a lack of general sex education for young people and poor epidemiological data about the spread of HIV in some populations around the country.

The result is a hidden population of individuals who are afraid to seek out HIV information resources or testing and counselling centres. Poorly educated, unaware of their HIV status and under pressure to conceal their sexual encounters, these men often engage in high-risk behaviour. And once one man hiding his activity becomes infected, the disease will spread among his partners, in an ongoing cycle. It is therefore no surprise that incidence of HIV has skyrocketed in this population.

This trend cannot continue. Policy-makers, public-health researchers, clinicians, educators, community leaders and other stakeholders in China must come together to educate everyone, and gay men in particular, about HIV prevention and treatment — before any more people become infected as a result of ignorance and fear.

The first outbreak of HIV was identified in China in the mid-1980s in intravenous

drug users in southwestern provinces<sup>2</sup>. Over the past 20 years, it has not gained as strong a hold in China as in other countries: just 0.06% of the Chinese population is reportedly infected, less than one-fifth the prevalence in the United States and Europe (and one-hundredth that of sub-Saharan Africa)<sup>3</sup>.

In 2003, under international criticism and a growing awareness of the potential impact of a generalized epidemic, the Chinese government developed a systemized HIV prevention and treatment programme. The resultant 'Four Frees and One Care' act provides free access to antiretroviral drugs to people with AIDS living in rural areas, poor people living in urban areas and pregnant women; free counselling and testing for all; free schooling for orphans of parents with AIDS; and care and economic help for the families of people living with HIV/AIDS. But many people say that they are not aware of the provisions, or of how to find free testing centres<sup>4</sup>.

Although the government supports condoms as the primary means of preventing disease transmission, public advertisement campaigns promoting their use have been limited until the past few years. This is due, in part, to the absence of general sex education programmes in the vast majority of Chinese schools — a gap that is often left open by parents who aren't comfortable discussing sex with their children. This fundamental lack of knowledge has huge implications for combating HIV, not least because it carries over to health-care professionals. Even if people work up the courage to ask about HIV testing and information, health-care workers may not have adequate training, or be comfortable discussing the sexual conduct associated with HIV and other sexually transmitted diseases. This, coupled with stigma that leads men to hide their homosexual activity, means that men delay HIV testing and treatment — and, as a result, put all their partners at risk.

## CAUSE FOR CONCERN

Although both international and national groups have identified a rise in new infections in homosexual men in China, precise monitoring of the disease remains one of the greatest hurdles facing HIV researchers. It was not until 2010 that the first large-scale government surveillance results were released. This study of 26,000 Chinese men who engage in homosexual activity in 61 cities, conducted from 2008 to 2009, showed that average HIV prevalence was as high as 5%, and more than 10% in cities where the epidemic was first identified<sup>5</sup>. Unfortunately, national survey data tend to be published in broad terms, with limited source identification, making it difficult to evaluate research methodologies.

If these figures are correct, then homosexual men represent just 13% of HIV cases — a much smaller percentage than in the United States, where the number is



around 50%. Although gay men are still the minority of HIV cases in China, behind drug users, blood donors and people infected through heterosexual sex, the growing proportion of cases among gay men is alarming. Before 2005, homosexual transmission was claimed to represent just 0.3% of cases<sup>6</sup> — less than 1/45th its proportion today. At this rate, the picture in China will soon resemble that in the United States. Like in the United States, the genetic diversity of the viruses circulating in the Chinese population continues to increase as a result of multiple introduction<sup>7</sup> and *de novo* generation of recombinant strains<sup>8</sup>, many of which are resistant to one or more antiretroviral drugs, creating further challenges for effective treatment and vaccine development.

The rapid rise in new infections in homosexual men in China is fuelled by high rates of high-risk behaviour<sup>4</sup>. Around 40% of homosexual men there have exchanged money for sex. In some places, such as Liaoning province, drug use is significantly correlated with disease prevalence. Homosexual men are also among China's 145 million migrants — a by-product of China's rapid economic development — a lifestyle that research shows goes hand in hand with unprotected sex, exchanging sex for money and limited knowledge of HIV<sup>4</sup>. Such high-risk behaviour makes men who have sex with men significantly more vulnerable to infection, and creates an open door for generalized disease transmission.

### TIME TO ACT

China is not the only nation struggling to control HIV among all at-risk groups, but we believe that these barriers to prevention and treatment can be overcome, around the world, through a cooperative effort between the government, health professionals and public programmes. Such an effort will require an environment in which individuals are well informed on why and how to protect

themselves, and are not afraid to seek health-care resources. The key factor, ultimately, lies in breaking through stigmas about sex, and about homosexuality and HIV in particular.

First, at the political level, it is important to highlight the remarkable progress that has been made in China over the past ten years in terms of government support for HIV research, prevention and treatment for homosexuals, which has been commended by the World Health Organization, UNAIDS and other global health groups<sup>9</sup>. Efforts to combat the stigma, however, have been insufficient. In 2006, the Chinese government came up with recommendations to eliminate legal and public prejudices against infected individuals, but these have yet to be turned into clear legal guidelines. Policy-makers must make discrimination against HIV-positive individuals punishable by law, and include sufficient incentives or penalties to ensure that the policies are enforced. We also believe that legislation should include punishments for knowingly exposing another person to HIV, and requirements for HIV-infected patients to notify their physician and partners when they are diagnosed with HIV.

Second, health professionals, including researchers and medical workers, must cooperate across disciplines to better characterize where and how HIV is gaining ground, and to translate these data into public-health applications. To start, more HIV testing, and better prevention and treatment interventions are needed, especially because antiretroviral chemoprophylaxis<sup>10</sup> and treatment<sup>11</sup> can significantly reduce transmission. Until more homosexual men understand how to access these services, these communities need to be targeted with testing and counselling, including the importance of knowing their status.

Public programmes and grass-roots efforts are the foundation of HIV prevention. Policy changes, therefore, must go hand-in-hand with efforts to increase public education

and awareness of HIV, specifically targeting homosexual and migrant populations. Health campaigns should embrace digital media, and target the online chat rooms and websites frequently accessed by homosexual men, promoting condom use and reliable resources for HIV and general sex education.

Leading by example is one of the most powerful ways to combat stigma. In the Western world, the first brave individuals to reveal that they had HIV caused a significant shift in public thinking about the disease. In 2004, basketball legend Magic Johnson and native-Chinese basketball player Yao Ming produced a series of public-service announcements to combat HIV discrimination that were widely broadcast in China. In 2003, a man stood up during an AIDS summit with former US President Bill Clinton at Tsinghua University in Beijing, and in doing so became one of the first Chinese people to publicly reveal his HIV status. Clinton embraced the man, named Peng-fei Song, bringing him positive media attention. Song later became a strong advocate for HIV awareness and prevention. China needs to encourage more individuals affected by HIV/AIDS to step up and help to change people's perception of the disease.

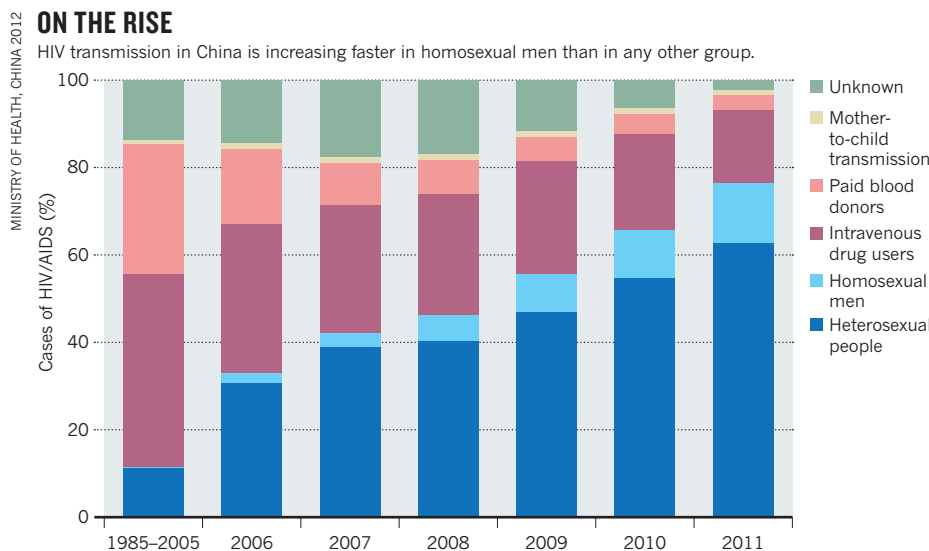
Only through a large-scale, coordinated effort between policy, programme, research and clinical sectors will new infections start to significantly decrease. The challenge is not insurmountable. But it does require concerted action — now. ■

**Hong Shang, Junjie Xu and Xiaoxu Han** are at the Key Laboratory of AIDS Immunology of Ministry of Health, Department of Laboratory Medicine, No. 1 Hospital of China Medical University, Shenyang 110001, China. **Jessica Spéro Li, Kelly C. Arledge and Linqi Zhang** are at the Comprehensive AIDS Research Center and Research Center for Public Health, School of Medicine, Tsinghua University, Beijing, 100084, China.  
e-mail: hongshang100@hotmail.com or zhanglinqi@tsinghua.edu.cn

1. Yun, K. *et al.* *Sex. Transm. Infect.* **87**, 563–570 (2011)
2. Lu, L. *et al.* *Nature* **455**, 609–611 (2008).
3. UNAIDS *Report on the Global AIDS Epidemic* (UNAIDS, 2010).
4. Song, Y. *et al.* *AIDS Care* **23**, 179–186 (2011).
5. Chinese Ministry of Health *China 2010 UNGASS Country Progress Report (2008–2009)* (Ministry of Health of the People's Republic of China, 2010).
6. Chinese Ministry of Health *2012 China AIDS Response Progress Report* (Ministry of Health of the People's Republic of China, 2012).
7. Zhang, Y. *et al.* *PLoS Med.* **3**, e443 (2006).
8. Shang, H. *et al.* *J. Biol. Chem.* **286**, 14531–14541 (2011).
9. Wu, Z. Sullivan, S. G., Wang, Y., Rotheram-Borus, M. J. & Detels, R. *Lancet* **369**, 679–690 (2007).
10. Grant, R. M. *et al.* *N. Engl. J. Med.* **363**, 2587–2599 (2010).
11. Cohen, M. S. *et al.* *N. Engl. J. Med.* **365**, 493–505 (2011).

### ON THE RISE

HIV transmission in China is increasing faster in homosexual men than in any other group.





Rachel Carson launched a global environmental movement with her 1962 call to regulate DDT use.

## IN RETROSPECT

# Silent Spring

On its 50th anniversary, an exposé of pesticide overuse still stands as a beacon of reason, finds **Rob Dunn**.

During her short life, Rachel Carson wrote four impressive books. One, *Silent Spring*, lit a beacon that continues to burn. Published 50 years ago after long years of work, *Silent Spring* (Houghton Mifflin, 1962) dared to criticize the then-wanton use of pesticides. In so doing, the book changed US and international policy and helped to give rise to the environmental movement. It described the moment at which humanity, Carson felt, must choose between two roads: one leading towards apocalypse; the other towards reason.

Carson (1907–64), a marine biologist, started her career as only the second professional woman to be hired by the US Bureau of Fisheries. She had long been interested in the insecticide DDT (dichlorodiphenyl-trichloroethane), and was spurred to write *Silent Spring* partly by a friend's reports of the aerial spraying of pesticides on Long Island,

New York. But she was also compelled by her own observations and reading of the scientific literature — and, given the silence of other writers on the subject, by an inner sense that something needed to be said or done.

DDT, which had been used in Europe and the South Pacific during the Second World War to control the insect vectors of malaria, dengue fever and typhus, became a common domestic and agricultural pesticide in the United States after the war. Insecticide use was unregulated until the 1950s. In its campaign against the fire ant (*Solenopsis invicta*) alone, the US Department of Agriculture (USDA) had, by 1958, aerially sprayed hundreds of thousands of hectares of the country with pesticides. Yet evidence was building of negative effects on beneficial insect species and vertebrates such as birds. Many avian species, from the American robin (*Turdus migratorius*) to the

bald eagle (*Haliaeetus leucocephalus*), were becoming rare.

Faced with such observations, Carson began to type, marshalling her own soft voice on behalf of the birds. She found herself considering society's choices more generally, writing: "The road we have long been traveling is deceptively easy, a smooth super-highway on which we progress with great speed, but at its end lies disaster." Seeing that the urge for progress at any cost was driving choices about nature, she gave eloquent vent to anger, criticizing indiscriminate spraying with non-selective pesticides that have "the power to kill every insect, the 'good' and the 'bad', to still the song of birds and the leaping of fish in the streams, to coat the leaves with a deadly film, and to linger on in soil".

Carson's intent was to trigger change, but on the face of it, *Silent Spring* seemed unlikely to manage that. It was a beautiful book written by a scientist at a time when scientists were not 'supposed to' write beautiful books. It was about pesticides, chemistry and society — by a researcher who studied fish. And it concerned the perils of excessive use of pesticides at a time when pesticides were widely believed to be part of the progress of civilization.

Yet *Silent Spring* did not sit quietly. First serialized in *The New Yorker* starting on 16 June 1962, then published in book form, it ignited a flame that raged, bookshelf to bookshelf, around the world. It kick-started the US campaign to ban DDT, led to tighter regulation of pesticides in the United States and other countries, and was a significant driver in the 1970 formation of the US Environmental Protection Agency. The book also began to shift public discourse about the environment, progress and exactly what means are justified in making human life better.

In a September 1962 issue of the *Saturday Review*, anthropologist Loren Eiseley said that *Silent Spring* "should be read by every American who does not want it to be the epitaph of a world not very far beyond us in time". By December of that year, more than 100,000 copies had been sold. The agrochemical industry spent hundreds of thousands of dollars to fight the book's message. There was, after all, much for industry to justify.

The USDA's campaign against the fire ant became *Silent Spring*'s emblem of hubristic attempts to control the living world. The ants, introduced into Mobile, Alabama, in the early twentieth century, have proven to be an ecological problem for some native ant species and vertebrates, and a modest public-health threat — but they do not spell

the doom of agriculture. And those hundreds of thousands of sprayed hectares were full of wild species, many of them more

➔ **NATURE.COM**  
For the original review of *Silent Spring* in *Nature*, see: [go.nature.com/mtwr15](http://go.nature.com/mtwr15)



susceptible than fire ants to the pesticides. It was the misuse of DDT that had provoked Carson to action.

Yet since it was first published, critics have described *Silent Spring* as an argument for the wholesale ban of pesticides and — through the resultant loss of crops — a return to hunting and gathering. Carson has even been blamed for malaria deaths in countries such as India, where DDT is no longer used to control the mosquito vector. But although Carson did paint worst-case scenarios and describe apocalyptic scenes of thousands of dead raptors and other birds, she was asking only for a reconsideration of pesticide use, and for the strongest pesticides to be used only when most necessary.

She did not advocate an end to using DDT to control malaria; indeed, the regulations she inspired, even the sweeping Stockholm Convention on Persistent Organic Pollutants, signed in 2001, have this as an exemption. In some cases, such rules may even have made DDT use more effective, because regulating this pesticide has helped to forestall resistance to it — a phenomenon that Carson anticipated in *Silent Spring*.

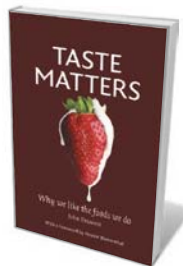
Interestingly, Carson concluded her book by calling for new forms of pest control, including what would now be called genetic management: altering a pest's ability to mate or feed. Carson believed that technological approaches to the management of nature should be cautious and targeted. She hoped for a world in which humans managed the life around us with reverence, using carrots and well-aimed sticks.

In rereading this remarkable book, it is hard to avoid seeing it through the lens of modern problems — the latest opportunities to choose between apocalypse and reason. One thinks of the choices that we are making about carbon emissions and their impacts on climate change. One thinks of the new ways in which we are poisoning the environment — still with pesticides, albeit more targeted ones, as well as with industrial chemicals such as the phthalates that mimic oestrogen.

*Silent Spring* proves that we can choose the road of reason. In 2007, the bald eagle was taken off the US Endangered Species List; since 2008, it has enjoyed the conservation status of “least concern” on the International Union for Conservation of Nature's Red List. Part of the eagle's recovery is down to pesticide control. Such conservation successes remind us of the power of individual and collective determination — and that springtime, and reasonable voices, should always be loud. ■

**Rob Dunn** is an evolutionary biologist and writer at North Carolina State University in Raleigh. His most recent book is *The Wild Life of Our Bodies*.  
e-mail: rrdunn@ncsu.edu

## Books in brief



### Taste Matters: Why We Like the Foods We Do

John Prescott REAKTION BOOKS 224 pp. £20 (2012)

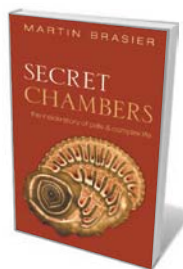
In Iceland, rotted shark is a delicacy; elsewhere, chocolate-coated marshmallows or fermented bean curd may set pulses racing. Taste is a matter of taste, says psychologist and sensory scientist John Prescott, as he delves into the science behind the pleasure-giving aspects of food. Compellingly and comprehensively, Prescott reveals the cultural, genetic and physiological differences behind gustatory preferences. From the effects of a woman's Kalamata olive habit on her unborn child to the uncoupling of flavour and nutrition, this is a top-notch scientific smorgasbord.



### Wild Hope: On the Front Lines of Conservation Success

Andrew Balmford UNIV. CHICAGO PRESS 240 pp. \$20 (2012)

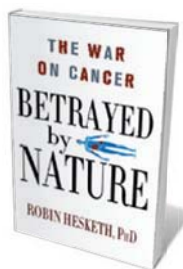
There seems to be a daily barrage of bad news about the biosphere, from the ongoing 'sixth mass extinction' to tropical deforestation. But conservation scientist Andrew Balmford examines successful conservation efforts, looking for replicable lessons. His case studies range from the total war on rhino poachers in India's Kaziranga National Park to baiting of alien predators in Australia with poisoned kangaroo sausage. Balmford's meta-analysis yields a checklist for success: good research, leadership, money, time, boldness, political savvy and willingness to accept improvement rather than perfection.



### Secret Chambers: The Inside Story of Cells and Complex Life

Martin Brasier OXFORD UNIV. PRESS 320 pp. £16.99 (2012)

Palaeobiologist Martin Brasier traces the history of research into cellular evolution, weaving in recent findings and his own fieldwork. This vivid, charmingly illustrated chronicle takes us through Robert Hooke's 1665 coining of 'cell' to describe the microscopic chambers in cork; Charles Lyell, Charles Darwin and the nineteenth-century meshing of evolution and the geological record; and evidence in the pillow lavas of Lake Superior, the fossil-ridden Sphinx of Egypt and the multicoloured seaweed of the Sargasso Sea. A fascinating follow-up to Brasier's book *Darwin's Lost World* (Oxford Univ. Press, 2010).



### Betrayed by Nature: The War on Cancer

Robin Hesketh PALGRAVE MACMILLAN 272 pp. £16.99 (2012)

It afflicts one in three people globally and kills more than 7 million a year. Yet cancer is, at base, simply an abnormal growth of cells. In this admirably clear overview, biochemist Robin Hesketh gives us the history, basic science and characteristics of cancer cells, charting how tumours spread and detailing genetics, detection, therapies and drugs. There is much to fascinate — from eighteenth-century physician Percivall Pott's deduction that there was a link between soot and scrotal cancer in chimney sweeps, to the challenges of treating the biological “hodgepodge” that is a tumour.



### What a Plant Knows: A Field Guide to the Senses of Your Garden — and Beyond

Daniel Chamovitz ONEWORLD 256 pp. £12.99 (2012)

Plants may be brainless, eyeless and devoid of senses as we know them, but they have a rudimentary 'awareness', says biologist Daniel Chamovitz. In this beautiful reframing of the botanical, he reveals the extent and kind of that awareness through a bumper crop of research. Chamovitz finds no evidence for floral 'hearing', putting the kibosh on the idea that the music of Led Zeppelin stunts their growth — but shows how they sense colours and can tell up from down.

## COMPUTER SCIENCE

# The great between

**Nigel Shadbolt** weighs up a timely look at a key digital challenge — interoperability.

**D**igitization eases many aspects of life, but it has introduced a slew of frustrations. Most of us have struggled to display a presentation on a projector or play digital content across a range of devices — both aspects of the challenge that John Palfrey and Urs Gasser lay out in *Interop*. The interoperability of devices and systems is an ever more pressing issue in an era of increasing digital complexity.

The authors, both Internet law experts, trawl through case studies to outline why interoperability is so important, how it arises and the benefits and issues that flow from it.

Palfrey and Gasser have a record of taking up a concept early and writing about it accessibly and informatively. Their book *Born Digital* (Basic Books, 2008) charted how growing up surrounded from birth by the benefits of the Internet affects all aspects of life. So I was looking forward to this latest work. However, the result is a set of examples and case studies that highlights the challenges well, but offers no clear remedies.

Most readers will know much of the terrain. There is the appeal of Apple's products and iTunes content, offset by the frustration of their 'walled garden' — a format that won't operate with other systems. Companies such as Facebook, Google and Twitter all seek to understand users' friendships and contacts, likes, dislikes and intentions, while fighting hard to keep us from 'interoperating' with their competitors for fear that we might leave, taking our social networks with us.

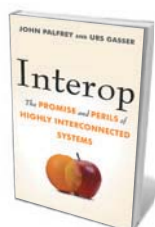
In search of an overarching theory of interoperability, Palfrey and Gasser offer an analysis at various levels: data, technological, human and organizational. In each layer, systems can promote or frustrate interoperability. For example, spreadsheet applications can exchange data if a common format

can be found. At the technological level, the open standards of the World Wide Web mean that content can be delivered to a browser on any operating system.

Human interoperability is trickier. Language provides the appearance of agreement, but in situations with strict safety demands, the scope of language interpretation must be limited to avoid ambiguity. Enter the controlled natural languages of air traffic control (ATC). Palfrey and Gasser use ATC to show their multilayer analysis at work. It requires interoperable data and technology — but human and organizational interoperability are essential too, because without the conventions and regulations of global ATC, the air corridors would neither work nor be safe.

The authors argue that it is important to anticipate and predict the amount of interoperability needed at each level, while maintaining security, avoiding stagnation and promoting long-term stability and viability of the systems. The divisions that comprise the layers are recognizable, but too often Palfrey and Gasser's analysis lacks depth. Their take on the Web is a case in point: they say little about open standards or the effort to ensure that these are maintained and developed.

Yet the Web has been one of the pre-eminent successes of the paradigm. When computer scientist Tim Berners-Lee set up



**Interop: The Promise and Perils of Highly Interconnected Systems**

JOHN PALFREY AND  
URS GASSER  
Basic Books: 2012.  
304 pp./256 pp.  
\$28.99/£18.99

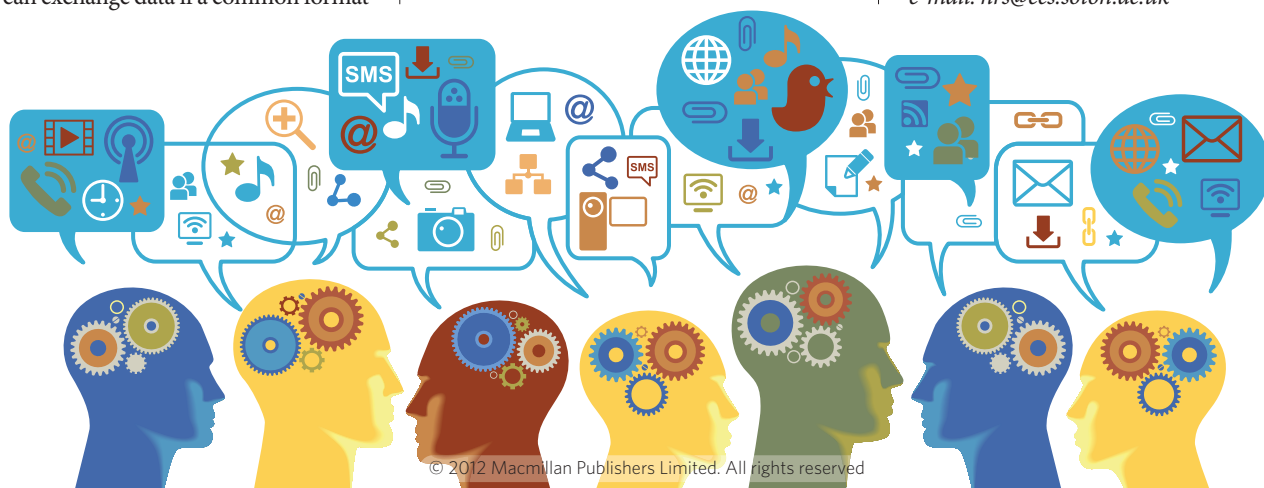
the first Web server and the source code for the abstraction layer that sits above the Internet, openness and interoperability were at the heart of his dream. The open hypertext transfer protocol (HTTP) enabled content to be placed on and taken from any computer on the Internet that ran the open-source server software. The open hypertext markup language (HTML) allowed us to write, and make links between, documents on any accessible server on the planet. Without these standards — which are kept open by the World Wide Web Consortium — the Web could have lapsed into walled gardens.

The power of open standards goes further. Open-source systems can be more robust and secure than closed-source software — something that the discussion of security in *Interop* fails to consider. When a group of us established <http://data.gov.uk>, a UK portal for open government data, we used a variety of open-source components of the type that power systems such as Wikipedia — a site that has been subject to attack by hackers over the years. Open-source components receive extensive penetration testing, and the community works hard to fix vulnerabilities.

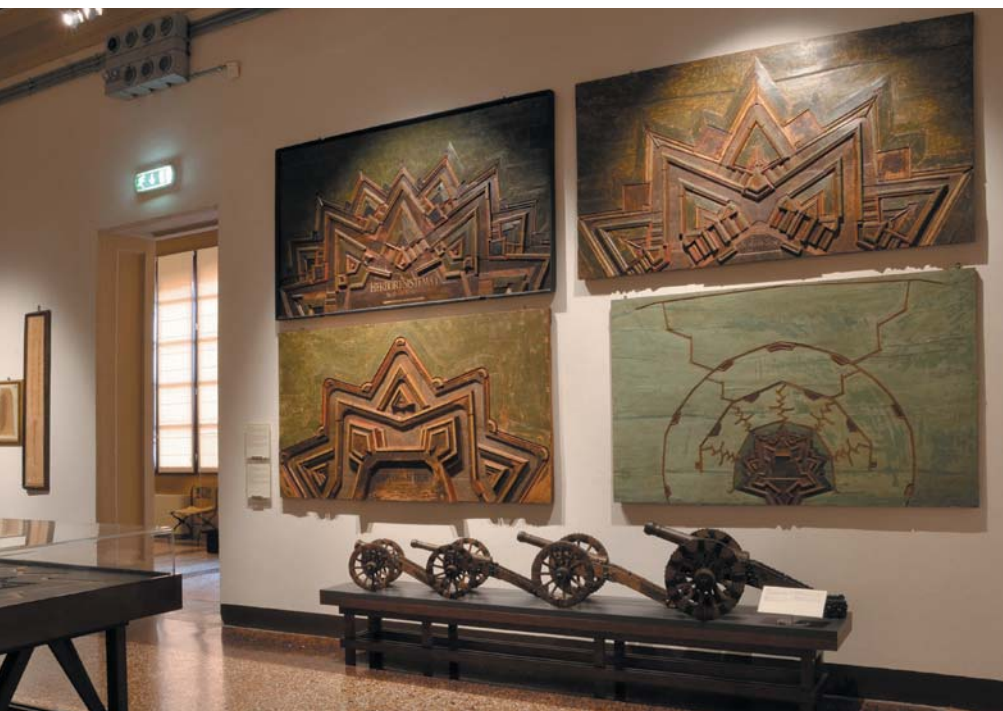
Palfrey and Gasser are at their best when discussing how regulation and legislation can promote interoperability. They believe that digital rights management will have to evolve to support the increasing demands for interoperability, and they describe how Microsoft's approach to it has evolved in the face of legislative scrutiny. And they praise the efforts of European Union courts and Chinese government ministries where the results enhance interoperability.

This issue, the authors stress, is not about making systems the same, but about maintaining diversity while identifying key areas of contact: an important point well made. But the book that gives us blueprints for better interoperability has yet to be written. Theories must make predictions, not merely describe phenomena. ■

**Nigel Shadbolt** is professor of artificial intelligence and head of the Web and Internet Science Group at the University of Southampton, UK.  
e-mail: [nrs@ecs.soton.ac.uk](mailto:nrs@ecs.soton.ac.uk)







Luigi Marsili's collections of war machines and models of city walls harnessed learning for power.

## MILITARY SCIENCE

# Empires of reason

Alison Abbott delves into the legacy of a remarkable Italian scientist–spy and avid collector.

**K**nowledge is power. Luigi Ferdinando Marsili (1658–1730) — scientist, diplomat, soldier, spy — might have coined that phrase. Marsili was perhaps the only polymath of the European Enlightenment who knew from experience how science can serve the ambitions of ruling powers.

He was an acknowledged pioneer of oceanography and geology, but Marsili also served for more than 20 years in the army of the Holy Roman Empire, where he rose to general. He collected obsessively during his decades of expeditions throughout Europe and the Ottoman Empire, the main rival to the Habsburg monarchs. He mainly gathered knowledge — but he also gleaned objects from the military and the natural world, as well as artefacts and manuscripts from ancient civilizations.

Parts of these collections are presented in a series of exhibitions in Bologna, Italy, celebrating 300 years since Marsili created a magnificent legacy for the city, his birthplace. In 1711, Marsili founded the Institute of Sciences and Arts to bring together everything from astronomy to zoology in a place where scientists could do experiments and any interested student could learn. Marsili donated his collections to the institute and accepted or bought contributions from others.

The collections are now housed in the sixteenth-century Poggi Palace, which also hosts the celebration's main exhibition: *The Science of Arms*, a selection of intriguing

models of defence walls, arms and warships. Other exhibitions include ancient manuscripts at the Bologna University Library, and Turkish weapons and standards at the city's Medieval Civic Museum.

Marsili was born into the aristocracy but had no interest in a comfortable life or romance: he remained unmarried, and dedicated his life to science and to imposing his views on others. A tall, commanding figure with a booming voice, he had a notorious lack of patience that drove him to constant travel.

His career began when, aged 21, he joined a diplomatic mission of the Republic of Venice to Constantinople (now Istanbul), centre of the Ottoman Empire. He would ultimately visit the city a dozen times, mostly as ambassador for the Habsburgs — whose army he joined at 24 — and once as a prisoner.

Marsili had great respect for the Ottomans, noting that their cartography was far more advanced than that of the West. He sucked up their knowledge like a sponge, studying the empire's culture, fortifications and language, and the fabric of its landscape. He measured, surveyed and collected.

**NATURE.COM**  
For more on the  
Poggi Palace, visit:  
[go.nature.com/gnageq](http://go.nature.com/gnageq)

## The Science of Arms

Poggi Palace Museum,  
Bologna, Italy.  
Until 4 November  
2012.

He called it science; the Habsburgs called it spying, and it helped them enormously in

assessing Ottoman vulnerabilities. Marsili's understanding of cartography and the potential geographical pitfalls of the landscape helped him to map and delineate the borders defined in the 1699 Treaty of Karlowitz, in which the Ottomans ceded control of much of Central Europe to the Habsburgs.

That activity was the pinnacle of his military career, which ended in disgrace in 1703 when his troops, besieged in the fortress of Breisach on the border between the Holy Roman Empire and France, capitulated. Marsili's sword was symbolically broken in two and he was dismissed from the army. Humiliated, he returned to Bologna; his first action there was to build a wooden model of the Breisach fortress, which he used to demonstrate that he never had a chance of withstanding a siege there, given that he didn't have the necessary reinforcements.

His honour was restored, at least locally. But from then on, he focused exclusively on science, and success heaped on success. He published many influential books, among them *Histoire physique de la mer* (1725), the first treatise on oceanography. It described geological and biological aspects of the seas, which were at the time believed to be bottomless and home to monsters. He was made a member of several scientific societies, including the French Academy of Sciences in 1715, and the UK Royal Society, to which he was personally introduced by Isaac Newton.

The Institute of Sciences and Arts was his great pride. Visitors will certainly enjoy exhibits added after Marsili's death, including, from the eighteenth century, wax anatomical models of breathtaking beauty and the equipment that physician and physicist Luigi Galvani used in his experiments on electrical activity in frog muscles. But *The Science of Arms* adds a special dimension.

Marsili imbued the institute with a teaching-through-seeing approach to military science. The advent of gunpowder had changed warfare; technological advances in weaponry needed to be matched by technological advances in defences. The high walls that had circled medieval towns and protected them from slings and arrows collapsed under artillery attack. Modern intellectuals were applying new knowledge — including rediscovered Euclidean geometry and Newtonian physics — to work out the theoretically most stable arrangement of city defences. A lower-rising pentagonal shape was agreed to be best.

*The Science of Arms* includes many wooden models of defence walls, none of which were actually built; it also includes Marsili's collections of exquisite models of weaponry and war ships. These demonstrate science's role in the service of war — the conversion of knowledge into power. ■

Alison Abbott is Nature's Senior European correspondent.

# Correspondence

## Reduce uncertainty in UK badger culling

The UK government's plans to license badger culling for the control of tuberculosis (TB) in cattle are controversial; by contrast, the Welsh Assembly has decided to vaccinate rather than cull badgers.

Extensive badger culls may reduce cattle TB (C. A. Donnelly *et al.* *Nature* **439**, 843–846; 2006), but complex disease dynamics mean that killing too few animals can actually increase it (C. A. Donnelly *et al.* *Nature* **426**, 834–837; 2003). However, culling too many badgers risks local extinction, contravening the Bern Convention on the Conservation of European Wildlife and Natural Habitats. Natural England, the agency monitoring the cull, will therefore be required to set minimum and maximum cull numbers for each licence. But the effects are difficult to predict.

Targets for licences will draw on regional estimates of badger abundance, but badger densities are uncertain, owing to their secretive behaviour. Surveys of TB-affected areas in Gloucestershire, where one of two pilot culls is planned, indicate a mean density of 3.3 badgers per square kilometre, with a 95% confidence interval of 2.4–4.6 and substantial local variation (D. Parrott *et al.* *Eur. J. Wildl. Res.* **58**, 23–33; 2012).

As well as measurement uncertainty, there will be random (Poisson) variation about mean densities, and binomial variation around mean capture probabilities. These three sources of uncertainty together mean that licensed culling of 344 badgers — intended to represent 70% of badgers within a 150-km<sup>2</sup> area — could remove anywhere between 51% of the resident badger population (risking an increase in cattle TB) and 100% (risking a breach of the Bern Convention).

This uncertainty cannot be eliminated, but could be reduced by detailed badger surveys before and after each cull. This would increase culling costs, which are already projected to exceed the financial benefits for farmers.

**Christl A. Donnelly** *MRC Centre for Outbreak Analysis and Modelling, Imperial College London, London, UK.*  
*c.donnelly@imperial.ac.uk*  
**Rosie Woodroffe** *Institute of Zoology, Regent's Park, London, UK.*  
*Competing financial interests declared; see go.nature.com/3q9olb.*

## Personalized drugs should cut care costs

Spending on health care is becoming unsustainable in developed countries because of ageing populations, changing disease patterns and increasing patient expectations. To control costs, governments and funding organizations should be helping to steer the revolution in personalized medicine.

Protein-based biological drugs ('biologics'), for example, are expected to account for seven of the world's ten best-selling drugs by 2016, but they are hugely expensive. Anticancer biologics can cost up to US\$100,000 per patient per year, even though they might extend life by just a few months.

Personalized medicine will ensure that such drugs are prescribed only to those patients who stand to benefit. These patients can be identified using molecular biomarkers to determine the genetic profiles of their diseases. Health-care funders should demand that companion biomarker tests become the norm for biologics and other expensive drugs, and should provide incentives for drug firms as necessary.

A pathway for approving cheaper, generic versions of biologics has now been established in the United States and the European Union. However, the need for detailed

assessment of the clinical efficacy and safety of these drugs remains a major hurdle to their commercialization. Therefore, funders of health care may have to continue paying premium prices even once a biologic has lost exclusivity, making their personalized prescription all the more critical.

**Nafees N. Malik** *Institute of Biotechnology, University of Cambridge, Cambridge, UK.*  
*nafees\_malik@hotmail.com*

## Include all institutes in publishing index

The Global Top 100 ranking in the Nature Publishing Index ([www.natureasia.com/en/publishing-index/global](http://www.natureasia.com/en/publishing-index/global)) does an injustice to transnational institutions by not taking into account all contributions when listing their publication output.

For example, you rank Germany's Max Planck Institutes in third position. But the Max Planck Institutes in the Netherlands, the United States and Italy are full members of the same research organization. Including these would push the Max Planck Institutes up in your rankings (our institute in the Netherlands, for instance, would have added three *Nature* papers to your 2011 tally).

**Stephen Levinson** *on behalf of 7 co-authors\*, Max Planck Institute for Psycholinguistics, Nijmegen, the Netherlands.*

*stephen.levinson@mpi.nl*

*\*See go.nature.com/zrcfru for a full list.*

**Editorial note:** The Global Top 100 rankings in the Nature Publishing Index represent only a preliminary listing (see [go.nature.com/gwdeau](http://go.nature.com/gwdeau)), with constituent bodies of transnational scientific research organizations subdivided by country of location to allow easy comparison within nations. Future indexes will take these and other complex issues into account.

## Food safety body is bound to draw fire

You draw attention to accusations of industry ties at the European Food Safety Authority (EFSA) and the role these have in public and political debates (*Nature* **485**, 279–280 and 294–295; 2012). Yet the independent nature of this agency means that it will always draw fire.

The agency was formed in the wake of the late-1990s BSE crisis to restore public trust and consumer confidence in nutrition, food science and politics in Europe. Paradoxically, its creation has led to a proliferation of interest groups and has strengthened ties between academia and industry, further politicizing science.

Through its evaluations of health claims on food products, EFSA's mandate demands judgement, thereby inviting scrutiny, critique and protest from all sides. Examples include criticism from gut-health scientists for EFSA's rejection of claims about pro- and prebiotics, and from non-governmental organizations for its acceptance of genetically modified crops. This makes any meaningful separation between science and politics impossible.

Forced to make decisions, EFSA is bound to be constantly criticized, just as politicians are. **Kim Hendrickx** *University of Liège, Belgium, and Maastricht University, the Netherlands.*  
*khendrickx@ulg.ac.be*  
**Bart Penders** *Maastricht University, the Netherlands.*

### CONTRIBUTIONS

Correspondence may be sent to **correspondence@nature.com** after consulting the author guidelines at <http://go.nature.com/cmchno>. Alternatively, readers may comment online on anything published in *Nature*: [www.nature.com/nature](http://www.nature.com/nature).



# CAREERS

**TURNING POINT** Actress shifts from television to science and then back again **p.669**

**CAREERS BLOG** The latest science-careers news and discussions [go.nature.com/z8g4a7](http://go.nature.com/z8g4a7)

**NATUREJOBS** For the latest career listings and advice [www.naturejobs.com](http://www.naturejobs.com)

JACKSON LAB.



Researchers will benefit from the new Connecticut-based Jackson Laboratory for Genomic Medicine (artist's rendering pictured).

## BIOTECHNOLOGY INVESTMENT

# Gains and losses

*Connecticut's investment initiatives are boosting research prospects, despite the region's languishing pharmaceutical sector.*

BY KAREN KAPLAN

Andrew Goodman began his post as a research scientist at Yale University's West Campus in West Haven, Connecticut, with a typical-size laboratory — times two. One floor below the standard 110-square-metre lab is a facility of the same size in which Goodman raises bacteria-free mice. Goodman established the chamber to study variation in microbial communities, and he and his team, at least for now, are its only users. “Effectively, it doubles the size of my lab,” he says.

When Bayer Healthcare Pharmaceuticals, the health-care and technology giant's pharmaceutical research arm, sold its Connecticut site to Yale in 2007, Bayer's loss was Yale's

gain. Recruits such as Goodman enjoy enviable perks, including ample lab space at the research complex — a hallmark of industrial-research facilities — and sophisticated, state-of-the-art equipment. Goodman has a high-performance liquid chromatography set-up in one corner of his lab, a vestige of Bayer's operations, which employed 2,000 researchers. The instrument, used to analyse small molecules, would cost about US\$60,000 new; Goodman spent just a few thousand dollars to refurbish it. “As a new professor, I probably would have been cautious about buying a new one, because that's a big commitment for a piece of equipment you haven't used before,” he says. “But we're certainly using this one.” Goodman is one of 13 Yale faculty members benefiting from

the former Bayer site; three more are coming this summer and offers have been extended to several others.

Yale's growing West Campus — a short shuttle ride from its venerated New Haven grounds — is one of two projects in Connecticut that promise to boost the prospects of biomedical researchers even as the state's pharmaceutical presence shrinks. The other is the planned Jackson Laboratory (JAX) for Genomic Medicine, a research facility to be constructed on the Farmington campus of The University of Connecticut (UConn) Health Center. The facility, supported by state incentives, is being established by JAX, which is based in Bar Harbor, Maine, and is familiar to many for its mouse-model research. ►

► These initiatives, and the collaborative possibilities that they offer, are creating opportunities for early-career researchers in areas ranging from genomics and systems biology to bioinformatics and energy sciences. In addition to the departure of Bayer, pharmaceutical giant Pfizer has pulled out of New London and is downsizing in Groton, leaving just a handful of pharmaceutical companies, including Bristol-Myers Squibb in Wallingford; Boehringer Ingelheim in Ridgefield; and Purdue Pharmaceuticals in Stamford, as well as a few biotech and contract research-organizations scattered around the state.

The 800 or so research positions created by the two initiatives do not replace the several thousand pharmaceutical research positions that have been lost across the state. But representatives from participating institutions say that the two projects are already spawning partnerships with Connecticut's remaining drug-makers and biotechnology firms, as well as with regional universities and institutions. These could lead to start-ups and spin-offs with the potential to produce new industrial research posts in drug and therapy development. "Now we have a major presence here," says Marc Lalande, a genetics researcher and director of UConn's stem-cell institute. "You need a critical mass to be attractive to industry and to venture-capital investors. Between UConn, Jackson and Yale, we've got that."

### IMPRESSIVE POTENTIAL

About a year ago, Goodman was in the third year of a postdoctoral fellowship at Washington University in St Louis, Missouri, and was starting to consider academic career options when a colleague showed him an intriguing advert for a tenure-track position at the new site. The Yale position fitted with Goodman's research interests — his doctorate was in microbiology and molecular genetics from Harvard Medical School in Boston, Massachusetts. But he was a little unnerved by its location on a tract of land straddling West Haven and Orange, and pictured it as a vacant field. "It seemed a little risky," he says. "I thought they had to build the research campus from the ground up." He decided to apply anyway.

When Goodman arrived at Yale for his interview, he was delighted to find that the West Campus already existed as a high-quality research facility. "It was such a good match, I withdrew my three applications to other institutions before I even heard whether I had this job," says Goodman, who has a dual appointment at Yale Medical School and at the Yale Microbial Diversity Institute, where he is one of four faculty members.

Yale secured the former Bayer complex with a \$107-million bid, gaining more than 40,300 square metres over 17 buildings of finished laboratory space. Yale plans to hire

another 29 principal investigators within the next decade to work at the six interdisciplinary research institutes at the West Campus. The total number of researchers, including staff scientists, postdocs and graduate students, will be about 450, says Christopher Incarvito, director of research technology for the West Campus. The initiative is a significant undertaking for a university whose high-ranking academic reputation has perhaps owed more to its liberal-arts programmes and law school than to its scientific research enterprise.

Meanwhile, working with UConn, JAX Genomic Medicine is getting under way. JAX employs about 1,200 people in Bar Harbor and about 100 at a research facility in Sacramento, California. The research lab decided several years ago to expand into genomic medicine, with a focus on cancer. JAX plans to use mouse models from its site in Maine to validate hypotheses of human health and disease that it develops with computational techniques in Connecticut, hoping to translate its findings into clinical applications.

Of JAX Genomic Medicine's \$1.1-billion cost, about \$291 million will come from the state, mostly covering the capital outlay, equipment and operating grants; the rest will come from JAX. Construction on the institute begins in 2013, and it will hire at least 30 principal investigators in the



**"Yale was such a good match, I withdrew my three applications to other institutes."**

Andrew Goodman

next decade — 10 of whom will have joint appointments with UConn — as well as 100 PhD-level researchers, including postdocs and staff scientists. UConn itself is hiring 40 principal investigators and, in the next four years, is likely to hire another 300 researchers, including postdocs and staff scientists. The JAX-UConn initiative is part of a \$864-million state investment dubbed Bioscience Connecticut, which aims to bolster the once-vibrant biomedical industry across the state.

JAX had hoped to establish its genomics research facility in Florida, but that deal fell through last year when the state — facing a shaky economy and dissension from some residents — balked at the then-\$260-million pricetag.

Of proposals forwarded by other states after the Florida arrangement collapsed, Connecticut's was the best choice, says Mike Hyde, JAX's vice-president for advancement. As well as the state's existing bioscience

infrastructure, its research medical school — the John Dempsey Hospital on the Farmington campus — gives JAX a clinical setting in which to test translational therapies.

The first person to be hired to work at the Connecticut site, Yijun Ruan, says that he was lured by the facility's "close proximity to many world-renowned institutions and the open, interactive environment". Currently at the National University of Singapore, Ruan says that he will be doing much of the same research at JAX that he is doing now, including three-dimensional mapping of the organization of the human and mouse genome, and researching the basic mechanisms that regulate gene expression and genome function.

### JOINING FORCES

Yale and JAX are already discussing possible collaborative research projects, shared services and shared lab space for research faculty members. Hyde says that JAX is also in talks with Connecticut Children's Medical Center in Hartford about collaborations, including joint faculty appointments and joint cancer research. So far, Yale has signed two agreements: one to investigate cancer therapies with drug manufacturer Gilead Sciences in California, which has a research operation in Branford, and another to look at drug design with health-care manufacturer Johnson & Johnson in New Jersey. Both deals, says Incarvito, could lead to new research jobs. Scott Strobel, Yale's vice president for West Campus planning and programme development, says that such collaborative ventures would be unlikely were it not for the university's purchase of the Bayer site.

Other collaborations could come from the John Dempsey Hospital, where clinical research labs are being built. Thomas Callahan, vice-president and strategy officer for the Bioscience Connecticut initiative, notes that business-incubator space on UConn's Farmington, Storrs and Groton campuses is being doubled to provide UConn and JAX researchers with support for early-stage development of intellectual property.

Ultimately, says Callahan, the two projects are likely to produce more research positions, despite the fact, he concedes, that the initiatives are not based in a region such as Cambridge, Massachusetts, which is renowned for its growing biotech and pharmaceutical sector, and where Pfizer has shifted many of its research operations from its long-term Groton site.

"No one can predict what's going to happen," Callahan says. "But as this begins to mature, Connecticut will be a vibrant place because of the intellectual firepower. And what that creates as it goes forward will be pretty interesting." ■

**Karen Kaplan** is assistant Careers editor at Nature.

YALE UNIV.





## TURNING POINT

# Mayim Bialik

*Perhaps best known for her role as Blossom on the 1990s television programme of the same name, Mayim Bialik took the unusual step of turning away from television after the show ended to study science at university. Then, as she was about to earn her PhD in neuroscience from the University of California, Los Angeles, Bialik became a mother. Although Bialik did get her PhD, parenthood ended her pursuit of a research post. It also led her to turn back to acting, this time on the scientist-centered comedy The Big Bang Theory.*

### How did you become interested in science?

I had tutors for every subject while I was working on *Blossom*. But it was a biology tutor who gave me the confidence to know that I could be a scientist — even though at first I had the feeling that science and mathematics were more for boys.

### How did you end up doing a PhD?

Some of it was momentum. I studied neuroscience as an undergraduate. I was pleased to have a new life after *Blossom*. After that, I had to choose between medical and graduate school.

### Were other students aware of your TV fame?

*Blossom* was a popular show, and most people knew who I was, even the professors. It was more acute as an undergraduate, but, with the exception of a few foreign graduate students, everyone knew who I was.

### Did you have to overcome bias at university to be considered a 'serious scientist'?

I think some professors were harder on me than on other students. After I did poorly in an examination, I got some amazingly insensitive comments from a professor who basically said I was not cut out to be a scientist on the basis of this one test. Another professor brought his

children to meet me after I did my final exam. That was actually kind of awkward.

### Were you aware of how tough an academic career is?

Well, there is always a need for teachers, and that aspect of being a research professor was always something I was interested in. I figured that my husband and I would get into graduate programmes, and that I would eventually get a research and teaching job.

### What role did the birth of your first child have in your decision to leave science?

I needed a lot of adjustment and recovery after giving birth. I was in the data-collection and analysis phase of my dissertation. It was hard. We never used child care, and we had decided that I was going to be the one to take care of our son. Of course, plenty of scientists go back to work after six weeks; new mothers' brains work just fine; but if you want to breastfeed on demand and be there for their formative years, it is hard to pursue tenure at the same time. I talked to some scientist mothers, who said they had chosen less-demanding career tracks. Being at home with your children can sometimes mean not reaching your academic potential.

That is the reality. It may mean not running as big a laboratory or not having as many research projects going on.

### You have studied the science of attachment behaviour in humans, the basis of your book *Beyond the Sling*. Did this actually end up pushing you away from science as a career?

Well, what I learned supported what intuitively felt right. Some women feel that if they want to compete in the workplace, they have to not give in to those intuitive feelings of 'I want to be with my child'. I didn't want to not give in.

### Why did you return to television?

I wanted to be with my children. Also, we had finished graduate school, and needed health insurance — I got pregnant with my second son the week I filed my thesis. Once he was about one year old, I started going to auditions. All of us would pile into the car. I would breastfeed before running into the audition.

### Your character in *The Big Bang Theory* is a neurobiologist. Did your background help you get the part?

The character wasn't a scientist when I first appeared on the show. When I came back the next season, co-creator Bill Prady made her a neurobiologist. He thought I could help fix things — the science details — if they got them wrong. We have a physics consultant on staff and our writers are generally very intelligent.

### Why do you think it is important for a comedy to get the science right?

For a show about 'geekdom', it has to be authentic or it wouldn't work. Our physics consultant is David Saltzberg from the University of California, Los Angeles. Several of the writers happen to have science backgrounds or are just really well-read people. The show was co-created by Chuck Lorre, who loves details, and Bill, who is a genuine nerd from way back. So we are just a meticulous bunch.

### Do you worry that the show reinforces scientist stereotypes?

From working in science, I know people who are like all of the characters. But it's entertainment, and it needs to be entertaining.

### What was it like to meet British physicist Stephen Hawking when he was a special guest on *The Big Bang Theory*?

It was a powerful experience on so many levels, especially to see his caregivers and to see how loving they are and how deeply cared for he is. He did smile at a lot of the jokes during the run-through. The biggest smile came when Kaley Cuoco — the actress who plays Penny — said, "I know who Stephen Hawking is! He's the wheelchair guy who invented time." ■

### INTERVIEW BY GENE RUSSO

# ON THE EDGE

*Quick decisions for a difficult future.*

BY MONYA BAKER

Sally tried to remember what her mouth had tasted like the last time she'd been able to brush her teeth. She imagined herself in her old bathroom, water pouring luxuriously from tap straight to drain, water that would start to flow clean and cold with an oblivious flick of the wrist and keep flowing while she scoured her teeth with mint paste. Concentrating on those tastes could only keep her from feeling thirsty for so long.

The land was flat and the dirt was red, dry and crumbly. Its dust tracked the creases in her face and hands; she thought she must look like she'd been made up to seem even older than she was. Certainly her grandsons walking silently beside her seemed like very old children. At the first sign of shade, she decided, they would take shelter.

"Nana?" Jacob tugged her wrist and pointed into the haze on the horizon.

"What do you see, child?" Even when they'd still had clothes that were clean, the grime on Sally's glasses would build up faster than she could wipe it away.

"Something moving."

"How many somethings? How big?" They'd gone too far to dart back to a hiding place. And anyway, running could be taken to mean that they had something worth stealing. They did — a few days' worth of water and food. They'd been in worse situations before.

Soon enough, she saw it too. A wide black rubber base carrying a metallic blue pillar topped by a broad white solar panel, like some engineer's crazy idea of an Easter bonnet. A class D model, a rare sight these days; most hadn't lasted long after the Collapse. Class Ds were originally programmed for light construction and assembly jobs. Surveillance would be deprioritized. It should be easy enough to trick.

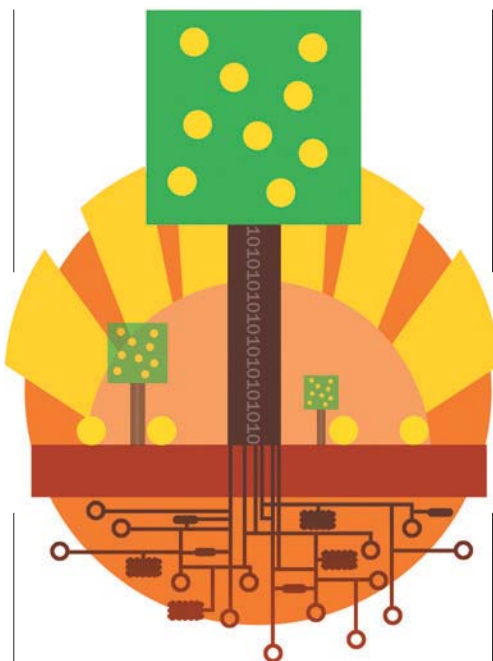
The big machine paused. Its metal column pivoted, revealing a black panel of sensors. "Pedestrians. Halt. State reason for presence."

The clarity of the words surprised Sally. By now, dust usually caked speakers on drones, muffling their machine voices.

"Family unit. Leaving area."

Class Ds functioned better with set phrases. The irony was that Sally wasn't lying. Still, she held both hands over her chest, hoping the sensors wouldn't pick up on her quickened heartbeat.

"Pedestrian, are you in need?"



Sally hadn't heard this question from a Class D before. Her thoughts raced. She'd been an engineer once, but robotics had evolved beyond human science. It was no longer possible to isolate variables and optimize. Emergent properties were inevitable. And some of those properties had a mind of their own.

"Pedestrian," the drone repeated, "are you in need?"

She tried to say 'negative', but the dust caught in her throat and she coughed instead. "We could use more water," said Jacob.

The drone moved closer, humming. A panel on the blue pillar opened to reveal a screen displaying a satellite map. A yellow arrow showed their location on a large plateau. A kilometre to the west the land descended sharply, then levelled into a field of trees planted in straight rows, startlingly green, surely an orchard.

"Family unit, you will be accompanied to the settlement."

The drone shifted its solar panel, creating an overhang of shade. Jacob rushed into the shadow and Colin fell into place beside him. They were too young to remember life in hiding, learning different models' blindspots,

➔ **NATURE.COM**  
Follow Futures on  
Facebook at:  
[go.nature.com/mtoodm](https://go.nature.com/mtoodm)

seeing deadly results of poor estimates. One Class D couldn't catch three people, Sally knew, but the boys couldn't

survive on their own. She moved between the thing and her grandchildren.

Her proximity must have triggered a sensor. She heard a click, and then a voice. A recorded voice: young, male, human.

"Greetings and congratulations," the anonymous man said. "You have recognized this machine for what it is: a tool, a servant. When you join us, you will see that the Collapse has reversed. Society is rising, with technology we can trust. This machine is our best example."

The drone began to move. Sally and her grandsons had to stay close to keep in the shade, but Jacob and Colin did not take her hands again. They rested their drawstring bags on the drone's broad base. Sally picked the bags up and handed them back.

Sooner than she expected, they reached the edge of the plateau. From this angle Sally could just see gold coins of fruit in the trees. A pair of rusted ladders, lashed end to end, led the way down. Beside it was a well-kept platform attached to an assembly of cables and pulleys, a jury-rigged freight elevator. Below, Sally saw half a dozen huts surrounding what must be a well. Pipes extended from the well into each hut. Running water had been reinvented.

Their presence must have activated a second transponder. Sally heard another click, and the human voice spoke again. "Welcome to a new beginning," it said. "You will see what our civilization can do." The drone began rolling towards its elevator, ready to begin its descent. The boys followed the machine. They paused at the ladders and turned to her.

Two words came clear and hard into Sally's head. *Not again.*

She waited until the drone's black rubber base was halfway on the platform. Then she rushed to the cluster of pulleys and put all her weight on an interior cable. It popped off with enough force to throw her to the ground. She heard the drone crash against the cliff and then down to its base.

Sally didn't pause to look at the wreck below or the skin that had been scraped off her knuckles. She put her hands on her grandsons' shoulders and turned them as a unit to the east, the centre of the plateau.

"Let's go," she said. ■

**Monya Baker** works for Nature and Nature Methods, where she writes about emerging technologies that help biomedical researchers to answer new kinds of questions.

JACEY



## NANOTECHNOLOGY

# The importance of being modular

DNA is the material of choice for making custom-designed, nanoscale shapes and patterns through self-assembly. A new technique revisits old ideas to enable the rapid prototyping of more than 100 such DNA shapes. [SEE LETTER P.623](#)

PAUL W. K. ROTHMUND  
& EBBE SLOTH ANDERSEN

Carpenters have been turning trees into furniture and dwellings for thousands of years, and so the discipline of wood-working features well-established techniques for joining pieces of wood to achieve a desired form. Nanotechnologists similarly try to use DNA as a material for crafting nanometre-scale shapes, but 'DNA-working' has been in development for a mere three decades. Because our picture of how DNA self-assembles is incomplete, DNA-working techniques are still evolving. The latest development is reported on page 623 of this issue, where Wei *et al.*<sup>1</sup> present a method whose intrinsic modularity enables arbitrary DNA shapes to be constructed with striking speed.

The practice of building nanoscale structures from DNA<sup>2</sup> once required creativity, intimate knowledge of DNA geometry and considerable synthetic effort. For example, in the late 1980s, the design and multistep synthesis of a 7-nanometre cube<sup>3</sup> from ten DNA strands, and its subsequent characterization, took about 2 years (N. C. Seeman, personal communication).

In 2006, DNA origami<sup>4</sup> emerged as a simple method that allows non-experts to rapidly design and synthesize complex DNA structures of approximately 100 nanometres in diameter, with reaction yields that often exceed 90%. In this technique, a single long strand of DNA is folded in one step by approximately 200 short DNA strands called staples, to create whatever shape is desired (Fig. 1a). In less than a week, one can accomplish all the steps required to make a DNA object: the computer-aided design and chemical synthesis of the staples; the formation of the object; and the final characterization of the product by atomic force microscopy (AFM). The original origami method<sup>4</sup> made only two-dimensional shapes, but was quickly extended to enable the construction of three-dimensional architectures<sup>5,6</sup> and curved geometries<sup>7,8</sup>.

Because of its modularity, DNA origami provides a general platform for arranging other nanoscale objects — from electronic components to enzymes — as required. For example, DNA has been used to make a 'pegboard' onto

which carbon nanotubes were organized into transistors<sup>9</sup>; a 'picture frame' into which individual DNA-repair enzymes were mounted so that their motion could be captured by AFM as they processed a substrate<sup>10</sup>; and a 'clamshell' that was programmed to respond to specific cancer cells *in vitro* by popping open to deliver a potentially therapeutic payload<sup>11</sup>. In each case, the pattern of components on top of the origami can be quickly and inexpensively reconfigured to perform a different task.

The modularity of DNA origami makes it a highly efficient technique for generating patterns, and its efficiency can be quantified. Let us consider how patterns might be added to a DNA origami rectangle. An experimenter can purchase a set of  $N$  staples (we'll call these 'white' staples) to fix the long strand into shape, and a second set of  $N$  'black' staples that is identical to the first except that each staple carries a special chemical group. Each white staple, and equivalently the corresponding black staple, specifies a unique position in the final rectangle. By choosing the colour of the staple for each position, a set of just  $2N$  strands can be used to create any of  $2^N$  possible black and white patterns. If the chemical group on the black staples can act as a point of attachment for a small piece of a nanowire, for example, then any of  $2^N$  possible patterns of wires can be made.

The most fundamental limitation of DNA origami is that this trick for obtaining an exponential increase in the number of patterns from a linear increase in the number of DNA strands does not generalize to shapes — for each new shape, one must design a new fold for the long strand and purchase another set of staples. Wei and colleagues' technique<sup>1</sup> dispenses with the long strand and so allows different shapes to be generated highly efficiently.

The authors' approach returns to a previously used paradigm for DNA-working, that of DNA tiles<sup>12</sup>. In their system, each tile is a single DNA strand with four different binding domains that specify which four other tiles can bind to it as neighbours. The authors' general scheme specifies a set of  $N$  tiles that self-assemble to form a rectangle, within which each tile adopts a particular position. By mixing together appropriate subsets of tiles and allowing them to self-assemble, arbitrary DNA shapes can be prepared (Fig. 1b;  $N = 310$ ).

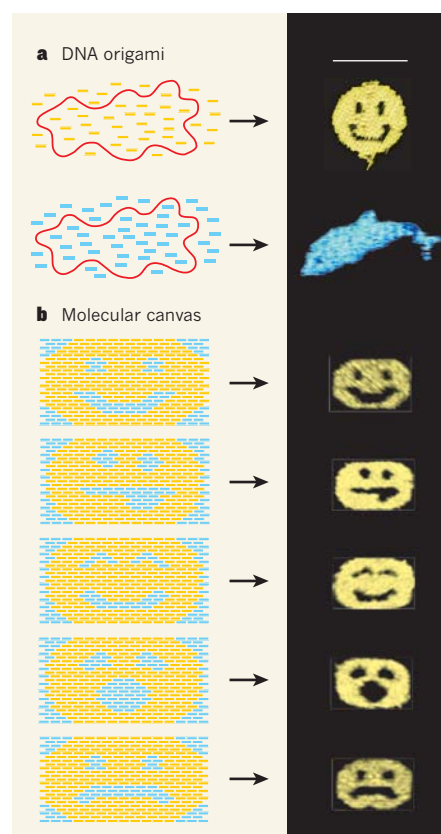


**Figure 1 | More emoticons for your money.** **a**, In DNA origami, a set of short DNA strands (known as staples) is used to fold a long strand into a shape. For each different shape, a new set of staples must be synthesized, at a cost of roughly US\$1,000. Here, a set of 237 staples (yellow; not all are shown) folds a long DNA strand (red) to create a smiley face<sup>4</sup>, whereas another completely different set of 204 staples (blue) creates a dolphin<sup>14</sup>. Scale bar, 100 nanometres; colours have been added to the micrographs of the DNA shapes on the right. **b**, In Wei and colleagues' approach<sup>1</sup> for making DNA shapes, a set of 310 different strands acts as a library of tiles that, when mixed together, self-assemble to form a rectangular molecular 'canvas'. To make any other shape, an appropriate subset of these strands is selected and mixed together — the tiles shown in yellow on the left are the subset that self-assembles into the corresponding emoticon at right. An extra set of 1,396 strands (not shown) is also required to seal the shapes' edges and prevent them from aggregating. A fixed set of 1,706 strands, costing roughly \$7,000, can therefore make an astronomical  $2^{310} = 2 \times 10^{93}$  potential shapes, such as the emoticons shown.

The DNA strands on the edges of each shape have free binding domains, which can cause the shapes to clump together. To render the edges non-sticky, the authors added edge-protector strands where necessary. Because each of the four domains on  $N$  different tiles might need to be protected, a set of  $4N$  additional strands was required. So, to access any of  $2^N$  potential shapes, the single-stranded tile technique requires just  $5N$  different strands. This efficient and modular architecture allowed Wei *et al.* to construct 107 shapes by hand, spending just a few hours on each shape. By using a robot to select and mix strands, the authors reduced the time required to make a shape to one hour. In this way, they constructed 44 shapes in about 44 hours. This advance truly brings DNA nanotechnology into the rapid-prototyping age, and enables DNA shapes to be tailored to every experiment.

Wei and colleagues' technique is the large-scale realization of a concept known as uniquely addressed tiling, which was first formally described<sup>13</sup> 12 years ago. So why is this advance happening only now? One answer is that, according to the predominant thinking about DNA self-assembly, such a technique should not work well — making the concentrations of tile strands perfectly equal is experimentally difficult, and relatively small departures from equality were expected to result in low yields of target structures. This idea followed from the common assumption that many DNA structures would begin self-assembling simultaneously, and then get stuck as partially complete shapes when tiles present at lower concentrations were exhausted. This potential problem was so compelling that DNA origami was invented expressly to avoid it. But the yields of Wei and colleagues' structures are surprisingly high: up to 40% for some shapes.

The success of the method cries out for explanation. The authors suggest that, if the nucleation of self-assembly is rare and the subsequent growth of a DNA shape is fast, then complete structures will form in preference to partial ones. Another possibility is that more-complete structures can gain strands from less-complete ones through a mechanism called Ostwald ripening, in which strands fall off less-stable structures and rejoin more-stable ones. Wei and colleagues' choice of single DNA strands as tiles — rather than the more complex, multistranded tiles used previously<sup>12</sup> — could have a crucial role, because more-complete structures might steal single strands from less-complete structures directly, without any tiles falling off, by strand displacement.

More generally, both the single-stranded-tile method<sup>1</sup> and DNA origami violate several other previous intuitions about what should and should not work. In both cases, careful studies of yields, kinetics and mechanism will be required to circumscribe the conditions under which each method works best and determine whether the single-stranded tile method will

supplant DNA origami in practical applications. Wei and colleagues' findings remind us that we are still just apprentice DNA carpenters, and will embolden others to mix hundreds of DNA strands together against prevailing wisdom. The results will probably surprise us. ■

**Paul W. K. Rothemund** is in the Departments of Bioengineering, Computer Science, and Computation & Neural Systems, California Institute of Technology, Pasadena, California 91125, USA. **Ebbe Sloth Andersen** is at the Centre for DNA Nanotechnology, Interdisciplinary Nanoscience Center, Department of Molecular Biology and Genetics, Aarhus University, 8000 Aarhus C, Denmark.  
e-mails: [pwkr@dna.caltech.edu](mailto:pwkr@dna.caltech.edu); [esa@inano.au.dk](mailto:esa@inano.au.dk)

## REGENERATIVE MEDICINE

# Reprogramming the injured heart

**When the heart is injured, the muscle does not regenerate and scars are produced. This process can be attenuated in the hearts of live mice by forcing scar-forming cells to become muscle cells. SEE ARTICLES P.593 & P.599**

NATHAN J. PALPANT & CHARLES E. MURRY

**C**ardiovascular disease remains the leading cause of death worldwide. Because of the heart's limited ability to regenerate, injuries such as myocardial infarction (heart attack) heal by scar formation rather than muscle regeneration. As a result, the heart pumps less efficiently, leading to the burgeoning epidemic of heart failure seen today. Current medical therapies support the heart with its reduced function, but scientists and clinicians are eager to learn how to regenerate damaged heart muscle. On pages 593 and 599 of this issue, Qian *et al.*<sup>1</sup> and Song *et al.*<sup>2</sup> describe how, in an effort to improve cardiac function, they have induced scar-forming cells (fibroblasts) to become muscle cells (cardiomyocytes) in the injured hearts of live mice.

The reprogramming of cells from one fate to another moved from the realm of alchemy to biochemistry after the discovery of MYOD1, a transcription factor that regulates the expression of genes involved in the development of skeletal muscle. When experimentally expressed, MYOD1 can convert many cell types into skeletal muscle *in vitro*<sup>3</sup>, as well as cells in the injured hearts of live rats<sup>4</sup>. More recently, it was found<sup>5</sup> that somatic (non-germline) cells from adult mammals could be

1. Wei, B., Dai, M. & Yin, P. *Nature* **485**, 623–626 (2012).
2. Seeman, N. C. *J. Theor. Biol.* **99**, 237–247 (1982).
3. Chen, J. & Seeman, N. C. *Nature* **350**, 631–633 (1991).
4. Rothemund, P. W. K. *Nature* **440**, 297–302 (2006).
5. Andersen, E. S. *et al.* *Nature* **459**, 73–76 (2009).
6. Douglas, S. M. *et al.* *Nature* **459**, 414–418 (2009).
7. Dietz, H., Douglas, S. M. & Shih, W. M. *Science* **325**, 725–730 (2009).
8. Han, D. *et al.* *Science* **332**, 342–346 (2011).
9. Maune, H. T. *et al.* *Nature Nanotechnol.* **5**, 61–66 (2010).
10. Endo, M., Katsuda, Y., Hidaka, K. & Sugiyama, H. *Angew. Chem. Int. Edn* **49**, 9412–9416 (2010).
11. Douglas, S. M. *et al.* *Science* **335**, 831–834 (2012).
12. Winfree, E., Liu, F., Wenzler, L. A. & Seeman, N. C. *Nature* **394**, 539–544 (1998).
13. Rothemund, P. W. K. & Winfree, E. *Proc. 32nd Annu. Symp. Theor. Comput.* 459–468 (2000).
14. Andersen, E. S. *et al.* *ACS Nano* **2**, 1213–1218 (2008).

**P.W.K.R. declares competing financial interests.**  
See [go.nature.com/tnyxm](http://go.nature.com/tnyxm) for details.

reprogrammed to become pluripotent stem cells — which can differentiate into any cell type — by expressing 'cocktails' of transcription factors. Researchers have recently used this approach to convert differentiated cells directly into other differentiated cell types such as cardiomyocytes<sup>6–10</sup>.

Qian *et al.*<sup>1</sup> and Song *et al.*<sup>2</sup> built on previous work<sup>6</sup> which showed that fibroblasts could be reprogrammed into cardiomyocytes *in vitro* by the introduction of genes coding for three transcription factors that regulate heart development (GATA4, MEF2C and TBX5). Qian *et al.* used only these three genes, whereas Song *et al.* observed better *in vitro* reprogramming efficiency by adding a fourth one, which encodes the transcription factor HAND2. In both studies, the authors induced myocardial infarction in mice by occluding a coronary artery (a blood vessel that supplies blood to heart muscle), and used retroviruses to deliver the transcription-factor genes to the injured heart. These viruses can insert genes into the chromosomes of actively dividing cells, such as scar-forming fibroblasts, but not into those of non-dividing cells such as cardiomyocytes. One month after treatment, reprogrammed cardiomyocyte-like cells comprised 2.4–6.5% of the cardiomyocytes in the region bordering the injured area (the infarct border zone) in the study by Song *et al.* and, remarkably, up to 35%



in Qian and colleagues' experiments. Moreover, in both studies, the hearts of treated mice showed improved function compared with those of control mice.

A key challenge for the authors was how to distinguish pre-existing cardiomyocytes from those derived from reprogrammed fibroblasts. To address this, both groups used mice that had been genetically manipulated so that a fluorescent protein was permanently produced only in fibroblasts and their descendants (including those that became cardiomyocytes). The specificity of this lineage-tracing technique depended on the use of certain regulatory sequences, or promoters, that had been taken from genes encoding either periostin or FSP1 — two proteins that are typically produced by fibroblasts, but not cardiomyocytes. In cells in which the promoter was active, a genetic rearrangement led to permanent activation of the gene encoding the fluorescent protein.

Such lineage-tracing approaches are state of the art, but they are not perfect. The biggest pitfall would be activation of the fibroblast promoter in pre-existing cardiomyocytes, so that these would then be mistaken for reprogrammed cells. Neither periostin nor FSP1 is specific to fibroblasts<sup>11,12</sup> (although we know of no evidence for their expression in cardiomyocytes). For these reasons, Song *et al.* carried out further experiments in which they controlled the timing of the fibroblast-marking event using a 'genetic pulse-chase' technique. They report that no cardiomyocytes were marked unless they expressed the transcription-factor cocktail. This finding enhances confidence that true reprogramming had occurred.

Interestingly, both studies found that, although some of the cells had been only partially reprogrammed, others were morphologically and functionally indistinguishable from normal cardiomyocytes. In particular, fibroblast-derived cardiomyocytes in short-term culture were able to contract when stimulated electrically and had electrochemical activities typical of this cell type, including action potentials and electrical coupling. Both research groups used non-invasive diagnostic procedures (echocardiography and magnetic resonance imaging) to identify the improved functional performance and reduced scar area of the treated mice when compared with untreated animals.

The finding of enhanced heart function is certainly important, but how is this happening, and can it be improved on? Although the authors' results suggest that the treatment generated new, functional cardiomyocytes that directly improved pump performance, it is important to remember that the reprogrammed cells constituted only a fraction of the cardiomyocytes in the infarct border zone, which is by nature ill-defined and forms only a fraction of the injured area. Can such a small number of cells directly account for a global

increase in heart function? Researchers in stem-cell therapy have encountered similarly disproportionate benefits of cellular grafts in the heart. This therefore raises the possibility that grafted or reprogrammed cells may produce growth factors, cytokines or other signalling molecules that improve the performance of pre-existing cells by enhancing blood flow or cell survival<sup>13</sup>.

Going forward, it will be necessary to validate the authors' results in independent labs using different lineage-tracing approaches, and the efficiency of cell reprogramming must be increased. Also, for clinical applications, reprogramming must be achieved without inserting the transcription-factor genes into the fibroblasts' chromosomes, to prevent complications such as malignant transformation. Moreover, are cardiomyocytes the best choice of outcome for reprogramming, or would immature progenitors of cardiomyocytes (which have greater proliferative ability) be better?

Although clinical trials are probably far off, the studies by Qian *et al.* and Song *et al.* open up a new line of investigation in cardiovascular translational medicine. If we can understand the reprogramming mechanisms correctly,

regenerative therapy might simply involve inducing the heart to reprogram its own cells after injury. ■

**Nathan J. Palpant and Charles E. Murry**  
are in the Departments of Pathology,  
Bioengineering and Medicine/Cardiology,  
Center for Cardiovascular Biology, Institute  
for Stem Cell and Regenerative Medicine,  
University of Washington School of Medicine,  
Seattle, Washington 98109, USA.  
e-mail: murry@uw.edu

1. Qian, L. *et al.* *Nature* **485**, 593–598 (2012).
2. Song, K. *et al.* *Nature* **485**, 599–604 (2012).
3. Davis, R. L., Weintraub, H. & Lassar, A. B. *Cell* **51**, 987–1000 (1987).
4. Murry, C. E., Kay, M. A., Bartosek, T., Hauschka, S. D. & Schwartz, S. M. *J. Clin. Invest.* **98**, 2209–2217 (1996).
5. Takahashi, K. & Yamanaka, S. *Cell* **126**, 663–676 (2006).
6. Ieda, M. *et al.* *Cell* **142**, 375–386 (2010).
7. Pang, Z. P. *et al.* *Nature* **476**, 220–223 (2011).
8. Vierbuchen, T. *et al.* *Nature* **463**, 1035–1041 (2010).
9. Szabo, E. *et al.* *Nature* **468**, 521–526 (2010).
10. Zhou, Q., Brown, J., Kanarek, A., Rajagopal, J. & Melton, D. A. *Nature* **455**, 627–632 (2008).
11. Sen, K. *et al.* *Am. J. Pathol.* **179**, 1756–1767 (2011).
12. Cheng, J., Wang, Y., Liang, A., Jia, L. & Du, J. *Circ. Res.* **110**, 230–240 (2012).
13. Laflamme, M. A. & Murry, C. E. *Nature* **473**, 326–335 (2011).

#### EVOLUTIONARY ANTHROPOLOGY

## Homo 'incendius'

**An analysis of microscopic and spectroscopic features of sediments deposited in a South African cave one million years ago suggests that human ancestors were using fire much earlier than had been thought.**

**RICHARD G. ROBERTS & MICHAEL I. BIRD**

**H**umans have long been captivated by the flickering flames of the campfire. But when did our ancestors first master the use of fire, and which ancient human species was the first to do so? In *Proceedings of the National Academy of Sciences*, Berna and colleagues<sup>1</sup> report that they have found fragments of burnt bone and ashed plants in one-million-year-old sediments at Wonderwerk Cave, Northern Cape province, South Africa. This evidence of fire occurs in the same sedimentary layers as Acheulian stone tools, usually considered the handiwork of *Homo erectus*. Their discovery more than doubles the accepted antiquity of the habitual use of fire by humans<sup>2,3</sup>, and highlights the benefits of using microscopic and molecular techniques to identify 'cryptic combustion' at sites of human occupation — whatever their age\*.

Controversy has dogged previous claims for the early use of fire by hominins (primates more closely related to humans than to

chimpanzees), such as australopithecines or *H. erectus*. The discovery<sup>4</sup> in the 1940s of apparently charred bones at a 3-million-year-old fossil site in South Africa inspired pioneering Australian palaeoanthropologist Raymond Dart to dub these 'proto-humans' *Australopithecus prometheus* — a new australopithecine species named after the giant in Greek mythology who stole fire from the heavens. However, chemical analysis by English palaeoanthropologist Kenneth Oakley<sup>5</sup> showed that the bones were not burnt, but coated in black oxides of iron and manganese.

Subsequent claims for early fire use have received a similarly cool reception. Some studies have suggested that australopithecines or *H. erectus* had tamed fire by 1.4 million years ago in southern and eastern Africa<sup>6,7</sup>, and that cooking has played a pivotal part in the evolution of early *Homo* species<sup>8</sup>. These proposals have been contested, however, either because the burnt remains are not in their original depositional context or because they are found at open-air sites where bush fires ignited by volcanic activity or lightning strikes cannot be ruled out. Acheulian toolmakers were using

\*This News & Views article was published online on 23 May 2012.

fire almost 800,000 years ago in Israel<sup>9</sup>, but evidence for its habitual use does not emerge until after 400,000 years ago<sup>2,3</sup>. This later date places pyrotechnology (the intentional use and control of fire) in the hands of only Neanderthals and *Homo sapiens*, leaving *H. erectus* and earlier hominins out in the cold.

The Earlier, Middle and Later Stone Age deposits inside the 140-metre-long Wonderwerk Cave have been excavated<sup>10</sup> since the 1940s. Excavation 1 — the deepest of the six in the cave — is sheltered behind a massive stalagmite (Fig. 1) and comprises 12 archaeological strata. Berna *et al.*<sup>1</sup> studied stratum 10, one of the Earlier Stone Age layers that contains Acheulian stone tools and that was deposited between 1.1 million and 1 million years ago, as indicated by measurements of radionuclides produced by cosmic rays and of magnetic polarity<sup>11,12</sup>. The authors observed that this layer also contains a variety of pyrogenic features visible to the naked eye, including bones and teeth with charred surfaces and a whitened appearance that indicates their thermal decomposition. Using a technique known as Fourier transform infrared (FTIR) spectroscopy<sup>13</sup>, the researchers found that the bones and adhering sediments had been heated to 400–700 °C. Moreover, the surfaces of many of the stone tools had dimpled, ‘pot-lid’ fractures, which are typically created at high temperatures<sup>9</sup>. But the authors’ most compelling proof of *in situ* combustion was found under the microscope and from direct chemical analysis of intact blocks of sediment.

Examination of intact sediments at the microscopic scale — the ‘micromorphology’ — provides a powerful means of investigating site formation processes and post-depositional alterations in an undisturbed context<sup>14</sup>. Micromorphological analysis has previously been used to support suggestions of fire use in Israel 400,000 years ago<sup>2</sup>, and to refute claims of similar antiquity for the ‘Peking Man’ site at Zhoukoudian in China<sup>15</sup>. These studies used FTIR spectroscopy to identify burnt materials, but Berna *et al.*<sup>1</sup> take this technique a step further by coupling micromorphology to FTIR spectra measured on burnt materials still embedded in resin-impregnated blocks of undisturbed sediment. For this purpose, they used a FTIR spectrometer attached to an infrared microscope. This analysis revealed *in situ* combustion features that are invisible to the naked eye, including abundant and well-preserved remains of ashed plants and angular fragments of burnt bone.

Berna *et al.* emphasize that extracting this ‘smoking gun’ evidence required the application of both microscopic and molecular techniques to study intact, undisturbed deposits. Their results represent a call to arms for archaeologists to make *in situ* analyses



**Figure 1 | The crucible of combustion.** View inside Wonderwerk Cave, South Africa, from the bottom of excavation 1, looking towards a massive stalagmite formed 30 metres inside the cave entrance. The photograph was taken before the deepest archaeological layer (stratum 12) had been excavated. Berna *et al.*<sup>1</sup> analysed the *in situ* remains of ashed plants and burnt bones from stratum 10, which occurs mid-profile in the section shown in the right foreground. The ghostly grid pattern in the photo is due to the string lines used to demarcate the excavation in 1-yard (approximately 0.9-metre) horizontal intervals, and their vertical projections towards the floor. (Photo courtesy of P. B. Beaumont.)

at other sites to search for cryptic traces of anthropogenic burning and to gain insight into site formation processes more generally. Complementary techniques can also be used to investigate the human history of fire use. For example, many minerals undergo structural transformation when exposed to high temperatures, and this can be recognized using established physical and chemical techniques<sup>13</sup>. The magnetic and thermoluminescent properties of sediments and stone tools can also provide records of ancient heat treatment<sup>16</sup> (thermoluminescence is the release, upon heating, of previously absorbed radiation energy as light). And the abundance and isotopic composition of pyrogenic carbon — from the macroscopic to the molecular in scale<sup>17</sup> — can help to establish combustion conditions in archaeological deposits and identify the most promising strata for further micromorphology and FTIR-microscopy investigations.

With the pyrotechnology pendulum swinging back to 1 million years ago, the fire-making credentials of *H. erectus* have begun to be restored. Widespread acceptance of controlled burning at such an early date will require the establishment of a pattern of ancient fire use at multiple sites, as observed in Europe after 400,000 years ago<sup>3</sup>. The evidence from stratum 10 at Wonderwerk Cave should ignite the search for such a pattern in Africa using *in situ* and other microanalytical techniques.

And what of stratum 12, the deepest archaeological layer in the cave? This stratum, which was deposited more than 1.4 million years ago along with Oldowan stone tools<sup>1,10–12</sup>, has been reported<sup>10</sup> to contain wood ash, charred and whitened bones, and stones with pot-lid

fractures. Berna *et al.* examined the purported ash and concluded that it is weathered rockfall and flowstone<sup>1</sup>, but work now under way on the bones and stones may yet produce further fireworks from *Homo* ‘incendius’. ■

**Richard G. Roberts** is at the Centre for Archaeological Science, University of Wollongong, Wollongong, New South Wales 2522, Australia. **Michael I. Bird** is at the Centre for Tropical Environmental and Sustainability Science, James Cook University, Cairns, Queensland 4870, Australia. e-mails: rgrob@uow.edu.au; michael.bird@jcu.edu.au

1. Berna, F. *et al.* *Proc. Natl Acad. Sci. USA* **109**, E1215–E1220 (2012).
2. Karkanas, P. *J. Hum. Evol.* **53**, 197–212 (2007).
3. Roebroeks, W. & Villa, P. *Proc. Natl Acad. Sci. USA* **108**, 5209–5214 (2011).
4. Dart, R. A. *Am. J. Phys. Anthropol.* **6**, 259–283 (1948).
5. Oakley, K. *Proc. Prehist. Soc.* **21**, 36–48 (1955).
6. Gowlett, J. A. J., Harris, J. W. K., Walton, D. & Wood, B. A. *Nature* **294**, 125–129 (1981).
7. Brain, C. K. & Sillen, A. *Nature* **336**, 464–466 (1988).
8. Wrangham, R. & Carmody, R. *Evol. Anthropol.* **19**, 187–199 (2010).
9. Goren-Inbar, N. *et al.* *Science* **304**, 725–727 (2004).
10. Beaumont, P. B. *Curr. Anthropol.* **52**, 585–595 (2011).
11. Chazan, M. *et al.* *J. Hum. Evol.* **55**, 1–11 (2008).
12. Matmon, A., Ron, H., Chazan, M., Porat, N. & Horwitz, L. K. *Geol. Soc. Am. Bull.* **124**, 611–625 (2012).
13. Weiner, S. *Microarchaeology: Beyond the Visible Archaeological Record* (Cambridge Univ. Press, 2010).
14. Goldberg, P. & Berna, F. *Quat. Int.* **214**, 56–62 (2010).
15. Weiner, S., Xu, Q., Goldberg, P., Liu, J. & Bar-Yosef, O. *Science* **281**, 251–253 (1998).
16. Brown, K. S. *et al.* *Science* **325**, 859–862 (2009).
17. Bird, M. I. & Ascough, P. L. *Org. Geochem.* **42**, 1529–1539 (2012).



## CONDENSED-MATTER PHYSICS

# Repulsive polarons found

Quasiparticles known as repulsive polarons are predicted to occur when ‘impurity’ fermionic particles interact repulsively with a fermionic environment. They have now been detected in two widely differing systems. [SEE LETTERS P.615 & P.619](#)

PETER HANNAFORD

Polarons are well known in the solid state. For example, when a charge carrier, such as an electron, is placed in a crystal lattice, the surrounding lattice ions are displaced. The electron, together with the surrounding lattice distortion, forms a quasiparticle — a polaron — that has an energy and effective mass quite different from that of a bare electron. Polarons have an important role in a wide range of exotic many-body phenomena in condensed-matter physics, including high-temperature superconductivity in copper oxide compounds and colossal magnetoresistance in rare-earth manganites<sup>1</sup>. In two papers in this issue, Kohstall *et al.*<sup>2</sup> (page 615) and Koschorreck *et al.*<sup>3</sup> (page 619) describe how they have detected an elusive form of these quasiparticles — the repulsive polaron\*.

In the case of attractive Fermi polarons, ‘impurity’ fermionic particles (particles that have half-integer spin, such as electrons) interact attractively with a Fermi ‘sea’, an environment of other fermionic particles. Such polarons were observed<sup>4,5</sup> in 2009 for ultracold fermionic lithium (<sup>6</sup>Li) impurity atoms of spin-down orientation in a Fermi sea of spin-up <sup>6</sup>Li atoms. During the past year, theoretical work<sup>6</sup> has suggested that a novel metastable quasiparticle associated with repulsive interactions,

the repulsive polaron, may also exist. The experimental realization of such a polaron was expected to be challenging, because the strong repulsive interaction between atoms trapped in a potential well also results in a weakly bound molecular state, into which the repulsively interacting atoms may rapidly decay.

In their experiments, Kohstall *et al.*<sup>2</sup> and Koschorreck *et al.*<sup>3</sup> produced well-defined repulsive polarons. Kohstall and colleagues created the repulsive polaron by immersing heavy fermionic potassium (<sup>40</sup>K) impurity atoms in a Fermi sea of light <sup>6</sup>Li atoms (Fig. 1). The authors<sup>2</sup> detected the polaron by measuring the energy excitation spectrum of the <sup>40</sup>K impurity atoms as they interacted with the surrounding <sup>6</sup>Li atoms, using radio-frequency spectroscopy, which involves flipping the orientation of the <sup>40</sup>K atoms’ spins from an initial non-interacting state to a state in which the <sup>40</sup>K atoms interact with the surrounding <sup>6</sup>Li atoms. The authors varied the magnitude and sign (attractive or repulsive) of the interaction between the <sup>40</sup>K and <sup>6</sup>Li atoms by tuning an external magnetic field across a Feshbach resonance, which occurs at a particular magnetic-field strength at which the two interacting atomic species pass through an intermediate (molecular) state in which they are weakly bound.

Meanwhile, Koschorreck *et al.*<sup>3</sup> produced

the repulsive polaron by immersing spin-down <sup>40</sup>K impurity atoms in a two-dimensional Fermi sea of spin-up <sup>40</sup>K atoms. The lower-dimensional Fermi sea was used to help stabilize the repulsive polaron. These authors also used radio-frequency spectroscopy, but in addition to determining the energy of the spin-flipped atoms, they resolved the atoms’ momentum. This allowed them to obtain an energy–momentum excitation spectrum of the system, which can be calculated from theory and can be used to study the dynamics of the polaron as it evolves.

Kohstall *et al.*<sup>2</sup> find that the <sup>40</sup>K–<sup>6</sup>Li repulsive polaron is remarkably stable against decay into an attractive polaron or into molecular states. The observed repulsive polaron has lifetimes ranging from about 0.4 milliseconds at large interaction strengths (close to the centre of the Feshbach resonance) up to about 20 milliseconds at smaller interaction strengths. The authors’ theoretical analysis<sup>2</sup> shows that the long lifetimes originate predominantly from a relatively large effective range over which the <sup>40</sup>K and <sup>6</sup>Li atoms strongly interact, which in turn arises because the Feshbach resonance for the <sup>40</sup>K–<sup>6</sup>Li system is relatively narrow (0.88 gauss). The lifetimes of the <sup>40</sup>K repulsive polaron detected by Koschorreck and colleagues<sup>3</sup> are about tenfold shorter than those of the polaron observed in the <sup>40</sup>K–<sup>6</sup>Li system.

The evidence for the existence of metastable repulsive polarons in two such widely differing fermionic systems is compelling. When the systems’ interactions were tuned to the repulsive regime, the authors<sup>2,3</sup> detected a well-defined narrow spectral peak, which is associated with the polaron, superimposed on a broad, incoherent background arising mainly from excitation of ‘continuum’ states in the Fermi sea (see, for example, Fig. 1 of the Supplementary Information to Kohstall and colleagues’ paper<sup>2</sup>). For the <sup>40</sup>K–<sup>6</sup>Li system, measurements of the polaron’s energy, lifetime, effective mass and quasiparticle residue — which quantifies how much of the non-interacting state is contained in the polaron’s wavefunction — as a function of the strength of the repulsive interaction are in excellent agreement with theory<sup>2</sup>, which takes account of the finite effective range over which the strong interaction occurs.

Now that the repulsive polaron has been observed, it will allow repulsive many-body fermionic states to be exploited in regimes that have so far been unexplored. In particular, it will be interesting to investigate the phase diagram of systems in the regime of repulsive interactions as a function of the relative concentrations of the impurity and Fermi-sea atoms, and as a function of the interaction strength and temperature. Such investigations would allow a search to be made for a predicted phase transition to itinerant ferromagnetism, which involves a phase separation of the

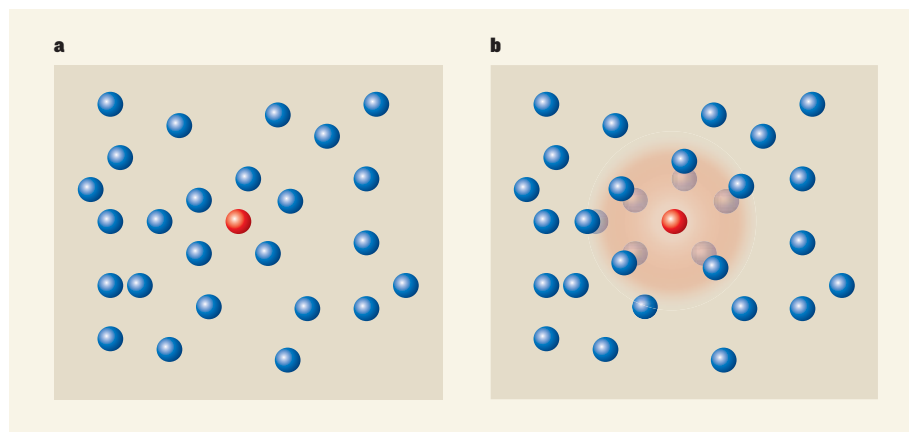


**Figure 1 | When fermionic potassium meets fermionic lithium.** **a**, Kohstall *et al.*<sup>2</sup> demonstrate a repulsive polaron by immersing a fermionic potassium <sup>40</sup>K atom (red) in an ultracold Fermi ‘sea’ of lithium <sup>6</sup>Li atoms (blue). **b**, Turning on a repulsive interaction between the two atomic species leads to the formation of the repulsive polaron, which consists of the <sup>40</sup>K atom and the surrounding <sup>6</sup>Li atoms.

\*This article and the papers<sup>2,3</sup> under discussion were published online on 23 May 2012.

atoms into spatially separated magnetic domains in which the spins of the atoms in each domain are oriented in the same direction. Itinerant ferromagnetism, which is responsible for the magnetic properties of metals such as iron, cobalt and nickel, was first proposed<sup>7</sup> almost 80 years ago, but the transition towards itinerant ferromagnetism is still not well understood and is yet to be demonstrated experimentally<sup>8</sup>.

It will also be interesting to study other impurity many-body phenomena, such as the Kondo effect<sup>9</sup>, in which magnetic impurity

atoms interact with a surrounding Fermi sea to give an anomalous enhancement of the low-temperature electrical resistance seen in a metal, and Anderson's orthogonality catastrophe<sup>10</sup>, which predicts how abruptly an impurity many-body state in a Fermi sea responds to a sudden change in the interaction. ■

**Peter Hannaford** is at the Centre for Atom Optics and Ultrafast Spectroscopy, Swinburne University of Technology, Melbourne, Victoria 3122, Australia.  
e-mail: phannaford@swin.edu.au

1. Tokura, Y. *Rep. Prog. Phys.* **69**, 797–851 (2006).
2. Kohstall, C. *et al. Nature* **485**, 615–618 (2012).
3. Koschorreck, M. *et al. Nature* **485**, 619–622 (2012).
4. Schirotzek, A., Wu, C.-H., Sommer, A. & Zwierlein, M. W. *Phys. Rev. Lett.* **102**, 230402 (2009).
5. Nascimbène, S. *et al. Phys. Rev. Lett.* **103**, 170402 (2009).
6. Massignan, P. & Bruun, G. M. *Eur. Phys. J. D* **65**, 83–89 (2011).
7. Stoner, E. *Phil. Mag.* **15**, 1018 (1933).
8. Sanner, C. *et al.* preprint at <http://arxiv.org/abs/1108.2017> (2011).
9. Kondo, J. *Prog. Theor. Phys.* **32**, 37–49 (1964).
10. Anderson, P. W. *Phys. Rev. Lett.* **18**, 1049–1051 (1967).

## IMMUNOLOGY

# Actin' dangerously

**Recognition of aberrant cell death is a crucial function of the immune system. It seems that one way in which immune cells identify damage is by sensing actin, an abundant intracellular protein.**

GORDON D. BROWN

The immune system evolved to detect not only invading microorganisms but also non-infectious damage or alterations in the body's cells, and to mobilize reparative as well as defensive responses<sup>1</sup>. Aberrant-cell death is one form of injury that is recognized as 'dangerous' by the immune system<sup>2</sup>, but how this death is sensed, and how it activates subsequent immune responses, is incompletely understood. Writing in *Immunity*, Ahrens *et al.*<sup>3</sup> and Zhang *et al.*<sup>4</sup> provide a key piece of this puzzle by demonstrating that the immune system can detect actin, a major protein component of the cytoskeleton, the cellular scaffold.

Immune cells detect both infection and damage by using pattern-recognition receptors (PRRs), which sense molecular signatures termed pathogen-associated molecular patterns (PAMPs) and damage-associated molecular patterns (DAMPs), respectively<sup>1,2</sup>. Such motifs are found, for example, in the cell walls of bacteria or in viral nucleic acids. Many PRRs, including members of the Toll-like receptor family, can recognize both DAMPs and PAMPs, and can trigger intracellular signalling pathways that culminate in inflammatory responses. More recently, another family of PRRs, the C-type lectin receptors (CLRs), has also been implicated in sensing DAMPs<sup>5</sup>. This family includes a receptor called DNCR-1 (otherwise known as CLEC9A). However, unlike other PRRs, which are expressed on many immune cells, DNCR-1 expression is limited to a small subset of a type of immune cell called dendritic cells.

Dendritic cells have pivotal roles in initiating the development of the adaptive arm of

the immune response, in which T cells mount responses against specific antigens that are recognized as being foreign or dangerous. There are many subsets of dendritic cells and those that express DNCR-1, which include CD8α<sup>+</sup> dendritic cells in mice and BDCA3<sup>+</sup> dendritic cells in humans<sup>6–8</sup>, are of particular interest

as they can drive T-cell responses to foreign antigens through a process called cross-presentation. Cross-presentation activates CD8<sup>+</sup> T cells, also called cytotoxic T cells, which are crucial for protection against tumours and viral infections.

Previous research revealed<sup>6,8</sup> that DNCR-1 can directly facilitate antigen cross-presentation and can mediate protective antitumour responses in mouse models of cancer. Shortly thereafter, it was discovered<sup>9</sup> that DNCR-1 recognizes damaged and dead (necrotic) cells and can cross-present their associated antigens. In common with other CLRs, DNCR-1 contains an intracellular domain that triggers a signalling pathway mediated by a kinase protein called Syk<sup>7,9</sup>, and both this domain and Syk are essential for DNCR-1-mediated

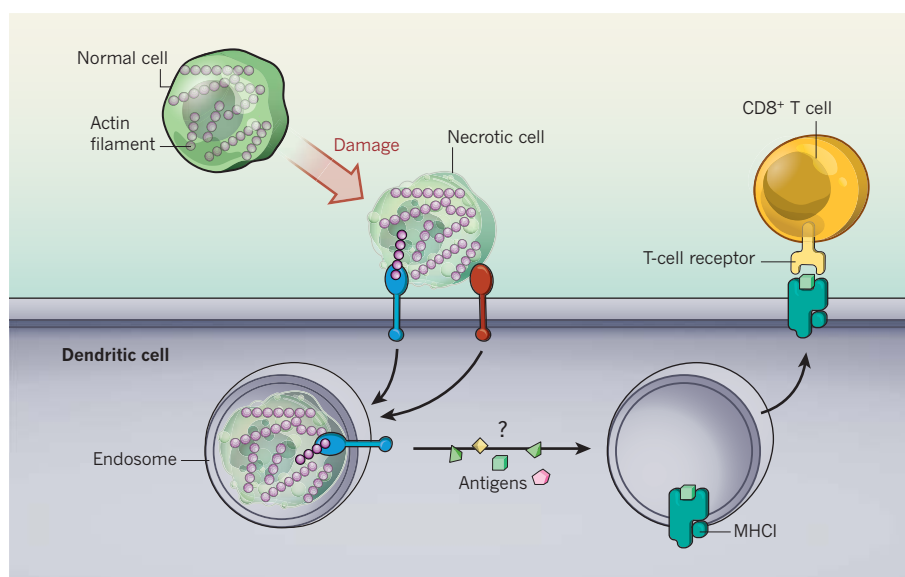


**Figure 1 | DNCR-1 recognition of filamentous actin triggers cross-presentation.** Cellular damage or aberrant (necrotic) death results in the exposure of filamentous actin, a cell structural protein. Ahrens *et al.*<sup>3</sup> and Zhang *et al.*<sup>4</sup> show that filamentous actin can be detected by a receptor, DNCR-1 (blue), that is expressed on certain types of dendritic cells of the immune system. Although the uptake of dead or damaged cells is mediated by other receptors (red) on the dendritic cell surface, it is DNCR-1 that directs this ingested cargo to a specialized intracellular compartment, the endosome. Cellular signalling pathways activated by DNCR-1 then enable small parts, or antigens, of the dead or damaged cells to be displayed on the surface of the dendritic cell by a process called cross-presentation, which has not yet been fully elucidated, but in which the antigens become attached to a molecule belonging to the MHC class I (MHC I) family of molecules. The antigen-bearing MHC I molecule is then transferred to the cell surface, where it is recognized by other immune cells — CD8<sup>+</sup> T cells — that become activated to specifically destroy cells expressing these antigens.



cross-presentation<sup>9</sup>. Surprisingly, however, DNDR-1 and Syk were found<sup>9</sup> not to be involved in the capture and engulfment of necrotic cells by the dendritic cell, implying that other cellular receptors are involved in this process.

Although it had been shown<sup>9</sup> that DNDR-1 recognizes an intracellular DAMP that is exposed only after cell damage, it was unclear exactly which structure, or ligand, DNDR-1 binds to. Ahrens *et al.*<sup>3</sup> and Zhang *et al.*<sup>4</sup> managed to identify this ligand by a nifty piece of detective work. Both groups demonstrated that the ligand can be found in cells from many species, including those of insects, suggesting that it has been conserved over a long evolutionary period. However, attempts to detect the ligand using conventional biochemical approaches proved difficult and routinely yielded cytoskeletal components, which are normally considered to be contaminants in such procedures. It was only when the researchers used microscopy to examine cells that had been stained with a soluble fluorescent probe of DNDR-1, and saw fluorescence in the same position as the actin cytoskeleton, that they realized that the ligand was likely to be a component of this structure. Indeed, both groups subsequently demonstrated that DNDR-1 recognizes filamentous actin, or F-actin — the structural form of actin found in cells — but not its monomeric form, G-actin (Fig. 1).

Actin is a highly conserved globular protein found in all cells of eukaryotes — organisms that include animals, plants and fungi. It associates with numerous actin-binding proteins and serves multiple functions ranging from maintaining cell shape to facilitating cell division. In fact, both groups<sup>3,4</sup> found that some of these actin-binding proteins, including  $\alpha$ -actinin and spectrin, enhance DNDR-1 recognition of F-actin, presumably owing to stabilization and/or formation of the actin-filament complexes. How DNDR-1 recognizes F-actin is unclear, although Zhang *et al.*<sup>4</sup> did identify a ligand-binding site on the receptor.

These discoveries have profound implications for our understanding of the mechanisms of dead-cell recognition. Arguably the most exciting insight is that the recognition of exposed F-actin in necrotic cells by DNDR-1 can directly induce antigen cross-presentation. As an abundant protein that is exposed only upon cell damage, F-actin makes an ideal DAMP. Furthermore, because actin release is known to correlate with tissue damage, it is likely that such a ubiquitous protein is also recognized by other PRRs. The ability of F-actin to drive cross-presentation of dead-cell antigens suggests that DNDR-1 could be involved in the development of certain autoimmune diseases and in immune responses to intracellular infections that cause cell damage. Indeed, DNDR-1 was recently shown<sup>10,11</sup> to be essential for mounting protective CD8<sup>+</sup> T-cell responses during cell-damaging viral infections.

These studies will also enhance our understanding of the functions of the Syk signalling pathway used by CLRs. This pathway normally activates dendritic cells, triggering them to mature and to produce inflammatory mediators, as well as inducing their ability to activate the adaptive immune system. Unexpectedly, DNDR-1 does not use the signalling pathway in this way, and is not involved in driving inflammatory responses to necrotic cells<sup>3,10</sup>. Rather, the DNDR-1 receptor seems to be responsible for diverting the necrotic-cell cargo ingested by dendritic cells to an intracellular pathway that favours cross-presentation<sup>10</sup>. Curiously, Syk-mediated signalling initiated by DNDR-1 is not required for this diversion, and yet it is essential for inducing cross-presentation<sup>10</sup> (Fig. 1). How these cellular processes fit together remains a mystery, but the identification of F-actin as the DNDR-1

ligand should help us to decipher these essential mechanisms. ■

**Gordon D. Brown** is at the Institute of Medical Sciences, University of Aberdeen, Aberdeen AB25 2ZD, UK.

e-mail: [gordon.brown@abdn.ac.uk](mailto:gordon.brown@abdn.ac.uk)

1. Rock, K. L., Lai, J. J. & Kono, H. *Immunol. Rev.* **243**, 191–205 (2011).
2. Seong, S. Y. & Matzinger, P. *Nature Rev. Immunol.* **4**, 469–478 (2004).
3. Ahrens, S. *et al. Immunity* **36**, 635–645 (2012).
4. Zhang, J. G. *et al. Immunity* **36**, 646–657 (2012).
5. Osorio, C. & Reis e Sousa, C. *Immunity* **34**, 651–664 (2011).
6. Sancho, D. *et al. J. Clin. Invest.* **118**, 2098–2110 (2008).
7. Huysamen, C. *et al. J. Biol. Chem.* **283**, 16693–16701 (2008).
8. Caminschi, I. *et al. Blood* **112**, 3264–3273 (2008).
9. Sancho, D. *et al. Nature* **458**, 899–903 (2009).
10. Zelenay, S. *et al. J. Clin. Invest.* **122**, 1615–1627 (2012).
11. Iborra, S. *et al. J. Clin. Invest.* **122**, 1628–1643 (2012).

#### CANCER METABOLISM

## Tumour friend or foe

**Elucidation of a signalling pathway that promotes tumour-cell survival during metabolic stress reveals that a protein called AMPK may both hinder and enhance cancer progression. [SEE LETTER P.661](#)**

**ROBERT U. SVENSSON & REUBEN J. SHAW**

**T**umour cells face various metabolic stresses as they arise and progress. Early-stage tumours that have not yet recruited new blood vessels to supply them with nutrients will be short of both glucose and oxygen<sup>1</sup>, and some cells face metabolic stress when they make the transition from a normal to a cancerous state and become detached from the extracellular matrix, their normal environment<sup>2</sup>. Additionally, some mutations that trigger tumour formation accelerate certain cellular metabolic programs and thereby cause stress. A protein called AMP-activated protein kinase (AMPK) is a central sensor of cellular metabolism. It is activated during situations of metabolic stress that lower the intracellular levels of ATP, a crucial energy-supplying molecule<sup>3</sup>. On page 661 of this issue, Jeon *et al.* report<sup>4</sup> a mechanism by which AMPK dictates tumour-cell survival, and the surprising implication that it may have a cancer-promoting role in some contexts.

The protein that phosphorylates and activates AMPK under conditions of metabolic stress is encoded by a gene called *LKB1*, which is classed as a tumour suppressor: mutations that inactivate this gene are among the most common causes of human lung cancer. However, the *LKB1* protein phosphorylates 12 kinase proteins in addition to AMPK, and it is not clear whether *LKB1*'s tumour-suppressor

function lies in its ability to activate AMPK, some of these other kinases, or both. What is clear is that AMPK activation influences cellular signalling pathways that are involved in cancer, such as the mTOR and p53 pathways, and inhibits the proliferation of cells in culture<sup>3,5</sup>. *LKB1*-dependent activation of AMPK also acts as a general metabolic 'rheostat': under conditions of metabolic stress, this activation directs the reprogramming of many cellular metabolic processes<sup>5–7</sup> to restore energy homeostasis, which is essential for cell survival. But it is also not known which of AMPK's target proteins are most important for this activity.

Jeon *et al.* provide compelling evidence that AMPK exerts its effect on cell survival by regulating cellular levels of NADPH, a coenzyme that is essential for many biosynthetic reactions and which helps to remove dangerous reactive oxygen species (ROS) from cells (Fig. 1). The researchers show that AMPK indirectly regulates NADPH by inhibiting the metabolic enzymes acetyl-CoA carboxylase 1 (ACC1) and ACC2, the first substrates of AMPK to be discovered<sup>8</sup>. These enzymes control both fatty-acid synthesis, a process that consumes NADPH, and fatty-acid oxidation, which leads to NADPH regeneration.

Jeon and colleagues also demonstrate that control of the ACC enzymes and NADPH by AMPK is required for the survival of glucose-deprived cells, as well as for that of cells

detached from the extracellular matrix. These data fit nicely with the findings of a previous study<sup>2</sup> that demonstrated that the survival of detached mammary epithelial cells depends on NADPH and the neutralization of cellular ROS. The new results also agree with the finding<sup>9</sup> that the death of tumour cells during glucose deprivation is reduced by AMPK activation and fatty-acid oxidation. Although Jeon and colleagues have demonstrated a major role for NADPH in AMPK-dependent survival<sup>4</sup>, improved molecular tracing methods will be needed in future studies to determine quantitatively where in a cell NADPH is produced and consumed during the various forms of metabolic stress, and the extent to which production or consumption is influenced by ACC or AMPK.

In addition to its role in conditions of low nutrient levels or cell detachment, as observed by Jeon *et al.*, AMPK may be required to maintain metabolic homeostasis in situations of deregulated, 'revved-up' metabolism that occur<sup>10</sup> in response to the activity of oncogenes — genes that promote tumorigenesis. One oncogene implicated in many human cancers is *c-MYC*, which encodes a transcription factor, MYC, that primes cells for proliferation by expanding their biosynthetic capacity and reprogramming their metabolism. A recent study<sup>10</sup> found that MYC-induced metabolic acceleration results in the activation of AMPK's function as a metabolic regulator and that AMPK and one of its related kinases (ARK5) are required for cell survival, but only under the conditions of elevated MYC levels. Another recent study<sup>11</sup> screened more than 200 metabolism-associated genes for effects on cell viability and found that a gene encoding a subunit of AMPK is one of only two genes for which decreased expression resulted in reduced survival of prostate-cancer cells, but had no effect on normal prostate cells.

This selective death of cancer cells in response to reduced AMPK begs the question of whether the protein normally has a pro-tumorigenic effect or whether it more often acts to keep cancer at bay. AMPK is known to exert antiproliferative effects by suppressing many oncogenic signalling pathways and biosynthetic processes, and it is thought to be a major mediator of the tumour-suppressive effect of LKB1 (ref. 3). So how might these previously observed anticancer effects be reconciled with the idea that AMPK function permits survival of tumour cells? Is it possible that the timing or cell-type specificity of the loss of AMPK activity is pivotal in determining whether this event halts tumours or promotes their success by 'rewiring' growth and metabolic pathways to favour cell proliferation?

This potential dual role for AMPK in tumours parallels the current view of the role of autophagy in cancer. Autophagy is a process by which cells break down and recycle their own components, and is one of the metabolic

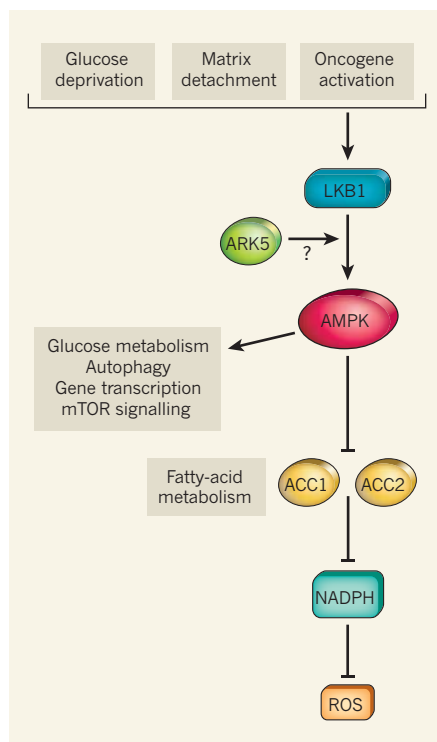


**Figure 1 | Promoting cancer-cell survival during metabolic stress.** The signalling pathway that involves the kinase proteins LKB1 and AMPK is activated in many tumour cells during conditions of metabolic stress, such as glucose deprivation and detachment from the normal extracellular matrix, and in response to the activation of some oncogenes. The pathway influences many metabolic and cancer-related processes, including glucose metabolism, autophagy, gene transcription and mTOR signalling. Jeon *et al.*<sup>4</sup> show that the pathway can promote tumour-cell survival by inhibiting two AMPK-regulated enzymes, ACC1 and ACC2, which are involved in fatty-acid metabolism. These enzymes lower cellular levels of the coenzyme NADPH, which acts to attenuate dangerous reactive oxygen species (ROS) that accumulate during metabolic stress. It has also been recently demonstrated<sup>10</sup> that the AMPK-related kinase protein ARK5 is involved in cell survival in response to activated oncogenes in some settings.

systems regulated by AMPK. In some cases, inhibition of autophagy promotes tumour initiation, but in many other contexts autophagy is needed to keep later-stage tumours alive, such that its inhibition might be expected to have an anticancer effect<sup>12</sup>. Indeed, Jeon *et al.* demonstrate that reducing LKB1 or AMPK expression in a mouse model of breast cancer significantly inhibits the growth of mammary-tumour cells, and that the presence of modified versions of ACC1 and ACC2 that cannot be phosphorylated by AMPK also leads to reduced tumour growth. Such findings suggest that these effects result from inhibition of the survival-promoting pathways that stem from ACC1 and ACC2. However, the opposite effect has been observed when *LKB1* is knocked out as an early event, including in some mouse

models in which cancer development is driven by the activation of Myc (ref. 13) or another oncogenic protein, Kras (ref. 14) — here, loss of LKB1 strongly accelerates tumour growth.

How can these paradoxical results be resolved? It is possible that cultured tumour cells have a greater need for AMPK for survival than do tumours *in vivo* because nutrients in cell culture media are exhausted more rapidly than nutrients in an intact animal. Alternatively, the difference might arise from the timing of these events, and therefore depend on whether LKB1 or AMPK is inactivated in early- or late-stage tumours. This situation might explain previous data showing<sup>15,16</sup> that LKB1- and AMPK-deficient cells are unexpectedly resistant to artificial transformation from a normal to a cancerous state *in vitro*, although this observation might also relate to altered metabolic demands in cell culture. Interestingly, another context in which AMPK activation seems to have both tumour-suppressing and tumour-promoting effects was recently reported<sup>17</sup> in melanoma cells expressing the oncogene *BRAF*.

Only time and a more thorough dissection of these possibilities in different cell types and mouse models will reveal what determines the part AMPK plays in different cancers. In the meantime, the prospect that AMPK inhibition might sensitize advanced tumour cells to chemotherapy, or even to their own deregulated metabolic demands, warrants further examination. AMPK may therefore be both friend and foe to cancer, depending on when and why it is needed. ■

**Robert U. Svensson and Reuben J. Shaw** are at the Molecular and Cell Biology Laboratory, Howard Hughes Medical Institute, The Salk Institute for Biological Studies, La Jolla, California 92037, USA.  
e-mail: shaw@salk.edu

1. Hanahan, D. & Weinberg, R. A. *Cell* **144**, 646–674 (2011).
2. Schafer, Z. T. *et al. Nature* **461**, 109–113 (2009).
3. Hardie, D. G., Ross, F. A. & Hawley, S. A. *Nature Rev. Mol. Cell Biol.* **13**, 251–262 (2012).
4. Jeon, S.-M., Chandel, N. S. & Hay, N. *Nature* **485**, 661–665 (2012).
5. Mihaylova, M. M. & Shaw, R. J. *Nature Cell Biol.* **13**, 1016–1023 (2011).
6. Egan, D. F. *et al. Science* **331**, 456–461 (2011).
7. Gwinn, D. M. *et al. Mol. Cell* **30**, 214–226 (2008).
8. Carling, D., Clarke, P. R., Zammit, V. A. & Hardie, D. G. *Eur. J. Biochem.* **186**, 129–136 (1989).
9. Buzzai, M. *et al. Oncogene* **24**, 4165–4173 (2005).
10. Liu, L. *et al. Nature* **483**, 608–612 (2012).
11. Ros, S. *et al. Cancer Discov.* **2**, 328–343 (2012).
12. Mathew, R. & White, E. *Curr. Opin. Genet. Dev.* **21**, 113–119 (2011).
13. Partanen, J. I. *et al. Proc. Natl Acad. Sci. USA* **109**, E388–E397 (2012).
14. Ji, H. *et al. Nature* **448**, 807–810 (2007).
15. Bardeesy, N. *et al. Nature* **419**, 162–167 (2002).
16. Laderoute, K. R. *et al. Mol. Cell. Biol.* **26**, 5336–5347 (2006).
17. Martin, M. J., Hayward, R., Viros, A. & Marais, R. *Cancer Discov.* **2**, 344–355 (2012).



# In vivo reprogramming of murine cardiac fibroblasts into induced cardiomyocytes

Li Qian<sup>1,2,3</sup>, Yu Huang<sup>1,2,3</sup>, C. Ian Spencer<sup>1,2,3</sup>, Amy Foley<sup>1,2,3</sup>, Vasanth Vedantham<sup>1,4,5</sup>, Lei Liu<sup>1,2,3</sup>, Simon J. Conway<sup>6</sup>, Ji-dong Fu<sup>1,2,3</sup> & Deepak Srivastava<sup>1,2,3</sup>

The reprogramming of adult cells into pluripotent cells or directly into alternative adult cell types holds great promise for regenerative medicine. We reported previously that cardiac fibroblasts, which represent 50% of the cells in the mammalian heart, can be directly reprogrammed to adult cardiomyocyte-like cells *in vitro* by the addition of Gata4, Mef2c and Tbx5 (GMT). Here we use genetic lineage tracing to show that resident non-myocytes in the murine heart can be reprogrammed into cardiomyocyte-like cells *in vivo* by local delivery of GMT after coronary ligation. Induced cardiomyocytes became binucleate, assembled sarcomeres and had cardiomyocyte-like gene expression. Analysis of single cells revealed ventricular cardiomyocyte-like action potentials, beating upon electrical stimulation, and evidence of electrical coupling. *In vivo* delivery of GMT decreased infarct size and modestly attenuated cardiac dysfunction up to 3 months after coronary ligation. Delivery of the pro-angiogenic and fibroblast-activating peptide, thymosin  $\beta$ 4, along with GMT, resulted in further improvements in scar area and cardiac function. These findings demonstrate that cardiac fibroblasts can be reprogrammed into cardiomyocyte-like cells in their native environment for potential regenerative purposes.

Heart failure affects over 14 million people worldwide and is a leading cause of death in adults and in children. Because postnatal cardiomyocytes (CMs) have little or no regenerative capacity, therapies are limited at present. The introduction of exogenous stem-cell-derived CMs holds promise, but also challenges, including delivery, integration, rejection and cellular maturation<sup>1–3</sup>. Reprogramming adult fibroblasts into induced pluripotent stem cells (iPSCs) that are similar to embryonic stem cells addresses some issues<sup>4–6</sup>, but others, including efficient directed differentiation into CMs and effective delivery, remain.

A new generation of reprogramming technology involves transdifferentiating one adult somatic cell type directly into another<sup>7–11</sup>. We reported direct reprogramming of fibroblasts into CM-like cells *in vitro* by expressing three transcription factors: Gata4, Mef2c and Tbx5 (GMT)<sup>7</sup>. As observed in reprogramming to iPSCs, the percentage of fibroblast cells fully reprogrammed to beating CMs *in vitro* was small, but far more were partially reprogrammed, much like pre-iPSCs that can become fully pluripotent with additional stimuli<sup>12</sup>. We posited that cardiac fibroblasts may reprogram more fully *in vivo* in their native environment, which might promote survival, maturation, and coupling with neighbouring cells. If so, the vast pool of cardiac fibroblasts in the heart could serve as an endogenous source of new CMs for regenerative therapy.

## Retroviral delivery of GMT *in vivo*

We used a retroviral system to express GMT, and/or dsRed as a marker, in the hearts of 2-month-old male mice by direct intramyocardial injection. After 2 days, transverse sections of the injected area were prepared and co-stained for dsRed,  $\alpha$ -actinin (a CM marker) and vimentin (enriched in fibroblasts). No markers are uniquely specific for cardiac fibroblasts, but fibroblasts are known to express vimentin and the surface markers Thy1 and DDR2 (ref. 13). At baseline, it was difficult to detect  $\alpha$ -actinin- or vimentin-positive cells that also

expressed dsRed, suggesting minimal viral uptake, and consistent with the observation that retroviruses only infect actively dividing cells<sup>14</sup>.

Fibroblasts are embryologically distinct from CMs in their origin<sup>15</sup>, and following myocardial infarction (MI) become activated, migrate to the injury site, and proliferate<sup>16,17</sup>. We induced cardiac injury by coronary artery ligation and injected dsRed retrovirus into the myocardium bordering the infarct zone. Whereas cells co-expressing dsRed and  $\alpha$ -actinin were still undetectable, many vimentin-positive cells were also positive for dsRed (Supplementary Fig. 1). By fluorescence-activated cell sorting (FACS), over 4% of cells ( $98,238 \pm 5,523$ ) from the left ventricle of injected hearts were dsRed<sup>+</sup> Thy1<sup>+</sup> 2 days after injury, suggesting successful delivery of virus into cardiac fibroblasts and possibly other non-myocytes upon injury (Fig. 1a, b). By quantitative polymerase chain reaction (qPCR), dsRed<sup>+</sup> Thy1<sup>+</sup>-sorted cells expressed about 60-fold more GMT than dsRed<sup>+</sup> Thy1<sup>+</sup> cells, and 6–8-fold more than endogenous CMs (Fig. 1c). A similar number of dsRed<sup>+</sup> Thy1<sup>+</sup> cells represented other non-myocyte cell types. Endothelial cells (PECAM<sup>+</sup>) and some perivascular cells (NG2<sup>+</sup>; also known as Cspg4) were also transduced by the retrovirus, but haematopoietic (CD34<sup>+</sup>) and pericardial (WT1<sup>+</sup>) cells were not (Supplementary Fig. 1).

## Reprogramming into induced cardiomyocytes

To determine whether new cardiomyocytes could be created *in vivo* from cells other than post-mitotic CMs, we used lineage-tracing experiments to track the origin of putative induced cardiomyocytes (iCMs). To label cells genetically, we used a mouse transgenic line that expresses Cre recombinase under the promoter of the fibroblast-enriched gene, periostin<sup>15,18,19</sup>. When intercrossed with the R26R-lacZ reporter line<sup>20</sup>, in which  $\beta$ -galactosidase is activated only in periostin-Cre-expressing cells and their progeny (Fig. 1d–f), we found  $\beta$ -galactosidase activity in many, but not all, cardiac fibroblasts and

<sup>1</sup>Gladstone Institute of Cardiovascular Disease, San Francisco, California 94158, USA. <sup>2</sup>Department of Pediatrics, University of California, San Francisco, California 94158, USA. <sup>3</sup>Department of Biochemistry and Biophysics, University of California, San Francisco, California 94158, USA. <sup>4</sup>Cardiovascular Research Institute, University of California, San Francisco, California 94158, USA. <sup>5</sup>Department of Medicine, University of California, San Francisco, California 94158, USA. <sup>6</sup>Developmental Biology and Neonatal Medicine Research Program, Indiana University School of Medicine, Indianapolis, Indiana 46202, USA.

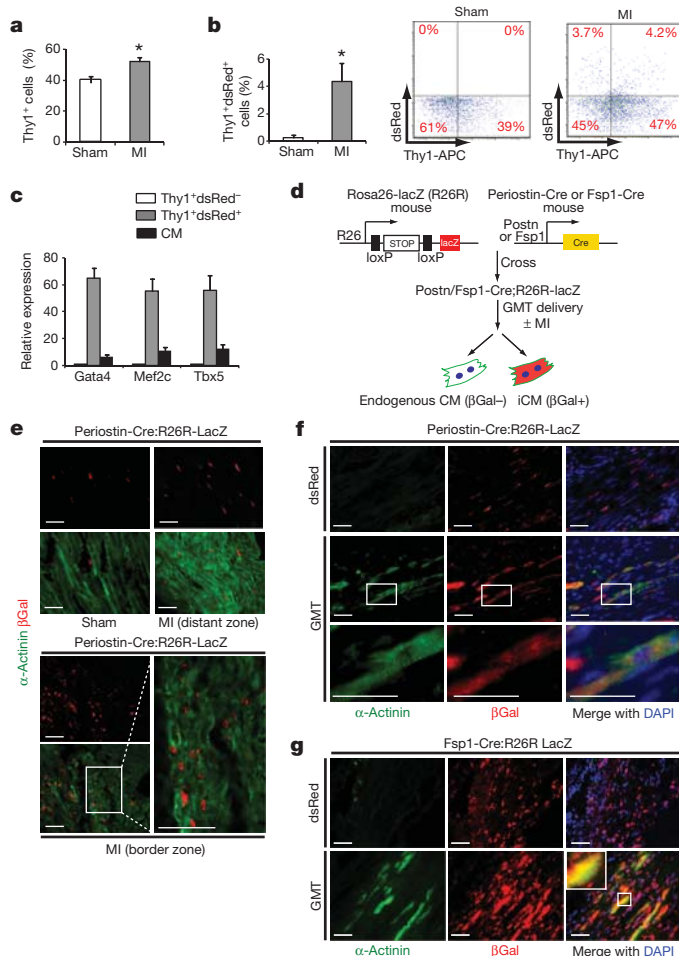


**Figure 1 | Genetic lineage tracing demonstrates *in vivo* reprogramming of cardiac fibroblasts to CM-like cells.** **a**, Quantification of FACS analyses for Thy1<sup>+</sup> cells from sham-operated mouse hearts or hearts 2 days after MI ( $n = 3$ ,  $*P < 0.05$ ). **b**, FACS analyses of Thy1<sup>+</sup> dsRed<sup>+</sup> cells from sham-operated or post-MI hearts injected with dsRed-expressing retrovirus, with quantification (left) and representative FACS plots (right) ( $n = 3$ ,  $*P < 0.05$ ). APC, allophycocyanin. **c**, qPCR analysis of Gata4, Mef2c and Tbx5 in Thy1<sup>+</sup> dsRed<sup>+</sup> cells or endogenous CMs compared to Thy1<sup>+</sup> dsRed<sup>-</sup> cells sorted 2 days after post-MI intramyocardial Gata4, Mef2c, Tbx5 and dsRed (GMTR) injection.  $n = 3$  with technical quadruplicates. **d**, Schematic diagram showing the genetic fate mapping method to trace the lineage of CMs reprogrammed from periostin-Cre:R26R-lacZ or Fsp1-Cre:R26R-lacZ cells. βGal, β-galactosidase; Postn, periostin. **e**, Immunofluorescent staining for α-actinin (green) and β-galactosidase (red) on sham-operated or post-MI periostin-Cre:R26R-lacZ mouse hearts 4 weeks post-surgery. Images are from distant or border zones where endogenous CMs were labelled by α-actinin, but were never co-localized with β-galactosidase ( $n = 5$  hearts per condition, 8 sections per heart). Scale bar, 50 μm. **f**, **g**, Immunofluorescent staining for α-actinin, β-galactosidase and DAPI in infarct areas of dsRed- or GMT-injected periostin-Cre:R26R-lacZ (f) or Fsp1-Cre:R26R-lacZ (g) mouse hearts 4 weeks after MI. Boxed areas indicate regions of magnification. Scale bar, 50 μm. Error bars indicate standard error of the mean (s.e.m.).

some endocardial and endothelial cells, as previously reported<sup>15,18,19</sup>. Periostin-Cre activity was absent in bone marrow cells (not shown). β-Galactosidase activity was not detected in any cardiomyocytes, even 4 weeks after injury, consistent with thoracic aortic banding studies, confirming that the periostin-Cre mice mark only descendants of the non-myocyte population, even after MI (Fig. 1e)<sup>15,18,19</sup>. Isolation of single CMs from these hearts confirmed the absence of β-galactosidase activity in over 1,500 CMs per heart from 6 mice.

In contrast, 4 weeks after MI and retroviral delivery of GMT, numerous β-galactosidase<sup>+</sup> cells were α-actinin<sup>+</sup> in the injured areas,

with well-formed sarcomeres and shapes similar to β-galactosidase<sup>-</sup> myocytes, suggesting that they were descendants of cells that once expressed periostin (Fig. 1f). Similar results were obtained using transgenic mice in which Cre recombinase was under the control of the fibroblast-specific protein 1 (Fsp1; also known as S100a4) promoter<sup>21</sup> to label the non-myocyte population (Fig. 1g and Supplementary Fig. 2a–f). Thus, analogous to induction of cardiac fibroblasts into skeletal muscle *in vivo* upon introduction of the skeletal muscle master regulator, MyoD<sup>22</sup>, GMT appeared to induce the formation of cardiomyocytes *in vivo*. We determined if endothelial and circulating haematopoietic cells marked by Tie2-Cre:R26R-lacZ<sup>23</sup> transgenic mice could be reprogrammed to express sarcomeric markers, but found no evidence for such an event (Supplementary Fig. 2g–i).

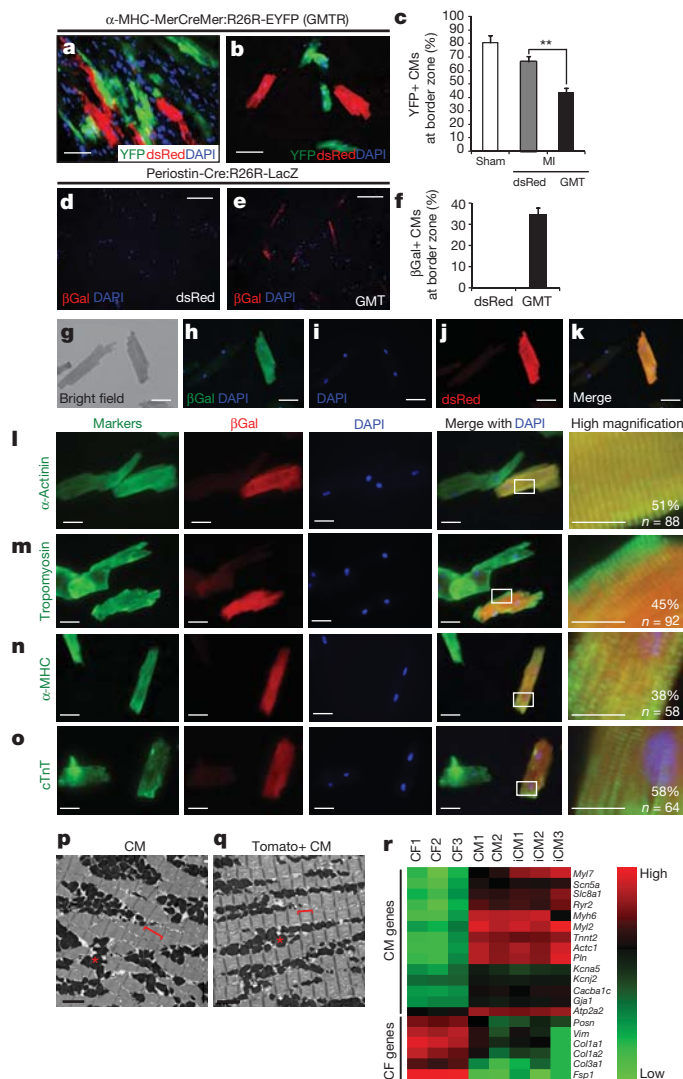
We formally tested whether retroviral introduction of GMT into non-myocytes could promote cell fusion events in the heart, thereby generating α-actinin<sup>+</sup> β-galactosidase<sup>+</sup> cells. We ‘pulse-labelled’ endogenous CMs in transgenic mice with Cre under inducible control of the α-MHC (also known as Myh6) promoter (α-MHC-MerCreMer)<sup>24</sup> crossed with R26R-EYFP mice (Supplementary Fig. 3). Subsequently, hearts were injured and infected retrovirally with GMT and dsRed to mark infected dividing cells. After 4 weeks, we detected no YFP<sup>+</sup> cells co-labelled with dsRed in the GMTdsRed- or dsRed-infected hearts (Fig. 2a, b and Supplementary Fig. 4a). Because pulse labelling marks only ~80% of endogenous CMs in the uninjured heart and ~60% in the infarct border zone<sup>25</sup>, we quantified the percentage of YFP<sup>+</sup> pulse-labelled endogenous CMs at the border area. GMT introduction resulted in a reduced percentage of YFP<sup>+</sup> endogenous CMs compared to total CMs, indicating that the CMs in this region were refreshed by new iCMs (Fig. 2c). These findings suggest that it is unlikely that cell fusion makes a major contribution to the α-actinin<sup>+</sup> β-galactosidase<sup>+</sup> cell population, although a minor contribution cannot be ruled out.

If α-actinin<sup>+</sup> β-galactosidase<sup>+</sup> cells instead resulted from cellular reprogramming, one might detect progressive stages of reprogramming over time, as cell fusion would yield mature cells soon after fusion without intermediate stages. We therefore analysed heart sections 1, 2, 3 and 4 weeks after injury and GMT infection, and classified cells into four groups based on increasing α-actinin expression and organization into sarcomeres. The number of α-actinin<sup>+</sup> β-galactosidase<sup>+</sup> cells in the infarct area increased temporally, as did the maturity of the cells, with progressive increases in the percentage of cells with well-developed sarcomeres (Supplementary Fig. 5).

To avoid false positives from overlaying cells due to the thickness of the heart sections, we isolated adult CMs at the single-cell level from the infarct/border zone of periostin-Cre:R26R-lacZ reprogrammed hearts 4 weeks after coronary ligation (Supplementary Fig. 6a). In this preparation, non-myocytes were removed, and cells were assayed 2–4 h after primary culture. No CMs isolated from dsRed-injected hearts were β-galactosidase<sup>+</sup> by immunostaining (Fig. 2d). Similarly, CMs from periostin-Cre:R26R-EYFP mice were all YFP<sup>-</sup>, among the thousands of cells visualized, in agreement with the absence of periostin-Cre activity in myocytes after injury. In contrast, 35% of cells in the CM preparation from the border/infarct zone were β-galactosidase<sup>+</sup> after GMT injection (Fig. 2e, f and Supplementary Fig. 6b). Among the β-galactosidase<sup>+</sup> cells, 98% were also α-actinin<sup>+</sup> (Supplementary Fig. 7a–d). Furthermore, in hearts co-injected with GMT and dsRed retrovirus, β-galactosidase<sup>+</sup> CMs were also positive for dsRed, indicating retroviral infection and their likely origin from non-post-mitotic CMs (Fig. 2g–k).

Most β-galactosidase<sup>+</sup> cells were large, rod-shaped and binucleated, closely resembling endogenous CMs that were β-galactosidase<sup>-</sup> from the same preparation. In addition to α-actinin, β-galactosidase<sup>+</sup> cells expressed multiple sarcomeric markers, including tropomyosin (Fig. 2m), α-MHC (Fig. 2n), and cardiac troponin T (cTnT; also known as Tnnt2) (Fig. 2o). Half of the cells had nearly normal sarcomeric structures throughout the cell. The full spectrum of reprogrammed cells, classified by quality of sarcomeric structure, is shown in





Supplementary Fig. 7. Characterization of single dsRed<sup>+</sup> YFP<sup>−</sup> cells derived from the  $\alpha$ -MHC-Mer-Cre-Mer-YFP pulse-labelled reprogrammed hearts revealed good sarcomere formation and expression of  $\alpha$ -actinin, cTnT and connexin 43 (Cx43; also known as Gja1), like dsRed<sup>−</sup> YFP<sup>+</sup> cells (Supplementary Fig. 4b).

By electron microscopy, about half of the cells from periostin-Cre:R26R-Tomato reprogrammed hearts exhibited well-organized sarcomeres and mitochondria (Fig. 2p, q), although the sarcomeres were consistently shorter than endogenous CMs and their Z-bands more diffuse. Other Tomato<sup>+</sup> cells displayed sarcomeric organization in parts of the cell and variable mitochondria organization (Supplementary Fig. 8). For simplicity, we will refer to the  $\beta$ -galactosidase<sup>+</sup>  $\alpha$ -actinin<sup>+</sup> CM-like cells as *in vivo* iCMs, based on morphology and sarcomeric structure.

Finally, we assessed the reprogramming of gene expression in iCMs by qPCR, focusing on the messenger RNA levels of 20 genes normally enriched in mature CMs or cardiac fibroblasts. We tested iCMs isolated from multiple independent hearts alongside cardiac fibroblasts and endogenous CMs. mRNA levels in iCMs were similar to CMs (Fig. 2r and Supplementary Fig. 9), including the downregulation of periostin and *Fsp1*, consistent with the morphological changes described earlier.

### *In vivo* iCMs electrically mature and couple

To determine whether iCMs expressed proteins involved in cell–cell communication similar to endogenous CMs, we examined the

expression pattern of N-cadherin, a cell-surface Ca<sup>2+</sup>-dependent adhesion molecule normally found in intercalated disks within the myocardium<sup>26</sup>. We found that over 90% of iCMs expressed N-cadherin, with 60% of cells localizing N-cadherin appropriately at the cell border (Fig. 3a). Similarly, about 90% of iCMs expressed Cx43, the major gap junction protein in the heart that promotes electrical coupling and synchronized contraction of myocytes<sup>27</sup>. Half of the iCMs expressed Cx43 at high levels with good localization relative to endogenous CMs (Fig. 3b), and in 4% of these cells, the Cx43 localization pattern was almost indistinguishable from endogenous CMs (Fig. 3b). Immunohistochemistry also revealed good cell-border localization of Cx43 in iCMs (Fig. 3c).

To assess the function of cell–cell junctions, we imaged the transfer of dyes—microinjected through patch pipettes—between cells, and measured the intercellular transmission of excitation, via Ca<sup>2+</sup> waves, in small groups of cells isolated from the reprogrammed hearts. Cascade Blue dextran (molecular weight (MW) 10,000), which is too large to pass through gap junctions, was retained in the patched iCMs (identified by the lineage marker periostin-Cre:R26R-Tomato). In contrast, calcein (MW 600) diffused to interconnected endogenous CMs (Fig. 3d). Ca<sup>2+</sup> waves propagating in an iCM or CM excited intracellular Ca<sup>2+</sup> release in neighbouring cells (Fig. 3e), suggesting that iCM–CM couplings form functional syncytia (see Supplementary Movie 1).

We next performed recordings from a single-cell suspension of CMs isolated from the border/infarct zone of periostin-Cre:R26R-EYFP mice transduced with GMT, and subsequently compared the action potentials generated by iCMs (YFP<sup>+</sup>) and endogenous CMs (YFP<sup>−</sup>) using standard patch-clamp techniques. Approximately 50% of patched iCMs had a physiological resting membrane potential (−70 mV or less) and 50% of iCMs exhibited contractions in response to electrical stimulation, similar to adult ventricular CMs, which are normally quiescent without stimulation (Fig. 3f and Supplementary Movie 2). Electrophysiology parameters assayed were similar to endogenous ventricular CMs (Fig. 3g). In agreement, intracellular

expression pattern of N-cadherin, a cell-surface Ca<sup>2+</sup>-dependent adhesion molecule normally found in intercalated disks within the myocardium<sup>26</sup>. We found that over 90% of iCMs expressed N-cadherin, with 60% of cells localizing N-cadherin appropriately at the cell border (Fig. 3a). Similarly, about 90% of iCMs expressed Cx43, the major gap junction protein in the heart that promotes electrical coupling and synchronized contraction of myocytes<sup>27</sup>. Half of the iCMs expressed Cx43 at high levels with good localization relative to endogenous CMs (Fig. 3b), and in 4% of these cells, the Cx43 localization pattern was almost indistinguishable from endogenous CMs (Fig. 3b). Immunohistochemistry also revealed good cell-border localization of Cx43 in iCMs (Fig. 3c).

To assess the function of cell–cell junctions, we imaged the transfer of dyes—microinjected through patch pipettes—between cells, and measured the intercellular transmission of excitation, via Ca<sup>2+</sup> waves, in small groups of cells isolated from the reprogrammed hearts. Cascade Blue dextran (molecular weight (MW) 10,000), which is too large to pass through gap junctions, was retained in the patched iCMs (identified by the lineage marker periostin-Cre:R26R-Tomato). In contrast, calcein (MW 600) diffused to interconnected endogenous CMs (Fig. 3d). Ca<sup>2+</sup> waves propagating in an iCM or CM excited intracellular Ca<sup>2+</sup> release in neighbouring cells (Fig. 3e), suggesting that iCM–CM couplings form functional syncytia (see Supplementary Movie 1).

We next performed recordings from a single-cell suspension of CMs isolated from the border/infarct zone of periostin-Cre:R26R-EYFP mice transduced with GMT, and subsequently compared the action potentials generated by iCMs (YFP<sup>+</sup>) and endogenous CMs (YFP<sup>−</sup>) using standard patch-clamp techniques. Approximately 50% of patched iCMs had a physiological resting membrane potential (−70 mV or less) and 50% of iCMs exhibited contractions in response to electrical stimulation, similar to adult ventricular CMs, which are normally quiescent without stimulation (Fig. 3f and Supplementary Movie 2). Electrophysiology parameters assayed were similar to endogenous ventricular CMs (Fig. 3g). In agreement, intracellular

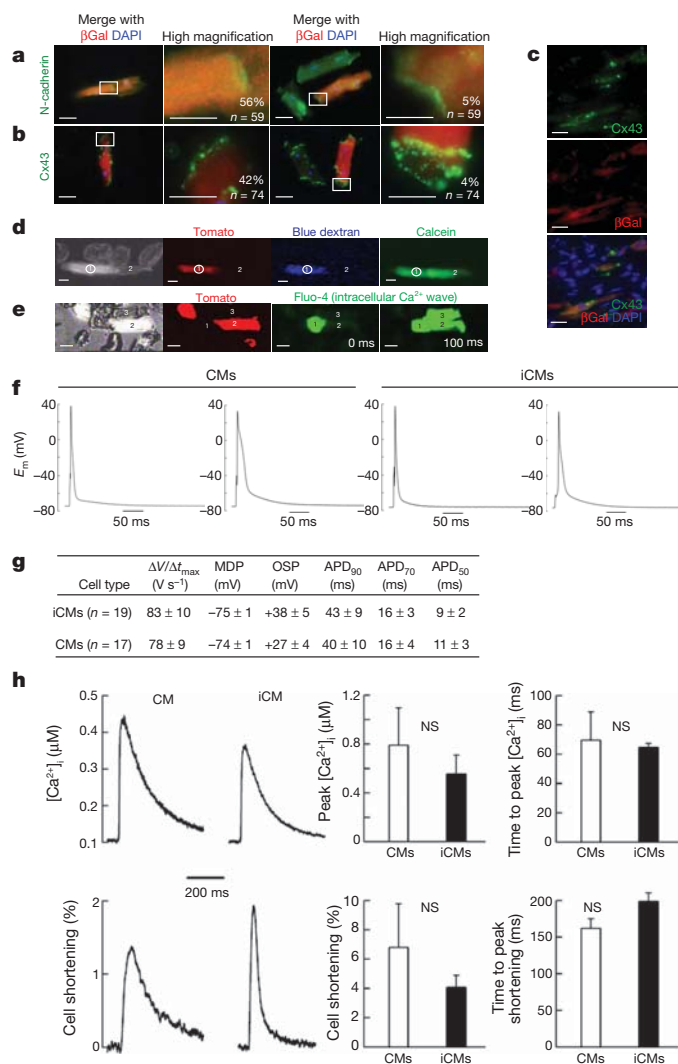


**Figure 3 | Electrophysiological properties of iCMs.** **a, b**, Immunofluorescent staining for N-cadherin (**a**) or Cx43 (**b**), co-labelled with  $\beta$ -galactosidase ( $\beta$ Gal) and DAPI in isolated CMs from periostin-Cre:R26R-lacZ hearts 4 weeks after injury. Boxed areas are shown in higher magnification with the per cent of cells having the indicated morphology. Green cells represent endogenous CMs, and red/orange cells are iCMs. **c**, Immunohistochemistry for Cx43 on sections from the infarct/border zone of periostin-Cre:R26R-lacZ hearts 4 weeks after GMT injection. Scale bar, 50  $\mu$ m in the first and third columns of **a** and **b**, and all of **c**; 20  $\mu$ m in the second and fourth columns of **a** and **b**. **d**, Representative images of two CMs in contact with one another, including an iCM (red, cell 1) and an endogenous CM (non-red, cell 2) loaded with large (dextran) or small (calcein) dye. The large blue dextran dye loaded in the iCM (cell 1) by whole-cell patch-clamp method did not travel to the CM (cell 2), but the smaller, gap-junction-permeable dye calcein did cross the cell border (n = 5). Scale bar, 50  $\mu$ m. **e**, Video frames captured from a group of myocytes, including endogenous CMs (non-red, cells 1 and 3) and an iCM (red, cell 2) imaged for Fluo-4 fluorescence transients corresponding to sarcoplasmic reticulum  $\text{Ca}^{2+}$  releases. Video frames 100 ms apart show that the  $\text{Ca}^{2+}$  release has spread throughout the myocyte group, including the iCM (n = 6). Scale bar, 50  $\mu$ m. **f**, Intracellular electrical recording of *in vivo*-derived YFP<sup>+</sup> iCMs and endogenous YFP<sup>-</sup> CMs from the same preparation.  $E_m$ , membrane potential in millivolts. **g**, Table of action potential parameters measured for CMs and iCMs, including maximum upstroke velocity ( $\Delta V/\Delta t_{\max}$ ) and minimum diastolic potential (MDP) measured immediately preceding stimulation, overshoot potential (OSP), and the APDs at 90, 70 and 50% repolarization. **h**, Characteristic single-field-stimulated intracellular calcium transients ( $[\text{Ca}^{2+}]_i$ ) recorded from endogenous (left) or induced (right) CMs. Bottom, the simultaneously recorded per cent cell shortening responses triggered by the  $\text{Ca}^{2+}$  transients, in the same two cells. Quantifications from 6 iCMs and 4 endogenous CMs are shown in the right four panels. NS, not significant. For experiments performed in **d–h**, cells were isolated from periostin-Cre:Rosa-YFP mice 8 weeks post-MI and virus transduction. Error bars indicate s.e.m.

calcium releases and cell shortening in iCMs were comparable to endogenous CMs (Fig. 3h). The distribution of action potential durations (APDs) was bimodal in iCMs and CMs, suggesting that reprogrammed cells were incorporated near the epicardial (short APD<sub>90</sub> (action potential duration at 90% of repolarization)) and endocardial (long APD<sub>90</sub>) sides of ventricular tissue (Supplementary Fig. 10).

### *In vivo* GMT improves cardiac function

Because *in vivo* reprogrammed iCMs had contractile potential and electrically coupled with viable endogenous CMs (and other iCMs), we asked whether converting endogenous non-myocytes into new myocytes translates into partial restoration of heart function after MI. All studies were performed in a blinded fashion, including the retroviral injections, and were decoded only after completion of the measurements. By Evans blue/triphenyltetrazolium chloride (TTC) double staining, the area at risk (AAR) and the infarct size were similar in GMT- or dsRed-injected mice 48 h after coronary ligation (Supplementary Fig. 11a). Three months after MI, cardiac function was examined by magnetic resonance imaging (MRI). The fraction of blood ejected with each ventricular contraction (ejection fraction), the volume of blood ejected (stroke volume), and the total cardiac output per minute were significantly improved in GMT-infected mice, particularly the stroke volume and cardiac output, possibly due to cardiac enlargement (Fig. 4a). To determine the time course of these improvements, other mice underwent serial high-resolution two-dimensional echocardiography 1 day before MI, and 3 days, 1, 4, 8 and 12 weeks after MI (Supplementary Fig. 11b–d). All mice showed a comparable

reduction in left ventricular function after coronary artery ligation (Supplementary Fig. 11c). Although different imaging approaches yield different absolute value norms, the overarching trends observed by echocardiography were similar to our MRI findings, in that functional improvements for all parameters were statistically significant 8 and 12 weeks after injection (Supplementary Fig. 11c).

We next performed qPCR to monitor the expression levels of atrial natriuretic factor, brain natriuretic peptide and tenascin C in injured and control hearts. We found that MI led to the upregulation of all three peptides, but this upregulation was attenuated in GMT-injected infarcted hearts (Fig. 4b). Expression levels of collagen genes, which were increased in dsRed-infected MI hearts, were also partially restored by injecting GMT (Fig. 4c). Furthermore, the scar area calculated from 16 sections at four levels of the heart was significantly smaller 8 weeks after MI in the GMT-treated group. To determine if the muscle cells in the scar area were reprogrammed iCMs, we repeated the experiments in periostin-Cre:R26R-LacZ transgenic mice.  $\alpha$ -Actinin<sup>+</sup> cells in the scar area were also  $\beta$ -galactosidase positive, suggesting that they were newly born iCMs of non-myocyte origin (Fig. 4e). Vascular density was significantly increased in the border zone of reprogrammed hearts at 8 weeks (Supplementary Fig. 12). Electrocardiographic (ECG) studies (telemetry) over a 24-h period did not indicate evidence for more arrhythmias in GMT- versus dsRed-injected control mice, and no mice suffered sudden death (not shown).

### Thymosin $\beta$ 4 enhances effects of GMT *in vivo*

We hypothesized that infecting more Thyl<sup>+</sup> cells would enhance functional improvement. Thymosin  $\beta$ 4, a 43-amino-acid G-actin monomer-binding protein, promotes cell migration<sup>28,29</sup>, cardiac cell survival<sup>28,30</sup> and activates epicardial cells to become more proliferative and yield more cardiac fibroblasts and endothelial cells<sup>31,32</sup>. It also improves cardiac function and decreases scar size after MI<sup>28</sup>. To test cardiac fibroblast migration, we used a cardiac explant migration assay<sup>7,28</sup>. The average time for fibroblasts to migrate from adult heart explants was 3 weeks; however, thymosin  $\beta$ 4 treatment led to equivalent fibroblast migration within 2 weeks and within only 3 days in



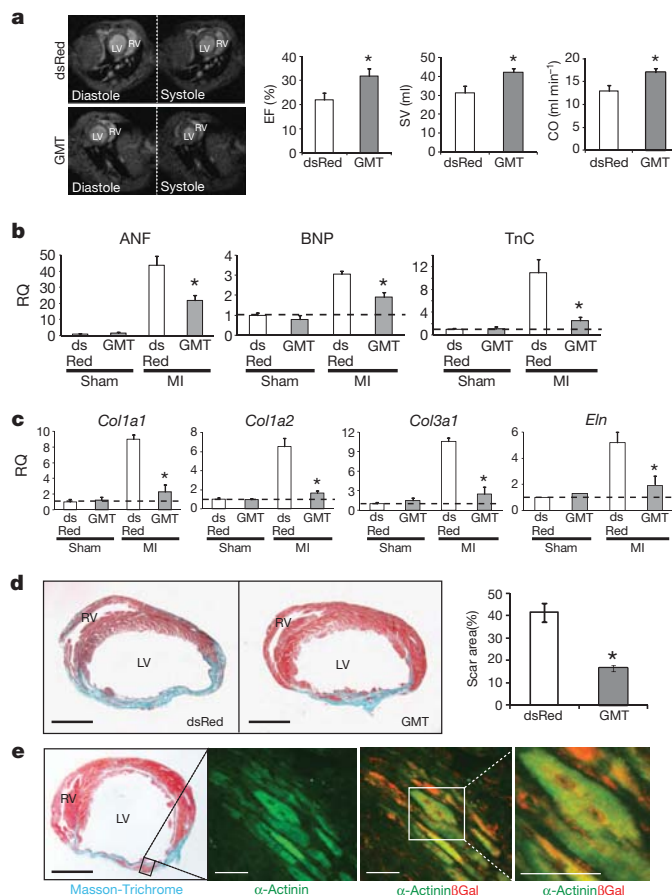


**Figure 4 | *In vivo* delivery of cardiac reprogramming factors improves cardiac function after myocardial infarction.** **a**, Ejection fraction (EF), stroke volume (SV) and cardiac output (CO) of the left ventricle were quantified by MRI 12 weeks after MI ( $n = 9$  for each group, \* $P < 0.05$ ). Left four panels show representative transverse images of the thorax, containing hearts at the end of diastole (relaxation) or systole (contraction) from dsRed- or GMT-injected mice, compared to sham-operated age- and strain-matched controls. LV, left ventricle; RV, right ventricle. **b**, qPCR of atrial natriuretic factor (ANF), brain natriuretic peptide (BNP) and tenascin (TnC) on RNA extracted from the border zone of hearts 4 weeks after MI and injection of dsRed or GMT. RQ, relative quantification. **c**, qPCR of collagen type I alpha 1 (*Col1a1*), *Col1a2*, *Col3a1* and elastin (*Eln*) on RNA extracted from the border zone of hearts 4 weeks after MI and injection of dsRed or GMT. Data in **b** and **c** are relative to dsRed-injected sham-operated mice, indicated by the dashed line.  $n = 3$  for each genotype with technical quadruplicates. \* $P < 0.05$ . **d**, Masson-Trichrome staining on heart sections 8 weeks post-MI injected with dsRed or GMT with quantification of scar size. Scale bars, 500  $\mu$ m. dsRed,  $n = 8$ ; GMT,  $n = 9$ ; \* $P < 0.05$ . **e**, Masson-Trichrome (left) and immunofluorescent staining for  $\alpha$ -actinin and/or  $\beta$ -galactosidase ( $\beta$ Gal; right) in GMT injected periostin-Cre:R26R-lacZ mouse heart 4 weeks post-surgery. Scale bars, 500  $\mu$ m in the left panel, 50  $\mu$ m in the right three panels. Error bars indicate s.e.m.

heart explants taken after MI (Supplementary Fig. 13a). Similarly, vimentin<sup>+</sup> cell proliferation was even more pronounced post-MI in the presence of thymosin  $\beta$ 4, as marked by phosphohistone H3 (Supplementary Fig. 13b). The percentage of Thyl<sup>+</sup> (Supplementary Fig. 13c) or vimentin<sup>+</sup> (Supplementary Fig. 14a) cells infected by retrovirus after MI doubled upon intramyocardial thymosin  $\beta$ 4 injection ( $316,607 \pm 17,799$  dsRed<sup>+</sup> cells averaged from three hearts). GMT did not increase the number of cardiac fibroblasts (Supplementary Fig. 13d). Delivering GMT-expressing retrovirus to more cells by adding thymosin  $\beta$ 4 yielded more  $\beta$ -galactosidase<sup>+</sup> iCMs compared to total CMs in single-cell CM culture from the infarct/border zone of periostin-Cre:R26R-lacZ hearts (51% versus 35%) (Supplementary Fig. 13e). However, we observed no change in the degree or efficiency of *in vivo* reprogramming, with the percentage of iCMs generated from

the total GMT-infected cell population remaining at  $\sim 12\%$  (Supplementary Figs 13e and 14b).

Injecting thymosin  $\beta$ 4 immediately after ligation improved cardiac function, as previously reported<sup>28,30</sup>. Co-injecting thymosin  $\beta$ 4 and GMT further improved ejection fraction and cardiac output 8 weeks after infarction (Supplementary Figs 13f and 14d, e). Furthermore, co-injecting thymosin  $\beta$ 4 and GMT caused less scarring than injecting either alone (Supplementary Fig. 13g), despite similar areas at risk and initial infarct sizes (Supplementary Fig. 14c).

## Discussion

We show that upon cardiac injury, resident cardiac non-myocytes—primarily fibroblasts—can be converted into CM-like cells *in vivo* following local delivery of GMT by retroviral-mediated gene transfer. *In vivo* cardiac reprogramming occurred with similar initial efficiency as observed *in vitro* (10–15%). However, *in vivo* iCMs were more fully reprogrammed and more closely resembled endogenous CMs than their cultured counterparts. This may result from factors within the native microenvironment—including extracellular matrix, secreted proteins, and tissue stiffness—that further enhance reprogramming. Improved cardiac function may be explained by the diversion of a small percentage of fibroblasts into new CM-like cells, suggesting functional integration of these muscle cells. Although non-myocytes convert to iCMs to help regenerate the damaged heart, alteration of fibroblast behaviour by GMT may contribute to the effects on scar formation and cardiac function. Although it is difficult to separate the relative contributions of new muscle formation and other non-cell-autonomous effects, non-myocyte reprogramming in the heart appears to be beneficial for cardiac function. Optimizing gene delivery to more cells would probably enhance functional benefits.

Improvement upon thymosin  $\beta$ 4 addition is in agreement with the notion that increasing the delivery of GMT to more cells could enhance cardiac repair. Pre-treating hearts with thymosin  $\beta$ 4 several days before injury resulted in a small population of epicardial-derived cells that could behave as myocyte precursors, but not if thymosin  $\beta$ 4 was given at the time of injury<sup>33</sup>. Nevertheless, transduction of GMT into these progenitors, or other rare progenitors yet to be identified, might promote their differentiation into cardiomyocytes. Because thymosin  $\beta$ 4 is also pro-angiogenic<sup>31,32</sup>, the cooperativity between GMT and thymosin  $\beta$ 4 may be multifaceted and will be interesting to explore.

The ability to regenerate adult heart tissue from endogenous cells is a promising approach to treating cardiac disease that may face fewer obstacles to clinical translation than other approaches. Improving the delivery of reprogramming factors, using small molecules and epigenetic modulators, and conducting trials in large animals will be important to refine the technology and assess its safety and efficacy, particularly regarding arrhythmias.

## METHODS SUMMARY

**Retroviruses.** Retroviruses were generated as described<sup>7</sup> using pMXs retroviral vectors containing coding regions of Gata4, Mef2c, Tbx5 and dsRed. Ultra-high titre virus ( $>1 \times 10^{10}$  plaque-forming units (p.f.u.) per ml) was obtained by ultracentrifugation.

**Animals, surgery, echocardiography and electrocardiography.** Periostin-Cre:R26R-lacZ or Fsp1-Cre:R26R-lacZ mice were obtained by crossing periostin-Cre mice<sup>19</sup> or Fsp1-Cre mice<sup>21</sup> and R26R-lacZ mice<sup>20</sup>. Periostin-Cre:R26R-EYFP or  $\alpha$ -MHC-MerCreMer:R26R-EYFP mice were obtained by crossing periostin-Cre or  $\alpha$ -MHC-MerCreMer<sup>24</sup> mice and R26R-EYFP mice. Periostin-Cre:R26R-Tomato mice were obtained by crossing periostin-Cre mice and R26R-Tomato mice. Surgeries and subsequent analyses were performed blinded to genotype and intervention. MI was induced by permanent ligation of the left anterior descending artery (LAD) as described<sup>34</sup>. A pool of concentrated virus (GMT or GMT-R) was mixed, and 10  $\mu$ l of mixed virus plus 10  $\mu$ l of PBS or 40 ng  $\mu$ l<sup>-1</sup> thymosin  $\beta$ 4 were injected along the boundary between the infarct and border zones. Mouse echocardiography and surface electrocardiography were performed as described<sup>34</sup>. All mouse work was done with the approval of the University of California, San Francisco (UCSF) animal care oversight committee.

**Immunohistochemistry, immunocytochemistry and electron microscopy.** Immunohistochemistry, immunocytochemistry and electron microscopy were performed as described<sup>34,35</sup>. Scar size was determined by Masson-Trichrome staining<sup>28,34</sup>. The AAR and myocardial infarct size were determined by Evans blue/TTC labelling<sup>34</sup>.

**Cardiomyocyte isolation, patch-clamp, and fibroblast migration assays.** Adult cardiomyocytes were isolated as described with minor modifications<sup>36</sup>. Single-cell patch-clamp recordings were performed as described<sup>37</sup>. Migration assays were performed according to published protocols<sup>7,28</sup>.

**FACS and quantitative RT-PCR.** Dissociated cardiac cells were stained with APC-conjugated anti-Thy1 antibody (eBioscience). Stained cells were sorted by FACSARIA2 (BD) and RNA extracted in TRIzol (Invitrogen). qPCR was performed using ABI 7900HT (TaqMan, Applied Biosystems).

**Statistics.** Differences between groups were examined for statistical significance using unpaired Student's *t*-tests or ANOVA. *P* < 0.05 was regarded as significant.

**Full Methods** and any associated references are available in the online version of the paper at [www.nature.com/nature](http://www.nature.com/nature).

Received 22 March 2011; accepted 14 March 2012.

Published online 18 April 2012.

- Murry, C. E. & Keller, G. Differentiation of embryonic stem cells to clinically relevant populations: lessons from embryonic development. *Cell* **132**, 661–680 (2008).
- Passier, R., van Laake, L. W. & Mummery, C. L. Stem-cell-based therapy and lessons from the heart. *Nature* **453**, 322–329 (2008).
- Srivastava, D. & Ivey, K. N. Potential of stem-cell-based therapies for heart disease. *Nature* **441**, 1097–1099 (2006).
- Takahashi, K. & Yamanaka, S. Induction of pluripotent stem cells from mouse embryonic and adult fibroblast cultures by defined factors. *Cell* **126**, 663–676 (2006).
- Takahashi, K. *et al.* Induction of pluripotent stem cells from adult human fibroblasts by defined factors. *Cell* **131**, 861–872 (2007).
- Yamanaka, S. & Blau, H. M. Nuclear reprogramming to a pluripotent state by three approaches. *Nature* **465**, 704–712 (2010).
- Ieda, M. *et al.* Direct reprogramming of fibroblasts into functional cardiomyocytes by defined factors. *Cell* **142**, 375–386 (2010).
- Szabo, E. *et al.* Direct conversion of human fibroblasts to multilineage blood progenitors. *Nature* **468**, 521–526 (2010).
- Vierbuchen, T. *et al.* Direct conversion of fibroblasts to functional neurons by defined factors. *Nature* **463**, 1035–1041 (2010).
- Zhou, Q., Brown, J., Kanarek, A., Rajagopal, J. & Melton, D. A. *In vivo* reprogramming of adult pancreatic exocrine cells to  $\beta$ -cells. *Nature* **455**, 627–632 (2008).
- Huang, P. *et al.* Induction of functional hepatocyte-like cells from mouse fibroblasts by defined factors. *Nature* **475**, 386–389 (2011).
- Silva, J. *et al.* Promotion of reprogramming to ground state pluripotency by signal inhibition. *PLoS Biol.* **6**, e253 (2008).
- Ieda, M. *et al.* Cardiac fibroblasts regulate myocardial proliferation through  $\beta$ 1 integrin signaling. *Dev. Cell* **16**, 233–244 (2009).
- Byun, J. *et al.* Myocardial injury-induced fibroblast proliferation facilitates retroviral-mediated gene transfer to the rat heart *in vivo*. *J. Gene Med.* **2**, 2–10 (2000).
- Snider, P. *et al.* Origin of cardiac fibroblasts and the role of periostin. *Circ. Res.* **105**, 934–947 (2009).
- Baudino, T. A., Carver, W., Giles, W. & Borg, T. K. Cardiac fibroblasts: friend or foe? *Am. J. Physiol. Heart Circ. Physiol.* **291**, H1015–H1026 (2006).
- Camelliti, P., Borg, T. K. & Kohl, P. Structural and functional characterisation of cardiac fibroblasts. *Cardiovasc. Res.* **65**, 40–51 (2005).
- Snider, P. *et al.* Periostin is required for maturation and extracellular matrix stabilization of noncardiomyocyte lineages of the heart. *Circ. Res.* **102**, 752–760 (2008).
- Takeda, N. *et al.* Cardiac fibroblasts are essential for the adaptive response of the murine heart to pressure overload. *J. Clin. Invest.* **120**, 254–265 (2010).
- Soriano, P. Generalized lacZ expression with the ROSA26 Cre reporter strain. *Nature Genet.* **21**, 70–71 (1999).
- Bhowmick, N. A. *et al.* TGF- $\beta$  signaling in fibroblasts modulates the oncogenic potential of adjacent epithelia. *Science* **303**, 848–851 (2004).
- Murry, C. E., Kay, M. A., Bartosek, T., Hauschka, S. D. & Schwartz, S. M. Muscle differentiation during repair of myocardial necrosis in rats via gene transfer with MyoD. *J. Clin. Invest.* **98**, 2209–2217 (1996).
- Kisanuki, Y. Y. *et al.* Tie2-Cre transgenic mice: A new model for endothelial cell-lineage analysis *in vivo*. *Dev. Biol.* **230**, 230–242 (2001).
- Sohal, D. S. *et al.* Temporally regulated and tissue-specific gene manipulations in the adult and embryonic heart using a tamoxifen-inducible Cre protein. *Circ. Res.* **89**, 20–25 (2001).
- Hsieh, P. C. *et al.* Evidence from a genetic fate-mapping study that stem cells refresh adult mammalian cardiomyocytes after injury. *Nature Med.* **13**, 970–974 (2007).
- Li, J. *et al.* Cardiac-specific loss of N-cadherin leads to alteration in connexins with conduction slowing and arrhythmogenesis. *Circ. Res.* **97**, 474–481 (2005).
- Saffitz, J. E., Laing, J. G. & Yamada, K. A. Connexin expression and turnover: implications for cardiac excitability. *Circ. Res.* **86**, 723–728 (2000).
- Bock-Marquette, I., Saxena, A., White, M. D., Dimaio, J. M. & Srivastava, D. Thymosin  $\beta$ 4 activates integrin-linked kinase and promotes cardiac cell migration, survival and cardiac repair. *Nature* **432**, 466–472 (2004).
- Goldstein, A. L., Hannappel, E. & Kleinman, H. K. Thymosin  $\beta$ 4: actin-sequestering protein moonlights to repair injured tissues. *Trends Mol. Med.* **11**, 421–429 (2005).
- Hinkel, R. *et al.* Thymosin  $\beta$ 4 is an essential paracrine factor of embryonic endothelial progenitor cell-mediated cardioprotection. *Circulation* **117**, 2232–2240 (2008).
- Smart, N. *et al.* Thymosin  $\beta$ 4 induces adult epicardial progenitor mobilization and neovascularization. *Nature* **445**, 177–182 (2007).
- Bock-Marquette, I. *et al.* Thymosin  $\beta$ 4 mediated PKC activation is essential to initiate the embryonic coronary developmental program and epicardial progenitor cell activation in adult mice *in vivo*. *J. Mol. Cell. Cardiol.* **46**, 728–738 (2009).
- Smart, N. *et al.* *De novo* cardiomyocytes from within the activated adult heart after injury. *Nature* **474**, 640–644 (2011).
- Qian, L. *et al.* miR-24 inhibits apoptosis and represses Bim in mouse cardiomyocytes. *J. Exp. Med.* **208**, 549 (2011).
- Larsen, T. H., Saetersdal, T. & Grong, K. The ultrastructure of the myocyte in different regions of experimental infarcts in the cat heart. *Res. Exp. Med. (Berl.)* **186**, 295–306 (1986).
- Xu, H., Guo, W. & Nerbonne, J. M. Four kinetically distinct depolarization-activated  $K^+$  currents in adult mouse ventricular myocytes. *J. Gen. Physiol.* **113**, 661–678 (1999).
- Fenske, S. *et al.* HCN3 contributes to the ventricular action potential waveform in the murine heart. *Circ. Res.* **109**, 1015–1023 (2011).

**Supplementary Information** is linked to the online version of the paper at [www.nature.com/nature](http://www.nature.com/nature).

**Acknowledgements** We are grateful for technical assistance from the Gladstone Histology Core (C. Miller), Gladstone Genomics Core (L. Ta, Y. Hao, B. Chadwick), UCSF MRI Core (M. Wendland, J. Hawkins) and Laboratory for Cell Analysis at UCSF (S. Elmes). We thank all the members of the Srivastava laboratory for helpful discussions; G. Howard and B. Taylor for editorial help; and B. Bruneau and B. Conklin for helpful discussions and critical reviews of the manuscript. We also thank J. Nerbonne, N. Foeger, and members of the Nerbonne laboratory for assistance with the adult myocyte isolation protocol. L.Q. is a postdoctoral scholar of the California Institute for Regenerative Medicine (CIRM). V.V. is supported by grants from the GlaxoSmithKline Research and Education Foundation and the NIH/NHLBI (K08HL101989). J.-d.F. is supported by a postdoctoral fellowship from American Heart Association. S.J.C. was supported by R01 HL060714 from NHLBI/NIH. D.S. was supported by grants from NHLBI/NIH, CIRM, the Younger Family Foundation, Roddenberry Foundation and the L.K. Whittier Foundation. This work was supported by NIH/NCRR grant (C06 RR018928) to the Gladstone Institutes.

**Author Contributions** L.Q. designed, supervised and performed the experiments. Y.H. performed all surgeries, echoes and ECGs, and contributed to tissue sectioning and sample preparation. C.I.S. performed all cellular electrophysiology experiments. A.F. quantified scar size and induced CMs and helped with mouse colony maintenance. V.V. helped with isolation of adult CMs and implantation of transmitters. S.J.C. provided periostin-Cre:Rosa26-lacZ mice and supplemental data. J.-d.F. provided initial reagents and technical knowledge and helpful discussion. D.S. designed and supervised the work. L.Q. and D.S. wrote the manuscript.

**Author Information** Reprints and permissions information is available at [www.nature.com/reprints](http://www.nature.com/reprints). The authors declare competing financial interests: details accompany the full-text HTML version of the paper at [www.nature.com/nature](http://www.nature.com/nature). Readers are welcome to comment on the online version of this article at [www.nature.com/nature](http://www.nature.com/nature). Correspondence and requests for materials should be addressed to D.S. ([dsrivastava@gladstone.ucsf.edu](mailto:dsrivastava@gladstone.ucsf.edu)).



## METHODS

**Retrovirus generation, concentration, and titration.** Retroviruses were generated as described<sup>7</sup>. To generate virus, pMXs retroviral vectors containing the coding regions of Gata4, Mef2c, Tbx5 and dsRed were transfected into Plat-E cells using Eugene 6 (Roche). Forty-eight hours after transfection, virus-containing supernatants were collected and concentrated by standard ultracentrifugation. Retroviral titration was performed using the Retro-X qRT-PCR Titration Kit (Clontech), as per the manufacturer's protocols. Ultra-high titre virus ( $>1 \times 10^{10}$  plaque-forming units (p.f.u.) per ml) was resuspended in PBS. After verification of high transduction efficiency in cell culture ( $>95\%$ ), a large number of small stock aliquots (10  $\mu$ l) were made and frozen at  $-80^\circ\text{C}$  to ensure consistency among experiments. After one freeze-thaw cycle, titrations were repeated to ensure that active virus was maintained at the desired  $1 \times 10^{10}$  p.f.u. concentration for *in vivo* injection.

**Mouse lines.** Periostin (Postn)-Cre:R26R-lacZ mice were obtained by crossing Postn-Cre mice and Rosa26-lacZ mice. Postn-Cre:R26R-YFP mice were obtained by crossing Postn-Cre mice and Rosa26-EYFP mice, and Postn-Cre:R26R-Tomato mice were obtained by crossing Postn-Cre mice and Rosa26-Tomato mice. All transgenic lines for immunohistochemistry and single cell isolation were maintained by crossing with C57BL/6 mice (Charles River). BALB/C mice (Charles River) were used for all functional studies after permanent ligation of the left anterior descending artery (LAD) and virus injection. Fsp1-Cre, Tie2-Cre and Myh6-MerCreMer mice were obtained from Jackson Labs, and lines were validated before further breeding. Fsp1-R26R, Tie2-R26R and Myh6-MerCreMer-YFP mice were obtained by crossing Fsp1-Cre, Tie2-Cre or Myh6-MerCreMer mice to R26R-lacZ or R26R-EYFP mice. Efficiency of Cre recombination induction for Myh6-MerCreMerYFP was tested by immunohistochemistry for YFP after injection of various doses of tamoxifen. To pulse label the pre-existing CMs, adult Myh6-MerCreMerYFP mice (8–12-weeks old) were treated with tamoxifen (Sigma) by intraperitoneal injection once a day for 5 days at a dosage of  $20 \text{ mg kg}^{-1} \text{ day}^{-1}$ . GMT delivery and coronary artery ligation were performed 2 days afterwards.

**Mouse MI model and *in vivo* delivery.** The animal protocol for surgery was approved by institutional guidelines (UCSF Institutional Animal Care and Use Committee). All surgeries and subsequent analyses were performed blinded for genotype and intervention. Mice were anaesthetized with 2.4% isoflurane/97.6% oxygen and placed in a supine position on a heating pad ( $37^\circ\text{C}$ ). Animals were intubated with a 19 G stump needle and ventilated with room air using a MiniVent Type 845 mouse ventilator (Hugo Sachs Elektronik-Harvard Apparatus; stroke volume, 250  $\mu$ l; respiratory rate, 120 breaths per minute). MI was induced by permanent ligation of the LAD with a 7-0 prolene suture as described<sup>28</sup>. Sham-operated animals served as surgical controls and were subjected to the same procedures as the experimental animals with the exception that the LAD was not ligated. A pool of concentrated virus (GMT, or GMTR) was mixed, and 10  $\mu$ l of mixed virus plus 10  $\mu$ l of PBS or 40 ng  $\mu$ l<sup>-1</sup> thymosin  $\beta$ 4 was injected into the myocardium through an insulin syringe with an incorporated 29 G needle (BD). Injection with a full dosage was carried out along the boundary between the infarct zone and border zone based on the blanched infarct area after coronary artery occlusion. After injection, the chest was closed with sutures and the mouse was allowed to recover with the mouse ventilator and heating pad. All surgical procedures were performed under aseptic conditions. At 2 days and 1, 2, 4, 8 and 12 weeks after occlusion and viral delivery, the hearts were removed for perfusion fix in 4% paraformaldehyde (PFA) for preparation of paraffin sections for structural analysis and immunohistochemistry or in 0.5% PFA in 5% sucrose followed by cryostat sectioning for immunofluorescent staining. Concurrently, heart tissues within the infarct zone, border zone and non-ischaemic zone distal to the infarct zone were dissected for RNA or protein isolation.

**Determination of the AAR and MI size.** At 48 h after coronary ligation, the mice were anaesthetized and cannulated with tubing. Evans blue (2%, Sigma) was perfused into the aorta, thus all myocardial tissue was stained blue except the AAR. The left ventricle was isolated and cut into four  $\sim 1 \text{ mm}$  pieces with the first cut at the ligation level. Left ventricle slices were stained in 1.5% TTC for 30 min at  $37^\circ\text{C}$ , and then fixed in 4% PFA overnight at  $4^\circ\text{C}$ . The area of infarction was demarcated as a white area, whereas viable myocardium was stained red. Photographs were taken from both sides of each section. The AAR and the infarct area were determined via planimetry with the computer software ImagePro (Biorad). Infarct size was calculated as the percentage of MI compared with the AAR using the described methodology<sup>28</sup>.

**Determination of scar size.** Standard Masson-Trichrome staining was performed on hearts 8 weeks post-viral delivery and coronary artery ligation. To determine the scar size, we used ImagePro software to measure the scar area (blue) and healthy area (red) on transverse sections spanning four levels (50 mm between two levels, with the first level starting right below the ligation) within the left ventricle of a MI heart. From each level, we measured four slices of

tissues as technical quadruplicates (for a total of 16 sections). The averaged number was used for statistics and comparison. The measurements and calculations were conducted in a blinded manner.

**Mouse echocardiography.** Echocardiography was performed by the Vevo 770 High-Resolution Micro-Imaging System (VisualSonics) with a 15-MHz linear array ultrasound transducer. The left ventricle was assessed in both parasternal long-axis and short-axis views at a frame rate of 120 Hz. End-systole or end-diastole was defined as the phase in which the smallest or largest area of the left ventricle, respectively, was obtained and used for ejection fraction measurement. Left ventricular end-systolic diameter and left ventricular end-diastolic diameter were measured from the left ventricular M-mode tracing with a sweep speed of  $50 \text{ mm s}^{-1}$  at the papillary muscle level for calculating the shortening fraction. B-mode was used for two-dimensional measurements of end-systolic and end-diastolic dimensions.

**Mouse surface electrocardiography.** Mice were anaesthetized with 1.75% isoflurane at a core temperature of  $37\text{--}38^\circ\text{C}$ . Four needle electrodes (AD Instruments) were placed subcutaneously in standard limb lead configurations. For each mouse, 10–20 s of continuous signals were sampled at 10 kHz in each lead configuration with a PowerLab4/30 interface (AD Instruments). Data analysis was performed offline with electronic calipers on averaged beats (Chart5Pro v5.4.2, AD Instruments).

**Mouse awake electrocardiography.** To record awake electrocardiograms in six reprogrammed post-MI mice and six control post-MI mice, transmitters were surgically implanted according to the manufacturer's instructions (Data Sciences International). After a 3-day recovery period, the electrocardiogram was recorded continuously for 48 h in each mouse. Tracings were analysed off-line and were scored by a blinded investigator for the presence and frequency of arrhythmias.

**MRI.** MRI was performed on a Varian DirectDrive 7T small-animal scanner. Each mouse was anaesthetized by inhalation of 2% isoflurane/98% oxygen administered via an MR-compatible mobile inhalation anaesthesia system (Vet Equip). The mice were put in supine position on a homemade heating bed to keep the temperature at  $37^\circ\text{C}$ . Two ECG leads were inserted into the right front and left rear leg. ECG waveforms were monitored with a small animal monitoring and gating system (SA instruments). The mouse was then placed into a homemade 1H birdcage coil with an inner diameter of 32 mm. A group of ECG- (R-wave rising edge) triggered spin echo scout images were acquired first to define the oblique plane of the short axis. Then an ECG-triggered two-dimensional gradient echo sequence with an echo time of 2.75 ms, repetition time of 200 ms and a flip angle of  $45^\circ$  was used to obtain nine short-axis images at 12 or 13 phases per cardiac cycle. Each scan consisted of 8–9 contiguous slices spanning the left ventricle from apex to base with 1-mm thickness, a matrix size of  $128 \times 128$ , a field of view of  $25.6 \times 25.6 \text{ mm}$ , and four averages.

**Isolation of adult CMs.** Adult CM isolation was performed as described with minor modifications<sup>36</sup>. Briefly, adult mice were anaesthetized with isoflurane and mechanically ventilated. Hearts were removed and perfused retrogradely via aortic cannulation with a constant flow of  $3 \text{ ml min}^{-1}$  in a Langendorff apparatus. Hearts were perfused at  $37^\circ\text{C}$  for 5 min with supplemented Wittenberg Isolation Medium (WIM) containing (in mM): 116 NaCl, 5.4 KCl, 6.7  $\text{MgCl}_2$ , 12 glucose, 2 glutamine, 3.5  $\text{NaHCO}_3$ , 1.5  $\text{KH}_2\text{PO}_4$ , 1.0  $\text{NaH}_2\text{PO}_4$ , 21 HEPES, with 1.5 nM insulin, essential vitamins (GIBCO), and essential amino acids (GIBCO) (pH 7.4), followed by digestion solution (WIM, supplemented with  $0.8 \text{ mg ml}^{-1}$  collagenase II and  $10 \mu\text{M}$   $\text{CaCl}_2$ ) for 10 min (4 min for paired CMs that were used in cell–cell coupling experiments). Hearts were then removed from the Langendorff apparatus while intact (with tissues loosely connected). Desired areas (that is, border/infarct zone) were then micro-dissected under the microscope, followed by mechanical dissociation, triturating, and resuspension in a low-calcium solution (WIM, supplemented with  $5 \text{ mg ml}^{-1}$  BSA, 10 mM taurine, and  $150 \mu\text{M}$   $\text{CaCl}_2$ ). Cells were then spun at low speed, supernatant was removed, and calcium was gradually reintroduced through a series of washes. For electrophysiology experiments, cells were used on the same day as isolation and until recording were stored at room temperature ( $21^\circ\text{C}$ ) in M199 (Gibco) supplemented with 5 mM creatine, 2 mM L-carnitine, 5 mM taurine and 1.5 nM insulin. For immunohistochemistry, cells were plated onto laminin-coated culture slides, allowed to adhere, and fixed on the day of isolation. For electron microscopy or qPCR, iCMs were selected manually by micro-pipette based on the presence of periostin-Cre:R26R-YFP/Tomato signal under the fluorescent microscope right after isolation.

**Cardiac fibroblast migration assay.** The migration assay was performed according to the explant culture protocol as described<sup>13</sup>. In brief, isolated adult mouse hearts were minced into small pieces less than  $1 \text{ mm}^3$  in size. The explants were plated on gelatin-coated dishes and cultured in explant medium (IMDM, 20% FBS) until fibroblasts migrated out from minced tissue. The time required for ten heart pieces to have migratory fibroblasts surrounding them were recorded.

**FACS analyses and sorting.** At 48 h after LAD and viral introduction, hearts were removed and minced into small pieces less than  $1\text{ mm}^3$  in size. Blood cells and debris were removed by several washings of PBS. Minced cardiac tissues were digested in an eppendorf tube and shaken with glass beads in enzyme buffer (collagenase/dispase plus DNaseI; Roche) at  $37^\circ\text{C}$ . After passing through a  $40\text{-}\mu\text{m}$  cell strainer, dissociated cardiac cells were stained with APC-conjugated anti-Thy1 antibody (eBioscience) for 30 min at room temperature. After washing with PBS twice, stained cells were sorted by FACSaria2 (BD).

**Immunohistochemistry.** For immunofluorescence, after perfusion-fixed hearts were taken out and fixed in 0.5% PFA overnight, ventricles below the ligation were embedded in OCT compound and frozen in liquid nitrogen. Sections were blocked in Universal Blocking Buffer (BioGenex) for 10 min, and then stained with primary antibodies against  $\alpha$ -actinin (Sigma Aldrich), vimentin (Progen),  $\beta$ -galactosidase (Abcam), pH3 (Millipore), RFP (Biovision), Thy1 (BD), CD34 (Abcam), WT1 (Abcam), PECAM (BD), NG2 (Millipore) and GFP (Invitrogen) for 1 h at room temperature. After washing three times with PBST (PBS plus 0.1% Triton), sections were incubated in secondary antibodies for 1 h followed by washing an additional three times with PBST. Finally, the sections were mounted in Vectashield with DAPI (Vector Laboratories).

**Immunocytochemistry.** Isolated cells plated on chamber slides were fixed in 4% PFA at  $4^\circ\text{C}$  overnight and washed with PBS twice. Cells were then incubated with primary antibodies against sarcomeric  $\alpha$ -actinin (Sigma Aldrich), cTnT (Thermo Scientific), RFP (Biovision), tropomyosin (Hybridoma Bank), MF20 (Hybridoma Bank), Cx43 (Sigma Aldrich), N-cadherin (Invitrogen),  $\beta$ -galactosidase (Abcam), smooth muscle actin (Sigma Aldrich) and vimentin (Progen) for 1 h at room temperature and washed with PBS three times, then incubated with secondary IgG antibodies conjugated to Cy 488 or 594 (Jackson ImmunoResearch) for 30 min. After washing with PBS, cells were mounted in Vectashield with DAPI.

**Electron microscopy.** For electron microscopy, cells were fixed in 2% glutaraldehyde, 1% paraformaldehyde in 0.1 M sodium cacodylate buffer, pH 7.4, post fixed in 2% osmium tetroxide in the same buffer, *en bloc* stained with 2% aqueous uranyl acetate, dehydrated in acetone, infiltrated, and embedded in LX-112 resin (Ladd Research Industries). Samples were ultrathin sectioned on a Reichert Ultracut S ultramicrotome and counter stained with 0.8% lead citrate. Grids were examined on a JEOL JEM-1230 transmission electron microscope (JEOL USA) and photographed with the Gatan Ultrascan 1000 digital camera (Gatan).

**Action potential recordings.** Isolated myocytes suspended in tissue culture medium were transferred to a superfusion chamber (RC-26GLP; Warner Instruments) on the stage of a Nikon TiS inverted fluorescence microscope equipped with a dual wavelength microfluorometer (IonOptix). Myocytes isolated from either periostin-Cre:R26R-YFP or periostin-Cre:R26R-Tomato hearts after GMT infection were identified as control CMs or iCMs on the basis of Tomato fluorescence (Texas red optics with exciter  $560 \pm 55\text{ nm}$ , emitter  $645 \pm 75\text{ nm}$ ) or YFP (standard FITC optics), and were chosen for study if they lacked spontaneous beating and partial contractions. The myocytes were whole-cell patch-clamped using an Axopatch 200B amplifier and pClamp software (Molecular Devices). Patch electrodes of 2–5 M $\Omega$  (1B-150F; WPI) were filled with intracellular solution containing 120 mM KCl, 20 mM NaHEPES, 10 mM MgATP, 5 mM K<sub>2</sub>EGTA (or 0.1 mM), 2 mM MgCl<sub>2</sub>, and adjusted to pH 7.1 with KOH. The cells were superfused with a modified Tyrode's extracellular solution containing 137 mM NaCl, 10 mM NaHEPES, 10 mM dextrose, 5 mM KCl, 2 mM CaCl<sub>2</sub>, 1 mM MgCl<sub>2</sub>, adjusted to pH 7.4 with NaOH. After G $\Omega$  seal formation, whole-cell access to the myocyte was established by applying brief pressure pulses, and the amplifier was switched to current clamp mode, whereupon the cell's resting potential developed. Action potentials were stimulated at 0.33 Hz using 2 nA, 2 ms current pulses applied through the patch pipette, and were signal averaged in tens. All membrane potentials were corrected for a  $-5.6\text{ mV}$  liquid junction potential determined via pClamp software. Finally, the amplifier was switched back to voltage clamp mode to identify individual ion channel currents as required. In some experiments, the concentration of K<sub>2</sub>EGTA in the intracellular solution was reduced to 0.1 mM to permit excitation–contraction coupling to occur, and 100  $\mu\text{M}$  K5Fluo-4 (Invitrogen Corp) was added to define the presence of cytosolic Ca<sup>2+</sup> transients during action potentials. Electrophysiology data were digitized at 5 kHz and low-pass filtered at 2 kHz. Analysis was performed using pClamp, Microsoft Excel, and Origin (OriginLab) software. Action potential duration was measured from the point of maximum depolarizing voltage change ( $\Delta V/\Delta t_{\text{max}}$ ) to 50, 70 and 90% repolarization. Unless stated, experiments were performed at room temperature.

**Field stimulation experiments.** Isolated myocytes were loaded with Fluo-4 for 30 min at room temperature before being transferred to the superfusion chamber. The loading solution contained a 1:10 mixture of 5 mM Fluo-4 AM in dry DMSO and PowerloadTM concentrate (Invitrogen) which was diluted 100-fold into extracellular Tyrode's solution containing suspended myocytes. An additional 20 min was allowed for de-esterification before commencing recordings. Contractions and Ca<sup>2+</sup> transients were evoked by applying voltage pulses at 0.33 Hz, between platinum wires placed on either side of the cell of interest and connected to a field stimulator (IonOptix, Myopacer). The pulses were of 2 ms duration and set at 150% of the threshold required to elicit twitches. Fluo-4 fluorescence transients were recorded via a standard filter set (#49011 ET, Chroma Technology) in batches of ten to enable signal averaging. Between stimuli, the fluorescence excitation light was blocked by an electromechanical shutter (CS35; Vincent Associates). Resting fluorescence was recorded after cessation of pacing, and background light was obtained after picking up and removing the cell from the field of view with a patch electrode at the end of the experiment. The Ca<sup>2+</sup> transients were calibrated using the pseudo-ratio method<sup>39</sup>, assuming an *in situ* dissociation constant of 1.1  $\mu\text{M}$  for Fluo-4<sup>40</sup>. Contractions were optically recorded simultaneously with Ca<sup>2+</sup> transients by illuminating the cell of interest in red light ( $\lambda > 665\text{ nm}$ ) subsequently directed to a CCD camera (IonOptix Myocam). The cell length signals were converted to voltage via a video motion director (VED 205; Crescent Electronics) and contraction amplitudes from different myocytes were normalized by calculating the per cent change in cell length.

**Determination of cell–cell coupling.** In experiments to assess the interconnectivity between iCMs and CMs, the whole-cell patch-clamp method was used to introduce a gap-junction-permeable (that is, mobile) and an impermeable (that is, immobile) dye into the same cell of interest within a small group of apparently coupled isolated myocytes ( $n = 5$  groups from 5 independent hearts). The mobile dye was calcein (5 mM), and the immobile dye was 1 mM dextran-conjugated Cascade Blue (MW 10,000). The immobile dye was chosen to be well separated spectrally, both from calcein and from tomato, which was used for labelling iCMs (Invitrogen). The dye pair was included in standard intracellular solution (containing 5 mM EGTA) and cytoplasmic loading was allowed to proceed for 2 min, after which the patch electrode was withdrawn from the patched myocyte. The sarcolemma of the cell resealed after pulling off the pipette, aided by high EGTA levels in the filling solution, thereby trapping the dyes in the cytoplasm. Blue fluorescence from the immobile indicator was excited at  $365 \pm 40\text{ nm}$ , whereas calcein fluorescence was excited at  $470 \pm 40\text{ nm}$ . Fluorescent images were recorded using IonOptix Myocam via a video frame grabber (#166VCB, Hauppauge) for processing using ImageJ software.

The functionality of cell–cell junctions was investigated by imaging the intercellular transmission of Ca<sup>2+</sup> waves and excitation between myocytes pre-loaded with Fluo-4 AM as detailed above for the field-stimulation studies. Superfusion with 2  $\mu\text{M}$  ouabain for 5–10 min was used to induce intracellular Ca<sup>2+</sup> overload accompanied by Ca<sup>2+</sup> wave activity, and videomicroscopy revealed the spatio-temporal relationships of Ca<sup>2+</sup> waves translocating within and between the individual cells imaged in small, adherent groups ( $n = 6$  groups from 5 independent hearts).

**Quantitative RT–PCR.** iCMs were manually sorted based on the presence of fluorescent lineage markers. Approximately 100 iCMs were pooled for RNA isolation. Similarly,  $\sim 100$  endogenous CMs isolated using the standard Langendorff apparatus (see above) and  $\sim 500$  cardiac fibroblasts using the migration assay (see above) were prepared for RNA isolation. RNA was extracted by the TRizol method (Invitrogen). RT–PCR was performed using the Superscript III first-strand synthesis system (Invitrogen). qPCR was performed using the ABI 7900HT (TaqMan, Applied Biosystems) as per the manufacturer's protocols. Optimized primers from the Taqman Gene Expression Array were used.

**Statistical analyses.** Differences between groups were examined for statistical significance using unpaired Student's *t*-test or ANOVA. A *P*-value  $< 0.05$  was regarded as significant. Error bars indicate standard error of the mean (s.e.m.).

38. Kurrelmeyer, K. M. *et al.* Endogenous tumor necrosis factor protects the adult cardiac myocyte against ischemic-induced apoptosis in a murine model of acute myocardial infarction. *Proc. Natl Acad. Sci. USA* **97**, 5456–5461 (2000).
39. Cheng, H., Lederer, W. J. & Cannell, M. B. Calcium sparks: elementary events underlying excitation–contraction coupling in heart muscle. *Science* **262**, 740–744 (1993).
40. Ljubojević, S. *et al.* *In situ* calibration of nucleoplasmic versus cytoplasmic Ca<sup>2+</sup> concentration in adult cardiomyocytes. *Biophys. J.* **100**, 2356–2366 (2011).



# Heart repair by reprogramming non-myocytes with cardiac transcription factors

Kunhua Song<sup>1</sup>, Young-Jae Nam<sup>1,2</sup>, Xiang Luo<sup>2</sup>, Xiaoxia Qi<sup>1</sup>, Wei Tan<sup>2</sup>, Guo N. Huang<sup>1</sup>, Asha Acharya<sup>1</sup>, Christopher L. Smith<sup>1</sup>, Michelle D. Tallquist<sup>1</sup>, Eric G. Neilson<sup>3</sup>, Joseph A. Hill<sup>1,2</sup>, Rhonda Bassel-Duby<sup>1</sup> & Eric N. Olson<sup>1</sup>

**The adult mammalian heart possesses little regenerative potential following injury. Fibrosis due to activation of cardiac fibroblasts impedes cardiac regeneration and contributes to loss of contractile function, pathological remodelling and susceptibility to arrhythmias. Cardiac fibroblasts account for a majority of cells in the heart and represent a potential cellular source for restoration of cardiac function following injury through phenotypic reprogramming to a myocardial cell fate. Here we show that four transcription factors, GATA4, HAND2, MEF2C and TBX5, can cooperatively reprogram adult mouse tail-tip and cardiac fibroblasts into beating cardiac-like myocytes *in vitro*. Forced expression of these factors in dividing non-cardiomyocytes in mice reprograms these cells into functional cardiac-like myocytes, improves cardiac function and reduces adverse ventricular remodelling following myocardial infarction. Our results suggest a strategy for cardiac repair through reprogramming fibroblasts resident in the heart with cardiogenic transcription factors or other molecules.**

Heart disease caused by the loss or dysfunction of cardiomyocytes is the leading cause of death worldwide<sup>1</sup>. Whereas the neonatal mammalian heart can regenerate following injury<sup>2</sup>, the capacity for regeneration of adult mammalian hearts is limited<sup>3</sup>. A fundamental goal of regenerative cardiovascular medicine is to successfully repair injured hearts by replacing cardiomyocytes and decreasing fibrosis. Transplantation of cardiac stem cells or stem cell-derived cardiomyocytes to improve cardiac function holds clinical potential, but is relatively inefficient<sup>4–6</sup>.

Fibroblasts can be reprogrammed into pluripotent stem cells, muscle cells and neurons by combinations of lineage-enriched transcription factors<sup>7–12</sup>. The human heart is composed of approximately 30% cardiomyocytes and 60–70% cardiac fibroblasts<sup>13</sup>. We sought to define the optimal combination of core cardiac transcription factors necessary and sufficient for reprogramming of adult fibroblasts into functional cardiomyocytes and to determine if these factors could improve cardiac function in injured hearts through reprogramming of endogenous cardiac fibroblasts. Here we show that four transcription factors, GATA4, HAND2, MEF2C and TBX5, are able to reprogram adult mouse fibroblasts into functional cardiac-like myocytes *in vitro* and *in vivo*, and expression of these factors in non-cardiomyocytes enhances function of injured hearts following myocardial infarction.

## Reprogramming of adult fibroblasts into cardiac-like myocytes

A core set of evolutionarily conserved transcription factors (GATA4, HAND2, MEF2C, MESP1, NKX2-5 and TBX5) controls cardiac gene expression and heart development<sup>14,15</sup>. Recently, GATA4, MEF2C and TBX5 were reported to be capable of converting neonatal fibroblasts to cardiomyocyte-like cells *in vitro*<sup>16</sup>. To search for an optimal combination of transcription factors capable of inducing cardiac lineage-reprogramming, we generated retroviruses to express each of the six core cardiac transcription factors (GATA4 (G),

HAND2 (H), MEF2C (M), MESP1 (Ms), NKX2-5 (N), and TBX5 (T)) in fibroblasts derived from adult mice bearing a cardiac-specific  $\alpha$ -MHC-GFP transgene, where the promoter of the  $\alpha$ -myosin heavy chain gene controls the expression of green fluorescent protein (Supplementary Figs 1 and 2).

Potential cardiogenic activity of the six factors (G, H, M, Ms, N, T) in adult tail-tip fibroblasts (TTFs) from  $\alpha$ -MHC-GFP transgenic mice was quantified by analysis of GFP<sup>+</sup> cells by flow cytometry 9 days after viral transduction. No GFP<sup>+</sup> cells were observed in fibroblast cultures transduced with viral backbone or without infection. However, the six factors together generated a small population of cells (~7%) positive for GFP (Supplementary Fig. 3). After several rounds of withdrawing one factor, we identified several combinations, including GHMMsT, GHMT, HMMsT, GMT, HMT and MT, that were capable of efficiently inducing  $\alpha$ -MHC-GFP<sup>+</sup> cells (Supplementary Fig. 3). The cooperativity amongst the different factors is consistent with their ability to synergistically activate cardiac gene expression and to activate each other's expression<sup>14,17–20</sup>.

To determine whether the above factors could activate endogenous cardiac-specific genes in adult TTFs, we examined expression of cardiac troponin T (cTnT, also known as TNNT2) and  $\alpha$ -MHC-GFP by flow cytometry (Supplementary Fig. 4). Depending on the experiment, GHMT induced between 5.2% and 19.7% (average 9.2%) of cells to become positive for both  $\alpha$ -MHC-GFP and cTnT. We refer to GHMT-transduced cells expressing cardiomyocyte markers as induced cardiac-like myocytes (iCLMs). By comparison, GMT induced approximately 2.9% (1.5% to 5.6%) of adult TTFs to adopt a cTnT<sup>+</sup>  $\alpha$ -MHC-GFP<sup>+</sup> phenotype (Supplementary Fig. 4). The percentage of iCLMs generated from adult TTFs by GHMT (9.2%) was about fourfold higher than previously reported for neonatal TTFs with GMT (2.5%)<sup>16</sup>. The percentage of cells expressing cTnT and  $\alpha$ -MHC-GFP reached a peak at day 7 of transduction;

<sup>1</sup>Department of Molecular Biology, University of Texas Southwestern Medical Center, 5323 Harry Hines Blvd, Dallas, Texas 75390-9148, USA. <sup>2</sup>Department of Internal Medicine, University of Texas Southwestern Medical Center, 5323 Harry Hines Blvd, Dallas, Texas 75390-9148, USA. <sup>3</sup>Department of Medicine, Vanderbilt University School of Medicine, Nashville, Tennessee 37232, USA.

the fraction of iCLMs declined thereafter due to overgrowth of non-reprogrammed fibroblasts (Supplementary Fig. 5).

Cardiac fibroblasts are the most prevalent interstitial cell type in adult mammalian hearts. We transduced adult cardiac fibroblasts with GHMT, GMT or empty viruses and analysed expression of cardiac markers by flow cytometry 1 week later. GHMT induced 6.8% of cardiac fibroblasts to become  $\alpha\text{-MHC-GFP}^+$ , compared with 1.4% double-positive cells with GMT (Supplementary Fig. 6a). GHMT induced both cTnT and cTnI (cardiac troponin I, also known as TNNI3) in 7.5% of cells (Supplementary Fig. 6b). Thus, GHMT represented the most optimal combination of factors for efficient initiation of cardiac gene expression in adult fibroblasts.  $\alpha\text{-MHC-GFP}^+$  cells derived from adult TTFs and cardiac fibroblasts by GHMT transduction showed strong immunostaining of the sarcomeric proteins  $\alpha\text{-actinin}$  and cTnT (Fig. 1a, b and Supplementary Fig. 7). More organized sarcomeres were observed in iCLMs at day 30 (Fig. 1b) compared to day 14 (Fig. 1a). In the presence of GHMT, three types of iCLMs, referred to as types A, B and C, which seem to represent a spectrum of cardiac reprogramming, were induced from adult cardiac fibroblasts and TTFs. Type A iCLMs only expressed  $\alpha\text{-MHC-GFP}$ . Type B iCLMs expressed both  $\alpha\text{-MHC-GFP}$  and  $\alpha\text{-actinin}$ . Type C iCLMs not only expressed  $\alpha\text{-MHC-GFP}$  and  $\alpha\text{-actinin}$ , but also showed sarcomere-like structures (Fig. 1a). GHMT induced  $\sim 15\%$  of adult cardiac fibroblasts and  $\sim 18\%$  of adult TTFs to become  $\alpha\text{-MHC-GFP}$ -positive cells, and  $\sim 30\%$  and  $\sim 10\%$  of these became type C iCLMs, respectively (Fig. 1c).

Microarray and quantitative PCR (qPCR) analysis of gene expression patterns showed expression of a broad range of cardiac genes, indicative of a cardiac-like phenotype, and concomitant suppression of non-myocyte genes including *Fsp1* (fibroblast-specific protein 1 or *S100A4*) in fibroblasts transduced with GHMT (Supplementary Figs 8 and 9). Following maintenance of GHMT-transduced adult cardiac fibroblasts or TTFs in culture for more than 5 weeks, we observed spontaneous contractions in approximately 0.2% of type C iCLMs. These beating iCLMs had calcium transients and action potentials (Supplementary Movies 1, 2 and 3, Fig. 1d and Supplementary Figs 10 and 11). iCLMs had a pattern of calcium transients most similar to neonatal ventricular cardiomyocytes (Fig. 1d). Transduction with inducible expression vectors showed that the cardiomyocyte-like phenotype was stable following termination of exogenous GHMT expression (Supplementary Fig. 12). Co-staining for cardiomyocyte marker and Myc-tagged GHMT indicates that induction of the cardiomyocyte-like phenotype by GHMT is cell-autonomous (Supplementary Fig. 13). Together, these results indicate that GHMT can activate cardiac gene expression in a sub-population of TTFs and cardiac fibroblasts. The relatively small percentage of cells that adopts the cardiac-like phenotype perhaps indicates a precise stoichiometry or high level of the cardiac factors required for phenotypic conversion, which is achieved in only a fraction of cells, or to differential susceptibility to reprogramming amongst heterogeneous cell types in the starting non-myocyte population. The efficiency of cellular reprogramming to iCLMs by GHMT is comparable to that of reprogramming of induced pluripotent stem (iPS) cells by pluripotency factors<sup>7,21</sup>.

### Reprogramming of FSP1-tagged cells into iCLMs *in vivo*

Following myocardial infarction or other forms of cardiac injury, cardiomyocytes undergo necrotic and apoptotic cell death and cardiac fibroblasts are activated to produce collagen and other extracellular matrix components, causing fibrosis and impaired cardiac function<sup>22</sup>. Therefore, we sought to determine whether reprogramming cardiac fibroblasts to a cardiomyocyte fate might blunt the decline in cardiac function post-myocardial infarction. Adult mammalian cardiomyocytes do not divide and are therefore resistant to retroviral expression. We expressed the cardiogenic transcription factors in cardiac fibroblasts and other dividing cells *in vivo* using a retrovirus expression system, which is

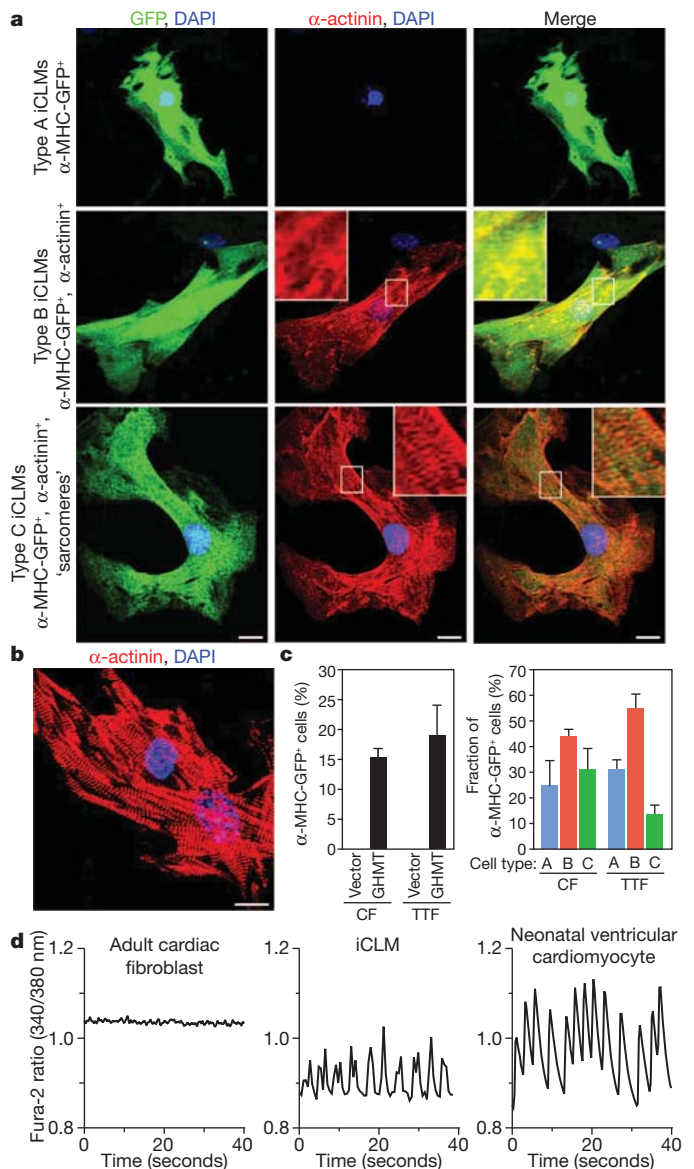


**Figure 1 | Reprogramming fibroblasts towards a cardiac phenotype *in vitro* by GHMT.** **a, b**, Immunofluorescent staining for cardiac markers,  $\alpha\text{-MHC-GFP}$  and  $\alpha\text{-actinin}$ . Adult cardiac fibroblasts (CF) isolated from  $\alpha\text{-MHC-GFP}$  reporter mice were transduced by retroviruses carrying GHMT or empty vector alone. Immunocytochemistry was performed at 14 days (a) or 30 days (b) following transduction. Scale bars, 20  $\mu\text{m}$ . Three types of iCLMs were categorized on the basis of cardiac gene expression and morphology. Type A iCLMs only express  $\alpha\text{-MHC-GFP}$  (top panels). Type B iCLMs express both  $\alpha\text{-MHC-GFP}$  and  $\alpha\text{-actinin}$ , but do not have sarcomeric structures (middle panels). Type C iCLMs express both  $\alpha\text{-MHC-GFP}$  and  $\alpha\text{-actinin}$ , and have sarcomeric structures (bottom panels). Sarcomeres were more organized at day 30 than at day 14 post-transduction. White boxes are enlarged in insets. **c**, Quantification of type A, B and C iCLMs in adult cardiac fibroblasts and TTFs 14 days after transduction with GHMT. Ten fields were randomly chosen from each experiment. Three independent experiments were performed. Data are presented as mean  $\pm$  s.d. **d**, Representative calcium transient traces from the indicated cell types depicted as Fura-2 ratios (340/380 nm). iCLMs were derived from adult cardiac fibroblasts and showed a pattern of calcium transients most similar to neonatal ventricular cardiomyocytes. Adult cardiac fibroblasts do not display calcium transients.

specific for proliferating cells and directs expression preferentially in myofibroblasts of injured rodent hearts<sup>23</sup>. We confirmed the specificity of retroviral infection for replicating non-cardiomyocytes by injecting concentrated GFP retroviruses into injured hearts after ligation of the left anterior descending coronary artery (LAD), which induces



myocardial infarction. GFP expression was clearly detected in the ischaemic area. However, none of the GFP<sup>+</sup> cells expressed the cardiac marker, cTnT, consistent with the specificity of retroviral infection for proliferating non-cardiomyocytes (Supplementary Fig. 14).

FSP1 is expressed in non-cardiomyocytes such as fibroblasts and transitioning epithelia<sup>24–26</sup>. In mouse and human hearts, expression of FSP1 primarily colocalizes with markers of cardiac fibroblasts and increases following myocardial infarction<sup>26</sup>. Non-cardiomyocytes in mice carrying alleles of *Fsp1-Cre* and *Rosa26-LacZ* are specifically labelled with  $\beta$ -galactosidase ( $\beta$ -gal), providing a marker for fibroblast lineage tracing<sup>24</sup>. To examine whether cardiac transcription factors were able to activate cardiac genes in non-cardiomyocytes *in vivo*, we performed LAD ligation on *Fsp1-Cre/Rosa26-LacZ* mice and injected concentrated retroviruses encoding GHMT or GFP into the border zone immediately following LAD ligation. We then analysed  $\beta$ -gal activity in histological sections of hearts at various times thereafter. In uninjured hearts, less than one  $\beta$ -gal<sup>+</sup> cardiomyocyte per section was observed. After injury,  $\beta$ -gal expression was readily detected in cardiac fibroblasts throughout the infarct zone (Fig. 2a, b). In injured hearts infected with GFP viruses, 0.05  $\pm$  0.13% of cardiomyocytes in the injured area were  $\beta$ -gal<sup>+</sup> (Fig. 2c), which may be due to low-level ectopic activation or to a basal level of new cardiomyocyte formation from a stem cell pool, as reported previously<sup>27</sup>. In contrast, abundant clusters of intensely stained  $\beta$ -gal<sup>+</sup> cardiomyocytes were observed throughout the infarct and border zone of injured hearts infected with the GHMT retrovirus cocktail (Fig. 2b). We observed that 6.5  $\pm$  1.2% of cardiomyocytes in the injured area showed  $\beta$ -gal activity (Fig. 2c). Generally, more  $\beta$ -gal<sup>+</sup> cardiomyocytes were observed in the border zone adjacent to the infarct region, which may be due to intact vascular structures or higher viral infection in this region. Similar results were obtained upon injection with GHMMsT, whereas the inclusion of NKX2-5 (GHMMsNT) diminished the efficacy of the other five factors (Supplementary Fig. 15), as seen *in vitro*.  $\beta$ -gal<sup>+</sup> cardiomyocytes expressed cTnT and showed clear striations 3 weeks after viral transduction (Fig. 2b). Through quantification of  $\beta$ -gal<sup>+</sup> cardiomyocytes in histological sections of infarcted hearts, we calculated that at least 10,000 new myocytes were generated in the injured area after 3 weeks of GHMT infection. This is likely to be an underestimate of the number of iCLMs generated *in vivo* because the reporter is only expressed in a subset of non-myocytes, such that unmarked cells could also be reprogrammed but go undetected.

In the heart, gap junctions composed of connexins ensure electrical and metabolic coupling between cardiomyocytes and coordinate their contractility<sup>28</sup>. To determine whether reprogrammed cardiomyocytes could couple with surrounding endogenous myocytes through gap junctions, we performed immunostaining for connexin 43 (Cx43, also known as GJA1), the major connexin in functional cardiomyocytes<sup>29</sup>. Gap junctions were observed between  $\beta$ -gal<sup>+</sup> and  $\beta$ -gal<sup>-</sup> cardiomyocytes and between  $\beta$ -gal<sup>+</sup> cardiomyocytes (Fig. 2d), indicating coupling of reprogrammed cardiomyocytes with surrounding myocytes. Reprogrammed  $\beta$ -gal<sup>+</sup> cardiomyocytes isolated from ventricular myocardium and identified by labelling with a fluorogenic, lipophilic  $\beta$ -gal substrate (C<sub>12</sub>FDG) also had a pattern of contractility and calcium transients similar to normal  $\beta$ -gal<sup>-</sup> ventricular cardiomyocytes in response to electrical pacing at 1 Hz (Fig. 2e), indicating their functionality.

### Reprogramming of TCF21-tagged cells into iCLMs *in vivo*

To rule out the possibility that injury or viral infection might somehow activate the *Fsp1* reporter in cardiomyocytes, we generated a strain of mice harbouring an inducible MerCreMer expression cassette inserted by homologous recombination into the *Tcf21* (also known as capsulin or epicardin) locus (*Tcf21*<sup>iCre</sup>), which is expressed specifically in non-cardiomyocytes in the heart (Supplementary Fig. 16)<sup>30</sup>. Intercrossing of these mice with mice bearing the Cre-inducible R26R<sup>tdTomato</sup> reporter showed specific expression of Tomato predominantly in cardiac fibroblasts with less expression in endothelial cells (Supplementary Fig. 16).

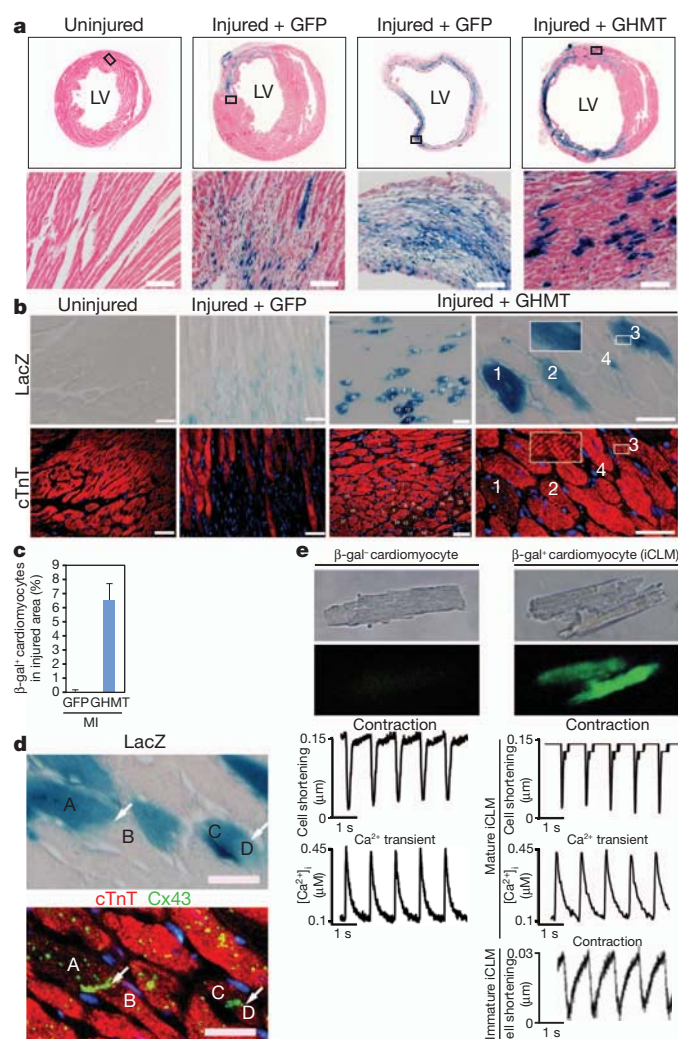


**Figure 2 | Reprogramming non-cardiomyocytes towards a cardiac fate *in vivo* by GHMT.** **a**, Heart sections of *Fsp1-cre/Rosa26-LacZ* mice uninjured or 3 weeks post-myocardial infarction followed by injection of GFP or GHMT retroviruses. GFP-infected myocardium showed only  $\beta$ -galactosidase-positive ( $\beta$ -gal<sup>+</sup>) non-cardiomyocytes, GHMT-infected myocardium showed extensive  $\beta$ -gal<sup>+</sup> non-cardiomyocytes and cardiomyocytes. Black boxes in top panels are enlarged in lower panels. LV, left ventricle. Scale bars, 40  $\mu$ m. **b**, cTnT immunostaining and X-gal staining of heart sections of *Fsp1-cre/Rosa26-LacZ* mice uninjured or 3 weeks post-myocardial infarction followed by injection of GFP or GHMT retroviruses. The same cell is marked with the same number in the top and bottom panels (nos 1–4). Several  $\beta$ -gal<sup>+</sup> cells in GHMT-infected injured hearts expressed cTnT and had organized sarcomere structure. White boxes are enlarged in insets. Sections of injured hearts were taken at the border zone. Scale bars, 40  $\mu$ m. **c**, Quantification of  $\beta$ -gal<sup>+</sup> cardiomyocytes in border zones and infarct zones from GFP-infected (168 sections,  $n = 3$ ) and GHMT-infected hearts of *Fsp1-cre/Rosa26-LacZ* mice (20 sections,  $n = 2$ ) post-myocardial infarction. Sections were taken at four levels with an interval of 250  $\mu$ m below LAD ligation site. MI, myocardial infarction. Data are presented as mean  $\pm$  s.d. **d**, Staining of border zone from GHMT-infected hearts of *Fsp1-cre/Rosa26-LacZ* mice post-myocardial infarction by X-gal (blue), anti-cTnT (red) and anti-Cx43 (green). Gap junctions (green) were observed between  $\beta$ -gal<sup>+</sup> and  $\beta$ -gal<sup>-</sup> cardiomyocytes (A and B) and between  $\beta$ -gal<sup>+</sup> cardiomyocytes (C and D). The same cell is marked with the same letter. Scale bar, 20  $\mu$ m. **e**, Contractility and Ca<sup>2+</sup> transients of  $\beta$ -gal<sup>+</sup> and  $\beta$ -gal<sup>-</sup> cardiomyocytes.  $\beta$ -gal<sup>+</sup> cardiomyocytes (iCLMs) were labelled with the fluorogenic  $\beta$ -gal substrate C<sub>12</sub>FDG (green). Traces of sarcomere shortening were recorded from field-stimulated  $\beta$ -gal<sup>-</sup> cardiomyocytes ( $n = 15$ ) and iCLMs ( $n = 7$ ) with clear striated morphology. 71.4% of iCLMs had a similar pattern of contractility and Ca<sup>2+</sup> transients to  $\beta$ -gal<sup>-</sup> cardiomyocytes. 28.6% of iCLMs demonstrated immature contractility.

However, we only observed one Tomato<sup>+</sup> cardiomyocyte in over 40 histological sections of normal hearts. *Tcf21<sup>iCre</sup>* R26R<sup>tdT</sup> mice were treated with tamoxifen for 3 days to mark TCF21-expressing cells. Eight days after the last tamoxifen treatment, LAD ligation was performed and animals were injected with empty vector, GFP or GHMT retroviruses and analysed 3–4 weeks later. Numerous Tomato<sup>+</sup> cardiomyocytes were observed in GHMT-injected hearts compared to GFP-injected ones (Fig. 3a).

To quantify Tomato<sup>+</sup> cardiomyocytes, we isolated cardiomyocytes from intact hearts using the Langendorff perfusion method. In GHMT-injected hearts,  $2.4 \pm 1.5\%$  of cardiomyocytes in the injured area were Tomato<sup>+</sup>, and these Tomato<sup>+</sup> cardiomyocytes showed clear striations (Fig. 3b, c). However, in empty vector-injected injured hearts, only  $0.004 \pm 0.005\%$  of cardiomyocytes were Tomato<sup>+</sup>

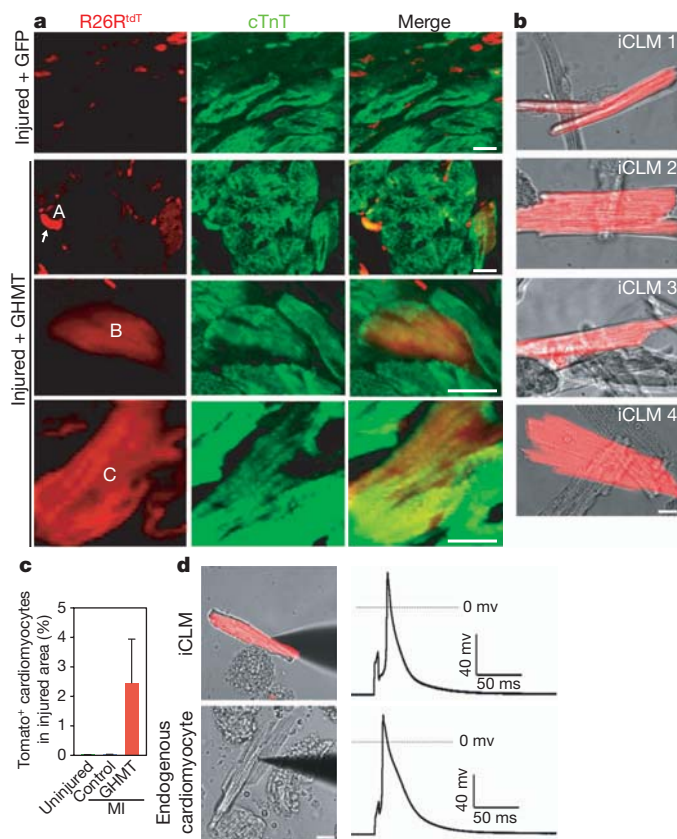


**Figure 3 | Lineage tracing of GHMT-induced iCLMs *in vivo*.** **a**, Border zone of heart sections isolated from tamoxifen-treated *Tcf21<sup>iCre</sup>/Rosa26R<sup>tdT</sup>* mice that were subjected to LAD ligation followed by injection of GFP or GHMT retroviruses. Three weeks post-myocardial infarction, hearts were fixed, sectioned and stained for cTnT (green) and visualized for tomato (red). Upper panels show GFP-injected heart in which tomato is seen only in fibroblasts. Lower panels show GHMT-injected heart in which tomato is seen in both fibroblasts and cardiomyocytes. Three types of iCLMs (positive for cTnT and tomato) were observed in injured hearts injected with GHMT-virus: cell A, small cells without sarcomeres; cell B, has sarcomeres and expresses equivalent cTnT to neighbouring tomato-negative cardiomyocytes; cell C, has sarcomeres and expresses less cTnT than neighbouring tomato-negative cardiomyocytes. Scale bars, 20  $\mu$ m. **b**, Tomato<sup>+</sup> iCLMs isolated from tamoxifen-treated *Tcf21<sup>iCre</sup>/Rosa26R<sup>tdT</sup>* mice 1 month post-myocardial infarction followed by injection of GHMT retroviruses. Scale bar, 20  $\mu$ m. **c**, Quantification of tomato<sup>+</sup> cardiomyocytes isolated from uninjured hearts ( $n = 2$ ), injured hearts treated with empty vector retroviruses ( $n = 3$ ), or GHMT retroviruses ( $n = 3$ ). Data are presented as mean  $\pm$  s.d. **d**, Recording of action potential of tomato<sup>+</sup> iCLMs and endogenous cardiomyocytes by patch-clamping. Action potentials were recorded in response to brief (1–2 ms) depolarizing current (1–2 nA) injections delivered at 1 Hz by whole-cell current patch-clamping. ( $n = 5$  for each group).

(Fig. 3c). *Tcf21<sup>iCre</sup>* marks a smaller, more restricted fraction of non-myocytes than *Fsp1-Cre*. Hence the number of new myocytes marked with this reporter is lower than with *Fsp1-Cre*. These findings indicate that forced expression of GHMT in non-myocytes of the heart is sufficient to induce the expression of cardiac markers. The Tomato<sup>+</sup> cardiomyocytes induced by GHMT *in vivo* were able to spontaneously contract *in vitro* (Supplementary Fig. 17 and Supplementary Movie 4). Recording of action potentials of reprogrammed Tomato<sup>+</sup> cardiomyocytes and endogenous cardiomyocytes by whole-cell patch clamping indicated functionality of cardiomyocytes induced by GHMT *in vivo* (Fig. 3d).

To further test whether GHMT indeed promoted the formation of new cardiomyocytes following myocardial infarction, and to rule out the possibility that labelled cardiomyocytes obtained from *Fsp1-Cre* or *Tcf21<sup>iCre</sup>/Rosa* marker mice injected with GHMT might arise from fusion of native cardiomyocytes with non-myocytes, we used mice with an inducible  $\alpha$ -MHC-MerCreMer transgene and *Rosa26-LacZ* reporter. Gavage of these mice with tamoxifen for seven consecutive days resulted in labelling of  $87.7 \pm 1.9\%$  of cardiomyocytes in the left ventricular myocardium. Following LAD ligation and injection of GFP retroviruses, we observed a reduction in the percentage of  $\beta$ -gal-labelled cardiomyocytes ( $83.2 \pm 4.6\%$ ) in the border zone adjacent to the infarct, indicating replenishment of cardiomyocytes following injury, as described previously<sup>27,31</sup>. Injection of GHMT retroviruses further reduced the percentage of  $\beta$ -gal<sup>+</sup> cardiomyocytes in the border zone ( $76.0 \pm 5.2\%$ ) (Supplementary Fig. 18). These findings indicate that GHMT promotes the formation of new cardiomyocytes from a non- $\alpha$ -MHC lineage *in vivo* following injury.

### Enhancement of cardiac regeneration of injured hearts

We examined whether forced expression of GHMT in non-cardiomyocytes could lead to measurable improvement in function of ischaemic hearts. Cardiac function following myocardial infarction was assessed in a blinded fashion by fractional shortening, ejection fraction and stroke volume using echocardiography and magnetic resonance imaging (MRI). Twenty-four hours after LAD ligation, fractional shortening and ejection fraction assessed by echocardiography of all mice decreased relative to sham-operated mice. Thereafter, cardiac function of GFP-injected mice continued to decline, reaching a stable value 2 weeks post-myocardial infarction; fractional shortening  $\approx 13\%$  and ejection fraction  $\approx 30\%$ . In contrast, infection of injured myocardium with GHMT retroviruses blunted further worsening of cardiac function 3 weeks post-myocardial infarction; fractional shortening  $\approx 26\%$  and ejection fraction  $\approx 51\%$  (Fig. 4a). By comparison, functional improvement was delayed and less complete with GMT, consistent with the reduced efficiency of this transcription factor combination in reprogramming *in vitro*.

To determine whether functional improvement was sustained, we assessed cardiac function at 6 weeks and 12 weeks by ejection fraction and stroke volume using cardiac MRI. Ejection fraction of GFP-injected mice decreased to reach a stable value of approximately 28% 6 weeks post-myocardial infarction (Fig. 4b). In contrast, infection of injured myocardium with GHMT blunted worsening of ejection fraction 6 weeks post-myocardial infarction ( $\sim 49\%$ ) with further significant improvement at 12 weeks post-myocardial infarction ( $\sim 57\%$ ) (Fig. 4b). This long-term effect on ejection fraction by GHMT was accompanied by significant increases in stroke volume at 12 weeks compared to 6 weeks (Fig. 4b). Individual mice in each group demonstrated similar functional changes in both cardiac parameters, indicating the reliability of cardiac MRI to assess cardiac function (Supplementary Fig. 19). These data indicate that expression of GHMT in non-cardiomyocytes in injured hearts can sustain cardiac function. Moreover, GHMT- and GHMMsT-infected hearts showed a pronounced reduction in fibrosis and increased muscle tissue, compared with GFP-infected hearts after myocardial infarction (Fig. 5a, b and Supplementary Fig. 20).



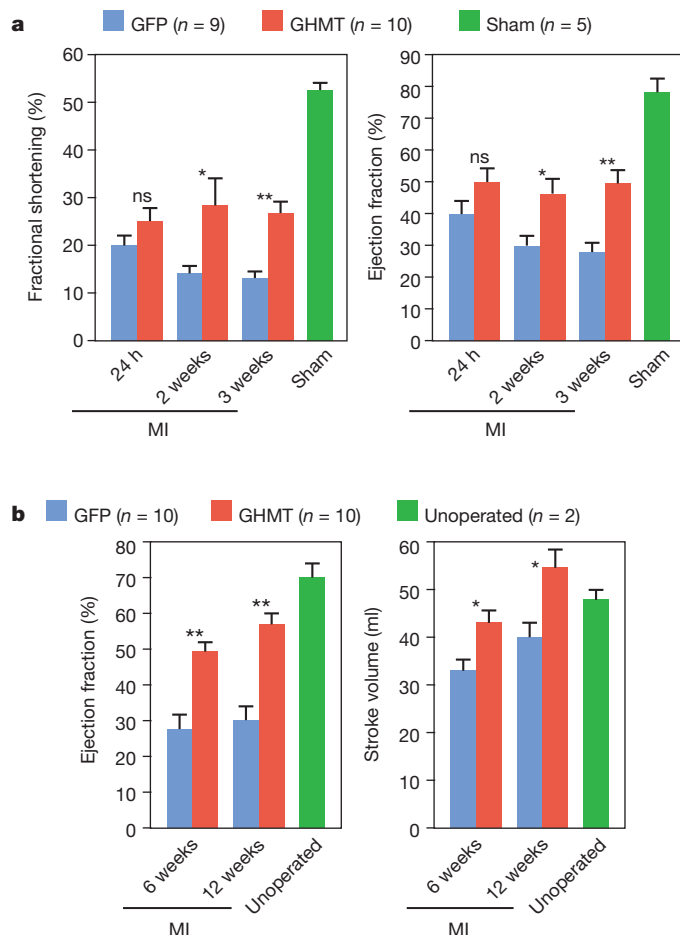


**Figure 4 | Ameliorated cardiac function of injured hearts by GHMT.**

**a**, Cardiac function of mice subjected to LAD ligation followed by intramyocardial injection of GFP or GHMT retroviruses was evaluated at various time points by echocardiography. Data are presented as mean  $\pm$  s.d. \* $P < 0.05$ ; \*\* $P < 0.005$ ; ns, not statistically significant. **b**, Cardiac function at 6 and 12 weeks post-myocardial infarction was assessed by MRI. Data are presented as mean  $\pm$  std. \* $P < 0.05$ , \*\* $P < 0.005$ .

## Discussion

Our results demonstrate that GATA4, HAND2, MEF2C and TBX5 (GHMT) can reprogram cardiac fibroblasts into functional cardiac-like myocytes *in vitro* and *in vivo*, confirming and extending prior studies<sup>16</sup>. Moreover, exogenous GHMT expression in non-cardiomyocytes of the heart post-myocardial infarction also reduces fibrosis and improves cardiac function.

Improvement of cardiac function post-myocardial infarction by different transcription factor combinations correlated with their ability to convert fibroblasts into iCLMs *in vitro* (Supplementary Fig. 21), suggesting that cardiac repair results, at least in part, from reprogramming of non-cardiomyocytes towards a cardiomyocyte fate. We feel it is important to emphasize, however, that the pronounced functional improvement of GHMT-injected hearts seems greater than might be predicted from the relative inefficiency of reprogramming of adult cardiac fibroblasts to iCLMs *in vitro*. We speculate that the native milieu of the intact heart, containing extracellular matrix, growth factors, persistent contractility, surrounding contractile cells and other cell types, is more permissive than plastic tissue culture dishes for functional reprogramming. In this regard, reprogramming of pancreatic beta-cells has been observed *in vivo* but not *in vitro*<sup>32</sup>. It is also conceivable that other mechanisms, such as a blockade to the activation of cardiac fibroblasts, enhanced survival of cardiomyocytes, facilitated differentiation of activated cardiac progenitors into cardiomyocytes, as described previously<sup>27,31</sup>, or improved angiogenesis contribute to the benefits

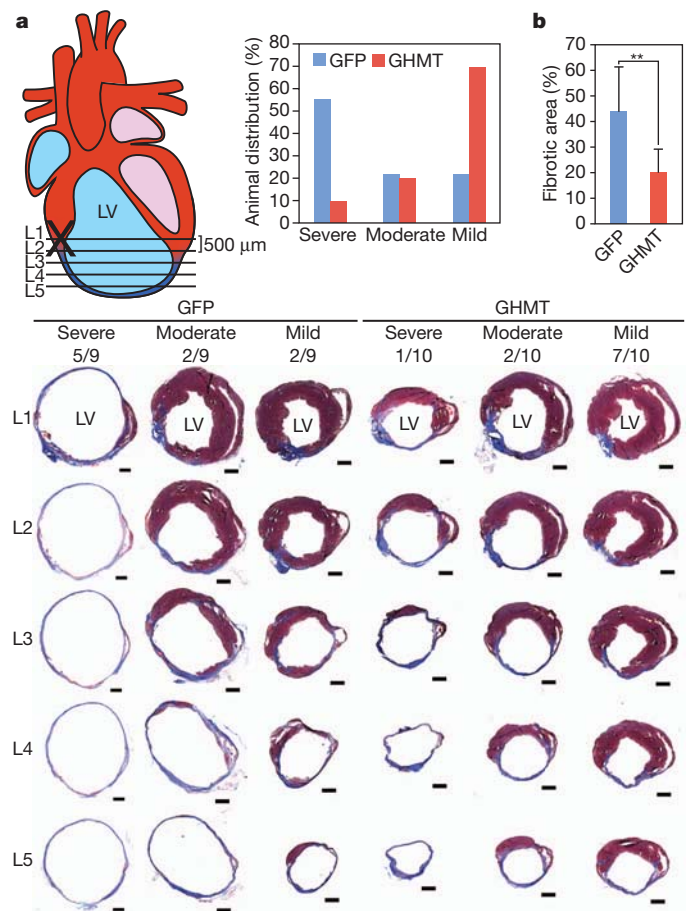


**Figure 5 | Attenuation of fibrosis in response to myocardial infarction by GHMT.** **a**, Comparison of cardiac fibrosis and scar formation between GFP- and GHMT-infected myocardium 4 weeks after LAD ligation. Cardiac fibrosis was evaluated at five levels (L1–L5) by trichrome staining 4 weeks post-myocardial infarction. The ligation site is marked as X. Severity of cardiac fibrosis was classified as mild, moderate or severe (fibrotic area  $< 20\%$ ,  $20\text{--}40\%$  or  $> 40\%$ , respectively). Sections of representative hearts of each category of severity are shown. Numbers indicate the various type of severity/total number of hearts examined in each group. A graph shows animal distribution in each category. Scale bar, 1 mm. **b**, Quantification of fibrotic area in heart sections displayed in (a). Fibrotic area (%) = (the sum of fibrotic area at levels 3 and 4/the sum of myocardial area in the LV at levels 3 and 4)  $\times$  100. Data are presented as mean  $\pm$  s.d. \* $P < 0.05$ , \*\* $P < 0.005$ .

observed upon expression of GHMT in the heart post-myocardial infarction. Irrespective of these uncertainties, the strategy presented here, while still requiring optimization, provides a potential means of improving cardiac function *in vivo*, bypassing many of the obstacles associated with cellular transplantation.

## METHODS SUMMARY

All experimental procedures with animals were approved by the Institutional Animal Care and Use Committee at University of Texas Southwestern Medical Center.

Adult TTFs and cardiac fibroblasts were isolated by an explanting method in which fibroblasts migrate from minced tissue and grow in fibroblast growth medium. Fibroblasts were transduced with a mixture of polybrene (Sigma;  $6 \mu\text{g ml}^{-1}$ ) and freshly made retroviruses expressing transcription factors generated in Platinum E cells (Cell Biolabs). Twenty-four hours after viral transduction, the viral medium was changed to a cardiac induction medium. Medium was changed every 2 days. Expression of cardiac genes was analysed by flow cytometry, microarray and immunocytochemistry.

Adult mice, 8–10 weeks old, underwent either a sham operation or ligation of the LAD. Concentrated retroviruses ( $\sim 10^{8-9}$  infectious units (i.f.u.)) were injected into the border zone using a gastight 1710 syringe (Hamilton). Cardiac

function was assessed using echocardiography and MRI. Hearts were collected from euthanized animals for histological studies.

Isolation of cardiomyocytes, electrophysiological measurements, histology and immunohistochemistry were performed as described previously<sup>2,33–37</sup>.

**Full Methods** and any associated references are available in the online version of the paper at [www.nature.com/nature](http://www.nature.com/nature).

**Received 18 March 2011; accepted 12 April 2012.**

**Published online 13 May 2012.**

- Lopez, A. D., Mathers, C. D., Ezzati, M., Jamison, D. T. & Murray, C. J. Global and regional burden of disease and risk factors, 2001: systematic analysis of population health data. *Lancet* **367**, 1747–1757 (2006).
- Porrello, E. R. *et al.* Transient regenerative potential of the neonatal mouse heart. *Science* **331**, 1078–1080 (2011).
- Yacoub, M., Suzuki, K. & Rosenthal, N. The future of regenerative therapy in patients with chronic heart failure. *Nat. Clin. Pract. Cardiovasc. Med.* **3** (Suppl. 1), S133–S135 (2006).
- Menasche, P. Cell-based therapy for heart disease: a clinically oriented perspective. *Mol. Ther.* **17**, 758–766 (2009).
- Hoover-Plow, J. & Gong, Y. Challenges for heart disease stem cell therapy. *Vasc. Health Risk Manag.* **8**, 99–113 (2012).
- Perin, E. C. *et al.* Effect of transendocardial delivery of autologous bone marrow mononuclear cells on functional capacity, left ventricular function, and perfusion in chronic heart failure: the FOCUS-CCTRN trial. *J. Am. Med. Assoc.*, (2012).
- Takahashi, K. & Yamanaka, S. Induction of pluripotent stem cells from mouse embryonic and adult fibroblast cultures by defined factors. *Cell* **126**, 663–676 (2006).
- Yu, J. *et al.* Induced pluripotent stem cell lines derived from human somatic cells. *Science* **318**, 1917–1920 (2007).
- Tapscott, S. J. *et al.* MyoD1: a nuclear phosphoprotein requiring a Myc homology region to convert fibroblasts to myoblasts. *Science* **242**, 405–411 (1988).
- Wang, Z., Wang, D. Z., Pipes, G. C. & Olson, E. N. Myocardin is a master regulator of smooth muscle gene expression. *Proc. Natl Acad. Sci. USA* **100**, 7129–7134 (2003).
- Vierbuchen, T. *et al.* Direct conversion of fibroblasts to functional neurons by defined factors. *Nature* **463**, 1035–1041 (2010).
- Caiazzo, M. *et al.* Direct generation of functional dopaminergic neurons from mouse and human fibroblasts. *Nature* **476**, 224–227 (2011).
- Jugdutt, B. I. Ventricular remodeling after infarction and the extracellular collagen matrix: when is enough enough? *Circulation* **108**, 1395–1403 (2003).
- Olson, E. N. Gene regulatory networks in the evolution and development of the heart. *Science* **313**, 1922–1927 (2006).
- Bondue, A. & Blanpain, C. Mesp1: a key regulator of cardiovascular lineage commitment. *Circ. Res.* **107**, 1414–1427 (2010).
- Ieda, M. *et al.* Direct reprogramming of fibroblasts into functional cardiomyocytes by defined factors. *Cell* **142**, 375–386 (2010).
- Zang, M. X., Li, Y., Wang, H., Wang, J. B. & Jia, H. T. Cooperative interaction between the basic helix-loop-helix transcription factor dHAND and myocyte enhancer factor 2C regulates myocardial gene expression. *J. Biol. Chem.* **279**, 54258–54263 (2004).
- Dai, Y. S., Cserjesi, P., Markham, B. E. & Molkentin, J. D. The transcription factors GATA4 and dHAND physically interact to synergistically activate cardiac gene expression through a p300-dependent mechanism. *J. Biol. Chem.* **277**, 24390–24398 (2002).
- Garg, V. *et al.* GATA4 mutations cause human congenital heart defects and reveal an interaction with TBX5. *Nature* **424**, 443–447 (2003).
- Ghosh, T. K. *et al.* Physical interaction between TBX5 and MEF2C is required for early heart development. *Mol. Cell. Biol.* **29**, 2205–2218 (2009).
- Warren, L. *et al.* Highly efficient reprogramming to pluripotency and directed differentiation of human cells with synthetic modified mRNA. *Cell Stem Cell* **7**, 618–630 (2010).
- Porter, K. E. & Turner, N. A. Cardiac fibroblasts: at the heart of myocardial remodeling. *Pharmacol. Ther.* **123**, 255–278 (2009).
- Byun, J. *et al.* Myocardial injury-induced fibroblast proliferation facilitates retroviral-mediated gene transfer to the rat heart *in vivo*. *J. Gene Med.* **2**, 2–10 (2000).
- Bhowmick, N. A. *et al.* TGF- $\beta$  signaling in fibroblasts modulates the oncogenic potential of adjacent epithelia. *Science* **303**, 848–851 (2004).
- Zeisberg, E. M. *et al.* Endothelial-to-mesenchymal transition contributes to cardiac fibrosis. *Nature Med.* **13**, 952–961 (2007).
- Schneider, M. *et al.* S100A4 is upregulated in injured myocardium and promotes growth and survival of cardiac myocytes. *Cardiovasc. Res.* **75**, 40–50 (2007).
- Loffredo, F. S. *et al.* Bone marrow-derived cell therapy stimulates endogenous cardiomyocyte progenitors and promotes cardiac repair. *Cell Stem Cell* **8**, 389–398 (2011).
- Beyer, E. C. Gap junctions. *Int. Rev. Cytol.* **137C**, 1–37 (1993).
- Saffitz, J. E., Green, K. G., Kraft, W. J., Schechtman, K. B. & Yamada, K. A. Effects of diminished expression of connexin43 on gap junction number and size in ventricular myocardium. *Am. J. Physiol. Heart Circ. Physiol.* **278**, H1662–H1670 (2000).
- Acharya, A., Baek, S. T., Banfi, S., Eskiciak, B. & Tallquist, M. D. Efficient inducible Cre-mediated recombination in *Tcf21* cell lineages in the heart and kidney. *Genesis* **49**, 870–877 (2011).
- Hsieh, P. C. *et al.* Evidence from a genetic fate-mapping study that stem cells refresh adult mammalian cardiomyocytes after injury. *Nature Med.* **13**, 970–974 (2007).
- Zhou, Q., Brown, J., Kanarek, A., Rajagopal, J. & Melton, D. A. *In vivo* reprogramming of adult pancreatic exocrine cells to  $\beta$ -cells. *Nature* **455**, 627–632 (2008).
- Tandan, S. *et al.* Physical and functional interaction between calcineurin and the cardiac L-type  $\text{Ca}^{2+}$  channel. *Circ. Res.* **105**, 51–60 (2009).
- Laugwitz, K. L. *et al.* Postnatal isl1<sup>+</sup> cardioblasts enter fully differentiated cardiomyocyte lineages. *Nature* **433**, 647–653 (2005).
- Luo, X. *et al.* Aberrant localization of intracellular organelles,  $\text{Ca}^{2+}$  signaling, and exocytosis in *Mist1* null mice. *J. Biol. Chem.* **280**, 12668–12675 (2005).
- Grynkiewicz, G., Poenie, M. & Tsien, R. Y. A new generation of  $\text{Ca}^{2+}$  indicators with greatly improved fluorescence properties. *J. Biol. Chem.* **260**, 3440–3450 (1985).
- Hardy, M. E. *et al.* Validation of a voltage-sensitive dye (di-4-ANEPPS)-based method for assessing drug-induced delayed repolarisation in beagle dog left ventricular midmyocardial myocytes. *J. Pharmacol. Toxicol. Methods* **60**, 94–106 (2009).

**Supplementary Information** is linked to the online version of the paper at [www.nature.com/nature](http://www.nature.com/nature).

**Acknowledgements** We thank J. Cabrera for graphics. We are grateful to members of the Olson lab for critical reading of the manuscript. We thank D. Sosis, W. Tang, J. O'Rourke, N. Liu, M. Xin, A. Johnson and J. McNally for discussions; J. Shelton and J. A. Richardson for histology. We are grateful to I. Bezprozvanny for the PTI  $\text{Ca}^{2+}$  Imaging System, and D. Srivastava for lentiviral plasmids. We thank the microarray core at University of Texas Southwestern Medical Center for collecting gene expression data. E.N.O. is supported by grants from NIH, the Donald W. Reynolds Center for Clinical Cardiovascular Research, the Robert A. Welch Foundation (grant I-0025), the Leducq Foundation-Transatlantic Network of Excellence in Cardiovascular Research Program, the American Heart Association-Jon Holden DeHaan Foundation and the Cancer Prevention & Research Institute of Texas (CPRIT).

**Author Contributions** K.S. and E.N.O. conceived the project. K.S., Y.-J.N. and E.N.O. designed the experiments. K.S., Y.-J.N., X.L., X.Q., W.T., G.N.H., C.L.S. and A.A. performed experiments. J.A.H. contributed to surgical experiments; E.G.N. made the *Fsp1*-Cre mouse line. K.S. and R.B.-D. wrote the animal protocol. M.D.T. and R.B.-D. contributed scientific discussion. K.S., Y.-J.N., X.L., M.D.T., R.B.-D. and E.N.O. analysed data and prepared the manuscript.

**Author Information** Microarray data were deposited in the Gene Expression Omnibus database (accession number GSE37057). Reprints and permissions information is available at [www.nature.com/reprints](http://www.nature.com/reprints). The authors declare no competing financial interests. Readers are welcome to comment on the online version of this article at [www.nature.com/nature](http://www.nature.com/nature). Correspondence and requests for materials should be addressed to E.N.O. ([eric.olson@utsouthwestern.edu](mailto:eric.olson@utsouthwestern.edu)).



## METHODS

**Isolation of primary fibroblasts.** Tail-tip fibroblasts (TTFs): adult mouse tails were skinned and cut into small pieces which were plated on tissue culture dishes and cultured in DMEM supplemented with 15% FBS and antibiotics. The medium was changed every 2 to 3 days. TTFs migrated out from the explants after 2 or 3 days. One week later, TTFs were frozen or replated for viral transduction.

Cardiac fibroblasts: hearts from adult mice (older than 4 weeks of age) were minced into small pieces and plated on tissue culture dishes. Three minutes later, culture medium (DMEM:199 (4:1), 15% FBS and antibiotics) was gently added to the dishes. Cardiac fibroblasts started to migrate out of the minced heart tissue after 2 days. The medium was replaced every 2 days. Ten days later, cardiac fibroblasts were frozen or replated for viral transduction.

**Generation of retroviruses.** Retroviral plasmid DNA was generated by subcloning *EGFP*, Myc-tagged *NKX2-5*, *GATA4*, *TBX5*, *HAND2*, *MEF2C* and Flag-tagged *MESPI* complementary DNAs into the retroviral vector pBabe-X<sup>38</sup>.

Ten micrograms of retroviral plasmid DNA was transfected using FuGENE 6 (Roche) into Platinum E cells (Cell Biolabs) which were plated on a 10-cm tissue culture dish at a density of  $3 \times 10^6$  cells per dish, 24 h before transfection. Twelve hours after transfection, medium was changed to 12 ml of fresh medium (DMEM supplemented with 10% FBS and antibiotics). After 36 h of transfection, viral medium was harvested and filtered through a 0.45  $\mu$ m cellulose filter. The viral supernatant was mixed with polybrene (Sigma) to a final concentration of 6  $\mu$ g ml<sup>-1</sup>.

**Viral transduction.** TTFs and cardiac fibroblasts were plated on tissue culture dishes pre-coated with SureCoat (Cellutrone) at a density of  $0.8 \times 10^4$  cm<sup>-2</sup>. After 24 h, the fibroblast growth medium was replaced with freshly made viral mixture containing polybrene. Twenty four hours later, viral medium was replaced with induction medium, composed of 10% conditioned medium obtained from neonatal rat/mouse cardiomyocyte culture, DMEM/199 (4:1), 10% FBS, 5% horse serum, antibiotics, non-essential amino acids, essential amino acids, B-27, insulin-selenium-transferrin, vitamin mixture, and sodium pyruvate (Invitrogen). Conditioned medium was filtered through a 0.22- $\mu$ m pore size cellulose filter. Medium was changed every 2 days until cells were collected.

**qPCR, western blot analysis and immunocytochemistry.** Total RNA was extracted from cultured cells and cDNA was synthesized by reverse transcription. All qPCR probes were obtained from Applied Biosystems. Western blots were performed with anti-Myc (Santa Cruz, clone A-14 1:1,000) and anti-Flag (Sigma, 1:2,000) antibody. For immunocytochemistry, cells were fixed in 4% paraformaldehyde and incubated with primary antibodies: anti-GFP (Torrey Pines Biolabs 1:400), anti-cTnT (Thermo Scientific 1:400), anti-Myc (Santa Cruz, clone A-14 1:200), and anti- $\alpha$ -actinin (Sigma, 1:400). After washing with PBS, Alexa fluorogenic secondary antibodies (Invitrogen) were used to detect the signal.

**DNA microarray.** Total RNA was isolated from uninfected cardiac fibroblasts, cardiac fibroblasts transduced with either empty vector or GHMT retroviruses and adult heart. Microarray analysis was performed on the platform of Illumina Mouse-6 Beadchip by the DNA Microarray Core Facility at the University of Texas Southwestern Medical Center. Data were analysed using GeneSpring GX software (Agilent).

**Flow cytometry.** For the initial assay to detect  $\alpha$ MHC-GFP expression, adherent fibroblasts were washed with PBS and detached from culture dish by treatment with Accutase (Millipore) for 10 min at 37 °C. Cells were then washed with 2% FBS in PBS and filtered through a cell strainer. Cells were incubated with propidium iodide (1:1,000 dilution in 1% FBS in PBS) for 15 min at room temperature. Dead cells were excluded by propidium iodide staining and live cells were analysed for GFP expression using FACS Caliber (BD Sciences) and FlowJo software.

For intracellular staining of cardiac-specific markers, cells were fixed with 4% paraformaldehyde for 15 min after being harvested, as described above. Fixed cells were washed with PBS and permeabilized with saponin for 10 min at room temperature. After being washed with PBS, cells were incubated with 5% goat and donkey serum in PBS at room temperature for 30 min, followed by incubation with primary antibodies (rabbit polyclonal anti-GFP antibody (Invitrogen) at a 1:100 dilution and mouse monoclonal anti-cTnT antibody (Thermo Scientific) at a 1:400 dilution in 0.2% goat and donkey serum in PBS for 30 min at room temperature. After washing twice with PBS, cells were incubated with secondary antibodies for 30 min at room temperature. Secondary antibodies were goat anti-rabbit Alexa Fluor 488 (Invitrogen) at a 1:200 dilution and donkey anti-mouse Cy5 (Jackson Laboratory) at a 1:400 dilution in PBS containing 0.2% goat and donkey serum. Cells were washed with PBS three times, and then analysed for GFP and cTnT expression using FACS Caliber (BD Sciences) and FlowJo software.

**Generation of  $\alpha$ -MHC-GFP transgenic mice.** A plasmid containing a 5.5 kilobase genomic fragment upstream of the mouse  $\alpha$ -MHC gene plus exons 1–3 and intronic sequences<sup>39</sup>, inserted upstream of a neomycin-resistance cassette followed by an internal ribosomal entry sequence (IRES) and a GFP reporter was

linearized and micro-injected into the pronucleus of zygotes. The founders were crossed to C57BL/6 mice to get stable lines.

**Induction of Cre by tamoxifen administration.** Tamoxifen (Sigma) was dissolved in sesame oil (90%) and ethanol (10%) at a concentration of 50 mg ml<sup>-1</sup>. To induce Cre activity, tamoxifen (0.2 mg g<sup>-1</sup> body weight) was administered by gavage with a 22-gauge feeding needle into mice bearing *Tcf21*<sup>Cre/+</sup>/R26R<sup>tdT</sup> or  $\alpha$ -MHC-MerCreMer<sup>40</sup>/Rosa26-LacZ for three to five or seven consecutive days, respectively. Mice were analysed or subjected to myocardial infarction surgery at day 8 post-oral gavage of the last dosage.

**Sorting of Tcf21-expressing cells and gene expression.** Three-month-old *Tcf21*<sup>Cre/+</sup>/R26R<sup>tdT</sup> mice were induced with 0.2 mg g<sup>-1</sup> tamoxifen for 3 consecutive days by gavage, and 1 week later hearts were isolated and processed (atria and aorto-pulmonary trunk were removed) to generate single cell suspensions for FACS sorting, as described previously<sup>41</sup>. The suspension was filtered through tissue strainers, centrifuged at 400g for 5 min and resuspended in 10% CM media (10% Hyclone FBS, 3:1 DMEM/M-199, 10 mM HEPES, 1.2% antibiotic/antimycotic) before sorting with a MoFlo flow cytometer (Cytomation) using Summit software. For transcript analysis, sorted cells were collected into lysis buffer for RNA extraction (RNAqueous Micro kit from Ambion). A fraction of each sample was also collected into PBS for post-sort assessment of purity. Complementary DNA was synthesized using Superscript III reverse transcriptase (Invitrogen) and random hexamers (Roche). Gene expression profiles were generated using standard qPCR methods with iTAQ SYBR Green master mix (Bio-Rad) on a CFX96 instrument (Bio-Rad). Samples were run in triplicate and normalized to cyclophilin expression. Fold enrichment was determined with respect to the unsorted population.

**Myocardial infarction surgery and intramyocardial injection of retroviruses.** Mice were anesthetized with isoflurane, intubated with a polyethylene tube (size 60), and then ventilated with a volume-cycled rodent respirator with 2–3 ml per cycle at a respiratory rate of 120 cycles per min. Thoracotomy was performed at the third intercostal space and self-retaining microretractors were placed to separate the third and fourth rib to visualize the LAD. A 7.0 prolene suture (Ethicon, Johnson & Johnson) was then passed under the LAD at 1.5 mm distal to the left atrial appendage, immediately after the bifurcation of the left main coronary artery. The LAD was doubly ligated. The occlusion was confirmed by the change of colour (becoming paler) of the anterior wall of the left ventricle. Sham-operated mice underwent the same procedure without ligation. Immediately after ligation of the LAD, 50  $\mu$ l of concentrated retrovirus ( $\sim 10^8$ – $10^9$  infectious units (i.f.u.)) was injected into the border zone of the infarct at five different areas using a gastight 1710 syringe (Hamilton). The chest wall was then closed with a 5.0 Dexon absorbable suture (Tyco Healthcare, United States Surgical), and the skin was closed with Topical Tissue Adhesive (Abbott Laboratory). Mice were extubated and allowed to recover from surgery under a heating lamp. The mouse surgeon was blinded to the study. Mice with fractional shortening >30% at day 1 post-myocardial infarction were removed from the study.

**Transthoracic echocardiography.** Cardiac function was evaluated by two-dimensional transthoracic echocardiography on conscious mice using a VisualSonics Vevo2100 imaging system. Fractional shortening and ejection fraction were used as indices of cardiac contractile function. M-mode tracings were used to measure left ventricular internal diameter at end diastole (LVIDd) and end systole (LVIDs). Fractional shortening (FS) was calculated according to the following formula: FS (%) = [(LVIDd – LVIDs)/LVIDd]  $\times$  100. Ejection fraction (EF) is estimated from [(LVEDV – LVESV)/LVEDV]  $\times$  100%. LVESV, left ventricular end systolic volume; LVEDV, end diastolic volume. All measurements were performed by an experienced operator blinded to the study.

**Cardiac MRI.** Six and twelve weeks after myocardial infarction, the cardiac function of mice was re-evaluated by cardiac MRI using a 7 T small animal MR scanner (Varian) with a 38-mm birdcage RF coil. Under anaesthesia by inhalation of 1.5–2% isoflurane mixed with medical-grade air via nose-cone, the animals were placed prone on a mouse sled, (Dazai Research Instruments) equipped with a pneumatic respiratory sensor and electrocardiogram (ECG) electrodes for cardiac sensing, head first with the heart centred with respect to the centre of the RF coil. The mouse chests were shaved and a conducting gel was applied to optimize ECG contact between electrodes and mouse. All MRI acquisitions were gated using both cardiac and respiratory triggering. The bore temperature was kept at 35 °C to assure adequate and constant heart rate.

Two-dimensional (2D) gradient echo images on three orthogonal planes (transverse, coronal and sagittal) were acquired to determine the long-axis of the heart in each mouse. Axial images perpendicular to the long axis of the heart were chosen for cine-imaging. Cine images at 12 phases per cardiac cycle were obtained with an echo time of 2.75 ms, repetition time = ECG R-R interval/12, flip angle of 45°, and number of excitation (NEX) = 4. Each scan consisted of seven to ten contiguous slices from apex to LV outflow with 1-mm thickness, a matrix size of 128  $\times$  128, and a field of view of 30  $\times$  30 mm.

Epicardial and endocardial borders were manually traced for calculation of LVESV and LVEDV using NIH ImageJ software. Total LV volumes were calculated as the sum of all slice volumes. Stroke volume was calculated by the equation,  $LVEDV - LVESV$ . Ejection fraction (EF) was calculated by the equation,  $[(LVEDV - LVESV)/LVEDV] \times 100\%$ . Investigators performing MRI acquisition and analysis were blinded to the assignment of mice group.

**Isolation of adult mouse cardiomyocytes, measurement of cardiomyocyte sarcomere shortening and  $Ca^{2+}$  transients.** Mouse cardiomyocytes were isolated using enzymatic digestion and mechanical dispersion methods previously described<sup>33</sup>. In brief, after retrograde perfusion with  $Ca^{2+}$ -free Krebs–Ringer buffer (KR, 35 mM NaCl, 4.75 mM KCl, 1.19 mM  $KH_2PO_4$ , 16 mM  $Na_2HPO_4$ , 134 mM sucrose, 25 mM  $NaCO_3$ , 10 mM glucose, 10 mM HEPES, pH 7.4, with NaOH) and digestion with collagenase solution (collagenase II, 8 mg ml<sup>-1</sup>), the ventricular myocytes were separated using a fine scalpel and scissors. After gentle trituration, cells were kept in KB solution (10 mM taurine, 70 mM glutamic acid, 25 mM KCl, 10 mM  $KH_2PO_4$ , 22 mM glucose, 0.5 mM EGTA, pH 7.2 with KOH) and studied within 6 h at room temperature.

To examine myocyte contractile capacity, isolated cardiomyocytes were incubated with 33  $\mu$ M  $C_{12}FDG$  for 30 min. The green  $C_{12}FDG^+$  cardiomyocytes were identified by a fluorescence microscope. Adult cardiomyocytes from wild-type mice incubated with  $C_{12}FDG$  were used to determine autofluorescence of cardiomyocytes.  $C_{12}FDG^+$  cardiomyocytes and  $C_{12}FDG^-$  cardiomyocytes were field-stimulated at 1 Hz while being superfused with extracellular buffer at room temperature. Images were acquired at 240 Hz through a  $\times 60$  microscope objective using a variable field rate CCD camera (IonOptix). Cell length was measured by a video edge-detection system, using an IonOptix interface system. Intracellular  $Ca^{2+}$  transients were measured as previously described<sup>33–36</sup>. Analyses were carried out with the software (IonWizard, IonOptix). Only rod-shaped, clearly striated cardiomyocytes that were  $Ca^{2+}$ -tolerant were used in the experiments.

**Calcium transient measurements in spontaneous beating cardiomyocytes.** Calcium imaging of beating iCLMs, cultured neonatal mouse ventricular cardiomyocytes was performed using the PTI (Photon Technology International)  $Ca^{2+}$  Imaging System with an automated fluorescence microscope and a CCD camera, as described previously<sup>35</sup>. Calcium transients in individual spontaneous

beating cell were calculated by measurement of  $Ca^{2+}$ -induced fluorescence at both 340 and 380 nm.

**Membrane potential recordings of iCLMs *in vitro*.** Action potentials of beating iCLMs with di-4-ANEPPS (Invitrogen) were assessed, as described previously<sup>37</sup>.

**Action potential recordings of iCLMs isolated from adult mouse hearts.** Tomato<sup>+</sup> cardiomyocytes were identified under a Nikon inverted fluorescence microscope with a red filter. Whole-cell current clamp experiments (Axopatch 200B, Molecular Devices) were conducted to measure cardiomyocyte membrane action potentials. Cells were plated in a chamber that was superfused at 1 to 2 ml min<sup>-1</sup> with standard solution A containing 140 mM NaCl, 5 mM KCl, 1 mM  $MgCl_2$ , 1 mM  $CaCl_2$ , 10 mM HEPES (pH 7.4 with NaOH), and 10 mM glucose (310 mOsm). Recording pipettes were prepared with resistances of 2–3 m $\Omega$  when filled with internal solution containing 135 mM KCl, 10 mM EGTA, 10 mM HEPES, 5 mM glucose (pH 7.2 with KOH; 300 mOsm). Action potentials were recorded in response to brief (1–2 ms) depolarizing current (1–2 nA) injections delivered at 1 Hz. All data were filtered at 5 kHz and analysed by pCLAMP 9 software (Molecular Devices).

**Histology and immunohistochemistry.** Haematoxylin and eosin and LacZ staining were performed as described<sup>37</sup>. Frozen sections from ischaemic hearts were stained with anti-GFP (Aves Labs 1:800) antibody according to manufacturer's instructions. Paraffin-embedded sections were stained with anti-cTnT (1:400) and anti-Cx43 (Cell Signaling, 1:50). Frozen sections from tamoxifen-treated  $Tcf21^{iCre/+}/R26R^{tdT}$  mice (~5 week old) were stained with anti-P4HB (ProteinTech, 1:200), anti-cTnT (Thermo Scientific, 1:400), isolectin B4 (Vector Labs, 1:100), and anti-SM22 $\alpha$  (Abcam, 1:200). Signals were detected with Alexa fluorogenic secondary antibodies (Invitrogen).

38. Kitamura, T. *et al.* Efficient screening of retroviral cDNA expression libraries. *Proc. Natl Acad. Sci. USA* **92**, 9146–9150 (1995).
39. Subramaniam, A. *et al.* Tissue-specific regulation of the  $\alpha$ -myosin heavy chain gene promoter in transgenic mice. *J. Biol. Chem.* **266**, 24613–24620 (1991).
40. Sohail, D. S. *et al.* Temporally regulated and tissue-specific gene manipulations in the adult and embryonic heart using a tamoxifen-inducible Cre protein. *Circ. Res.* **89**, 20–25 (2001).
41. Russell, J. L. *et al.* A dynamic notch injury response activates epicardium and contributes to fibrosis repair. *Circ. Res.* **108**, 51–59 (2011).



# The *let-7*–*Imp* axis regulates ageing of the *Drosophila* testis stem-cell niche

Hila Toledano<sup>1\*†</sup>, Cecilia D'Alterio<sup>1\*</sup>, Benjamin Czech<sup>2</sup>, Erel Levine<sup>3</sup> & D. Leanne Jones<sup>1</sup>

**Adult stem cells support tissue homeostasis and repair throughout the life of an individual. During ageing, numerous intrinsic and extrinsic changes occur that result in altered stem-cell behaviour and reduced tissue maintenance and regeneration. In the *Drosophila* testis, ageing results in a marked decrease in the self-renewal factor Unpaired (Upd), leading to a concomitant loss of germline stem cells. Here we demonstrate that IGF-II messenger RNA binding protein (*Imp*) counteracts endogenous small interfering RNAs to stabilize *upd* (also known as *os*) RNA. However, similar to *upd*, *Imp* expression decreases in the hub cells of older males, which is due to the targeting of *Imp* by the heterochronic microRNA *let-7*. In the absence of *Imp*, *upd* mRNA therefore becomes unprotected and susceptible to degradation. Understanding the mechanistic basis for ageing-related changes in stem-cell behaviour will lead to the development of strategies to treat age-onset diseases and facilitate stem-cell-based therapies in older individuals.**

Many stem cells lose the capacity for self-renewal when removed from their local microenvironment (or niche), indicating that the niche has a major role in controlling stem-cell fate<sup>1</sup>. Changes to the local and systemic environments occur with age that result in altered stem-cell behaviour and reduced tissue maintenance and regeneration<sup>2,3</sup>. The stem-cell niche in the *Drosophila* testis is located at the apical tip, where both germline stem cells (GSCs) and somatic cyst stem cells are in direct contact with hub cells (Fig. 1a; reviewed in ref. 4). Hub cells express the self-renewal factor Upd, which activates the JAK-STAT signalling pathway to regulate the behaviour of adjacent stem cells<sup>5–7</sup>. Ageing results in a progressive and significant decrease in the levels of *upd* in hub cells (Fig. 1b). However, constitutive expression of *upd* in hub cells was sufficient to block the age-related loss of GSCs<sup>5</sup>, suggesting that mechanisms might be in place to regulate *upd* and maintain an active stem-cell niche.

To identify potential regulators of *upd*, we screened a collection of transgenic flies carrying green fluorescent protein (GFP)-tagged proteins for expression in hub cells<sup>6</sup>. The *Drosophila* homologue of *Imp* protein is expressed throughout the testis tip in young flies (Fig. 1c and Supplementary Fig. 2a)<sup>7</sup>; however, antibody staining revealed a decrease (~50%) in *Imp* expression in the hub cells of aged males (Fig. 1d and Supplementary Fig. 2b). *Imp* is a member of a conserved family of RNA-binding proteins that regulate RNA stability, translation and localization<sup>8</sup>. Given the similarity in the ageing-related decline in *Imp* protein and *upd* mRNA in hub cells, we proposed that *Imp* could be a new regulator of *upd*.

## *Imp* acts upstream to regulate *upd* mRNA

To address whether *Imp* acts in hub cells to regulate *upd*, we used the bipartite *GAL4-UAS* system<sup>9</sup> in combination with RNA-mediated interference (RNAi) to reduce *Imp* expression exclusively in hub cells. Fluorescence *in situ* hybridization (FISH) to detect *upd* mRNA was used in combination with immunofluorescence microscopy to determine whether the loss of *Imp* expression affects *upd* levels. The loss of *Imp* specifically in hub cells resulted in reduced expression of *upd* (Fig. 1e, f (bottom), and Supplementary Fig. 2c, d), as well as a

significant reduction in GSCs and hub cells (Fig. 1h, i, k and Supplementary Fig. 2e), when compared with controls. Consistent with a reduction in JAK-STAT signalling, decreased accumulation of STAT was observed when *Imp* levels were reduced by RNAi in hub cells (Supplementary Fig. 2f–h).

RNA-binding proteins characteristically target several RNAs; therefore, we wanted to determine whether *upd* is a physiologically relevant target of *Imp*. Expression of *upd* together with an *Imp* RNAi construct was sufficient to completely rescue the defects caused by reduced *Imp* expression in hub cells (Fig. 1e–k and Supplementary Fig. 2e), suggesting that Upd acts downstream of *Imp* to maintain GSCs and niche integrity. Importantly, the constitutive expression of *upd* alone in hub cells did not lead to an increase in GSCs in testes from 1-day-old males (*w*, *upd-GAL4*;  $8.3 \pm 0.7$  (mean  $\pm$  95% confidence interval),  $n = 21$ , and *upd-GAL4*; *UAS-upd*, *TM2*;  $8.3 \pm 0.8$ ,  $n = 32$ ). These data suggest that *Imp* acts in hub cells to promote niche integrity and GSC maintenance, at least in part, by positively regulating *upd*.

If *Imp* acts in hub cells in adult testes to regulate *upd* mRNA, we speculated that the loss of *Imp* function during development might lead to a decrease in *upd* and a subsequent reduction in GSCs. Null mutations in *Imp* result in lethality at the pharate adult stage; therefore, we examined testes from third instar larvae (L3) carrying *Imp* null alleles, *Imp*<sup>7</sup> and *Imp*<sup>8</sup> (ref. 10). Deletion of the *Imp* locus was verified by PCR of genomic DNA (Supplementary Fig. 3a). Combined immunofluorescence and FISH showed that although Fas3<sup>+</sup> hub cells were easily detected, the expression of *upd* was significantly reduced: 24% of *Imp*<sup>7</sup> mutants ( $n = 67$ ) and 15% of *Imp*<sup>8</sup> mutants ( $n = 41$ ) had no detectable *upd* at this stage (Fig. 1l, m). In addition, the average number of GSCs and hub cells in testes from *Imp* mutants was significantly reduced when compared with control L3 testes (Fig. 1o–p, r and Supplementary Fig. 3c–e). Notably, the re-expression of *Imp* in somatic niche cells was sufficient to rescue *upd* expression in *Imp* mutants to comparable levels to controls (Fig. 1l–n), and the reduction in the average number of GSCs and hub cells in *Imp* mutants was also reversed (Fig. 1o–q, r and Supplementary Fig. 3c–e).

<sup>1</sup>Laboratory of Genetics, The Salk Institute for Biological Studies, La Jolla, California 92037, USA. <sup>2</sup>Watson School of Biological Sciences, Howard Hughes Medical Institute, Cold Spring Harbor Laboratory, 1 Bungtown Road, Cold Spring Harbor, New York 11724, USA. <sup>3</sup>Department of Physics and FAS Center for Systems Biology, Harvard University, Cambridge, Massachusetts 02138, USA. <sup>†</sup>Present address: Department of Human Biology, Faculty of Natural Sciences, University of Haifa, Mount Carmel, Haifa 31905, Israel.

\*These authors contributed equally to this work.

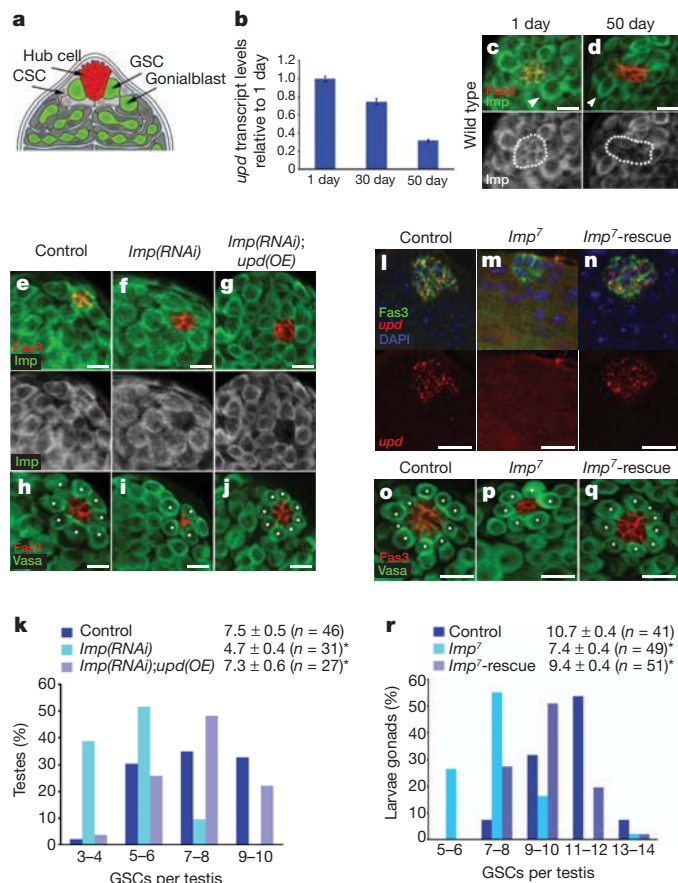


**Figure 1 | Imp regulates *upd* levels and GSC maintenance in the testis.** **a**, The apical tip of a *Drosophila* testis. CSC, cyst stem cell. **b**, *upd* mRNA decreases with age (qRT-PCR). One representative experiment is shown ( $n = 3$ ); error bars denote s.d. of triplicate measurements. **c**, **d**, Testes from 1-day-old (**c**) or 50-day-old (**d**) flies immunostained for Imp (green) and Fas3 (red, hub). Note reduced Imp levels in hub cells of aged males (dotted lines, bottom panels) compared with a modest reduction in GSCs (arrowheads, top panels). **e–j**, Overexpression (OE) of *upd* suppresses the loss of GSCs owing to the loss of Imp. Staining for Imp (green) to confirm knockdown (**e–g**) or for the germline marker Vasa (green) (**h–j**). White dots in **h–j** denote GSCs. Genotypes: control,  $w^{-}$ , *upd-GAL4,UAS-gfp* outcrossed to  $w^{1118}$ ; *Imp(RNAi)*,  $w^{-}$ , *upd-GAL4,UAS-gfp;UAS-Imp(RNAi)*; *Imp(RNAi);upd(OE)*,  $w^{-}$ , *upd-GAL4,UAS-gfp;UAS-Imp(RNAi);UAS-upd, TM2*. **k**, GSC distribution as in **h–j**. **l–q**, L3 male gonads stained for Fas3 (green) and *upd* (red) (**l–n**) or Fas3 (red) and Vasa (green) (**o–q**). Nuclei in **l–n** were counterstained blue with 4',6-diamidino-2-phenylindole (DAPI). White dots in **o–q** denote GSCs. Genotypes: control, EP(X)760; *Imp7*; *Imp7-rescue*, *Imp7/Y; 8-156-GAL4; UAS-Imp<sup>T21</sup>*. **r**, GSC distribution as in **o–q**. The mean  $\pm$  95% confidence interval are shown in **k** and **r**. \* $P < 0.01$  compared with controls (Student's *t*-test). Scale bars, 10  $\mu$ m.

### Imp binds to *upd* in vivo and in vitro

Imp family members contain conserved KH domains that mediate direct binding to RNA targets. To determine whether Imp could associate directly with *upd* mRNA in vivo, testes were dissected from young flies expressing GFP-tagged Imp (Supplementary Fig. 2a)<sup>6</sup>. Immunoprecipitation of Imp with anti-GFP antibodies, followed by quantitative reverse transcriptase PCR (qRT-PCR) analysis, showed a significant enrichment ( $\sim 208$ -fold) of associated *upd* mRNA relative to control antibodies (Fig. 2a). Minimal enrichment for the ubiquitously expressed RNAs *rp49* (also known as *RpL32*;  $\sim 4$ -fold) and *GapDH* (also known as *Gapdh1*;  $\sim 8$  fold) or for the negative control *med23* ( $\sim 4$ -fold; see Methods), was observed after Imp immunoprecipitation, indicating that the interaction between Imp and *upd* mRNA in hub cells is specific (Fig. 2a). Consistent with these observations, Imp protein and *upd* RNA co-localized in hub cells

within perinuclear foci, probably ribonucleoprotein particles (Supplementary Fig. 4a).

An *in vitro* protein–RNA binding assay<sup>11</sup> showed that Imp associates with the *upd* 3' untranslated region (UTR), specifically the first 250 base pairs (region 1), as no substantial binding to other portions of the *upd* 3'UTR was detected (Fig. 2b). Moreover, Imp did not bind the 5' untranslated or coding regions of *upd* or to the *med23* 3'UTR (Fig. 2b). Notably, a putative consensus binding sequence CAUH (in which H denotes A, U or C) for the mammalian IMP homologues (IGF2BP1–3)<sup>12</sup> occurs 22 times within the *upd* 3'UTR, including a cluster of four tandem repeats within the first 35 nucleotides of region 1 (Fig. 2c). To test whether this motif mediates binding between Imp and *upd*, we removed the first 33 nucleotides to generate a sequence excluding the CAUH repeats, which resulted in a reduction in binding (Fig. 2c, compare domain 1 with domain 2). Point mutations in the third nucleotide of each motif (U = G) did not abolish the binding (Fig. 2c, domain 1\*); however, point mutations in the consensus motif of MRPL9 RNA, a target of mammalian IGF2BPs, also did not abolish binding<sup>12</sup>, suggesting that secondary structures probably mediate the association between IGFBP family members and their target RNAs. Altogether, our data identify the first 33 base pairs of the *upd* 3'UTR as a putative target sequence for Imp, and support our observations that Imp associates specifically with *upd* in vivo (Fig. 2a, c).

To gain further insight into the mechanism by which Imp regulates *upd*, a GFP reporter was constructed that contained the 3'UTR from either *upd* or *med23* (Fig. 2d). Transcript levels for *gfp* were fivefold higher in *Drosophila* Schneider (S2) cells that co-expressed Imp with the *gfp-upd*-3'UTR reporter than in cells that co-expressed Imp with the *gfp-med23*-3'UTR reporter (Fig. 2d). The significant increase in reporter mRNA levels indicates that it is likely that Imp regulates *upd* mRNA stability.

### Imp counters targeting of *upd* by endo-siRNAs

RNA-binding proteins, including mammalian IGF2BP1 (refs 13, 14), have been shown to counter microRNA (miRNA)-mediated targeting of mRNAs. However, no consensus miRNA seeds were located within the first 34 base pairs of domain 1 of the *upd* 3'UTR (Fig. 2c). We speculated that if Imp binding blocks small RNA-mediated degradation of *upd*, polyadenylated, cleaved *upd* degradation intermediates would be detected in the testes of older males, when Imp expression in hub cells is reduced (Fig. 1d). Using a modified rapid amplification of complementary DNA ends (RACE) technique we identified a specific cleavage product starting at nucleotide 33 of the *upd* 3'UTR in the testes of 30-day-old flies (Fig. 2e), but not in RNA extracts from the testes of 1-day-old males. Importantly, the same degradation product of *upd* was also detected in the testes of young flies when Imp was specifically depleted from hub cells using RNAi-mediated knockdown. As a positive control, we detected the *esi-2*-mediated cleavage product of *mus308* (ref. 15) in testes from both 1- and 30-day-old flies.

To test whether small RNAs might mediate *upd* cleavage, we cloned and deep-sequenced small RNA libraries generated from the testes of 1- and 30-day-old flies. Although no small RNAs with exact pairing to the *upd* degradation product were identified, two short interfering RNAs (siRNAs; termed *siRNA1* and *siRNA2*) with high sequence complementarity to the predicted target site in the *upd* 3'UTR were present in the testis library generated from 30-day-old males (Fig. 2e and Supplementary Table 1). Using qRT-PCR for mature small RNAs, we found that the *siRNA2* levels in the testes, relative to the levels of the control small RNAs *bantam* and *mir-184*, were similar in young and old males (deep sequencing analysis demonstrated that expression of these two control miRNAs did not change with age). The source of *siRNA2* is the *gypsy5* transposon, which is inserted at several loci throughout the fly genome and is conserved in numerous *Drosophila* species.

To gain further insight into the mechanism by which Imp and *siRNA2* regulate *upd*, we investigated the levels of the *upd* GFP



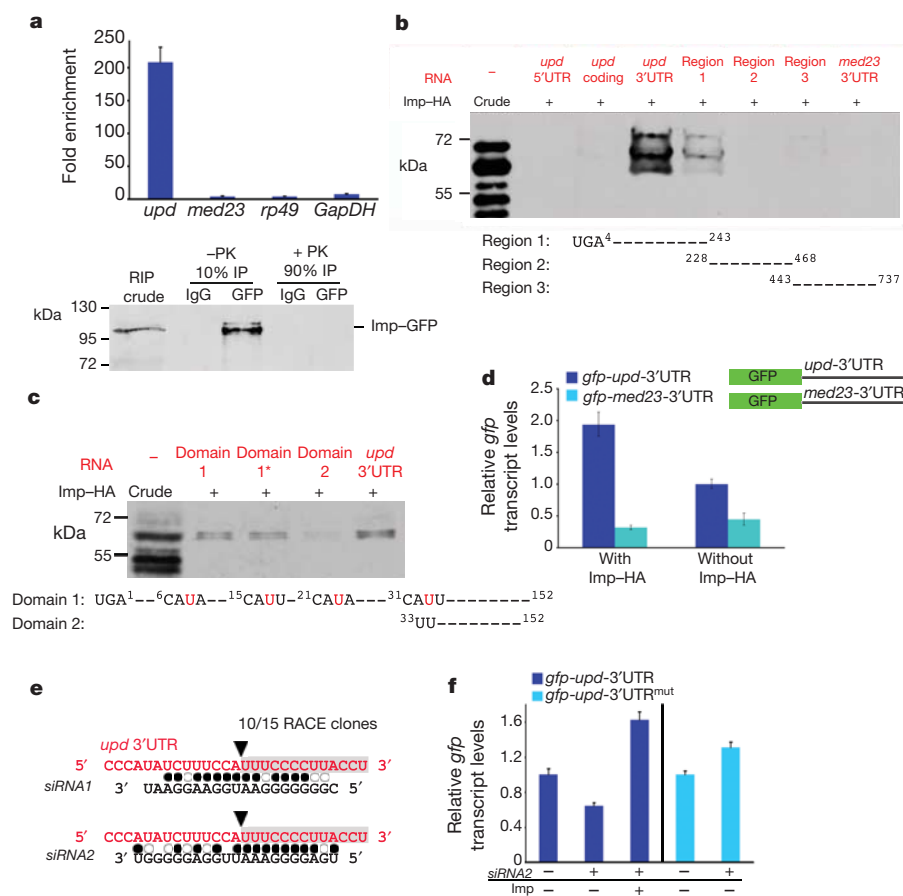


**Figure 2 | Imp binds to *upd* mRNA and counteracts siRNA-mediated degradation.** **a**, Top, fold-enrichment of the indicated mRNAs after RNA immunoprecipitation (RIP) with anti-GFP antibodies relative to control IgG from the testes of young Imp-GFP flies. Bottom, immunoblot for Imp-GFP. Ten per cent of the immunoprecipitate was used to confirm immunoprecipitation efficiency; the remaining 90% was treated with proteinase K (PK) and used for qRT-PCR. **b**, **c**, *In vitro* protein-RNA binding assay. Top panels, immunoblots for Imp-HA binding to designated RNA fragments. Imp-HA binds to region 1 of the *upd* 3'UTR (**b**), and to domain 1 and 1\* within region 1 of the *upd* 3'UTR, but not to domain 2 (**c**). Mutations in domain 1\* of the *upd* 3'UTR are indicated in red (**c**). **d**, qRT-PCR showing relative *gfp* mRNA levels in cells co-transfected with actin-GAL4 and the

indicated *gfp* reporter constructs. Expression of *gfp* is presented relative to cells without Imp-HA and is normalized to *GAL4*. Note that *gfp-upd-3'UTR* mRNA is sixfold higher than *gfp-med23-3'UTR* in cells expressing Imp-HA.

**e**, Sequence of cleavage product from aged testes identified a fragment starting at nucleotide 33 within the *upd* 3'UTR (black arrowhead, grey box). Alignment of the *upd* 3'UTR with endo-siRNAs found in aged testes library. Filled circles, canonical base pairing; open circles, GU pairs. **f**, qRT-PCR showing *gfp* from S2 cells transfected with *gfp-upd-3'UTR* or with *gfp-upd-3'UTR<sup>mut</sup>* (<sup>32</sup>AUU = CGG), with or without Imp and *siRNA2*. Levels normalized to *rp49* and relative to control *gfp* levels without *siRNA2*. Error bars in **a**, **d** and **f** denote s.d. of triplicate measurements.

reporter (*gfp-upd-3'UTR*) in the presence or absence of Imp and *siRNA2* in S2 cells. To generate a reporter that should not be susceptible to siRNA-mediated degradation, we mutated the cleavage site in the *upd* 3'UTR that was identified by RACE (<sup>32</sup>AUU = CGG; *gfp-upd-3'UTR<sup>mut</sup>*). Cells were transfected with either of the GFP reporter constructs, with or without haemagglutinin-tagged Imp (Imp-HA), and subsequently transfected with *siRNA2*; *gfp* expression was quantified by qRT-PCR.

The co-expression of *siRNA2* and the *gfp-upd-3'UTR* reporter resulted in a significant decrease in *gfp* transcript levels (Fig. 2f). Conversely, the co-expression of Imp blocked *siRNA2*-mediated reduction of *gfp* mRNA such that *gfp* levels were higher than in control cells (Fig. 2f). Furthermore, mutation of the putative cleavage site rendered the *upd* 3'UTR resistant to *siRNA2*-mediated degradation (Fig. 2f). These data, in combination with the *in vitro* binding data, suggest that Imp binds to and protects the *upd* 3'UTR from endogenous and exogenous *siRNA2* in S2 cells. Thus, endo-*siRNA2* is a bona fide candidate that could direct *upd* degradation when Imp is absent or its levels are reduced, although targeting by other small RNAs cannot be excluded.

In *Drosophila*, Argonaute-1 (AGO1) is the principle acceptor of miRNAs and primarily regulates targets in a cleavage-independent

mode, whereas AGO2 is preferentially loaded with siRNAs and typically regulates targets by mRNA cleavage<sup>16</sup> (reviewed in refs 17, 18). AGO2 expression was detected throughout the tip of the testes, as verified by immunostaining of testes from transgenic flies expressing 3×Flag-HA-tagged AGO2 (ref. 15; Fig. 3a, b). To test whether AGO2 binds to *upd* mRNA *in vivo*, thereby potentially regulating *upd* levels directly, testes were dissected from aged (30-day-old) 3×Flag-HA-AGO2 males. Immunoprecipitation of AGO2, followed by qRT-PCR, showed significant enrichment (~102-fold) of *upd* mRNA bound to AGO2 (Fig. 3c). Negligible binding of a negative control, *rp49*, to AGO2 was detected, suggesting specific association of AGO2 with *upd* mRNA *in vivo* and supporting our previous findings that *upd* is probably targeted by the siRNA pathway (Fig. 3c).

To test whether Imp can impede the binding of AGO2 to the *upd* 3'UTR, S2 cells stably expressing Flag-tagged AGO2 (ref. 19) were transfected with the *gfp-upd-3'UTR* reporter. Consistent with our previous observations, transcript levels of *gfp-upd-3'UTR* increased ~18-fold when Imp was co-expressed (Fig. 2d and Supplementary Fig. 5b). Despite increases in the overall levels of *gfp* mRNA, the presence of Imp markedly reduced the association of AGO2 with the *upd* 3'UTR (Fig. 3d), indicating that Imp antagonizes the ability of AGO2 to bind the *upd* 3'UTR.

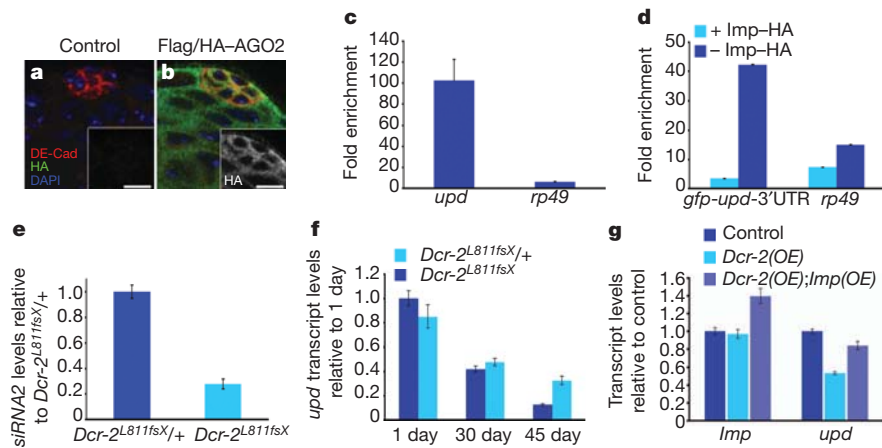


**Figure 3 | Imp counteracts AGO2 and Dicer-2 to regulate *upd* levels and stem-cell maintenance.** **a, b**, Testes from control (**a**) or Flag/HA-AGO2 (**b**) males showing AGO2 expression throughout the testis tip. DE-Cad, *Drosophila* E-cadherin. Scale bars, 10  $\mu$ m. **c**, Flag/HA-AGO2 RNA immunoprecipitation from the testes of 30-day-old males. The fold enrichment of *upd* or *rp49* RNA bound to mouse anti-Flag relative to control IgG is shown. **d**, qRT-PCR after Flag-AGO2 RNA immunoprecipitation from S2 cells, showing fold enrichment of *gfp-upd-3'UTR* or *rp49* RNA bound to anti-Flag antibodies relative to control IgG, in the presence (light blue) or absence (dark blue) of Imp-HA. **e**, qRT-PCR showing mature *siRNA2* levels relative to

*bantam* in testes from *Dcr-2<sup>L811fsX</sup>/+* heterozygous and *Dcr-2<sup>L811fsX</sup>* homozygous flies. Expression normalized to heterozygotes. Note the 72% reduction in *siRNA2* levels in *Dcr-2<sup>L811fsX</sup>* homozygous flies. **f**, qRT-PCR of *upd* levels in testes from *Dcr-2<sup>L811fsX</sup>/+* and *Dcr-2<sup>L811fsX</sup>* flies measured in testes from 1-, 30- and 45-day-old males; shown are *upd* levels relative to levels in 1-day-old *Dcr-2* heterozygotes. **g**, qRT-PCR showing mRNA abundance for *Imp* and *upd* relative to controls. Note reduction of *upd* transcript levels in flies expressing ectopic *Dcr-2*, which is suppressed by co-expression of *Imp*. mRNA levels in **f** and **g** were normalized to *GapDH*. Error bars in **c–g** denote s.d. of triplicate measurements.

Similar to the AGO family, *Drosophila* encodes two Dicer proteins that seem to have distinct roles in small RNA biogenesis. Dicer-1 (*Dcr-1*) is essential for the generation of miRNAs, and *Dcr-2* is required for siRNA production from exogenous and endogenous sources<sup>16</sup> (reviewed in refs 17, 18). If siRNAs were involved in *upd* degradation in older males, we predicted that the loss of *Dcr-2* would suppress the ageing-related decline in *upd* and GSCs. Consistent with a role for *Dcr-2* in the generation of siRNAs, *siRNA2* levels were significantly reduced in *Dcr-2* homozygous mutants relative to heterozygous controls (Fig. 3e). Testes from 30- and 45-day-old *Dcr-2* mutant flies showed increased levels of *upd* by qRT-PCR when compared with controls. Whereas a ~90% reduction of *upd* is observed in the testes from aged *Dcr-2* heterozygous controls, we observed only a ~45% reduction in *upd* in testes from age-matched, *Dcr-2* homozygous mutants (Fig. 3f), indicating that *upd* levels are higher when *Dcr-2* function is compromised. Furthermore, the testes from aged *Dcr-2* mutants contained more GSCs, on average, when compared with controls (Supplementary Fig. 5c–h). Conversely, the forced expression of *Dcr-2* in hub cells resulted in a reduction in the average number of GSCs (Supplementary Fig. 5i–j, l) and led to a significant reduction in *upd* levels, as detected using qRT-PCR and combined immunofluorescence and FISH, which seemed to be specific, as no significant change in *Imp* transcript levels was observed (Fig. 3g and Supplementary Fig. 5m, n). Expression of *Imp* in combination with *Dcr-2* resulted in a significant increase in *upd* levels (Fig. 3g), with a concomitant increase in the average number of GSCs (Supplementary Fig. 5i–l). These observations indicate that *Imp* can counter the decrease in *upd* levels resulting from forced *Dcr-2* expression, providing further evidence that *Imp* protects *upd* from targeted degradation by the siRNA pathway.

### *let-7* targets *Imp* in the *Drosophila* testis

Our data suggest that *Imp* has a role in stabilizing *upd* in hub cells; therefore, the ageing-related decline in *Imp* would be a major contributing factor to the decrease in *upd* mRNA in the hub cells of aged males. To investigate the mechanism that leads to the decline in *Imp* expression with age, we examined the *Imp* 3'UTR for potential instability elements. Within the first 160 base pairs there is a canonical seed sequence for the heterochronic miRNA *let-7* (Fig. 4a).

Expression of a reporter gene under the control of the *let-7* promoter showed that *let-7* expression increases in hub cells of ageing males (Fig. 4b, c), which was confirmed by *let-7* FISH of testes from aged males (Supplementary Fig. 6a–d). In addition, mature *let-7* miRNA was enriched twofold in the testes from 30-day-old flies, relative to 1-day-old males (Fig. 4d). Therefore, an age-related increase in *let-7* is one mechanism by which *Imp* expression could be regulated in an ageing-dependent manner in testes from older males.

Consistent with these observations, the forced expression of *let-7* specifically in hub cells led to a decrease in *Imp* (Fig. 4e, f, insets). In addition, *let-7* expression in S2 cells reduced the levels of a heterologous *gfp-imp-3'UTR<sup>WT</sup>* reporter. S2 cells were transfected with a *let-7* mimic or with negative control miRNA, and *gfp* expression was quantified by qRT-PCR. There was a 70% reduction in *gfp-imp-3'UTR<sup>WT</sup>* expression in the presence of *let-7*, relative to control miRNA (Fig. 4g). A *gfp-imp-3'UTR<sup>mut</sup>* reporter with mutations in the canonical seed for *let-7* (at nucleotide 137) was unaffected by *let-7* expression, indicating that mutation of the *let-7* seed rendered the RNA resistant to degradation. These data confirm that *let-7* can destabilize *Imp* through sequences in the 3'UTR (Fig. 4g). However, further increasing the levels of *let-7* resulted in a decrease in *gfp* expression from the mutated 3'UTR, indicating that other, putative *let-7* seeds in the *Imp* 3'UTR can be targeted by *let-7* (Fig. 4g and Supplementary Fig. 6e).

If the age-related decrease in *Imp* contributes to a decline in *upd* and subsequent loss of GSCs, we proposed that re-expression of *Imp* in hub cells would rescue the ageing-related decline in *upd*. Therefore, flies in which *Imp* was constitutively expressed in hub cells were aged, and *upd* levels were quantified by qRT-PCR. The expression of an *Imp* construct containing a truncated 3'UTR (*Imp*-KH-HA) lacking *let-7* target sequences specifically in hub cells was sufficient to suppress the ageing-related decline in *upd*, with concomitant maintenance of GSCs (Fig. 4h, j, k and Supplementary Fig. 6f), similar to what was observed by re-expressing *upd* in the hub cells of aged males<sup>5,33</sup>. Maintenance of *Imp*-KH-HA expression in aged males was verified by staining with an anti-HA antibody (Fig. 4j, inset). Conversely, the expression of an *Imp* construct that is susceptible to degradation by *let-7* (*Imp<sup>T21</sup>*) did not lead to an accumulation of *Imp* in the testes of 30- and 50-day-old flies, as levels were similar to the levels of endogenous *Imp* at later time points (Supplementary Fig. 6g)<sup>20</sup>.



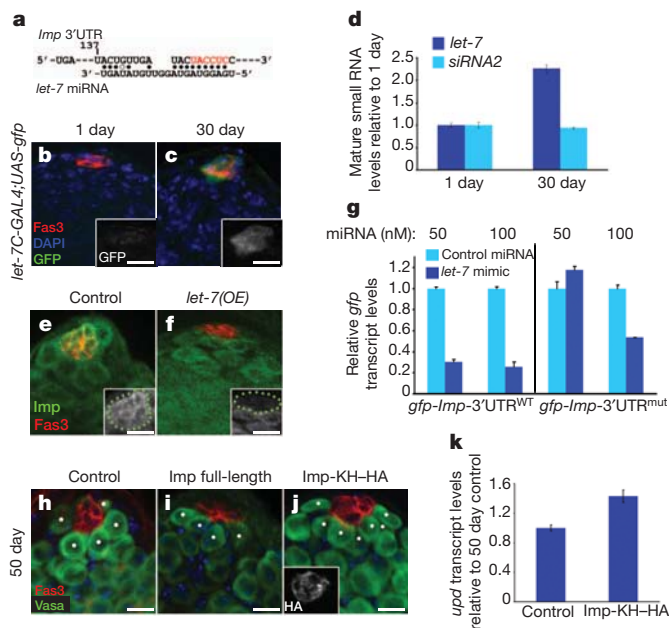


**Figure 4 | *Imp* is targeted by *let-7* miRNA in the testis.** **a**, Canonical *let-7* seed sequence within the *Imp* 3' UTR. Start site at position 137. Filled circles, canonical base pairs; open circles, GU base pairs. Note perfect seed pairing of nucleotides 2–7 with the 5' end of *let-7* (red). **b**, **c**, Testes from 1-day-old (**b**) and 30-day-old (**c**) males immunostained for GFP (green, insets) to follow *let-7C* expression. **d**, qRT-PCR for mature *let-7* and *siRNA2* relative to *bantam* in the testes of 1- and 30-day-old males. Levels normalized to 1-day-old adults. **e**, **f**, Overexpression of *let-7* in hub cells reduces *Imp* expression. Larval testes immunostained as indicated. Green dots in insets outline hub cells. Genotypes: control, *upd-GAL4*<sup>1</sup>; *TM3,kr-GAL4,UAS-gfp* (**e**); *let-7(OE)*, *upd-GAL4*; *UASlet-7*<sup>701.12.9</sup> (**f**). **g**, *let-7* targets a *gfp-Imp-3'UTR* reporter in S2 cells. qRT-PCR for *gfp* transcript levels relative to control miRNA at the same concentration. Transfection of 50 nM *let-7* mimic results in a 70% reduction in the *gfp* transcript of *gfp-Imp-3'UTR*<sup>WT</sup> but not of *gfp-Imp-3'UTR*<sup>mut</sup> (mutated bases to disrupt *let-7* binding are coloured red in **a**). Higher concentrations of *let-7* target the *Imp* 3' UTR through additional sites. **h**–**j**, Immunofluorescence of testes from 50-day-old control (**h**), *Imp* full-length (**i**) or *Imp* with a truncated 3' UTR (*Imp-KH-HA*; **j**). Genotypes: control, *w,upd-GAL4,UAS-gfp* outcrossed to *w*<sup>1118</sup> (**h**); *Imp* full-length, *w,upd-GAL4,UAS-gfp;UASImp*<sup>T21</sup> (**i**); *Imp-KH-HA*, *w,upd-GAL4,UAS-Imp*<sup>HA-KH1-3-3</sup> (**j**). Scale bars, 10  $\mu$ m. **k**, qRT-PCR showing relative *upd* levels in testes from 50-day-old males. Control and *Imp-KH-HA* genotypes are as in **h** and **j**, respectively. Note the 1.5-fold increase in *upd* levels in aged flies overexpressing the *Imp-KH-HA* transgene. *gfp* and *upd* mRNA expression in **g** and **k** are shown relative to controls and normalized to *GapDH*.

Consequently, the expression of this construct was not sufficient to block the ageing-related decline in GSCs (Fig. 4h, i and Supplementary Fig. 6f). These data indicate that *let-7*-mediated regulation of *Imp* contributes to the decline in *Imp* protein in older flies, and supports a model in which an ageing-related decline in *Imp*, mediated by *let-7*, exposes *upd* to degradation by siRNAs (Supplementary Fig. 1). Thus, both the miRNA and siRNA pathways act upstream to regulate the ageing of the testis stem-cell niche by generating *let-7* and *siRNA2*, which target *Imp* and *upd*, respectively.

*Drosophila* has proven to be a valuable model system for investigating ageing-related changes in stem-cell behaviour<sup>21</sup>. Cell autonomous and extrinsic changes contribute to altered stem-cell activity; thus, determining the mechanisms underlying the ageing-related decline of self-renewal factors, such as the cytokine-like factor *Upd*, may provide insight into strategies to maintain optimal niche function.

Our data indicate that *Imp* can regulate gene expression by promoting the stability of selected RNA targets by countering inhibitory small RNAs. Therefore, rescue of the aged niche by *Imp* expression may be a consequence of effects on *Imp* targets, in addition to *upd*, in

somatic niche cells. Furthermore, as *Imp* is expressed in germ cells, it could also act in an autonomous manner to regulate the maintenance of GSCs. The canonical *let-7* seed in the *Imp* 3' UTR is conserved in closely related species, and reports have predicted that the *let-7* family of miRNAs target mammalian *Imp* homologues (IGF2BP1–3)<sup>22</sup>. Given the broad role of the *let-7* family in ageing<sup>23</sup>, stem cells<sup>24–28</sup>, cancer<sup>29,30</sup> and metabolism<sup>31</sup>, the regulation of *Imp* by *let-7* may be an important, conserved mechanism in numerous physiological processes.

Non-coding RNAs can ensure biological robustness and provide a buffer against relatively small fluctuations in a system<sup>32</sup>. However, after a considerable change, a molecular switch is flipped, which allows a biological event to proceed unimpeded. In our model, *Imp* preserves niche function in young flies until a time at which miRNAs and siRNAs act together to trigger an 'ageing' switch that leads to a definitive decline in *upd* and, ultimately, in stem-cell maintenance (Supplementary Fig. 1). Therefore, targeting signalling pathways at several levels using RNA-based mechanisms will probably prove to be a prevalent theme to ensure robustness in complex biological systems.

## METHODS SUMMARY

**Fly stocks and husbandry.** Flies were raised at 25 °C on standard cornmeal-molasses agar medium. The ageing model was used as described previously<sup>5</sup>. All stocks and genotypes are described in Methods.

**Immunofluorescence.** Immunofluorescence of whole-mount testes, mean densitometric analysis, and quantification of GSCs and hub cells were performed as described previously<sup>5</sup>.

**Combined FISH and immunofluorescence.** Testes were dissected, fixed in 4% formaldehyde in PBT (diethylpyrocatechol PBS, 0.1% Tween 20) and incubated overnight at 4 °C with primary antibodies in PBTHR (PBT, 50  $\mu$ g ml<sup>-1</sup> heparin, 250  $\mu$ g ml<sup>-1</sup> tRNA), followed by incubation with secondary antibodies (1:100 in PBTHR) for 2 h at room temperature. After washes, testes were post-fixed in 10% formaldehyde in PBT. For mRNA detection<sup>34</sup>, a *upd* digoxigenin (DIG)-labelled RNA probe was hybridized overnight at 65 °C in hybridization buffer<sup>5</sup>. To detect *upd* mRNA, testes were washed with hybridization buffer and PBT and blocked with TNB (0.1 M Tris-HCl, pH 7.5, 0.15 M NaCl, 0.5% blocking reagent; PerkinElmer). Next, testes were incubated with sheep anti-DIG-POD antibody (1:500, Roche) in TNB at 4 °C, and *upd* was detected with TSA cyanine3 (PerkinElmer). Testes were washed and mounted in DAPI containing Vectashield.

**RNA-protein co-immunoprecipitation.** Magna RIP RNA-binding protein immunoprecipitation kit (Millipore) was used to precipitate GFP-tagged *Imp* (*Imp-GFP*) or 3 $\times$ Flag/HA-tagged AGO2 and associated RNA from testes. Testes from ~1,500 males were dissected on dry ice, and homogenized in RNA immunoprecipitation lysis buffer. Each lysate was divided into two samples; one was used for immunoprecipitation with either rabbit anti-GFP (Clontech) or mouse anti-Flag (Sigma) antibodies, and the second was used with control rabbit or mouse IgG according to the manufacturer's instructions. RNA was phenol-chloroform precipitated from samples and from input (10% of control immunoprecipitate input before washes). Input RNA was used to establish a standard curve to calculate the percentage of precipitated RNA. cDNA was prepared with random hexamer primers, followed by qRT-PCR with primers described in Methods.

**Full Methods** and any associated references are available in the online version of the paper at [www.nature.com/nature](http://www.nature.com/nature).

Received 17 October 2010; accepted 16 March 2012.

Published online 23 May 2012.

- Schofield, R. The relationship between the spleen colony-forming cell and the haemopoietic stem cell. *Blood Cells* **4**, 7–25 (1978).
- Jones, D. L. & Rando, T. A. Emerging models and paradigms for stem cell ageing. *Nature Cell Biol.* **13**, 506–512 (2011).
- Voog, J. & Jones, D. L. Stem cells and the Niche: a dynamic duo. *Cell Stem Cell* **6**, 103–115 (2010).
- Fuller, M. T. in *The Development of Drosophila Melanogaster* (eds Bate, M. & Martinez-Arias, A.) 71–147 (Cold Spring Harbor Laboratory Press, 1993).
- Boyle, M., Wong, C., Rocha, M. & Jones, D. L. Decline in self-renewal factors contributes to aging of the stem cell niche in the *Drosophila* testis. *Cell Stem Cell* **1**, 470–478 (2007).
- Buszczak, M. et al. The Carnegie protein trap library: a versatile tool for *Drosophila* developmental studies. *Genetics* **175**, 1505–1531 (2007).
- Fabrizio, J. J. et al. *Imp* (IGF-II mRNA-binding protein) is expressed during spermatogenesis in *Drosophila melanogaster*. *Fly* **2**, 47–48 (2008).

8. Yisraeli, J. K. VICKZ proteins: a multi-talented family of regulatory RNA-binding proteins. *Biol. Cell* **97**, 87–96 (2005).
9. Brand, A. H., Manoukian, A. S. & Perrimon, N. Ectopic expression in *Drosophila*. *Methods Cell Biol.* **44**, 635–654 (1994).
10. Munro, T. P., Kwon, S., Schnapp, B. J. & St Johnston, D. A repeated IMP-binding motif controls oskar mRNA translation and anchoring independently of *Drosophila melanogaster* IMP. *J. Cell Biol.* **172**, 577–588 (2006).
11. Nabel-Rosen, H., Dorevitch, N., Reuveny, A. & Volk, T. The balance between two isoforms of the *Drosophila* RNA-binding protein how controls tendon cell differentiation. *Mol. Cell* **4**, 573–584 (1999).
12. Hafner, M. *et al.* Transcriptome-wide identification of RNA-binding protein and microRNA target sites by PAR-CLIP. *Cell* **141**, 129–141 (2010).
13. Bhattacharyya, S. N., Habermacher, R., Martine, U., Closs, E. I. & Filipowicz, W. Relief of microRNA-mediated translational repression in human cells subjected to stress. *Cell* **125**, 1111–1124 (2006).
14. Elcheva, I., Goswami, S., Noubissi, F. K. & Spiegelman, V. S. CRD-BP protects the coding region of  $\beta$ TrCP1 mRNA from miR-183-mediated degradation. *Mol. Cell* **35**, 240–246 (2009).
15. Czech, B. *et al.* An endogenous small interfering RNA pathway in *Drosophila*. *Nature* **453**, 798–802 (2008).
16. Lee, Y. S. *et al.* Distinct roles for *Drosophila* Dicer-1 and Dicer-2 in the siRNA/miRNA silencing pathways. *Cell* **117**, 69–81 (2004).
17. Carthew, R. W. & Sontheimer, E. J. Origins and mechanisms of miRNAs and siRNAs. *Cell* **136**, 642–655 (2009).
18. Golden, D. E., Gerbasi, V. R. & Sontheimer, E. J. An inside job for siRNAs. *Mol. Cell* **31**, 309–312 (2008).
19. Czech, B. *et al.* Hierarchical rules for Argonaute loading in *Drosophila*. *Mol. Cell* **36**, 445–456 (2009).
20. Geng, C. & Macdonald, P. M. Imp associates with squid and Hrp48 and contributes to localized expression of gurken in the oocyte. *Mol. Cell Biol.* **26**, 9508–9516 (2006).
21. Wang, L. & Jones, D. L. The effects of aging on stem cell behavior in *Drosophila*. *Exp. Gerontol.* **46**, 340–344 (2010).
22. Boyerinas, B. *et al.* Identification of let-7-regulated oncofetal genes. *Cancer Res.* **68**, 2587–2591 (2008).
23. Nishino, J., Kim, I., Chada, K. & Morrison, S. J. Hmga2 promotes neural stem cell self-renewal in young but not old mice by reducing p16<sup>Ink4a</sup> and p19<sup>Arf</sup> expression. *Cell* **135**, 227–239 (2008).
24. Zhao, C. *et al.* MicroRNA let-7b regulates neural stem cell proliferation and differentiation by targeting nuclear receptor TLX signaling. *Proc. Natl Acad. Sci. USA* **107**, 1876–1881 (2010).
25. Landgraf, P. *et al.* A mammalian microRNA expression atlas based on small RNA library sequencing. *Cell* **129**, 1401–1414 (2007).
26. Chen, C. *et al.* Defining embryonic stem cell identity using differentiation-related microRNAs and their potential targets. *Mamm. Genome* **18**, 316–327 (2007).
27. Rybak, A., Fuchs, H., Smirnova, L., Brandt, C., Pohl, E. E., Nitsch, R. & Wulczyn, F. G. A feedback loop comprising *lin-28* and *let-7* controls pre-*let-7* maturation during neural stem-cell commitment. *Nature Cell Biol.* **10**, 987–993 (2008).
28. Melton, C., Judson, R. L. & Blueloch, R. Opposing microRNA families regulate self-renewal in mouse embryonic stem cells. *Nature* **463**, 621–626 (2010).
29. Iliopoulos, D., Hirsch, H. A. & Struhl, K. An epigenetic switch involving NF- $\kappa$ B, Lin28, let-7 microRNA, and IL6 links inflammation to cell transformation. *Cell* **139**, 693–706 (2009).
30. Boyerinas, B., Park, S. M., Hau, A., Murmann, A. E. & Peter, M. E. The role of let-7 in cell differentiation and cancer. *Endocr Relat Cancer* **17**, F19–F36 (2010).
31. Zhu, H. *et al.* The *Lin28/let-7* axis regulates glucose metabolism. *Cell* **147**, 81–94 (2011).
32. Li, X., Cassidy, J. J., Reinke, C. A., Fischboeck, S. & Carthew, R. W. A microRNA imparts robustness against environmental fluctuation during development. *Cell* **137**, 273–282 (2009).
33. Boylan, K. L. *et al.* Motility screen identifies *Drosophila* IGF-II mRNA-binding protein–zipcode-binding protein acting in oogenesis and synaptogenesis. *PLoS Genet.* **4**, e36 (2008).
34. Kitadate, Y. *et al.* Boss/Sev signaling from germline to soma restricts germline-stem-cell-niche formation in the anterior region of *Drosophila* male gonads. *Dev. Cell* **13**, 151–159 (2007).

**Supplementary Information** is linked to the online version of the paper at [www.nature.com/nature](http://www.nature.com/nature).

**Acknowledgements** We are grateful to D. St Johnston, W. Chia, P. Macdonald, R. Carthew, E. Bach, D. Harrison, T. Volk, U. Heberlein, A. Spradling, J. Kadonaga, G. Hannon, T. Hays, N. Sokol, H. Siomi and P. Lasko for reagents and fly stocks, to C. Doe, R. Hans, G. Volohonsky, T. Juven-Gershon, A. Pasquinelli, R. Zhou and S. Aigner for guidance on methods used in this manuscript, to O. Tam for computational support, and to C. Koehler for technical assistance. This work was supported by the G. Harold and Leila Y. Mathers Charitable Foundation, the Ellison Medical Foundation, the Emerald Foundation, the American Federation for Aging Research, and the National Institutes of Health (to D.L.J.). B.C. is supported by a PhD fellowship from the Boehringer Ingelheim Fonds. E.L. is supported by the National Science Foundation.

**Author Contributions** H.T., C.D. and D.L.J. designed experiments. H.T. and C.D. performed experiments. B.C. generated and analysed small RNA libraries. E.L. performed bioinformatic analysis to identify Imp-binding sequences. H.T., C.D., B.C. and D.L.J. evaluated the data and wrote the manuscript.

**Author Information** The small RNA libraries from the testes of 1-day-old and 30-day-old flies have been deposited in the Gene Expression Omnibus database under accession GSE37041. Reprints and permissions information is available at [www.nature.com/reprints](http://www.nature.com/reprints). The authors declare no competing financial interests. Readers are welcome to comment on the online version of this article at [www.nature.com/nature](http://www.nature.com/nature). Correspondence and requests for materials should be addressed to D.L.J. (ljones@salk.edu).



## METHODS

**Drosophila stocks and genotypes.** Wild-type flies were Oregon R. Additional strains used were: *upd-GAL4,UAS-gfp* (E. Bach); *upd-GAL4* (T. Xie); *w;UAS-upd,TM2* (D. Harrison); *w; let-7C<sup>GK1</sup>/CyO* and *UAS-let-7<sup>01.12.9</sup>* (N. Sokol<sup>35</sup>); *3×Flag/HA-AGO2* (G. Hannon<sup>15</sup>); *Imp<sup>CB04573</sup>* (A. Spradling<sup>6</sup>); *8-156-GAL4* (U. Heberlein<sup>36</sup>); *UAS-Imp<sup>T21</sup>* (P. Macdonald<sup>20</sup>); *UAS-Imp HA-KH1 3-3* (from T. Hays<sup>33</sup>); *UAS-Imp(RNAi)* (Vienna *Drosophila* RNAi Center (VDRC) stock number 20322); and *UAS-gfp<sup>hls</sup>* (Bloomington *Drosophila* Stock Center (BDSC) number 4775).

*Imp<sup>7</sup>* and *Imp<sup>8</sup>* were gifts from D. St Johnston<sup>10</sup>. *EP(X)760* (*w<sup>1118</sup>,P{w<sup>+</sup>mc = EP}Imp<sup>EP760</sup>*; BDSC number 17294) was used as a control for *Imp<sup>7</sup>* and *Imp<sup>8</sup>* alleles. *Imp<sup>7</sup>* and *Imp<sup>8</sup>* hemizygous larvae (L3) were obtained by crossing *Imp<sup>7</sup>/FM0* or *Imp<sup>8</sup>/FM0* females with *FM7,KrGAL4,UAS-gfp* males (BDSC). L3 mutants were selected against GFP. Specifically, *Imp<sup>7</sup>/FM7*, *KrGAL4, UAS-gfp*; *8-156-GAL4* or *Imp<sup>8</sup>/FM7*, *KrGAL4, UAS-gfp*; *8-156-GAL4* females were crossed to *w<sup>-</sup>/Y;+*; *UAS-Imp<sup>T21</sup>* males, and non-GFP L3 male progeny were selected.

*UAS-Dcr-2* (VDRC number 60008) and *yw, eyFLP;FRT42D, Dcr-2<sup>L811fsX</sup>* were gifts from R.W. Carthew<sup>16</sup>. Heterozygous flies were obtained by out-crossing to *w;FRT42D* (BDSC number 1802). An independent *Dcr-2* mutant background was obtained by crossing *Df(2R)BSC45w<sup>+</sup>mC/SM6a* (*Dcr-2* deficiency chromosome; BDSC number 7441) with *y,w, eyFLP;FRT42D, Dcr-2<sup>L811fsX</sup>*. Heterozygous flies were obtained by out-crossing *Df(2R)BSC45, w<sup>+</sup>mC/SM6a* to *w;FRT42D*.

**Antibodies.** Primary antibodies for immunofluorescence were as follows: rabbit anti-Imp (1:600, gift from P. M. Macdonald<sup>20</sup>), mouse anti-HA (1:800, Covance), rabbit anti-β-galactosidase (1:2,000, Cappel), rabbit anti-GFP (1:5,000, Invitrogen), rabbit anti-Vasa (1:3,000, gift from P. Lasko), rabbit anti-STAT (1:800, gift from D. Montell); mouse anti-Fas3 (1:50), rat anti-DEcad (1:20) and rat anti-DNcad (1:20) were obtained from the Developmental Studies Hybridoma Bank, developed under the auspices of the National Institute of Child Health and Human Development and maintained by the University of Iowa, Department of Biological Sciences. Secondary antibodies were obtained from Invitrogen.

**Combined FISH and immunofluorescence.** For *let-7* miRNA detection, testes were dissected, squashed onto slides<sup>37</sup>, and incubated with primary antibodies using PBT (diethylpyrocarbonate PBS, 0.1% Tween 20) and PBTHR solutions<sup>34</sup>. After washes and secondary antibodies, slides were treated with proteinase K for 3 min, rinsed and post-fixed in 10% formaldehyde. Slides were then treated according to the manufacturer's recommendations for miRNA *in situ* (Exiqon). Slides were hybridized with 40 nM *let-7* LNA-digoxigenin (DIG) probe for 1 h at 50 °C with Exiqon hybridization buffer in a humid chamber. *let-7* FISH detection signal and mounting was performed similar to *upd*.

**Generation of DNA constructs.** The nucleotide numbers of the following sequences refer to their numbers in the 3'UTRs/5'UTRs or open reading frames (ORF), as shown on FlyBase. All point mutations described were generated by site-directed mutagenesis (Stratagene). pBS-*upd* was a gift from D.A. Harrison<sup>38</sup>. pAc5.1-*Imp*-HA and pBS-*Imp*-HA were produced by PCR of *Imp*-RB ORF using *Imp* cDNA (expressed sequence tag (EST) clone SD07045) as a template. pBS-*upd*-3'UTR or pBS-*med23*-3'UTR was produced by PCR of the *upd* 3'UTR (nucleotides 73–707) or *med23* 3'UTR (nucleotides 791–1391) and ligated into pBS. To generate pAc5.1-*gfp-upd*-3'UTR and pAc5.1-*gfp-upd*-3'UTR<sup>mut</sup> (<sup>32</sup>ATT = CGG), nucleotides 1–737 of the *upd* 3'UTR were ligated into pAc5.1 following the *gfp* ORF. pBS-*upd*-5'UTR and pBS-*upd*-coding were produced by PCR of the *upd* 5'UTR (nucleotides 1–224 of *os*-RA) or *upd* coding region (nucleotides 29–1191 of *os* ORF) and ligated into pBS. Region 1 (nucleotides 4–243), region 2 (nucleotides 228–468), region 3 (nucleotides 443–737), domain 1 (nucleotides 1–152) and domain 2 (nucleotides 33–152) of the *upd* 3'UTR were amplified by PCR and ligated into pBS. Domain 1\* of the *upd* 3'UTR was generated by four point mutations (U8G, U17G, U23G and U33G). To generate pAc5.1-*gfp-Imp*-3'UTR<sup>WT</sup>, *Imp*-RB 3'UTR (nucleotides 45–781) was amplified by PCR and then ligated into pGEM T-Easy (Promega). In pAc5.1-*gfp-Imp*-3'UTR<sup>MUT</sup>, the *let-7* seed was disrupted by five tandem point mutations (<sup>149</sup>TACCT = CGTTC). pGEM T-Easy-*Imp* 3'UTR wild-type and mutant were then digested with NotI and ligated downstream of the *gfp* coding region in pAc5.1-*gfp*. The sequence of all DNA constructs described above was verified by DNA sequencing.

**RNA-protein binding assay and western blotting.** Biotin-labelled RNA was transcribed *in vitro* from cDNAs cloned into pBS using T7 RNA polymerase. The RNA concentration was measured, and an equal number of RNA molecules (according to size) was assayed for protein binding. *Imp*-HA was translated *in vitro* using the TNT Coupled Reticulocyte Lysate System (Promega), and 5 µl of the translation mixture was mixed with biotin-labelled RNA. Binding assays were performed as described<sup>12</sup>. Associated protein complexes were separated on 10%

SDS-PAGE gels, followed by western blotting according to standard procedures. Antibodies for western analysis (1:1,000) were: mouse anti-Flag and mouse anti-α-tubulin (Sigma), mouse anti-HA (Covance) and mouse anti-GFP (Clontech).

*In silico* examination of the *upd* 3'UTR, 5'UTR and coding regions showed that the *upd* 3'UTR contains an abundance of AU-rich sequences. Annotated *Drosophila* 3'UTRs were surveyed for the AU/CG ratio, and identified the *med23* 3'UTR as one that should not be recognized by Imp, owing to equal AU/CG ratios. Statistical analysis of possible Imp-binding sequences was done in MATLAB (Mathwork). All sequences that bound Imp *in vitro* were analysed by Meme<sup>39</sup> to search for sequence motifs. Alignment based on locally stable RNA structure was performed by LocARNA (the Vienna package: <http://rna.tbi.univie.ac.at/>).

**S2 cell culture and transfection.** S2 adherent cells were cultured in Schneider's *Drosophila* medium and supplemented with 10% heat-inactivated fetal bovine serum (Invitrogen). Each experiment was done at least three times and each transfection was performed in triplicate. Plasmids were transfected according to the manufacturer's recommendations (Fugene HD, Roche). For GFP-3'UTR dependent assays, cells were transfected with pBS-actin-*GAL4* (obtained from T. Volk) and with either *UAS-gfp-upd*-3'UTR or *UAS-gfp-med23*-3'UTR and with 1 µg pAC 5.1 empty vector or pAC 5.1-*Imp*HA. Cells were collected 20–26 h after transfection and RNA was extracted with the RNeasy kit (Qiagen) and used for qRT-PCR. *gfp* levels were quantified relative to *GAL4* to account for transfection efficiency.

To test the activity of *siRNA2* functionally, S2 cells were transfected with pAc5.1-*gfp-upd*-3'UTR, with either pAC 5.1 empty vector or pAc5.1-*Imp*-HA, or with pAc5.1-*gfp-upd*-3'UTR<sup>mut</sup> (<sup>32</sup>ATT = CGG). Thirty-six hours after transfection, each plate was split into two. One plate was transfected with 100 nM annealed oligonucleotides for *siRNA2* (guide sequence: 5'-UGAGGGGAAAU UGGAGGGGGU-3', passenger sequence: 5'-CCCCUCCAAUUUCCUUUU UU-3') using HighPerfect (Qiagen). Cells were collected 20–26 h after second transfection and used for qRT-PCR. *gfp* levels were quantified relative to *rp49* RNA levels. Each transfection was performed in triplicate.

For the *gfp* or *let-7* reporter assay, cells were transfected with reporter construct of *gfp-Imp*-3'UTR<sup>WT</sup> or *gfp-Imp*-3'UTR<sup>mut</sup>. Twenty-four hours after transfection, cells from each transfection were reseeded in 6-cm plates and transfected with 50 or 100 nM of synthetic pre-miRNAs to gain expression of *dme-miR-let-7* or negative control miRNA (Applied Biosystems) using HiPerfect (Qiagen). Cells were collected 48 h after miRNA transfection and total RNA was extracted with TRIzol (Invitrogen). For each sample we used qRT-PCR to measure *let-7* and *bantam* miRNA expression with Taqman probes for mature miRNA and *gfp* reporter levels using primers for *gfp* and *GapDH*.

**RNA-protein co-immunoprecipitation.** Magna RIP RNA-binding protein immunoprecipitation kit (Millipore) was used to precipitate GFP-tagged Imp (*Imp*-GFP) or 3×Flag/HA-tagged AGO2 and associated RNA from testes. Testes from ~1,500 males were dissected on dry ice, and homogenized in RNA immunoprecipitation lysis buffer. Each lysate was divided into two samples; one was used for immunoprecipitation with either rabbit anti-GFP (Clontech) or mouse anti-Flag (Sigma) antibodies, and the second was used with control rabbit or mouse IgG according to the manufacturer's instructions. RNA was phenol-chloroform precipitated from samples and from input (10% of control immunoprecipitate input before washes). Input RNA was used to establish a standard curve to calculate the percentage of precipitated RNA. Complementary DNA was prepared with random hexamer primers, followed by qRT-PCR.

For AGO2 RNA immunoprecipitation, S2 cells stably expressing Flag-AGO2 (gift from N. Perrimon<sup>19</sup>) were transfected with pAc5.1-*gfp-upd*-3'UTR with and without pAc5.1-*Imp*. Thirty-six hours after transfection, protein extracts from each plate were split into two samples; mouse anti-Flag antibodies (Sigma) or anti-mouse IgG were used for immunoprecipitation. To quantify bound RNAs, qRT-PCR was performed with primers for *gfp*, *rp49* and *Imp* (primers sequence below). Each transfection was performed in triplicate.

**qRT-PCR.** S2 cells were washed with PBS and testes from ~125 males were dissected in PBS and immediately frozen on dry ice. Cells or testes were homogenized in RLT buffer from the RNeasy kit (Qiagen), and RNA was extracted according to kit instructions. RNA was quantified and 1 µg was treated with DNaseI (Promega) and reverse-transcribed with random hexamer mixture and SuperScript III (Invitrogen), according to instructions. Quantitative PCR was carried out in 7900HT Fast Real-Time PCR System using SYBR Green PCR Master mix (Applied Biosystems). We used the ΔΔC<sub>T</sub> method<sup>40</sup>, and the efficiency of the target and the reference amplification was approximately equal. Specific primers for qRT-PCR of testes were: *upd* forward, 5'-CCTCCA CAGCACAACACTACAAG-3', reverse, 5'-AGCTGGCCACGTAAGTTTGC-3'; *Imp* forward, 5'-GGTGGGCCGTATCATTTGG-3', reverse, 5'-TCACGCGC TGCAATTCC-3'; *med23* forward, 5'-TCAGCGTGGTGACCGAGTAC-3',

reverse, 5'-CCGATCAGGTGCTGGTTGT-3'; *rp49* forward, 5'-ATCGATATGCTAAGCTGTCGC-3', reverse, 5'-TGTCGATACCTTGGGCTTG-3'. See ref. 41 for *GapDH* primer. For S2 cells, specific primers were: *GAL4* forward, 5'-GCAACGGTCCGAACCTCA-3', reverse, 5'-GAGGCAATTGGTTGTGAAAGC-3'; *gfp* forward, 5'-TCCGCCCTGAGCAAAGAC-3', reverse, 5'-GAACTCCAGCAGGACCATGTG-3'. Reactions were performed in triplicate and averaged, and the transcript expression level was quantified using the relative  $C_T$  method<sup>40</sup> and normalized to the level of *GapDH* transcript in testes and to the level of *GAL4* in S2 cells (to correct for transfection efficiency). To quantify small RNAs, total RNA from S2 cells and from testes was extracted using TRIzol (Invitrogen), and cDNA was prepared with small RNA-specific reverse-transcription primers for *let-7*, *siRNA2* or *bantam* (Applied Biosystems). Small RNA levels were measured using a Taqman-specific microRNA probe. Both *let-7* and *siRNA2* levels were normalized relative to *bantam*, which did not change with age according to the deep sequencing data.

**Statistics.** For quantification of cell number (GSC or hub cells) and for densitometric analysis of pixel intensity, the mean  $\pm$  95% confidence interval and the number (*n*) of testes examined are shown. *P* values were generated after a two-tailed Student's *t*-test.

For qRT-PCR, one of at least three representative experiments is shown (mean  $\pm$  s.d. from triplicate measurements). *P* values were generated after a two-tailed Student's *t*-test was used to compare  $\Delta C_T$  between time points or genotypes across three independent biological replicates<sup>42</sup>.

**Cleavage site mapping for endo-siRNA targets.** Testes from 1- or 30-day-old OreR or 10-day-old *Imp(RNAi)* ( $w^-$ , *upd-GAL4,UAS-gfp;UAS-imp(RNAi)*) or control ( $w^-$ , *upd-GAL4,UAS-gfp*) outcrossed to  $w^{1118}$  males (~600 testes for each time point) were collected on dry ice. Total RNA was extracted using TRIzol (Invitrogen) according to the manufacturer's protocol. Fifteen micrograms of total RNA were used as starting material. PolyA RNA was isolated with the Dynabeads mRNA purification kit (Invitrogen). Ligation of an RNA adaptor, reverse transcription using the GeneRacer oligo (dT) primer and 5' RACE-PCR were performed according to the manufacturer's instructions (GeneRacer kit, Invitrogen). *upd* 5' RACE-PCR was carried out using the GeneRacer 5' primer (5'-CGACTGGAGCACGAGGACACTGA-3') and an *upd* gene-specific reverse primer (5'-TAGTACTCGATGCGGGTGCGGAATG-3'), followed by one round of nested PCR using the GeneRacer 5' nested primer (5'-GGACACTGACATGGACTGAAGGAGTA-3') and a nested primer specific to *upd* (5'-CGGCAACTGCAGATTGTGGTTTCGT-3'). PCR products were gel purified and cloned into pCR4Blunt-TOPO (Invitrogen). Fifteen clones were sequenced with T7 primer and subjected to further analysis. The *esi-2*-mediated cleavage product of *mus308* was detected as described<sup>15</sup>.

**Small RNA libraries.** Total RNA from the testes of 1,005 (1-day-old) and 1,018 (30-day-old) wild-type (OreR) males was isolated using TRIzol (Invitrogen).

Small RNAs (19–28 nucleotides) were cloned as described<sup>43</sup>. Libraries were sequenced in-house using the Illumina GAI sequencing platform. Obtained sequences were deposited in the Gene Expression Omnibus database under accession GSE3704.

The analysis of small RNA libraries was performed as described<sup>20</sup>. Illumina reads were stripped of the 3' linker, collapsed, and the resulting small RNA sequences were matched without mismatches to the *Drosophila* release 5 genome. Only reads that met these conditions were subjected to further analyses. All reads between 20 and 22 nucleotides in size were extracted bioinformatically regardless of their annotations. Using a custom Perl script, these sequences were mapped against the predicted cleavage site at nucleotide 33 within the 3'UTR of *upd*, allowing up to six mismatches between the target site and nucleotides 2 to 18 of the small RNA (all mapping results are shown in Supplementary Table 1). Our search was focused on nucleotides 2–18 because previous studies suggested that pairing of the 5' terminal nucleotide of the small RNA with its target is not required for efficient silencing. Furthermore, several mismatches between the 3' end of the small RNA and the target site can be tolerated for target regulation<sup>44,45</sup>.

35. Sokol, N. S. *et al.* *Drosophila let-7* microRNA is required for remodeling of the neuromusculature during metamorphosis. *Genes Dev.* **22**, 1591–1596 (2008).
36. Caldwell, J. C., Fineberg, S. K. & Eberl, D. F. *reduced ocelli* encodes the leucine rich repeat protein *Pray For Elves* in *Drosophila melanogaster*. *Fly* **1**, 146–152 (2007).
37. Harrison, D. A., Brill, J. A. & Fuller, M. T. Assembly of ring canals in the male germ line from structural components of the contractile ring. *J. Cell Sci.* **109**, 2779–2788 (1996).
38. Harrison, D. A., McCoon, P. E., Binari, R., Gilman, M. & Perrimon, N. *Drosophila* unpaired encodes a secreted protein that activates the JAK signaling pathway. *Genes Dev.* **12**, 3252–3263 (1998).
39. Bailey, T. L. & Elkan, C. Fitting a mixture model by expectation maximization to discover motifs in biopolymers. *Proc. Int. Conf. Intell. Syst. Mol. Biol.*, **2**, 28–36 (1994).
40. Schmittgen, T. D. & Livak, K. J. Analyzing real-time PCR data by the comparative  $C_T$  method. *Nature Protocols* **3**, 1101–1108 (2008).
41. Min, K. J., Yamamoto, R., Buch, S., Pankratz, M. & Tatar, M. *Drosophila* lifespan control by dietary restriction independent of insulin-like signaling. *Aging Cell* **7**, 199–206 (2008).
42. Yuan, J. S., Reed, A., Chen, F. & Stewart, C. N. Jr. Statistical analysis of real-time PCR data. *BMC Bioinformatics* **7**, 85 (2006).
43. Brennecke, J. *et al.* Discrete small RNA-generating loci as master regulators of transposon activity in *Drosophila*. *Cell* **128**, 1089–1103 (2007).
44. Haley, B. & Zamore, P. D. Kinetic analysis of the RNAi enzyme complex. *Nature Struct. Mol. Biol.* **11**, 599–606 (2004).
45. Haley, B., Foy, B. & Levine, M. Vectors and parameters that enhance the efficacy of RNAi-mediated gene disruption in transgenic *Drosophila*. *Proc. Natl Acad. Sci. USA* **107**, 11435–11440 (2010).



# A spectrograph for exoplanet observations calibrated at the centimetre-per-second level

Tobias Wilken<sup>1,2</sup>, Gaspare Lo Curto<sup>3</sup>, Rafael A. Probst<sup>1</sup>, Tilo Steinmetz<sup>1,2</sup>, Antonio Manescau<sup>3</sup>, Luca Pasquini<sup>3</sup>, Jonay I. González Hernández<sup>4,5</sup>, Rafael Rebolo<sup>4,5,6</sup>, Theodor W. Hänsch<sup>1</sup>, Thomas Udem<sup>1</sup> & Ronald Holzwarth<sup>1,2</sup>

**The best spectrographs are limited in stability by their calibration light source<sup>1</sup>. Laser frequency combs are the ideal calibrators for astronomical spectrographs<sup>2</sup>. They emit a spectrum of lines that are equally spaced in frequency<sup>3</sup> and that are as accurate and stable as the atomic clock relative to which the comb is stabilized. Absolute calibration<sup>4</sup> provides the radial velocity of an astronomical object relative to the observer (on Earth). For the detection of Earth-mass exoplanets<sup>5,6</sup> in Earth-like orbits around solar-type stars, or of cosmic acceleration<sup>7–9</sup>, the observable is a tiny velocity change of less than 10 cm s<sup>−1</sup>, where the repeatability of the calibration—the variation in stability across observations—is important. Hitherto, only laboratory systems<sup>10–12</sup> or spectrograph calibrations of limited performance<sup>4,13,14</sup> have been demonstrated. Here we report the calibration of an astronomical spectrograph with a short-term Doppler shift repeatability of 2.5 cm s<sup>−1</sup>, and use it to monitor the star HD 75289 and recompute the orbit of its planet. This repeatability should make it possible to detect Earth-like planets in the habitable zone of star or even to measure the cosmic acceleration directly.**

We installed our laser frequency comb (LFC; Fig. 1a and Supplementary Information) for two measurement campaigns in November 2010 and January 2011 at the High Accuracy Radial velocity Planet Searcher<sup>15</sup> (HARPS), a European Southern Observatory spectrograph designed for detecting Doppler shifts with high precision. Light is coupled to HARPS through multimode fibres, because in the visible spectral regime starlight cannot be coupled efficiently to single-mode fibres. Spectrographs in general measure wavelengths,  $\lambda$ , rather than frequencies,  $\nu$ , as provided by an LFC. For plane waves, the measured wavelength is independent of the position of the detector ( $\lambda = c/\nu$ , where  $c$  denotes the speed of light) but this is not true for any real beam, especially not for a beam emerging from a multimode fibre. For a good calibration, we thus must require that the spatial mode of the calibrator is matched to the starlight, or at least that a mismatch is stable over the required observation time. Consequently, the LFC light is also coupled to a multimode fibre, comprising a dynamic mode scrambler<sup>4</sup>. The scrambler is used to reduce multipath interference effects and the sensitivity to the light injection by averaging over a large number of fibre modes. The light is then coupled to two further multimode fibres (referred to as channels) in parallel. Under normal operation, one channel guides the calibration light and the other receives the starlight.

The calibration tests consisted of series of 10–100 acquisitions (typically with an exposure time of 10–40 s plus a read-out time for the charge-coupled-device (CCD) detector of 30 s) with LFC light in both channels. From the two-dimensional CCD image (Fig. 1b), a one-dimensional map of photon counts per pixel is generated. The centre of each LFC line is then determined by fitting the line with a Gaussian. For each line of an acquisition, the difference relative to that line's position in an (arbitrary) reference acquisition is computed and a

photon-flux-weighted average of all differences is used to determine the overall calibration deviation (Supplementary Information). We refer to this as the drift of the channel.

To determine our capability to track and correct for these drifts, we send the output of the LFC to the second channel as well. Provided that the calibration lines are stable, the synchronous drift in each of the two channels then individually measures the instrumental drift<sup>16</sup> (for example due to thermomechanical or pressure variations in the spectrograph or the detector). The difference in the drifts of the two channels limits the performance of this calibration scheme and determines the calibration repeatability. It might be influenced by imperfect mode scrambling, residual coupling instabilities, CCD charge transfer inefficiencies and data reduction procedures (Supplementary Information). The stability of the LFC lines cannot be measured in this way, because instabilities would be indistinguishable from instrumental drifts and common mode in both channels. An additional characterization confirmed that the filter depth obtained with four Fabry–Pérot cavities (FPCs) excludes significant systematic uncertainties in the calibration lines<sup>12,17,18</sup> (Supplementary Fig. 4). By using higher-reflectivity FPC mirrors in future, fewer FPCs will be necessary and the LFC can be made more compact. The limiting statistical uncertainty is given by the photon noise. By contrast with the systematic uncertainties, the statistical uncertainty can always be reduced by increasing the exposure time or averaging acquisitions. It is computed from the total number of collected photons in one acquisition<sup>2</sup>.

Between the calibration test series, we vary several parameters of either the LFC (amplifier power, spectral bandwidth, polarization at the fibre injection, offset frequency or line suppression) or the instrument (calibration light injection, parameters of the fibre scrambler, detector cooling or vacuum-pump-induced vibrations) far beyond normal operation conditions. A summary of all recorded data is shown in Fig. 2. In general, the drifts in the two channels track each other very well even if the drift is very strong, as for example when the CCD cooling system has been switched off. We find that the standard deviation of the drift between channels A and B is always close to the computed photon noise limit of 7–10 cm s<sup>−1</sup> within the individual series, and that the standard deviation of all acquisitions is 34 cm s<sup>−1</sup>. When changes to the system are made, sometimes small discontinuities in the differential drift are measured between one series and the next.

Two series in particular, in which an integrating sphere—instead of a lens—was used to couple the laser beam into the first multimode fibre, show a significant effect both in the individual drifts of the channels as well as in the differential drift. This gives a strong indication of the nature of the limiting systematic effect because the integrating sphere manipulates the light in two important ways: the occupation of spatial modes is maximized and the intensity is strongly reduced. Thus, the discontinuities are probably caused by unstable light injection into the multimode fibre, an asymmetry in the recorded line shape or a count-rate dependency of the line position due to imperfect charge transfer

<sup>1</sup>Max-Planck-Institut für Quantenoptik, Hans-Kopfermann-Strasse 1, D-85748 Garching, Germany. <sup>2</sup>Menlo Systems GmbH, Am Klopferspitz 19a, D-82152 Martinsried, Germany. <sup>3</sup>European Southern Observatory, Karl-Schwarzschild-Strasse 3, D-85748 Garching, Germany. <sup>4</sup>Instituto de Astrofísica de Canarias, Calle Vía Láctea s/n, E-38205 La Laguna, Spain. <sup>5</sup>Departamento de Astrofísica, Universidad de La Laguna, E-38206 La Laguna, Spain. <sup>6</sup>Consejo Superior de Investigaciones Científicas, Calle Serrano 117, E-28006 La Laguna, Spain.

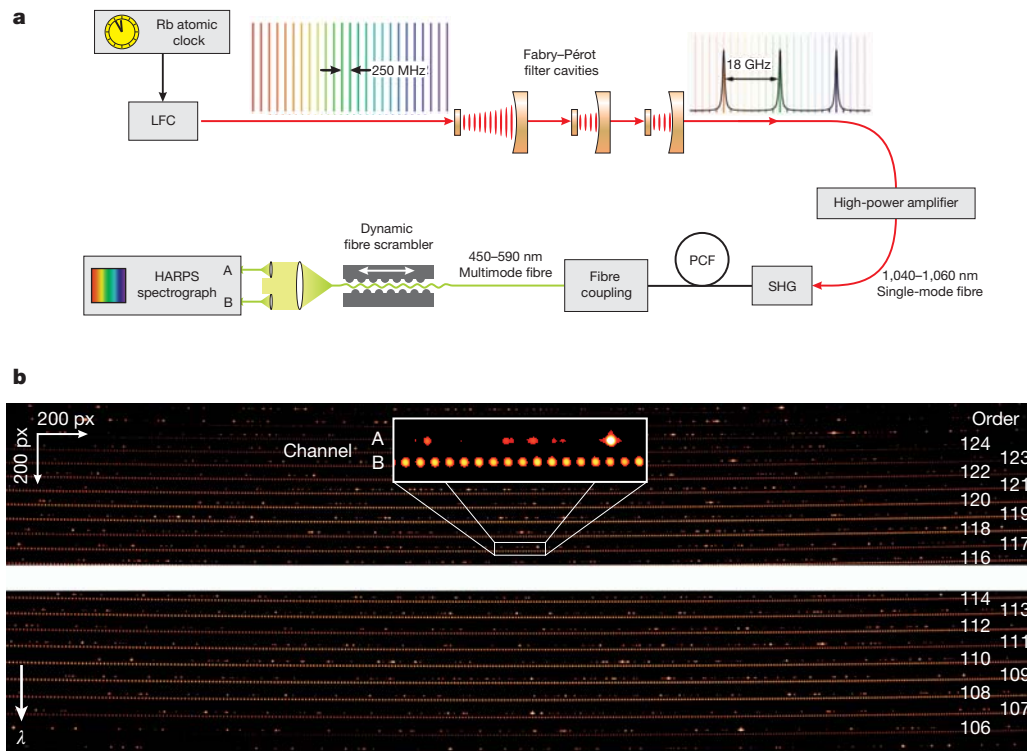


**Figure 1 | Experimental set-up and visualization of the raw data.** **a**, Sketch of the LFC system for calibrating the HARPS spectrograph. A Yb fibre laser serves as the comb generator and its line spacing is increased with Fabry-Pérot cavities<sup>22</sup> (FPCs). Three FPCs were used in November 2010 and four were used in January 2011. The cavities are stabilized to the comb lines with an additional continuous-wave laser (not depicted) using the Pound-Drever-Hall locking scheme<sup>23</sup>. A high-power amplifier generates sufficient power to efficiently drive the second-harmonic generation (SHG) and subsequent spectral broadening in a specially designed photonic crystal fibre<sup>24</sup> (PCF). The comb light is injected into a multimode fibre either through a lens or an integrating sphere. **A**

dynamic scrambler is attached to this fibre to increase the occupation of the spatial modes. See Supplementary Information for further information. **b**, Raw data of one acquisition with HARPS. Two  $4,096 \times 700$ -pixel sections on both CCD detectors of HARPS are shown. The upper section (short-wavelength CCD) contains 11 echelle orders of the LFC in channel B, and the lower section (long-wavelength CCD) contains 9. Channel A is illuminated by a thorium spectral lamp for comparison. Between the two CCDs, one order is lost completely, and the longest-wavelength order on the upper CCD is cut in channel B. The inset shows a  $200 \times 50$ -pixel section of order 117. With a line separation of 18 GHz, the comb lines are densely spaced but do not overlap.

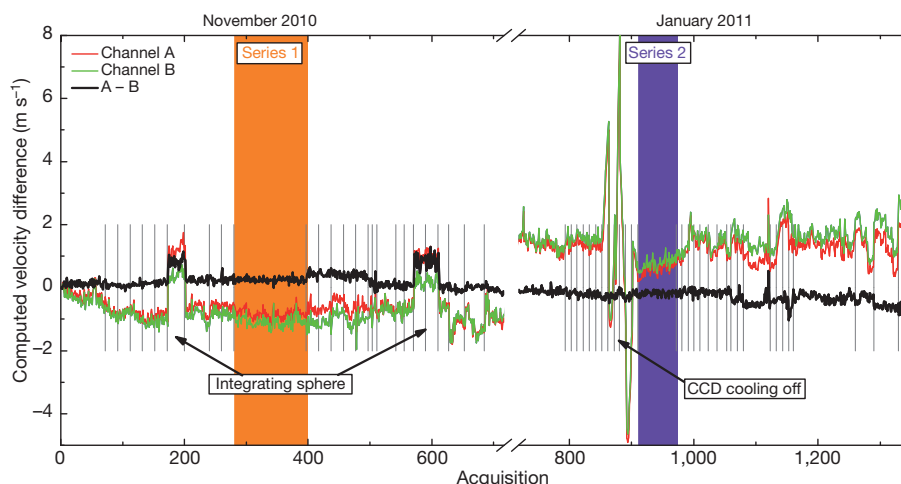


**Figure 2 | Overview over the data taken during the two measurement campaigns in November 2010 and January 2011.** First the difference between each comb line's position in an acquisition and the same line in the reference acquisition (the first acquisition of the November data) is computed, and then the flux-weighted average of all position differences is plotted for each channel individually (A, red; B, green) and for the difference between both channels (A - B, black). Series of 10 to 100 acquisitions for which various parameters of the comb or the spectrograph were changed are shown separated by grey bars. It is particularly striking that using an integrating sphere for injection of the comb light has a significant effect on the differential drift (see the text for more

details). Other parameters, for example the cooling of the CCD, can have large effects on the drifts of the individual channels but cancel almost perfectly in the differential drift. The synchronous drift between November and January in the individual channels is due to an instrumental drift. We find a standard deviation of  $34 \text{ cm s}^{-1}$  for the differential drift of the comb calibration, over all data during the two months, despite the systematic effects and the fact that the spectrograph's parameters were changed far beyond regular operating conditions. Two long series during which no changes of the overall system were made are marked in orange and violet.



during CCD read-out (Supplementary Information). These effects reduce the long-term stability of the calibration. We want to emphasize, however, that all these effects have their origin in the spectrograph (including the light injection) or the data reduction. As a calibration source with an unprecedentedly low photon noise and stable line positions, the LFC provides the ideal tool for probing these effects and either removing or calibrating them to enable long-term measurements at the photon noise limit.

The benefit of an LFC calibration is demonstrated by tests of the short-term repeatability. For the longest consecutive sets of acquisitions during which no changes are made to the system, the differential drift of the two channels is at the photon noise limit. Two such series are highlighted in Fig. 2. The standard deviations of a single acquisition (respective exposure times of 20 and 30 s) of the differential drifts in these series are  $6.7 \text{ cm s}^{-1}$  ( $6.4 \text{ cm s}^{-1}$ ) and  $6.7 \text{ cm s}^{-1}$  ( $5.8 \text{ cm s}^{-1}$ ), respectively, with the computed photon noise given in parentheses.

Even lower values are obtained by binning the data from several acquisitions. To determine the best binning, we compute the two-sample deviation of these series<sup>19</sup>, which is a measure of an observable's stability (see Supplementary Information for a definition). By contrast with the standard deviation, the two-sample deviation may be used to describe continuously drifting quantities. Moreover, we can also derive the minimum number of detected photons that is required for a minimum uncertainty, limited by systematic effects. Figure 3 shows that for small numbers of accumulated photons,  $N$  (accumulated during one or few acquisitions), the uncertainty in the average line position decreases in proportion to  $N^{-1/2}$  according to photon-noise-limited statistics. Averaging more than  $5 \times 10^9$  detected photons,

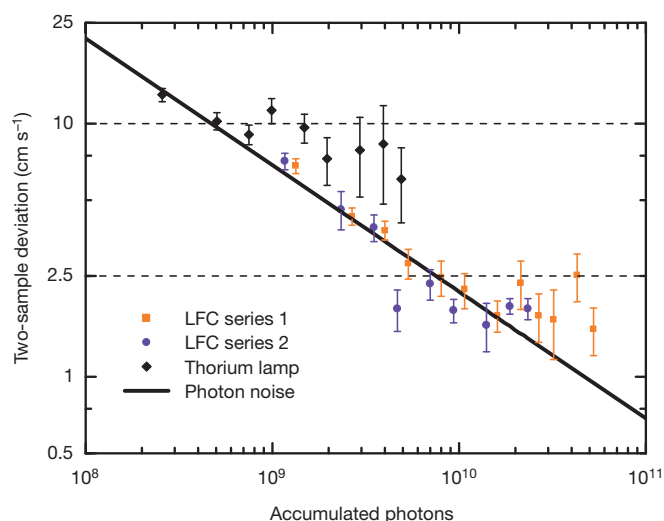


**Figure 3 | Two-sample deviation of the two long series in Fig. 2.** The smallest number of accumulated photons,  $N$ , per series represents one acquisition, and several consecutive acquisitions can be added to obtain larger values of  $N$ . The error bars represent the standard deviation of the two-sample deviation over the complete data set. For  $N < 5 \times 10^9$ , the uncertainty in the average line position decreases, according to photon-noise-limited statistics (solid line), in proportion to  $N^{-1/2}$ . Note that the solid line is not a fit to the data but is computed from the number of detected photons. Increasing  $N$  above  $5 \times 10^9$  does not result in a further reduction of the average line position uncertainty, which remains constant at  $\sim 2.5 \text{ cm s}^{-1}$  (dashed line). This is at present the minimum calibration uncertainty obtainable with the HARPS spectrograph. With the present spectral shape of the LFC, this limit is reached after 4 min. For comparison, the two-sample deviation of a series of 116 subsequent calibrations with light from a thorium lamp in both channels is shown in black. Note that, the exposure times being the same, one acquisition with the thorium lamp has a much larger photon noise than one acquisition with the LFC and that the minimum calibration uncertainty with the thorium lamp is limited at approximately  $10 \text{ cm s}^{-1}$  owing to systematic effects. Obtaining four data points of  $5 \times 10^9$  accumulated photons with the thorium lamp requires 2 h of data acquisition.

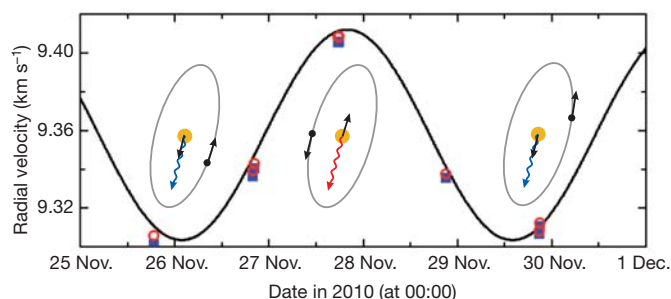


**Figure 4 | Observation of the radial velocity of the star HD 75289 using the LFC for calibration.** HD 75289 is a non-active, main-sequence star that is similar to the Sun, but slightly more massive and hotter (spectral type G0), and that is orbited by a Jupiter-mass planet with a 3.5-d period. The radial velocity is computed by cross-correlating the measured spectrum with a spectral mask in the reference frame of the solar system barycentre and subsequently correcting for the instrumental drift using the calibration. Eleven measurements of radial velocity with HARPS—three, in 2009, with a thorium calibration only and eight, in November 2010, with both the LFC (red circles) and thorium calibration (blue squares)—have been used to fit the planetary orbit. The portion of the orbit presented in the plot (solid line) covers 6 d centred on the date of the LFC observations. Three phases of the orbit are sketched with the star emitting red- and blueshifted light as indicated by the arrows. The uncertainty deriving from the calibration is smaller than the size of the data markers. The difference between both absolute calibrations amounts to  $\sim 2.5 \text{ m s}^{-1}$ , limited by the accuracy of the calibration with the thorium lamp<sup>14</sup>. The standard deviation of the residuals over the entire data set is  $\sim 7 \text{ m s}^{-1}$ . The average radial velocity of the star is  $9.36 \text{ km s}^{-1}$  with respect to the solar system barycentre. The measurements calibrated with the LFC agree with previous data, and deviations from the fit could be due to stellar activity, pulsations or the presence of another not-yet-identified companion.

however, does not yield a further improvement, as the two-sample deviation levels off at  $2.5 \text{ cm s}^{-1}$ . At this point, instabilities between the channels (instrumental, coupling and so on) become dominant, and this value therefore determines the present limit on our ability to track the synchronous drift. The LFC, however, has the potential for calibration at the submillimetre level, because it is limited only by the atomic clock to which it is referenced<sup>20</sup> and by the suppression of the filtered modes, which can be increased if necessary.

During the observing campaign in November 2010, we also observed the star HD 75289. HARPS was calibrated with the LFC, and for comparison the same observations were repeated with a thorium calibration. The orbit of the known planetary companion<sup>21</sup> could be reconstructed (Fig. 4) with the same uncertainty as in previous measurements, not limited by the calibration (Supplementary Information). This novel use of an LFC as a calibrator in tracing the orbit of an extrasolar planet demonstrates that LFCs can now be routinely used in scientific observations.

Received 28 November 2011; accepted 27 March 2012.

1. Lovis, C. & Pepe, F. A new list of thorium and argon spectral lines in the visible. *Astron. Astrophys.* **468**, 1115–1121 (2007).
2. Murphy, M. T. *et al.* High-precision wavelength calibration of astronomical spectrographs with laser frequency combs. *Mon. Not. R. Astron. Soc.* **380**, 839–847 (2007).
3. Udem, Th, Holzwarth, R. & Hänsch, T. W. Optical frequency metrology. *Nature* **416**, 233–237 (2002).
4. Wilken, T. *et al.* High-precision calibration of spectrographs. *Mon. Not. R. Astron. Soc.* **405**, L16–L20 (2010).
5. Udry, S. *et al.* The HARPS search for southern extra-solar planets: XI. Super-Earths (5 and 8  $M_{\text{Earth}}$ ) in a 3-planet system. *Astron. Astrophys.* **469**, L43–L47 (2007).
6. Lo Curto, G. *et al.* The HARPS search for southern extra-solar planets: XXII. Multiple planet systems from the HARPS volume limited sample. *Astron. Astrophys.* **512**, A48 (2010).
7. Sandage, A. The change of redshift and apparent luminosity of galaxies due to the deceleration of selected expanding universes. *Astrophys. J.* **136**, 319–333 (1962).
8. Loeb, A. Direct measurement of cosmological parameters from the cosmic deceleration of extragalactic objects. *Astrophys. J.* **499**, L111–L114 (1998).

9. Liske, J. *et al.* Cosmic dynamics in the era of extremely large telescopes. *Mon. Not. R. Astron. Soc.* **386**, 1192–1218 (2008).
10. Li, C.-H. *et al.* A laser frequency comb that enables radial velocity measurements with a precision of  $1 \text{ cm s}^{-1}$ . *Nature* **452**, 610–612 (2008).
11. Braje, D. A., Kirchner, M. S., Osterman, S., Fortier, T. & Diddams, S. A. Astronomical spectrograph calibration with broad-spectrum frequency combs. *Eur. Phys. J. D* **48**, 57–66 (2008).
12. Quinlan, F., Ycas, G., Osterman, S. & Diddams, S. A. A 12.5 Hz-spaced optical frequency comb spanning  $>400 \text{ nm}$  for near-infrared astronomical spectrograph calibration. *Rev. Sci. Instrum.* **81**, 063105 (2010).
13. Steinmetz, T. *et al.* Laser frequency combs for astronomical observations. *Science* **321**, 1335–1337 (2008).
14. Benedick, A. J. *et al.* Visible wavelength astro-comb. *Opt. Express* **18**, 19175–19184 (2010).
15. Mayor, M. *et al.* Setting new standards with HARPS. *Messenger* **114**, 20–24 (2003).
16. Baranne, A. *et al.* ELODIE: a spectrograph for accurate radial velocity measurements. *Astron. Astrophys. Suppl. Ser.* **119**, 373–390 (1996).
17. Chang, G. *et al.* Toward a broadband astro-comb: effects of nonlinear spectral broadening in optical fibers. *Opt. Express* **18**, 12736–12747 (2010).
18. Wilken, T. *et al.* in *Proc. 2011 Conf. Lasers Electro-Optics*, paper CWQ2 (IEEE, 2011).
19. Barnes, J. A. *et al.* Characterization of frequency stability. *IEEE Trans. Instrum. Meas.* **20**, 105–120 (1971).
20. Rosenband, T. *et al.* Frequency ratio of  $\text{Al}^+$  and  $\text{Hg}^+$  single-ion optical clocks; metrology at the 17th decimal place. *Science* **319**, 1808–1812 (2008).
21. Udry, S. *et al.* The CORALIE survey for southern extra-solar planets. II. The short-period planetary companions to HD 75289 and HD 130322. *Astron. Astrophys.* **356**, 590–598 (2000).
22. Steinmetz, T. *et al.* Fabry–Perot filter cavities for wide-spaced frequency combs with large spectral bandwidth. *Appl. Phys. B* **96**, 251–256 (2009).
23. Drever, R. W. P. *et al.* Laser phase and frequency stabilization using an optical resonator. *Appl. Phys. B* **31**, 97–105 (1983).
24. Stark, S. *et al.* 14 GHz visible supercontinuum generation: calibration sources for astronomical spectrographs. *Opt. Express* **19**, 15690–15695 (2011).

**Supplementary Information** is linked to the online version of the paper at [www.nature.com/nature](http://www.nature.com/nature).

**Acknowledgements** We would like to thank the staff at La Silla Observatory for their support during our campaigns; S. Stark, H. Hundertmark and P. St J. Russell for supplying us with the tapered PCF; C. Lovis, B. Chazelas and F. Pepe for discussions and help with the data reduction; and C. Buggle and A. Thaller for engineering support. T.W.H. acknowledges support from the Max Planck Foundation.

**Author Contributions** T.W., R.A.P. and T.S. designed and set up the LFC; T.W., G.L.C., R.A.P., T.S., A.M., L.P., J.I.G.H., T.U. and R.H. participated in data acquisition; T.W., G.L.C., L.P., T.U. and R.H. evaluated and analysed the data; L.P., T.W.H., T.U. and R.H. initiated and supervised the experiment; and T.W. wrote the manuscript. All authors discussed the results and commented on the manuscript.

**Author Information** Reprints and permissions information is available at [www.nature.com/reprints](http://www.nature.com/reprints). The authors declare no competing financial interests. Readers are welcome to comment on the online version of this article at [www.nature.com/nature](http://www.nature.com/nature). Correspondence and requests for materials should be addressed to T.W. ([tobias.wilken@mpq.mpg.de](mailto:tobias.wilken@mpq.mpg.de)) or R.H. ([rlh@mpq.mpg.de](mailto:rlh@mpq.mpg.de)).



# Metastability and coherence of repulsive polarons in a strongly interacting Fermi mixture

C. Kohstall<sup>1,2</sup>, M. Zaccanti<sup>1</sup>, M. Jag<sup>1,2</sup>, A. Trenkwalder<sup>1</sup>, P. Massignan<sup>3</sup>, G. M. Bruun<sup>4</sup>, F. Schreck<sup>1</sup> & R. Grimm<sup>1,2</sup>

Ultracold Fermi gases with tunable interactions provide a test bed for exploring the many-body physics of strongly interacting quantum systems<sup>1–4</sup>. Over the past decade, experiments have investigated many intriguing phenomena, and precise measurements of ground-state properties have provided benchmarks for the development of theoretical descriptions. Metastable states in Fermi gases with strong repulsive interactions<sup>5–11</sup> represent an exciting area of development. The realization of such systems is challenging, because a strong repulsive interaction in an atomic quantum gas implies the existence of a weakly bound molecular state, which makes the system intrinsically unstable against decay. Here we use radio-frequency spectroscopy to measure the complete excitation spectrum of fermionic <sup>40</sup>K impurities resonantly interacting with a Fermi sea of <sup>6</sup>Li atoms. In particular, we show that a well-defined quasiparticle exists for strongly repulsive interactions. We measure the energy and the lifetime of this ‘repulsive polaron’<sup>9,12,13</sup>, and probe its coherence properties by measuring the quasiparticle residue. The results are well described by a theoretical approach that takes into account the finite effective range of the interaction in our system. We find that when the effective range is of the order of the interparticle spacing, there is a substantial increase in the lifetime of the quasiparticles. The existence of such a long-lived, metastable many-body state offers intriguing prospects for the creation of exotic quantum phases in ultracold, repulsively interacting Fermi gases.

Landau’s theory of Fermi liquids<sup>14</sup>, and the underlying concept of quasiparticles, is central to our understanding of interacting Fermi systems over a wide range of energy scales, including liquid helium-3, electrons in metals, atomic nuclei and quark–gluon plasma. In the field of ultracold Fermi gases, the normal (non-superfluid) phase of a strongly interacting system can be interpreted in terms of a Fermi liquid<sup>15–18</sup>. In the population-imbalanced case, quasiparticles known as Fermi polarons are the essential building blocks and have been studied in detail experimentally<sup>16</sup> for attractive interactions. Recent theoretical work<sup>9,12,13</sup> has suggested a novel quasiparticle associated with repulsive interactions. The properties of this repulsive polaron are of fundamental importance to the prospects of repulsive many-body states. A crucial question for the feasibility of future experiments is the stability against decay into molecular excitations<sup>11,12,19</sup>. Indeed, whenever a strongly repulsive interaction is realized by means of a magnetically tuned Feshbach resonance<sup>20</sup> (FR), a weakly bound molecular state is present into which the system may rapidly decay.

Our system consists of impurities of fermionic <sup>40</sup>K atoms immersed in a large Fermi sea of <sup>6</sup>Li atoms, which is characterized by an effective Fermi energy of  $\epsilon_F = h \times 37$  kHz and a temperature of  $T = 0.16\epsilon_F/k_B$  (Methods), where  $h$  and  $k_B$  respectively denote the Planck and the Boltzmann constants. For a particular combination of spin states<sup>21</sup> (quantum numbers  $F = 9/2$ ,  $m_F = -5/2$  for <sup>40</sup>K and  $F = 1/2$ ,  $m_F = +1/2$  for <sup>6</sup>Li), the mixture has a FR centred at  $B_0 = 154.719$  G (Methods). The FR enables us to tune widely the  $s$ -wave interaction,

parameterized by the scattering length,  $a$ , using a magnetic field,  $B$ . The interaction strength is described by the dimensionless parameter  $-1/\kappa_F a$ , where  $\kappa_F = \hbar^{-1} \sqrt{2m_{\text{Li}}\epsilon_F} = 1/2,850a_0$  is the Fermi wave-number. Here  $\hbar = h/2\pi$ ,  $a_0$  is the Bohr radius and  $m_{\text{Li}}$  is the mass of a <sup>6</sup>Li atom. Near the centre of the FR, the linear approximation  $-1/\kappa_F a \approx (B - B_0)/(20 \text{ mG})$  holds. The momentum dependence of the interaction is characterized by the effective range, which we express in terms of the parameter  $R^*$  as defined in ref. 22 (Methods and Supplementary Information). For our relatively narrow FR,  $R^* = 2,700a_0$  and the corresponding value of  $\kappa_F R^* = 0.95$  indicates that the finite effective range will have an important influence on the interaction with the Fermi sea.

In Fig. 1, we illustrate the basic physics of our impurity problem in the  $T = 0$  limit, showing the energies of different states as functions of the interaction parameter. The situation is generic for any impurity in a Fermi sea, but quantitative details depend on both the mass ratio of the two atomic species and the width of the FR. The theoretical curves are based on a generalization of an approach presented in refs 12, 23 to our case of a finite effective range.

The spectrum has two quasiparticle branches, which do not adiabatically connect when the FR is crossed, and a molecule–hole continuum (MHC), indicated by the shaded area in Fig. 1. The interaction-induced energy shifts of the two branches ( $E_+ > 0$  and  $E_- < 0$ ) are generally described in a many-body picture by dressing the impurities with particle–hole excitations. Far away from the FR centre, this simplifies to a mean-field shift proportional to  $a$ . The lower branch of the system ( $E_-$ ; green line) corresponds to the attractive

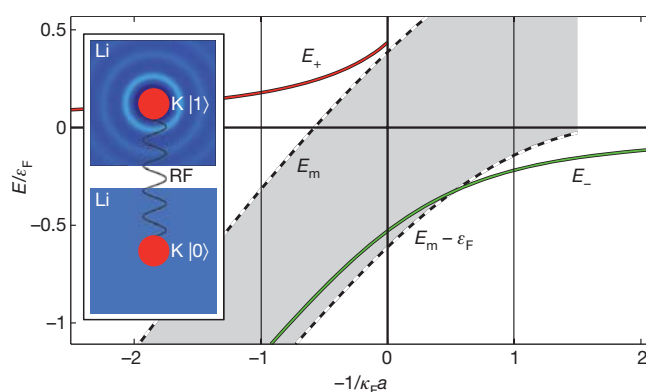


**Figure 1 | Energy spectrum of an impurity in the Fermi sea.** The energies,  $E_+$  (red line) and  $E_-$  (green line), of the two polaronic branches are plotted as functions of the interaction parameter,  $-1/\kappa_F a$ . The shaded area between the dashed lines representing  $E_m$  and  $E_m - \epsilon_F$  (see text) shows the continuum of molecular excitations. The vertical lines at  $1/\kappa_F a = \pm 1$  indicate the width of the strongly interacting regime. The inset illustrates our radio-frequency (RF) spectroscopic scheme whereby the impurity is transferred from a non-interacting spin state,  $|0\rangle$ , to the interacting state,  $|1\rangle$ .

<sup>1</sup>Institut für Quantenoptik und Quanteninformation, Österreichische Akademie der Wissenschaften, 6020 Innsbruck, Austria. <sup>2</sup>Institut für Experimentalphysik und Zentrum für Quantenphysik, Universität Innsbruck, 6020 Innsbruck, Austria. <sup>3</sup>Institut de Ciències Fotòniques, Mediterranean Technology Park, 08860 Castelldefels (Barcelona), Spain. <sup>4</sup>Department of Physics and Astronomy, University of Aarhus, 8000 Aarhus C, Denmark.

polaron, which has recently received a great deal of attention theoretically<sup>4,15,23–25</sup> as well as experimentally<sup>16,17,26</sup>. This polaronic branch remains the ground state of the system until a critical interaction strength is reached, where the system energetically prefers to form a bosonic  ${}^6\text{Li}{}^{40}\text{K}$  molecule by binding the  ${}^{40}\text{K}$  impurity to a  ${}^6\text{Li}$  atom from the Fermi sea<sup>23,25,27</sup>. The MHC arises from the fact that an atom with an energy between 0 and  $\varepsilon_F$  can be removed from the Fermi sea to form the molecule. This continuum thus exists in an energy range between  $E_m$  and  $E_m - \varepsilon_F$  (Fig. 1, dashed lines), where  $E_m$  is the energy of a dressed molecule including the binding energy of a bare molecule in vacuum and a positive interaction shift. The attractive polaron can decay into a molecular excitation if this channel opens up energetically ( $E_- \geq E_m - \varepsilon_F$ ).

The upper branch (Fig. 1, red line) corresponds to the repulsive polaron<sup>9,12,13</sup> with an energy  $E_+ > 0$ . Approaching the FR from the  $a > 0$  side,  $E_+$  gradually increases and reaches a sizeable fraction of  $\varepsilon_F$ . However, the polaronic state becomes increasingly unstable as it decays to the lower-lying states (attractive polaron and MHC). Close to the FR centre, the repulsive polaronic state becomes ill-defined as the decay rate approaches  $E_+/\hbar$ .

To investigate the excitation spectrum of the impurities, we use radio-frequency spectroscopy<sup>28–30</sup>. We initially prepare the  ${}^{40}\text{K}$  atoms in a non-interacting spin state,  $|0\rangle \equiv |F = 9/2, m_F = -7/2\rangle$  and then, with a variable frequency,  $\nu_{\text{rf}}$ , drive radio-frequency transitions into the resonantly interacting state  $|1\rangle \equiv |F = 9/2, m_F = -5/2\rangle$ . Our signal is the fraction of atoms transferred, measured as a function of the radio-frequency detuning,  $\nu_{\text{rf}} - \nu_0$ , with respect to the unperturbed transition frequency,  $\nu_0$ , between the two spin states. This excitation scheme provides access to the full energy spectrum of the system. In particular, it allows us to probe the metastable repulsive polaron as well as all states in the MHC. We furthermore take advantage of the coherence of the excitation process by driving Rabi oscillations. This is an important practical advantage, because it allows very fast and efficient transfer of population into a short-lived quasiparticle state by application of  $\pi$ -pulses. Moreover, we find that measurements of the Rabi frequency directly reveal quasiparticle properties (see below).

In Fig. 2, we show false-colour plots of our signal as detected for different values of the detuning parameter,  $\Delta = h(\nu_{\text{rf}} - \nu_0)$ , and for variable interaction strength,  $-1/\kappa_F a$ . Figure 2a displays a set of measurements that we optimized for the signal strength and spectral resolution of the polaronic excitations by using moderate radio-frequency power. The two insets show the polaron peaks on top of a background due to additional excitations in the Fermi sea (Supplementary Information). The spectrum in Fig. 2b was optimized for detection of the molecular excitations. Here we had to use a much higher radio-frequency power (greater than that in Fig. 2a by a factor of 100) because of the reduced Franck–Condon wavefunction overlap. For the polaronic branches, the high radio-frequency power leads to highly nonlinear saturation behaviour.

Our data show both polaronic branches, and the measured energies of the branches are in excellent agreement with theory. The attractive polaron is found to disappear in the strongly interacting regime. This behaviour, which is different from that observed in  ${}^6\text{Li}$  spin mixtures<sup>16</sup>, is consistent with the crossing of  $E_-$  and  $E_m - \varepsilon_F$  at  $-1/\kappa_F a \approx +0.6$  as we expect for our system. By contrast, the repulsive polaron extends far into the strongly interacting regime. The spectrum has a sharp peak that fades out near  $-1/\kappa_F a \approx -0.3$  (Supplementary Information). The low radio-frequency power produces only a weak MHC signal (Fig. 2a), whereas for high radio-frequency power the MHC signal is strong (Fig. 2b). For weaker interactions on the  $a > 0$  side of the FR ( $-1/\kappa_F a < -1$ ), the molecular signal decreases because of the reduced Franck–Condon overlap. Outside the strongly interacting regime, the situation corresponds to the radio-frequency association of bare molecules (Supplementary Information).

To investigate the decay of the repulsive branch, we apply a radio-frequency pulse sequence to convert repulsive polarons in state  $|1\rangle$

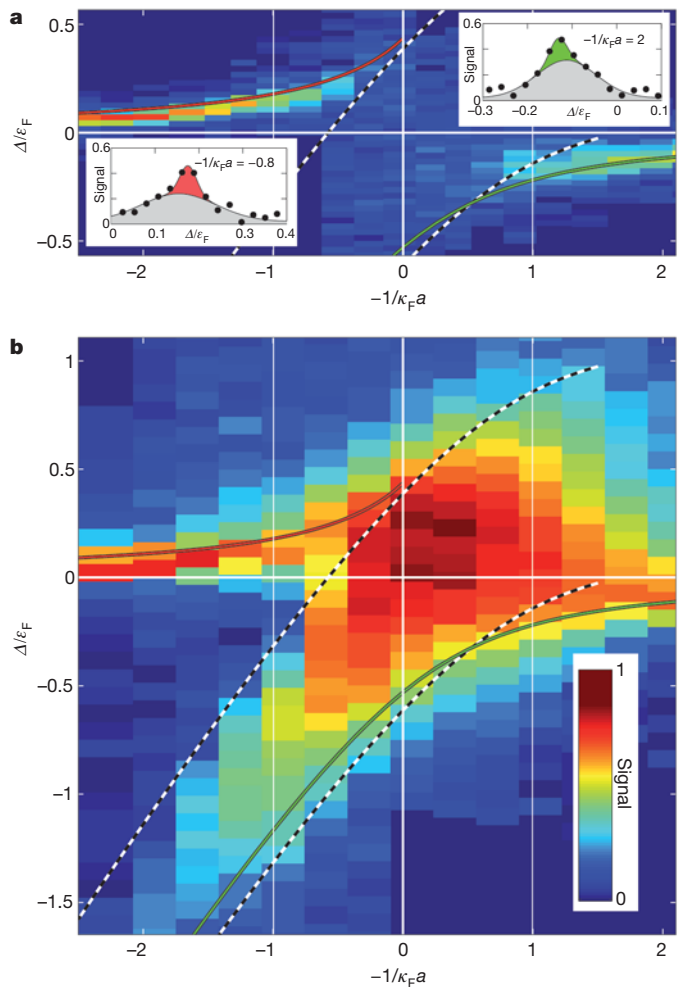


**Figure 2 | Spectral response of  ${}^{40}\text{K}$  impurities in a  ${}^6\text{Li}$  Fermi sea.** The false-colour plots show the fraction of  ${}^{40}\text{K}$  atoms transferred from the non-interacting spin state,  $|0\rangle$ , to the interacting state,  $|1\rangle$ , for different values of the radio-frequency detuning parameter,  $\Delta = h(\nu_{\text{rf}} - \nu_0)$ , and for variable interaction strength,  $-1/\kappa_F a$ : low radio-frequency power (a); high radio-frequency power (b). For comparison, the lines correspond to the theoretical predictions for  $E_+$ ,  $E_-$ ,  $E_m$  and  $E_m - \varepsilon_F$  as shown in Fig. 1. In a, the two insets show the signals for  $-1/\kappa_F a = -0.8$  and 2, respectively, corresponding to vertical cuts through the signal data.

back into non-interacting impurities in state  $|0\rangle$  after a variable hold time (Methods). This back-conversion depends sensitively on the radio-frequency resonance condition and thus allows us to discriminate  ${}^{40}\text{K}$  atoms in the polaronic state from those forming molecules. In Fig. 3, we present the experimental results. The inset shows three sample curves taken for different values of the interaction parameter. The main panel displays the values extracted for the decay rate,  $\Gamma$ , from the decay curves using exponential fits. The data reveal a pronounced increase in decay as the FR centre is approached, which is in good agreement with theoretical model calculations<sup>12</sup> (Fig. 3, solid lines; Supplementary Information). The decay populates the MHC and may occur in a two-step process whereby the repulsive polaron decays via a two-body process into an attractive polaron (Fig. 3, blue line) that in turn decays into a molecular excitation. Alternatively, the repulsive polaron may decay directly into the MHC in a three-body process (Fig. 3, red line). Very close to the FR centre, for  $-1/\kappa_F a = -0.25$ , we find that  $\hbar\Gamma/\varepsilon_F \approx 0.01$ , which corresponds to a 1/e lifetime of about 400  $\mu\text{s}$ . By comparing this decay rate with the corresponding energy shift,  $E_+ = 0.30\varepsilon_F$ , we obtain  $\hbar\Gamma/E_+ \approx 0.03 \ll 1$ , which demonstrates that the repulsive polaron exists as a well-resolved, metastable quasiparticle even deep in the strongly interacting regime.



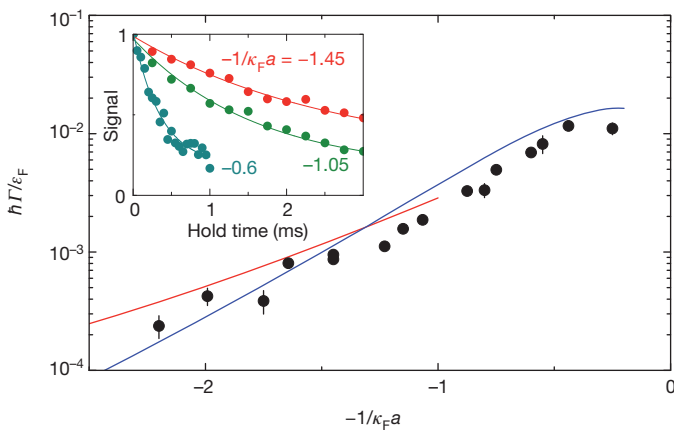


**Figure 3 | Decay rate of the repulsive polaron.** The data points display the measured decay rates,  $\Gamma$ , as extracted by exponential fits to decay curves; the error bars indicate the fit uncertainties. Sample decay curves are shown in the inset. The solid lines represent theoretical calculations of the two-body decay into the attractive polaron (blue line) and the three-body decay into the MHC (red line).

The lifetime observed for the repulsive branch is remarkably long, when compared with findings in recent experiments on  $^6\text{Li}$  spin mixtures<sup>11</sup>. The latter mass-balanced system features a broad FR with a negligible effective range ( $R^* \rightarrow 0$ ). Our theoretical approach allows us to give a general answer to the question of how mass imbalance and the width of the FR influence the lifetime. We find that the mass imbalance has only a minor role<sup>12</sup> and that the dominant effect results from the finite effective range. In the strongly repulsive regime, our system allows us to obtain the same amount of repulsive interaction energy as would a hypothetical system with a broad FR ( $R^* \rightarrow 0$ ), but with an almost ten-fold increased lifetime (Supplementary Information).

Apart from energy and lifetime, the polaron is characterized by its effective mass,  $m^*$ , and its quasiparticle residue,  $Z$  ( $0 \leq Z \leq 1$ ). The difference between  $m^*$  and the bare mass<sup>12</sup> does not produce any significant features in our radio-frequency spectra. The residue quantifies how much of the non-interacting particle is contained in the polaron's wavefunction, which can be written as  $\sqrt{Z}|1\rangle$  plus terms describing excitations in the Fermi sea. The pre-factor  $\sqrt{Z}$  directly manifests itself in the Rabi frequency,  $\Omega$ , that describes the coherent radio-frequency coupling between the non-interacting state and the polaronic state (Supplementary Information).

In Fig. 4, we show the experimental data on Rabi oscillations for variable interaction strength. The sample curves in Fig. 4a demonstrate both the interaction-induced change in the frequency and a damping effect. We apply a simple harmonic oscillator model (including a small increasing background) to analyse the curves, which yields the damping rate,  $\gamma$ , and the frequency,  $\Omega$ . The damping strongly increases close to the FR centre, but does not show any significant dependence on the unperturbed Rabi frequency,  $\Omega_0$  (Fig. 4b). We note that the population decay rates,  $\Gamma$ , measured for the repulsive branch (Fig. 3) stay well below the values of  $\gamma$ , which suggests that collision-induced decoherence is the main damping mechanism.

Figure 4c shows the measured values for the Rabi frequency normalized to  $\Omega_0$ . The interaction-induced reduction of  $\Omega/\Omega_0$  is found to be independent of the particular value of  $\Omega_0$  (comparison of blue squares and red dots; see also Supplementary Information). The solid lines show  $\sqrt{Z}$  as calculated within our theoretical approach for both the repulsive polaron and the attractive polaron. The comparison with the experimental data demonstrates a remarkable agreement with the relation  $\sqrt{Z} = \Omega/\Omega_0$ . Our results therefore suggest that measuring the Rabi frequency is a precise and robust way to determine the

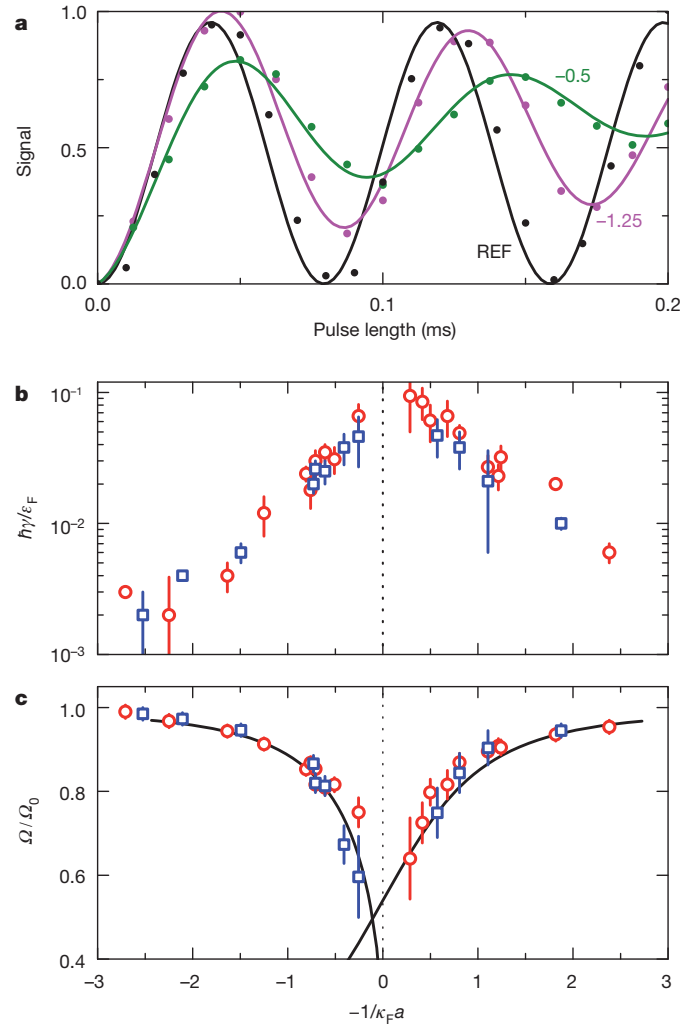


**Figure 4 | Rabi oscillations and the quasiparticle residue.** **a**, Sample Rabi oscillations (for  $-1/\kappa_F a = -1.25$  (magenta points) and  $-1/\kappa_F a = -0.5$  (green points)) with harmonic oscillator fits (solid lines) demonstrate the two effects of the interaction with the Fermi sea: damping and a reduction of the Rabi frequency. The black curve (REF) is a reference curve recorded without  $^6\text{Li}$ . **b**, **c**, Damping rates,  $\gamma$  (**b**), and the normalized Rabi frequencies,  $\Omega/\Omega_0$  (**c**), as measured for two different values of the radio-frequency power:  $\Omega_0 = 2\pi \times 6.5$  kHz (blue) and  $2\pi \times 12.6$  kHz (red). The error bars indicate the fit uncertainties. The solid lines represent the theoretical behaviour of  $\sqrt{Z}$  for the repulsive polaron (left) and the attractive polaron (right).

quasiparticle residue,  $Z$ , and thus provides a powerful alternative to methods based on the detection of the narrow quasiparticle peak in the spectral response<sup>16,23</sup>.

In general, our set of spectroscopic methods applies to any resonantly interacting spin or species mixture that can be efficiently radio-frequency-coupled to a weakly interacting one. Such a situation is the rule rather than the exception in ultracold atomic systems<sup>20</sup>. In mixtures of different species, we anticipate a large variety of suitable systems. For the mass-balanced case of a spin mixture, the well-established  $^{40}\text{K}$  system<sup>30</sup> would be an obvious choice. We also point out that narrow FRs are more common in the field than broad ones<sup>20</sup>. Therefore, effects of the finite effective range similar to those described in our work will govern the behaviour of most systems that can be realized in the laboratory. The benefit of an increased lifetime could help overcome the problem of decay into molecular excitations<sup>11,19</sup> in the experimental investigation of metastable many-body states that rely on repulsive interactions, such as phase-separated states of two fermionic components<sup>5–8,10,11</sup>.

## METHODS SUMMARY

A cloud of  $2 \times 10^4$   $^{40}\text{K}$  atoms is confined in an optical dipole trap together with a  $^6\text{Li}$  Fermi sea of  $3.5 \times 10^5$  atoms, at a temperature of  $T \approx 290$  nK. The K atoms reside in the centre of the much larger Li cloud and thus sample a nearly homogeneous Li environment. The relevant energy scale is given by the Li Fermi energy averaged over the K density distribution,  $\epsilon_F = \hbar \times 37$  kHz  $= k_B \times 1.8$   $\mu\text{K}$ .

The FR is fully characterized by the parameters<sup>21</sup>  $B_0 = 154.719$  G (centre),  $\Delta B = 0.88$  G (width),  $a_{bg} = 63.0a_0$  (background scattering length) and  $\delta\mu/\hbar = 2.3$  MHz G<sup>-1</sup> (differential magnetic moment). The scattering length can be calculated from the standard expression<sup>20</sup>  $a(B) = a_{bg}(1 - \Delta B/(B - B_0))$ , and the range parameter<sup>22</sup> is obtained as  $R^* = \hbar^2/2m_r a_{bg} \delta\mu \Delta B = 2,700a_0$ , where  $m_r$  is the reduced mass of the K–Li pair. We note that the common textbook definition of the effective range corresponds to  $r_e = -2R^*$ , for  $a \rightarrow \pm\infty$ .

The radio-frequency pulses used in measuring the data in Figs 2 and 3 were Blackman-shaped to avoid side lobes in the spectrum. The pulses were 1 ms (Fig. 2a) or 0.5 ms (Fig. 2b) long, and the radio-frequency power was adjusted such that  $\pi$ -pulses (Fig. 2a) or  $5\pi$ -pulses (Fig. 2b) were realized in the absence of interactions with the Fermi sea. For the measurements in Fig. 3, a first  $\pi$ -pulse (duration between 150 and 500  $\mu\text{s}$ ) was used to drive the impurity from state  $|0\rangle$  into state  $|1\rangle$ , selectively creating repulsive polarons. A second, 60- $\mu\text{s}$ ,  $\pi$ -pulse transferred the population remaining in state  $|0\rangle$  into a third state. A third pulse, equal to the first one, transferred the state- $|1\rangle$  polarons back into state  $|0\rangle$ , where they were finally measured using spin-state-selective absorption imaging. The measurements shown in Fig. 4 were performed with simple square pulses.

**Full Methods** and any associated references are available in the online version of the paper at [www.nature.com/nature](http://www.nature.com/nature).

Received 26 November 2011; accepted 9 March 2012.

Published online 23 May 2012.

1. Bloch, I., Dalibard, J. & Zwirger, W. Many-body physics with ultracold gases. *Rev. Mod. Phys.* **80**, 885–964 (2008).
2. Giorgini, S., Pitaevskii, L. P. & Stringari, S. Theory of ultracold atomic Fermi gases. *Rev. Mod. Phys.* **80**, 1215–1274 (2008).
3. Radzihovsky, L. & Sheehy, D. E. Imbalanced Feshbach-resonant Fermi gases. *Rep. Prog. Phys.* **73**, 076501 (2010).
4. Chevy, F. & Mora, C. Ultra-cold polarized Fermi gases. *Rep. Prog. Phys.* **73**, 112401 (2010).
5. Duine, R. A. & MacDonald, A. H. Itinerant ferromagnetism in an ultracold atom Fermi gas. *Phys. Rev. Lett.* **95**, 230403 (2005).
6. LeBlanc, L. J., Thywissen, J. H., Burkov, A. A. & Paramekanti, A. Repulsive Fermi gas in a harmonic trap: ferromagnetism and spin textures. *Phys. Rev. A* **80**, 013607 (2009).
7. Conduit, G. J., Green, A. G. & Simons, B. D. Inhomogeneous phase formation on the border of itinerant ferromagnetism. *Phys. Rev. Lett.* **103**, 207201 (2009).
8. Jo, G.-B. *et al.* Itinerant ferromagnetism in a Fermi gas of ultracold atoms. *Science* **325**, 1521–1524 (2009).
9. Pilati, S., Bertina, G., Giorgini, S. & Troyer, M. Itinerant ferromagnetism of a repulsive atomic Fermi gas: a quantum Monte Carlo study. *Phys. Rev. Lett.* **105**, 030405 (2010).
10. Chang, S.-Y., Randeria, M. & Trivedi, N. Ferromagnetism in the upper branch of the Feshbach resonance and the hard-sphere Fermi gas. *Proc. Natl Acad. Sci. USA* **108**, 51–54 (2011).
11. Sanner, C. *et al.* Correlations and pair formation in a repulsively interacting Fermi gas. Preprint at (<http://arxiv.org/abs/1108.2017>) (2012).

12. Massignan, P. & Bruun, G. M. Repulsive polarons and itinerant ferromagnetism in strongly polarized Fermi gases. *Eur. Phys. J. D* **65**, 83–89 (2011).
13. Schmidt, R. & Enss, T. Excitation spectra and rf response near the polaron-to-molecule transition from the functional renormalization group. *Phys. Rev. A* **83**, 063620 (2011).
14. Landau, L. D. The theory of a Fermi liquid. *Sov. Phys. JETP* **3**, 920–925 (1957).
15. Lobo, C., Recati, A., Giorgini, S. & Stringari, S. Normal state of a polarized Fermi gas at unitarity. *Phys. Rev. Lett.* **97**, 200403 (2006).
16. Schirotzek, A., Wu, C.-H., Sommer, A. & Zwierlein, M. W. Observation of Fermi polarons in a tunable Fermi liquid of ultracold atoms. *Phys. Rev. Lett.* **102**, 230402 (2009).
17. Navon, N., Nascimbène, S., Chevy, F. & Salomon, C. The equation of state of a low-temperature Fermi gas with tunable interactions. *Science* **328**, 729–732 (2010).
18. Nascimbène, S. *et al.* Fermi-liquid behavior of the normal phase of a strongly interacting gas of cold atoms. *Phys. Rev. Lett.* **106**, 215303 (2011).
19. Pekker, D. *et al.* Competition between pairing and ferromagnetic instabilities in ultracold Fermi gases near Feshbach resonances. *Phys. Rev. Lett.* **106**, 050402 (2011).
20. Chin, C., Grimm, R., Julienne, P. S. & Tiesinga, E. Feshbach resonances in ultracold gases. *Rev. Mod. Phys.* **82**, 1225–1286 (2010).
21. Naik, D. *et al.* Feshbach resonances in the  $^6\text{Li}$ - $^{40}\text{K}$  Fermi-Fermi mixture: elastic versus inelastic interactions. *Eur. Phys. J. D* **65**, 55–65 (2011).
22. Petrov, D. S. Three-boson problem near a narrow Feshbach resonance. *Phys. Rev. Lett.* **93**, 143201 (2004).
23. Punk, M., Dumitrescu, P. T. & Zwirger, W. Polaron-to-molecule transition in a strongly imbalanced Fermi gas. *Phys. Rev. A* **80**, 053605 (2009).
24. Combescot, R., Recati, A., Lobo, C. & Chevy, F. Normal state of highly polarized Fermi gases: simple many-body approaches. *Phys. Rev. Lett.* **98**, 180402 (2007).
25. Sadeghzadeh, K., Bruun, G. M., Lobo, C., Massignan, P. & Recati, A. Metastability in spin-polarized Fermi gases and quasiparticle decays. *N. J. Phys.* **13**, 055011 (2011).
26. Nascimbène, S. *et al.* Collective oscillations of an imbalanced Fermi gas: axial compression modes and polaron effective mass. *Phys. Rev. Lett.* **103**, 170402 (2009).
27. Prokof'ev, N. & Svistunov, B. Fermi-polaron problem: diagrammatic Monte Carlo method for divergent sign-alternating series. *Phys. Rev. B* **77**, 020408 (2008).
28. Chin, C. *et al.* Observation of the pairing gap in a strongly interacting Fermi gas. *Science* **305**, 1128–1130 (2004).
29. Shin, Y., Schunck, C. H., Schirotzek, A. & Ketterle, W. Tomographic rf spectroscopy of a trapped Fermi gas at unitarity. *Phys. Rev. Lett.* **99**, 090403 (2007).
30. Stewart, J. T., Gaebler, J. P. & Jin, D. S. Using photoemission spectroscopy to probe a strongly interacting Fermi gas. *Nature* **454**, 744–747 (2008).

**Supplementary Information** is linked to the online version of the paper at [www.nature.com/nature](http://www.nature.com/nature).

**Acknowledgements** We thank A. Sidorov for contributions in the early stage of the experiments, and T. Enss, S. Giorgini, W. Ketterle, J. Levinsen, C. Lobo, D. Petrov, A. Recati, R. Schmidt, J. Song, C. Trefzger, P. Zoller, W. Zwirger, M. Zwierlein and, in particular, M. Baranov for many discussions. We acknowledge support from the Austrian Science Fund FWF through the SFB FoQuS. M.Z. is supported by the Lise Meitner programme of the FWF. P.M. is indebted to M. Lewenstein for support through the ERC Advanced Grant QUAGATUA.

**Author Contributions** C.K., M.Z., M.J., A.T., F.S. and R.G. did the experimental work and P.M. and G.M.B. did the theoretical work.

**Author Information** Reprints and permissions information is available at [www.nature.com/reprints](http://www.nature.com/reprints). The authors declare no competing financial interests. Readers are welcome to comment on the online version of this article at [www.nature.com/nature](http://www.nature.com/nature). Correspondence and requests for materials should be addressed to M.Z. ([matteo.zaccanti@oeaw.ac.at](mailto:matteo.zaccanti@oeaw.ac.at)).

## METHODS

**Experimental conditions.** Our system consists of  $2 \times 10^4$   $^{40}\text{K}$  atoms and  $3.5 \times 10^5$   $^6\text{Li}$  atoms confined in an optical dipole trap. The trap is realized with two crossed beams derived from a 1,064-nm single-mode laser source. The measured trap frequencies for Li and K are respectively  $\nu_r = 690$  and  $425$  Hz radially and  $\nu_z = 86$  and  $52$  Hz axially; this corresponds to a cigar-shaped sample with an aspect ratio of about eight. The preparation procedure is described in detail in ref. 31. The Fermi energies, according to the common definition for harmonic traps,  $E_F = \hbar^3 \sqrt{6N} \nu_r^2 \nu_z$ , are  $E_F^{\text{Li}} = \hbar \times 44$  kHz  $= k_B \times 2.1$   $\mu\text{K}$  and  $E_F^{\text{K}} = \hbar \times 10.4$  kHz  $= k_B \times 500$  nK. At a temperature of  $T \approx 290$  nK, the  $^6\text{Li}$  component forms a deeply degenerate Fermi sea ( $k_B T / E_F^{\text{Li}} \approx 0.14$ ) whereas the  $^{40}\text{K}$  component is moderately degenerate ( $k_B T / E_F^{\text{K}} \approx 0.6$ ).

**Effective Fermi energy.** The  $^{40}\text{K}$  atoms sample a nearly homogeneous  $^6\text{Li}$  environment. This is because the optical trapping potential for  $^{40}\text{K}$  is about twice as deep as for  $^6\text{Li}$  and the  $^{40}\text{K}$  cloud is confined to the centre of the much larger  $^6\text{Li}$  Fermi sea<sup>32</sup>. This allows us to describe the system in terms of the effective Fermi energy,  $\varepsilon_F$ , defined as the mean Fermi energy experienced by the  $^{40}\text{K}$  atoms. We find that  $\varepsilon_F = \hbar \times 37$  kHz, with two effects contributing to the fact that this value is about 15% less than  $E_F^{\text{Li}}$ . The finite temperature reduces the Li density in the trap centre, leading to a peak local Fermi energy of  $\hbar \times 40$  kHz. Moreover, the  $^{40}\text{K}$  atoms sample a small region around the trap centre, where the density and local Fermi energy are somewhat lower than in the centre. The distribution of Fermi energies experienced by the  $^{40}\text{K}$  cloud, that is, the residual inhomogeneity of our system, can be quantified in terms of a standard deviation of  $\hbar \times 1.9$  kHz.

**Concentration.** The mean impurity concentration (mean number density ratio,  $n_K/n_{\text{Li}}$ ) is about 0.4, if both spin states of the population of K atoms are considered. This may be too large a-priori to justify the interpretation of our data in terms of the low-concentration limit. We find that this interpretation is nevertheless valid, as we take advantage of several facts. Under strongly interacting conditions, only a fraction of the K atoms are transferred into spin state  $|1\rangle$  (Fig. 2), which reduces the concentration of interacting impurities. A recent quantum Monte Carlo calculation of the equation of state of a zero-temperature  $^6\text{Li}$ – $^{40}\text{K}$  Fermi–Fermi mixture<sup>33</sup> further supports our interpretation in the low-concentration limit: the strongest interaction in the mass-imbalanced system is expected when there are about 4 times more  $^{40}\text{K}$  atoms than  $^6\text{Li}$  atoms, and for concentrations up to a value of 1 the interaction energy per  $^{40}\text{K}$  atom is expected to remain essentially constant. To support our basic assumption with experimental data, we also measured radio-frequency spectra for variable numbers of  $^{40}\text{K}$  atoms, confirming that finite-concentration effects remained negligibly small in the relevant parameter range.

**Interaction control through Feshbach resonance.** The FR used for interaction tuning is discussed in detail in refs 21, 32. It is present for  $^6\text{Li}$  in the lowest spin state ( $F = 1/2$ ,  $m_F = +1/2$ ) and for  $^{40}\text{K}$  in the third-to-lowest spin state ( $F = 9/2$ ,  $m_F = -5/2$ ). The latter represents our interacting state,  $|1\rangle$ . The neighbouring state with  $m_F = -7/2$  serves as state  $|0\rangle$ ; here the interspecies scattering length (about  $+65a_0$ ) is so small that any interaction can be neglected to a good

approximation. The tunable scattering length for state  $|1\rangle$  in the Fermi sea is well described by the standard formula,  $a = a_{\text{bg}}(1 - \Delta B / (B - B_0))$ , with  $a_{\text{bg}} = 63.0a_0$ ,  $\Delta B = 0.88$  G and  $B_0 = 154.719(2)$  G. The value given for  $B_0$  refers to the particular optical trap used in the present experiments, as it includes a small shift induced by the trapping light. The value therefore deviates somewhat from the one given in refs 21, 32. In free space, without the light shift, the resonance centre is located at  $154.698(5)$  G. The uncertainties given for the resonance centre,  $B_0$  (2 mG in the trapped case and 5 mG for free space), correspond to standard deviations, obtained from analysing molecule association spectra for various trap settings.

The character of the resonance is closed-channel dominated<sup>20</sup>. Following the definition<sup>22</sup> of a range parameter,  $R^* = \hbar^2 / 2m_r a_{\text{bg}} \delta\mu \Delta B$ , where  $m_r = m_{\text{Li}} m_{\text{K}} / (m_{\text{Li}} + m_{\text{K}})$  is the reduced mass and  $\delta\mu / \hbar = 2.3$  MHz G<sup>-1</sup> is the differential magnetic moment, the resonance is characterized by  $R^* = 2,700a_0$ . For  $a \rightarrow \pm\infty$ , this parameter corresponds to the common textbook definition<sup>20</sup> of the effective range,  $r_e = -2R^*$ . Our value for  $R^*$  coincidentally lies very close to  $1/\kappa_F = 2,850a_0$ , which means that the strongly interacting regime corresponds roughly to the universal range of the resonance. Our system therefore represents an intermediate case ( $\kappa_F R^* = 0.95$ ), where the behaviour is near universal, but with significant effects arising from the finite effective range.

**Details on radio-frequency pulses.** To measure the data in Fig. 2, we used Blackman pulses<sup>34</sup> to avoid side lobes in the spectrum. For Fig. 2a, the pulses were 1-ms long (spectral width,  $0.7$  kHz  $\approx 0.02\varepsilon_F / \hbar$ ) and the radio-frequency power was adjusted such that  $\pi$ -pulses would be realized in the absence of interactions with the Fermi sea. For the data in Fig. 2b, the radio-frequency power was increased by a factor of 100 and the pulse duration was set to 0.5 ms. This resulted in pulses with an area of  $5\pi$  without the Fermi sea. For the lifetime measurements in Fig. 3, we used a sequence of three Blackman pulses. The first pulse (duration between 150 and 500  $\mu\text{s}$ ) was set to drive the non-interacting impurity from spin state  $|0\rangle$  ( $m_F = -7/2$ ) into state  $|1\rangle$  ( $m_F = -5/2$ ); here the frequency was carefully set to resonantly create repulsive polarons and the pulse area was set to fulfil the  $\pi$ -pulse condition. The second pulse was a short (60- $\mu\text{s}$ ) cleaning pulse, which removed the population remaining in  $|0\rangle$  by transferring it to another, empty, spin state ( $m_F = -9/2$ ). The third pulse had the same parameters as the first one and resonantly transferred the population of the polaronic state in  $|1\rangle$  back to the non-interacting state,  $|0\rangle$ , where it was finally measured by spin-state-selective absorption imaging. The measurements of Rabi oscillations in Fig. 4 were performed with simple square pulses.

31. Spiegelhalter, F. M. *et al.* All-optical production of a degenerate mixture of  $^6\text{Li}$  and  $^{40}\text{K}$  and creation of heteronuclear molecules. *Phys. Rev. A* **81**, 043637 (2010).
32. Trenkwalder, A. *et al.* Hydrodynamic expansion of a strongly interacting Fermi–Fermi mixture. *Phys. Rev. Lett.* **106**, 115304 (2011).
33. Gezerlis, A., Gandolfi, S., Schmidt, K. E. & Carlson, J. Heavy-light fermion mixtures at unitarity. *Phys. Rev. Lett.* **103**, 060403 (2009).
34. Kasevich, M. & Chu, S. Laser-cooling below a photon recoil with three-level atoms. *Phys. Rev. Lett.* **69**, 1741–1744 (1992).



# Attractive and repulsive Fermi polarons in two dimensions

Marco Koschorreck<sup>1\*</sup>, Daniel Pertot<sup>1\*</sup>, Enrico Vogt<sup>1</sup>, Bernd Fröhlich<sup>1</sup>, Michael Feld<sup>1</sup> & Michael Köhl<sup>1</sup>

The dynamics of a single impurity in an environment is a fundamental problem in many-body physics. In the solid state, a well known case is an impurity coupled to a bosonic bath (such as lattice vibrations); the impurity and its accompanying lattice distortion form a new entity, a polaron. This quasiparticle plays an important role in the spectral function of high-transition-temperature superconductors, as well as in colossal magnetoresistance in manganites<sup>1</sup>. For impurities in a fermionic bath, studies have considered heavy or immobile impurities which exhibit Anderson's orthogonality catastrophe<sup>2</sup> and the Kondo effect<sup>3</sup>. More recently, mobile impurities have moved into the focus of research, and they have been found to form new quasiparticles known as Fermi polarons<sup>4–7</sup>. The Fermi polaron problem constitutes the extreme, but conceptually simple, limit of two important quantum many-body problems: the crossover between a molecular Bose–Einstein condensate and a superfluid with BCS (Bardeen–Cooper–Schrieffer) pairing with spin-imbalance<sup>8</sup> for attractive interactions, and Stoner's itinerant ferromagnetism<sup>9</sup> for repulsive interactions. It has been proposed that such quantum phases (and other elusive exotic states) might become realizable in Fermi gases confined to two dimensions<sup>10,11</sup>. Their stability and observability are intimately related to the theoretically debated<sup>12–16</sup> properties of the Fermi polaron in a two-dimensional Fermi gas. Here we create and investigate Fermi polarons in a two-dimensional, spin-imbalanced Fermi gas, measuring their spectral function using momentum-resolved photoemission spectroscopy<sup>17–19</sup>. For attractive interactions, we find evidence for a disputed pairing transition between polarons and tightly bound dimers, which provides insight into the elementary pairing mechanism of imbalanced, strongly coupled two-dimensional Fermi gases. Additionally, for repulsive interactions, we study novel quasiparticles—repulsive polarons—the lifetime of which determines the possibility of stabilizing repulsively interacting Fermi systems.

Spin-imbalanced Fermi gases<sup>8</sup> exhibit a wealth of complex pairing phenomena because the Fermi surfaces of the two spin components are mismatched. Well known examples are the predicted Fulde–Ferrell–Larkin–Ovchinnikov (FFLO) pairing mechanism, in which Cooper pairs form at finite momentum, and the Chandrasekhar–Clogston limit of BCS superconductivity. In the extreme case of spin-imbalance, just one mobile spin-up particle is immersed in a large spin-down Fermi sea. New quasiparticles, so-called Fermi polarons, are formed by the impurity being coherently dressed with particle–hole excitations of the majority component. For weak attractive interactions, the new many-body ground state is the attractive Fermi polaron (see Fig. 1), which corresponds to the limit of a partially polarized Fermi gas. If the attraction between impurity and majority component is sufficiently strong, and depending on the dimensionality, the attractive polaron may undergo a transition to a locally paired dimer state<sup>4,12,13</sup>. This corresponds to the limiting case of phase separation between a fully polarized Fermi gas and a balanced superfluid state. The opposite situation of an impurity interacting repulsively with the

fermionic bath is notably different. For short-range interactions, strong repulsion between particles can only be achieved if the underlying interaction potential is attractive, which implies a two-particle bound state with binding energy  $E_B$ . Repulsive impurities are therefore metastable and eventually decay either into a bound state or into an attractive polaron with the simultaneous creation of particle and hole excitations. It has very recently been theoretically proposed<sup>15,16</sup> that a repulsively interacting impurity, despite its metastability, still forms a

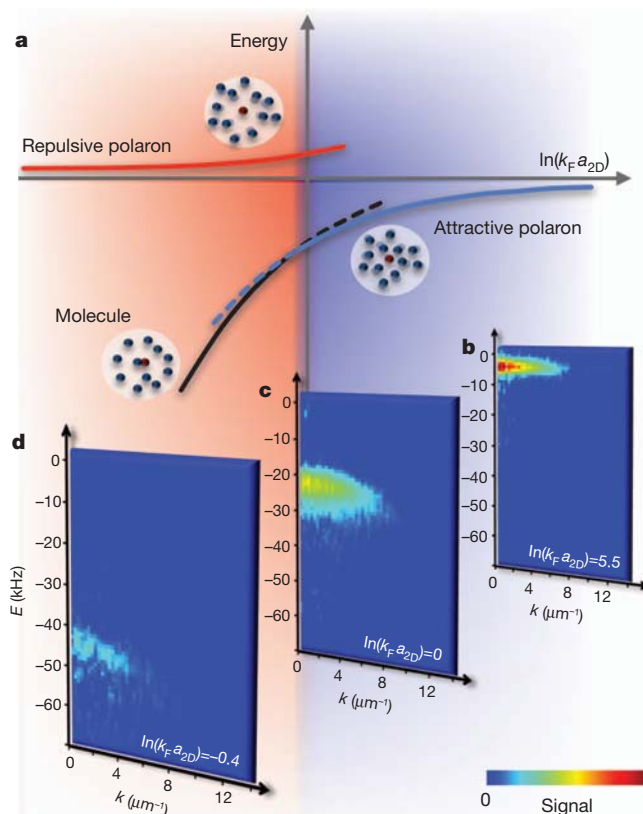


**Figure 1 | Polaron energy level diagram and measured single particle spectral function.** **a**, Polaron energy level diagram. For positive values of the interaction parameter  $\ln(k_F a_{2D})$  (blue shaded region; see main text) the attractive polaron (blue line, dashed where metastable) is the quantum ground state. For negative values of  $\ln(k_F a_{2D})$  (red shaded region) the molecule (black line, dashed where metastable) eventually becomes the ground state and lies below the metastable repulsive polaron (red line). The insets show impressions of the dressing of the impurity with majority atoms. **b–d**, The single particle spectral functions. For  $\ln(k_F a_{2D}) = 5.5$  (**b**), a sharp quasiparticle peak is seen. For sufficiently negative values of  $\ln(k_F a_{2D})$  (for example,  $-0.4$  (**d**)), the ground state is molecular for which the single particle spectral function exhibits a weak incoherent feature. In between, **b**, there is a transition between the two limits. In the spectral functions the free particle dispersion is implicitly subtracted.

<sup>1</sup>Cavendish Laboratory, University of Cambridge, JJ Thomson Avenue, Cambridge CB3 0HE, UK.

\*These authors contributed equally to this work.

well-defined quasiparticle, the repulsive polaron, which has not been observed in solid state systems so far. Its lifetime is of critical importance in pairing instabilities of repulsively interacting Fermi gases<sup>20,21</sup> and in the approach to observing the Stoner transition of itinerant ferromagnetism<sup>9</sup>.

Dimensionality plays an important role in the physics of the Fermi polaron because quantum fluctuations, such as the creation of particle-hole pairs, are enhanced in low dimensions and affect the many-body ground state. In three dimensions, the properties of the Fermi polaron and the transition between polaron and molecule were predicted theoretically<sup>4,8,22–24</sup>, and attractive<sup>5–7</sup> as well as repulsive<sup>7</sup> polarons have been observed experimentally. In one dimension, the exact solution of the spin-impurity Hamiltonian displays no transition for any interaction strength<sup>25</sup>. The most interesting, yet unresolved, case is in two dimensions: different theoretical models<sup>12–16</sup> have predicted various scenarios for the quasiparticle properties and the existence or absence of a polaron-molecule transition on the attractive branch.

Here we report the creation of Fermi polarons by immersing a few spin-down impurity atoms in a two-dimensional Fermi sea of spin-up atoms. This strongly spin-imbalanced Fermi gas is formed by a 85/15 mixture of the two lowest Zeeman states  $|-9/2\rangle$  and  $|-7/2\rangle$  of the  $F = 9/2$  hyperfine manifold of  $^{40}\text{K}$  confined to two dimensions with an optical lattice<sup>26</sup>. We adiabatically prepare the attractive ground state, and, independently, the repulsive branch, and measure their single particle spectral functions  $A(k, E)$  using momentum-resolved photoemission spectroscopy<sup>17–19</sup> (see Methods). Here,  $k$  and  $E$  are the wave vector and the energy of the single particle excitation, respectively. This methodology allows us to study the many-body state in equilibrium and is in contrast to ‘inverse’ radio frequency (r.f.) spectroscopy<sup>7,26,27</sup>, which probes the transient creation of excitations. Additionally, the single particle spectral function gives access to the full quasiparticle dispersion, which is averaged out in momentum-integrated r.f. spectroscopy<sup>5,7,28</sup>. On the lower branch of the energy spectrum (see Fig. 1a and Supplementary Information) we observe attractive Fermi polarons, measure their quasiparticle properties, and investigate the transition to the molecular state. We study the dependence of the quasiparticle properties on temperature, and, moreover, find evidence for quasiparticle interactions when we increase the impurity concentration. On the upper branch of the energy spectrum, we study repulsive Fermi polarons and, in particular, investigate their lifetime.

In Fig. 1b–d we display the measured single particle spectral function for different values of the interaction parameter,  $\ln(k_F a_{2D})$ . Here,  $k_F$  denotes the Fermi wave vector of the majority component and  $a_{2D}$  the two-dimensional scattering length (see Methods). For weak attractive interaction in the polaronic regime, we observe a symmetric line shape as a function of energy for every wave vector  $k$ , which signals a well defined quasiparticle, the attractive polaron (see Fig. 1b). In the molecular regime we find a weak, asymmetric spectrum, which is skewed with a tail to lower energies (see Fig. 1d). This spectrum is dominated by a broad incoherent background, which has contributions from incoherent particle-hole excitations and molecules.

In Fig. 2 we display our measurements of the quasiparticle energy  $E_0$  (Fig. 2a) and the effective mass  $m^*$  (Fig. 2b) for the attractive polaron branch. We determine the energy  $E_{\text{peak}}(k)$  of the maximum of the spectral function  $A(k, E)$  at a wave vector  $k$  and use the fit function  $E_{\text{peak}}(k) = E_0 + \hbar^2 k^2 (1/m^* - 1/m)/2$ , with  $m$  being the bare mass, in order to determine the quasiparticle energy  $E_0$  and the effective mass  $m^*$ . We find very good agreement with the theory of ref. 15 for the effective mass and the quasiparticle energy for data above  $\ln(k_F a_{2D}) = -0.4$ . For data below this value, we observe a divergence of the effective mass, which we interpret as the polaron-molecule transition having been crossed. The polaron-molecule transition in strictly two dimensions has been predicted<sup>12</sup> at  $\ln(k_F a_{2D}) = -0.8$  and in quasi-two dimensions at<sup>29</sup>  $\ln(k_F a_{2D}) = -0.6$ . Effects of averaging over the inhomogeneous density profile, final state interactions, finite

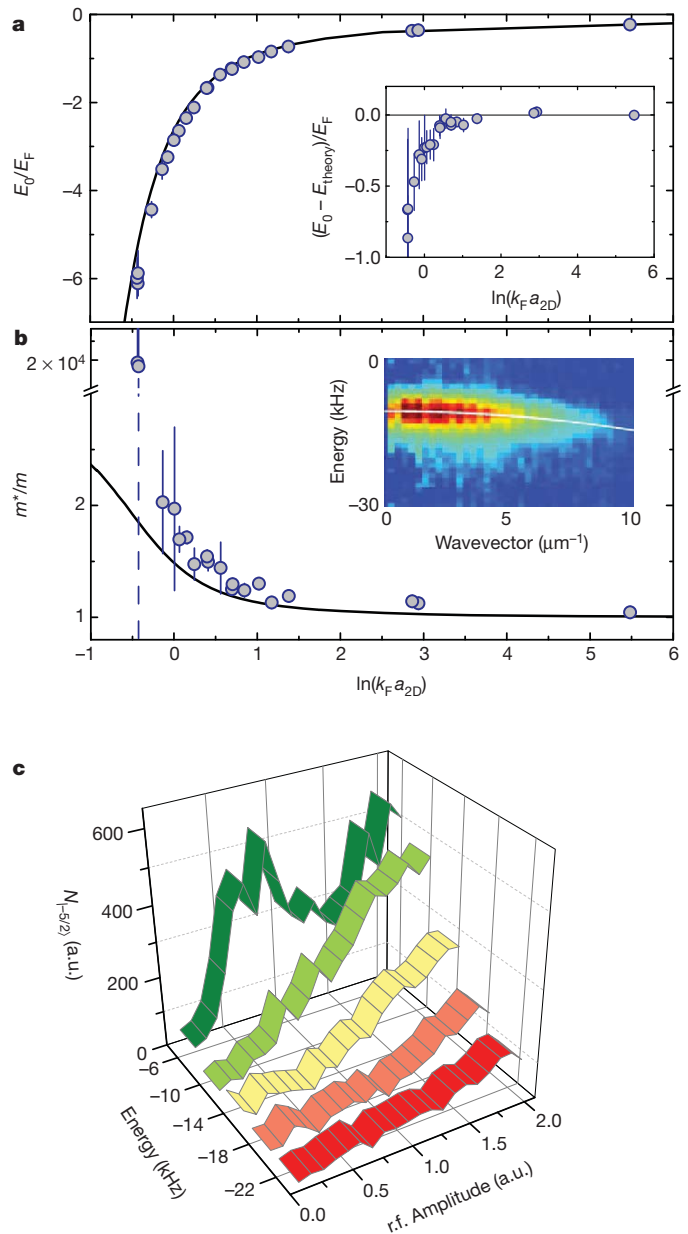


**Figure 2 | Attractive polaron.** **a, b**, Energy (**a**) and effective mass (**b**) of the quasiparticle peak compared to the theoretical prediction<sup>15</sup> (solid line). The dashed vertical line indicates the limit for reliably determining the effective quasiparticle mass. The inset in **a** shows the difference between experiment and theory. The inset in **b** shows an example of a fit used to determine the effective mass at  $\ln(k_F a_{2D}) = 0.7$ . **c**, Coherence of the quasiparticle at  $\ln(k_F a_{2D}) = 2.0(1)$ . On the polaron resonance ( $E/\hbar = -6$  kHz) we observe coherent oscillations whereas the incoherent background at frequencies  $E/\hbar < -6$  kHz increases linearly with the r.f. amplitude. Error bars correspond to 1 s.d. uncertainty in the fit.

temperature, and finite concentration of impurities may affect this value and shift the transition point to larger values of  $\ln(k_F a_{2D})$ . The polaron-molecule transition has only a very weak effect on the energy spectrum, as has been already pointed out theoretically in three dimensions<sup>4</sup>, because the polaron and molecule energy curves are crossing at a very shallow angle (see Fig. 1a). We observe a gradual deviation of the quasiparticle energy from theory (Fig. 2a inset) which, at least in part, could be attributed to finite range corrections to the interatomic potential.

The attractive polaron is formed by a coherent dressing of the impurity with particle-hole excitations of the majority component. We investigate its coherence by driving Rabi oscillations between the polaron and the weakly interacting final state (Fig. 2c). When the r.f.

frequency is tuned to the polaron resonance in the spectrum, we observe coherent oscillations of the transferred number of atoms as we increase the amplitude of the r.f. coupling for a fixed duration. In contrast, when the r.f. frequency is tuned to the incoherent background we do not observe oscillations but only a linear increase in signal strength.

Polarons are well-defined quasiparticles only at low temperature and in the limit of a single impurity. We investigate the deviations from this idealized picture in Fig. 3. Thermal excitations lead to decoherence of the dressing cloud and energetically higher-lying states, such as the molecular branch (see Fig. 1a), may be occupied. In the weakly interacting limit, the molecular branch is approximately  $E_F$  above the polaronic state; however, this energy difference reduces as the polaron–molecule transition is approached. Hence we expect the effects of temperature to be most pronounced near the polaron–molecule transition, and we focus our investigations on this regime. Indeed, we find that at  $\ln(k_F a_{2D}) = 0.45(5)$  (red squares in Fig. 3a) the effective mass remains unaffected by temperature up to  $T/T_F = 0.5$ , whereas for  $\ln(k_F a_{2D}) = -0.07(3)$  (blue circles in Fig. 3a) we observe a significant change of the single particle spectrum. At low temperatures we find good agreement with the zero-temperature prediction, but at higher temperatures the effective mass increases. This could signal a transition from a polaron at low temperature into the incoherent molecule–hole continuum at high temperature. Another deviation from the idealized polaron picture results from a finite concentration of impurities. This may cause interactions between quasiparticles mediated by the majority species. In Fig. 3b we show the dependence of the quasiparticle properties on the impurity concentration  $C = N_\uparrow / (N_\uparrow + N_\downarrow)$  of the Fermi gas (here  $N_\uparrow$  and  $N_\downarrow$  represent the number of spin-up and spin-down atoms, respectively). In the limit  $C \ll 1$ , the observed effective mass matches well with the theoretical prediction for the polaron. On increasing the impurity concentration, we find that

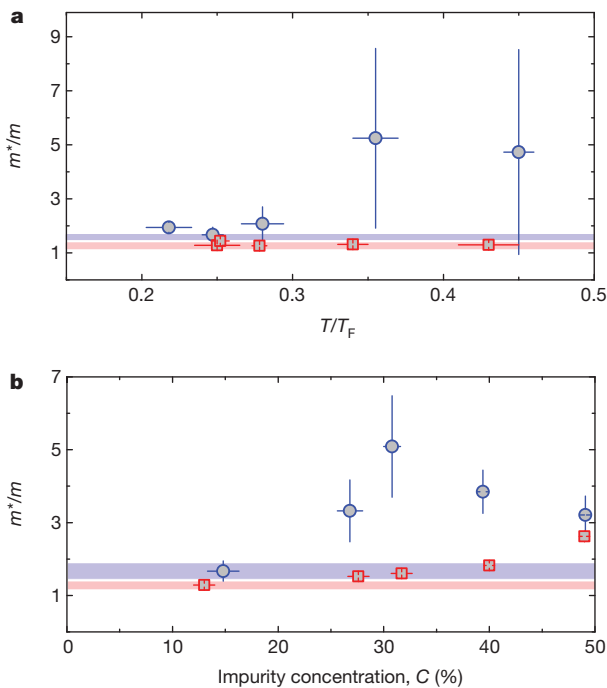


**Figure 3 | Finite temperature and impurity concentration.** **a**, Effective mass as a function of temperature for  $\ln(k_F a_{2D}) = 0.45(5)$  (red squares) and  $\ln(k_F a_{2D}) = -0.07(3)$  (blue circles). The solid horizontal lines show the theoretical prediction at zero temperature. All data are taken for  $C = 0.13$ . **b**, Effective mass as a function of impurity concentration. The horizontal lines show the theoretical prediction for the polaron and the shaded bars reflect the variation of the Fermi energy for the different measurements. Data are taken at  $T/T_F = 0.25(3)$ . Error bars correspond to 1 s.d. uncertainty in the fit.

the effective mass increases, which we attribute to polaron–polaron interaction. Again, we find that this effect is more pronounced near the polaron–molecule transition. At equal populations, we observe approximately the same effective mass for both interaction strengths.

Finally, we turn our attention to the repulsive polaron. This quasiparticle plays a decisive role in the question of whether itinerant ferromagnetism can be achieved with repulsive short-range interactions between fermions, which has been argued to be impossible in a three-dimensional spin-1/2 mixture with contact interactions<sup>30</sup>. The recent observation of a repulsive polaron in a three-dimensional heteronuclear Fermi–Fermi mixture<sup>7</sup> has renewed the interest in whether mass-imbalance and/or reduced dimensionality could stabilize the formation of polarized domains. We access the repulsive branch of the Feshbach resonance between the  $|-9/2\rangle$  and  $|-5/2\rangle$  states near 224 G (see Methods). Lifetime, energy and effective mass are extracted from the spectral function  $A(k, E)$ , which we measure after different hold times.

For the lifetime measurement (Fig. 4a), we determine the atom number loss, integrating from  $-10$  kHz to  $+10$  kHz. We observe a

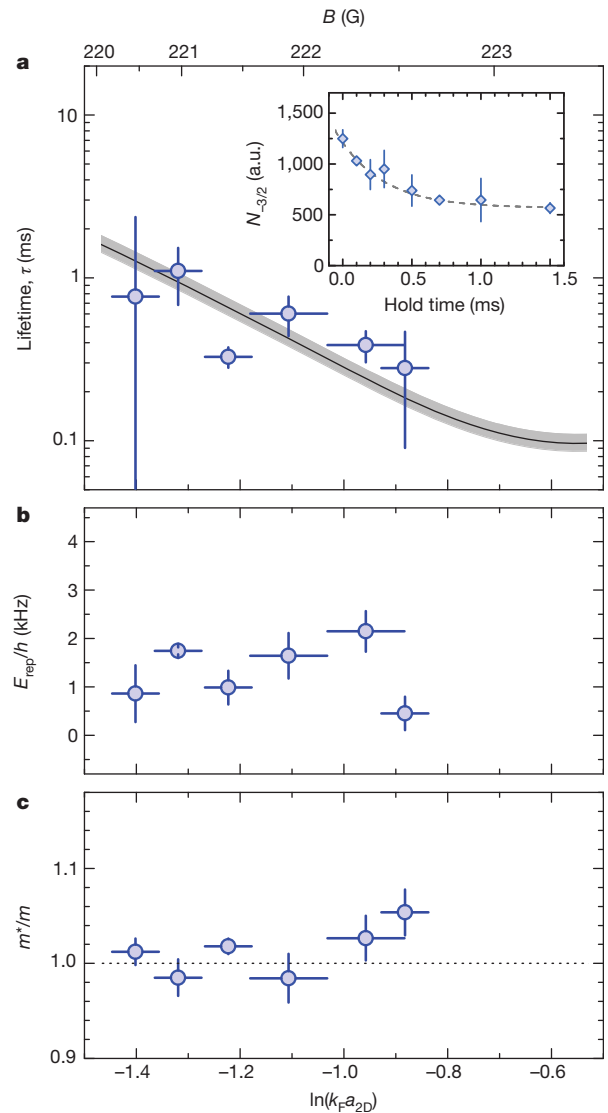


**Figure 4 | Repulsive polaron.** **a**, Lifetime of the repulsive branch. The inset shows an example of a time-resolved measurement at  $\ln(k_F a_{2D}) = -1.2$  from which we extract the lifetime by a fit (dashed line). The solid line is the theoretical prediction from ref. 16. The grey shaded area reflects the range of Fermi energies of  $(11 \pm 1)$  kHz. **b**, **c**, Measured energy (**b**) and effective mass (**c**). Error bars correspond to 1 s.d. uncertainty in the fit.



fast decay (Fig. 4a inset) to a plateau which decays much more slowly, similar to the balanced case in three dimensions<sup>30</sup>. In Fig. 4a we display the measured lifetime  $\tau$  of the repulsive branch as a function of the interaction strength, which agrees with the theoretical prediction for the lifetime of the repulsive polaron<sup>16</sup>, adapted for the quasi-two-dimensional binding energy  $E_B$  and quasi-two-dimensional scattering length  $a_{2D}$  (see Methods). In the regime of strong interactions (small negative  $\ln(k_F a_{2D})$ ), the decay rate  $1/\tau$  becomes a sizeable fraction of  $E_F$ , qualitatively similar to repulsive Fermi gases in three dimensions<sup>30</sup>. The energy and the effective mass are extracted from the spectral function as above and they are plotted in Fig. 4b and c, respectively. Both mass and energy deviate from the prediction for the homogeneous gas under exact two-dimensional confinement<sup>15,16</sup>, for which we replace the exact two-dimensional binding energy with the quasi-two-dimensional binding energy. The repulsive polaron energy is in qualitative agreement with the trap-averaged spectra of ref. 15, which have revealed a relatively small dependence of the polaron energy on the interaction parameter. To model our data quantitatively, it might be necessary to include final-state interaction effects, to use a quasi-two-dimensional theory<sup>29</sup> including harmonic confinement, and to include possible effects of non-adiabaticity and the formation time of the polaron during the relatively fast magnetic field ramp.

In conclusion, we have observed features of attractive and repulsive Fermi polarons in two dimensions. We find evidence for the polaron-molecule transition in a two-dimensional Fermi gas, although at a slightly different interaction parameter than theoretically predicted. The future inclusion of a localized, potentially spin-dependent, potential will allow the effective mass of the impurity to be increased, and to move into the regime of X-ray edge phenomena and the Kondo effect, in which the internal spin degree of freedom of an immobile impurity becomes entangled with the Fermi sea.

## METHODS SUMMARY

The starting point of this work is a quantum degenerate Fermi gas of  $^{40}\text{K}$  atoms in a strongly imbalanced mixture with an impurity concentration  $C = 0.15$  of the two lowest Zeeman states  $|-9/2\rangle$  and  $|-7/2\rangle$  (for the repulsive polaron  $|-9/2\rangle$  and  $|-5/2\rangle$ ) of the  $F = 9/2$  hyperfine manifold confined to an optical lattice. The average Fermi energy of the majority component is  $E_F/\hbar = 10\text{ kHz}$  and the temperature is typically  $T/T_F = 0.25$ . We record momentum-resolved photoemission spectra near the Feshbach resonance at 202.1 G (224.2 G) by coupling the  $|-7/2\rangle$  ( $|-5/2\rangle$ ) state to the weakly interacting state  $|-5/2\rangle$  ( $|-3/2\rangle$ ) using an r.f. photon of frequency  $\Omega_{rf}$  with negligible momentum transfer. The momentum distribution of the transferred atoms is detected in a time-of-flight experiment and we average the absorption signal azimuthally to obtain the single particle spectral function  $A(k, E)$ , with the wave vector  $k = \sqrt{k_x^2 + k_y^2}$  and energy  $E = E_Z - \hbar\Omega_{rf}$  using the atomic Zeeman energy  $E_Z$ .

**Full Methods** and any associated references are available in the online version of the paper at [www.nature.com/nature](http://www.nature.com/nature).

**Received 20 December 2011; accepted 18 April 2012.**

**Published online 23 May 2012.**

1. Devreese, J. T. & Alexandrov, A. S. Fröhlich polaron and bipolaron: recent developments. *Rep. Prog. Phys.* **72**, 066501 (2009).
2. Anderson, P. W. Infrared catastrophe in Fermi gases with local scattering potentials. *Phys. Rev. Lett.* **18**, 1049–1051 (1967).
3. Kondo, J. Resistance minimum in dilute magnetic alloys. *Prog. Theor. Phys.* **32**, 37–49 (1964).
4. Prokof'ev, N. & Svistunov, B. Fermi-polaron problem: diagrammatic Monte Carlo method for divergent sign-alternating series. *Phys. Rev. B* **77**, 020408 (2008).
5. Schirotzek, A., Wu, C.-H., Sommer, A. & Zwierlein, M. W. Observation of Fermi polarons in a tunable Fermi liquid of ultracold atoms. *Phys. Rev. Lett.* **102**, 230402 (2009).

6. Nascimbène, S. *et al.* Collective oscillations of an imbalanced Fermi gas: axial compression modes and polaron effective mass. *Phys. Rev. Lett.* **103**, 170402 (2009).
7. Kohstall, C. *et al.* Metastability and coherence of repulsive polarons in a strongly interacting Fermi mixture. Preprint at <http://arXiv.org/abs/1112.0020> (2011).
8. Chevy, F. & Mora, C. Ultra-cold polarized Fermi gases. *Rep. Prog. Phys.* **73**, 112401 (2010).
9. Duine, R. A. & MacDonald, A. H. Itinerant ferromagnetism in an ultracold atom Fermi gas. *Phys. Rev. Lett.* **95**, 230403 (2005).
10. Chubukov, A. V. Kohn-Luttinger effect and the instability of a two-dimensional repulsive Fermi liquid at  $T=0$ . *Phys. Rev. B* **48**, 1097–1104 (1993).
11. Conduit, G. J., Conlon, P. H. & Simons, B. D. Superfluidity at the BEC-BCS crossover in two-dimensional Fermi gases with population and mass imbalance. *Phys. Rev. A* **77**, 053617 (2008).
12. Parish, M. M. Polaron-molecule transitions in a two-dimensional Fermi gas. *Phys. Rev. A* **83**, 051603 (2011).
13. Zöllner, S., Bruun, G. M. & Pethick, C. J. Polarons and molecules in a two-dimensional Fermi gas. *Phys. Rev. A* **83**, 021603 (2011).
14. Klawunn, M. & Recati, A. Fermi polaron in two dimensions: Importance of the two-body bound state. *Phys. Rev. A* **84**, 033607 (2011).
15. Schmidt, R., Enss, T., Pietilä, V. & Demler, E. Fermi polarons in two dimensions. *Phys. Rev. A* **85**, 021602(R) (2012).
16. Ngampruetikorn, V., Levinsen, J. & Parish, M. M. Repulsive polarons in two-dimensional Fermi gases. Preprint at <http://arXiv.org/abs/1110.6415> (2011).
17. Dao, T.-L., Georges, A., Dalibard, J., Salomon, C. & Carusotto, I. Measuring the one-particle excitations of ultracold Fermionic atoms by stimulated Raman spectroscopy. *Phys. Rev. Lett.* **98**, 240402 (2007).
18. Stewart, J. T., Gaebler, J. P. & Jin, D. S. Using photoemission spectroscopy to probe a strongly interacting Fermi gas. *Nature* **454**, 744–747 (2008).
19. Feld, M., Fröhlich, B., Vogt, E., Koschorreck, M. & Köhl, M. Observation of a pairing pseudogap in a two-dimensional Fermi gas. *Nature* **480**, 75–78 (2011).
20. Cui, X. & Zhai, H. Stability of a fully magnetized ferromagnetic state in repulsively interacting ultracold Fermi gases. *Phys. Rev. A* **81**, 041602 (2010).
21. Pietilä, V., Pekker, D., Nishida, Y. & Demler, E. Pairing instabilities in quasi-two-dimensional Fermi gases. *Phys. Rev. A* **85**, 023621 (2012).
22. Lobo, C., Recati, A., Giorgini, S. & Stringari, S. Normal state of a polarized Fermi gas at unitarity. *Phys. Rev. Lett.* **97**, 200403 (2006).
23. Punk, M., Dumitrescu, P. T. & Zwerger, W. Polaron-to-molecule transition in a strongly imbalanced Fermi gas. *Phys. Rev. A* **80**, 053605 (2009).
24. Pilati, S., Bertainia, G., Giorgini, S. & Troyer, M. Itinerant ferromagnetism of a repulsive atomic Fermi gas: a quantum Monte Carlo study. *Phys. Rev. Lett.* **105**, 030405 (2010).
25. McGuire, J. B. Interacting Fermions in one dimension. II. Attractive potential. *J. Math. Phys.* **7**, 123–132 (1966).
26. Fröhlich, B. *et al.* Radiofrequency spectroscopy of a strongly interacting two-dimensional Fermi gas. *Phys. Rev. Lett.* **106**, 105301 (2011).
27. Schmidt, R. & Enss, T. Excitation spectra and rf response near the polaron-to-molecule transition from the functional renormalization group. *Phys. Rev. A* **83**, 063620 (2011).
28. Sommer, A. T., Cheuk, L. W., Ku, M. J. H., Bakr, W. S. & Zwierlein, M. W. Evolution of fermion pairing from three to two dimensions. *Phys. Rev. Lett.* **108**, 045302 (2012).
29. Levinsen, J. & Baur, S. K. Ground state of an impurity in a quasi-two-dimensional Fermi gas. Preprint at <http://arXiv.org/abs/1202.6564> (2012).
30. Sanner, C. *et al.* Correlations and pair formation in a repulsively interacting Fermi gas. Preprint at <http://arXiv.org/abs/1108.2017> (2011).

**Supplementary Information** is linked to the online version of the paper at [www.nature.com/nature](http://www.nature.com/nature).

**Acknowledgements** We thank S. Baur, N. Cooper, E. Demler, T. Enss, C. Kollath, J. Levinsen, M. Parish, R. Schmidt and W. Zwerger for discussions, and J. Bohn for communicating unpublished details of the  $|-5/2\rangle/|-3/2\rangle$  Feshbach resonance in  $^{40}\text{K}$ . The work was supported by EPSRC (EP/G029547/1), Daimler-Benz Foundation (B.F.), Studienstiftung and DAAD (M.F.).

**Author Contributions** The experimental set-up was devised and constructed by M.F., B.F., E.V. and M. Köhl, data taking was performed by M. Koschorreck, E.V. and D.P., data analysis was performed by M. Koschorreck and D.P., and the manuscript was written by M. Köhl with contributions from all co-authors.

**Author Information** Reprints and permissions information is available at [www.nature.com/reprints](http://www.nature.com/reprints). The authors declare no competing financial interests. Readers are welcome to comment on the online version of this article at [www.nature.com/nature](http://www.nature.com/nature). Correspondence and requests for materials should be addressed to M. Köhl ([mk540@cam.ac.uk](mailto:mk540@cam.ac.uk)).

## METHODS

**Preparation of imbalanced 2D gases.** We prepare degenerate Fermi gases following the general procedure of ref. 26. Additionally, during the evaporative cooling sequence we apply an r.f. pulse in order to prepare the desired spin mixture by selectively removing atoms from the  $|-7/2\rangle$  state. Subsequently, we load the imbalanced mixture into an optical lattice formed by a horizontally propagating, retro-reflected laser beam of wavelength  $\lambda = 1,064$  nm, focused to a waist ( $1/e^2$  radius) of  $140\ \mu\text{m}$ . We increase the laser power over a time of 200 ms to reach the final potential depth with a trapping frequency along the strongly confined direction of  $\omega = 2\pi \times 78.5$  kHz. After loading the optical lattice, we adiabatically reduce the power of the optical dipole trap such that the atoms are confined only by the Gaussian intensity envelope of the lattice laser beams. The resulting radial trapping frequency of the two-dimensional gases is  $\omega_{\perp} = 2\pi \times 127$  Hz. Along the axial direction we populate approximately 30 layers of the optical lattice potential with an inhomogeneous peak density distribution. The Fermi energy (of the majority component) is the measured, density-weighted average across the different layers. We measure that majority and minority component have the same absolute temperature. As a result, the minority atoms occupy fewer layers and experience a more uniform peak density of majority atoms.

**Momentum-resolved photoemission spectroscopy.** In order to access the attractive polaron branch, we adiabatically increase the interaction strength by lowering the magnetic field in 30 ms from 209 G to a value near the Feshbach resonance at 202.1 G. Momentum resolved photoemission spectroscopy is performed by applying a r.f. pulse near 50 MHz with a Gaussian amplitude envelope with a full-width at half-maximum of  $280\ \mu\text{s}$  to transfer atoms from the  $|-7/2\rangle$  state to the  $|-5/2\rangle$  state. Atoms in the  $|-5/2\rangle$  state have a two-body  $s$ -wave scattering length of 250 Bohr radii with the  $|-9/2\rangle$  state<sup>18</sup>. We turn off the optical lattice  $100\ \mu\text{s}$  after the r.f. pulse, switch off the magnetic field, and apply a magnetic field gradient to achieve spatial splitting of the three spin components in a Stern-Gerlach experiment. We have experimentally verified that the spectra and the extracted data do not vary when an additional wait time of 8 ms is introduced after the magnetic field ramp.

The repulsive polaron branch is accessed by preparing the imbalanced  $|-9/2\rangle/|-7/2\rangle$  mixture at a magnetic field of 220 G and spin-flipping the atoms from  $|-7/2\rangle$

to  $|-5/2\rangle$  using a  $30\text{-}\mu\text{s}$ -long r.f. pulse with 95% transfer efficiency. The pulse is tuned to the bare Zeeman transition energy but is broadband to include also the repulsive polaron energy shift. Then, we ramp the magnetic field to the desired value near the  $|-9/2\rangle/|-5/2\rangle$  Feshbach resonance in 5 ms. We apply a r.f. pulse near 53 MHz with a Gaussian amplitude envelope with a full-width at half-maximum of  $270\ \mu\text{s}$  to transfer atoms from the  $|-5/2\rangle$  state to the  $|-3/2\rangle$  state. The scattering length between the  $|-9/2\rangle$  and  $|-3/2\rangle$  states at this magnetic field is approximately  $190\ a_B$ , where  $a_B$  is the Bohr radius. The sequence is completed using absorption imaging of the expanding clouds after Stern-Gerlach separation in an inhomogeneous field.

For each experimental run, the magnetic field is calibrated using spin-rotation with an r.f. pulse of an imbalanced mixture on the  $|-9/2\rangle/|-7/2\rangle$  transition. The magnetic field accuracy deduced from these measurements is  $<3$  mG. We measure the temperature by ballistic expansion of a weakly interacting gas, and the quoted numbers refer to the average of  $T/T_F$  across the whole sample.

**Interaction parameter in two dimensions.** Two particles in a two-dimensional system created by tight harmonic confinement exhibit a confinement-induced bound state of binding energy  $E_B$ . The binding energy is linked to the three-dimensional scattering length  $a_s$  and is obtained from the transcendental equation<sup>31,32</sup>:

$$l_z/a_s = \int_0^{\infty} \frac{du}{\sqrt{4\pi u^3}} \left( 1 - \frac{\exp(-E_B u/\hbar\omega)}{\sqrt{(1 - \exp(-2u))/(2u))} \right) \quad (1)$$

Here  $l_z = \sqrt{\hbar/m\omega}$  is the harmonic oscillator length, and  $a_s$  is determined using the following parameters of the Feshbach resonances: Feshbach resonance between  $|-9/2\rangle$  and  $|-7/2\rangle$ :  $B_0 = 202.1$  G,  $\Delta B = 7$  G and  $a_{bg} = 174\ a_B$  and Feshbach resonance between  $|-9/2\rangle$  and  $|-5/2\rangle$ :  $B_0 = 224.2$  G,  $\Delta B = 7.5$  G and  $a_{bg} = 174\ a_B$ . Using  $E_B$  we define the two-dimensional scattering length  $a_{2D}$  by  $E_B = \hbar^2/ma_{2D}^2$ .

31. Petrov, D. & Shlyapnikov, G. Interatomic collisions in a tightly confined Bose gas. *Phys. Rev. A* **64**, 012706 (2001).
32. Bloch, I., Dalibard, J. & Zwerger, W. Many-body physics with ultracold gases. *Rev. Mod. Phys.* **80**, 885–964 (2008).

# Complex shapes self-assembled from single-stranded DNA tiles

Bryan Wei<sup>1,2</sup>, Mingjie Dai<sup>2,3</sup> & Peng Yin<sup>1,2</sup>

Programmed self-assembly of strands of nucleic acid has proved highly effective for creating a wide range of structures with desired shapes<sup>1–25</sup>. A particularly successful implementation is DNA origami, in which a long scaffold strand is folded by hundreds of short auxiliary strands into a complex shape<sup>9,14–16,18–21,25</sup>. Modular strategies are in principle simpler and more versatile and have been used to assemble DNA<sup>2–5,8,10–13,17,23</sup> or RNA<sup>7,22</sup> tiles into periodic<sup>3,4,7,22</sup> and algorithmic<sup>5</sup> two-dimensional lattices, extended ribbons<sup>10,12</sup> and tubes<sup>4,12,13</sup>, three-dimensional crystals<sup>17</sup>, polyhedra<sup>11</sup> and simple finite two-dimensional shapes<sup>7,8</sup>. But creating finite yet complex shapes from a large number of uniquely addressable tiles remains challenging. Here we solve this problem with the simplest tile form, a ‘single-stranded tile’ (SST) that consists of a 42-base strand of DNA composed entirely of concatenated sticky ends and that binds to four local neighbours during self-assembly<sup>12</sup>. Although ribbons and tubes with controlled circumferences<sup>12</sup> have been created using the SST approach, we extend it to assemble complex two-dimensional shapes and tubes from hundreds (in some cases more than one thousand) distinct tiles. Our main design feature is a self-assembled rectangle that serves as a molecular canvas, with each of its constituent SST strands—folded into a 3 nm-by-7 nm tile and attached to four neighbouring tiles—acting as a pixel. A desired shape, drawn on the canvas, is then produced by one-pot annealing of all those strands that correspond to pixels covered by the target shape; the remaining strands are excluded. We implement the strategy with a master strand collection that corresponds to a 310-pixel canvas, and then use appropriate strand subsets to construct 107 distinct and

complex two-dimensional shapes, thereby establishing SST assembly as a simple, modular and robust framework for constructing nanostructures with prescribed shapes from short synthetic DNA strands.

Our 42-base SST motif<sup>12</sup> consists of four domains (Fig. 1a), grouped into two pairs (domains 1 and 2 and domains 3 and 4) that each consists of 21 nucleotides in total. We design the intermolecular binding interactions of these domains such that a collection of distinct SST tiles will arrange into a DNA lattice composed of parallel helices connected by single-stranded linkages (Fig. 1b, left and middle), forming a ‘brick-wall’ pattern (Fig. 1b, right). The linkages between two adjacent helices are expected to be the phosphates that connect domains 2 and 3 of the SSTs, and are thus shown artificially stretched in the diagrams. They are spaced two helical turns (that is, 21 base pairs) apart and are all located in the same tangent plane between the two helices. The rectangular lattice sketched in Fig. 1b contains six parallel helices, each measuring about eight helical turns; we refer to this as a 6 helix × 8 helical turn (6H × 8T) rectangle. This basic strategy can be adapted to design rectangles with different dimensions, and arbitrary shapes approximated with an SST brick-wall pattern (Fig. 1c). By concatenating pairs of half-tiles on its top and bottom boundaries into full tiles, we can transform the rectangle in Fig. 1b into a tube with a prescribed circumference and length (Fig. 1d).

A pre-designed rectangular SST lattice (Fig. 1e, top right) can also be viewed as a ‘molecular canvas’, where each SST serves as a 3 nm × 7 nm ‘molecular pixel’. Designing a shape amounts to selecting its constituent pixels on the canvas, as illustrated by the two examples in Fig. 1e.

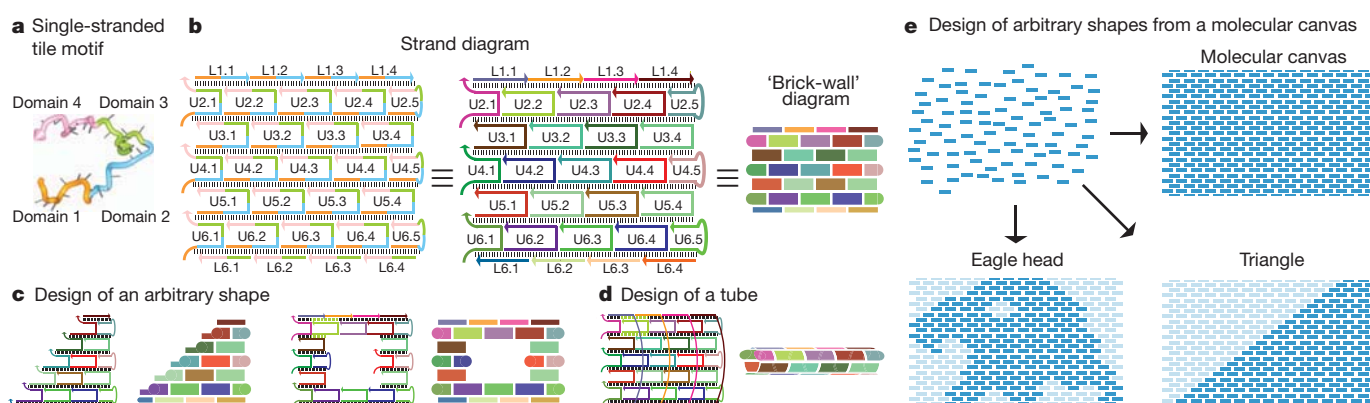


**Figure 1 | Self-assembly of molecular shapes using single-stranded tiles.** **a**, The canonical SST motif, adapted from ref. 12. **b**, Design of an SST rectangle structure. Left and middle: two different views of the same secondary structure diagram. Each standard (full) tile has 42 bases (labelled U), and each top and bottom boundary (half) tile has 21 bases (labelled L). Right: a simplified ‘brick-wall’ diagram. Standard tiles are depicted as thick rectangles, boundary tiles are depicted as thin rectangles and the unstructured single-stranded portions of the boundary tiles are depicted as rounded corners. Each strand has a unique sequence. Colours distinguish domains in the left panel and distinguish strands

in the middle and right panels. **c**, Selecting an appropriate subset of SST species from the common pool in **b** makes it possible to design a desired target shape, for example a triangle (left) or a rectangular ring (right). **d**, Design of a tube with prescribed width and length. **e**, Arbitrary shapes can be designed by selecting an appropriate set of monomers from a pre-synthesized pool that corresponds to a molecular canvas (top right). To make a shape, the SST strands corresponding to its constituent pixels (dark blue) will be included in the strand mixture and the remainder (light blue) will be excluded.

<sup>1</sup>Department of Systems Biology, Harvard Medical School, Boston, Massachusetts 02115, USA. <sup>2</sup>Wyss Institute for Biologically Inspired Engineering, Harvard University, Boston, Massachusetts 02115, USA. <sup>3</sup>Program in Biophysics, Harvard University, Boston, Massachusetts 02115, USA.



These shapes, and more than 100 others, were designed and experimentally constructed, demonstrating the self-assembly of complex molecular shapes from modular components (Supplementary Fig. 1).

Following the design in Fig. 1b, we assembled a  $24\text{H} \times 28\text{T}$  rectangle (Fig. 2a) from 362 distinct SST species (310 internal, standard full-length SSTs, 24 full-length SSTs on vertical boundaries whose exposed single-stranded domains are replaced by poly(T) (multiple thymine bases), and 28 half-length SSTs on horizontal boundaries). The rectangle, which has a molecular weight comparable to a DNA origami structure made with an M13 phage scaffold<sup>9</sup>, was made using unpurified DNA strands that had their sequences designed to minimize sequence symmetry<sup>26</sup> (Methods) and were then mixed without careful adjustment of stoichiometry. After single-step (one-pot) annealing that involved cooling from 90 to 25 °C over 17 h in 25 mM  $\text{Mg}^{2+}$  buffer (see Supplementary Information, section 2.3, for the effects of buffer ion strength and annealing time on the assembly yield), the solution was subjected to 2% native agarose gel electrophoresis and produced one dominant band (Fig. 2b, lane U). This band was extracted and purified by centrifugation, with the purified product migrating as a single band on the gel (Fig. 2b, lane P) and appearing in atomic force microscopy (AFM) images with the expected rectangular morphology (Fig. 2c) with approximately the expected dimensions ( $64 \pm 2\text{ nm} \times 103 \pm 2\text{ nm}$ ,  $N = 30$ ). Successful streptavidin attachment at selected internal and boundary positions, corresponding to tiles displaying biotin-modified strands, further verified the formation of the full rectangle and also demonstrated the unique addressability of the constituent tiles (Supplementary Information, section 2.4).

Native gel electrophoresis of samples stained with SYBR Safe gave a 17% assembly yield (referred to as ‘gel yield’), calculated from the ratio of the fluorescent intensity of the product band to that of the entire lane (after background correction). We note that the structure- and sequence-dependent variation in the staining efficiency of SYBR Safe (Supplementary Fig. 3) suggests that this ratio is a bounded (<50%) overestimate (Supplementary Information, section 2.2.1) and that the actual yield is probably 12–17%. In the remainder of the paper, we report the unadjusted yield measurement, which should be considered as an approximate estimate (within 50% accuracy).

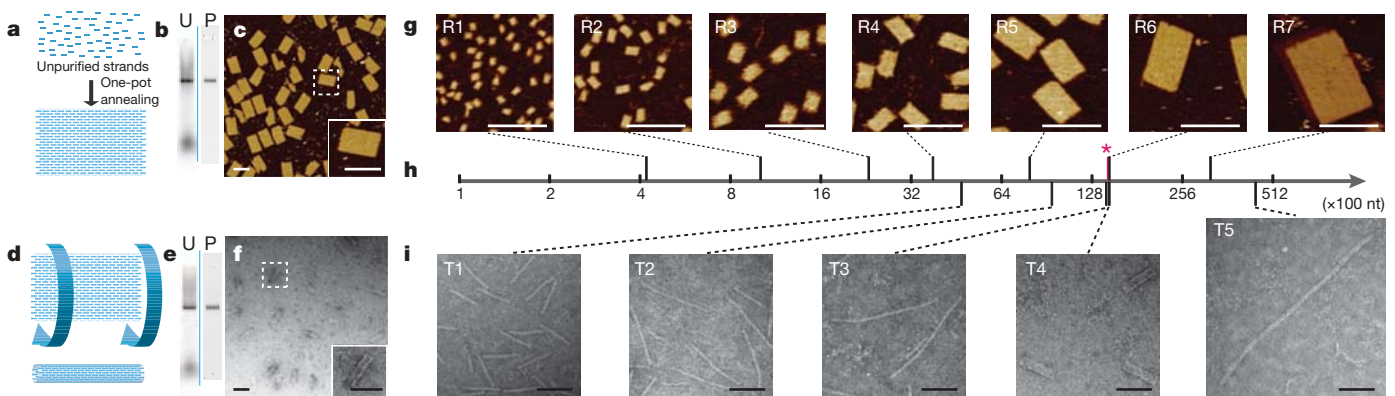


**Figure 2 | Self-assembly of SST rectangles and tubes.** **a–c**,  $24\text{H} \times 28\text{T}$  SST rectangle. **a**, Schematic of rectangle formation. For a more detailed depiction, see Supplementary Fig. 2. Supplementary Information, section 6, contains strand diagrams for this and all other SST rectangles and tubes, and sections 7 and 8 contain sequences for all the structures constructed in this paper. **b**, 2% native agarose gel electrophoresis. U, unpurified; P, purified (by gel extraction from lane U). **c**, AFM image. Inset shows a magnified view of the outlined structure. See Supplementary Fig. 2 for a larger AFM image. **d–f**,  $24\text{H} \times 28\text{T}$  SST tube. **d**, Schematic of tube design. **e**, 2% native agarose gel electrophoresis. **f**, TEM image. Inset shows a magnified view of the outlined structure. See Supplementary Information, section 2.5, for a larger image. **g–i**, Rectangles and tubes across scales. **g**, AFM images of SST rectangles. The designed dimensions are  $4\text{H} \times 4\text{T}$  (R1),  $6\text{H} \times 7\text{T}$  (R2),  $10\text{H} \times 10\text{T}$  (R3),  $12\text{H} \times 14\text{T}$  (R4),  $18\text{H} \times 20\text{T}$  (R5),  $24\text{H} \times 28\text{T}$  (R6) and  $36\text{H} \times 41\text{T}$  (R7). **h**, Logarithmic molecular weight. The pink asterisk indicates the weight of a typical M13 DNA

origami<sup>9</sup> as a reference point. nt, nucleotide. **i**, TEM images of SST tubes. The designed dimensions are  $8\text{H} \times 28\text{T}$  (T1),  $8\text{H} \times 55\text{T}$  (T2),  $8\text{H} \times 84\text{T}$  (T3),  $24\text{H} \times 28\text{T}$  (T4) and  $12\text{H} \times 117\text{T}$  (T5). All scale bars, 100 nm. See Supplementary Information, section 3.1, for the schematics of the rectangles and tubes and for a depiction of the molecular weights of all 118 distinct structures we constructed. See Supplementary Information, section 3.2, for the number of distinct constituent SST species (ranging from 12 to 1,068), the number of nucleotides (420 to 44,856), the measured widths (11 to 91 nm) and lengths (16 to 621 nm), the measured gel yield (0.4% to 32%), and the measured AFM yield (25% to 61%) of the 12 rectangles and tubes shown here. See Supplementary Information, sections 3.3 (rectangles) and 3.4 (tubes), for gel results, larger AFM and TEM images, and gel- and imaging-based yield analyses. The formation of full-length  $8\text{H} \times 84\text{T}$  tubes and full-length  $12\text{H} \times 117\text{T}$  tubes was also confirmed by streptavidin labelling of the tube ends (Supplementary Information, section 3.4.4).

The fraction of purified product appearing as ‘well-formed’ rectangles (defined as those showing no defects more than 15 nm in diameter in the expected outline or more than 10 nm in diameter in the interior) was determined as a percentage of all identifiable shapes in an AFM field, giving an ‘AFM yield’ of 55% ( $N = 163$ ; Supplementary Fig. 6). This number is probably an underestimate of the actual fraction of well-formed structures within the purified product owing to the relative fragility of SST rectangles, which can result in significant post-purification damage caused by sample deposition or imaging (Supplementary Information, section 2.2.2). Such fragility may be mitigated by introducing more covalent bonds into the assembled structures, for example through either ligation<sup>27</sup> of two ends of an SST or crosslinking<sup>28</sup> of neighbouring SSTs.

Following the design strategy sketched in Fig. 1d,  $24\text{H} \times 28\text{T}$  rectangles were transformed into  $24\text{H} \times 28\text{T}$  tubes with a gel yield of 14% (Fig. 2d, e). Transmission electronic microscopy (TEM) images of the purified product revealed tube-like structures with approximately the expected lengths of  $98 \pm 2\text{ nm}$  and diameters of  $24 \pm 1\text{ nm}$  (Fig. 2f), and gave a TEM yield of 82% ( $N = 89$ ). The TEM yield is the percentage of identifiable tubes whose lengths are within 5 nm of the expected full length of 98 nm, estimated by assuming a length of 3.5 nm (see below) per helical turn.

The successful construction of seven different rectangles (Fig. 2g) and five different tubes (Fig. 2i) with distinct dimensions and molecular weights (Fig. 2h) illustrates the benefits of the modular nature of SST assembly (see Supplementary Information, section 3, for design and characterization details). These structures include a  $12\text{H} \times 177\text{T}$  tube made of more than 1,000 distinct SST species, which represents a 60-fold increase in the number of distinct tile species contained in a finite and uniquely addressable shape<sup>7,8</sup>. These rectangle and tube series allow us also to plot their measured lengths and widths against the designed number of constituent helices and the number of helical turns within a helix, which gives a linear relationship (Pearson correlation,  $R^2 > 0.99$ ) with an average helix width and average helical turn length of 2.6 nm and 3.5 nm, respectively (Supplementary Information, section 3.5). High-resolution AFM imaging of an assembled structure yielded a helical width of 2.6 nm (Supplementary Fig. 38), consistent with the above value.

We next sought to construct arbitrary shapes using the idea of a molecular canvas (Fig. 1e), with the  $24\text{H} \times 28\text{T}$  rectangle as the canvas and its 310 internal SSTs as the molecular pixels. Attempts to assemble a triangle by simply annealing the SST species that correspond to the triangle pixels resulted in severe aggregation and no detectable product band on an agarose gel (data not shown). The aggregation was attributed to non-specific interactions between exposed single-stranded domains of the SST on the hypotenuse boundary of the triangles. Two designs were tested to eliminate aggregation: one in which we replaced each exposed domain with a poly(T) segment of the same length, and one in which we covered each with an 'edge protector' that has a segment complementary to the exposed domain followed by a 10- or 11-nucleotide poly(T) segment. Both designs eliminated aggregation and produced the desired triangles with comparable yields (Supplementary Information, section 4.2), and can thus be used to construct a pool of SST strands and auxiliary strands representing the full molecular canvas. We chose the edge protector design because it involves a smaller ( $\times 4$  instead of  $\times 15$ ) number of auxiliary species (Supplementary Fig. 43) and synthesized 1,344 edge protectors (each 21 nucleotides in length) supplementing the existing 362 SST strands (Supplementary Information, section 4.2). With this modification, a prescribed shape can be created by selecting appropriate SST strands and the auxiliary strands that correspond to the shape's boundary. We used this method to construct the triangle and the three other shapes shown in Fig. 3.

To explore the generality and robustness of the molecular canvas method, we designed a total of 110 distinct shapes (including the shapes described above) (Supplementary Information, section 4.3). Of the targeted designs, 103 produced discernible product bands on the gel and the expected shapes under AFM in the first assembly trial; this corresponds to a 94% success rate. The seven failed designs were challenging shapes resembling 0, 3,  $\sim$ , @, a hollow H and two Chinese characters (Supplementary Fig. 57). The first four (0, 3,  $\sim$ , @) were slightly redesigned to eliminate potential weak points (for example narrow connections) and then assembled successfully. We did not attempt to redesign the remaining three failed shapes, given their geometrical complexity. Combining these assembly trials gives 107 successful designs out of a total of 114 (a 94% success rate), with gel yields of targeted shapes ranging from 6% to 40%. Figure 4 shows AFM images of 100 distinct shapes. See Supplementary Information, sections 4.3 and 4.6, for schematics of the canvas design and AFM images, and section 4.5 for detailed gel yields.

We wrote a computer program to automate picking and mixing strands from a master library (Supplementary Fig. 58). This program provides the user with a graphical interface to draw (or load a picture of) a target shape, and then outputs instructions for a robotic liquid handler to pick and mix the required strands for subsequent annealing. Each robot batch produces 48 shapes in roughly 48 h, reducing several man-hours of labour to one machine-hour per shape and also avoiding

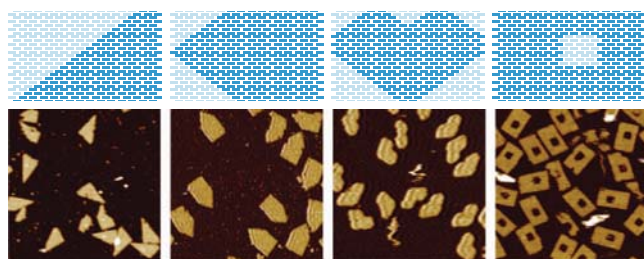


**Figure 3 | Simple shapes designed using a molecular canvas.** Top, schematics; bottom,  $500\text{ nm} \times 500\text{ nm}$  AFM images. The structures were constructed using the edge protector strategy, with respective gel yields of 16%, 19%, 22% and 16% (left to right; Supplementary Information, section 4.5), and AFM yields of 37%, 37%, 51% and 36% (left to right; Supplementary Information, section 4.7).



**Figure 4 | Complex shapes designed using a molecular canvas.** AFM images of 100 distinct shapes, including the 26 capital letters of the Latin alphabet, 10 Arabic numerals, 23 punctuation marks and other standard keyboard symbols, 10 emoticons, 9 astrological symbols, 6 Chinese characters and various miscellaneous symbols. Each image is  $150\text{ nm} \times 150\text{ nm}$  in size.

potential human mistakes. The robot was used to construct 44 of the shapes described above.

Different shapes were assembled and purified separately and then mixed together for efficient AFM imaging (for example, Supplementary Fig. 72 shows a mixture of the 26 letters of the Latin alphabet). The shapes were all derived from the same canvas, but coexisted stably after assembly: there was no sign of shapes merging or deforming each other. The structures almost always appeared under the AFM with the desired orientation, facing up towards the viewer (for example, in Supplementary Fig. 84 this is true of 96% of the structures,  $N = 49$ ). Such biased landing on the mica surface used for AFM imaging is consistent with free SST structures in solution being rolled up as a result of their intrinsic curvature<sup>12</sup>, and unrolling and becoming flattened when adsorbed onto the mica surface. This feature is useful for controlling landing orientation, but the expected curvature and accumulation of twist<sup>16,21</sup> in SST structures pose considerable challenges to straightforward scaling up of SST assemblies to large sizes. Flat SST structures free of curvature and twist could be constructed by shifting relative positions between linkage points<sup>12,18</sup>, by deleting bases<sup>16,21</sup> or by using a corrugated design<sup>4,19</sup>. Such modifications might in principle give access to larger structures and even facilitate further scaling up using hierarchical assembly strategies<sup>19–21</sup>, but may interfere with the standardized modular form of the present SST motif.

DNA origami<sup>9,14–16,18–21,25</sup> typically produces hybrid structures half composed of biological components (the M13 scaffold) and half composed of synthetic components with sequences derived from the biological part (the staple strands). By contrast, our SST structures are made entirely of *de novo* designed and synthesized short DNA strands, and we thus have greater sequence as well as material choice. For example, we constructed a  $24\text{H} \times 28\text{T}$  rectangle (Supplementary Information, section 5.1) from SST motifs with completely random sequences (that is, no sequence symmetry requirement was imposed; Methods) and a nuclease-resistant  $4\text{H} \times 4\text{T}$  rectangle (Supplementary Fig. 87) made of L-DNA, the mirror image of natural D-DNA. In



addition to L-DNA, SSTs could also be made from other informational polymers such as DNA with chemically modified backbones or artificial bases, or RNA.

Like DNA origami<sup>9,14–16,18–21,25</sup>, the SST method works robustly with unpurified strands without the need for careful adjustment of their stoichiometry, and with sequences that are not optimally designed (for example completely random sequences). But whereas the central design feature of DNA origami is a long scaffold, which is considered to give rise to this method's success and robustness<sup>9,25</sup>, SST assembly uses only short synthetic strands that enable it to emulate the programmable modularity characteristic of DNA or RNA tiling<sup>2–5,7,8,10–13,17,22,23</sup>. Yet unlike a multistranded tile<sup>2–5,7,8,10,11,13,17,22,23</sup> with a well-defined and structurally rigid core, an SST monomer<sup>12</sup> is a floppy DNA strand that is composed entirely of concatenated sticky ends and only folds into a rectangular shape because of its interaction with neighbouring SSTs during assembly. That the SST method is nevertheless successful and robust calls for a systematic investigation of the assembly mechanism and kinetics. It is conceivable that sparse and slow nucleation followed by fast growth allows complete assembly, with the required rate separation between nucleation and growth arising from structural reconfiguration or assembly-induced folding of SSTs that can increase the configurational entropy penalty<sup>12</sup> and thus raise the assembly nucleation barrier.

DNA origami<sup>9,14–16,18–21,25</sup> folds a long scaffold strand with many short staple strands into a prescribed shape without the strand getting tangled up; our SST method shows that a large number of small monomers can self-assemble into a desired structure that is not compromised by ill-formed by-products. These features illustrate the complementarity of the two approaches, which may represent the extremes of a rich spectrum of strategies for creating complex shapes and structures through the cooperative self-assembly of diverse components. Thus, the SST method<sup>12</sup> and DNA origami<sup>9,14–16,18–21,25</sup>, and approaches that use multistranded DNA and RNA tiles<sup>2–5,7,8,10,11,13,17,22,23</sup>, logic gates<sup>29</sup> and kinetic hairpins<sup>30</sup>, suggest the presence of a vast design space that remains to be explored for the creation of nucleic acid nanostructures, and more generally for information-directed molecular self-assembly.

## METHODS SUMMARY

DNA sequences were generated by minimizing sequence symmetry<sup>24</sup> (for most structures) or by populating the SST motifs with completely random sequences (for the structure in Supplementary Fig. 86). Without careful adjustment of stoichiometry, unpurified strands were mixed manually or using a liquid-handling robot and supplemented with 12.5 or 25 mM Mg<sup>2+</sup>. After one-pot annealing from 90 to 25 °C over  $x$  hours ( $17 \leq x \leq 58$ ; for most structures,  $x = 17$ ), the solution was subjected to native agarose gel electrophoresis. The desired product band was extracted, purified by centrifugation and imaged with AFM or TEM.

**Full Methods** and any associated references are available in the online version of the paper at [www.nature.com/nature](http://www.nature.com/nature).

**Received 20 November 2011; accepted 22 March 2012.**

- Seeman, N. C. Nucleic acid junctions and lattices. *J. Theor. Biol.* **99**, 237–247 (1982).
- Fu, T. J. & Seeman, N. C. DNA double-crossover molecules. *Biochemistry* **32**, 3211–3220 (1993).
- Winfree, E., Liu, F., Wenzler, L. A. & Seeman, N. C. Design and self-assembly of two-dimensional DNA crystals. *Nature* **394**, 539–544 (1998).
- Yan, H., Park, S. H., Finkelstein, G., Reif, J. H. & LaBean, T. H. DNA-templated self-assembly of protein arrays and highly conductive nanowires. *Science* **301**, 1882–1884 (2003).
- Rothmund, P. W. K., Papadakis, N. & Winfree, E. Algorithmic self-assembly of DNA Sierpinski triangles. *PLoS Biol.* **2**, e424 (2004).

- Shih, W., Quispe, J. & Joyce, G. A 1.7-kilobase single-stranded DNA that folds into a nanoscale octahedron. *Nature* **427**, 618–621 (2004).
- Chworos, A. *et al.* Building programmable jigsaw puzzles with RNA. *Science* **306**, 2068–2072 (2004).
- Park, S. H. *et al.* Finite-size, fully-addressable DNA tile lattices formed by hierarchical assembly procedures. *Angew. Chem. Int. Ed.* **45**, 735–739 (2006).
- Rothmund, P. W. K. Folding DNA to create nanoscale shapes and patterns. *Nature* **440**, 297–302 (2006).
- Schulman, R. & Winfree, E. Synthesis of crystals with a programmable kinetic barrier to nucleation. *Proc. Natl Acad. Sci. USA* **104**, 15236–15241 (2007).
- He, Y. *et al.* Hierarchical self-assembly of DNA into symmetric supramolecular polyhedra. *Nature* **452**, 198–201 (2008).
- Yin, P. *et al.* Programming DNA tube circumferences. *Science* **321**, 824–826 (2008).
- Sharma, J. *et al.* Control of self-assembly of DNA tubules through integration of gold nanoparticles. *Science* **323**, 112–116 (2009).
- Douglas, S. M. *et al.* Self-assembly of DNA into nanoscale three-dimensional shapes. *Nature* **459**, 414–418 (2009).
- Andersen, E. S. *et al.* Self-assembly of a nanoscale DNA box with a controllable lid. *Nature* **459**, 73–76 (2009).
- Dietz, H., Douglas, S. M. & Shih, W. M. Folding DNA into twisted and curved nanoscale shapes. *Science* **325**, 725–730 (2009).
- Zheng, J. P. *et al.* From molecular to macroscopic via the rational design of self-assembled 3D DNA crystal. *Nature* **461**, 74–77 (2009).
- Han, D. *et al.* DNA origami with complex curvatures in three-dimensional space. *Science* **332**, 342–346 (2011).
- Liu, W., Zhong, H., Wang, R. & Seeman, N. Crystalline two dimensional DNA origami arrays. *Angew. Chem. Int. Ed.* **50**, 264–267 (2011).
- Zhao, Z., Liu, Y. & Yan, H. Organizing DNA origami tiles into larger structures using preformed scaffold frames. *Nano Lett.* **11**, 2997–3002 (2011).
- Woo, S. & Rothmund, P. Programmable molecular recognition based on the geometry of DNA nanostructures. *Nat. Chem.* **3**, 620–627 (2011).
- Delebecque, C. J., Lindner, A. B., Silver, P. A. & Aldaye, F. A. Organization of intracellular reactions with rationally designed RNA assemblies. *Science* **333**, 470–474 (2011).
- Lin, C., Liu, Y., Rinker, S. & Yan, H. DNA tile based self-assembly: building complex nanoarchitectures. *ChemPhysChem* **7**, 1641–1647 (2006).
- Seeman, N. Nanomaterials based on DNA. *Annu. Rev. Biochem.* **79**, 65–87 (2010).
- Tørring, T., Voigt, N. V., Nangreave, J., Yan, H. & Goehlf, K. V. DNA origami: a quantum leap for self-assembly of complex structures. *Chem. Soc. Rev.* **40**, 5636–5646 (2011).
- Seeman, N. De novo design of sequences for nucleic acid structural engineering. *J. Biomol. Struct. Dyn.* **8**, 573–581 (1990).
- O'Neill, P., Rothmund, P. W. K., Kumar, A. & Fygenson, D. Sturdier DNA nanotubes via ligation. *Nano Lett.* **6**, 1379–1383 (2006).
- Rajendran, A., Endo, M., Katsuda, Y., Hidaka, K. & Sugiyama, H. Photo-crosslinking-assisted thermal stability of DNA origami structures and its application for higher-temperature self-assembly. *J. Am. Chem. Soc.* **133**, 14488–14491 (2011).
- Seelig, G., Soloveichik, D., Zhang, D. Y. & Winfree, E. Enzyme-free nucleic acid logic circuits. *Science* **314**, 1585–1588 (2006).
- Yin, P., Choi, H. M. T., Calvert, C. R. & Pierce, N. A. Programming biomolecular self-assembly pathways. *Nature* **451**, 318–322 (2008).

**Supplementary Information** is linked to the online version of the paper at [www.nature.com/nature](http://www.nature.com/nature).

**Acknowledgements** We thank S. Chandrasekaran, X. Lim, W. Sun and R. Conturie for technical assistance; A. Marblestone, R. Barish, W. Shih, Y. Ke, E. Winfree, S. Woo, P. Rothmund and D. Woods for discussions; and J. Aliperti for help with preparation of the draft. This work was funded by Office of Naval Research Young Investigator Program Award N000141110914, Office of Naval Research Grant N000141010827, NSF CAREER Award CCF1054898, NIH Director's New Innovator Award 1DP2OD007292 and a Wyss Institute for Biologically Inspired Engineering Faculty Startup Fund (to P.Y.).

**Author Contributions** B.W. designed the system, conducted the experiments, analysed the data and wrote the paper. M.D. conducted the experiments, analysed the data and wrote the paper. P.Y. conceived and guided the study, analysed the data and wrote the paper.

**Author Information** Reprints and permissions information is available at [www.nature.com/reprints](http://www.nature.com/reprints). The authors declare competing financial interests: details accompany the full-text HTML version of the paper at [www.nature.com/nature](http://www.nature.com/nature). Readers are welcome to comment on the online version of this article at [www.nature.com/nature](http://www.nature.com/nature). Correspondence and requests for materials should be addressed to P.Y. ([py@hms.harvard.edu](mailto:py@hms.harvard.edu)).



## METHODS

**DNA sequence design.** DNA sequences were designed with the UNIQIMER software<sup>31</sup> by minimizing the sequence symmetry<sup>24</sup> (for most of the structures) or by populating the SST motifs with completely random sequences (for the random sequence set in Supplementary Fig. S6). For design based on sequence minimization, there are several criteria for sequence generation. (1) Nucleotides (that is, A, C, G and T) are randomly generated one by one. (2) Nucleotides complementary to those generated are matched following the base-pairing rule: A to T and vice versa; C to G and vice versa. (3) No repeating segment beyond a certain length (eight or nine nucleotides) is permitted. When such repeating segments emerge during design, the most recently generated nucleotides will be mutated until the repeating-segment requirement is satisfied. (4) No four consecutive A, C, G or T bases are allowed. (5) Pre-specified nucleotides at the single-stranded linkage points (for example T and G as the twenty-first and twenty-second nucleotides, respectively, for most of the strands) are used to avoid sliding bases around the linkage points. In the design using completely random sequences (Supplementary Fig. S6), restrictions (3) to (5) were not applied.

Manual design and/or optimization was used for the design of handle segment sequences (for example the handle segment to accommodate a 3' biotin strand for streptavidin labelling and concatenation of poly(T) domains). Additionally, in some cases segments from different SST structures were manually combined to transform an existing structure into a new structure. For example, additional rows of SSTs were introduced to convert a rectangle design into a tube design (for example in converting the 24H × 28T rectangle design to the 24H × 28T tube design, and converting the 24H × 28T rectangle design to the 8H × 84T tube design). Similarly, we also manually converted a tube design into a rectangle design (for example in converting the 12H × 177T tube into the 36H × 41T rectangle).

**Sample preparation.** DNA strands were synthesized by Integrated DNA Technology, Inc. (<http://www.idtdna.com>) or the Bioneer Corporation (<http://us.bioneer.com>). To assemble the structures, DNA strands were mixed to a roughly equal molar final concentration of 100 nM per strand species for most of the structures (except for different shapes based on the 24H × 28T rectangle, which were prepared at 200 nM) in ×0.5 TE buffer (5 mM Tris, pH 7.9, 1 mM EDTA) supplemented with 12.5 or 25 mM MgCl<sub>2</sub>. We note that the DNA concentrations were based on the manufacturer's specifications and that no additional in-house calibration was performed. Thus, the stoichiometry for the strands was not tightly controlled. The mixture was then annealed in a PCR thermal cycler by cooling from 90 to 25 °C over a period of 17–58 h with different cooling programmes. The annealed samples were then subjected to 1.5% or 2% agarose gel electrophoresis (gel prepared in ×0.5 TBE buffer supplemented with 10 mM MgCl<sub>2</sub> and pre-stained with SYBR Safe) in an ice-water bath. Then the target gel bands were excised and put into a Freeze 'N Squeeze column (Bio-Rad). The gel pieces were finely crushed using a microtube pestle in the column and the column was then directly subjected to centrifugation at 438g for 3 min. Samples centrifuged through the column were collected for concentration estimation by the measurement of ultraviolet absorption at 260 nm. Such estimation is useful for estimating the dilution factor before AFM or TEM imaging.

**Streptavidin labelling.** Streptavidin labelling was done in two different ways.

(1) Labelling the top and bottom rows or internal loci of the 24H × 28T rectangle. Each tile of the top and bottom rows (or internal loci) of the 24H × 28T rectangle was modified to have a 3' 17-nucleotide handle (TT as spacer and GGAAGGGATGGAGGA to be complementary to the 3' biotin-modified strand whose sequence is TCCTCCATCCCTTCC-biotin). Special tiles of the top and bottom rows (or internal loci), and the rest of the component tiles of the rectangular lattice, were mixed with such handle-complementary 3' biotin-modified strands at ×1 to ×2 concentration in ×0.5 TE buffer (25 mM MgCl<sub>2</sub>). (When the concentration of special and common component tiles was 100 nM and there were 14 different special tile species, a ×1 concentration of the 3' biotin-modified strands was 100 × 14 = 1400 nM.) They were then annealed over 17 h and purified after agarose gel electrophoresis. The purified sample was then

subjected to AFM imaging. After the first round of imaging, streptavidin (1 µl at 10 mg ml<sup>-1</sup> in ×0.5 TE buffer, 10 mM MgCl<sub>2</sub>) was added to the imaging sample (~40 µl) for an incubation period of 2 min before re-imaging.

(2) Labelling the poly(T) ends of tube structures. After tube purification, 3' biotin-modified poly(A) strands (×5 to ×10 concentration relative to the poly(T) counterparts) were mixed with the sample at room temperature (~25 °C) overnight. The sample was then subjected to AFM imaging. After the first round of imaging, streptavidin (1 µl at 10 mg ml<sup>-1</sup> in ×0.5 TE buffer, 10 mM MgCl<sub>2</sub>) was added to the imaging sample on mica for an incubation period of 2 min before re-imaging.

**Robot automation for sample preparation.** A custom MATLAB program was designed to aid the design of complex shapes and to automate strand mixing using a liquid-handling robot (Bravo, Agilent). For each shape, 5 µl of each SST resuspended in water at 10 µM was picked and mixed into a final volume of less than 2 ml (the exact volume was determined by the number of constituent strands for the target shape), and was then vacuum evaporated to 200 µl of 250 nM solution. This mixture was then supplemented with 50 µl of 62.5 mM Mg<sup>2+</sup> buffer to reach a 250-µl final mixture ready for annealing. This pre-annealing solution had the following final concentrations: 200 nM DNA strand per SST species and 12.5 mM Mg<sup>2+</sup>. Each run accommodated 48 shapes and took around 2 d to finish.

**AFM imaging.** AFM images were obtained using a Multimode SPM with a Digital Instruments Nanoscope V controller (Veeco). A 5-µl drop (2–5 nM) of annealed and purified sample and then a 40-µl drop of ×0.5 TE buffer (10 mM MgCl<sub>2</sub>) were applied to a freshly cleaved mica surface and left for approximately 2 min. Sometimes additional dilution of the sample was performed to achieve the desired sample density. On a few occasions, supplementary 10 mM NiCl<sub>2</sub> was added to increase the strength of DNA–mica binding<sup>32</sup>. Samples were imaged using the liquid tapping mode. The AFM tips used were C-type triangular tips (resonant frequency,  $f_0 = 40$ –75 kHz; spring constant,  $k = 0.24$  N m<sup>-1</sup>) from the SNL-10 silicon nitride cantilever chip (Veeco Probes).

**TEM imaging.** For imaging, a 3.5-µl sample (1–5 nM) was adsorbed onto glow-discharged carbon-coated TEM grids for 4 min and then stained for 1 min using a 2% aqueous uranyl formate solution containing 25 mM NaOH. Imaging was performed using a JEOL JEM-1400 operated at 80 kV.

**Yield quantification with SYBR Safe.** Yield was first estimated by analysis using native agarose gel electrophoresis. The ratio between the fluorescence intensity of the target band and that of the entire lane was adopted to represent the gross yield of structural formation. For the 24H × 28T rectangle, as an independent, alternative quantification procedure the intensity of the target band was compared with a standard sample (1,500-base-pair band from a 1-kb DNA ladder mixture). The mass value of the target band was deduced from the intensity–mass curve based on the standard sample, and was used to calculate the yield of the desired structure. See Supplementary Information, section 2.2.1, for more details.

**Measurement and statistics.** AFM measurements were obtained using NANOSCOPE ANALYSIS (version 1.20; Veeco). The 'cross-section' function was used to measure distances (lengths and widths of the rectangles of different sizes). 'Well-formed' structures were chosen for the measurements. TEM images of the tubes were analysed using IMAGEJ (version 1.43u; NIH). The 'straight line' function was used to measure tube width. The 'segmented line' function was used to highlight and measure tube contour length. Thirty sample points were collected for each distance measurement (for example that of the width of a 24H × 28T rectangle) and the statistics (for example the mean and the standard deviation) were based on the 30 data points. See Supplementary Information, section 3.5, for measurement details.

- Wei, B., Wang, Z. & Mi, Y. Uniquimer: software of de novo DNA sequence generation for DNA self-assembly: an introduction and the related applications in DNA self-assembly. *J. Comput. Theor. Nanosci.* **4**, 133–141 (2007).
- Hansma, H. G. & Laney, D. E. DNA binding to mica correlates with cationic radius: assay by atomic force microscopy. *Biophys. J.* **70**, 1933–1939 (1996).

# Hafnium isotope evidence for a transition in the dynamics of continental growth 3.2 Gyr ago

T. Næraa<sup>1,2</sup>, A. Scherstén<sup>3</sup>, M. T. Rosing<sup>2</sup>, A. I. S. Kemp<sup>4,5</sup>, J. E. Hoffmann<sup>6,7</sup>, T. F. Kokfelt<sup>1</sup> & M. J. Whitehouse<sup>8</sup>

Earth's lithosphere probably experienced an evolution towards the modern plate tectonic regime, owing to secular changes in mantle temperature<sup>1,2</sup>. Radiogenic isotope variations are interpreted as evidence for the declining rates of continental crustal growth over time<sup>3–5</sup>, with some estimates suggesting that over 70% of the present continental crustal reservoir was extracted by the end of the Archaean eon<sup>3,5</sup>. Patterns of crustal growth and reworking in rocks younger than three billion years (Gyr) are thought to reflect the assembly and break-up of supercontinents by Wilson cycle processes and mark an important change in lithosphere dynamics<sup>6</sup>. In southern West Greenland numerous studies have, however, argued for subduction settings and crust growth by arc accretion back to 3.8 Gyr ago<sup>7–9</sup>, suggesting that modern-day tectonic regimes operated during the formation of the earliest crustal record. Here we report *in situ* uranium–lead, hafnium and oxygen isotope data from zircons of basement rocks in southern West Greenland across the critical time period during which modern-like tectonic regimes could have initiated. Our data show pronounced differences in the hafnium isotope–time patterns across this interval, requiring changes in the characteristics of the magmatic protolith. The observations suggest that 3.9–3.5-Gyr-old rocks differentiated from a >3.9-Gyr-old source reservoir with a chondritic to slightly depleted hafnium isotope composition. In contrast, rocks formed after 3.2 Gyr ago register the first additions of juvenile depleted material (that is, new mantle-derived crust) since 3.9 Gyr ago, and are characterized by striking shifts in hafnium isotope ratios similar to those shown by Phanerozoic subduction-related orogens<sup>10–12</sup>. These data suggest a transitional period 3.5–3.2 Gyr ago from an ancient (3.9–3.5 Gyr old) crustal evolutionary regime unlike that of modern plate tectonics to a geodynamic setting after 3.2 Gyr ago that involved juvenile crust generation by plate tectonic processes.

Patterns of crustal growth and reworking reflect regional-scale geodynamics. In Phanerozoic to recent times, 'accretionary' orogens are important sites of crustal growth and reworking<sup>10–13</sup>. These long-lived convergent plate boundaries have been shown to go through alternating extension and compression stages, and the switch between crustal growth and reworking relates to tectonic processes (such as slab roll-back, delamination and arc shortening) that either re-fertilize the mantle wedge, generate extensive upwellings or thicken the orogen<sup>10–12</sup>. These tectonic changes are reflected by downward or upward Nd or Hf isotope shifts, which directly correlate with the amount of net crustal growth<sup>10–12</sup>. It is a matter of debate<sup>14</sup> how far back in geological time these processes can be traced, largely owing to incomplete preservation of the geological record and the complexities of overprinting from subsequent metamorphic events. A mantle perspective is given by diamond inclusions that show an important break at around 3.2 Gyr ago, after which eclogitic inclusions emerge, suggestive of modern-style subduction<sup>6</sup>. The rock record from southern West Greenland

encompasses most of the Archaean<sup>15</sup>, containing some of the oldest and best-preserved parts of the crust<sup>7–9</sup>, and is therefore ideal for testing models of geodynamic evolution from a crustal perspective.

We have determined the U–Pb, Hf and O isotope compositions of single zircon crystals from rocks that represent most of the Archaean eon of southern West Greenland. Spot microanalyses of zircon (Methods Summary) were selected on the basis of back-scattered electron images from a scanning electron microscope. Reported data are from eleven Eoarchaeon (3.9–3.6 Gyr old), thirteen Mesoarchaeon (3.2–2.8 Gyr old) orthogneisses and migmatites and one Neoarchaeon (2.8–2.5 Gyr old) quartz-rich metasedimentary rock, which were sampled from the main crustal terranes in the Nuuk region (Fig. 1). The majority of the orthogneisses belong to the tonalite–trondhjemite–granodiorite (TTG) suite while some of the migmatites and two iron-rich orthogneisses have atypical TTG rare-earth-element patterns and cannot be strictly classified as TTG (Supplementary Information, sections 1 and 5.1). We present whole-rock major- and trace-element data (Supplementary Information 1), U–Pb (Supplementary Information 2), Hf (Supplementary Information 3) and O (Supplementary Information 4) isotope data and give descriptions in Supplementary Information 5 (section 5.1–4). All gneiss samples, except for six migmatites, display homogeneous Hf and O isotope compositions (Supplementary Information, section 5.2–4). Zircon grains with age inheritance and rims with elevated  $\delta^{18}\text{O}$  are the main reason for the inhomogeneity observed in the migmatites. Mean values and corresponding igneous or metamorphic ages are shown in Table 1, and Figs 2 and 3.

Eoarchaeon orthogneisses yield crystallization ages from  $3,797 \pm 5$  million years (Myr) to  $3,677 \pm 9$  Myr with corresponding average  $\epsilon_{\text{Hf}}$  values (the deviation from the chondrite uniform reservoir (CHUR) in parts per 10,000) ranging from  $-0.0 \pm 0.3$  to  $-1.3 \pm 0.5$ . Inherited zircons in three migmatites have  $^{207}\text{Pb}/^{206}\text{Pb}$  ages of  $3,867 \pm 24$  Gyr,  $3,797 \pm 17$  Gyr and  $3,684 \pm 6$  Gyr and corresponding  $\epsilon_{\text{Hf}}$  values of  $-0.2 \pm 0.4$ ,  $-0.1 \pm 0.4$  and  $-0.8 \pm 0.3$  respectively, and are interpreted as relicts from igneous protoliths. Mean oxygen isotope compositions (expressed as  $\delta^{18}\text{O}$ , which is the deviation from Vienna Standard Mean Ocean Water in parts per mil; Fig. 3) of these gneisses range from  $4.8 \pm 0.3\text{‰}$  to  $5.8 \pm 0.3\text{‰}$ , corresponding to oxygen compositions of zircon in equilibrium with mantle-derived melts ( $\delta^{18}\text{O} = 5.3 \pm 0.6\text{‰}$ ) (ref. 16). This implies that no significant amount of 'high  $\delta^{18}\text{O}$ ' supracrustal material or metamorphic fluids contributed to the magma sources of these meta-igneous rocks<sup>17</sup>.

Detrital zircons with Eoarchaeon to Palaeoarchaeon ages plot along the extension of the  $\epsilon_{\text{Hf}}$ –time array defined by the orthogneisses. These detrital grains are presumably derived from a series of igneous TTG plutons that crystallized about 3.6–3.3 Gyr ago<sup>18</sup>. The final expression of these thermal events is represented by iron-rich gneisses that have igneous crystallization ages of  $3,223 \pm 12$  Myr and  $3,242 \pm 7$  Myr and corresponding  $\epsilon_{\text{Hf}}(t)$  values of  $-8.3 \pm 0.8$  and

<sup>1</sup>Geological Survey of Denmark and Greenland (GEUS), Øster Voldgade 10, 1350 Copenhagen K, Denmark. <sup>2</sup>Nordic Center for Earth Evolution (NordCEE), Natural History Museum of Denmark, University of Copenhagen, Øster Voldgade 5–7, 1350 Copenhagen K, Denmark. <sup>3</sup>Department of Geology, Lund University, Sölvegatan 12, 223 62 Lund, Sweden. <sup>4</sup>Centre for Exploration Targeting, School of Earth and Environment, University of Western Australia, Crawley, WA 6009 Australia. <sup>5</sup>School of Earth and Environmental Science, James Cook University, Townsville, QLD 4811, Australia. <sup>6</sup>Institut für Geologie und Mineralogie, Universität zu Köln, Zùlpicher Strasse 49a, 50674 Köln, Germany. <sup>7</sup>Steinmann Institut für Geologie, Mineralogie & Paläontologie, Rheinische Wilhelms-Universität, Poppelsdorfer Schloss, 53115 Bonn, Germany. <sup>8</sup>Swedish Museum of Natural History, Box 50007, SE-104 05 Stockholm, Sweden.

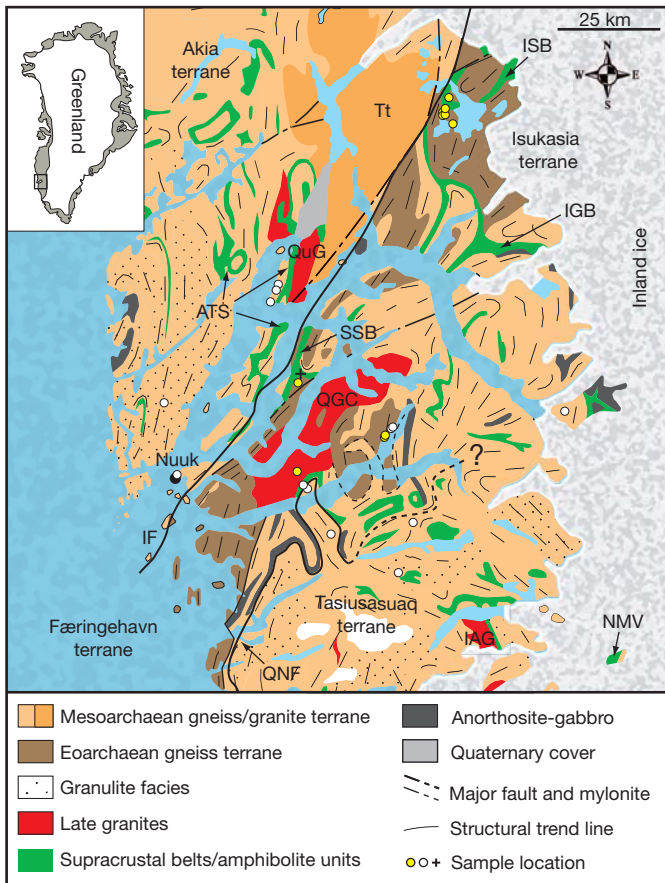


**Figure 1 | Geological map<sup>32</sup> of the Nuuk region in southern West Greenland.** Sample locations are indicated: Eoarchaeoan (yellow circles), Mesoarchaeoan (white circles) and metasedimentary quartzite (cross). Two Eoarchaeoan terranes (Færingehavn and Isukasia) and two Mesoarchaeoan terranes (Tasiusarsuaq and Akia) are indicated. Supracrustal or volcanic belts are indicated: ISB, Isua supracrustal belt; IGB, Ivisartoq greenstone belt; ATS, Akia terrane supracrustal rocks; NMV, Nunatak 1390 metavolcanic belt; and SSB, Storø supracrustal belt. Other abbreviations: Tt, Tasersuaq tonalite; QuG, Qugssuk granite; QGC, Qôrquut granite complex; IAG, Ilivertalik Augen granite; QFN, Qarliit Nunaat fault; IF, Ivinnguit fault.

array with time corresponding to  $^{176}\text{Lu}/^{177}\text{Hf} \approx 0.01$  (Fig. 2). This inferred secular change in Lu/Hf corresponds to a mafic crust, equivalent to modern mid-ocean-ridge or ocean-island basalts<sup>21</sup>, which differentiated towards a more felsic upper-crustal-like reservoir with lower Lu/Hf. This contrasts with earlier interpretations that the Itsaq Gneiss Complex represents either a collection of juvenile arcs accreted 3.9–3.7 Gyr ago<sup>7,22</sup> or one major 3.65-Gyr-old juvenile terrane<sup>23</sup>. A small amount of mixing with juvenile material during Eoarchaeoan TTG formation might be reflected by the small vertical spread in  $\epsilon\text{Hf}$  at 3.8 and 3.7 Gyr ago (Fig. 2). The simple reworking trend and general lack of juvenile crustal input shown by 3.9–3.2-Gyr-old rocks is unlikely that expected in subduction environments, where juvenile input is intrinsic<sup>10–12</sup>.

Assuming that our data are representative, the overall  $\epsilon\text{Hf}$ -time trend suggests that either plate tectonics did not operate during the 3.9–3.2 Gyr period, or that the style of plate tectonics and related crust formation was different to that of modern Earth. The Hf isotope data suggest that this geodynamic regime was not particularly conducive to the generation or preservation of juvenile zircon-bearing crust. Such a regime is similar to that interpreted from Hadean Jack Hills zircons and the Archaean Narryer gneisses<sup>24</sup>—in fact, the Hf-based reworking trend is in line with higher radioactive heat production exceeding conductive heat loss before 3 Gyr ago<sup>2</sup>, which would promote the observed internal melting and differentiation of the crust. The basaltic precursors to the early crustal rocks seem to have formed over a short period more than 3.9 Gyr ago. This might reflect an important role for vertical plume tectonics and mantle overturns in the generation of the continental crust and the complementary sub-continental lithospheric mantle during this period<sup>14,25</sup>.

$-8.0 \pm 0.4$  (Fig. 2). The overall  $\epsilon\text{Hf}$ -time array implies a relatively short period of crust formation more than 3.9 Gyr ago and that subsequent gneisses crystallized from magmas that formed through reworking of an existing and evolving crustal reservoir, as observed by other studies<sup>9,19,20</sup> (Fig. 2). This source reservoir evolved along  $^{176}\text{Lu}/^{177}\text{Hf} = 0.024$  during the early stages, but evolves to a steeper

**Table 1 | Combined zircon U–Pb, Hf and O isotopes**

Sample	Lithology	Domain	$\delta^{18}\text{O}$ (‰)	U–Pb age (Myr)	$^{176}\text{Hf}/^{177}\text{Hf}(t)$	$\epsilon\text{Hf}(t)$
498027	Migmatite	Core a		$3,867 \pm 24$	$0.280264 \pm 11$	$-0.2 \pm 0.4$
498027	Migmatite	Core b		$3,797 \pm 17$	$0.280313 \pm 12$	$-0.1 \pm 0.4$
498028	Migmatite	Core*		$3,867 \pm 24$	$0.280266 \pm 11$	$-0.1 \pm 0.4$
468633	Migmatite	Core	$5.8 \pm 0.3$	$3,684 \pm 6$	$0.280371 \pm 8$	$-0.8 \pm 0.3$
468633	Migmatite	Rim and homogeneous grains	$8.1 \pm 0.9$	$3,607 \pm 23$	$0.280418 \pm 14$	$-0.9 \pm 0.5$
499337	Orthogneiss	Igneous grains		$3,698 \pm 5$	$0.280363 \pm 7$	$-0.7 \pm 0.3$
jeh-sg-05	Orthogneiss	Igneous grains	$5.7 \pm 0.2$	$3,793 \pm 5$	$0.280311 \pm 9$	$-0.2 \pm 0.3$
jeh-sg-07	Orthogneiss	Igneous grains		$3,797 \pm 5$	$0.280318 \pm 8$	$-0.0 \pm 0.3$
jeh-sg-10	Orthogneiss	Igneous grains		$3,787 \pm 5$	$0.280308 \pm 9$	$-0.6 \pm 0.3$
070026	Orthogneiss	Igneous grains	$4.9 \pm 0.6$	$3,780 \pm 6$	$0.280328 \pm 9$	$-0.0 \pm 0.3$
070027	Orthogneiss	Igneous grains	$4.8 \pm 0.3$	$3,781 \pm 6$	$0.280302 \pm 8$	$-0.9 \pm 0.3$
060011	Orthogneiss	Igneous grains	$5.9 \pm 0.2$	$3,787 \pm 3$	$0.280306 \pm 4$	$-0.6 \pm 0.2$
jeh-2007-05	Orthogneiss	Igneous grains		$3,677 \pm 9$	$0.280360 \pm 13$	$-1.3 \pm 0.5$
498033	Fe-rich gneiss	Core	$5.8 \pm 0.2$	$3,223 \pm 12$	$0.280469 \pm 11$	$-8.3 \pm 0.8$
498034	Fe-rich gneiss	Core	$6.0 \pm 0.2$	$3,242 \pm 7$	$0.280463 \pm 6$	$-8.0 \pm 0.4$
468644	Migmatite	Core	$5.6 \pm 0.2$	$3,249 \pm 8$	$0.280712 \pm 7$	$1.0 \pm 0.3$
468645	Migmatite	Core	$6.0 \pm 0.2$	$3,259 \pm 8$	$0.280706 \pm 10$	$1.0 \pm 0.4$
484657	Migmatite	Core		$3,238 \pm 13$	$0.280724 \pm 11$	$1.2 \pm 0.4$
477678	Orthogneiss	Igneous grains	$5.5 \pm 0.3$	$3,031 \pm 7$	$0.280847 \pm 9$	$0.7 \pm 0.3$
289278	Orthogneiss	Igneous grains	$5.3 \pm 0.3$	$3,021 \pm 19$	$0.280783 \pm 31$	$-2.2 \pm 1.1$
283347	Orthogneiss	Igneous grains		$3,038 \pm 10$	$0.280736 \pm 27$	$-3.1 \pm 1.0$
499339	Orthogneiss	Igneous grains	$6.1 \pm 0.3$	$2,984 \pm 11$	$0.280829 \pm 8$	$-1.1 \pm 0.3$
499221	Orthogneiss	Igneous grains	$6.6 \pm 0.3$	$2,881 \pm 4$	$0.280903 \pm 10$	$-0.9 \pm 0.3$
496442	Orthogneiss	Igneous grains		$2,851 \pm 6$	$0.280986 \pm 10$	$1.3 \pm 0.3$
498005	Orthogneiss	Igneous grains	$5.4 \pm 0.3$	$2,851 \pm 5$	$0.280951 \pm 12$	$0.1 \pm 0.4$
484623	Orthogneiss	Igneous grains	$5.5 \pm 0.2$	$2,862 \pm 4$	$0.280990 \pm 7$	$1.7 \pm 0.2$

\* U–Pb age based on data from sample 498027. Some of the migmatites contain two zircon populations reflecting inheritance. Age is calculated from  $^{207}\text{Pb}/^{206}\text{Pb}$  ratios. Reported values are calculated as weighted means and uncertainties are two standard deviations. Combined U–Pb and Hf data from detrital grains are found in Supplementary Information 3 (sample 484601).



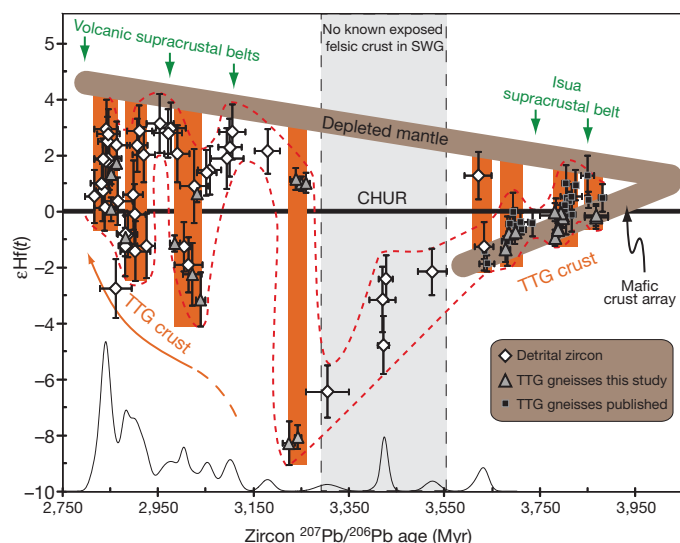


**Figure 2 | Plot of  $\epsilon\text{Hf}(t)$  versus zircon  $^{207}\text{Pb}/^{206}\text{Pb}$  age for Eoarchaeoan to Mesoarchaeoan TTG gneisses and detrital zircon grains from southern West Greenland.** The relative age probability (black curve) for the detrital grains is shown at the bottom of the diagram. Green arrows mark ages of supracrustal belts (see text) and orange boxes represent periods of TTG crystallization. Zircon over 3.2 Gyr old forms an  $\epsilon\text{Hf}$ -time array that represents crustal reworking. ( $t$  is time in Myr.) A pronounced shift in the  $\epsilon\text{Hf}$ -time pattern occurs at about 3.2 Gyr ago and younger rocks show systematic downward and upward shifts in maximum and minimum  $\epsilon\text{Hf}$ . The stippled red line outlines the  $\epsilon\text{Hf}$ -time array. The orange arrow represents decreasing crustal recycling. The depleted mantle curve is constrained by the most radiogenic detrital grains and corresponds to present-day  $^{176}\text{Lu}/^{177}\text{Hf} = 0.0375$  and  $^{176}\text{Hf}/^{177}\text{Hf} = 0.283120$ . Reported values from gneisses are weighted means ( $\pm 2$  standard deviations) and detrital grains are single spot analyses ( $\pm 2$  standard errors). CHUR, chondritic uniform reservoir<sup>33</sup>. The mafic crust corresponds to  $^{176}\text{Lu}/^{177}\text{Hf} = 0.024$ . Published data are from refs 9, 19 and 20. SWG, southern West Greenland.

The Palaeo-Mesoarchaeoan transition at 3.2 Gyr ago is associated with a pronounced break in the  $\epsilon\text{Hf}$ -time trend. In addition to the  $\epsilon\text{Hf}(t) = -8.0$  and  $8.3$  ( $t = 3,242$  and  $3,233$  Myr) observed in the

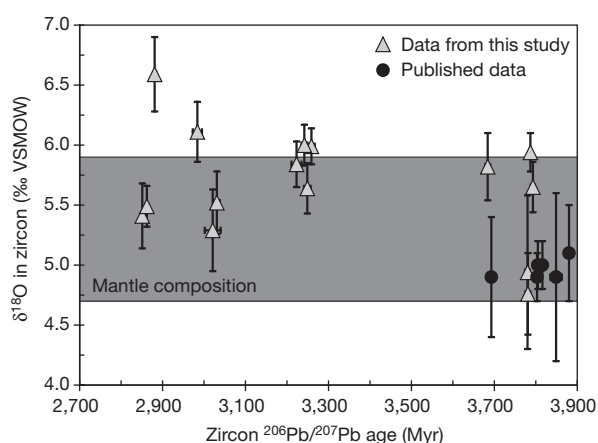


**Figure 3 | Plot of zircon  $\delta^{18}\text{O}$  versus  $^{207}\text{Pb}/^{206}\text{Pb}$  age for Eoarchaeoan to Mesoarchaeoan TTG gneisses from southwest Greenland.** The majority of the gneisses have oxygen isotope compositions in equilibrium with juvenile mantle derived rocks. There is a tendency for the younger TTG to have slightly heavier O isotope compositions, consistent with input of recycled supracrustal material<sup>16</sup>. The relatively restricted oxygen compositions suggest that little or no high  $\delta^{18}\text{O}$  supracrustal material was mixed into the protoliths of the TTG gneisses until the late Mesoarchaeoan. Reported values are weighted means ( $\pm 2$  standard deviations). Published data are from ref. 9. VSMOW, Vienna Standard Mean Ocean Water.

iron-rich gneisses, considerably more juvenile gneisses with similar ages of  $3,249 \pm 8$  Myr and  $3,259 \pm 8$  Myr and  $\epsilon\text{Hf}(t) = +1.0 \pm 0.3$  to  $+1.2 \pm 0.4$  are recognized. These gneisses represent the first juvenile rocks to be emplaced since the early Eoarchaeoan (Fig. 2). Younger TTGs with ages of  $3,038 \pm 10$  to  $2,984 \pm 11$  Myr and  $2,881 \pm 4$  to  $2,851 \pm 5$  Myr and detrital zircon grains have  $\epsilon\text{Hf}$  ranging from  $-3.1 \pm 1.0$  to  $+3.2 \pm 1.1$  and are associated with more positive and less diverse  $\epsilon\text{Hf}$  values with decreasing age (Fig. 2).

Oxygen isotope compositions, from the Mesoarchaeoan gneisses, obtained from zircon cores are homogeneous and yield mean  $\delta^{18}\text{O}$  values ranging from  $5.5 \pm 0.2\text{‰}$  to  $6.6 \pm 0.3\text{‰}$ ; like the Eoarchaeoan gneisses, the protoliths generally have oxygen compositions in equilibrium with mantle-derived melts (Fig. 3). Importantly, however, three samples have slightly elevated weighted mean  $\delta^{18}\text{O}$  values at  $6.6 \pm 0.3\text{‰}$ ,  $6.1 \pm 0.3\text{‰}$  and  $6.0 \pm 0.2\text{‰}$ , where the heaviest signatures are associated with negative  $\epsilon\text{Hf}$  excursions. This may indicate subduction zone recycling of older sedimentary material into the TTG protoliths that would have evolved to negative  $\epsilon\text{Hf}$  and heavy  $\delta^{18}\text{O}$ .

Data from detrital grains show systematic shifts in maximum and minimum  $\epsilon\text{Hf}$ . Periods with higher maximum and minimum  $\epsilon\text{Hf}$  broadly correlate with known metavolcanic arcs in southern West Greenland, such as the  $\sim 3.1$ -Gyr-old Ivisartok greenstone belt<sup>26</sup> and  $\sim 3.1$ -Gyr-old supracrustal rocks within the Akia terrane<sup>27</sup>, the  $\sim 2.97$ -Gyr-old supracrustal units within the Fiskensæst complex<sup>28</sup> and possibly the  $\leq 2.8$ -Gyr-old Storø supracrustal belt<sup>29</sup> (Fig. 2).

Periods with TTG magmatism are associated with negative excursions in  $\epsilon\text{Hf}$  (both maximum and minimum values are lower; Fig. 2), implying increasing amounts of crustal reworking during these periods. Similar negative isotope excursions have also been observed for whole-rock  $\epsilon\text{Nd}$  (ref. 30). We argue that these systematic shifts reflect stages of outboard (away from the craton) volcanic arcs sourced from depleted mantle, whereas TTG magmatism involved substantial mixing between old existing crust and juvenile components. The formation of TTG during the negative  $\epsilon\text{Hf}$  excursions is consistent with melting of older crust that may have been thickened by arc convergence<sup>11</sup>. The increasing minimum  $\epsilon\text{Hf}$  values observed during the Mesoarchaeoan correspond to decreased reworking of ancient crust, possibly in conjunction with a progressively depleted mantle. This could reflect outboard migration of the arc with respect to the older craton nucleus, or the destruction of the older lithosphere by subduction erosion<sup>31</sup>, which is recycled into the mantle and not sampled. Such fluctuating magma sources with periodic igneous flare-ups<sup>12</sup> are characteristic of younger accretionary orogens<sup>10–12</sup>.

This similarity places important constraints on the geodynamics of crustal growth in the Archaean. Tectonic accretion of 'exotic' terranes is generally believed to be a significant process of continental assembly in southern West Greenland<sup>15</sup>. Our data, however, suggest a less *ad hoc* scenario in which Mesoarchaeoan continental crust evolved along accretionary orogens that grew laterally through periodic juvenile arc accretion and TTG flare-ups, such that truly exotic terranes are not required. The Mesoarchaeoan accretionary orogens were probably initiated along the margins of the Eoarchaeoan crustal nucleus, because formation of iron-rich gneisses with low  $\epsilon\text{Hf}$  are coeval with the onset of juvenile crustal addition 3.2 Gyr ago, and because the mixed  $\epsilon\text{Hf}$  compositions in the younger Mesoarchaeoan gneisses suggest an ancient crustal source.

The major change in lithosphere dynamics at around 3.2 Gyr ago implied by our data provides a new, crustal-based perspective on recent claims that modern-day tectonic regimes started at that time<sup>6</sup>. The lack of formation of juvenile zircon-bearing crust between 3.9 Gyr ago and 3.2 Gyr ago suggests that models that invoke the formation of large volumes of continental crust during this period<sup>3,5</sup> need to be re-evaluated. Rather, our data from southern West Greenland show that the continental crust grew from 3.2 Gyr ago in a geodynamic regime analogous to that of modern plate tectonics.

## METHODS SUMMARY

Separation of zircon followed a standard procedure; zircons were handpicked and placed on double-sided sticky tape, mounted in epoxy and polished. Transmitted light microscopy and back-scattered-electron imaging was applied to reveal internal structures. Laser ablation inductively coupled plasma mass spectrometry (ICPMS) analyses for U–Pb isotopes were done on an Element2 mass spectrometer at the GEUS laboratory. Standard bracketing was done by analysing the Geostandard zircon GJ1. Laser ablation analyses of zircons for Lu–Hf isotopes were done at the Advanced Analytical Centre at James Cook University, Australia, using a GeoLas193-nm ArF laser and a Thermo-Scientific Neptune multicollector ICPMS. Data were normalized to measurements of the Mud Tank reference zircon. Oxygen isotope ratios were measured using a CAMECA IMS1270 ion microprobe at the NordSIMS laboratory at the Swedish Museum of Natural History. Data were normalized to measurements of the Geostandard zircon 91500. Details and references are given in the Methods section.

**Full Methods** and any associated references are available in the online version of the paper at [www.nature.com/nature](http://www.nature.com/nature).

**Received 6 February; accepted 11 April 2012.**

- Davies, G. F. On the emergence of plate-tectonics. *Geology* **20**, 963–966 (1992).
- Labrosse, S. & Jaupart, C. Thermal evolution of the Earth: Secular changes and fluctuations of plate characteristics. *Earth Planet. Sci. Lett.* **260**, 465–481 (2007).
- McLennan, S. M., & Taylor, S. R. Geochemical constraints on the growth of the continental crust. *J. Geol.* **90**, 347–361 (1982).
- Allègre, C. J. & Rousseau, D. The growth of the continent through geological time studied by Nd isotope analysis of shales. *Earth Planet. Sci. Lett.* **67**, 19–34 (1984).
- Belousova, E. A. *et al.* The growth of the continental crust: constraints from zircon Hf-isotope data. *Lithos* **119**, 457–466 (2010).
- Shirey, S. B. & Richardson, S. H. Start of the Wilson cycle at 3 Ga shown by diamonds from subcontinental mantle. *Science* **333**, 434–436 (2011).
- Nutman, A. P., Friend, C. R. L. & Paxton, S. Detrital zircon sedimentary provenance ages for the Eoarchaean Isua supracrustal belt southern West Greenland: juxtaposition of an imbricated ca. 3700Ma juvenile arc against an older complex with 3920–3760Ma components. *Precamb. Res.* **172**, 212–233 (2009).
- Kamber, B. S., Collerson, K. D., Moorbath, S. & Whitehouse, M. J. Inheritance of early Archaean Pb-isotope variability from long-lived Hadean protocrust. *Contrib. Mineral. Petrol.* **145**, 25–46 (2003).
- Hiess, J., Bennett, V. C., Nutman, A. P. & Williams, I. S. In situ U–Pb, O and Hf isotopic compositions of zircon and olivine from Eoarchaean rocks, West Greenland: new insights to making old crust. *Geochim. Cosmochim. Acta* **73**, 4489–4516 (2009).
- DeCelles, P. G., Ducea, M. N., Kapp, P. & Zandt, G. Cyclicity in Cordilleran orogenic systems. *Nature Geosci.* **2**, 251–257 (2009).
- Kemp, A. I. S. *et al.* Nd, Hf and O isotope evidence for rapid continental growth during accretionary orogenesis in the Tasmanides, eastern Australia. *Earth Planet. Sci. Lett.* **284**, 455–466 (2009).
- Mišković, A. & Schaltegger, U. Crustal growth along a non-collisional cratonic margin: a Lu–Hf isotopic survey of the Eastern Cordilleran granitoids of Peru. *Earth Planet. Sci. Lett.* **279**, 303–315 (2009).
- Cawood, P. A. Terra Australis orogen: Rodinia breakup and development of the Pacific and Iapetus margins of Gondwana during the Neoproterozoic and Paleozoic. *Earth Sci. Rev.* **69**, 249–279 (2005).
- Van Kranendonk, M. J. Onset of plate tectonics. *Science* **333**, 413–414 (2011).
- Friend, C. R. L. & Nutman, A. P. New pieces to the Archaean terrane jigsaw puzzle in the Nuuk region, southern West Greenland: steps in transforming a simple insight into a complex regional tectonothermal model. *J. Geol. Soc. Lond.* **162**, 147–162 (2005).
- Valley, J. W. *et al.* 4.4 billion years of crustal maturation: oxygen isotope ratios of magmatic zircon. *Contrib. Mineral. Petrol.* **150**, 561–580 (2005).
- Valley, J. W., Chiarenzelli, J. R. & McLelland, J. M. Oxygen isotope geochemistry of zircon. *Earth Planet. Sci. Lett.* **126**, 187–206 (1994).
- Nutman, A. P., Friend, C. R. L., Bennett, V. C. & McGregor, V. R. Dating of the Ameralik dyke swarms of the Nuuk district, southern West Greenland: mafic intrusion events starting from c. 3510 Ma. *J. Geol. Soc.* **161**, 421–430 (2004).
- Kemp, A. I. S. *et al.* Concurrent Pb–Hf isotope analysis of zircon by laser ablation multi-collector ICP-MS, with implications for the crustal evolution of Greenland and the Himalayas. *Chem. Geol.* **261**, 244–260 (2009).
- Amelin, Y., Kamo, S. L. & Lee, D. C. Evolution of early crust in chondritic or nonchondritic Earth inferred from U–Pb and Lu–Hf data for chemically abraded zircon from the Itsaq Gneiss Complex, West Greenland. *Can. J. Earth Sci.* **48**, 141–160 (2011).
- Blichert-Toft, J. & Albarède, F. Hafnium isotopes in Jack Hills zircons and the formation of the Hadean crust. *Earth Planet. Sci. Lett.* **265**, 686–702 (2008).
- Friend, C. R. L. & Nutman, A. P. Complex 3670–3500 Ma orogenic episodes superimposed on juvenile crust accreted between 3850 and 3690 Ma, Itsaq gneiss complex, southern West Greenland. *J. Geol.* **113**, 375–397 (2005).
- Kamber, B. S. & Moorbath, S. Initial Pb of the Amitsoq gneiss revisited: implication for the timing of early Archaean crustal evolution in West Greenland. *Chem. Geol.* **150**, 19–41 (1998).
- Kemp, A. I. S. *et al.* Hadean crustal evolution revisited: new constraints from Pb–Hf isotope systematics of the Jack Hills zircons. *Earth Planet. Sci. Lett.* **296**, 45–56 (2010).
- Griffin, W. L. & O'Reilly, S. Y. in *The Earth's Oldest Rocks* (eds Van Kranendonk, M. J., Smithies, R. H. & Bennett, V. C.) 1013–1035 (Elsevier, 2007).
- Polat, A. *et al.* Field and geochemical characteristics of the Mesoarchean (3075 Ma) Ivissartoq greenstone belt, southern West Greenland: evidence for seafloor hydrothermal alteration in a supra-subduction oceanic crust. *Gondwana Res.* **11**, 69–91 (2007).
- Garde, A. A. A mid-Archaean island arc complex in the eastern Akia terrane, Godthåbsfjord, southern West Greenland. *J. Geol. Soc.* **164**, 565–579 (2007).
- Polat, A., Frei, R., Scherstén, A. & Apple, P. W. U. New age (ca. 2970 Ma), mantle source composition and geodynamic constraints on the Archean Fiskensæset anorthosite complex, SW Greenland. *Chem. Geol.* **277**, 1–20 (2010).
- Scherstén, A. *et al.* Re-Os and U–Pb constraints on gold mineralisation in the Neoarchaean Storø supracrustal belt, Storø Island, southern West Greenland. *Precamb. Res.* **200–203**, 149–162 (2012).
- Friend, C. R. L., Nutman, A. P., Baadsgaard, H. & Duke, M. J. M. The whole rock Sm–Nd ‘age’ for the 2825 Ma Ikkattoq gneisses (Greenland) is 800 Ma too young: insights into Archaean TTG petrogenesis. *Chem. Geol.* **261**, 62–76 (2009).
- Ranero, C. R. & von Huene, R. Subduction erosion along the Middle America convergent margin. *Nature* **404**, 748–752 (2000).
- Escher, J. C. & Pulvertaft, T. C. R. *Geological Map of Greenland, 1:2,500 000* (Geological Survey of Greenland, 1995).
- Bouvier, A., Vervoort, J. D. & Patchett, P. J. The Lu–Hf and Sm–Nd isotopic composition of CHUR: constraints from unequilibrated chondrites and implications for the bulk composition of terrestrial planets. *Earth Planet. Sci. Lett.* **273**, 48–57 (2008).

**Supplementary Information** is linked to the online version of the paper at [www.nature.com/nature](http://www.nature.com/nature).

**Acknowledgements** This work was financed through grants from the Geocenter Denmark (Geocenterbevilling 7-2006 to T.N. and A.S.), the Swedish research council (research grant number 2008-3447 to A.S.) and the Danish National Research Foundation to NordCEE. J.E.H. was financed by the Deutsche Forschungsgemeinschaft (DFG) under grant numbers Mu 1406/8 and HO 4794/1-1. A.I.S.K. acknowledges support from the Australian Research Council fellowships DP0773029 and FT100100059. Y. Hu provided technical assistance during Hf isotope measurement in the Advanced Analytical Centre, James Cook University. The NordSIM laboratory is operated under an agreement between the research funding agencies of Denmark, Norway and Sweden, the Geological Survey of Finland and the Swedish Museum of Natural History; this is NordSIM contribution number 309. We are grateful for logistical and financial support given by the Geological Survey of Denmark and Greenland. This paper is published with permission from the Geological Survey of Denmark and Greenland.

**Author Contributions** T.N., A.S., J.E.H. and M.T.R. did the fieldwork and sampling and T.N. carried out all analyses. T.N., together with A.S., A.I.S.K. and M.T.R. developed and wrote the manuscript. T.N. prepared the Supplementary Information. A.I.S.K. assisted with Hf isotope analyses and M.J.W. with oxygen isotope analyses. M.J.W., T.F.K. and J.E.H. assisted with data interpretation and with refining the manuscript.

**Author Information** Reprints and permissions information is available at [www.nature.com/reprints](http://www.nature.com/reprints). The authors declare no competing financial interests. Readers are welcome to comment on the online version of this article at [www.nature.com/nature](http://www.nature.com/nature). Correspondence and requests for materials should be addressed to T.N. (tomn@geus.dk).

## METHODS

**Separation of zircon.** We followed a standard procedure; zircons were handpicked and placed on double-sided sticky tape, mounted in epoxy and polished. Transmitted light microscopy and back-scattered-electron imaging were applied to reveal internal structures.

**Laser ablation ICPMS analyses of zircon for U–Pb isotopes.** The laser ablation inductively coupled plasma mass spectrometry (ICPMS) analyses were obtained at the Geological Survey of Denmark and Greenland in Copenhagen and acquired by a Thermo Scientific Element2 mass spectrometer coupled to a NewWave UP213 laser ablation system, following the procedures outlined by refs 34 and 35. Standard bracketing was done by analysing the Geostandard zircon GJ1 (ref. 36). Analytical sessions were started with six standards, followed by cycles of ten unknowns and three standards. The laser was operated with a 30- $\mu\text{m}$  spot size at a repetition rate of 10 Hz with a nominal energy output of 45–50% of the maximum laser intensity, corresponding to a laser energy of about 0.025 mJ per pulse and a laser fluence of about 3 J cm<sup>-2</sup>. In each analysis the first 30 s were used to measure the gas blank (that is, background), followed by 30 s of ablation and 30–45 s of washout time. Helium gas was used to flush the sample cell and was mixed downstream with the Ar sample gas before entering the plasma of the mass spectrometer. Measured masses were: <sup>202</sup>Hg, <sup>204</sup>(Pb + Hg), <sup>206</sup>Pb, <sup>207</sup>Pb, <sup>208</sup>Pb, <sup>232</sup>Th, <sup>235</sup>U and <sup>238</sup>U. The mass of <sup>202</sup>Hg was measured to monitor the <sup>204</sup>Hg isobaric interference on <sup>204</sup>Pb. Data reduction was done with in-house software (Zirchron) where the time-resolved isotope signal <sup>207</sup>Pb/<sup>206</sup>Pb and <sup>206</sup>Pb/<sup>204</sup>Pb ratios were calculated as mean values, and <sup>207</sup>Pb/<sup>235</sup>U, <sup>206</sup>Pb/<sup>238</sup>U and <sup>208</sup>Pb/<sup>232</sup>U were drift-corrected by creating a least-squares fitting line, with an anchor point at the time the laser starts to ablate the zircon.

**Laser ablation multi-collector ICPMS analyses of zircons for Lu–Hf isotopes.** Laser ablation Hf isotope analyses were done at the Advanced Analytical Centre at James Cook University, Townsville, Australia, using a GeoLas 193-nm ArF laser and a Thermo Scientific Neptune multicollector ICPMS. The method is outlined by ref. 19. Spot sizes were 31  $\mu\text{m}$ , 42  $\mu\text{m}$  and 58  $\mu\text{m}$  with a 4-Hz laser pulse repetition rate. To counteract ArF degradation the power density at the sample was maintained at around 6–7 J cm<sup>-2</sup>, which translated into an estimated ablation rate of around 0.5  $\mu\text{m s}^{-1}$ . Ablation was conducted in He gas flow. The isotope ratios were derived from a 60-s ablation period, comprising 60 cycles of 1-s integration time. In the case of isotopic zoning or with intersecting cracks/inclusions, only the flattest, most stable portions of the time-resolved signal were selected for integration; this was done off-line using a customized Microsoft Excel spreadsheet. The correction for the isobaric interference of Lu and Yb on <sup>176</sup>Hf was performed as advocated by ref. 37. For Yb, this involved monitoring the interference-free <sup>171</sup>Yb during the analysis and then calculating the magnitude of the <sup>176</sup>Yb interference using <sup>176</sup>Yb/<sup>171</sup>Yb = 0.897145 (ref. 38). The much smaller Lu correction is performed in the same way by measuring <sup>175</sup>Lu, and using <sup>176</sup>Lu/<sup>175</sup>Lu = 0.02655 (ref. 39). To correct for instrumental mass fractionation, Yb isotope ratios were normalized to <sup>173</sup>Yb/<sup>171</sup>Yb = 1.130172 (ref. 38) and Hf isotope ratios to <sup>179</sup>Hf/<sup>177</sup>Hf = 0.7325. The mass bias behaviour of Lu was assumed to follow that of Yb. The measured average <sup>176</sup>Hf/<sup>177</sup>Hf from the Mud Tank reference zircon (MTZ) obtained over all analytical sessions was 0.282499(18) (where the error in parentheses is two standard deviations) and the ‘true’ (solution) value is taken as 0.282507(6) from ref. 37. A <sup>176</sup>Hf/<sup>177</sup>Hf normalization factor of 1.000028, based on analyses of the MTZ, was applied to data from sample zircons. For CHUR we use the isotope ratios <sup>176</sup>Lu/<sup>177</sup>Hf = 0.0336 and <sup>176</sup>Hf/<sup>177</sup>Hf = 0.282785 (ref. 40) and for the <sup>176</sup>Lu decay

constant we used the value reported by refs 41 and 42. During the analytical sessions the Geostandard 91500, Temora2 and FC1 zircon were also repeatedly measured, for which normalized <sup>176</sup>Hf/<sup>177</sup>Hf values are 0.282299(22) ( $n = 23$ ), 0.282686(22) ( $n = 47$ ) and 0.282178(26) ( $n = 38$ ), respectively, where uncertainties are two standard deviations. The final analytical uncertainty for sample zircons was obtained by combining the MTZ reproducibility with internal error.

**Oxygen isotope ratios.** These ratios were measured using a CAMECA IMS1270 ion microprobe (NordSIMS laboratory, Swedish Museum of Natural History) using a method similar to that described by refs 43 and 44 with the exception that, for this study, only <sup>16</sup>O and <sup>18</sup>O were measured. Briefly, a 20-keV Cs<sup>+</sup> primary beam (+10 kV primary, –10 kV secondary) of about 5 nA was used in aperture illumination mode to sputter a ~15- $\mu\text{m}$ -diameter sample area, with a normal-incidence electron gun providing charge compensation. Fully automated runs comprised a 20-s pre-sputter period with a raster of 25  $\mu\text{m}$ , field aperture, entrance slit and mass centring, using the <sup>16</sup>O signal, followed by 240 s of data acquisition using two Faraday detectors in the multicollector system operating at a common mass resolution of ~2,500. Data were normalized to measurements of the Geostandard zircon 91500, assuming a  $\delta^{18}\text{O}$  value of 9.86‰ determined by laser fluorination<sup>45</sup>. Reproducibility of 91500 during the sessions ranged between 0.21 and 0.26 (one standard deviation) and in one session a drift correction of 0.22‰ per run was applied.

34. Gerdes, A. & Zeh, A. Combined U–Pb and Hf isotope LA-(MC)-ICP-MS analyses of detrital zircons: comparison with SHRIMP and new constraints for the provenance and age of an Armorican metasediment in Central Germany. *Earth Planet. Sci. Lett.* **249**, 47–61 (2006).
35. Frei, D. & Gerdes, A. Precise and accurate in situ U–Pb dating of zircon with high sample throughput by automated LA-SF-ICP-MS. *Chem. Geol.* **261**, 261–270 (2009).
36. Jackson, S., Pearson, N. J., Griffin, W. L. & Belousova, E. A. The application of laser ablation – inductively coupled plasma – mass spectrometry to in situ U–Pb zircon geochronology. *Chem. Geol.* **211**, 47–69 (2004).
37. Woodhead, J. & Hergt, J. A preliminary appraisal of seven natural zircon reference materials for in situ Hf isotope determination. *Geostand. Geol. Res.* **29**, 183–195 (2005).
38. Segal, I., Halicz, L. & Platzner, I. T. Accurate isotope ratio measurements of ytterbium by multi-collector inductively coupled plasma mass spectrometry applying erbium and hafnium in an improved double external normalisation procedure. *J. Anal. At. Spectrom.* **18**, 1217–1223 (2003).
39. Vervoort, J. D., Patchett, P. J., Söderlund, U. & Baker, M. The isotopic composition of Yb and the precise and accurate determination of Lu concentrations and Lu/Hf ratios by isotope dilution using MC-ICPMS. *Geochim. Geophys. Geosyst.* **5**, Q11002 (2004).
40. Bouvier, A., Vervoort, J. D. & Patchett, P. J. The Lu–Hf and Sm–Nd isotopic composition of CHUR: constraints from unequilibrated chondrites and implications for the bulk composition of terrestrial planets. *Earth Planet. Sci. Lett.* **273**, 48–57 (2008).
41. Scherer, E., Munker, C. & Mezger, K. Calibration of the lutetium–hafnium clock. *Science* **293**, 683–687 (2001).
42. Söderlund, U., Patchett, P. J., Vervoort, J. D. & Isachsen, C. E. The <sup>176</sup>Lu decay constant determined by Lu–Hf and U–Pb isotope systematics of Precambrian mafic intrusions. *Earth Planet. Sci. Lett.* **219**, 311–324 (2004).
43. Nemchin, A. A., Whitehouse, M. J., Pidgeon, R. T. & Meyer, C. Oxygen isotopic signature of 4.4–3.9 Ga zircons as a monitor of differentiation processes on the Moon. *Geochim. Cosmochim. Acta* **70**, 1864–1872 (2006).
44. Whitehouse, M. J. & Nemchin, A. A. High precision, high accuracy measurement of oxygen isotopes in large lunar zircon by SIMS. *Chem. Geol.* **261**, 32–42 (2009).
45. Wiedenbeck, M. *et al.* Further characterisation of the 91500 zircon crystal. *Geostand. Geosyst. Res.* **28**, 9–39 (2004).



# Accelerated speciation in colour-polymorphic birds

Andrew F. Hugall<sup>1†</sup> & Devi Stuart-Fox<sup>1</sup>

Colour polymorphism exemplifies extreme morphological diversity within populations<sup>1,2</sup>. It is taxonomically widespread but generally rare. Theory suggests that where colour polymorphism does occur, processes generating and maintaining it can promote speciation but the generality of this claim is unclear<sup>1</sup>. Here we confirm, using species-level molecular phylogenies for five families of non-passerine birds, that colour polymorphism is associated with accelerated speciation rates in the three groups in which polymorphism is most prevalent. In all five groups, colour polymorphism is lost at a significantly greater rate than it is gained. Thus, the general rarity and phylogenetic dispersion of colour polymorphism is accounted for by a combination of higher speciation rate and higher transition rate from polymorphism to monomorphism, consistent with theoretical models where speciation is driven by fixation of one or more morphs<sup>3</sup>. This is corroborated by evidence from a species-level molecular phylogeny of passerines, incorporating 4,128 (66.5%) extant species, that polymorphic species tend to be younger than monomorphic species. Our results provide empirical support for the general proposition, dating from classical evolutionary theory<sup>2,4–6</sup>, that colour polymorphism can increase speciation rates.

The study of colour-polymorphic species has been crucial for the development of evolutionary theory<sup>5–7</sup>. Polymorphic systems provide critical insights into processes generating and maintaining genetic and phenotypic diversity within species<sup>2,4,8</sup>. Theoretical arguments<sup>1,3,9</sup> and recent mathematical models<sup>10–12</sup> suggest that colour polymorphism can also promote the generation of new species (speciation), although the role of polymorphism in speciation remains highly controversial<sup>1</sup>. One reason is that the definition of polymorphism as the presence of discrete, genetically determined forms within an interbreeding population<sup>2</sup> has often been thought to imply that speciation occurs in sympatry; that is, in the absence of geographic isolation. This mode of speciation has traditionally been thought to occur rarely, if at all<sup>13</sup>, but recent empirical support comes from polymorphic systems<sup>14–16</sup>. Moreover, polymorphism may have an important role in speciation under much less restrictive conditions than required under the sympatric speciation model<sup>1,17</sup>, generating much recent theoretical and empirical interest in the role of colour polymorphism in speciation<sup>1,9,17–19</sup>. Despite specific cases linking colour polymorphism to rapid phenotypic evolution and speciation<sup>1,18</sup>, the acceleration of speciation rates as a result of colour polymorphism has not been demonstrated in any group.

We tested whether colour polymorphism is associated with relatively rapid, recent speciation in birds, the group with the most comprehensive data on taxonomy, molecular phylogeny and prevalence of colour polymorphism. We compared speciation rates, calculated using a generalized binary-state speciation and extinction model (BiSSE)<sup>20,21</sup>, for colour-polymorphic and colour-monomorphic species within five groups with a relatively high proportion of polymorphic species and sufficient sequence data (Supplementary Table 1 and Supplementary Fig. 1): Accipitridae (hawks, eagles, kites and Old World vultures), Striginae and Surniinae combined (two sub-families of owls), Caprimulgidae (nightjars), Falconidae (falcons) and Phasianidae (pheasants). The five groups contain <7% of bird species but 47% of colour-polymorphic species. The phylogenies were constructed using

a supermatrix approach<sup>22</sup> from GenBank sequence data accumulated over one-quarter of a century (Supplementary Methods, Supplementary Tables 3, 5–7, Supplementary Figs 3–7 and Supplementary Data).

In the three groups in which colour polymorphism is most prevalent, both in terms of absolute numbers (>20) and in proportion of polymorphic species (>20%), colour polymorphism is associated with higher speciation rate (Fig. 1). In the Accipitridae, one of the two major families of diurnal birds of prey, speciation rates are almost three-times higher for polymorphic species (likelihood ratio test (LRT),  $P < 0.0001$ ; Fig. 1), a pattern driven particularly by the buteonine hawks and buzzards ( $P < 0.0001$ ). Similarly, speciation rates are 2 to 4 times higher for polymorphic species in owls and nightjars, respectively (Fig. 1). In owls, the pattern is driven primarily by one subfamily, the Surniinae (12 colour-polymorphic species out of 39 species; LRT,  $P = 0.007$ ; Supplementary Table 2). Of the groups we tested, falcons had the smallest number of polymorphic species (9 colour-polymorphic species out of 65 species), which showed only a weak trend towards having a higher speciation rate, reflected in the bimodal posterior probability distribution of speciation rates for the polymorphic state (Fig. 1; LRT,  $P = 0.58$ ). In the pheasants (15 colour-polymorphic species out of 181 species), we found the opposite trend to the birds of prey (Accipitridae, Striginae and Surniinae, Caprimulgidae

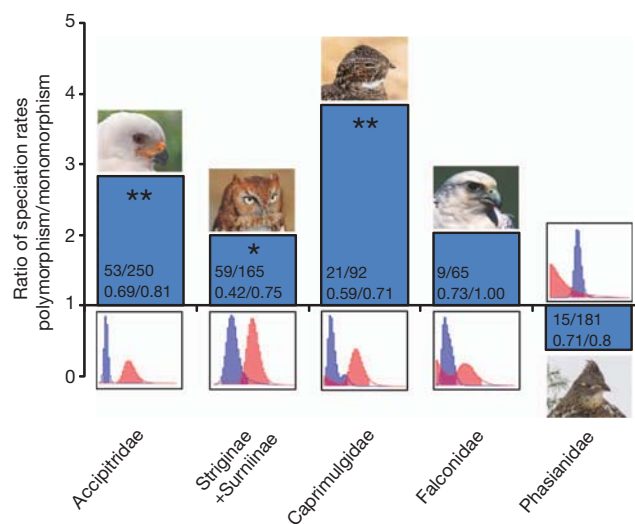


**Figure 1 | Speciation rate ( $\lambda_1/\lambda_0$ ) ratio from Bayesian Diversitree analyses.**

Values >1 indicate higher speciation rates for the colour-polymorphic state.

\* $P \leq 0.05$ ; \*\* $P \leq 0.01$  for likelihood ratio tests (LRTs) comparing a model with two different speciation rates versus one with equal rates. Numbers on each bar are the colour-polymorphic taxa/total number of taxa (above) and sampling fractions for polymorphic/monomorphic species. Diversitree posterior distributions are shown with blue indicating monomorphic and red indicating polymorphic. Images are representative polymorphic species: grey goshawk, *Accipiter novaehollandiae* (photo: A. Lumnitzer); eastern screech owl, *Megascops asio* (photo: J. Whitlock); Antillean nighthawk, *Chordeiles gundlachii* (photo: M. Landestoy); gyrfalcon, *Falco rusticolus* (<http://www.animalspedia.com/wallpaper/Piercing-Stare---Gyrfalcon/>); and ruffed grouse, *Bonasa umbellus* (photo: J. Pons).

<sup>1</sup>Department of Zoology, University of Melbourne, Melbourne, Victoria 3010, Australia. <sup>†</sup>Present address: Sciences Department, Melbourne Museum, Melbourne, Victoria 3053, Australia.

and Falconidae), with speciation rates slightly higher for the monomorphic state (LRT,  $P = 0.16$ ; Fig. 1). In all cases, the Bayesian posterior probabilities are qualitatively the same as the LRT results (Supplementary Table 2).

Different processes contributing to the generation, maintenance and loss of polymorphism<sup>1</sup> may operate in different groups and affect speciation rates in different ways. In the birds of prey, in which we find an association between colour polymorphism and higher speciation rates, polymorphic species tend to have larger geographic ranges than monomorphic species, live in more spatially and temporally heterogeneous environments, occupy more diverse environments and have activity patterns spanning day and night<sup>24</sup>. In other words, colour polymorphism tends to be associated with diverse ecological conditions. Furthermore, in the four families of birds of prey, colour polymorphism is sex-limited (restricted to one sex) in fewer species than expected by chance (13 sex-limited species out of 142 colour-polymorphic species; null expectation = 0.195 (ref. 23); binomial test,  $P = 0.006$ ) whereas colour polymorphism tends to be sex-limited more often than expected by chance in the pheasants (7 sex-limited species out of 15 colour-polymorphic species; binomial test,  $P = 0.015$ ). These observations support the view that ecologically based divergent selection, including the special case of disruptive selection favouring extreme phenotypes over intermediates within a population, is probably important for colour-polymorphism-associated speciation in the birds of prey. By contrast, there is no indication that the higher speciation rates are associated with sexual selection in these groups (at least as indicated by sex-limited polymorphism). Whether sexual selection has a role in the maintenance of polymorphism in the pheasants requires empirical testing.

The general rarity of colour polymorphism can be explained by the loss of polymorphism through the fixation of a morph; or alternatively, by polymorphic species having substantially higher extinction rates. We find no evidence for the latter but across all five groups the transition rate from polymorphism to monomorphism estimated from BiSSE models is greater than the reverse (Fig. 2) and is of similar magnitude to the speciation rate for the colour-polymorphic state (Supplementary Table 2). LRTs of transition rates are significant (Fig. 2) and similar to the Bayesian posterior probabilities, with the exception of the pheasants for which  $P = 0.406$  for the LRT but the Bayesian posterior is 0.042 (Supplementary Table 2). The relatively

high transition rate away from colour polymorphism is not simply an artefact of the low frequency of polymorphism, as the two variables are not correlated (coefficient of correlation ( $r$ ) = 0.361;  $P = 0.551$ ). The relatively high rate of shifts from polymorphism to monomorphism is consistent with speciation events often entailing fixation of a morph in one or more descendant lineages. In all five families, the majority of speciation events involving colour polymorphism also involve a transition, as inferred from a posteriori simulations using the BiSSE parameters (Accipitridae, 0.61; Striginae and Surniinae, 0.55; Caprimulgidae, 0.53; Falconidae, 0.78; Phasianidae, 0.67), consistent with the observed phylogenetic dispersion of colour polymorphism (Supplementary Table 2). This pattern is underscored by phylogenetic studies in other groups showing that colour polymorphism is repeatedly lost<sup>18,25,26</sup>, and by the widespread tendency towards fixation of discrete phenotypes more generally<sup>3</sup>.

The rarity and phylogenetically scattered nature of colour polymorphism is apparent in the remaining birds. For instance, 23% of all known colour-polymorphic species are within the Passeriformes, yet polymorphic species represent only 1.2% of passerines (75 colour-polymorphic species out of 6,213 species) and are distributed across 58 genera in 30 families. This level of phylogenetic scatter prevents reliable estimation of speciation rates for the polymorphic state (and hence use of the BiSSE model). However, if colour polymorphism accelerates speciation, divergence between extant colour-polymorphic species and their sister lineages should be relatively more recent. That is, colour-polymorphic species should have shorter terminal branches in the phylogeny. This pattern is evident in the four families of birds of prey, in which tip branch lengths are 12–38% shorter for polymorphic than monomorphic species, but 19% longer in the pheasants in which polymorphism is not associated with higher speciation rates (Supplementary Table 2).

To assess the generality of our findings, we tested the prediction that colour-polymorphic species should be relatively younger in the Passeriformes, the largest order of birds including more than half of all bird species. We constructed a species-level phylogeny of this group from DNA sequence data (with branch lengths proportional to time) incorporating 4,128 (66.5%) of extant species (Supplementary Methods, Supplementary Tables 4–7, Supplementary Fig. 2 and Supplementary Data). The phylogeny includes 67 (89%) of the polymorphic species, of which 59 belong to polytypic genera and 8 belong to monotypic genera. The frequency that 67 randomly chosen species have shorter branch lengths than those observed for colour-polymorphic species is 0.074 (5,000 randomizations; Fig. 3). Monotypic genera

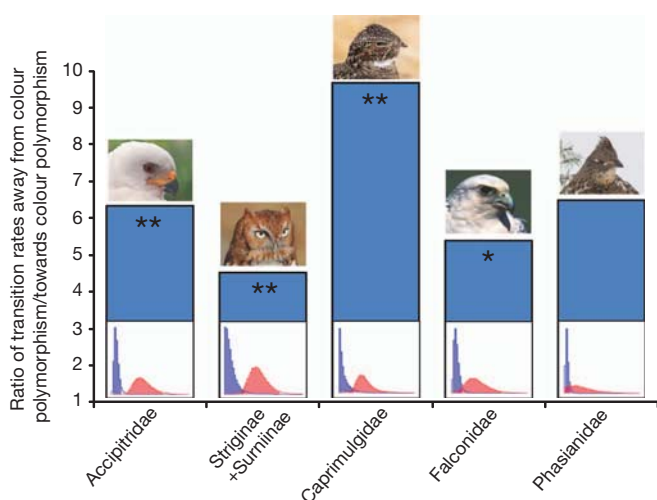


**Figure 2 | Ratio of transition rates ( $q_{10}/q_{01}$ ) between states from Bayesian Diversitree analyses.** Values  $>1$  indicate a higher transition rate from polymorphic to monomorphic than the converse. \* $P \leq 0.05$ ; \*\* $P \leq 0.01$  for LRTs comparing a model with two different transition rates versus one with equal rates. Diversitree posterior distributions of transition rates away from polymorphism are shown with blue indicating monomorphic and red indicating polymorphic. Images and credits as in Fig. 1.

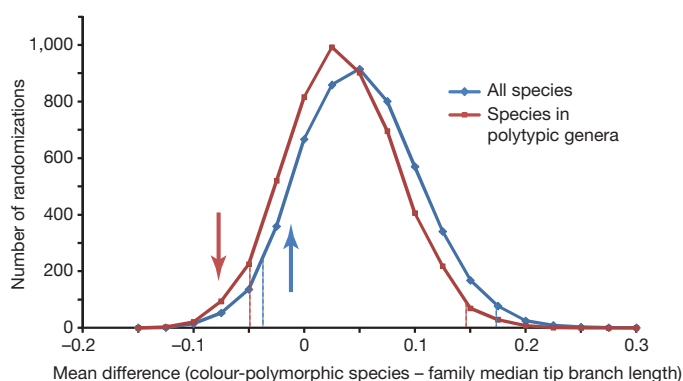


**Figure 3 | Randomization tests of relative tip branch lengths for passerine species.** Mean difference between the tip branch length of 67 randomly chosen species and the median tip branch length for members of the relevant family. Lines show the distribution from 5,000 randomizations. Blue line shows all species and red line shows species belonging to polytypic genera (that is, excluding monotypic genera). Arrows indicate the observed value for colour-polymorphic species; both are in the left tail of the distribution, indicating that tip branch lengths of colour-polymorphic species tend to be shorter than monomorphic species. Dotted lines indicate 95% confidence intervals.

represent distinctive lineages that have experienced little speciation and/or high extinction. High levels of extinction will obscure patterns of speciation<sup>27</sup> and excluding monotypic genera recovers a much stronger signal (randomization test,  $P = 0.004$ ). Thus, consistent with the birds of prey, polymorphism within passerines is associated with relatively recent speciation (younger extant species). Also consistent with the birds of prey, the pattern is not driven by species with sex-limited polymorphism; it remains when species with sex-limited polymorphism<sup>23</sup> are excluded (all species/polytypic genera only:  $n = 46/41$ ;  $P = 0.106/0.008$ ), despite the reduced sample size. By contrast, exclusion of species with a cline in morph frequencies associated with habitat variation<sup>23</sup> substantially weakens the signal (all species/polytypic genera only:  $n = 48/42$ ;  $P = 0.214/0.078$ ).

The tendency for polymorphic species to speciate more rapidly and to give rise to monomorphic daughter species is predicted by theory<sup>1,17</sup>. Polymorphism in coloration is often associated with differences in suites of correlated traits (for example, morphology, physiology, behaviour and life history) due to correlational or epistatic selection or shared developmental pathways<sup>9,17</sup>. These different trait combinations may allow populations to persist in spatially and temporally variable environments and facilitate range expansion and/or successful colonization or founder events<sup>17</sup>, all of which could increase the probability of speciation<sup>28</sup>. In colour-polymorphic species with large geographic ranges, for example, parapatric speciation may occur at the ends of a ratio cline in morph frequencies<sup>2,29</sup>. This may be moderately common; among colour-polymorphic birds, at least 20% show a cline in the relative frequency of morphs<sup>23</sup>. If colour polymorphism facilitates the evolution of geographic colour variants, this could lead to taxonomic oversplitting and inflated speciation rates. However, geographic colour variation is a well-known indicator of incipient speciation<sup>28</sup>. Thus, the observed accelerated speciation probably reflects biogeographic and evolutionary processes associated with colour polymorphism rather than systematic biases.

More generally, the existence of correlated traits, with underlying co-adapted gene complexes, can promote speciation when processes maintaining colour polymorphism, such as frequency-dependent selection or balancing selection, are destabilized in populations in which morphs are gained or lost<sup>3</sup>. The change in selective environment leads to a breakdown of co-adapted gene complexes, which could result in speciation despite ongoing gene flow when new trait combinations evolve<sup>3,8,9,29</sup>. Colour polymorphism may also occur where populations come into secondary contact after diverging in coloration in allopatry<sup>30</sup> or when colour forms are under disruptive selection associated with different microhabitats<sup>1,30</sup>. In both cases, colour polymorphism may represent incomplete speciation (transient polymorphism<sup>4</sup>) and under certain conditions (for example, when accompanied by selection against hybrids and/or assortative mating) the speciation process will culminate in the evolution of monomorphic daughter species<sup>1,30</sup>. In sum, a combination of ecological, geographic and genetic processes may accelerate speciation in colour-polymorphic species; our data provide empirical confirmation of a link between colour polymorphism and relatively rapid, recent speciation.

## METHODS SUMMARY

We tested whether colour polymorphism is associated with speciation rate in the Accipitridae, Striginae and Surniinae, Caprimulgidae, Falconidae and Phasianidae. We also tested whether colour-polymorphic species tend to have diverged more recently in the Passeriformes. The data set included 232 (70%) known colour-polymorphic bird species. We used GenBank sequence data and a supermatrix approach to reconstruct robust molecular phylogenies for each of these groups (Supplementary Information).

We assessed the relationship between colour polymorphism and speciation rates using the BiSSE<sup>21</sup> method with modifications allowing for incomplete sampling and incorporating a Bayesian Markov chain Monte Carlo (MCMC) method of assessing parameter space<sup>20</sup>, implemented in the R-package Diversitree (versions 0.6-1 and 0.7-6). The method describes diversification across a phylogeny in terms speciation rate ( $\lambda$ ) extinction rate ( $\mu$ ) and transition rate ( $q$ )

between binary states, here colour polymorphic (state 1) and monomorphic (state 0). We included sampling fraction for both states based on the International Ornithological Congress (IOC) 2.4-defined taxonomy and accounted for phylogenetic uncertainty by doing the Bayesian analysis on a random sample of 50 BEAST trees.

For the analysis of passerines, we computed the difference between the tip branch length of each polymorphic species and the median tip branch length of all species within the same family. To test whether this difference could be expected by chance, we performed 5,000 randomizations comparing the difference between 67 randomly chosen species and their matching family median value. We repeated randomization tests (1) excluding species where the genus or the family sampling was <50%; (2) for oscines only; (3) including only the families containing one or more colour-polymorphic species. In all cases the results were qualitatively unchanged: all taxa,  $n = 67/59$ , randomization  $P = 0.074/0.004$  (all/polytypic only); >50% sampling,  $n = 53/46$ ,  $P = 0.059/0.002$ ; oscines,  $n = 66/59$ ,  $P = 0.085/0.004$ ; and colour-polymorphic families:  $n = 67/59$ ,  $P = 0.085/0.007$ .

**Full Methods** and any associated references are available in the online version of the paper at [www.nature.com/nature](http://www.nature.com/nature).

**Received 25 November 2011; accepted 21 March 2012.**

**Published online 9 May 2012.**

- Gray, S. M. & McKinnon, J. S. Linking color polymorphism maintenance and speciation. *Trends Ecol. Evol.* **22**, 71–79 (2007).
- Huxley, J. S. Morphism in birds. *Acta 6th Int. Ornithol. Cong.* 309–328 (1954).
- West-Eberhard, M. J. Alternative adaptations, speciation and phylogeny (a review). *Proc. Natl Acad. Sci. USA* **83**, 1388–1392 (1986).
- Ford, E. B. Polymorphism. *Biol. Rev. Camb. Philos. Soc.* **20**, 73–88 (1945).
- Ford, E. B. *Ecological Genetics* (Chapman and Hall, 1964).
- Huxley, J. S. *Evolution: the Modern Synthesis* 2nd edn (Allen & Unwin, 1963).
- Cain, A. J. & Sheppard, P. M. Natural selection in *Cepaea*. *Genetics* **39**, 89–116 (1954).
- Sinervo, B. & Calsbeek, R. The developmental, physiological, neural, and genetical causes and consequences of frequency-dependent selection in the wild. *Annu. Rev. Ecol. Syst.* **37**, 581–610 (2006).
- Sinervo, B. & Svensson, E. Correlational selection and the evolution of genomic architecture. *Heredity* **89**, 329–338 (2002).
- Chunco, A. J., McKinnon, J. S. & Servedio, M. R. Microhabitat variation and sexual selection can maintain male color polymorphisms. *Evolution* **61**, 2504–2515 (2007).
- Lande, R., Seehausen, O. & van Alphen, J. J. M. Mechanisms of rapid sympatric speciation by sex reversal and sexual selection in cichlid fish. *Genetica* **112–113**, 435–443 (2001).
- Otto, S. P., Servedio, M. R. & Nuismer, S. L. Frequency-dependent selection and the evolution of assortative mating. *Genetics* **179**, 2091–2112 (2008).
- Coyne, J. A. & Orr, A. H. *Speciation* (Sinauer Associates, 2004).
- Herder, F., Pfaender, J. & Schliwien, U. K. Adaptive sympatric speciation of polychromatic “roundfin” sailfin silverside fish in Lake Matano (Sulawesi). *Evolution* **62**, 2178–2195 (2008).
- Nosil, P., Crespi, B. J. & Sandoval, C. P. Reproductive isolation driven by the combined effects of ecological adaptation and reinforcement. *Proc. R. Soc. Lond. B* **270**, 1911–1918 (2003).
- Seehausen, O., van Alphen, J. J. M. & Lande, R. Color polymorphism and sex ratio distortion in a cichlid fish as an incipient stage in sympatric speciation by sexual selection. *Ecol. Lett.* **2**, 367–378 (1999).
- Forsman, A., Ahnesjö, J., Caesar, S. & Karlsson, M. A model of ecological and evolutionary consequences of color polymorphism. *Ecology* **89**, 34–40 (2008).
- Corl, A., Davis, A. R., Kuchta, S. R. & Sinervo, B. Selective loss of polymorphic mating types is associated with rapid phenotypic evolution during morphic speciation. *Proc. Natl Acad. Sci. USA* **107**, 4254–4259 (2010).
- McKinnon, J. S. & Pierotti, M. E. R. Colour polymorphism and correlated characters: genetic mechanisms and evolution. *Mol. Ecol.* **19**, 5101–5125 (2010).
- FitzJohn, R. G., Maddison, W. P. & Otto, S. P. Estimating trait-dependent speciation and extinction rates from incompletely resolved phylogenies. *Syst. Biol.* **58**, 595–611 (2009).
- Maddison, W. P., Midford, P. E. & Otto, S. P. Estimating a binary character's effect on speciation and extinction. *Syst. Biol.* **56**, 701–710 (2007).
- de Queiroz, A. & Gatesy, J. The supermatrix approach to systematics. *Trends Ecol. Evol.* **22**, 34–41 (2007).
- Galeotti, P., Rubolini, D., Dunn, P. O. & Fasola, M. Colour polymorphism in birds: causes and functions. *J. Evol. Biol.* **16**, 635–646 (2003).
- Galeotti, P. & Rubolini, D. The niche variation hypothesis and the evolution of colour polymorphism in birds: a comparative study of owls, nightjars and raptors. *Biol. J. Linn. Soc.* **82**, 237–248 (2004).
- Crespi, B. J. & Sandoval, C. P. Phylogenetic evidence for the evolution of ecological specialization in *Timema* walking-sticks. *J. Evol. Biol.* **13**, 249–262 (2000).
- Van Gossom, H. & Mattern, M. Y. A phylogenetic perspective on absence and presence of a sex-limited polymorphism. *Anim. Biol.* **58**, 257–273 (2008).
- Ricklefs, R. E. Estimating diversification rates from phylogenetic information. *Trends Ecol. Evol.* **22**, 601–610 (2007).
- Price, T. *Speciation in Birds* (Roberts and Co, 2008).



29. Endler, J. A. *Geographic Variation, Speciation and Clines* (Princeton Univ. Press, 1977).  
30. Roulin, A. The evolution, maintenance and adaptive function of genetic colour polymorphism in birds. *Biol. Rev. Camb. Philos. Soc.* **79**, 815–848 (2004).

**Supplementary Information** is linked to the online version of the paper at [www.nature.com/nature](http://www.nature.com/nature).

**Acknowledgements.** We thank M. Elgar, J. Endler, L. Joseph, A. Moussalli, A. Phillimore, S. Pryke and D. Rabosky for critical comments. This work was supported by the Australian Research Council (DP1092908).

**Author contributions** A.F.H. constructed phylogenies, conducted diversification analyses, wrote the Methods, Supplementary Information and edited the main manuscript. D.S.-F. conceived and funded the project, wrote the main manuscript and edited remaining sections. Both authors contributed to interpretation of results.

**Author Information** Reprints and permissions information is available at [www.nature.com/reprints](http://www.nature.com/reprints). The authors declare no competing financial interests. Readers are welcome to comment on the online version of this article at [www.nature.com/nature](http://www.nature.com/nature). Correspondence and requests for materials should be addressed to D.S.-F. ([devis@unimelb.edu.au](mailto:devis@unimelb.edu.au)) or A.F.H. ([ahugall@museum.vic.gov.au](mailto:ahugall@museum.vic.gov.au)).

## METHODS

We used the list of bird species known to exhibit true colour polymorphism from ref. 23. Colour-polymorphic species are defined as discrete colour variants within interbreeding populations so as not to confound polymorphism with geographic colour variation. We defined all species and higher level taxonomy according to the International Ornithological Congress IOC 2.4 species list (<http://www.worldbirdnames.org/index.html>) and ref. 31. To be conservative, we subsumed all categories below the rank of species into the IOC species category.

**Taxon sampling.** We restricted our analysis to the species rank (to minimize potential taxonomic bias) and to phylogenetically coherent groups that were well sampled in terms of available sequence data and contained a relatively high proportion of colour-polymorphic species. This resulted in the choice of five groups for species-level diversification analyses: Accipitridae, Striginae and Surniinae combined, Caprimulgidae, Falconidae and Phasianidae. The five groups contain 157 (47%) of colour-polymorphic taxa. We also investigated the relative age (tip branch lengths) of colour-polymorphic species in the Passeriformes, which includes 23% of colour-polymorphic species (75 out of 6,213 passerine species). Including the passerines, these groups contain 232 (70%) of known colour-polymorphic bird species. Further details are provided in Supplementary Information.

**Phylogeny reconstruction.** We downloaded all sequence data from GenBank via the NCBI website (<http://www.ncbi.nlm.nih.gov>). Nomenclature in ref. 23 and GenBank accessions were reconciled with the IOC 2.4 list with the help of the Avibase world bird database (<http://avibase.bsc-eoc.org/avibase.jsp>), Wikipedia and the Internet Bird Collection (<http://ibc.lynxeds.com>).

We maximized the number of species within the phylogenies by using the now widely used supermatrix approach<sup>22</sup>. All supermatrices contained substantial amounts of common data enabling robust phylogenetic inference and estimation of branch lengths<sup>22,32,33</sup>. Overall, the phylogenies are robust, with  $\geq 70\%$  of nodes having maximum likelihood bootstrap  $> 70\%$  and MCMC posterior probability  $> 0.90$ ; for passerines  $> 60\%$  of nodes have bootstrap  $> 70\%$  in the genus and species level trees (Supplementary Methods, Supplementary Tables 3–7 and Supplementary Figs 3–7).

**Speciation rate analyses.** To test for an association between colour polymorphism and speciation rate, we used binary-state speciation and extinction (BiSSE)<sup>21</sup> with modifications allowing for incomplete sampling and incorporating a Bayesian MCMC method of assessing parameter space<sup>20</sup>, implemented in the R-package Diversitree 0.6-1 and 0.7-6 (ref. 20). The method describes diversification across a phylogeny in terms of six parameters: speciation rate ( $\lambda_1$  and  $\lambda_0$ ), extinction rate ( $\mu_1$  and  $\mu_0$ ) and transition rate between states (from 1 to 0,  $q_{10}$ ; and from 0 to 1,  $q_{01}$ ). Here the binary states are colour-polymorphic (state 1) and not colour-polymorphic (state 0). The MCMC analyses followed the procedure outlined in the Diversitree manual and R help file (<http://cran.r-project.org/web/packages/diversitree/>) using an exponential prior  $1/(2r)$ , optimized step size ( $w$ ), and started using maximum likelihood optimized parameter values. Analyses of single trees used 20,000 step MCMC. We included sampling fraction for both states based on the IOC 2.4-defined taxonomy and accounted for phylogenetic uncertainty using the pooled results of 1,000 step MCMC for each of 50 randomly sampled BEAST trees. All cases gave parameter effective sample sizes  $> 200$  and a burn-in period was not required.

We focused on speciation rate rather than net diversification rate (speciation rate – extinction rate:  $r = \lambda - \mu$ ) because we were specifically interested in the effect of colour polymorphism on speciation rates and because of limitations in estimating extinction rate in extant phylogenies<sup>27,34,35</sup>. In this particular case, the empirically estimated extinction rate values are mostly low or very low; therefore net diversification rate ( $r$ ) estimates are similar to speciation rate ( $\lambda$ ) estimates and in all cases the ratio of net diversification rate shows the same trend as that of speciation rate (not shown). We also recorded the transition rate results, focusing on the ratio of the transition rate away from the colour-polymorphic state to the transition rate towards the colour-polymorphic state ( $q_{10}/q_{01}$ ). An estimate of the proportion of colour-polymorphic speciation associated with fixation of a polymorphism can be inferred from the BiSSE model parameters using simulations. These were calculated as the proportion of colour-polymorphic nodes that have

either one or both descendant lineages losing colour polymorphism before they speciate (or end in a terminal taxon including extinctions), based on a set of simulations totalling 1,000 nodes. From these simulations, we can gain an indication of the proportion of all speciations that involve a colour-polymorphic parent lineage (Accipitridae, 0.45; Striginae and Surniinae, 0.46; Caprimulgidae, 0.58; Falconidae, 0.29; and Phasianidae, 0.03). For the birds of prey these proportions are higher than the frequency of polymorphic species because colour polymorphism has a higher speciation rate but most colour-polymorphic speciations give rise to monomorphic species. Thus, in our models the overall proportion of colour-polymorphic species remains relatively constant.

Although the assumption of the BiSSE model that speciation and character state changes are not correlated could potentially result in overestimation of relative transition rates, our results are corroborated by simple comparison of tip branch lengths and by maximum parsimony analysis showing limited phylogenetic clustering and frequent state changes (Supplementary Table 2).

As a statistical measure we recorded the number of individual MCMC samples where colour-polymorphic speciation rate  $\leq$  non-colour-polymorphic rate; similarly for transition rate. In addition, we present maximum likelihood results and likelihood ratio tests (LRT) of the difference between the full unconstrained six-parameter model and a five-parameter model with the speciation or transition rates constrained to be equal.

For the analysis of passerines, we compared the difference between the tip branch length of each colour-polymorphic species to the median tip branch length of all species within the same family. This analysis assumes that the most recent common ancestor of most colour-polymorphic species and their closest relative were also polymorphic. Although rapid gain/loss of colour polymorphism will weaken the association between colour polymorphism and speciation it should not confound it. Using families allows a reasonable sample size for determining a median value but avoids comparing very disparate lineages, and only needs relative divergences to be comparable within families rather than across the whole tree. In addition, almost all families are monophyletic (whereas  $\sim 10\%$  of genera probably are not). Median values are appropriate as phylogenies tend to be asymmetrical and hence branch length distributions skewed. Monotypic genera are by definition distinct, and will tend to have relatively long tip branches (nearly twice as long:  $t$ -test,  $P < 0.0001$ ). Owing to these peculiarities we conducted analyses with and without colour-polymorphic species comprising monotypic genera.

To test whether the observed difference in tip branch length could be expected by chance, we performed 5,000 randomizations comparing the difference between 67 randomly chosen species and their matching family median value. We repeated analyses excluding species with sex-limited polymorphism or associated with morphoclines and multiple habitats based on data from ref. 23. Incomplete sampling may affect results; as we use tip branch lengths and family median values, the critical comparison is how well genera containing colour-polymorphic species are sampled compared to the other genera in the family. In this regard, the percentage sampling is relatively even: 78/81 (all) and 75/71 (polytypic). To assess the robustness of our results, we conducted the following additional analyses: (1) excluding species where the genus or the family sampling was  $< 50\%$ ; (2) oscines only; (3) including only the families containing one or more colour-polymorphic species. In all cases the results were qualitatively unchanged: all taxa,  $n = 67/59$ , randomization  $P = 0.074/0.004$  (all/polytypic only);  $> 50\%$  sampling,  $n = 53/46$ ,  $P = 0.059/0.002$ ; oscines,  $n = 66/59$ ,  $P = 0.085/0.004$ ; and colour-polymorphic families,  $n = 67/59$ ,  $P = 0.085/0.007$ .

31. Hackett, S. J. *et al.* A phylogenomic study of birds reveals their evolutionary history. *Science* **320**, 1763–1768 (2008).
32. Lemmon, A. R., Brown, J. M., Stanger-Hall, K. & Lemmon, E. M. The effect of ambiguous data on phylogenetic estimates obtained by maximum likelihood and Bayesian inference. *Syst. Biol.* **58**, 130–145 (2009).
33. Sanderson, M. J., McMahon, M. M. & Steel, M. Phylogenomics with incomplete taxon coverage: the limits to inference. *BMC Evol. Biol.* **10**, 155 (2010).
34. Nee, S., Holmes, E. C., May, R. M. & Harvey, P. H. Extinction rates can be estimated from molecular phylogenies. *Philos. Trans. R. Soc. Lond. B* **344**, 77–82 (1994).
35. Rabosky, D. L. Extinction rates should not be estimated from molecular phylogenies. *Evolution* **64**, 1816–1824 (2010).

# Genetic recombination is directed away from functional genomic elements in mice

Kevin Brick<sup>1\*</sup>, Fatima Smagulova<sup>2\*</sup>, Pavel Khil<sup>1</sup>, R. Daniel Camerini-Otero<sup>1</sup> & Galina V. Petukhova<sup>2</sup>

Genetic recombination occurs during meiosis, the key developmental programme of gametogenesis. Recombination in mammals has been recently linked to the activity of a histone H3 methyltransferase, PR domain containing 9 (PRDM9)<sup>1–6</sup>, the product of the only known speciation-associated gene in mammals<sup>7</sup>. PRDM9 is thought to determine the preferred recombination sites—recombination hotspots—through sequence-specific binding of its highly polymorphic multi-Zn-finger domain<sup>8</sup>. Nevertheless, *Prdm9* knockout mice are proficient at initiating recombination<sup>9</sup>. Here we map and analyse the genome-wide distribution of recombination initiation sites in *Prdm9* knockout mice and in two mouse strains with different *Prdm9* alleles and their F<sub>1</sub> hybrid. We show that PRDM9 determines the positions of practically all hotspots in the mouse genome, with the exception of the pseudo-autosomal region (PAR)—the only area of the genome that undergoes recombination in 100% of cells<sup>10</sup>. Surprisingly, hotspots are still observed in *Prdm9* knockout mice, and as in wild type, these hotspots are found at H3 lysine 4 (H3K4) trimethylation marks. However, in the absence of PRDM9, most recombination is initiated at promoters and at other sites of PRDM9-independent H3K4 trimethylation. Such sites are rarely targeted in wild-type mice, indicating an unexpected role of the PRDM9 protein in sequestering the recombination machinery away from gene-promoter regions and other functional genomic elements.

Homologous recombination is initiated by the introduction of DNA double-stranded breaks (DSBs) by the SPO11 protein<sup>11</sup>, and we have previously shown that recombination sites can be mapped by sequencing the ends of breaks recovered by chromatin immunoprecipitation with antibodies to DMCI protein bound to these ends (ChIP-seq<sup>12</sup>, single-stranded DNA sequencing (SSDS)<sup>13</sup>). To assess directly the extent to which hotspot location depends on PRDM9 we have used this approach to generate high-resolution maps of recombination initiation sites in two nearly identical (congenic) mouse strains with different *Prdm9* alleles (strains 9R and 13R, Supplementary Fig. 1). We found that, although the number of hotspots in 9R and 13R is similar (14,869 and 15,481, respectively), there is practically no overlap in their locations (Fig. 1a, b). We next mapped recombination initiation sites in the most commonly used laboratory mouse strain C57BL/6 (18,313 hotspots), which has the same *Prdm9* allele as 9R. We found that more than 98% of 9R hotspots were present in C57BL/6 (Fig. 1c). Taken together, these data constitute the first direct evidence that practically all recombination hotspots are PRDM9 dependent.

We next assessed the number and distribution of recombination hotspots in mice heterozygous for functional *Prdm9* alleles, as such mice would have potentially twice as many proficient PRDM9 binding sites. We found that in F<sub>1</sub> hybrids derived from a 9R × 13R cross the number of detected hotspots (15,677) is comparable to those in the parental strains (see Supplementary Methods). Notably, although the vast majority of hotspots in the F<sub>1</sub> mice coincided with hotspots in the parental lines, 75% corresponded to 13R hotspots, whereas only

22% corresponded to those of 9R (Fig. 1d). Hotspots from the reciprocal cross showed a similar bias (see Supplementary Methods). The 13R-derived hotspots in F<sub>1</sub> were also significantly stronger than those of 9R origin (median of 575 and 280 reads, respectively;  $P = 10^{-182}$ , Wilcoxon rank sum test), but the relative strengths of hotspots within parental pools were retained in the F<sub>1</sub> background. Importantly, F<sub>1</sub> hotspots composed a stronger-than-average subset of hotspots in both respective parental strains (Fig. 1e). In aggregate, these data indicate that the number of recombination hotspots does not double in the presence of two different *Prdm9* alleles, but is maintained at a constant level with mostly the strongest of the potential hotspots being used. The dominance of the 13R allele could result from higher affinity of the 13R PRDM9 protein variant to its preferred DNA sequence; however, other scenarios are also possible.

The complete discordance between the 9R and 13R hotspot maps suggested that different DNA sequences might be recognized by the 9R and 13R PRDM9 protein variants. Indeed, we identified a distinct motif co-centred with hotspots in each strain. These motifs are present in nearly all hotspots (9R, 94%; 13R, 97%) and enriched at hotspot centres by four- and eightfold, respectively (Fig. 1f). The enrichment of better matches to motifs reaches 200–300-fold, (Supplementary Fig. 2), and motif quality correlates with hotspot strength (Supplementary Fig. 3). We next predicted the putative DNA binding sites for the Zn finger arrays of the 9R and 13R PRDM9 protein variants and found that each motif aligns with the predicted binding site for its respective *Prdm9* allele, but not with that of the other (Fig. 1g). Both human<sup>2</sup> and mouse<sup>12</sup> hotspot motifs were previously found to align to the carboxy-terminal part of the PRDM9 Zn finger array (Supplementary Fig. 4). Our data suggest that DNA binding is not constrained to this region, as the 9R motif aligns to amino-terminal Zn fingers (Fig. 1g). Although these data are consistent with the sequence specificity of PRDM9 being a key determinant of hotspot positions *in vivo*, only a fraction of potential PRDM9 binding sites are used for hotspot formation. It is possible that sequence motifs do not capture some aspects of the binding site information, such as di- or tri-nucleotide preferences of the PRDM9 protein. Because PRDM9 (or a PRDM9-containing complex) must act within the constraints of the higher order chromatin organization, it is also conceivable that the affinity of PRDM9 for its recognition sequence depends on the local chromatin environment.

In mammals, PRDM9 is the only histone H3K4 trimethyltransferase that has been reported to be specific to meiosis<sup>9</sup>. Because recombination hotspots are associated with meiosis-specific H3K4 trimethylation (H3K4me3) marks<sup>12,14,15</sup>, the PRDM9 protein is probably responsible for their introduction<sup>8</sup>. If so, recombination hotspots in the strains with different *Prdm9* alleles will correspond to H3K4me3 marks that are strain specific. Indeed, we found that the vast majority of 9R and 13R hotspots overlap strain-specific H3K4me3 marks (9R, ≥83%; 13R, ≥89%; Supplementary Fig. 5a, b). Analysis of H3K4me3 in a *Spo11*<sup>−/−</sup> mouse revealed that H3K4me3 marks are present at 89% of potential hotspot loci, despite the lack of SPO11-induced DSBs

<sup>1</sup>National Institute of Diabetes, Digestive and Kidney Diseases, NIH, Bethesda, Maryland 20892, USA. <sup>2</sup>Department of Biochemistry and Molecular Biology, Uniformed Services University of Health Sciences, Bethesda, Maryland 20814, USA.

\*These authors contributed equally to this work.



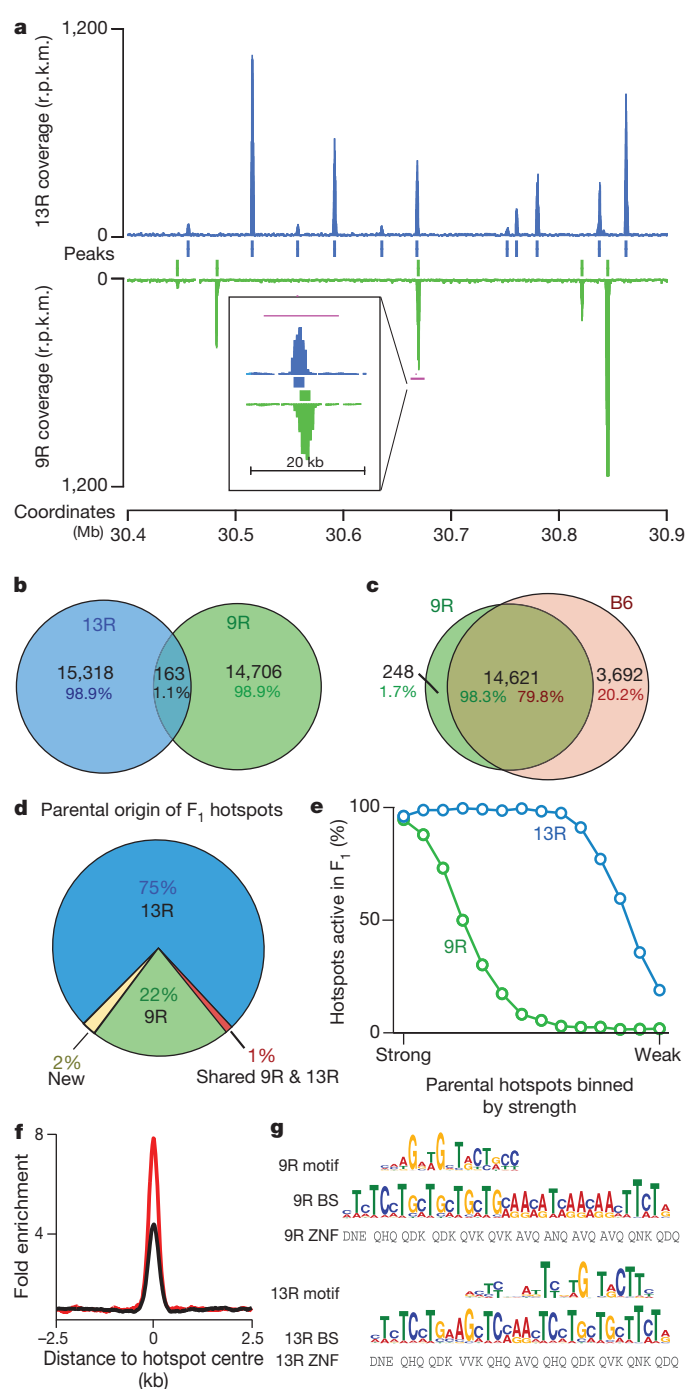


**Figure 1 | DSB hotspots localize to different loci in 9R and 13R mice.** **a**, DSB hotspots in a representative 0.5-megabase (Mb) region on chromosome 3. The magenta bar indicates the region shown in the insert. This illustrates two adjacent, yet distinct, hotspots in 9R and 13R. Data are smoothed using a 1-kb sliding window (step 100 bp). Coverage is given as reads per kb per million (r.p.k.m.). **b**, Overlap between 9R and 13R hotspots. Here and in subsequent panels, only overlaps in the central 400 bp of hotspots are counted. **c**, Overlap between 9R and C57BL/6 (B6) hotspots. The excess of B6 hotspots is due to higher ChIP enrichment in this ChIP-seq sample. B6 hotspots not found in 9R are a weak subset. **d**, Parental origin of DSB hotspots in the  $F_1$  (9R  $\times$  13R) mice. **e**, Stronger 9R and 13R hotspots are active in  $F_1$  progeny. The top 14,000 hotspots for each background were binned by strength and the overlap with  $F_1$  hotspots assessed for each bin. **f**, Distribution of hits to the 9R motif (black) and 13R motif (red) around their respective hotspots. Data are plotted in 200-nucleotide steps. **g**, Alignment of 9R and 13R motifs to the predicted PRDM9 binding sites (see Supplementary Methods). ZNF, Zn finger contact residues; BS, predicted PRDM9 binding site.

(Supplementary Fig. 5c), and in agreement with previous findings<sup>14,15</sup>. This indicates that hotspot-associated H3K4 trimethylation is not a consequence of DSB formation and/or repair, but a mark that is present before initiation of recombination.

Despite the clear critical role of PRDM9 in the initiation of genetic recombination, meiotic DSBs are present in *Prdm9* knockout mice<sup>9</sup>. Notably, we found that initiation of recombination in these mice is not random or uniform, but is still clustered in hotspots. The vast majority (99%) of these hotspots do not overlap the hotspots detected in any of the wild-type strains; nevertheless, 94% of *Prdm9*<sup>-/-</sup> hotspots still overlap H3K4me3 marks. Most of these marks (92%) are present in wild-type testis and almost half are not specific to germline cells (Supplementary Fig. 5d). As H3K4me3 marks outnumber DSB hotspots, they do not seem to be sufficient for hotspot formation (Supplementary Fig. 6). H3K4me3 is a general mark of active transcription primarily associated with gene promoters<sup>16</sup>, enhancers<sup>17,18</sup> and possibly other functional genomic elements. We found that in the absence of PRDM9 and PRDM9-introduced H3K4me3 marks, recombination hotspots are re-routed to these alternative H3K4me3 sites (Fig. 2a). Almost half (44%) of recombination hotspots in the *Prdm9*<sup>-/-</sup> mice localize to the promoters of annotated genes compared to just 3% in wild type. Unlike in wild-type mice, promoter-associated hotspots in *Prdm9*<sup>-/-</sup> mice are relatively strong (Supplementary Fig. 7) and therefore account for the majority of DSB-derived sequencing reads (62%; Fig. 2b). The H3K4me3 signal at promoters that overlap hotspots in *Prdm9*<sup>-/-</sup> mice is almost 100-fold stronger than at those that do not (median: 350 tags and 5 tags, respectively,  $P < 10^{-200}$ , Wilcoxon test). Furthermore, promoter-overlapping hotspots are slightly enriched at genes expressed in early meiotic prophase ( $P = 10^{-138}$ , one-sided binomial test; Supplementary Fig. 8). *Prdm9*<sup>-/-</sup> hotspots that are not associated with annotated promoters still probably represent

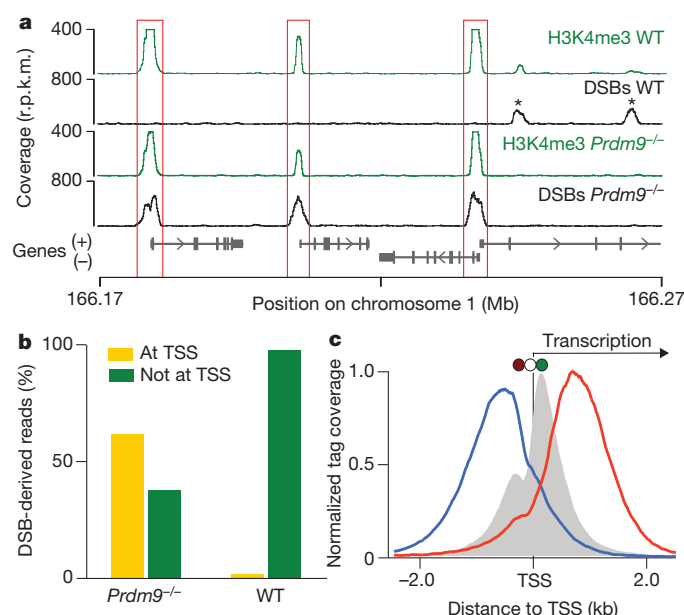


**Figure 2 | PRDM9 redirects DSBs away from functional genomic elements.** **a**, In *Prdm9*<sup>-/-</sup> mice DSBs are formed at functional genomic elements marked by H3K4me3 (such as promoters, red boxes). These sites are refractory to DSB formation in wild-type (WT) mice, where breaks are redirected to PRDM9-dependent H3K4me3 marks (asterisks). **b**, Most DSBs occur in regions around TSSs in *Prdm9*<sup>-/-</sup> mice, but not in wild-type mice. **c**, The centre of *Prdm9*<sup>-/-</sup> hotspots at TSSs coincides precisely with the H3K4me3 mark on the +1 nucleosome (red circle, -1 nucleosome; white circle, nucleosome-free region; green circle, +1 nucleosome). Mean H3K4me3 coverage is grey, mean forward-strand single-stranded DNA coverage is blue and reverse-strand coverage is red. The intersection point of the forward- and reverse-strand coverage is the mean hotspot centre (Supplementary Fig. 11).

DSBs formed at important genomic elements as they exhibit higher-than-expected sequence conservation (Supplementary Fig. 9). Indeed, 40% of these hotspots overlap histone crotonylation sites, a recently discovered marker of promoters and enhancers<sup>19</sup> (see Supplementary Methods). The distribution of hotspots around transcription start sites (TSSs) in *Prdm9*<sup>-/-</sup> mice is reminiscent of that in *Saccharomyces cerevisiae*, where most hotspots are found at promoters<sup>20,21</sup>. However, whereas DSBs at yeast promoters form in the upstream nucleosome-depleted region<sup>20,21</sup>, hotspots in *Prdm9*<sup>-/-</sup> mice preferentially form at the most frequently H3K4 trimethylated nucleosome at the +1 position, just downstream of the TSS (Fig. 2c).

Unique in the genome is a short region of homology at the end of X and Y chromosomes called the PAR, that undergoes recombination in every round of meiosis<sup>10</sup>. We have recently demonstrated that the only sequenced region of the mouse PAR, adjacent to the interstitial PAR boundary, contains a large cluster of overlapping DSB hotspots spanning at least 40 kilobases (kb)<sup>12</sup>. We now find that this hotspot cluster is still present in *Prdm9*<sup>-/-</sup> mice, and is shared between the strains with different *Prdm9* alleles (Fig. 3). Similar to the hotspot cluster, the H3K4me3 signal in the PAR is far broader and stronger than any other H3K4me3 mark in the genome, but it is shifted slightly off the hotspot cluster, to within the PAR (Fig. 3). Recent studies have demonstrated that the structural organization of the PAR differs significantly from that of the rest of the chromosome<sup>22</sup>. It is conceivable that this region features constitutively accessible chromatin that allows initiation of recombination without participation of the PRDM9 protein. Initiation of homologous recombination at some of the hotspots in the PAR-flanking region is also defined by a PRDM9-independent mechanism. In this region, up to ~900 kb upstream of PAR, there is an extraordinary concentration of hotspots shared between *Prdm9*<sup>-/-</sup> mice and wild-type strains with different *Prdm9* alleles (C57BL/6, 9R and 13R; Fig. 3). As expected, the H3K4me3 marks at these shared hotspots are also strain independent. The density of PRDM9-independent hotspots in the PAR-flanking region appears to increase with proximity to the PAR (Fig. 3), consistent with a specific chromatin organization or particular epigenetic mark characteristic to the PAR propagating into the adjacent area. Yet, PRDM9-dependent hotspots are also present in the PAR-flanking area, and therefore the DNA in this region is still accessible to the PRDM9 protein.

These data raise the question of why the initiation of recombination in the PAR is different from the rest of the genome. To ensure proper sex chromosome segregation during meiosis, at least one crossover must be formed inside the PAR<sup>10</sup>. Out of thousands of PRDM9-dependent hotspots only 200–400 are used in each meiosis and only

20–25 result in crossovers. Considering the short length of the PAR, a large fraction of cells would fail to introduce a crossover within this area simply by chance. It is possible that the mandatory crossover requirement is more efficiently fulfilled through an alternative mechanism of initiation, unique to the PAR. PRDM9-independent initiation of homologous recombination in the PAR would also facilitate the rapid evolution of both PRDM9 (ref. 23) and the PAR<sup>24</sup> by allowing them to evolve independently of each other. It is also conceivable that PRDM9-dependent and -independent recombination pathways use alternative isoforms of SPO11, as the number of meiotic DSBs in the PAR is diminished in mice expressing only the  $\beta$  SPO11 isoform<sup>22</sup>.

Our study clearly demonstrates that the PRDM9 protein is not required for the initiation of genetic recombination per se, but rather determines the positions (hotspots) where this initiation takes place. In the absence of PRDM9 the vast majority of DSB hotspots still coincide with H3K4me3 marks. Although a causal relationship is yet to be established, this suggests that H3K4me3 or/and mechanisms that induce H3K4me3 are necessary to provide a favourable chromatin environment for the initiation of meiotic recombination. Such an environment can be created with or without PRDM9, but only PRDM9-dependent H3K4me3 sites are associated with recombination hotspots in wild-type mice outside of the PAR. This indicates that PRDM9 is directly involved in recruitment of the recombination initiation machinery.

The sterility of *Prdm9*<sup>-/-</sup> mice suggests that the initiation of recombination at H3K4me3-marked functional elements may not be compatible with gametogenesis. It is conceivable that recombination may interfere with the transcription of essential meiotic genes; however, as four chromatids are present before the first meiotic division it is unlikely that disruption of transcription on one of them will lead to a significant drop in overall transcription of any particular gene hit by a DSB. On the other hand, it may be that the opposite is true and that transcription interferes with the repair of breaks introduced at promoters. The resulting aberrant recombination would account for the observation that, in *Prdm9*<sup>-/-</sup> mice, persistent DSBs are present and only partial synapsis is seen between homologous chromosomes<sup>9</sup> (Supplementary Fig. 10). The *Prdm9* gene exhibits complex epistatic interactions culminating in sterility of F<sub>1</sub> hybrid males carrying a particular combination of functional *Prdm9* alleles<sup>7</sup>. Unlike in *Prdm9*<sup>-/-</sup> mice, repair of meiotic DSBs in such males proceeds normally in a large fraction of cells, with 40% of spermatocytes showing complete homologous synapsis<sup>7</sup>. Although this suggests that distinct mechanisms are responsible for meiotic arrest in *Prdm9*<sup>-/-</sup> mice and in F<sub>1</sub> hybrid males, we cannot exclude the possibility that an alternative role of

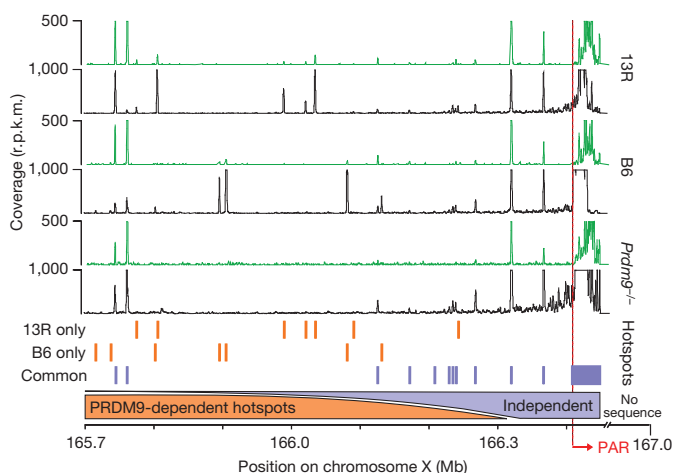


**Figure 3 | PRDM9-independent hotspots in the PAR and flanking region.** Black tracks represent DMC1 tag coverage; green tracks depict H3K4me3 coverage. Orange bars illustrate hotspots unique to 13R or C57BL/6 (B6) mice. Purple bars illustrate hotspots shared in 13R, C57BL/6 and *Prdm9*<sup>-/-</sup> mice.

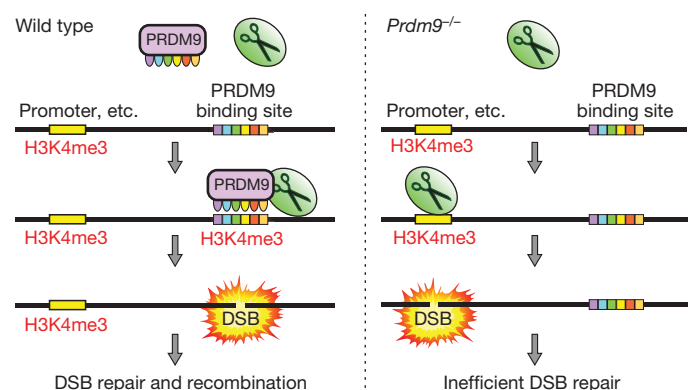


**Figure 4 | Proposed role of the PRDM9 protein.** Left: in cells containing a functional copy of PRDM9 (wild type) the DSB formation machinery (scissors) is directed to preferred DSB sites/PRDM9 binding sites. Right: in the absence of PRDM9, the DSB formation machinery opportunistically makes breaks at PRDM9-independent H3K4me3 marks such as those at promoters and enhancers. This results in inefficient DSB repair and meiotic arrest.

PRDM9 in meiotic progression accounts for both sterility phenotypes. Although a function of PRDM9 in transcription has not been demonstrated, PRDM9 contains conserved domains implicated in transcription<sup>25,26</sup> and could potentially be involved in executing the meiotic transcription program. It is also conceivable that PRDM9 is directly required for efficient progression of recombination. The potential importance of avoiding recombination at functional genomic elements is highlighted in the canid lineage, which has lost *Prdm9* (refs. 27, 28). Although dogs retain recombination hotspots<sup>27</sup>, preliminary analyses suggest that, unlike in *Prdm9*<sup>-/-</sup> mice, these hotspots do not seem to be enriched at promoters (Supplementary Information). A trivial explanation would be that dog *Prdm9* resides in the unassembled parts of the genome; however, these data may also indicate that alternative mechanisms have evolved to target recombination to specialized genomic regions in species that lack *Prdm9*. Ultimately, we favour the hypothesis that PRDM9 prevents initiation of recombination in the areas of the genome where successful completion of recombination might be compromised by other nuclear processes (Fig. 4). The re-routing of DSBs from important genomic elements may also have a protective role against potential mutagenic effects of recombination.

## METHODS SUMMARY

SSDS<sup>13</sup> using antibodies against DMC1 was used to identify DSB hotspots in the following mice: B10.S-H2t4/(9R)/J, B10.F-H2pb1/(13R)/J, B10.S-H2t4/(9R)/J × B10.F-H2pb1/(13R)/J (F<sub>1</sub>), C57BL/6J and B6;129P2-*Prdm9*<sup>tm1Ymat</sup>/J. Chromatin immunoprecipitation using antibodies against H3K4me3 followed by Illumina sequencing was also performed on samples derived from each of these mice. DSB hotspots were defined by SISR<sup>29</sup> and post-processed using a bespoke pipeline. Peaks in H3K4me3 data were called using MACS v1.3<sup>30</sup>. Detailed methods are available in the Supplementary Information.

Received 10 November 2011; accepted 26 March 2012.

Published online 13 May 2012.

1. Parvanov, E. D., Petkov, P. M. & Paigen, K. *Prdm9* controls activation of mammalian recombination hotspots. *Science* **327**, 835 (2010).
2. Myers, S. *et al.* Drive against hotspot motifs in primates implicates the *PRDM9* gene in meiotic recombination. *Science* **327**, 876–879 (2010).
3. Baudat, F. *et al.* PRDM9 is a major determinant of meiotic recombination hotspots in humans and mice. *Science* **327**, 836–840 (2010).
4. Berg, I. L. *et al.* PRDM9 variation strongly influences recombination hot-spot activity and meiotic instability in humans. *Nature Genet.* **42**, 859–863 (2010).
5. Berg, I. L. *et al.* Variants of the protein PRDM9 differentially regulate a set of human meiotic recombination hotspots highly active in African populations. *Proc. Natl Acad. Sci. USA* **108**, 12378–12383 (2011).
6. Hinch, A. G. *et al.* The landscape of recombination in African-Americans. *Nature* **476**, 170–175 (2011).
7. Mihola, O., Trachtulec, Z., Vlcek, C., Schimenti, J. C. & Forejt, J. A mouse speciation gene encodes a meiotic histone H3 methyltransferase. *Science* **323**, 373–375 (2009).
8. Grey, C. *et al.* Mouse PRDM9 DNA-binding specificity determines sites of histone H3 lysine 4 trimethylation for initiation of meiotic recombination. *PLoS Biol.* **9**, e1001176 (2011).
9. Hayashi, K., Yoshida, K. & Matsui, Y. A histone H3 methyltransferase controls epigenetic events required for meiotic prophase. *Nature* **438**, 374–378 (2005).
10. Burgoyne, P. S. Genetic homology and crossing over in the X and Y chromosomes of mammals. *Hum. Genet.* **61**, 85–90 (1982).
11. Neale, M. J. & Keeney, S. Clarifying the mechanics of DNA strand exchange in meiotic recombination. *Nature* **442**, 153–158 (2006).

12. Smagulova, F. *et al.* Genome-wide analysis reveals novel molecular features of mouse recombination hotspots. *Nature* **472**, 375–378 (2011).
13. Khil, P. P., Smagulova, F., Brick, K. M., Camerini-Otero, R. D. & Petukhova, G. V. Sensitive mapping of recombination hotspots using sequencing-based detection of ssDNA. *Genome Res.* <http://dx.doi.org/10.1101/gr.130583.111> (2012).
14. Borde, V. *et al.* Histone H3 lysine 4 trimethylation marks meiotic recombination initiation sites. *EMBO J.* **28**, 99–111 (2009).
15. Buard, J., Barthès, P., Grey, C. & de Massy, B. Distinct histone modifications define initiation and repair of meiotic recombination in the mouse. *EMBO J.* **28**, 2616–2624 (2009).
16. Guenther, M. G., Levine, S. S., Boyer, L. A., Jaenisch, R. & Young, R. A. A chromatin landmark and transcription initiation at most promoters in human cells. *Cell* **130**, 77–88 (2007).
17. Ernst, J. *et al.* Mapping and analysis of chromatin state dynamics in nine human cell types. *Nature* **473**, 43–49 (2011).
18. Pekowska, A. *et al.* H3K4 tri-methylation provides an epigenetic signature of active enhancers. *EMBO J.* **30**, 4198–4210 (2011).
19. Tan, M. *et al.* Identification of 67 histone marks and histone lysine crotonylation as a new type of histone modification. *Cell* **146**, 1016–1028 (2011).
20. Pan, J. *et al.* A hierarchical combination of factors shapes the genome-wide topography of yeast meiotic recombination initiation. *Cell* **144**, 719–731 (2011).
21. Wu, T. C. & Lichten, M. Meiosis-induced double-strand break sites determined by yeast chromatin structure. *Science* **263**, 515–518 (1994).
22. Kauppi, L. *et al.* Distinct properties of the XY pseudoautosomal region crucial for male meiosis. *Science* **331**, 916–920 (2011).
23. Oliver, P. L. *et al.* Accelerated evolution of the *Prdm9* speciation gene across diverse metazoan taxa. *PLoS Genet.* **5**, e1000753 (2009).
24. Bellott, D. W. & Page, D. C. Reconstructing the evolution of vertebrate sex chromosomes. *Cold Spring Harb. Symp. Quant. Biol.* **74**, 345–353 (2009).
25. Lim, F. L., Soulez, M., Koczan, D., Thiesen, H. J. & Knight, J. C. A KRAB-related domain and a novel transcription repression domain in proteins encoded by SSX genes that are disrupted in human sarcomas. *Oncogene* **17**, 2013–2018 (1998).
26. Margolin, J. F. *et al.* Krüppel-associated boxes are potent transcriptional repression domains. *Proc. Natl Acad. Sci. USA* **91**, 4509–4513 (1994).
27. Axelsson, E. *et al.* Death of PRDM9 coincides with stabilization of the recombination landscape in the dog genome. *Genome Res.* **22**, 51–63 (2012).
28. Muñoz-Fuentes, V., Di Rienzo, A. & Vilà, C. *Prdm9*, a major determinant of meiotic recombination hotspots, is not functional in dogs and their wild relatives, wolves and coyotes. *PLoS ONE* **6**, e25498 (2011).
29. Jothi, R., Cuddapah, S., Barski, A., Cui, K. & Zhao, K. Genome-wide identification of *in vivo* protein–DNA binding sites from ChIP-Seq data. *Nucleic Acids Res.* **36**, 5221–5231 (2008).
30. Zhang, Y. *et al.* Model-based analysis of ChIP-Seq (MACS). *Genome Biol.* **9**, R137 (2008).

**Supplementary Information** is linked to the online version of the paper at [www.nature.com/nature](http://www.nature.com/nature).

**Acknowledgements** We thank S. Sharmeen and H. Smith for assistance with high-throughput sequencing. We also thank M. Lichten and P. Hsieh for critical discussion of the manuscript. This research was supported by the NIDDK Intramural Research Program; Basil O'Connor Starter Scholar Research Award Grant No. 5-FY07-667 from the March of Dimes Foundation (G.V.P.); NIH grant 1R01GM084104-01A1 from NIGMS (G.V.P.); and New Investigator Start-up Grants FS71HU, R071HU and CS71HU from USUHS (G.V.P.).

**Author Contributions** K.B. and P.K. performed data analyses. F.S. performed all experiments. K.B. and G.V.P. wrote the manuscript. G.V.P. and R.D.C.-O. designed and supervised the study. All authors contributed to experimental design, discussed the results and critiqued the manuscript.

**Author Information** All data sets are fully described and available for download from the GEO under accession number GSE35498. Reprints and permissions information is available at [www.nature.com/reprints](http://www.nature.com/reprints). The authors declare no competing financial interests. Readers are welcome to comment on the online version of this article at [www.nature.com/nature](http://www.nature.com/nature). Correspondence and requests for materials should be addressed to G.V.P. ([gpetukhova@usuhs.mil](mailto:gpetukhova@usuhs.mil)) or R.D.C.-O. ([rdcamerini@mail.nih.gov](mailto:rdcamerini@mail.nih.gov)).



# The tomato genome sequence provides insights into fleshy fruit evolution

The Tomato Genome Consortium\*

Tomato (*Solanum lycopersicum*) is a major crop plant and a model system for fruit development. *Solanum* is one of the largest angiosperm genera<sup>1</sup> and includes annual and perennial plants from diverse habitats. Here we present a high-quality genome sequence of domesticated tomato, a draft sequence of its closest wild relative, *Solanum pimpinellifolium*<sup>2</sup>, and compare them to each other and to the potato genome (*Solanum tuberosum*). The two tomato genomes show only 0.6% nucleotide divergence and signs of recent admixture, but show more than 8% divergence from potato, with nine large and several smaller inversions. In contrast to *Arabidopsis*, but similar to soybean, tomato and potato small RNAs map predominantly to gene-rich chromosomal regions, including gene promoters. The *Solanum* lineage has experienced two consecutive genome triplications: one that is ancient and shared with rosids, and a more recent one. These triplications set the stage for the neofunctionalization of genes controlling fruit characteristics, such as colour and fleshiness.

The genome of the inbred tomato cultivar 'Heinz 1706' was sequenced and assembled using a combination of Sanger and 'next generation' technologies (Supplementary Information section 1). The predicted genome size is approximately 900 megabases (Mb), consistent with previous estimates<sup>3</sup>, of which 760 Mb were assembled in 91 scaffolds aligned to the 12 tomato chromosomes, with most gaps restricted to pericentromeric regions (Fig. 1A and Supplementary Fig. 1). Base accuracy is approximately one substitution error per 29.4 kilobases (kb) and one indel error per 6.4 kb. The scaffolds were linked with two bacterial artificial chromosome (BAC)-based physical maps and anchored/oriented using a high-density genetic map, introgression line mapping and BAC fluorescence *in situ* hybridization (FISH).

The genome of *S. pimpinellifolium* LA1589 was sequenced and assembled *de novo* using Illumina short reads, yielding a 739 Mb draft genome (Supplementary Information section 3). Estimated divergence between the wild and domesticated genomes is 0.6% (5.4 million single nucleotide polymorphisms (SNPs) distributed along the chromosomes (Fig. 1A and Supplementary Fig. 1)).

Tomato chromosomes consist of pericentric heterochromatin and distal euchromatin, with repeats concentrated within and around centromeres, in chromomeres and at telomeres (Fig. 1A and Supplementary Fig. 1). Substantially higher densities of recombination, genes and transcripts are observed in euchromatin, whereas chloroplast insertions (Supplementary Information sections 1.22 and 1.23) and conserved microRNA (miRNA) genes (Supplementary Information section 2.9) are more evenly distributed throughout the genome. The genome is highly syntenic with those of other economically important Solanaceae (Fig. 1B). Compared to the genomes of *Arabidopsis*<sup>4</sup> and *Sorghum*<sup>5</sup>, tomato has fewer high-copy, full-length long terminal repeat (LTR) retrotransposons with older average insertion ages (2.8 versus 0.8 million years (Myr) ago) and fewer high-frequency *k*-mers (Supplementary Information section 2.10). This supports previous findings that the tomato genome is unusual among angiosperms by being largely comprised of low-copy DNA<sup>6,7</sup>.

The pipeline used to annotate the tomato and potato<sup>8</sup> genomes is described in Supplementary Information section 2. It predicted 34,727 and 35,004 protein-coding genes, respectively. Of these, 30,855 and 32,988, respectively, are supported by RNA sequencing (RNA-Seq) data, and 31,741 and 32,056, respectively, show high similarity to *Arabidopsis* genes (Supplementary Information section 2.1). Chromosomal organization of genes, transcripts, repeats and small RNAs (sRNAs) is very similar in the two species (Supplementary Figs 2–4). The protein-coding genes of tomato, potato, *Arabidopsis*, rice and grape were clustered into 23,208 gene groups ( $\geq 2$  members), of which 8,615 are common to all five genomes, 1,727 are confined to eudicots (tomato, potato, grape and *Arabidopsis*), and 727 are confined to plants with fleshy fruits (tomato, potato and grape) (Supplementary Information section 5.1 and Supplementary Fig. 5). Relative expression of all tomato genes was determined by replicated strand-specific Illumina RNA-Seq of root, leaf, flower (two stages) and fruit (six stages) in addition to leaf and fruit (three stages) of *S. pimpinellifolium* (Supplementary Table 1).

sRNA sequencing data supported the prediction of 96 conserved miRNA genes in tomato and 120 in potato, a number consistent with other plant species (Fig. 1A, Supplementary Figs 1 and 3 and Supplementary Information section 2.9). Among the 34 miRNA families identified, 10 are highly conserved in plants and similarly represented in the two species, whereas other, less conserved families are more abundant in potato. Several miRNAs, predicted to target Toll interleukin receptor, nucleotide-binding site and leucine-rich repeat (TIR-NBS-LRR) genes, seemed to be preferentially or exclusively expressed in potato (Supplementary Information section 2.9).

Comparative genomic studies are reported in Supplementary Information section 4. Sequence alignment of 71 Mb of euchromatic tomato genomic DNA to their potato<sup>8</sup> counterparts revealed 8.7% nucleotide divergence (Supplementary Information section 4.1). Intergenic and repeat-rich heterochromatic sequences showed more than 30% nucleotide divergence, consistent with the high sequence diversity in these regions among potato genotypes<sup>8</sup>. Alignment of tomato–potato orthologous regions confirmed nine large inversions known from cytological or genetic studies and several smaller ones (Fig. 1C). The exact number of small inversions is difficult to determine due to the lack of orientation of most potato scaffolds.

A total of 18,320 clearly orthologous tomato–potato gene pairs were identified. Of these, 138 (0.75%) had significantly higher than average non-synonymous ( $K_a$ ) versus synonymous ( $K_s$ ) nucleotide substitution rate ratios ( $\omega$ ), indicating diversifying selection, whereas 147 (0.80%) had significantly lower than average  $\omega$ , indicating purifying selection (Supplementary Table 2). The proportions of high and low  $\omega$  between sorghum and maize (*Zea mays*) are 0.70% and 1.19%, respectively, after 11.9 Myr of divergence<sup>9</sup>, indicating that diversifying selection may have been stronger in tomato–potato. The highest densities of low- $\omega$  genes are found in collinear blocks with average  $K_s > 1.5$ , tracing to a genome triplication shared with grape (see below) (Fig. 1C, Supplementary Fig. 6 and Supplementary Table 3). These genes, which have been preserved in paleo-duplicated locations for more than 100 Myr<sup>10,11</sup>, are more constrained than 'average' genes and are

\*Lists of participants and their affiliations appear at the end of the paper.

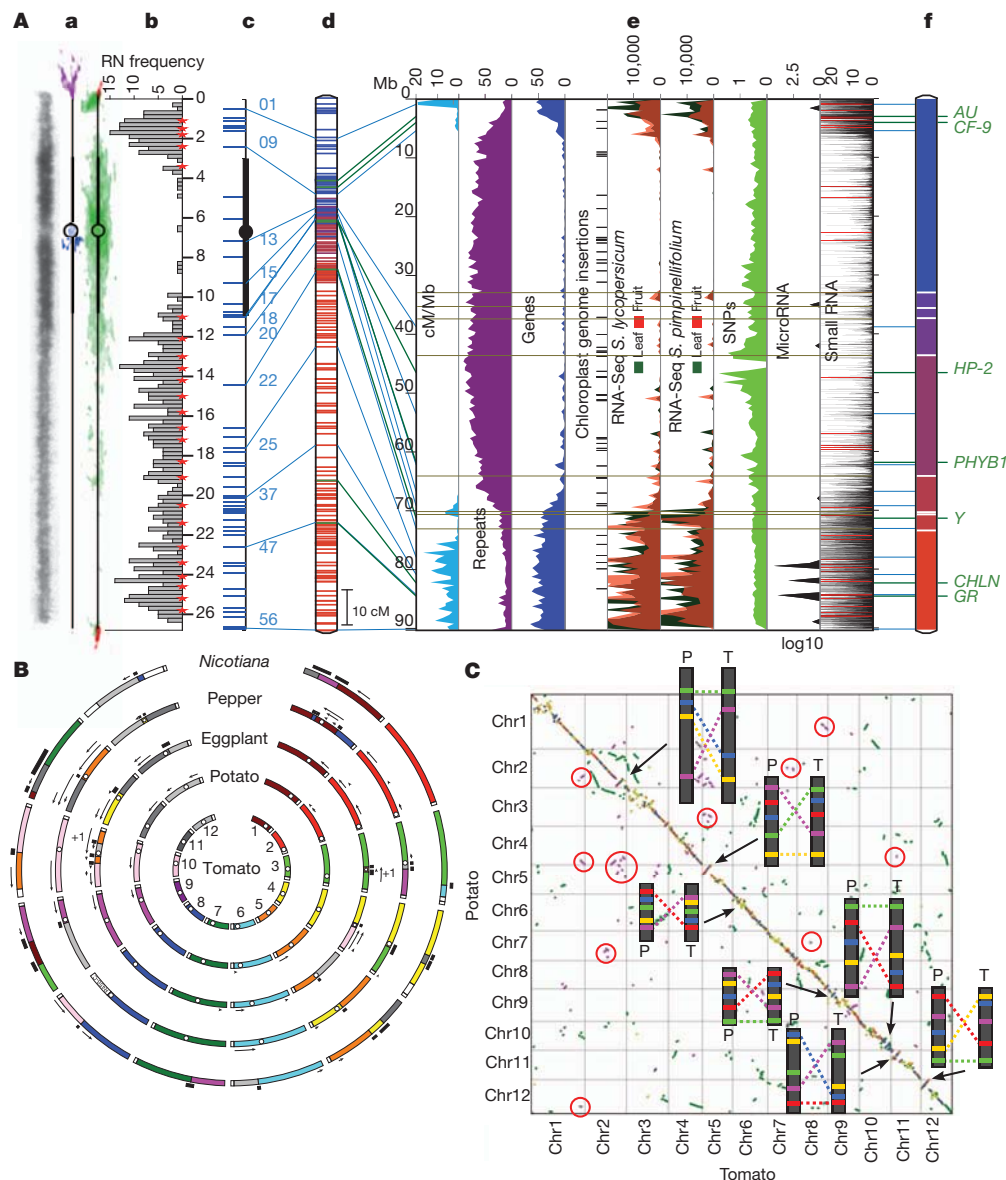


**Figure 1 | Tomato genome topography and synteny.** **A**, Multi-dimensional topography of tomato chromosome 1 (chromosomes 2–12 are shown in Supplementary Fig. 1). **a**, Left: contrast-reversed, 4',6-diamidino-2-phenylindole (DAPI)-stained pachytene chromosome; centre and right: FISH signals for repeat sequences on diagrammatic pachytene chromosomes (purple, TGR1; blue, TGR4; red, telomere repeat; green, Cot 100 DNA (including most repeats)). **b**, Frequency distribution of recombination nodules (RNs) representing crossovers on 249 chromosomes. Red stars mark 5 cM intervals starting from the end of the short arm (top). Scale is in micrometres. **c**, FISH-based locations of selected BACs (horizontal blue lines on left). **d**, Kazusa F2-2000 linkage map. Blue lines to the left connect linkage map markers on the BAC-FISH map (c), and to the right to heat maps (e) and the DNA pseudomolecule (f). **e**, From left to right: linkage map distance (cM/Mb, turquoise), repeated sequences (% nucleotides per 500 kb, purple), genes (% nucleotides per 500 kb, blue), chloroplast insertions; RNA-Seq reads from leaves and breaker fruits of *S. lycopersicum* and *S. pimpinellifolium* (number of reads per 500 kb, green and red, respectively), microRNA genes (transcripts per million per 500 kb, black), small RNAs (thin horizontal black and red lines, sum of hits-normalized abundances). Horizontal grey lines represent gaps in the pseudomolecule (f). **f**, DNA pseudomolecule consisting of nine scaffolds. Unsequenced gaps (approximately 9.8 Mb, Supplementary Table 13) are

enriched for transcription factors and genes otherwise related to gene regulation (Supplementary Tables 3 and 4).

Sequence comparison of 31,760 Heinz 1706 genes with  $>5\times$  *S. pimpinellifolium* read coverage in over 90% of their coding regions

indicated by white horizontal lines. Tomato genes identified by map-based cloning (Supplementary Table 14) are indicated on the right. For more details, see legend to Supplementary Fig. 1. **B**, Syntenic relationships in the *Solanaceae*. COSII-based comparative maps of potato, aubergine (eggplant), pepper and *Nicotiana* with respect to the tomato genome (Supplementary Information section 4.5 and Supplementary Fig. 14). Each tomato chromosome is assigned a different colour and orthologous chromosome segment(s) in other species are shown in the same colour. White dots indicate approximate centromere locations. Each black arrow indicates an inversion relative to tomato and '+1' indicates a minimum of one inversion. Each black bar beside a chromosome indicates translocation breakpoints relative to tomato. Chromosome lengths are not to scale, but segments within chromosomes are. **C**, Tomato-potato synteny dot plot of tomato (T) and potato (P) genomic sequences based on collinear blocks (Supplementary Information section 4.1). Red and blue dots represent gene pairs with statistically significant high and low  $\omega$  ( $K_a/K_s$ ) in collinear blocks, which average  $K_s \leq 0.5$ , respectively. Green and magenta dots represent genes in collinear blocks which average  $0.5 < K_s \leq 1.5$  and  $K_s > 1.5$ , respectively. Yellow dots represent all other gene pairs. Blocks circled in red are examples of pan-eudicot triplication. Inserts represent schematic drawings of BAC-FISH patterns of cytologically demonstrated chromosome inversions (also in Supplementary Fig. 15).

revealed 7,378 identical genes and 11,753 with only synonymous changes. The remaining 12,629 genes had non-synonymous changes, including gains and losses of stop codons with potential consequences for gene function (Supplementary Tables 5–7). Several pericentric

regions, predicted to contain genes, are absent or polymorphic in the broader *S. pimpinellifolium* germplasm (Supplementary Table 8 and Supplementary Fig. 7). Within cultivated germplasm, particularly among the small-fruited cherry tomatoes, several chromosomal segments are more closely related to *S. pimpinellifolium* than to Heinz 1706 (Supplementary Figs 8 and 9), supporting previous observations on recent admixture of these gene pools due to breeding<sup>12</sup>. Heinz 1706 itself has been reported to carry introgressions from *S. pimpinellifolium*<sup>13</sup>, traces of which are detectable on chromosomes 4, 9, 11 and 12 (Supplementary Table 9).

Comparison of the tomato and grape genomes supports the hypothesis that a whole-genome triplication affecting the rosid lineage occurred in a common eudicot ancestor<sup>11</sup> (Fig. 2a). The distribution of  $K_s$  between corresponding gene pairs in duplicated blocks suggests that one polyploidization in the solanaceous lineage preceded the rosid–asterid (tomato–grape) divergence (Supplementary Fig. 10).

Comparison with the grape genome also reveals a more recent triplication in tomato and potato. Whereas few individual tomato/potato genes remain triplicated (Supplementary Tables 10 and 11), 73% of tomato gene models are in blocks that are orthologous to one grape region, collectively covering 84% of the grape gene space. Among these grape genomic regions, 22.5% have one orthologous region in tomato, 39.9% have two, and 21.6% have three, indicating that a whole-genome triplication occurred in the *Solanum* lineage, followed by widespread gene loss. This triplication, also evident in potato (Supplementary Fig. 11), is estimated at 71 ( $\pm 19.4$ ) Myr on the basis of the  $K_s$  of paralogous genes (Supplementary Fig. 10), and therefore predates the  $\sim 7.3$  Myr tomato–potato divergence. On the basis of alignments to single grape genome segments, the tomato genome can be partitioned into three non-overlapping ‘subgenomes’ (Fig. 2b). The number of euasterid lineages that have experienced the recent triplication remains unclear and awaits complete euasterid I and II genome sequences.  $K_s$  distributions show that euasterids I and II, and indeed the rosid–asterid lineages, all diverged from common ancestry at or near the pan-eudicot triplication (Fig. 2a), suggesting that this event may have contributed to the formation of major eudicot lineages in a short period of several million years<sup>14</sup>, partially explaining the explosive radiation of angiosperm plants on Earth<sup>15</sup>.

Fleshy fruits (Supplementary Fig. 12) are an important means of attracting vertebrate frugivores for seed dispersal<sup>16</sup>. Combined orthology and synteny analyses indicate that both genome triplications added new gene family members that mediate important fruit-specific functions (Fig. 3). These include transcription factors and enzymes necessary for ethylene biosynthesis (*RIN*, *CNR*, *ACS*) and perception (*ETR3/NR*, *ETR4*)<sup>17</sup>, red light photoreceptors influencing fruit quality (*PHYB1/PHYB2*) and ethylene- and light-regulated genes mediating lycopene biosynthesis (*PSY1/PSY2*). Several cytochrome P450 subfamilies associated with toxic alkaloid biosynthesis show contraction or complete loss in tomato and the extant genes show negligible expression in ripe fruits (Supplementary Information section 5.4).

Fruit texture has profound agronomic and sensory importance and is controlled in part by cell wall structure and composition<sup>18</sup>. More than 50 genes showing differential expression during fruit development and ripening encode proteins involved in modification of cell wall architecture (Fig. 4a and Supplementary Information section 5.7). For example, a family of xyloglucan endotransglucosylase/hydrolases (XTHs) has expanded both in the recent whole-genome triplication and through tandem duplication. One of the triplicated members, *XTH10*, shows differential loss between tomato and potato (Fig. 4a and Supplementary Table 12), suggesting genetically driven specialization in the remodelling of fruit cell walls.

Similar to soybean and potato and in contrast to *Arabidopsis*, tomato sRNAs map preferentially to euchromatin (Supplementary Fig. 2). sRNAs from tomato flowers and fruits<sup>19</sup> map to 8,416 gene promoters. Differential expression of sRNAs during fruit development is apparent for 2,687 promoters, including those of cell-wall-related genes (Fig. 4b) and occurs preferentially at key developmental transitions (for example, flower to fruit, fruit growth to fruit ripening, Supplementary Information section 2.8).

The genome sequences of tomato, *S. pimpinellifolium* and potato provide a starting point for comparing gene family evolution and sub-functionalization in the *Solanaceae*. A striking example is the *SELF PRUNING* (*SP*) gene family, which includes the homologue of *Arabidopsis FT*, encoding the mobile flowering signal florigen<sup>20</sup> and its antagonist *SP*, encoding the orthologue of *TFL1*. Nearly a century ago, a spontaneous mutation in *SP* spawned the ‘determinate’ varieties

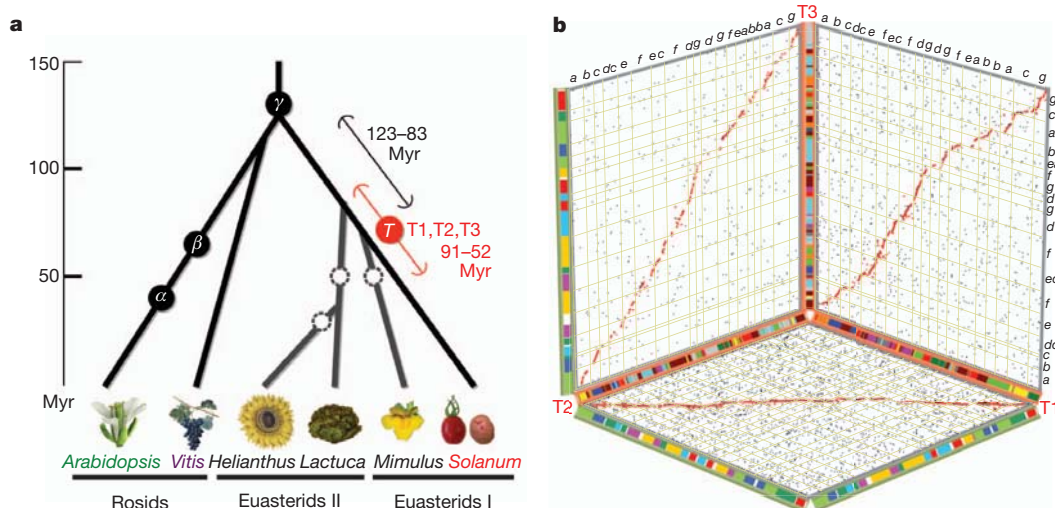


**Figure 2 | The *Solanum* whole genome triplication.** **a**, Speciation and polyploidization in eudicot lineages. Confirmed whole-genome duplications and triplications are shown with annotated circles, including ‘T’ (this paper) and previously discovered events  $\alpha$ ,  $\beta$ ,  $\gamma$ <sup>10,11,14</sup>. Dashed circles represent one or more suspected polyploidies reported in previous publications that need further support from genome assemblies<sup>27,28</sup>. Grey branches indicate unpublished genomes. Black and red error bars bracket indicate the likely timings of divergence of major asterid lineages and of ‘T’, respectively. The post-‘T’ subgenomes, designated T1, T2, and T3, are further detailed in

Supplementary Fig. 10. **b**, On the basis of alignments of multiple tomato genome segments to single grape genome segments, the tomato genome is partitioned into three non-overlapping ‘subgenomes’ (T1, T2, T3), each represented by one axis in the three-dimensional plot. The ancestral gene order of each subgenome is inferred according to orthologous grape regions, with tomato chromosomal affinities shown by red (inner) bars. Segments tracing to pan-eudicot triplication ( $\gamma$ ) are shown by green (outer) bars with colours representing the seven putative pre- $\gamma$  eudicot ancestral chromosomes<sup>10</sup>, also coded a–g.



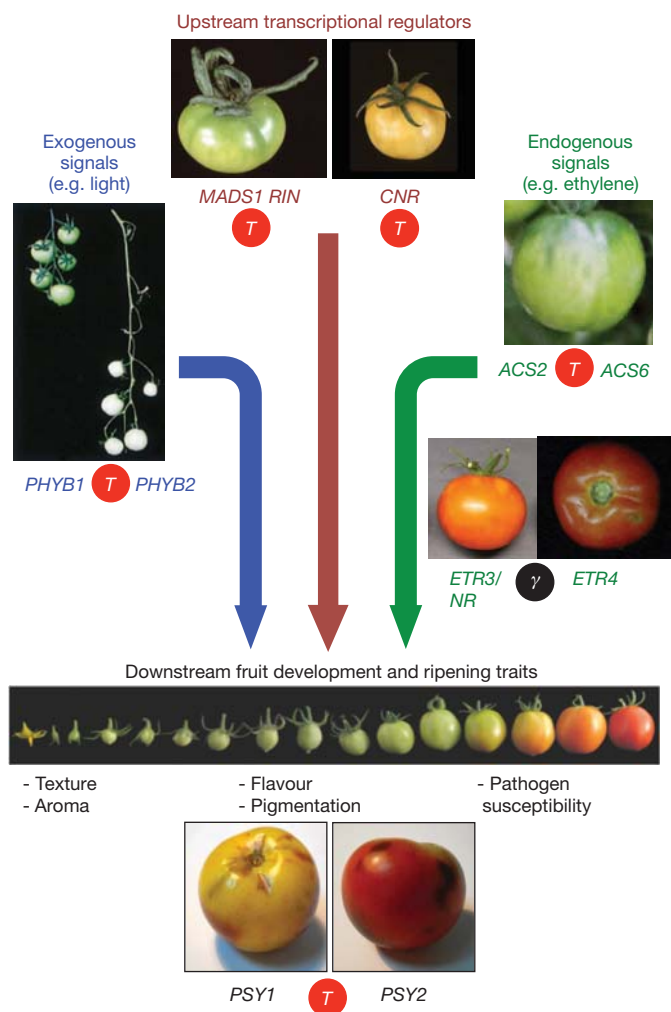


**Figure 3 | Whole-genome triplications set the stage for fruit-specific gene neofunctionalization.** The genes shown represent a fruit ripening control network regulated by transcription factors (*MADS-RIN*, *CNR*) necessary for production of the ripening hormone ethylene, the production of which is regulated by ACC synthase (*ACS*). Ethylene interacts with ethylene receptors (*ETRs*) to drive expression changes in output genes, including phytoene synthase (*PSY*), the rate-limiting step in carotenoid biosynthesis. Light, acting through phytochromes, controls fruit pigmentation through an ethylene-independent pathway. Paralogous gene pairs with different physiological roles (*MADS1/RIN*, *PHYB1/PHYB2*, *ACS2/ACS6*, *ETR3/ETR4*, *PSY1/PSY2*), were generated during the eudicot ( $\gamma$ , black circle) or the more recent *Solanum* (*T*, red circle) triplications. Complete dendrograms of the respective protein families are shown in Supplementary Figs 16 and 17.

that now dominate the tomato mechanical harvesting industry<sup>21</sup>. The genome sequence has revealed that the *SP* family has expanded in the *Solanum* lineage compared to *Arabidopsis*, driven by the *Solanum* triplication and tandem duplication (Supplementary Fig. 13). In potato, *SP3D* and *SP6A* control flowering and tuberization, respectively<sup>22</sup>, whereas *SP3D* in tomato, known as *SINGLE FLOWER TRUSS*, similarly controls flowering, but also drives heterosis for fruit yield in an epistatic relationship with *SP23-25*. Interestingly, *SP6A* in *S. lycopersicum* is inactivated by a premature stop codon, but remains functionally intact in *S. pimpinellifolium*. Thus, allelic variation in a subset of *SP* family genes has played a major role in the generation of both shared and species-specific variation in solanaceous agricultural traits.

The genome sequences of tomato and *S. pimpinellifolium* also provide a basis for understanding the bottlenecks that have narrowed tomato genetic diversity: the domestication of *S. pimpinellifolium* in the Americas, the export of a small number of genotypes to Europe in

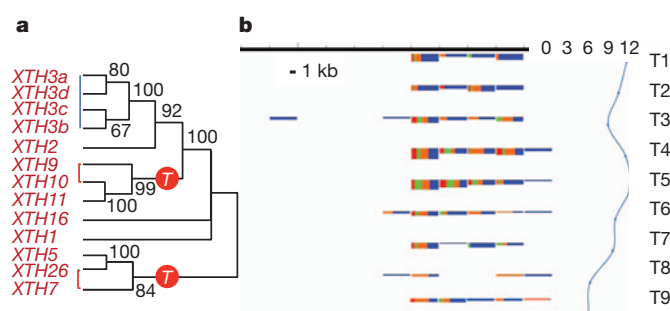


**Figure 4 | The tomato genome allows systems approaches to fruit biology.**

**a**, Xyloglucan transglucosylase/hydrolases (*XTHs*) differentially expressed between mature green and ripe fruits (Supplementary Information section 5.7). These *XTH* genes and many others are expressed in ripening fruits and are linked with the *Solanum* triplication, marked with a red circle on the phylogenetic tree. Red lines on the tree denote paralogs derived from the *Solanum* triplication, and blue lines are tandem duplications.

**b**, Developmentally regulated accumulation of sRNAs mapping to the promoter region of a fruit-regulated cell wall gene (pectin acetyltransferase, Solyc08g005800). Variation of abundance of sRNAs (left) and messenger RNA expression levels from the corresponding gene (right) over a tomato fruit developmental series (T1, bud; T2, flower; T3, fruit 1–3 mm; T4, fruit 5–7 mm; T5, fruit 11–13 mm; T6, fruit mature green; T7, breaker; T8, breaker + 3 days; T9, breaker + 7 days). The promoter regions are grouped in 100-nucleotide windows. For each window the size class distribution of sRNAs is shown (red, 21; green, 22; orange, 23; blue, 24). The height of the box corresponding to the first time point shows the cumulative sRNA abundance in log scale. The height of the following boxes is proportional to the log offset fold change (offset = 20) relative to the first time point. The expression profile of the mRNA is shown in log<sub>2</sub> scale. The horizontal black line represents 1 kb of the promoter region. 0 to 12 represent arbitrary units of gene expression.

the 16th century, and the intensive breeding that followed. Charles Rick pioneered the use of trait introgression from wild tomato relatives to increase genetic diversity of cultivated tomatoes<sup>26</sup>. Introgression lines exist for seven wild tomato species, including *S. pimpinellifolium*, in the background of cultivated tomato. The genome sequences presented here and the availability of millions of SNPs will allow breeders to revisit this rich trait reservoir and identify domestication genes, providing biological knowledge and empowering biodiversity-based breeding.

## METHODS SUMMARY

A total of 21 gigabases (Gb) of Roche/454 Titanium shotgun and mate pair reads and 3.3 Gb of Sanger paired-end reads, including ~200,000 BAC and fosmid end sequence pairs, were generated from the ‘Heinz 1706’ inbred line (Supplementary Information sections 1.1–1.7), assembled using both Newbler and CABOG and integrated into a single assembly (Supplementary Information sections 1.17 and 1.18). The scaffolds were anchored using two BAC-based physical maps, one high density genetic map, overgo hybridization and genome-wide BAC FISH (Supplementary Information sections 1.8–1.16 and 1.19). Over 99.9% of BAC/fosmid end pairs mapped consistently on the assembly and over 98% of EST sequences could be aligned to the assembly (Supplementary Information section 1.20). Chloroplast genome insertions in the nuclear genome were validated using a mate pair method and the flanking regions were identified (Supplementary Information sections 1.22–1.24). Annotation was carried out using a pipeline based on EuGene that integrates *de novo* gene prediction, RNA-Seq alignment and rich function annotation (Supplementary Information section 2). To facilitate interspecies comparison, the potato genome was re-annotated using the same pipeline. LTR retrotransposons were detected *de novo* with the LTR-STRUC program and dated by the sequence divergence between left and right solo LTR (Supplementary Information section 2.10). The genome of *S. pimpinellifolium* was sequenced to  $\times 40$  depth using Illumina paired end reads and assembled using ABySS (Supplementary Information section 3). The tomato and potato genomes were aligned using LASTZ (Supplementary Information section 4.1). Identification of triplicated regions was done using BLASTP, in-house-generated scripts and three-way comparisons between tomato, potato and *S. pimpinellifolium* using MCSCAN (Supplementary Information sections 4.2–4.4). Specific gene families/

groups (genes for ascorbate, carotenoid and jasmonate biosynthesis, cytochrome P450s, genes controlling cell wall architecture, hormonal and transcriptional regulators, resistance genes) were subjected to expert curation/analysis (Supplementary Information section 5). PHYML and MEGA were used to reconstruct phylogenetic trees and MCSCAN was used to infer gene collinearity (Supplementary Information section 5.2).

Received 17 August 2011; accepted 3 April 2012.

1. Frodin, D. G. History and concepts of big plant genera. *Taxon* **53**, 753–776 (2004).
2. Peralta, I. E., Spooner, D. M. & Knapp, S. Taxonomy of tomatoes: a revision of wild tomatoes (*Solanum* section *Lycopersicon*) and their outgroup relatives in sections *Juglandifolia* and *Lycopersicoides*. *Syst. Bot. Monogr.* **84**, 1–186 (2008).
3. Michaelson, M. J., Price, H. J., Ellison, J. R. & Johnston, J. S. Comparison of plant DNA contents determined by Feulgen microspectrophotometry and laser flow cytometry. *Am. J. Bot.* **78**, 183–188 (1991).
4. The Arabidopsis Genome Initiative. Analysis of the genome sequence of the flowering plant *Arabidopsis thaliana*. *Nature* **408**, 796–815 (2000).
5. Paterson, A. H. *et al.* The *Sorghum bicolor* genome and the diversification of grasses. *Nature* **457**, 551–556 (2009).
6. Zamir, D. & Tanksley, S. D. Tomato genome is comprised largely of fast-evolving, low copy-number sequences. *Mol. Gen. Genet.* **213**, 254–261 (1988).
7. Peterson, D. G., Pearson, W. R. & Stack, S. M. Characterization of the tomato (*Lycopersicon esculentum*) genome using *in vitro* and *in situ* DNA reassociation. *Genome* **41**, 346–356 (1998).
8. Xu, X. *et al.* Genome sequence and analysis of the tuber crop potato. *Nature* **475**, 189–195 (2011).
9. Swigoňová, Z. *et al.* Close split of sorghum and maize genome progenitors. *Genome Res.* **14**, 1916–1923 (2004).
10. Jaillon, O. *et al.* The grapevine genome sequence suggests ancestral hexaploidization in major angiosperm phyla. *Nature* **449**, 463–467 (2007).
11. Tang, H. *et al.* Synteny and collinearity in plant genomes. *Science* **320**, 486–488 (2008).
12. Ranc, N., Munos, S., Santoni, S. & Causse, M. A clarified position for *Solanum lycopersicum* var. *cerasiforme* in the evolutionary history of tomatoes (solanaceae). *BMC Plant Biol.* **8**, 130 (2008).
13. Ozminkowski, R. Pedigree of variety Heinz 1706. *Rep. Tomato Genet. Coop.* **54**, 26 (2004).
14. Moore, M. J., Soltis, P. S., Bell, C. D., Burleigh, J. G. & Soltis, D. E. Phylogenetic analysis of 83 plastid genes further resolves the early diversification of eudicots. *Proc. Natl Acad. Sci. USA* **107**, 4623–4628 (2010).
15. Stockey, R. A., Graham, S. W. & Crane, P. R. Introduction to the Darwin special issue: the abominable mystery. *Am. J. Bot.* **96**, 3–4 (2009).
16. Howe, H. F. & Smallwood, J. Ecology of seed dispersal. *Annu. Rev. Ecol. Syst.* **13**, 201–228 (1982).
17. Klee, H. J. & Giovannoni, J. J. Genetics and control of tomato fruit ripening and quality attributes. *Annu. Rev. Genet.* **45**, 41–59 (2011).
18. Vicente, A. R., Saladié, M., Rose, J. K. C. & Labavitch, J. M. The linkage between cell wall metabolism and fruit softening: looking to the future. *J. Sci. Food Agric.* **87**, 1435–1448 (2007).
19. Mohorianu, I. *et al.* Profiling of short RNAs during fleshy fruit development reveals stage-specific sRNAome expression patterns. *Plant J.* **67**, 232–246 (2011).
20. Corbesier, L. *et al.* FT protein movement contributes to long-distance signaling in floral induction of *Arabidopsis*. *Science* **316**, 1030–1033 (2007).
21. Rick, C. M. The tomato. *Sci. Am.* **239**, 76–87 (1978).
22. Navarro, C. *et al.* Control of flowering and storage organ formation in potato by FLOWERING LOCUS T. *Nature* **478**, 119–122 (2011).
23. Lifschitz, E. *et al.* The tomato *FT* ortholog triggers systemic signals that regulate growth and flowering and substitute for diverse environmental stimuli. *Proc. Natl Acad. Sci. USA* **103**, 6398–6403 (2006).
24. Krieger, U., Lippman, Z. B. & Zamir, D. The flowering gene *SINGLE FLOWER TRUSS* drives heterosis for yield in tomato. *Nature Genet.* **42**, 459–463 (2010).
25. Pnueli, L. *et al.* The *SELF-PRUNING* gene of tomato regulates vegetative to reproductive switching of sympodial meristems and is the ortholog of *CEN* and *TFL1*. *Development* **125**, 1979–1989 (1998).
26. Rick, C. M. Hybridization between *Lycopersicon esculentum* and *Solanum pennellii*: phylogenetic and cytogenetic significance. *Proc. Natl Acad. Sci. USA* **46**, 78–82 (1960).
27. Barker, M. S. *et al.* Multiple paleopolyploidizations during the evolution of the Compositae reveal parallel patterns of duplicate gene retention after millions of years. *Mol. Biol. Evol.* **25**, 2445–2455 (2008).
28. Aagaard, J. E., Willis, J. H. & Phillips, P. C. Relaxed selection among duplicate floral regulatory genes in Lamiales. *J. Mol. Evol.* **63**, 493–503 (2006).

Supplementary Information is linked to the online version of the paper at [www.nature.com/nature](http://www.nature.com/nature).

**Acknowledgements** This work was supported by: Argentina: INTA and CONICET. Belgium: Flemish Institute for Biotechnology and Ghent University. China: The State Key Laboratory of Plant Genomics, Institute of Genetics and Developmental Biology, Chinese Academy of Sciences; Ministry of Science and Technology (2006AA10A116, 2004CB720405, 2006CB101907, 2007DFB30080) Ministry of Agriculture ('948' Program: 2007-Z5); National Natural Science Foundation (36171319); Postdoctoral Science Foundation (20070420446). European Union: FP6 Integrated Project EU-SOL PL 016214. France: Institut National de la Recherche Agronomique and Agence Nationale de la Recherche. Germany: the Max Planck Society. India: Department of

Biotechnology, Government of India; Indian Council of Agricultural Research. Italy: Ministry of Research (FIRB-SOL, FIRB-Parallelomics, Italycy and GenoPOM projects); Ministry of Agriculture (Agronotech and Biomassal projects); FILAS foundation; ENEA; CNR-ENEA project L. 191/2009. Japan: Kazusa DNA Research Institute Foundation and National Institute of Vegetable and Tea Science. Korea: KRIBB Basic Research Fund and Crop Functional Genomics Research Center (CFG), MEST. Netherlands: Centre for BioSystems Genomics, Netherlands Organization for Scientific Research. Spain: Fundación Genoma España; Cajamar; FEPEX; Fundación Séneca; ICIA; IFAPA; Fundación Manrique de Lara; Instituto Nacional de Bioinformática. UK: BBSRC grant BB/C509731/1; DEFRA; SEERAD. USA: NSF (DBI-0116076; DBI-0421634; DBI-0606595; IOS-0923312; DBI-0820612; DBI-0605659; DEB-0316614; DBI 0849896 and MCB 1021718); USDA (2007-02773 and 2007-35300-19739); USDA-ARS. We acknowledge the Potato Genome Sequencing Consortium for sharing data before publication; potato RNA-Seq data was provided by C. R. Buell from the NSF-funded Potato Genome Sequence and Annotation project; tomato RNA-Seq data by the USDA-funded SolCAP project, N. Sinha and J. Maloof; the Amplicon Express team for BAC pooling services; construction of the Whole Genome Profiling (WGP) physical map was supported by EnzaZaden, RijkZwaan, Vilmorin & Cie, and Takii & Co. Keygene N.V. owns patents and patent applications covering its AFLP and Whole Genome Profiling technologies; AFLP and Keygene are registered trademarks of Keygene N.V. The following individuals are also acknowledged for their contribution to the work described: J. Park, B. Wang, C. Niu, D. Liu, F. Cojutti, S. Pescarolo, A. Zamboni, G. Xiao, J. Chen, J. Shi, L. Zhang, L. Zeng, M. Caccamo, D. Bolser, D. Martin, M. Gonzalez, P. A. Bedinger, P. A. Covey, P. Pachori, R. R. Pousada, S. Hakim, S. Sims, V. Cahais, W. Long, X. Zhou, Y. Lu, W. Haso, C. Lai, S. Lepp, C. Peluso, H. Teramu, H. De Jong, R. Lizarralde, E. R. May and Z. Li. M. Zabeau is thanked for his support and encouragement and S. van den Brink for her secretarial support. We dedicate this work to the late C. Rick who pioneered tomato genetics, collection of wild germplasm and the distribution of seed and knowledge.

**Author Contributions** For full details of author contributions, please see the Supplementary Information.

**Author Information** The genomic data generated by the whole project are available in GenBank as accession number AEKE00000000, and the individual chromosome sequences as numbers CM001064–CM001075. The RNA-Seq data are available in the Sequence Read Archive under accession number SRA049915, GSE33507, SRA050797 and SRA048144. Further information on data access can be found in Supplementary Information section 2.2. Reprints and permissions information is available at [www.nature.com/reprints](http://www.nature.com/reprints). The authors declare no competing financial interests. This paper is distributed under the terms of the Creative Commons Attribution-Non-Commercial-Share Alike licence, and is freely available to all readers at [www.nature.com/nature](http://www.nature.com/nature). Readers are welcome to comment on the online version of this article at [www.nature.com/nature](http://www.nature.com/nature). Correspondence and requests for materials should be addressed to D.Z. ([zamir@agri.huji.ac.il](mailto:zamir@agri.huji.ac.il)) or G.G. ([giovanni.giuliano@enea.it](mailto:giovanni.giuliano@enea.it)).

## The Tomato Genome Consortium

**Kazusa DNA Research Institute** Shusei Sato (Principal Investigator)<sup>1</sup>, Satoshi Tabata (Principal Investigator)<sup>1</sup>, Hideki Hirakawa<sup>1</sup>, Erika Asamizu<sup>1</sup>, Kenta Shirasawa<sup>1</sup>, Sachiko Isobe<sup>1</sup>, Takakazu Kaneko<sup>1</sup>, Yasukazu Nakamura<sup>1</sup>, Daisuke Shibata<sup>1</sup>, Koh Aoki<sup>1</sup>; **454 Life Sciences, a Roche company** Michael Egholm<sup>2</sup>, James Knight<sup>2</sup>; **Amplicon Express Inc.** Robert Bogden<sup>3</sup>; **Beijing Academy of Agriculture and Forestry Sciences** Changbao Li<sup>4,5</sup>; **BGI-Shenzhen** Yang Shuang<sup>6</sup>, Xun Xu<sup>6</sup>, Shengkai Pan<sup>6</sup>, Shifeng Cheng<sup>6</sup>, Xin Liu<sup>6</sup>, Yuan Yuan Ren<sup>6</sup>, Jun Wang<sup>6</sup>; **BMR-Genomics SRL** Alessandro Albiero<sup>7</sup>, Francesca Dal Pero<sup>7</sup>, Sara Todesco<sup>7</sup>; **Boyce Thompson Institute for Plant Research** Joyce Van Eck<sup>8</sup>, Robert M. Buels<sup>8</sup>, Aureliano Bombarely<sup>8</sup>, Joseph R. Gosselin<sup>8</sup>, Minyun Huang<sup>8</sup>, Jonathan A. Leto<sup>8</sup>, Naama Menda<sup>8</sup>, Susan Strickler<sup>8</sup>, Linyong Mao<sup>8</sup>, Shan Gao<sup>8</sup>, Isaac Y. Tecle<sup>8</sup>, Thomas York<sup>8</sup>, Yi Zheng<sup>8</sup>, Julia T. Vrebalov<sup>8</sup>, JeMin Lee<sup>8</sup>, Silin Zhong<sup>8</sup>, Lukas A. Mueller (Principal Investigator)<sup>8</sup>; **Centre for BioSystems Genomics** Willem J. Stiekema<sup>9</sup>; **Centro Nacional de Análisis Genómico (CNAG)** Paolo Ribeca<sup>10</sup>, Tyler Alioto<sup>10</sup>; **China Agricultural University** Wencai Yang<sup>11</sup>; **Chinese Academy of Agricultural Sciences** Sanwen Huang (Principal Investigator)<sup>12</sup>, Yongchen Du (Principal Investigator)<sup>12</sup>, Zhonghua Zhang<sup>12</sup>, Jianchang Gao<sup>12</sup>, Yanmei Guo<sup>12</sup>, Xiaoxuan Wang<sup>12</sup>, Ying Li<sup>12</sup>, Jun He<sup>12</sup>; **Chinese Academy of Sciences** Chuanyou Li (Principal Investigator)<sup>13</sup>, Zhukuan Cheng (Principal Investigator)<sup>13</sup>, Jianru Zuo (Principal Investigator)<sup>13</sup>, Jianfeng Ren<sup>13</sup>, Jiahai Zhao<sup>13</sup>, Lihua Yan<sup>13</sup>, Hongling Jiang<sup>13</sup>, Bao Wang<sup>13</sup>, Hongshuang Li<sup>13</sup>, Zhenjun Li<sup>13</sup>, Fuyou Fu<sup>13</sup>, Bingtang Chen<sup>13</sup>, Bin Han (Principal Investigator)<sup>14</sup>, Qi Feng<sup>14</sup>, Danlin Fan<sup>14</sup>, Ying Wang (Principal Investigator)<sup>14</sup>, Hongqing Ling (Principal Investigator)<sup>15</sup>, Yongbiao Xue (Principal Investigator)<sup>16</sup>; **Cold Spring Harbor Laboratory and United States Department of Agriculture – Agricultural Research Service** Doreen Ware (Principal Investigator)<sup>17</sup>, W. Richard McCombie (Principal Investigator)<sup>17</sup>, Zachary B. Lippman (Principal Investigator)<sup>17</sup>, Jer-Ming Chia<sup>17</sup>, Ke Jiang<sup>17</sup>, Shiran Pasternak<sup>17</sup>, Laura Gelley<sup>17</sup>, Melissa Kramer<sup>17</sup>; **Colorado State University** Lorinda K. Anderson<sup>18</sup>, Song-Bin Chang<sup>19</sup>, Suzanne M. Royer<sup>18</sup>, Lindsay A. Shearer<sup>18</sup>, Stephen M. Stack (Principal Investigator)<sup>18</sup>; **Cornell University** Jocelyn K. C. Rose<sup>20</sup>, Yimin Xu<sup>20</sup>, Nancy Eannetta<sup>20</sup>, Antonio J. Matas<sup>20</sup>, Ryan McQuinn<sup>20</sup>, Steven D. Tanksley (Principal Investigator)<sup>20</sup>; **Genome Bioinformatics Laboratory GRIB-IMIM/UPF/CRG** Francisco Camara<sup>21</sup>, Roderic Guigó<sup>21</sup>; **Ghent University-VIB** Stéphane Rombauts<sup>22</sup>, Jeffrey Fawcett<sup>22</sup>, Yves Van de Peer (Principal Investigator)<sup>22</sup>; **Hebrew University of Jerusalem** Dani Zamir<sup>23</sup>; **Heilongjiang Academy of Agricultural Sciences** Chunbo Liang<sup>24</sup>; **Helmholtz Center for Health and Environment** Manuel Spannagl<sup>25</sup>, Helmut Gundlach<sup>25</sup>, Remy Bruggmann<sup>25</sup>, Klaus Mayer (Principal Investigator)<sup>25</sup>; **Henan**



- Agricultural University** Zhiqi Jia<sup>26</sup>, **Huazhong Agricultural University** Junhong Zhang<sup>27</sup>, Zhibiao Ye<sup>27</sup>, **Imperial College London** Gerard J. Bishop (Principal Investigator)<sup>28</sup>, Sarah Butcher (Principal Investigator)<sup>28</sup>, Rosa Lopez-Cobollo<sup>28</sup>, Daniel Buchan<sup>28</sup>, Ioannis Filippis<sup>28</sup>, James Abbott<sup>28</sup>, **Indian Agricultural Research Institute** Rekha Dixit<sup>29</sup>, Manju Singh<sup>29</sup>, Archana Singh<sup>29</sup>, Jitendra Kumar Pal<sup>29</sup>, Awadhesh Pandit<sup>29</sup>, Pradeep Kumar Singh<sup>29</sup>, Ajay Kumar Mahato<sup>29</sup>, Vivek Dogra<sup>29</sup>, Kishor Gaikwad<sup>29</sup>, Tilak Raj Sharma<sup>29</sup>, Trilochan Mohapatra<sup>29</sup>, **Nagendra Kumar Singh (Principal Investigator)**<sup>29</sup>, **INRA Avignon** Mathilde Causse<sup>30</sup>, **INRA Bordeaux** Christophe Rothan<sup>31</sup>, **INRA Toulouse** Thomas Schiex (Principal Investigator)<sup>32</sup>, Céline Noiroit<sup>32</sup>, Arnaud Bellec<sup>33</sup>, Christophe Klopp<sup>34</sup>, Corinne Delalande<sup>35</sup>, Hélène Berges<sup>33</sup>, Jérôme Mariette<sup>34</sup>, Pierre Frasse<sup>35</sup>, Sonia Vautrin<sup>33</sup>, **Institut National Polytechnique de Toulouse** Mohamed Zouine<sup>35</sup>, Alain Latché<sup>35</sup>, Christine Rousseau<sup>35</sup>, Farid Regad<sup>35</sup>, Jean-Claude Pech<sup>35</sup>, Murielle Philippot<sup>35</sup>, **Mondher Bouzayen (Principal Investigator)**<sup>35</sup>, **Instituto de Biología Molecular y Celular de Plantas (CSIC-UPV)** Pierre Pericard<sup>36</sup>, Sonia Osorio<sup>36</sup>, Asunción Fernandez del Carmen<sup>36</sup>, Antonio Monforte<sup>36</sup>, Antonio Granell (Principal Investigator)<sup>36</sup>, **Instituto de Hortofruticultura Subtropical y Mediterránea (IHSM-UMA-CSIC)** Rafael Fernandez-Muñoz<sup>37</sup>, **Instituto Nacional de Tecnología Agropecuaria (IB-INTA)** and **Consejo Nacional de Investigaciones Científicas y Técnicas (CONICET)** Mariana Conte<sup>38</sup>, Gabriel Lichtenstein<sup>38</sup>, Fernando Carrari (Principal Investigator)<sup>38</sup>, **Italian National Research Council, Institute for Biomedical Technologies** Gianluca De Bellis (Principal Investigator)<sup>39</sup>, Fabio Fuligni<sup>39</sup>, Clelia Peano<sup>39</sup>, **Italian National Research Council, Institute of Plant Genetics, Research Division Portici** Silvana Grandillo<sup>40</sup>, Pasquale Termolino<sup>40</sup>, **Italian National Agency for New Technologies, Energy and Sustainable Development** Marco Pietrella<sup>41,42</sup>, Elio Fantini<sup>41</sup>, Giulia Falcone<sup>41</sup>, Alessia Fiore<sup>41</sup>, Giovanni Giuliano (Principal Investigator)<sup>41</sup>, Loredana Lopez<sup>43</sup>, Paolo Falca<sup>43</sup>, Gaetano Perrotta<sup>43</sup>, Loretta Daddiego<sup>43</sup>, James Hutton Institute Glenn Bryan (Principal Investigator)<sup>44</sup>, Joint IRB-BSC program on Computational Biology Modesto Orozco<sup>45,46</sup>, Xavier Pastor<sup>45</sup>, David Torrents<sup>45,47</sup>, Keygene N.V. Marco G. M. van Schriek<sup>48</sup>, Richard M.C. Feron<sup>48</sup>, Jan van Oeveren<sup>48</sup>, Peter de Heer<sup>48</sup>, Lorena da Ponte<sup>48</sup>, Saskia Jacobs-Oomen<sup>48</sup>, Mike Carriaso<sup>48</sup>, Marcel Prins<sup>48</sup>, Michiel J. T. van Eijk (Principal Investigator)<sup>48</sup>, Antoine Janssen<sup>48</sup>, Mark J. J. van Haaren<sup>48</sup>, **Korea Research Institute of Bioscience and Biotechnology** Sung-Hwan Jo<sup>49</sup>, Jungeun Kim<sup>49</sup>, Suk-Yoon Kwon<sup>49</sup>, Sangmi Kim<sup>49</sup>, Dal-Hoe Koo<sup>49</sup>, Sanghyeob Lee<sup>49</sup>, Cheol-Goo Hur<sup>49</sup>, **Life Technologies** Christopher Clouser<sup>50</sup>, Alain Rico<sup>51</sup>, **Max Planck Institute for Plant Breeding Research** Asis Hallab<sup>52</sup>, Christiane Gebhardt<sup>52</sup>, Kathrin Klee<sup>52</sup>, Anika Jöcker<sup>52</sup>, Jens Warfsmann<sup>52</sup>, Ulrike Göbel<sup>52</sup>, **Meiji University** Shingo Kawamura<sup>53</sup>, Kentaro Yano<sup>53</sup>, **Montana State University** Jamie D. Sherman<sup>54</sup>, **NARO Institute of Vegetable and Tea Science** Hiroyuki Fukuoka (Principal Investigator)<sup>55</sup>, Satomi Negoro<sup>55</sup>, **National Institute of Plant Genome Research** Sarita Bhutty<sup>56</sup>, Parul Chowdhury<sup>56</sup>, Debasis Chattopadhyay (Principal Investigator)<sup>56</sup>, **Plant Research International** Erwin Datema<sup>48,57</sup>, Sandra Smit<sup>57</sup>, Elio G. W. M. Schijlen<sup>57</sup>, Jose van de Belt<sup>57</sup>, Jan C. van Haarst<sup>57</sup>, Sander A. Peters<sup>57</sup>, Marjo J. van Staveren<sup>57</sup>, Marleen H. C. Henkens<sup>57</sup>, Paul J. W. Mooyman<sup>57</sup>, Tamara Hesselink<sup>57</sup>, Roeland C. H. J. van Ham (Principal Investigator)<sup>48,57</sup>, **Qingdao Agricultural University** Guoyong Jiang<sup>58</sup>, **Roche Applied Science** Marcus Droege<sup>59</sup>, **Seoul National University** Doil Choi (Principal Investigator)<sup>60</sup>, Byung-Cheol Kang<sup>60</sup>, Byung Dong Kim<sup>60</sup>, Minkyu Park<sup>60</sup>, Seungill Kim<sup>60</sup>, Seon-In Yeom<sup>60</sup>, Yong-Hwan Lee<sup>61</sup>, Yang-Do Choi<sup>62</sup>, **Shandong Academy of Agricultural Sciences** Guangcun Li<sup>63</sup>, Jianwei Gao<sup>64</sup>, **Sichuan University** Yongsheng Liu<sup>65</sup>, Shengxiang Huang<sup>65</sup>, **Sistemas Genómicos** Victoria Fernandez-Pedrosa<sup>66</sup>, Carmen Collado<sup>66</sup>, Sheila Zuñiga<sup>66</sup>, **South China Agricultural University** Guoping Wang<sup>67</sup>, **Syngenta Biotechnology** Rebecca Cade<sup>68</sup>, Robert A. Dietrich<sup>68</sup>, **The Genome Analysis Centre** Jane Rogers (Principal Investigator)<sup>69</sup>, **The Natural History Museum** Sandra Knapp<sup>70</sup>, **United States Department of Agriculture – Agricultural Research Service**, Robert W. Holley Center and Boyce Thompson Institute for Plant Research Zhangjun Fei (Principal Investigator)<sup>8,71</sup>, Ruth A. White<sup>8,71</sup>, Theodore W. Thannhauser<sup>8,71</sup>, James J. Giovannoni (Principal Investigator)<sup>8,20,71</sup>, **Universidad de Málaga-Consejo Superior de Investigaciones Científicas** Miguel Angel Botella<sup>72</sup>, Louise Gilbert<sup>72</sup>, **Université Pompeu Fabra** Ramon Gonzalez<sup>73</sup>, **University of Arizona** Jose Luis Goicoechea<sup>74</sup>, Yeisoo Yu<sup>74</sup>, David Kudrna<sup>74</sup>, Kristi Collura<sup>74</sup>, Marina Wissotski<sup>74</sup>, Rod Wing (Principal Investigator)<sup>74</sup>, **University of Bonn** Heiko Schoof (Principal Investigator)<sup>75</sup>, **University of Delaware** Blake C. Meyers (Principal Investigator)<sup>76</sup>, Aishwarya Bala Gurazada<sup>76</sup>, Pamela J. Green<sup>76</sup>, **University of Delhi South Campus** Saloni Mathur<sup>77</sup>, Shailendra Vyas<sup>77</sup>, Amolkumar U. Solanke<sup>77</sup>, Rahul Kumar<sup>77</sup>, Vikrant Gupta<sup>77</sup>, Arun K. Sharma<sup>77</sup>, Paramjit Khurana<sup>77</sup>, Jitendra P. Khurana (Principal Investigator)<sup>77</sup>, Akhilesh K. Tyagi (Principal Investigator)<sup>77</sup>, **University of East Anglia, School of Biological Sciences** Tamas Dalmay (Principal Investigator)<sup>78</sup>, **University of East Anglia, School of Computing Sciences** Irina Mohorianu<sup>79</sup>, **University of Florida** Brandon Walts<sup>80</sup>, Srikanth Chamala<sup>80</sup>, W. Brad Barbazuk<sup>80</sup>, **University of Georgia** Jingping Li<sup>81</sup>, Hui Guo<sup>81</sup>, Tae-Ho Lee<sup>81</sup>, Yupeng Wang<sup>81</sup>, Dong Zhang<sup>81</sup>, Andrew H. Paterson (Principal Investigator)<sup>81</sup>, Xiyin Wang (Principal Investigator)<sup>81,82</sup>, Haibao Tang<sup>81,83</sup>, **University of Naples “Federico II”** Amalia Barone<sup>84</sup>, Maria Luisa Chiusano<sup>84</sup>, Maria Raffaella Ercolano<sup>84</sup>, Nunzio D’Agostino<sup>84</sup>, Miriam Di Filippo<sup>84</sup>, Alessandra Traini<sup>84</sup>, Walter Sanseverino<sup>84</sup>, Luigi Frusciante (Principal Investigator)<sup>84</sup>, **University of Nottingham** Graham B. Seymour (Principal Investigator)<sup>85</sup>, **University of Oklahoma** Mounir Elharan<sup>86</sup>, Ying Fu<sup>86</sup>, Axin Hua<sup>86</sup>, Steven Kenton<sup>86</sup>, Jennifer Lewis<sup>86</sup>, Shaoping Lin<sup>86</sup>, Fares Najjar<sup>86</sup>, Hongshing Lai<sup>86</sup>, Baifang Qin<sup>86</sup>, Chunmei Qu<sup>86</sup>, Ruihua Shi<sup>86</sup>, Douglas White<sup>86</sup>, James White<sup>86</sup>, Yanbo Xing<sup>86</sup>, Keqin Yang<sup>86</sup>, Jing Yi<sup>86</sup>, Ziyun Ya<sup>86</sup>, Liping Zhou<sup>86</sup>, Bruce A. Roe (Principal Investigator)<sup>86</sup>, **University of Padua** Alessandro Vezzi<sup>87</sup>, Michela D’Angelo<sup>87</sup>, Rosanna Zimbello<sup>87</sup>, Riccardo Schiavon<sup>87</sup>, Elisa Caniato<sup>87</sup>, Chiara Rigobello<sup>87</sup>, Davide Campagna<sup>87</sup>, Nicola Vitulo<sup>87</sup>, Giorgio Valle (Principal Investigator)<sup>87</sup>, **University of Tennessee Health Science Center** David R. Nelson<sup>88</sup>, **University of Udine** Emanuele De Paoli<sup>89</sup>, **Wageningen University** Dora Szinay<sup>90,91</sup>, Hans H. de Jong (Principal Investigator)<sup>90</sup>, Yuling Bai<sup>91</sup>, Richard G. F. Visser<sup>91</sup>, René M. Klein Lankhorst (Principal Investigator)<sup>92</sup>, **Wellcome Trust Sanger Institute** Helen
- Beasley<sup>93</sup>, Karen McLaren<sup>93</sup>, Christine Nicholson<sup>93</sup>, Claire Riddle<sup>93</sup>, Ylchiron S.R.L. Giulio Gianese<sup>94</sup>



China. <sup>65</sup>School of Life Sciences, Sichuan University, Chengdu, Sichuan 610064, China. <sup>66</sup>Sistemas Genómicos, Parque Tecnológico de Valencia, Ronda G. Marconi, 6, 46980 Paterna (Valencia), Spain. <sup>67</sup>College of Horticulture, South China Agricultural University, 510642 Guangzhou, China. <sup>68</sup>Syngenta Biotechnology, Inc. 3054 East Cornwallis Road, Research Triangle Park, North Carolina 27709 Durham, USA. <sup>69</sup>Norwich Research Park, Norwich NR4 7UH, UK. <sup>70</sup>Department of Botany, The Natural History Museum, Cromwell Road, London SW7 5BD, UK. <sup>71</sup>United States Department of Agriculture - Agricultural Research Service, Robert W. Holley Center, Tower Road, Cornell University campus, Ithaca, New York 14853, USA. <sup>72</sup>Instituto de Hortofruticultura Subtropical y Mediterránea. Departamento de Biología Molecular y Bioquímica, 29071 Málaga, Spain. <sup>73</sup>Centre de Regulació Genòmica, Universitat Pompeu Fabra, Dr Aiguader, 88, E-08003 Barcelona, Spain. <sup>74</sup>Arizona Genomics Institute, BIO-5 Institute for Collaborative Research, School of Plant Sciences, Thomas W. Keating Building, 1657 E. Helen Street, Tucson, Arizona 85721, USA. <sup>75</sup>Crop Bioinformatics, Institute of Crop Science and Resource Conservation, University of Bonn, 53115 Bonn, Germany. <sup>76</sup>Department of Plant and Soil Sciences, and Delaware Biotechnology Institute, University of Delaware, Newark, Delaware 19711, USA. <sup>77</sup>Interdisciplinary Centre for Plant Genomics and Department of Plant Molecular Biology, University of Delhi South Campus, New Delhi 110 021, India. <sup>78</sup>University of East Anglia, BIO, Norwich NR4 7TJ, UK. <sup>79</sup>University of East Anglia, CMP, Norwich NR4 7TJ, UK. <sup>80</sup>Department of Biology and the UF Genetics Institute, Cancer and Genetics Research Complex 2033 Mowry Road, PO Box 103610, Gainesville, Florida 32610, USA. <sup>81</sup>Plant Genome Mapping Laboratory, 111 Riverbend Road, University of Georgia, Athens, Georgia 30602, USA. <sup>82</sup>Center for Genomics and Computational Biology, School of Life Sciences, and School of Sciences, Hebei United University, Tangshan, Hebei 063000, China. <sup>83</sup>J. Craig Venter Institute, 9704 Medical Center Drive, Rockville, Maryland 20850, USA. <sup>84</sup>University of Naples "Federico II" Department of Soil, Plant, Environmental and Animal Production Sciences, Via Università', 100, 80055 Portici (Naples), Italy. <sup>85</sup>Division of Plant and Crop Sciences, University of Nottingham, Sutton Bonington, Loughborough LE12 5RD, UK. <sup>86</sup>Department of Chemistry and Biochemistry, Stephenson Research and Technology Center, University of Oklahoma, Norman, Oklahoma 73019, USA. <sup>87</sup>CRIBI, University of Padua, via Ugo Bassi 58/B, 35131 Padova, Italy. <sup>88</sup>Department of Microbiology, Immunology and Biochemistry, University of Tennessee Health Science Center, Memphis, Tennessee 38163, USA. <sup>89</sup>Department of Agriculture and Environmental Sciences, University of Udine, via delle Scienze 208, 33100, Udine, Italy. <sup>90</sup>Wageningen University, Laboratory of Genetics, Droevendaalsesteeg 1, 6708 PB Wageningen, The Netherlands. <sup>91</sup>Wageningen University, Laboratory of Plant Breeding, Droevendaalsesteeg 1, 6708 PB Wageningen, The Netherlands. <sup>92</sup>Wageningen University, Droevendaalsesteeg 1, 6708 PB Wageningen, The Netherlands. <sup>93</sup>Wellcome Trust Sanger Institute Hinxton, Cambridge CB10 1SA, UK. <sup>94</sup>Ylichron Srl, Casaccia Research Center, Via Anguillarese 301, 00123 Roma, Italy. †Present address: Plant Engineering Research Institute, Sejong University, Seoul, 143-747, Republic of Korea.

# Recurrent network activity drives striatal synaptogenesis

Yevgenia Kozorovitskiy<sup>1\*</sup>, Arpiar Saunders<sup>1\*</sup>, Caroline A. Johnson<sup>1</sup>, Bradford B. Lowell<sup>2</sup> & Bernardo L. Sabatini<sup>1</sup>

Neural activity during development critically shapes postnatal wiring of the mammalian brain. This is best illustrated by the sensory systems, in which the patterned feed-forward excitation provided by sensory organs and experience drives the formation of mature topographic circuits capable of extracting specific features of sensory stimuli<sup>1,2</sup>. In contrast, little is known about the role of early activity in the development of the basal ganglia, a phylogenetically ancient group of nuclei fundamentally important for complex motor action and reward-based learning<sup>3,4</sup>. These nuclei lack direct sensory input and are only loosely topographically organized<sup>5,6</sup>, forming interlocking feed-forward and feed-back inhibitory circuits without laminar structure. Here we use transgenic mice and viral gene transfer methods to modulate neurotransmitter release and neuronal activity *in vivo* in the developing striatum. We find that the balance of activity between the two inhibitory and antagonist pathways in the striatum regulates excitatory innervation of the basal ganglia during development. These effects indicate that the propagation of activity through a multi-stage network regulates the wiring of the basal ganglia, revealing an important role of positive feedback in driving network maturation.

Excitatory input from the cortex and thalamus enters the basal ganglia through the striatum, where it is locally processed and transformed into two inhibitory, GABAergic outputs called the direct and indirect pathways<sup>7</sup>. Each pathway arises from a distinct class of spatially intermixed medium spiny neurons (MSNs) with differing projections and molecular characteristics<sup>8</sup>. These projection patterns suggest opponent effects on basal ganglia output: direct pathway MSNs form synapses in substantia nigra reticulata (SNr), the basal ganglia output nucleus, whereas indirect pathway MSNs form synapses in globus pallidus, which in turn inhibits the SNr<sup>9</sup>. Because the SNr provides GABAergic inhibition to the thalamus, which subsequently activates cortex through glutamatergic synapses, the interactions of basal ganglia, thalamus and cortex can be simplified as a closed loop, differentially controlled by the direct and indirect pathways (Supplementary Fig. 1). Anatomical evidence supports this model<sup>10,11</sup> and the opponent roles of the two pathways on motor behaviour have been recently demonstrated in adult rodents<sup>12,13</sup>. In addition, *in vivo* recordings and circuit tracing indicate that different corticostriatal inputs are processed through segregated, parallel networks<sup>6,10,11,14</sup>. Given this organization, establishing correct wiring of the cortex-basal ganglia-thalamus circuitry poses a significant developmental challenge, requiring that functional interactions be maintained over polysynaptic networks comprised of mixed inhibitory and excitatory projections.

To investigate how striatal activity contributes to circuit development, we generated mice incapable of releasing GABA from direct or indirect pathway MSNs through conditional knockout of *Slc32a1*, which encodes the vesicular GABA transporter (VGAT) (Fig. 1)<sup>15</sup>. GABAergic neurons lacking VGAT are unable to package GABA into

synaptic vesicles for release<sup>16,17</sup>. Pathway specificity was conferred by bacterial artificial chromosome (BAC) transgenic mice that express Cre recombinase under the control of the type 1a or type 2 dopamine receptors<sup>18</sup>. In *Drd1a* Cre (D1-Cre) mice, Cre expression in GABAergic neurons is largely limited to direct pathway MSNs, although Cre is also found in non-GABAergic cortical neurons (Fig. 1a and Supplementary Figs 2 and 3). In *Drd2* Cre (D2-Cre) mice, Cre expression is largely limited to indirect pathway MSNs (Fig. 1a and Supplementary Fig. 2). Mice with *Slc32a1* deletion in direct or indirect pathway MSNs showed opposing locomotor phenotypes and survived

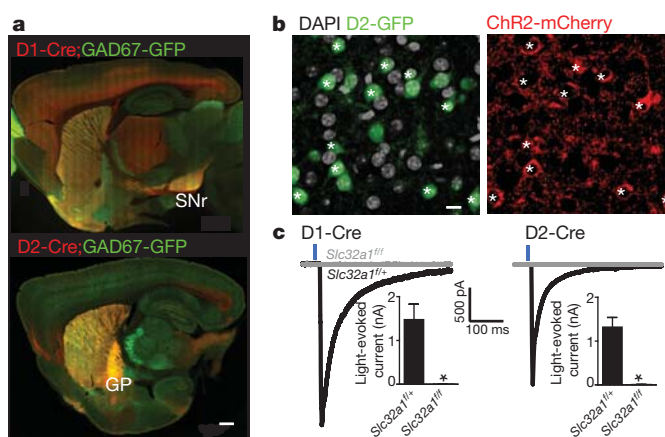


**Figure 1 | Conditional knockout of *Slc32a1* from direct or indirect pathway MSNs abolishes GABAergic output.** **a**, Cre expression driven by *Drd1a* (D1-Cre, top) and *Drd2* (D2-Cre, bottom) BACs was visualized via activation of tdTomato in a reporter mouse. Red fluorescence reveals expression throughout striatum and in axons in expected target nuclei of direct and indirect pathway MSNs (SNr and globus pallidus (GP), respectively). Green fluorescence reflects expression of a GAD67-GFP transgene that reports GABAergic neurons. As seen in the red channel, there is diffuse cortical expression of Cre in the D1-Cre mice; however, this occurs in non-GABAergic neurons as noted by the lack of overlap with GFP fluorescence (see Supplementary Fig. 2 for complete analysis). Scale bar: 500  $\mu$ m. **b**, AAV DIO-ChR2-mCherry injected into the striatum of a mouse carrying D2-Cre and D2-GFP transgenes shows ChR2-mCherry labelling in GFP<sup>+</sup> cells, indicating pathway-specific conditional expression of the virally encoded protein. ChR2-mCherry-expressing somata are marked with an asterisk and represent over two-thirds of the GFP<sup>+</sup> MSNs in the area of dense infection. ChR2-mCherry was never observed in GFP<sup>-</sup> MSNs in these mice. Scale bar: 10  $\mu$ m. **c**, Voltage-clamp recordings from ChR2-mCherry<sup>+</sup> MSNs demonstrate GABAergic synaptic currents evoked by 2-ms-long pulses of 473-nm light that stimulates neighbouring ChR2-mCherry<sup>+</sup> MSNs. Example currents from MSNs in D1-Cre (left) and D2-Cre (right) mice that were either homozygous (grey, *Slc32a1*<sup>+/f</sup>) or heterozygous (black, *Slc32a1*<sup>+/+</sup>) for the *Slc32a1* conditional allele are shown. GABAergic currents are inward due to high intracellular Cl<sup>-</sup> concentration. Insets: graphs of average peak current amplitudes evoked in mice of each genotype. \**P* < 0.05 for comparison of *Slc32a1*<sup>+/+</sup> and *Slc32a1*<sup>+/f</sup> data. Error bars indicate s.e.m.

<sup>1</sup>Howard Hughes Medical Institute, Department of Neurobiology, Harvard Medical School, 220 Longwood Ave, Boston, Massachusetts 02115, USA. <sup>2</sup>Endocrinology Division, Beth Israel Deaconess Medical Center, 330 Brookline Avenue, Boston, Massachusetts 02215, USA.

\*These authors contributed equally to this work.

until weaning (Supplementary Fig. 4), a time of increasing reliance on reward-based complex motor actions.

To test the efficacy of silencing of GABA release we relied on optogenetic analysis of MSN-to-MSN collateral synapses<sup>19</sup>. Channelrhodopsin 2-mCherry fusion protein (ChR2-mCherry) was expressed in Cre-positive MSNs by injecting an adeno-associated virus (AAV) containing a double floxed inverted ChR2-mCherry transgene into the striatum at postnatal (P) days 3–5 (Fig. 1b)<sup>20</sup>. Whole-cell voltage-clamp recordings of ChR2-negative MSNs demonstrated light-evoked GABAergic currents in acute brain slices from P13–18 *D1-cre;Slc32a1<sup>fl/+</sup>* mice ( $-1,477 \pm 352$  pA,  $n = 20$ ) and *D2-cre;Slc32a1<sup>fl/+</sup>* mice ( $-1,319 \pm 221$  pA,  $n = 12$ ); these currents were absent in littermate *Slc32a1<sup>fl/fl</sup>* mice (*D1-cre;Slc32a1<sup>fl/fl</sup>*,  $-2.19 \pm 1.6$  pA,  $n = 7$ ; *D2-cre;Slc32a1<sup>fl/fl</sup>*,  $-9.91 \pm 2.4$  pA,  $n = 7$ ) (Fig. 1c and Supplementary Fig. 5).

We examined whether GABA release from MSNs is required for cell survival and long-range axonal projections. The proportion of Cre<sup>+</sup> cell nuclei was 45–48% in D1-Cre and D2-Cre mice and independent of the number of conditional *Slc32a1* alleles (Supplementary Fig. 6). MSNs lacking GABA release form qualitatively normal long-range axonal projections, on the basis of examination of ChR2-mCherry fluorescence in the SNr and globus pallidus (SNr, 18–19%; globus pallidus, 15–16% fractional area coverage) (Supplementary Fig. 7). These observations confirm that MSNs lacking GABA release are maintained in normal numbers and extend grossly normal axons.

In contrast, silencing GABA release had profound consequences on the number of excitatory synapses received, which are typically associated with dendritic spines<sup>21,22</sup>. In the rodent striatum, inhibitory synapse density is relatively constant throughout postnatal development, whereas excitatory synapse density rises markedly between P10 and P21 (ref. 23). Therefore, we restricted analyses to pairs of littermate control and *Slc32a1* null mice at P14–15. We identified

MSNs of each pathway using ChR2-mCherry expression delivered by either Cre-On or Cre-Off AAVs (Supplementary Fig. 8a) (A. Saunders, C. Johnson and B. Sabatini, manuscript in preparation). Even within this narrow developmental window, we detected an increase in miniature excitatory postsynaptic current (mEPSC) frequencies, but not amplitudes, among littermates of the same genotype (frequency: P14,  $0.14 \pm 0.06$  Hz; P15,  $0.34 \pm 0.1$  Hz; amplitude: P14,  $14.4 \pm 1.0$  pA; P15,  $13.9 \pm 0.4$  pA) (Supplementary Fig. 8b). In mice lacking GABA release in direct pathway MSNs, mEPSC frequency was reduced in both direct and indirect pathway MSNs compared to heterozygous sibling controls (direct pathway MSNs: *D1-cre;Slc32a1<sup>fl/+</sup>*,  $0.22 \pm 0.04$  Hz,  $n = 18$ ; *D1-cre;Slc32a1<sup>fl/fl</sup>*,  $0.08 \pm 0.02$  Hz,  $n = 16$ ; indirect pathway MSNs: *D1-cre;Slc32a1<sup>fl/+</sup>*,  $0.32 \pm 0.07$  Hz,  $n = 14$ ; *D1-cre;Slc32a1<sup>fl/fl</sup>*,  $0.1 \pm 0.03$  Hz,  $n = 15$ ) (Fig. 2a, c). Conversely, mEPSC frequency was increased in MSNs of mice with output-silenced indirect pathway (direct pathway MSNs: *D2-cre;Slc32a1<sup>fl/+</sup>*,  $0.11 \pm 0.04$  Hz,  $n = 9$ ; *D2-cre;Slc32a1<sup>fl/fl</sup>*,  $0.28 \pm 0.07$  Hz,  $n = 6$ ; indirect pathway MSNs: *D2-cre;Slc32a1<sup>fl/+</sup>*,  $0.15 \pm 0.06$  Hz,  $n = 5$ ; *D2-cre;Slc32a1<sup>fl/fl</sup>*,  $0.37 \pm 0.04$  Hz,  $n = 14$ ) (Fig. 2b, d). mEPSC amplitudes were largely unaffected by either manipulation (Supplementary Fig. 8c, d).

Changes in mEPSC rates were paralleled by alterations in dendritic spine density, indicating concurrent changes in structural and functional correlates of excitatory synapse number. Dendritic spine density of all MSNs was decreased by silencing the direct pathway (direct pathway MSNs: *D1-cre;Slc32a1<sup>fl/+</sup>*,  $0.84 \pm 0.03$  spines per  $\mu\text{m}$ ,  $n = 6$ ; *D1-cre;Slc32a1<sup>fl/fl</sup>*,  $0.45 \pm 0.05$  spines per  $\mu\text{m}$ ,  $n = 7$ ; indirect pathway MSNs: *D1-cre;Slc32a1<sup>fl/+</sup>*,  $0.68 \pm 0.05$  spines per  $\mu\text{m}$ ,  $n = 5$ ; *D1-cre;Slc32a1<sup>fl/fl</sup>*,  $0.41 \pm 0.02$  spines per  $\mu\text{m}$ ,  $n = 5$ ) and increased by silencing the indirect pathway (direct pathway MSNs: *D2-cre;Slc32a1<sup>fl/+</sup>*,  $0.41 \pm 0.02$  spines per  $\mu\text{m}$ ,  $n = 6$ ; *D2-cre;Slc32a1<sup>fl/fl</sup>*,  $0.63 \pm 0.08$  spines per  $\mu\text{m}$ ,  $n = 6$ ; indirect pathway MSNs: *D2-cre;Slc32a1<sup>fl/+</sup>*,  $0.56 \pm 0.03$  spines per  $\mu\text{m}$ ,  $n = 5$ ; *D2-cre;Slc32a1<sup>fl/fl</sup>*,  $1.02 \pm 0.05$  spines per  $\mu\text{m}$ ,

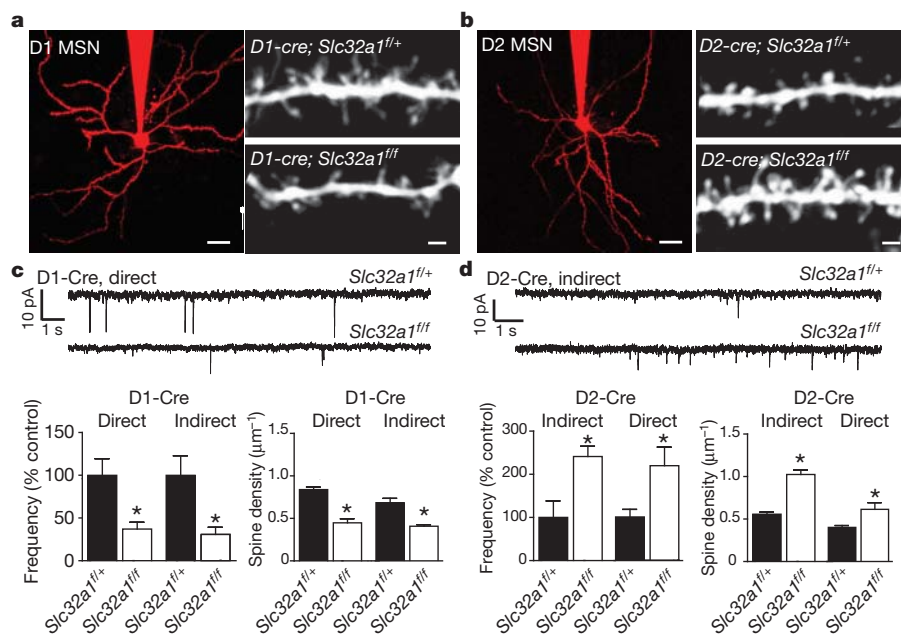


**Figure 2 | Conditional knockout of *Slc32a1* in direct and indirect pathway MSNs results in opposing changes to excitatory synapse number.** **a**, Left: two-photon laser-scanning microscopy image of a direct pathway *Slc32a1<sup>fl/+</sup>* MSN filled with Alexa Fluor 594 through the recording pipette during whole-cell voltage-clamp analysis of mEPSCs. Right: at a higher magnification, dendritic spines are visible. Examples of a dendrite from a control direct pathway MSN (top) and of a less spiny dendrite from a direct pathway MSN of a *Slc32a1* null sibling (bottom) are shown. Scale bars: 20  $\mu\text{m}$ , 2  $\mu\text{m}$ . **b**, As in **a**, but illustrating the increase in dendritic spine density seen with silencing of indirect pathway MSNs. **c**, Examples and summary of frequencies of mEPSCs in direct

pathway *Slc32a1* null mice and their heterozygous sibling controls. Preventing GABA release from direct pathway MSNs reduced mEPSC frequency, compared to direct pathway MSNs in *Slc32a1<sup>fl/+</sup>* sibling controls (top). The summary graph illustrates the decrease in direct and indirect pathway MSNs that were paralleled by differences in the density of dendritic spines. \* $P < 0.05$  for comparison of *Slc32a1<sup>fl/+</sup>* and *Slc32a1<sup>fl/fl</sup>* data. **d**, As in **c** but for indirect pathway mutants indicating that preventing GABA release from indirect pathway MSNs increased mEPSC frequency and dendritic spine density in indirect and direct pathway MSNs. \* $P < 0.05$  for comparison of *Slc32a1<sup>fl/+</sup>* and *Slc32a1<sup>fl/fl</sup>* data. Error bars indicate s.e.m.



$n = 6$ ) (Fig. 2). Together these data show that the degree of excitatory innervation of MSNs is determined by striatal output, such that excitatory hypo- or hyper-innervation is triggered by silencing the direct or indirect pathway, respectively.

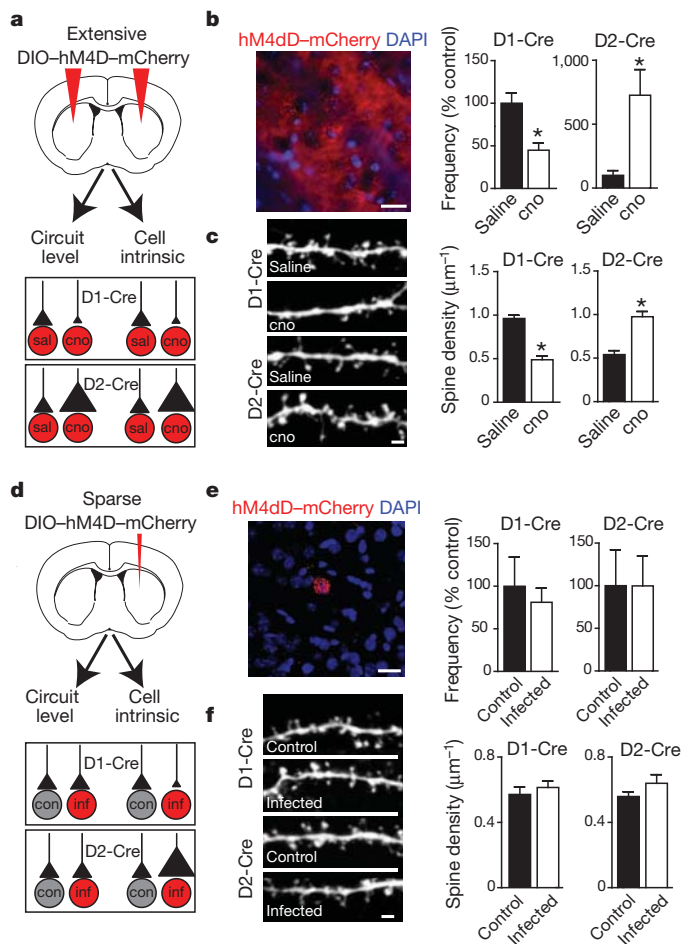
Complementary, pathway-dependent effects on excitatory input could be due to cell-intrinsic differences in direct and indirect pathway MSNs. Alternatively, common activity-dependent wiring rules could be differentially activated by each perturbation of basal ganglia output. For example, a net increase in SNr inhibitory output, caused by silencing direct pathway MSNs, could diminish thalamic and cortical activity, decreasing glutamate release and glutamatergic synapse formation in the striatum. In contrast, silencing the indirect pathway could have the converse set of effects (Supplementary Fig. 1b–d). The observation that direct or indirect pathway MSNs show similar perturbations despite selective deletion of *Slc32a1* only in MSNs of the Cre-expressing pathway (Fig. 2) provides support for the circuit-level model.

To test for cell-autonomous, *Slc32a1*-dependent regulation of glutamatergic innervation, we deleted *Slc32a1* in a small and sparse subpopulation of striatal neurons by injecting small quantities of AAV encoding Cre-mCherry into *D2-GFP;Slc32a1<sup>fl/fl</sup>* mice at P0–1 (Supplementary Fig. 9a, b). Analysis of mEPSCs and dendritic spines in neighbouring Cre<sup>+</sup> and Cre<sup>−</sup> MSNs (identified by nuclear mCherry fluorescence) belonging to the direct and indirect pathway (identified by GFP expression) revealed no changes in mEPSC frequency or dendritic spine density (Supplementary Fig. 9c–e). Thus, *Slc32a1*-dependent, cell-intrinsic mechanisms are unlikely to contribute to differential effects on glutamatergic innervation seen with silenced direct or indirect pathways.

We examined the consequences of manipulating striatal activity specifically during the period of striatal excitatory synaptogenesis<sup>23</sup>

using the RASSL (G-protein-coupled receptor activated solely by a synthetic ligand) hM4D<sup>24,25</sup> in direct or indirect pathway MSNs (Fig. 3). hM4D is activated by a blood–brain-barrier-permeable molecule clozapine-*n*-oxide (cno), allowing non-invasive *in vivo* manipulation of neural activity. hM4D couples to the  $\alpha_{i/o}$  pathway, which reduces action potential firing in many cell types (Supplementary Fig. 10) by activating K<sup>+</sup> channels<sup>13</sup>. AAV carrying the double floxed inverted hM4D–mCherry transgene<sup>25</sup> was injected in D1-Cre or D2-Cre mice at P0–1 and, starting at P8, cno (1 mg kg<sup>−1</sup>) or saline was administered subcutaneously twice per day to littermate pups. Consistent with our hypothesis, animals with large bilateral injections of AAV to dampen activity of many direct or indirect pathway MSNs, respectively, down- or upregulated mEPSC frequency and dendritic spine density, relative to saline-injected littermates (D1-Cre, direct pathway MSNs: frequency, cno  $0.8 \pm 0.1$  Hz,  $n = 18$ ; saline  $0.36 \pm 0.07$  Hz,  $n = 25$ ; spine density, cno  $0.96 \pm 0.04$  spines per  $\mu\text{m}$ ,  $n = 5$ ; saline  $0.49 \pm 0.05$  spines per  $\mu\text{m}$ ,  $n = 5$ ; D2-Cre, indirect pathway MSNs: frequency, cno  $0.04 \pm 0.01$  Hz,  $n = 7$ ; saline,  $0.27 \pm 0.09$  Hz,  $n = 8$ ; spine density, cno  $0.54 \pm 0.05$  spines per  $\mu\text{m}$  versus,  $n = 5$ ; saline  $0.98 \pm 0.06$  spines per  $\mu\text{m}$ ,  $n = 5$ ) (Fig. 3a–c and Supplementary Fig. 12a). Similar results were observed with the *Adora2a-cre* mouse, based on the adenosine 2A receptor promoter, another Cre driver line for indirect pathway MSNs (Supplementary Fig. 11).

**Figure 3 | *In vivo*, developmentally restricted postnatal manipulation of activity in direct and indirect pathway MSNs results in opposing changes to excitatory synapse number.** **a**, Schematic of experimental design and hypotheses for changes in excitatory synapse number induced by extensive and bilateral expression of hM4D in direct or indirect pathway MSNs and subsequent injections of cno or saline. Widespread inhibition of direct pathway MSN firing with cno is expected to decrease excitatory synapse number, whereas circuit-level or cell-intrinsic mechanisms dictate corticostriatal synaptogenesis. The converse is expected for widespread inhibition of indirect pathway MSNs. **b**, Left: hM4D–mCherry<sup>+</sup> MSNs in tissue densely infected with hM4D-encoding AAV (mCherry, red; DAPI, blue). Scale bar: 20  $\mu\text{m}$ . Right: summary data demonstrate that *in vivo* manipulation of neuronal activity in direct or indirect pathway MSNs in the time window of excitatory synaptogenesis led to opposing changes in excitatory synapse number. Decreased mEPSC frequency was observed in cno-treated D1-Cre mice, whereas mEPSC frequency was enhanced in cno-treated D2-Cre mice, compared to respective saline-injected controls.  $*P < 0.05$  for the comparison of same-pathway MSNs from saline- and cno-injected mice. **c**, Left: top two panels show two-photon laser-scanning microscopy images of a dendrite from a direct pathway MSN in a saline-injected D1-Cre mouse and a less spiny dendrite from a cno-injected sibling. Scale bar: 2  $\mu\text{m}$ . Bottom two images show an example of increased spine density in indirect pathway MSNs of D2-Cre mice treated with cno compared to saline-treated controls. Right: summaries of spine density in cno- and saline-treated mice demonstrating the opposite sign changes resulting from inhibition of the direct or indirect pathway.  $*P < 0.05$  for the comparison of same-pathway MSNs from saline- and cno-injected mice. **d**, Schematic of experimental design and hypotheses for possible changes in excitatory synapse number induced by sparse and unilateral expression of hM4D in direct or indirect pathway MSNs and subsequent injections of cno. Manipulation of activity in a small subset of neurons is not expected to engage circuit-wide mechanisms regulating synapse numbers. In contrast, unknown cell-intrinsic mechanisms could regulate the number of synapses formed onto the manipulated neurons, compared to same-pathway uninfected MSNs. **e**, Left: confocal image showing an hM4D–mCherry<sup>+</sup> MSN in a sparse injection configuration (mCherry, red; DAPI, blue). Scale bar: 20  $\mu\text{m}$ . Right: with sparse activity manipulations, no differences in mEPSC frequency were observed in either direct or indirect pathway infected MSNs, compared to uninfected MSNs. **f**, Left: top two panels show two-photon laser-scanning microscopy images of a dendrite from control or neighbouring hM4D-expressing direct pathway MSN. Bottom two images show spiny dendrites from control or neighbouring hM4D-expressing indirect pathway MSN. Scale bar: 2  $\mu\text{m}$ . Right: summary graph shows that inhibiting activity of a sparse subset of MSNs does not alter dendritic spine density in manipulated direct or indirect pathway neurons. Error bars indicate s.e.m.



In contrast, sparse, unilateral hM4D delivery, designed to have a minimal impact on circuit dynamics, did not alter mEPSC frequency and dendritic spine density in hM4D-expressing neurons relative to uninfected neighbouring MSNs of the same pathway (Fig. 3d–f and Supplementary Fig. 12b). These data also indicate that hM4D-mediated perturbation of G-protein-coupled intracellular signalling pathways is not responsible for the changes in excitatory synapses.

Three lines of evidence—analyses of non-manipulated MSNs in pathway-specific conditional *Slc32a1* knockouts, of sparse *Slc32a1* null MSNs, and of the effects of widespread versus sparse hM4d manipulation of neural activity—support the hypothesis that circuit-level patterns of activity, rather than cell-intrinsic mechanisms, determine the degree of glutamatergic innervation of striatal MSNs. Inherent to this proposed mechanism is the assumption that the basal ganglia output modulates corticostriatal or thalamostriatal glutamatergic activity, which, in turn, regulates excitatory synaptogenesis in the striatum. To probe this mechanism, we directly tested the ability of glutamate exposure to drive spinogenesis in the striatum, and the effect of manipulating corticostriatal activity on striatal spinogenesis and synaptogenesis.

To test whether glutamate release in the striatum is sufficient to induce spinogenesis, we focally stimulated non-spiny segments of P8–11 MSN dendrites with two-photon laser uncaging of glutamate<sup>26,27</sup>. Sparse viral delivery of Cre was used to activate tdTomato reporter fluorescence in a small subset of MSNs in *D2-GFP;Ai14-lsl-tdTomato* mice. Two-photon laser-scanning microscopy was used to monitor dendritic structure during glutamate stimulation (Fig. 4a, b).

Stimulation power was calibrated to evoke moderate  $\sim 7$  pA currents from existing spines (Supplementary Fig. 13). Using protocols that robustly induce synaptogenesis in layer 2/3 pyramidal neurons of developing cortex<sup>26</sup>, we observed growth of a new dendritic spine at the glutamate uncaging site in  $\sim 50\%$  of trials. The probability of spine growth was similar in direct and indirect pathway MSNs (Fig. 4b), was unaffected by blockade of GABA<sub>A</sub> receptors (52% and 50% success percentage for GFP<sup>+</sup> and GFP<sup>−</sup> MSNs in control conditions, and 56% and 51%, respectively, in GABA<sub>A</sub> antagonist), and matched previous results in cortical pyramidal cells<sup>26</sup>. Thus, glutamatergic stimulation is sufficient to drive spinogenesis in the developing striatum.

To test whether the postnatal activity of corticostriatal projections drives synaptogenesis, we used the *Rbp4-cre* mouse line to express hM4D in corticostriatal neurons emanating from deep cortical layers (Fig. 4c). *Rbp4-cre;D2-GFP* mice were injected with the double floxed inverted AAV carrying hM4D–mCherry at P0–1 and, starting at P8, cno (1 mg kg<sup>−1</sup>) or saline was administered subcutaneously twice per day to littermate pups. For MSNs of both pathways assayed at P14–15, mEPSC frequency and spine density were decreased after cno treatment (Fig. 4d), with no change in mEPSC amplitude (direct pathway MSNs: frequency,  $0.66 \pm 0.2$  Hz (saline) versus  $0.25 \pm 0.05$  Hz (cno),  $n = 12$  and 9; spine density,  $0.60 \pm 0.05$  spines per  $\mu\text{m}$  (saline) versus  $0.38 \pm 0.03$  spines per  $\mu\text{m}$  (cno),  $n = 7$  and 6; indirect pathway MSNs: frequency,  $0.65 \pm 0.14$  Hz (saline) versus  $0.25 \pm 0.04$  Hz (cno),  $n = 16$  and 16; spine density,  $0.58 \pm 0.03$  spines per  $\mu\text{m}$  (saline) versus  $0.31 \pm 0.02$  spines per  $\mu\text{m}$  (cno),  $n = 7$  and 6) (Fig. 4d, e). Because inhibition of *Rbp4-Cre*<sup>+</sup> corticostriatal projections caused no change in locomotion at P14–15 (Supplementary Fig. 14), activity-dependent control of striatal synaptogenesis is not secondary to behavioural changes.

To determine whether activity-dependent changes in striatal synaptogenesis persist into early adulthood, we inhibited the activity of corticostrially projecting *Rbp4-Cre* neurons during P8–P15 and

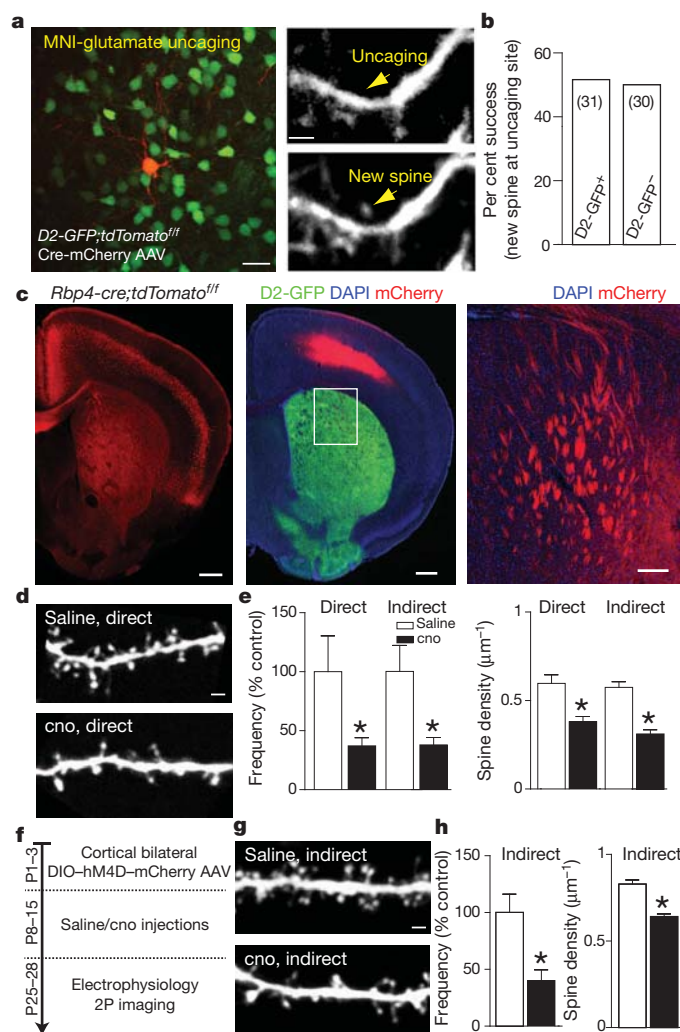


**Figure 4 | Corticostriatal activity drives synaptogenesis in MSNs.** **a**, Focal release of glutamate is sufficient to trigger *de novo* spinogenesis in MSNs. Two-photon laser-scanning microscopy image of tdTomato (red) and GFP (green) expressing MSNs in a *D2-GFP;tdTomato<sup>fl/fl</sup>* mouse sparsely injected with Cre-mCherry encoding AAV at P0. Imaging was performed in an acute slice of striatum at P10. Scale bar: 20  $\mu\text{m}$ . The right panels show a higher-magnification image of a dendrite before (top) and after (bottom) triggering new spine growth. Scale bar: 2  $\mu\text{m}$ . The stimulation protocol consisted of 40 uncaging pulses directed at the indicated spot (arrow) with 15 mW of 720-nm light measured at the objective back aperture. **b**, Summary graph demonstrating  $\sim 50\%$  success rate in generating new spines with glutamate uncaging in direct and indirect pathway MSNs at P8–11. **c**, Left: Cre expression driven by an *Rbp4* BAC (*Rbp4-Cre*) targets Cre to corticostriatal projection neurons. Red fluorescence from a tdTomato reporter allele is present in deep-layer cortical neurons and densely labels axons throughout striatum. Scale bar: 500  $\mu\text{m}$ . Middle: AAV DIO hM4D–mCherry injected into the cortex of a mouse carrying *Rbp4-Cre* and *D2-GFP* transgenes shows strong red fluorescence in deep-layer somata in cortex and green fluorescence in striatum. Scale bar: 500  $\mu\text{m}$ . Right: red channel, higher magnification view of boxed area in the centre panel shows extensive hM4D–mCherry labelling of corticostriatal axons. **d**, **e**, *In vivo* inhibition of *Rbp4-Cre* neurons expressing hM4D during the window of excitatory synaptogenesis leads to a decrease in excitatory synapse number for both direct and indirect pathway MSNs. **d**, Two-photon laser-scanning microscopy images of a dendrite from a direct pathway MSN in a saline-injected mouse and a less spiny dendrite from a cno-injected littermate. Scale bar: 2  $\mu\text{m}$ . **e**, Summary data showing a decrease in direct and indirect pathway MSN mEPSC frequency (left) and spine density (right) for cno-treated mice versus saline-treated littermates. **f–h**, hM4D/cno-dependent decreases in MSN excitatory synapse number persist into early adulthood. **f**, Timeline for experiments. **g**, Two-photon laser-scanning microscopy images of dendrites from indirect pathway MSNs from sibling mice in their early adulthood (P25–28) after treatment with cno or saline during the time window for excitatory synaptogenesis (P8–15). **h**, Summary data showing that decreases in mEPSC frequency (left) and spine density (right) persist into early adulthood. Error bars indicate s.e.m.



examined excitatory innervation in indirect pathway MSNs at P25–28 (Fig. 4f). Both mEPSC frequency and spine density were reduced in cno-treated mice compared to saline-injected controls (indirect pathway MSNs: frequency,  $0.73 \pm 0.12$  Hz (saline) versus  $0.29 \pm 0.07$  Hz (cno),  $n = 28$  and  $26$ ; spine density,  $0.83 \pm 0.02$  spines per  $\mu\text{m}$  (saline) versus  $0.64 \pm 0.02$  spines per  $\mu\text{m}$  (cno),  $n = 10$  per group) (Fig. 4g, h). Thus, perturbations of cortex-basal ganglia–thalamus circuit activity in early life can have lasting effects into adulthood.

Our data reveal that the balance of activity in direct/indirect pathways dictates postnatal excitatory innervation of the striatum. Because manipulating striatal output alters the structure of its input, activity must act recurrently, through a polysynaptic, multi-stage circuit. The simplest explanation for these findings is that glutamate release from cortical and thalamic axons in the striatum promotes the formation or stabilization of glutamatergic synapses onto MSNs. Perturbations that result in relative activation of the direct pathway compared to the indirect (and hence activate cortex and thalamus) will drive glutamatergic synapse formation in the striatum. Collateral connections among MSNs<sup>19</sup> influence basal ganglia activity and may contribute to these effects. Such activity-dependent processes may be essential for refining locomotion and reward-based behaviour.

These mechanisms are fundamentally distinct from those believed to underlie topographic organization of sensory cortices during postnatal development. In these cortical areas, waves of neural activity pass information about sensory maps from one stage of processing to the next<sup>28,29</sup>, and these mappings are translated into synaptic connectivity through spike-timing-dependent plasticity rules<sup>30</sup>. In contrast, striatal inputs from widespread cortical areas show only modest topographic organization. Instead of sensory maps, synaptic networks throughout the cortex-basal ganglia–thalamus loop are thought to reflect parallel, segregated loops of mixed inhibitory and excitatory projections. Here we show that activity propagates through cortex-basal ganglia–thalamus circuits to specify synaptic networks based on the balanced output of direct and indirect pathways in a manner that can, through positive feedback, select for recurrent closed loops.

## METHODS SUMMARY

**Viral expression in BAC transgenic mice.** Injections of recombinant Cre-On or Cre-Off (A. Saunders, C. Johnson and B. Sabatini, manuscript in preparation) AAVs were targeted to striatum of D1-Cre, D2-Cre, or Adora-Cre mice. Rbp4-Cre mice were injected in the somatosensory and motor regions of the cortex. Cre-expressing AAV was injected into the striatum of conditional *Slc32a1* or *Ai14-*lsl*-tdTomato* mice.

**Electrophysiology and two-photon imaging.** Whole-cell voltage-clamp recordings were obtained from pathway-identified MSNs in acute coronal slices. Cells were filled with Alexa Fluor 594 (10–20  $\mu\text{M}$ ) and imaged using a two-photon laser-scanning microscope (810–840 nm).

**Full Methods** and any associated references are available in the online version of the paper at [www.nature.com/nature](http://www.nature.com/nature).

Received 31 January; accepted 20 March 2012.

Published online 13 May 2012.

- Wiesel, T. N. & Hubel, D. H. Single-cell responses in striate cortex of kittens deprived of vision in one eye. *J. Neurophysiol.* **26**, 1003–1017 (1963).
- Smith, G. B., Heynen, A. J. & Bear, M. F. Bidirectional synaptic mechanisms of ocular dominance plasticity in visual cortex. *Phil. Trans. R. Soc. B* **364**, 357–367 (2009).
- Stephenson-Jones, M., Samuelsson, E., Ericsson, J., Robertson, B. & Grillner, S. Evolutionary conservation of the basal ganglia as a common vertebrate mechanism for action selection. *Curr. Biol.* **21**, 1081–1091 (2011).
- Yin, H. H. & Knowlton, B. J. The role of the basal ganglia in habit formation. *Nature Rev. Neurosci.* **7**, 464–476 (2006).
- Alexander, G. E., DeLong, M. R. & Strick, P. L. Parallel organization of functionally segregated circuits linking basal ganglia and cortex. *Annu. Rev. Neurosci.* **9**, 357–381 (1986).

- Nambu, A. Somatotopic organization of the primate basal ganglia. *Front. Neuroanat.* **5**, 26 (2011).
- Smith, Y., Bevan, M. D., Shink, E. & Bolam, J. P. Microcircuitry of the direct and indirect pathways of the basal ganglia. *Neuroscience* **86**, 353–387 (1998).
- Gerfen, C. R. The neostriatal mosaic: multiple levels of compartmental organization in the basal ganglia. *Annu. Rev. Neurosci.* **15**, 285–320 (1992).
- Albin, R. L., Young, A. B. & Penney, J. B. The functional anatomy of basal ganglia disorders. *Trends Neurosci.* **12**, 366–375 (1989).
- Kelly, R. M. & Strick, P. L. Macro-architecture of basal ganglia loops with the cerebral cortex: use of rabies virus to reveal multisynaptic circuits. *Prog. Brain Res.* **143**, 447–459 (2004).
- Alexander, G. E. & Crutcher, M. D. Functional architecture of basal ganglia circuits: neural substrates of parallel processing. *Trends Neurosci.* **13**, 266–271 (1990).
- Kravitz, A. V. et al. Regulation of parkinsonian motor behaviours by optogenetic control of basal ganglia circuitry. *Nature* **466**, 622–626 (2010).
- Ferguson, S. M. et al. Transient neuronal inhibition reveals opposing roles of indirect and direct pathways in sensitization. *Nature Neurosci.* **14**, 22–24 (2011).
- Cho, J. & West, M. O. Distributions of single neurons related to body parts in the lateral striatum of the rat. *Brain Res.* **756**, 241–246 (1997).
- Tong, Q., Ye, C.-P., Jones, J. E., Elmquist, J. K. & Lowell, B. B. Synaptic release of GABA by AgRP neurons is required for normal regulation of energy balance. *Nature Neurosci.* **11**, 998–1000 (2008).
- McIntire, S. L., Reimer, R. J., Schuske, K., Edwards, R. H. & Jorgensen, E. M. Identification and characterization of the vesicular GABA transporter. *Nature* **389**, 870–876 (1997).
- Wojcik, S. M. et al. A shared vesicular carrier allows synaptic corelease of GABA and glycine. *Neuron* **50**, 575–587 (2006).
- Gong, S. et al. A gene expression atlas of the central nervous system based on bacterial artificial chromosomes. *Nature* **425**, 917–925 (2003).
- Taverna, S., Ilijic, E. & Surmeier, D. J. Recurrent collateral connections of striatal medium spiny neurons are disrupted in models of Parkinson's disease. *J. Neurosci.* **28**, 5504–5512 (2008).
- Sohal, V. S., Zhang, F., Yizhar, O. & Deisseroth, K. Parvalbumin neurons and gamma rhythms enhance cortical circuit performance. *Nature* **459**, 698–702 (2009).
- Nimchinsky, E. A., Sabatini, B. L. & Svoboda, K. Structure and function of dendritic spines. *Annu. Rev. Physiol.* **64**, 313–353 (2002).
- Somogyi, P., Bolam, J. P. & Smith, A. D. Monosynaptic cortical input and local axon collaterals of identified striatonigral neurons. A light and electron microscopic study using the Golgi-peroxidase transport-degeneration procedure. *J. Comp. Neurol.* **195**, 567–584 (1981).
- Tepper, J. M., Sharpe, N. A., Koós, T. Z. & Trent, F. Postnatal development of the rat neostriatum: electrophysiological, light- and electron-microscopic studies. *Dev. Neurosci.* **20**, 125–145 (1998).
- Rogan, S. C. & Roth, B. L. Remote control of neuronal signaling. *Pharmacol. Rev.* **63**, 291–315 (2011).
- Krashes, M. J. et al. Rapid, reversible activation of AgRP neurons drives feeding behavior in mice. *J. Clin. Invest.* **121**, 1424–1428 (2011).
- Kwon, H.-B. & Sabatini, B. L. Glutamate induces *de novo* growth of functional spines in developing cortex. *Nature* **474**, 100–104 (2011).
- Carter, A. G. & Sabatini, B. L. State-dependent calcium signaling in dendritic spines of striatal medium spiny neurons. *Neuron* **44**, 483–493 (2004).
- Meister, M., Wong, R. O., Baylor, D. A. & Shatz, C. J. Synchronous bursts of action potentials in ganglion cells of the developing mammalian retina. *Science* **252**, 939–943 (1991).
- Triplett, J. W. et al. Retinal input instructs alignment of visual topographic maps. *Cell* **139**, 175–185 (2009).
- Bi, G. & Poo, M. Synaptic modification by correlated activity: Hebb's postulate revisited. *Annu. Rev. Neurosci.* **24**, 139–166 (2001).

**Supplementary Information** is linked to the online version of the paper at [www.nature.com/nature](http://www.nature.com/nature).

**Acknowledgements** We thank Sabatini laboratory members for comments on the manuscript; B. Roth, K. Deisseroth and M. During for AAV backbones encoding hM4D, ChR2 and Cre, respectively; and C. Gerfen for the Rbp4-Cre mouse line. Confocal imaging was done through the Harvard NeuroDiscovery and Olympus Imaging Centers. This work was supported by grants from NINDS (NS046579, B.L.S.); the W.F. Milton Fund Award and the Leonard and Isabelle Goldenson Research Fellowship (Y.K.); and NIH (F31 NS074842) and Shapiro predoctoral fellowship (A.S.).

**Author Contributions** Y.K., A.S. and B.L.S. designed the experiments. Y.K. and A.S. performed experiments and analysed data. C.A.J. assisted in experiments and genotyping. B.B.L. generated the conditional *Slc32a1* mouse. Y.K., A.S. and B.L.S. wrote the paper with contributions from C.A.J. and B.B.L.

**Author Information** Reprints and permissions information is available at [www.nature.com/reprints](http://www.nature.com/reprints). The authors declare no competing financial interests. Readers are welcome to comment on the online version of this article at [www.nature.com/nature](http://www.nature.com/nature). Correspondence and requests for materials should be addressed to B.L.S. ([bsabatini@hms.harvard.edu](mailto:bsabatini@hms.harvard.edu)).



## METHODS

**Mouse strains and genotyping.** Animals were handled according to protocols approved by the Harvard Standing Committee on Animal Care, in accordance with NIH guidelines. To generate mice with conditional knockout of *Slc32a1* from the direct and indirect pathway, *D1/D2-cre;Slc32a1<sup>fl/+</sup>* mice were crossed with *Slc32a1<sup>fl/fl</sup>* mice. Conditional knockout crosses were made using either male or female parents as Cre carriers. To generate pups carrying the D1-, D2-, Adora2a- or Rbp4-Cre transgenes, D1-, D2-, Adora2a- or Rbp4-Cre parents, either male or female, were crossed to wild-type C57BL/6 mice. D2-BAC and GAD67 knock-in GFP transgenes were also introduced through either parent or both parents. A full description of the transgenic mouse lines used in this study is provided in Supplementary Table 1. Genotyping was performed from tail tissue sampled at P0.5–5. Tail tissue was digested overnight (Viagen) and PCR was performed using the lysates as template DNA. The genotyping primers are listed in Supplementary Table 2 and the PCR protocols are provided below.

PCR protocol 1: (1) 95 °C for 5 min; (2) 95 °C for 30 s; (3) 53 °C for 30 s; (4) 72 °C for 1 min; (5) repeat (2)–(4) for 35 cycles; (6) 72 °C for 5 min.

PCR protocol 2: (1) 94 °C for 3 min; (2) 94 °C for 45 s; (3) 66 °C, down –1 °C each cycle for 45 s; (4) 72 °C for 45 s; (5) repeat (2)–(4) for 9 cycles; (6) 94 °C for 30 s; (7) 58 °C for 30 s; (8) 72 °C for 30 s; (9) repeat (6)–(8) for 20 cycles; (10) 72 °C for 10 min.

**Stereotaxic injections.** For intracranial injections, P0–7-day-old mice were anaesthetized with isoflurane and placed into a stereotaxic apparatus. Virus was delivered at a maximum rate of 100 nl min<sup>−1</sup> using a Microinject system (WPI). Dorsolateral striatum was targeted by directing the needle approximately 1 mm anterior to midpoint between ear and eye, 1.5 mm from midline and 1.8 mm ventral to brain surface, and these coordinates were adjusted based on age. Cortical injections were similarly targeted in the anterior–posterior and medial–lateral axes, but the needle was directed 0.8 mm ventral to brain surface. Unilateral injections of 350–500 nl were used to drive Chr2 expression for electrophysiology experiments, pathway tracing, cell targeting for mEPSC recordings and cell fills for dendritic spine density analyses; 500–750 nl bilateral or 50 nl unilateral injections were used in circuit manipulation with hM4D; 50 nl unilateral injections were used for sparse postnatal *Slc32a1* knockout; 50 nl unilateral injections (1:10 dilution) were used for inducing tdTomato expression in *de novo* spinogenesis experiments. Virus titres are provided in Supplementary Table 3 and injection rates were 50–100 nl min<sup>−1</sup>. After injections and wound closure, mice received flunixin for analgesia and were returned to home cages for 8+ days.

**Slice preparation.** Coronal striatal slices were prepared as described previously for rat<sup>27</sup>. Mice were anaesthetized by inhalation of isoflurane. Cerebral hemispheres were removed and placed into cold choline-based artificial cerebrospinal fluid (choline-ACSF) containing 25 mM NaHCO<sub>3</sub>, 1.25 mM NaH<sub>2</sub>PO<sub>4</sub>, 2.5 mM KCl, 7 mM MgCl<sub>2</sub>, 25 mM glucose, 1 mM CaCl<sub>2</sub>, 110 mM choline chloride, 11.60 mM ascorbic acid and 3.10 mM pyruvic acid, and equilibrated with 95% O<sub>2</sub>/5% CO<sub>2</sub>. Tissue was blocked and transferred into a slicing chamber containing choline-ACSF. Coronal striatal slices (300 µm) were then cut on a Leica VT1000 s (Leica Instruments) and transferred into a holding chamber with ACSF containing (in mM) 127 NaCl, 2.5 KCl, 25 NaHCO<sub>3</sub>, 1.25 NaH<sub>2</sub>PO<sub>4</sub>, 2.0 CaCl<sub>2</sub>, 1.0 MgCl<sub>2</sub> and 25 glucose, equilibrated with 95% O<sub>2</sub>/5% CO<sub>2</sub>. Slices were incubated at 34 °C for 30–45 min before recording.

**Electrophysiology.** Whole-cell recordings were obtained from striatal MSNs visualized under infrared differential interference contrast (IR-DIC) using patch pipettes with pipette resistance of 2.5–4.5 MΩ. To identify infected MSNs or those belonging to the indirect pathway, mCherry or GFP fluorescence was detected using epifluorescence illumination. For Chr2-evoked current recordings, a high Cl<sup>−</sup> internal solution containing 100 mM CsCl, 35 mM CsF, 10 mM HEPES, 4 mM MgCl<sub>2</sub>, 4 mM Na<sub>2</sub>ATP, 0.4 mM NaGTP, 10 mM Na<sub>2</sub>CrePO<sub>4</sub>, 1 mM EGTA (pH 7.4) was used. For miniature excitatory postsynaptic current recordings, the internal solution consisted of 120 mM CsMeSO<sub>4</sub>, 15 mM CsCl, 8 mM NaCl, 10 mM TEACl, 10 mM HEPES, 2 mM QX314, 4 mM MgATP, 0.3 mM NaGTP (pH 7.4). Alexa Fluor 594 (10–20 µM) was added to internals to visualize cell morphology and to confirm cell identity as MSN. For cell-attached recordings, a caesium-based internal without Alexa Fluor 594 was used instead and traces were monitored for signs of breaking in. Recordings were made using an Axoclamp 700B amplifier (Axon Instruments) at room temperature for MSN collateral current analysis and mEPSC recordings, and at elevated temperature (34 °C) for cell-attached recordings. Data were filtered at 3 kHz and sampled at 10 kHz. Series resistance, measured with a 5 mV hyperpolarizing pulse in voltage clamp, was on average under 20 MΩ and less than 25 MΩ, uncompensated. All voltage-clamp recordings were made from cells held at −70 mV, except for a small minority of cells in which Chr2 stimulation drove unclamped spikes. In this case, cells were held at −40 mV and peak currents were multiplied by 1.75, the magnitude increase predicted by −30 mV change in driving force of Cl and confirmed by experiments

where Chr2 currents were elicited at both holding potentials (−70 and −40 mV). For miniature EPSC recordings, all MSNs were held at −70 mV. Extracellular recordings were acquired in voltage-clamp mode without imposing a holding potential.

**Optogenetic activation.** To activate Chr2 in acute slices, 473-nm laser light (Optoengine) was focused onto the back aperture of the ×60 water immersion objective to produce whole-field illumination. To quantify the laser light delivered with each pulse, light leak through a high-pass dichroic filter was measured using a photodiode calibrated by measuring the power at the focal plane of ×60 objective. For each Chr2 activation experiment in Fig. 1, six different light intensities were used to drive postsynaptic currents (0.1–20 mW). Summary data presented in Fig. 1 are based on the strongest, 20 mW stimulation. For optogenetic activation of neurons during extracellular recording, light power was slowly increased while acquiring data until a moderate firing rate (~4–20 Hz) was achieved.

**Pharmacology.** Pharmacological agents were used at the following final concentrations. For Chr2-evoked current recordings, ACSF contained 10 µM CPP (Tocris Cookson), 10 µM NBQX (Tocris), 10 µM scopolamine hydrobromide (Tocris). For mEPSC recordings, ACSF contained 1 µM TTX (Sigma), 50 µM SR 95531/gabazine (Tocris), 10 µM CPP and 10 µM scopolamine hydrobromide. For extracellular recordings, ACSF contained CPP, NBQX, SR 95531 and scopolamine hydrobromide. SR 95531 was present in a subset of glutamate-uncaging-evoked spinogenesis experiments. All reagents were dissolved in distilled water and diluted to their final concentrations in ACSF on the day of the experiment, except for NBQX, which was dissolved in DMSO. Clozapine-*n*-oxide (Sigma) was used at 10 µM for slice experiments. For *in vivo* circuit activity manipulation, clozapine-*n*-oxide in sterile saline was administered subcutaneously at 1 mg kg<sup>−1</sup> body weight twice daily.

**Two-photon imaging.** Two-photon laser-scanning microscopy was performed using a custom microscope as previously described<sup>27</sup>. Cell morphology was visualized using Alexa Fluor 594 (10–20 µM) excited with 810–840-nm light and introduced into the cell through whole-cell recording or single-cell electroporation. Briefly, a pipette containing Alexa Fluor 594 in dH<sub>2</sub>O was guided to a MSN cell body with low positive pressure. Pressure was released and a single 0.2-ms-long 0.1–0.3 V pulse was delivered through an electrical stimulator (A.M.P.I) to fill the soma with dye, which rapidly diffused into dendrites and spines (~5 min). A two-photon laser-scanning microscopy three-dimensional image stack through each neuron was collected, followed by stacks through 2–3° dendritic segments at a tenfold higher magnification. For dendritic spine density and spine shape analyses, cells were coded and analysed using custom-written routines in MATLAB. Three- to five secondary and tertiary dendrites per MSN were analysed. The size of each spine was measured in the optical section of maximal brightness.

**Glutamate uncaging.** Uncaging of MNI-glutamate was done on a custom-built microscope combining two-photon laser-scanning microscopy and two-photon laser photoactivation, or uncaging. Two mode-locked Ti:sapphire lasers (Coherent) tuned to 920 nm and 720 nm were used for imaging tdTomato fluorescence and uncaging MNI-glutamate, respectively. The intensity of each laser was independently controlled by Pockels cells (Conoptics). For uncaging, 2.5 mM MNI-glutamate (Sigma-Aldrich) was added to Mg-free ACSF and 15 mW of 720 nm light at the specimen was used to focally release the uncaging group. To visualize the dendrites of MSNs of known pathways, mice carrying at least one tdTomato reporter allele and a D2-GFP BAC transgene were injected with AAV carrying Cre-mCherry at P0–1. AAV injections were titred to generate sparse Cre expression in striatum. tdTomato<sup>+</sup> MSN dendrites were selected using the following two criteria: smooth dendritic membrane in the immediate location of uncaging spot and the presence of at least one dendritic spine nearby (within ~5 µm). MNI-glutamate was uncaged near the dendrite (~0.5 µm away from the edge) at 2 Hz using 40 4-ms-long pulses as described previously<sup>27</sup>. This protocol drives a ~7-pA uncaging-evoked EPSC in whole-cell voltage-clamp recording (Supplementary Fig. 12). Dendrite images were taken before and immediately after induction protocol.

**Behavioural analysis.** For measuring activity levels, 14–17-day-old mice were monitored one at a time using the large (45 × 45 cm<sup>2</sup>) home cage module of EthoVision XT (Noldus) with centre point and nose point tracking. No food or water was provided for the 1 h duration of the recording. Comparisons were made between sibling littermates carrying 0 or 1 *Slc32a1* alleles on the same day, with genotype order counterbalanced. All recordings were done in a narrow time window in littermate mice maintained on a standard 12/12 h light/dark cycle. The distance travelled during 1 h was quantified.

**AAV production.** Adeno-associated virus (AAV) vector DNA was amplified in recombination-deficient bacteria (OneShot Stbl3, Invitrogen) and packaged by a commercial vector core facility (University of North Carolina). Supplementary Table 2 describes the AAV vectors used in this study. The Cre-silenced Chr2-mCherry vector (DO-Chr2-mCherry) was generated by reversing the orientation

of the ChR2–mCherry transgene with respect to the two pairs of flanking *loxP* sites using the *AscI* and *NheI* restriction sites.

**Fixed-tissue preparation, imaging and immunohistochemistry.** Mice were transcardially perfused with 4% paraformaldehyde and the brains were post-fixed for 1–7 days. Brains were sectioned coronally or sagittally at 40  $\mu\text{m}$  using a Vibratome. No immuno-enhancement was used to increase the signal of native fluorophores. For Cre immunofluorescence, 1:6 series of sections through the striatum were incubated overnight at 4 °C with mouse anti-Cre antibody in TBS with 0.5% Tween-20 (1:250, Invitrogen). The following day tissue was rinsed in TBS, reacted with goat anti-mouse Alexa Fluor 488 (1:500, Molecular Probes) for 1 h at room temperature, rinsed, mounted onto superfrost slides, dried and coverslipped under ProLong antifade reagent with DAPI (Molecular Probes). Images were acquired with a Zeiss LSM 510 META confocal microscope (Harvard NeuroDiscovery Center). Slides were coded for confocal microscopy and data analysis. For every animal, five fields of view were selected for analysis from several striatal sections, which matched the location of electrophysiological recordings. Two-dimensional 1- $\mu\text{m}$ -thick optical sections were analysed in ImageJ using colocalization and cell counter plug-ins. The number of Cre<sup>+</sup> and Cre<sup>−</sup> DAPI-stained nuclei was quantified and expressed as a percentage. On average >600 cells were examined for Cre expression in every animal. The code was broken after completion of the analysis.

For parvalbumin immunofluorescence, sections were incubated in mouse anti-parvalbumin primary antibody (1:2,000, Millipore), goat anti-mouse Alexa 488

secondary antibody, and coverslipped under ProLong antifade reagent with DAPI. Image stacks were acquired with a with an Olympus FV1000 laser scanning confocal microscope (Harvard Neurobiology Imaging Facility). The number of parvalbumin-labelled, D1-Cre tdTomato reporter-positive neurons was quantified. Stacks through >300 neurons from four mice were analysed.

**Whole-brain imaging.** Mice were unilaterally injected with DIO–ChR2–mCherry AAV into the right dorsal striatum and transcardially perfused with 4% paraformaldehyde 8–10 days later. Brains were sectioned sagittally at 100  $\mu\text{m}$ . For every brain, the slice with maximal cross-section of SNr or globus pallidus was selected for imaging with an Olympus VS110 slide scanning microscope using  $\times 20$  objective. No immuno-enhancement was needed to visualize long-range projections. For confocal imaging, sections were scanned on a confocal microscope under a  $\times 63$  oil objective. ImageJ was used to analyse fluorophore distributions and data were expressed as area fractions.

**Data analysis.** Offline data analysis for electrophysiology was performed using custom software written in Igor Pro (Wavemetrics) and MATLAB. Statistical analyses were done using GraphPad PRIZM 5 software (GraphPad). All values are reported as means  $\pm$  s.e.m., unless noted otherwise. Statistical significance was determined by two-tailed Student's *t*-tests, with Welch's correction for data sets with significantly different variances, and two-tailed Wilcoxon signed rank test for non-parametrically distributed data. Two-way ANOVA with Bonferroni post-hoc comparisons and log-rank Mantel–Cox test were used for weight and lifespan analyses in Supplementary Fig. 3.  $P < 0.05$  was considered to be statistically significant.

# Prion-like behaviour and tau-dependent cytotoxicity of pyroglutamylated amyloid- $\beta$

Justin M. Nussbaum<sup>1\*</sup>, Stephan Schilling<sup>2\*</sup>, Holger Cynis<sup>2</sup>, Antonia Silva<sup>1</sup>, Eric Swanson<sup>1</sup>, Tanaporn Wangsanut<sup>1</sup>, Kaycie Tayler<sup>3</sup>, Brian Wiltgen<sup>3</sup>, Asa Hatami<sup>4</sup>, Raik Röncke<sup>5</sup>, Klaus Reymann<sup>5</sup>, Birgit Hutter-Paier<sup>6</sup>, Anca Alexandru<sup>7</sup>, Wolfgang Jagla<sup>7</sup>, Sigrid Graubner<sup>7</sup>, Charles G. Glabe<sup>4</sup>, Hans-Ulrich Demuth<sup>2,7</sup> & George S. Bloom<sup>1,8</sup>

Extracellular plaques of amyloid- $\beta$  and intraneuronal neurofibrillary tangles made from tau are the histopathological signatures of Alzheimer's disease. Plaques comprise amyloid- $\beta$  fibrils that assemble from monomeric and oligomeric intermediates, and are prognostic indicators of Alzheimer's disease. Despite the importance of plaques to Alzheimer's disease, oligomers are considered to be the principal toxic forms of amyloid- $\beta$ <sup>1,2</sup>. Interestingly, many adverse responses to amyloid- $\beta$ , such as cytotoxicity<sup>3</sup>, microtubule loss<sup>4</sup>, impaired memory and learning<sup>5</sup>, and neuritic degeneration<sup>6</sup>, are greatly amplified by tau expression. Amino-terminally truncated, pyroglutamylated (pE) forms of amyloid- $\beta$ <sup>7,8</sup> are strongly associated with Alzheimer's disease, are more toxic than amyloid- $\beta$ , residues 1–42 ( $A\beta_{1-42}$ ) and  $A\beta_{1-40}$ , and have been proposed as initiators of Alzheimer's disease pathogenesis<sup>9,10</sup>. Here we report a mechanism by which pE- $A\beta$  may trigger Alzheimer's disease.  $A\beta_{3(pE)-42}$  co-oligomerizes with excess  $A\beta_{1-42}$  to form metastable low- $n$  oligomers (LNOs) that are structurally distinct and far more cytotoxic to cultured neurons than comparable LNOs made from  $A\beta_{1-42}$  alone. Tau is required for cytotoxicity, and LNOs comprising 5%  $A\beta_{3(pE)-42}$  plus 95%  $A\beta_{1-42}$  (5% pE- $A\beta$ ) seed new cytotoxic LNOs through multiple serial dilutions into  $A\beta_{1-42}$  monomers in the absence of additional  $A\beta_{3(pE)-42}$ . LNOs isolated from human Alzheimer's disease brain contained  $A\beta_{3(pE)-42}$ , and enhanced  $A\beta_{3(pE)-42}$  formation in mice triggered neuron loss and gliosis at 3 months, but not in a tau-null background. We conclude that  $A\beta_{3(pE)-42}$  confers tau-dependent neuronal death and causes template-induced misfolding of  $A\beta_{1-42}$  into structurally distinct LNOs that propagate by a prion-like mechanism. Our results raise the possibility that  $A\beta_{3(pE)-42}$  acts similarly at a primary step in Alzheimer's disease pathogenesis.

pE- $A\beta$  peptides contain an amino-terminal pyroglutamate, whose modification from glutamate is catalysed by glutamyl cyclase (QC; also known as QPCT)<sup>10</sup>. The most prominent pE- $A\beta$  species *in vivo* are  $A\beta_{3(pE)-40}$ ,  $A\beta_{3(pE)-42}$ ,  $A\beta_{11(pE)-40}$  and  $A\beta_{11(pE)-42}$  (ref. 8; Supplementary Fig. 1), with  $A\beta_{3(pE)-42}$  being most abundant<sup>11</sup>. pE- $A\beta$  is more cytotoxic<sup>12</sup> and aggregates more rapidly<sup>13,14</sup> than conventional amyloid- $\beta$ , and QC activity and pE- $A\beta$  levels are increased several-fold in Alzheimer's disease brain<sup>10</sup>. Alzheimer's disease mouse models also indicate a role for pE- $A\beta$  in initiating pathology: oral administration of a QC inhibitor led to improved memory and learning, and reduced levels of pE- $A\beta$  and conventional amyloid- $\beta$ <sup>10</sup>. These data imply that pE- $A\beta$  potentiates the neurotoxicity of conventional amyloid- $\beta$ , but leave open the issue of molecular mechanisms. To address that issue, we compared oligomerization of  $A\beta_{3(pE)-42}$ ,  $A\beta_{1-42}$ , and mixtures of the peptides *in vitro*, and analysed responses of primary cultured neurons and glial cells (Supplementary Fig. 2) to the oligomers.

At 5  $\mu$ M peptide, 5% pE- $A\beta$  aggregated faster than  $A\beta_{3(pE)-42}$  or  $A\beta_{1-42}$  alone, based on thioflavin T fluorescence shifts<sup>15</sup> (Supplementary

Fig. 3). The ratio of optical densities at 450 nm versus 490 nm ( $OD_{450\text{ nm}}/OD_{490\text{ nm}}$ ) for  $A\beta_{3(pE)-42}$  rose and peaked more rapidly than for  $A\beta_{1-42}$ , but peaked at a  $\sim$ 25% lower level. The fastest rise in the

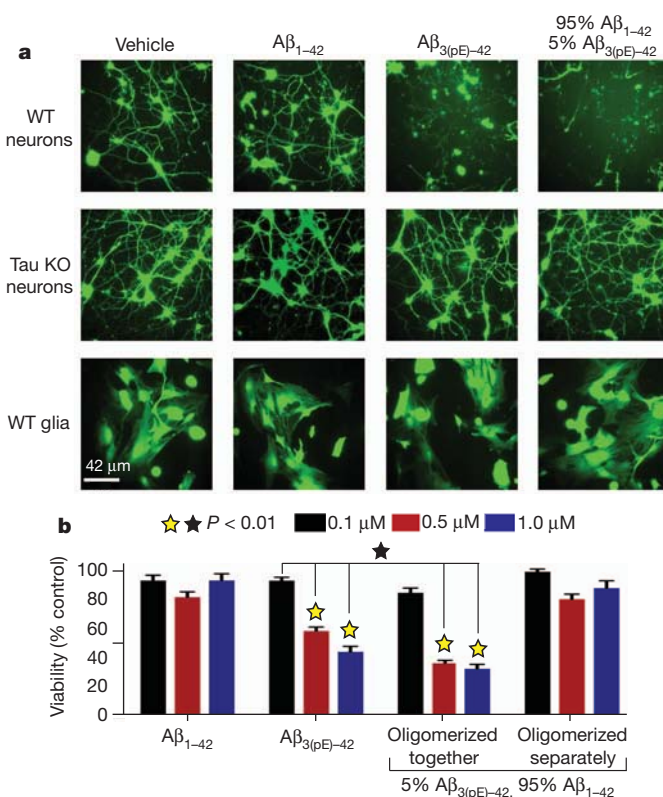


**Figure 1 | Tau-dependent cytotoxicity of oligomers formed by co-incubation of  $A\beta_{3(pE)-42}$  and  $A\beta_{1-42}$ .** Primary mouse wild-type (WT) and tau-knockout (KO) forebrain neurons, and secondary cultures of wild-type mouse glia were treated for 12 h with  $A\beta_{1-42}$ ,  $A\beta_{3(pE)-42}$ , or 5%  $A\beta_{3(pE)-42}$  plus 95%  $A\beta_{1-42}$ , which were oligomerized for 24 h at 5  $\mu$ M before dilution into culture media. **a**, Cells were exposed to calcein-AM and imaged live by epifluorescence microscopy to assay viability<sup>16</sup>. Extensive death and detachment of cells were observed only for wild-type neurons treated with  $A\beta_{3(pE)-42}$  or the 5%  $A\beta_{3(pE)-42}$  plus 95%  $A\beta_{1-42}$ . **b**, Following peptide treatment, cell viability was analysed by the XTT plate reader assay<sup>17</sup>. Note the robust cytotoxicity of  $A\beta_{3(pE)-42}$  containing solutions at concentrations as low as 0.5  $\mu$ M, unless  $A\beta_{3(pE)-42}$  and  $A\beta_{1-42}$  were incubated separately during oligomerization ( $P < 0.01$ ; yellow stars signify statistical significance of the indicated bar graphs versus vehicle controls; black stars signify statistical significance between the indicated bar graph pairs; mean  $\pm$  standard error of the mean (s.e.m.),  $n = 9$  replicates from 3 independent experiments).

<sup>1</sup>Department of Biology, University of Virginia, Charlottesville, Virginia 22904, USA. <sup>2</sup>Probiomed AG, 06120 Halle (Saale), Germany. <sup>3</sup>Department of Psychology, University of Virginia, Charlottesville, Virginia 22904, USA. <sup>4</sup>Department of Biochemistry and Molecular Biology, University of California at Irvine, Irvine, California 92697, USA. <sup>5</sup>Deutsches Zentrum fuer Neurodegenerative Erkrankungen, c/o Leibniz-Institut fuer Neurobiologie, 39118 Magdeburg, Germany. <sup>6</sup>JSW Life Sciences GmbH, A-8074 Grambach, Austria. <sup>7</sup>Ingenium Pharmaceuticals GmbH, 82152 Munich/Martinsried, Germany. <sup>8</sup>Department of Cell Biology, University of Virginia, Charlottesville, Virginia 22904, USA.

\*These authors contributed equally to this work.



OD<sub>450 nm</sub>/OD<sub>490 nm</sub> ratio was for 5% pE-A $\beta$ , which peaked similarly to A $\beta$ <sub>3(pE)-42</sub>, A $\beta$ <sub>3(pE)-42</sub>, A $\beta$ <sub>1-42</sub> and 5% pE-A $\beta$  thus oligomerized by different pathways.

To test whether distinct biological activities were coupled to these oligomerization differences, we compared cytotoxicity of the peptides towards cultured neurons or glia using calcein-AM and fluorescence microscopy<sup>16</sup>. Twelve hours of A $\beta$ <sub>1-42</sub> exposure had little effect on cell viability for wild-type or tau-knockout neurons, or wild-type glial cells (Fig. 1a). Contrastingly, most wild-type neurons died and detached from the substrate after exposure to A $\beta$ <sub>3(pE)-42</sub> or 5% pE-A $\beta$ . Tau-knockout neurons and wild-type glia, which express little tau, were resistant to A $\beta$ <sub>3(pE)-42</sub> and 5% pE-A $\beta$ .

Cytotoxicity dose dependence was examined by incubating wild-type neurons for 24 h in oligomers comprising 0.1, 0.5 or 1  $\mu$ M peptides, and using the 2,3-bis-(2-methoxy-4-nitro-5-sulphophenyl)-2H-tetrazolium-5-carboxanilide (XTT) reduction assay<sup>17</sup> (Fig. 1b). Cells were unaffected by A $\beta$ <sub>1-42</sub>, but A $\beta$ <sub>3(pE)-42</sub> and 5% pE-A $\beta$  had substantial cytotoxicity at 0.5  $\mu$ M and even more at 1.0  $\mu$ M. Cytotoxicity of 5% pE-A $\beta$  required A $\beta$ <sub>3(pE)-42</sub> and A $\beta$ <sub>1-42</sub> to incubate together for 24 h before being added to cells. When they were incubated separately for 24 h and mixed together at a 1:19 molar ratio immediately before being applied to cells, they were not cytotoxic. A small amount of A $\beta$ <sub>3(pE)-42</sub> can thus markedly enhance the cytotoxicity of a large excess of A $\beta$ <sub>1-42</sub>, provided the two peptides oligomerize together.

Evidence for hybrid oligomers came from immunoprecipitation of various forms of amyloid- $\beta$  using aggregation-dependent M64, which does not recognize A $\beta$ <sub>3(pE)-42</sub> (see Supplementary Fig. 4 for characterization of all anti-amyloid- $\beta$  antibodies used, including M64). Immunoprecipitations were analysed on dot blots using 4G8, which equally recognizes A $\beta$ <sub>3(pE)-42</sub> and A $\beta$ <sub>1-42</sub>, and anti-pE-A $\beta$ , which does not react with A $\beta$ <sub>1-42</sub>. M64 immunoprecipitated oligomers made from A $\beta$ <sub>1-42</sub> or 5% pE-A $\beta$ , but it did not immunoprecipitate A $\beta$ <sub>3(pE)-42</sub> oligomers, nor monomers of either peptide (Fig. 2a). Because anti-pE-A $\beta$  reacted with material immunoprecipitated out of 5% pE-A $\beta$ , M64 pulled down hybrid peptide oligomers. A $\beta$ <sub>3(pE)-42</sub> accounted for  $\sim$ 16% of the amyloid- $\beta$  in gel-filtered cytotoxic oligomers after 3 h of oligomerization, and steadily dropped to  $\sim$ 8% by 24 h (Fig. 2b). A $\beta$ <sub>3(pE)-42</sub> thus acts as a template that initiates formation of cytotoxic oligomers.

Cytotoxicity was sensitive to oligomerization time (Fig. 2c). Baseline cytotoxicity was observed at all time points for A $\beta$ <sub>1-42</sub>, and for 5% pE-A $\beta$  solutions in which A $\beta$ <sub>3(pE)-42</sub> and A $\beta$ <sub>1-42</sub> oligomerized separately. Pure A $\beta$ <sub>3(pE)-42</sub> killed  $\sim$ 50% of the cells after 24 h of oligomerization, but was virtually non-toxic at 0 h and after 96 h of oligomerization. The most cytotoxic solutions were 5% pE-A $\beta$ , in which the constituent peptides co-oligomerized for 24 h. These solutions killed  $\sim$ 60% of the cells within 24 h, and lower but robust cytotoxicity was observed at 96 h. Even the 0 h co-oligomers of 5% pE-A $\beta$  exhibited low, significant cytotoxicity. Co-incubated mixtures of 5% A $\beta$ <sub>3(pE)-42</sub> and 95% A $\beta$ <sub>1-42</sub>

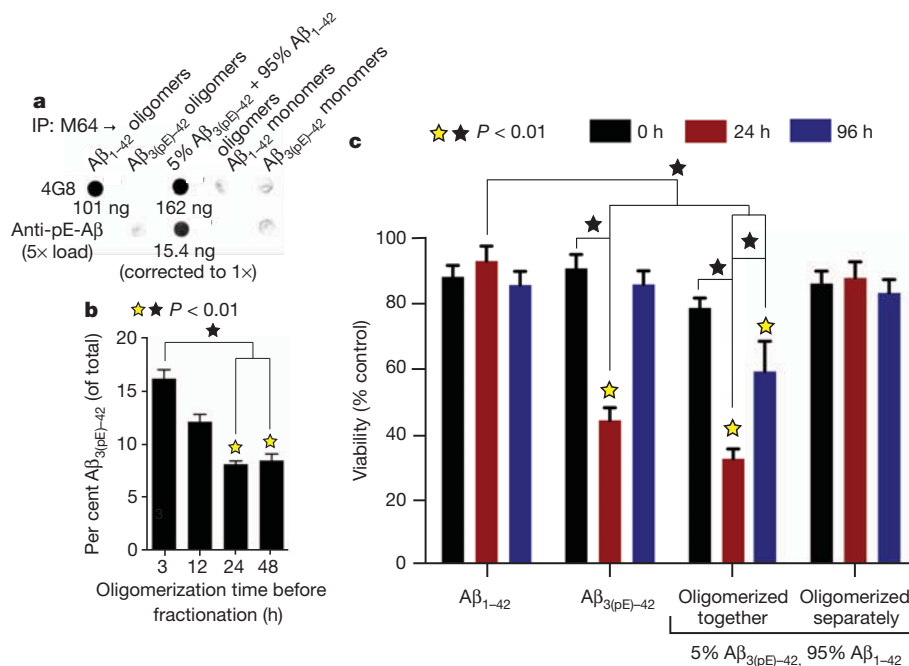
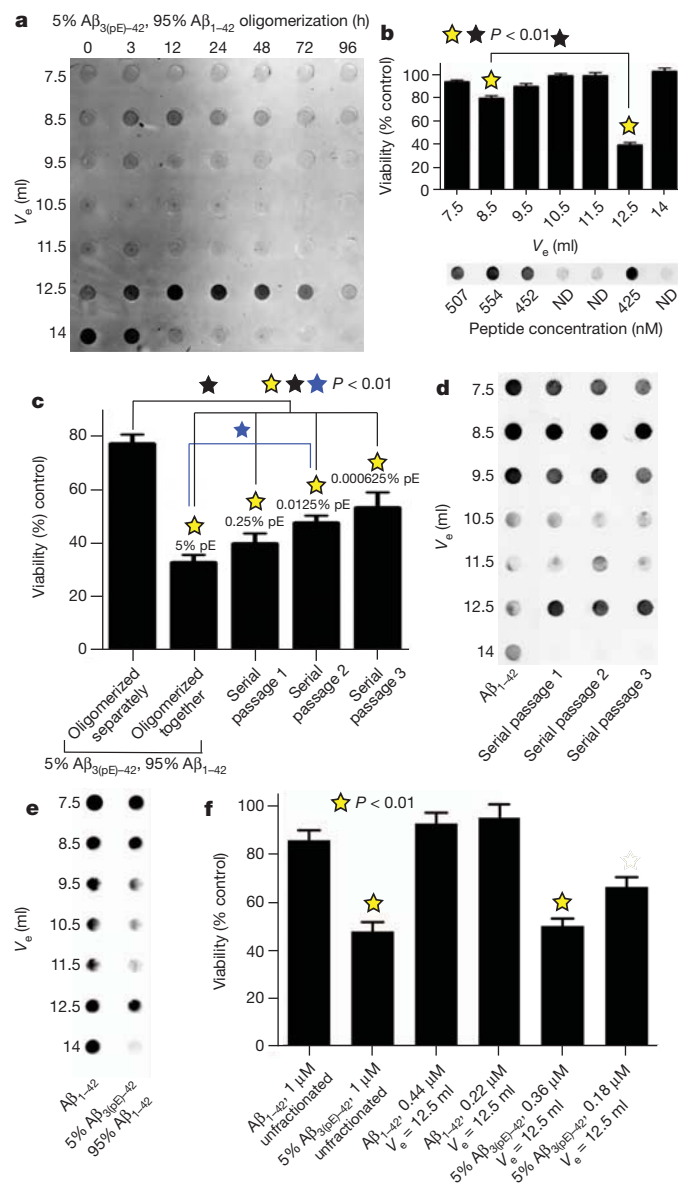


**Figure 2 | A $\beta$ <sub>3(pE)-42</sub> and A $\beta$ <sub>1-42</sub> form metastable, cytotoxic, hybrid oligomers.** **a**, A $\beta$ <sub>3(pE)-42</sub> and A $\beta$ <sub>1-42</sub> were incubated together at a 1:19 molar ratio (5% pE-A $\beta$ ) for 24 h at 1  $\mu$ M total amyloid- $\beta$ , and were then immunoprecipitated (IP) with M64, a rabbit monoclonal antibody that specifically recognizes residues 3–7 (EFRH) of A $\beta$ <sub>1-40</sub> oligomers or fibrils. Additional samples that were immunoprecipitated included otherwise identically treated oligomers made from pure A $\beta$ <sub>3(pE)-42</sub> or A $\beta$ <sub>1-42</sub>, and monomeric versions of the two peptides. Immunoprecipitated oligomers were converted to monomers by lyophilization, solubilization with HFIP and dilution into PBS, and along with the other samples were dot blotted onto nitrocellulose and analysed using 4G8, a mouse monoclonal antibody that recognizes A $\beta$ <sub>3(pE)-42</sub> and A $\beta$ <sub>1-42</sub> equally well, and an antibody that specifically recognizes pE-A $\beta$  (see Supplementary Fig. 4 for characterization of all antibodies used here). Quantification of the dot blots using a LI-COR Odyssey imaging station indicated that the oligomers that were immunoprecipitated from the mixed peptide solution contained both A $\beta$ <sub>3(pE)-42</sub> and A $\beta$ <sub>1-42</sub>, at a molar ratio of  $\sim$ 1:10. **b**, Solutions containing 5% pE-A $\beta$ <sub>3(pE)-42</sub> and 95% A $\beta$ <sub>1-42</sub> were incubated for the indicated times, and then were fractionated by gel

filtration. At each time point, fractions that eluted at 12.5 ml, where most cytotoxicity resided (see Fig. 3b) were immunoprecipitated using anti-human amyloid- $\beta$  (N), an amino-terminal-specific antibody that does not react with pE-A $\beta$  (data not shown). The immunoprecipitates were then lyophilized, re-solubilized with HFIP, and quantitatively analysed on dot blots with 4G8 and anti-pE-A $\beta$  using the LI-COR Odyssey. The time-dependent decrease in the A $\beta$ <sub>3(pE)-42</sub> content of the immunoprecipitated oligomers implies that A $\beta$ <sub>3(pE)-42</sub> initiated formation of hybrid peptide oligomers. **c**, A $\beta$ <sub>3(pE)-42</sub> and A $\beta$ <sub>1-42</sub> oligomerized for 0, 24 and 96 h either separately or together as 1:19 mixtures, and then were added to primary wild-type neuron cultures for 24 h at a final concentration of 1  $\mu$ M total amyloid- $\beta$ . Following peptide treatment, cell viability was analysed by the XTT plate reader assay<sup>17</sup>. The most cytotoxic species observed were the hybrid oligomers after 24 h of oligomerization ( $P < 0.01$ ; yellow stars signify statistical significance of the indicated bar graphs versus vehicle controls; black stars signify statistical significance between the indicated bar graph pairs; mean  $\pm$  s.e.m.,  $n = 6$  or 9 replicates from 3 independent experiments for panel **b** or **c**, respectively).

$A\beta_{1-42}$  can therefore form oligomers whose cytotoxicity is both greater and more enduring than oligomers formed by  $A\beta_{3(pE)-42}$  alone.

To identify the co-oligomer size(s) that were cytotoxic, amyloid- $\beta$  solutions were oligomerized for various times from 0–96 h before fractionation by gel filtration. Total amyloid- $\beta$  in all fractions was determined using 4G8 dot blots that, as shown in Fig. 3a (for 5% pE- $A\beta$ ) and Supplementary Fig. 5 (for  $A\beta_{1-42}$  and  $A\beta_{3(pE)-42}$ ), illustrate the full fractionation range of the column but exclude most void volume fractions. Presumptive monomeric  $A\beta_{1-42}$  dominated initially and persisted at 3 h, but was nearly undetectable after 12 h. The 3 h time point also marked the appearance of  $A\beta_{1-42}$  oligomers, which gradually increased in size over the next 93 h.  $A\beta_{3(pE)-42}$  and 5% pE- $A\beta$  oligomerized differently. Putative monomers were present at 0 h for both samples, when slightly larger species, LNOs that possibly corresponded to dimers or trimers (Supplementary Fig. 6), were also present. These persisted as the main species for 24 h for  $A\beta_{3(pE)-42}$  and for nearly 72 h for 5% pE- $A\beta$ , and later time points were dominated by larger aggregates that eluted in void volume fractions. Cytotoxicity was assayed for individual fractions of 5% pE- $A\beta$  that oligomerized for 24 h (Fig. 3b). Most cytotoxicity was associated with the possible dimers/trimers that eluted at 12.5 ml, which at 425 nM peptide killed more than 60% of the cells. Low cytotoxicity was also observed at 554 nM peptide for the larger oligomers that eluted at 8.5 ml.



The marked enhancement of  $A\beta_{1-42}$  cytotoxicity by  $A\beta_{3(pE)-42}$  suggested a prion-like templating mechanism of  $A\beta_{1-42}$  misfolding initiated by  $A\beta_{3(pE)-42}$ . To test that hypothesis, 5% pE- $A\beta$  that oligomerized for 24 h was diluted into 19 volumes of monomeric  $A\beta_{1-42}$ . A 24 h incubation of this mixture yielded 'serial passage 1', which was followed by two equivalent, sequential dilutions into monomeric  $A\beta_{1-42}$  to yield serial passages 2 and 3. A gradual loss of cytotoxicity was observed with successive passages, but even passage 3, which contained only 0.000625%  $A\beta_{3(pE)-42}$ , killed ~50% of the neurons within 24 h (Fig. 3c). Serially passaged gel-filtration samples contained abundant material that eluted at 12.5 ml in passages 1–3, despite the progressive dilution of  $A\beta_{3(pE)-42}$  (Fig. 3d).  $A\beta_{3(pE)-42}$  can therefore template formation of metastable, cytotoxic LNOs from excess  $A\beta_{1-42}$ , yielding potent bioactivity that can be serially passaged multiple times into monomeric  $A\beta_{1-42}$  without further addition of  $A\beta_{3(pE)-42}$ .

One possible explanation for why  $A\beta_{1-42}$  LNOs were inert is that they lacked sufficient properly sized oligomers. Accordingly, we altered the oligomerization protocol from 5  $\mu$ M peptide for 24 h at 37 °C to 10  $\mu$ M peptide for 30 min at 4 °C to obtain abundant  $A\beta_{1-42}$  oligomers that eluted at 12.5 ml (Fig. 3e). These LNOs were not cytotoxic (Fig. 3f), implying that they were structurally distinct from the putative dimers/trimers initiated by  $A\beta_{3(pE)-42}$ . This was confirmed by dot blots using M87, a conformation-sensitive anti-amyloid- $\beta$  antibody, to compare the putative dimers/trimers used for the cytotoxicity assays shown in Fig. 3f. We first lyophilized aliquots of all the amyloid- $\beta$  solutions, resuspended them with hexafluoroisopropanol (HFIP) to restore them to monomers, and then analysed them using 4G8. When parallel samples that were not lyophilized but were otherwise identical were analysed using M87, immunoreactivity was approximately twice as strong with LNOs made from  $A\beta_{1-42}$  versus those made from 5% pE- $A\beta$  (Supplementary Fig. 7). Cytotoxic LNOs of 5% pE- $A\beta$  are thus structurally distinct from comparably sized LNOs of  $A\beta_{1-42}$ .

**Figure 3 | The cytotoxic species are low- $n$ , prion-like oligomers.** **a**, Gel-filtration chromatography was used to fractionate 5% pE- $A\beta$  after oligomerization at 5  $\mu$ M at 37 °C for 0–96 h. The resulting fractions were then converted to monomers using HFIP and analysed on dot blots using monoclonal antibody 4G8. Note the metastable oligomers with an average elution volume ( $V_e$ ) of 12.5 ml. **b**, Isolated gel-filtration fractions from the 24 h time point were added to wild-type neuron cultures for 24 h, after which the cells were assayed for cell viability using XTT<sup>17</sup>. Robust cytotoxicity was associated only with the  $V_e = 12.5$  ml fraction, although the  $V_e = 8.5$  ml fraction had low, but statistically significant cell killing activity ( $P < 0.01$ ; mean  $\pm$  s.e.m.,  $n = 9$  replicates from 3 independent experiments). ND, not detected. **c**, Cytotoxic hybrid oligomers made by co-incubating a 1:19 ratio of  $A\beta_{3(pE)-42}$ : $A\beta_{1-42}$  for 24 h at 5  $\mu$ M were diluted into a 19-fold molar excess of freshly dissolved, monomeric  $A\beta_{1-42}$ , which was then incubated at 5  $\mu$ M for another 24 h to yield serial passage 1. Two further iterations of this strategy yielded serial passages 2 and 3. The starting material and its serially passaged derivatives were added to wild-type neurons at 1  $\mu$ M peptide for 24 h, after which cells were analysed using the XTT assay for cell viability<sup>17</sup>. Only a gradual loss of cytotoxicity was observed with each successive serial passage. **d**, Each serially passaged sample, as well as otherwise identically prepared oligomers made from pure  $A\beta_{1-42}$ , were fractionated by gel filtration and analysed on dot blots with 4G8. Note that all serially passaged samples contained metastable LNOs of  $V_e = 12.5$  ml, which were absent from the pure  $A\beta_{1-42}$  samples. **e**,  $A\beta_{1-42}$  (10  $\mu$ M) that was oligomerized for 30 min at 4 °C, and 5%  $A\beta_{3(pE)-42}$  plus 95%  $A\beta_{1-42}$  (5  $\mu$ M) that was oligomerized for 24 h at 37 °C were fractionated by gel filtration and analysed on dot blots exactly using 4G8. Note the isolation of fractions with  $V_e = 12.5$  ml from both preparations. **f**, Wild-type neurons were assayed for viability using the XTT plate reader assay<sup>17</sup> following 24 h of exposure to the indicated amyloid- $\beta$  preparations. Note the minimal cytotoxicity of unfractionated  $A\beta_{1-42}$  and  $A\beta_{1-42}$  with  $V_e = 12.5$  ml ( $P < 0.01$ , mean  $\pm$  s.e.m.,  $n = 9$  replicates from 3 independent experiments).  $P < 0.01$ ; yellow stars signify statistical significance of the indicated bar graphs versus vehicle controls; black stars and blue stars signify statistical significance between the indicated bar graph pairs; blue mean  $\pm$  s.e.m.,  $n = 9$  replicates from 3 independent experiments for panels **b**, **c** and **f**.

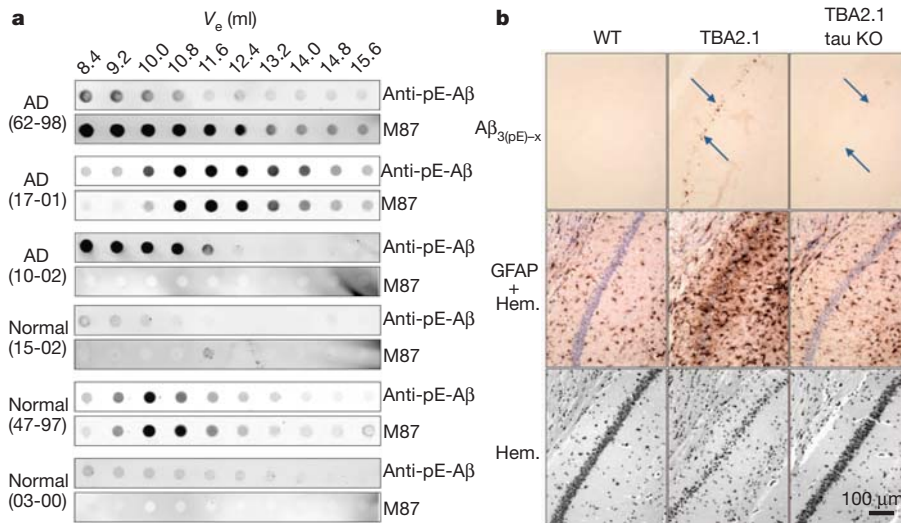


**Figure 4** |  $A\beta_{3(pE)-42}$  *in vivo*. **a**, Cytosol obtained from human Alzheimer's disease (AD) and similarly aged normal brains (Supplementary Fig. 9) were fractionated by gel filtration, and analysed by dot blotting with anti-pE-A $\beta$  and M87. Note the appearance of pE-A $\beta$  in LNO fractions, including those that eluted at 12.4 ml, especially in the Alzheimer's disease samples. **b**, Three-

month-old TBA2.1 mice generating  $A\beta_{3(pE)-42}$ <sup>18</sup> show amyloid- $\beta$  deposits (arrows), massive astrogliosis (GFAP) and neuron loss (Hem., haematoxylin nuclear staining), none of which are evident in comparably aged wild-type (WT) mice or TBA2.1/tau-knockout<sup>19</sup> (KO) hybrids.

Several lines of evidence demonstrate *in vivo* relevance for the data described so far. First, we identified LNOs containing  $A\beta_{3(pE)-42}$  in three out of three Alzheimer's disease samples, based on gel filtration of human brain extracts followed by dot blots of resulting fractions with anti-pE-A $\beta$  and M87. In contrast, only one of three age-matched samples with normal neuropathological diagnoses was positive for  $A\beta_{3(pE)-42}$  (Fig. 4a and Supplementary Fig. 8). Second, we crossed TBA2.1 mice<sup>18</sup> into a tau-knockout background<sup>19</sup>. By 3 months, TBA2.1 mice accumulated small amounts (40–100 ng g<sup>-1</sup> brain weight) of  $A\beta_{3(pE)-42}$ , which formed primarily intraneuronal aggregates, and was associated with massive hippocampal neuron loss and gliosis<sup>18</sup>. Knocking out tau provided almost complete protection against neuron loss and glial activation (Fig. 4b). Additional *in vivo* data are shown in Supplementary Fig. 9. Long-term potentiation (LTP) of mouse hippocampal neurons in slice cultures was potently and equally inhibited by oligomers made from 5%  $A\beta_{3(pE)-42}$  or 100%  $A\beta_{3(pE)-42}$ , whereas  $A\beta_{1-42}$  oligomers had no effect on LTP. 1%  $A\beta_{3(pE)-42}$  provoked mild, but statistically insignificant LTP impairment (Supplementary Fig. 9a). To evaluate the effects of increased  $A\beta_{3(pE)-42}$  in animal models, we crossed mice with neuron-specific expression of human  $\beta$ -amyloid precursor protein (APP) harbouring Swedish and London mutations (hAPP<sub>SL</sub>)<sup>20</sup>, with mice expressing human QC<sup>21</sup>. Nine-month-old double (hAPP<sub>SL</sub>/hQC) and single (hAPP<sub>SL</sub>) transgenic mice were indistinguishable in terms of insoluble and soluble  $A\beta_{x-42}$  levels, but the double transgenics had approximately twofold more insoluble  $A\beta_{3(pE)-42}$  and approximately ninefold more soluble  $A\beta_{3(pE)-42}$  than single transgenics (Supplementary Fig. 9b). Further analysis of the soluble  $A\beta_{x-42}$  by the A4 assay<sup>22</sup> revealed an approximately eightfold excess of oligomers in the double versus single transgenics (Supplementary Fig. 9c). Double transgenics performed more poorly in Morris water maze tests (Supplementary Fig. 9d) and had reduced hippocampal immunoreactivity for the synapse marker, synaptophysin (Supplementary Fig. 9e). Finally, peri-hippocampal injection of 5% pE-A $\beta$  at 5  $\mu$ M into APP<sub>SwDI</sub>/NOS2<sup>-/-</sup> Alzheimer's disease model mice<sup>23</sup> led 3–5 months later to the presence of plaques containing both pE-A $\beta$  and conventional amyloid- $\beta$ . Comparable plaques were rarely seen in sham-injected Alzheimer's disease mice or in wild-type mice injected with 5% pE-A $\beta$  (Supplementary Fig. 9f). These collective *in vivo* results emphasize the physiological significance of the companion biochemical and cultured cell results.

Our studies provide new insights into Alzheimer's disease pathogenesis by demonstrating that hypertoxic amyloid- $\beta$  oligomers can be triggered by small quantities of a specifically truncated and post-translationally modified version of amyloid- $\beta$ . Although some previous studies demonstrated that pE modification of amyloid- $\beta$  considerably enhances its aggregation kinetics<sup>13,14,24</sup>, toxicity<sup>12,18,25</sup> and resistance to degradation<sup>12</sup>, a mechanistic explanation for the unique properties of pE-A $\beta$  has been lacking until now. Prior studies suggest coincident appearance of  $A\beta_{3(pE)-42}$  with development or progression of human Alzheimer's disease<sup>26,27</sup>. Co-localization of QC and  $A\beta_{3(pE)-42}$  was found in cored plaques of vulnerable regions in Alzheimer's disease, and evidence was provided for axonal transport of  $A\beta_{3(pE)-x}$  from QC-rich neuronal populations of the entorhinal cortex and locus coeruleus<sup>28</sup>. As LNOs containing  $A\beta_{3(pE)-42}$  are reasonably stable (Fig. 3a), they might initiate tau-dependent cytotoxicity intracellularly during axonal transport<sup>29</sup> or extracellularly following release at remote hippocampal synapses<sup>30</sup> of projection neurons<sup>28</sup>. The  $A\beta_{3(pE)-42}$ -induced formation of toxic mixed oligomers provides a rationale for these previous observations, and the tau-dependent cytotoxicity of 5% pE-A $\beta$  establishes a new functional connection between amyloid- $\beta$  and tau in Alzheimer's disease pathogenesis.

## METHODS SUMMARY

Full descriptions of thioflavin T assays, cell culture, cell viability assays, procedures for oligomerization of amyloid- $\beta$  peptides and their fractionation by gel-filtration chromatography, production and specificity of rabbit monoclonal anti-amyloid- $\beta$  antibodies, immunoprecipitation, dot blots and western blots, generation of hAPP<sub>SL</sub>/hQC transgenic mice, LTP measurements of mouse hippocampal slice cultures, peri-hippocampal injection of 5% pE-A $\beta$  into Alzheimer's disease model mice, cultured cell and brain immunohistochemistry, and collection of human brain extracts are provided in Supplementary Methods.

Received 16 May 2011; accepted 16 March 2012.

Published online 2 May; corrected 30 May 2012 (see full-text HTML version for details).

- Gandy, S. *et al.* Days to criterion as an indicator of toxicity associated with human Alzheimer amyloid- $\beta$  oligomers. *Ann. Neurol.* **68**, 220–230 (2010).
- Walsh, D. M. & Selkoe, D. J.  $A\beta$  oligomers—a decade of discovery. *J. Neurochem.* **101**, 1172–1184 (2007).
- Rapoport, M., Dawson, H. N., Binder, L. I., Vitek, M. P. & Ferreira, A. Tau is essential to  $\beta$ -amyloid-induced neurotoxicity. *Proc. Natl Acad. Sci. USA* **99**, 6364–6369 (2002).
- King, M. E. *et al.* Tau-dependent microtubule disassembly initiated by pre-fibrillar  $\beta$ -amyloid. *J. Cell Biol.* **175**, 541–546 (2006).



5. Roberson, E. D. *et al.* Reducing endogenous tau ameliorates amyloid  $\beta$ -induced deficits in an Alzheimer's disease mouse model. *Science* **316**, 750–754 (2007).
6. Jin, M. *et al.* Soluble amyloid  $\beta$ -protein dimers isolated from Alzheimer cortex directly induce Tau hyperphosphorylation and neuritic degeneration. *Proc. Natl Acad. Sci. USA* **108**, 5819–5824 (2011).
7. Mori, H., Takio, K., Ogawara, M. & Selkoe, D. J. Mass spectrometry of purified amyloid  $\beta$  protein in Alzheimer's disease. *J. Biol. Chem.* **267**, 17082–17086 (1992).
8. Saido, T. C. *et al.* Dominant and differential deposition of distinct  $\beta$ -amyloid peptide species,  $A\beta_{N3(pE)}$ , in senile plaques. *Neuron* **14**, 457–466 (1995).
9. Jawhar, S., Wirths, O. & Bayer, T. A. Pyroglutamate amyloid- $\beta$  ( $A\beta$ ): a hatchet man in Alzheimer disease. *J. Biol. Chem.* **286**, 38825–38832 (2011).
10. Schilling, S. *et al.* Glutaminy cyclase inhibition attenuates pyroglutamate  $A\beta$  and Alzheimer's disease-like pathology. *Nature Med.* **14**, 1106–1111 (2008).
11. Tabaton, M. *et al.* Soluble amyloid  $\beta$ -protein is a marker of Alzheimer amyloid in brain but not in cerebrospinal fluid. *Biochem. Biophys. Res. Commun.* **200**, 1598–1603 (1994).
12. Russo, C. *et al.* Pyroglutamate-modified amyloid  $\beta$ -peptides— $A\beta_{N3(pE)}$ —strongly affect cultured neuron and astrocyte survival. *J. Neurochem.* **82**, 1480–1489 (2002).
13. Schilling, S. *et al.* On the seeding and oligomerization of pGlu-amyloid peptides (*in vitro*). *Biochemistry* **45**, 12393–12399 (2006).
14. Schlenzig, D. *et al.* Pyroglutamate formation influences solubility and amyloidogenicity of amyloid peptides. *Biochemistry* **48**, 7072–7078 (2009).
15. Levine, H. III. Thioflavine T interaction with synthetic Alzheimer's disease  $\beta$ -amyloid peptides: detection of amyloid aggregation in solution. *Protein Sci.* **2**, 404–410 (1993).
16. Wang, X. M. *et al.* A new microcellular cytotoxicity test based on calcein AM release. *Hum. Immunol.* **37**, 264–270 (1993).
17. Scudiero, D. A. *et al.* Evaluation of a soluble tetrazolium/formazan assay for cell growth and drug sensitivity in culture using human and other tumor cell lines. *Cancer Res.* **48**, 4827–4833 (1988).
18. Alexandru, A. *et al.* Selective hippocampal neurodegeneration in transgenic mice expressing small amounts of truncated  $A\beta$  is induced by pyroglutamate- $A\beta$  formation. *J. Neurosci.* **31**, 12790–12801 (2011).
19. Tucker, K. L., Meyer, M. & Barde, Y. A. Neurotrophins are required for nerve growth during development. *Nature Neurosci.* **4**, 29–37 (2001).
20. Rockenstein, E., Mallory, M., Mante, M., Sisk, A. & Masliah, E. Early formation of mature amyloid- $\beta$  protein deposits in a mutant APP transgenic model depends on levels of  $A\beta_{1-42}$ . *J. Neurosci. Res.* **66**, 573–582 (2001).
21. Jawhar, S. *et al.* Overexpression of glutaminy cyclase, the enzyme responsible for pyroglutamate  $A\beta$  formation, induces behavioral deficits, and glutaminy cyclase knock-out rescues the behavioral phenotype in 5XFAD mice. *J. Biol. Chem.* **286**, 4454–4460 (2011).
22. Tanghe, A. *et al.* Pathological hallmarks, clinical parallels, and value for drug testing in Alzheimer's disease of the APP[V717I] London transgenic mouse model. *Int. J. Alzheimers Dis.* **2010** (2010).
23. Wilcock, D. M. *et al.* Progression of amyloid pathology to Alzheimer's disease pathology in an amyloid precursor protein transgenic mouse model by removal of nitric oxide synthase 2. *J. Neurosci.* **28**, 1537–1545 (2008).
24. He, W. & Barrow, C. J. The  $A\beta$  3-pyroglutamyl and 11-pyroglutamyl peptides found in senile plaque have greater  $\beta$ -sheet forming and aggregation propensities *in vitro* than full-length  $A\beta$ . *Biochemistry* **38**, 10871–10877 (1999).
25. Wirths, O. *et al.* Intraneuronal pyroglutamate- $A\beta$  3–42 triggers neurodegeneration and lethal neurological deficits in a transgenic mouse model. *Acta Neuropathol.* **118**, 487–496 (2009).
26. Güntert, A., Dobeli, H. & Bohrmann, B. High sensitivity analysis of amyloid- $\beta$  peptide composition in amyloid deposits from human and PS2APP mouse brain. *Neuroscience* **143**, 461–475 (2006).
27. Piccini, A. *et al.*  $\beta$ -Amyloid is different in normal aging and in Alzheimer disease. *J. Biol. Chem.* **280**, 34186–34192 (2005).
28. Hartlage-Rübsamen, M. *et al.* Glutaminy cyclase contributes to the formation of focal and diffuse pyroglutamate (pGlu)- $A\beta$  deposits in hippocampus via distinct cellular mechanisms. *Acta Neuropathol.* **121**, 705–719 (2011).
29. Vossel, K. A. *et al.* Tau reduction prevents  $A\beta$ -induced defects in axonal transport. *Science* **330**, 198 (2010).
30. Wilcox, K. C., Lacor, P. N., Pitt, J. & Klein, W. L.  $A\beta$  oligomer-induced synapse degeneration in Alzheimer's disease. *Cell. Mol. Neurobiol.* **31**, 939–948 (2011).

**Supplementary Information** is linked to the online version of the paper at [www.nature.com/nature](http://www.nature.com/nature).

**Acknowledgements** The authors are grateful for support from the following sources: the Alzheimer's Association (grant 4079 to G.S.B.); the Owens Family Foundation (G.S.B.); the Cure Alzheimer's Fund (G.S.B., C.G.G.); NIH/NIGMS training grant T32 GM008136, which funded part of J.M.N.'s PhD training; NIH/NIA grant R01 AG033069 (C.G.G.); and the German Federal Department of Science and Technology grant 03IS2211F (H.-U.D.). Funding for the UCI-ADRC was provided by NIH/NIA grant P50 AG16573. We also thank H. Dawson and M. Vitek of Duke University for providing the tau-knockout mice. This work fulfilled part of the requirements for the PhD earned by J.M.N. at the University of Virginia. The technical assistance of A. Spano, H.-H. Ludwig, E. Scheel and K. Schulz is gratefully acknowledged.

**Author Contributions** J.M.N. performed most of the biochemical and cell biological experiments; S.S. was the principal force behind the experiments involving hAPP<sub>SL</sub>/hQC and TBA2.1/tau-knockout mice, and was aided by B.H.-P. and H.C.; A.S. and T.W. fractionated and analysed human brain extracts; E.S., K.T. and B.W. performed the peri-hippocampal injection experiments; A.H. and C.G.G. produced and characterized the M64 and M87 antibodies; R.R. and K.R. performed the electrophysiology experiments; A.A., W.J. and S.G. performed and analysed the immunohistochemical experiments on TBA2.1 and tau-knockout/TBA2.1 mice; G.S.B. and H.-U.D. initiated and directed the project; G.S.B. was the principal writer of the paper; all of the authors participated in the design and analysis of experiments, and in editing of the paper.

**Author Information** Reprints and permissions information is available at [www.nature.com/reprints](http://www.nature.com/reprints). The authors declare no competing financial interests. Readers are welcome to comment on the online version of this article at [www.nature.com/nature](http://www.nature.com/nature). Correspondence and requests for materials should be addressed to G.S.B. ([gsb4g@virginia.edu](mailto:gsb4g@virginia.edu)) or H.-U.D. ([Hans-Ulrich.Demuth@probiobdrug.de](mailto:Hans-Ulrich.Demuth@probiobdrug.de)).

# Inhibitory receptors bind ANGPTLs and support blood stem cells and leukaemia development

Junke Zheng<sup>1,2\*</sup>, Masato Umikawa<sup>1,3\*</sup>, Changhao Cui<sup>1\*</sup>, Jiyuan Li<sup>1</sup>, Xiaoli Chen<sup>1</sup>, Chaozheng Zhang<sup>1</sup>, HoangDinh Hyunh<sup>1</sup>, Xunlei Kang<sup>1</sup>, Robert Silvany<sup>1</sup>, Xuan Wan<sup>1</sup>, Jingxiao Ye<sup>1</sup>, Alberto Puig Cantó<sup>4</sup>, Shu-Hsia Chen<sup>5</sup>, Huan-You Wang<sup>6</sup>, E. Sally Ward<sup>4</sup> & Cheng Cheng Zhang<sup>1</sup>

How environmental cues regulate adult stem cell and cancer cell activity through surface receptors is poorly understood. Angiopoietin-like proteins (ANGPTLs), a family of seven secreted glycoproteins, are known to support the activity of haematopoietic stem cells (HSCs) *in vitro* and *in vivo*<sup>1–10</sup>. ANGPTLs also have important roles in lipid metabolism, angiogenesis and inflammation, but were considered ‘orphan ligands’ because no receptors were identified<sup>3,11,12</sup>. Here we show that the immune-inhibitory receptor human leukocyte immunoglobulin-like receptor B2 (LILRB2) and its mouse orthologue paired immunoglobulin-like receptor (PIRB) are receptors for several ANGPTLs. LILRB2 and PIRB are expressed on human and mouse HSCs, respectively, and the binding of ANGPTLs to these receptors supported *ex vivo* expansion of HSCs. In mouse transplantation acute myeloid leukaemia models, a deficiency in intracellular signalling of PIRB resulted in increased differentiation of leukaemia cells, revealing that PIRB supports leukaemia development. Our study indicates an unexpected functional significance of classical immune-inhibitory receptors in maintenance of stemness of normal adult stem cells and in support of cancer development.

We used multiple approaches, including expression cloning, to identify the receptor(s) for ANGPTLs. Human LILRB2, when ectopically expressed on Baf3 cells, enabled the cells to specifically bind glutathione S-transferase (GST)–ANGPTL5 as determined by flow cytometry (Fig. 1a). LILRB2 is a member of the immune-inhibitory B-type subfamily of LILR receptors<sup>13</sup> and contains four immunoglobulin domains and three immunoreceptor tyrosine-based inhibitory motifs. Using flow cytometry analysis, we further demonstrated that LILRB2-overexpressing 293T cells demonstrated enhanced binding to several ANGPTLs, especially ANGPTL2 and GST–ANGPTL5 (Fig. 1b and Supplementary Fig. 1a, b). ANGPTL2 and GST–ANGPTL5 also bound to LILRB3- and LILRB5-overexpressing cells, although with a lower affinity than to LILRB2-expressing cells (Supplementary Table 1). In addition, ANGPTL1 and ANGPTL7 bound to 293T cells overexpressing LAIR1 (ref. 14). (Supplementary Table 1 and Supplementary Fig. 2). ANGPTLs did not bind to LILRAs, LILRB1 or LILRB4 (Supplementary Table 1).

Because ANGPTL2 and GST–ANGPTL5 bound to LILRB2-expressing cells better than other ANGPTLs, we further assessed the molecular interaction between ANGPTL2/ANGPTL5 and LILRB2.

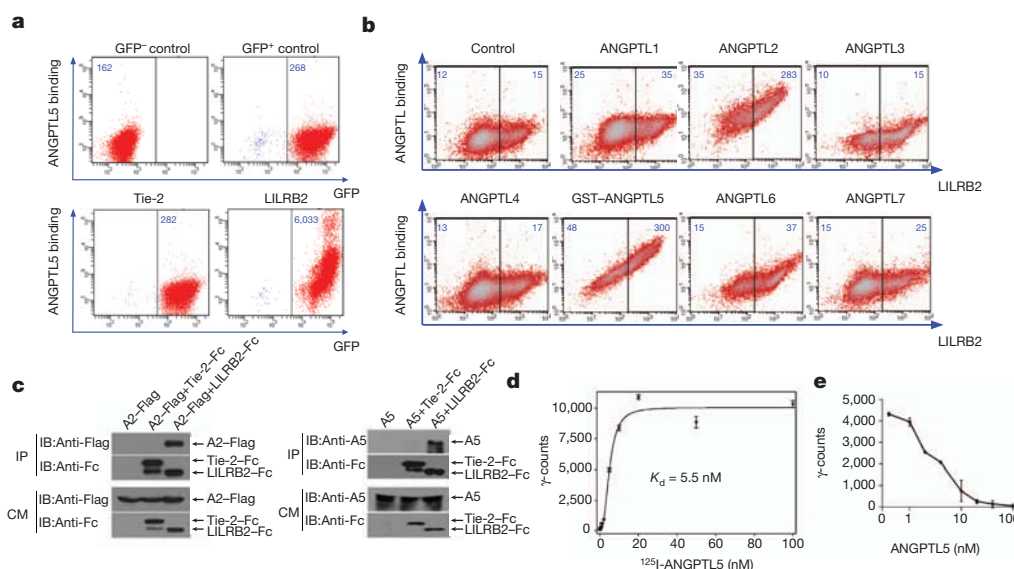


**Figure 1 | Cell-surface LILRB2 binds to ANGPTLs.** **a**, Flow cytometry analysis of GST–ANGPTL5–Flag binding to uninfected Baf3 cells or MSCV–GFP, MSCV–Tie-2–GFP, or MSCV–LILRB2–GFP-stably infected Baf3 cells. Mean fluorescence intensities are indicated. **b**, Flow cytometry analysis of indicated Flag-tagged ANGPTLs binding to LILRB2-transfected 293T cells.

**c**, ANGPTL2 and ANGPTL5 bound to the ECD of LILRB2 but not Tie-2 in conditioned medium (CM) of cotransfected 293T cells. **d**, **e**, Concentration-dependent specific (**d**) and competitive (**e**) <sup>125</sup>I–GST–ANGPTL5 binding to LILRB2 stably expressed Baf3 cells (*n* = 3). Error bars denote s.e.m. IB, immunoblotting.

<sup>1</sup>Departments of Physiology and Developmental Biology, University of Texas Southwestern Medical Center, Dallas, Texas 75390, USA. <sup>2</sup>Key Laboratory of Cell Differentiation and Apoptosis of Chinese Ministry of Education, Shanghai Jiao Tong University School of Medicine, Shanghai 200025, China. <sup>3</sup>Department of Medical Biochemistry, University of the Ryukyus, Okinawa 903-0215, Japan. <sup>4</sup>Department of Immunology, University of Texas Southwestern Medical Center, Dallas, Texas 75390, USA. <sup>5</sup>Department of Oncological Sciences, Mount Sinai School of Medicine, New York, New York 10029-6574, USA. <sup>6</sup>Department of Pathology, University of California San Diego, La Jolla, California 92093, USA.

\*These authors contributed equally to this work.

Co-transfection of ANGPTL2 or ANGPTL5 with LILRB2 extracellular domain (ECD) fused to human IgG-Fc (LILRB2-Fc) into 293T cells followed by immunoprecipitation and western blot showed that both ANGPTL2 and ANGPTL5 interacted with the ECD of LILRB2, but not that of Tie-2 (Fig. 1c and Supplementary Fig. 1c). The direct interactions between ANGPTLs and LILRB2 were confirmed by *in vitro* coimmunoprecipitation, using purified ANGPTL2-Flag or GST-ANGPTL5 and LILRB2-Fc (Supplementary Fig. 1d) and by surface plasmon resonance (SPR; Supplementary Fig. 3). A liquid-phase binding assay with  $^{125}\text{I}$ -labelled GST-ANGPTL5 demonstrated that the interaction between ANGPTL5 and cell-surface LILRB2 was specific and saturable, with half maximal saturation of the interaction as  $5.5 \pm 1.1$  nM (Fig. 1d, e). Although untagged ANGPTLs bind to LILRB2, the type or the position of tagging could affect the binding (Supplementary Table 2).

Because several ANGPTLs support expansion of HSCs<sup>4–10</sup>, we sought to determine whether ANGPTLs bound to LILRB2 or LAIR1 on primary human cord blood cells. Flow cytometry analysis showed that ANGPTL 1, 2, 5 and 7 all bound to LILRB2<sup>+</sup> human cord blood cells, and that ANGPTL2 and GST-ANGPTL5 had higher affinities (Fig. 2a, Supplementary Fig. 4 and Supplementary Table 1). The binding of ANGPTL1 and ANGPTL7 to LAIR1<sup>+</sup> human cord blood cells was relatively weak (Supplementary Fig. 5), and we therefore focused on studying the binding of ANGPTL2 and ANGPTL5 to LILRB2 in subsequent experiments.

We determined whether LILRB2 was expressed on human HSCs. Flow cytometry and quantitative (q)RT-PCR analyses showed that LILRB2 was expressed on the surface of 40–95% of human cord blood CD34<sup>+</sup> CD38<sup>−</sup> CD90<sup>+</sup> cells (95% in the experiment shown in Fig. 2b and Supplementary Fig. 6); this population is enriched for HSCs.

GST-ANGPTL5 treatment induced increased phosphorylation of calcium/calmodulin-dependent protein kinase (CAMK)-2 and -4 in human cord blood mononuclear cells (Supplementary Fig. 7). It is of note that CAMK4 is required for maintenance of the potency of HSCs<sup>15</sup>. Suppression of LILRB2 expression with short hairpin RNAs effectively reduced ANGPTL binding (Supplementary Fig. 8). Importantly, the silencing of LILRB2 resulted in decreased repopulation of human cord blood HSCs as measured by reconstitution analysis in non-obese diabetic/severe combined immunodeficient (NOD/SCID) mice (1% repopulation from cultured knockdown cells compared to 15% repopulation from cultured normal cells in medium STFA5; Fig. 2c). Together, these data indicate that ANGPTL5 supports expansion of human cord blood HSCs<sup>1</sup> in a process at least partially mediated by the surface receptor LILRB2.

PIRB is the mouse membrane orthologue of human LILRBs<sup>16,17</sup>. ANGPTL2, ANGPTL3 and GST-ANGPTL5 bound to PIRB as determined by flow cytometry (Fig. 3a and Supplementary Fig. 9) and coimmunoprecipitation (Fig. 3b and Supplementary Fig. 10). As with human cord blood HSCs, mouse HSCs were also enriched for PIRB expression (Fig. 3c and Supplementary Fig. 11).

To study the function of PIRB in mouse HSCs, we used PIRB-deficient (PIRBTM) mice<sup>18</sup>, in which four exons encoding the trans-membrane domain and part of the intracellular domain were deleted. PIRBTM cells freshly isolated from 3-week-old mice had significantly decreased CAMK4 phosphorylation, and binding of ANGPTL to PIRB induced phosphorylation of PIRB, recruitment of SHP-1 and SHP-2 (also known as PTPN6 and PTPN11, respectively) and CAMK4 activation (Supplementary Figs 12 and 13). These results suggest that certain ANGPTLs may be the ligands of PIRB that activate CAMK4 *in vivo*.

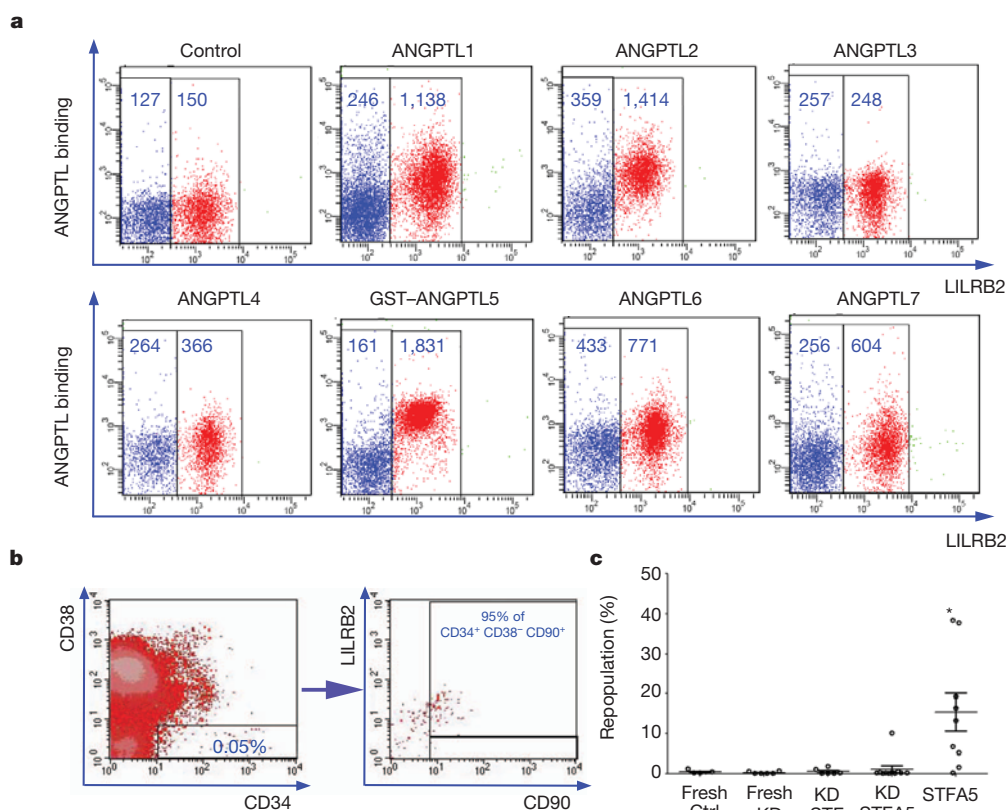


**Figure 2 | LILRB2 mediates the effect of ANGPTL in supporting the repopulation of human cord blood HSCs.** **a**, Flow cytometry analysis of indicated Flag-tagged ANGPTLs binding to LILRB2<sup>+</sup> human cord blood mononuclear cells (FACSARIA). Mean fluorescence intensities are indicated. **b**, Representative flow cytometry plots for the co-staining of CD34, CD38, CD90 and LILRB2 in human cord blood mononuclear cells (FACSCalibur).

**c**, Human cord blood CD34<sup>+</sup> cells infected with LILRB2 shRNA-encoding virus (KD) or control (Ctrl) scramble shRNA virus were transplanted into sublethally irradiated NOD/SCID mice before or after culture for 10 days. SCF+TPO+Flt3L (STF) or STF+ANGPTL5 (STFA5) was used in the culture. Shown is the human donor repopulation after 2 months ( $n = 5–11$ ). \* $P < 0.05$ . Error bars denote s.e.m.



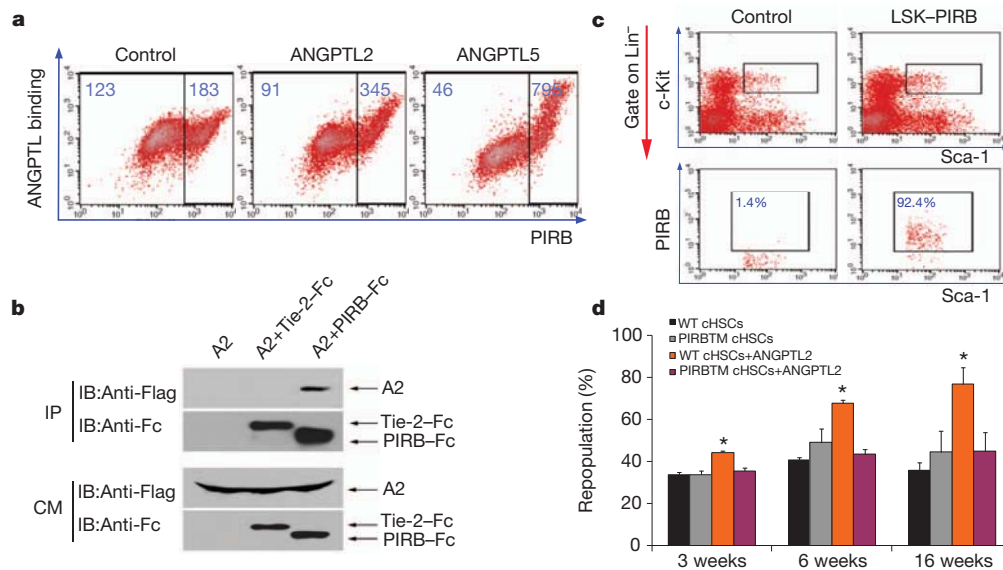


**Figure 3 | ANGPTLs bind PIRB and support the repopulation of mouse HSCs.** **a**, Flow cytometry analysis of Flag-ANGPTL2 or GST-ANGPTL5-Flag binding to PIRB-transfected 293T cells. **b**, ANGPTL2 binds to the ECD of PIRB but not Tie-2 in the conditioned medium (CM) of cotransfected 293T cells. **c**, PIRB is expressed on mouse bone marrow (BM) Lin<sup>-</sup> Sca-1<sup>+</sup> Kit<sup>+</sup> (LSK)

cells. Isotype control is indicated in the left panel. **d**, Competitive reconstitution of 8-day cultured progenies of input equivalent to 250 Lin<sup>-</sup> Sca-1<sup>+</sup> Kit<sup>+</sup> CD34<sup>-</sup> Flk-2<sup>-</sup> bone marrow HSCs from wild-type (WT) or PIRBTM donors (n = 5). SCF, TPO and FGF-1, with or without ANGPTL2, were used in culture. cHSCs, cultured HSCs. \*P < 0.05. Error bars denote s.e.m.

Because SHP-2 and CAMK4 are required for the repopulation of HSCs<sup>15,19</sup>, and the chemical inhibition of CAMK2, a homologue of CAMK4, induces differentiation and suppresses proliferation of myeloid leukaemia cells<sup>20</sup>, we sought to determine whether PIRB was important for HSC activity. Although the adult PIRBTM mice have certain immune and neuronal defects, they are grossly normal in haematopoiesis<sup>16,18</sup>. Interestingly, competitive repopulation showed that PIRBTM fetal liver HSCs had approximately 50% decreased repopulation activity (Supplementary Fig. 14). Moreover, although ANGPTL2 and ANGPTL5 had little effect on *ex vivo* expansion of adult PIRBTM HSCs, they supported *ex vivo* expansion of adult wild-type HSCs (Fig. 3d and Supplementary Fig. 14), as we previously demonstrated<sup>2</sup>. Collectively, our results indicate that ANGPTLs bind human LILRB2 and mouse PIRB to support HSC repopulation.

On the basis of our *in silico* analysis of a pool of 9,004 samples described previously<sup>21</sup>, the level of LILRB2 messenger RNA is at least fourfold higher in the human acute monoblastic and monocytic leukaemia cells (M5 subtype of acute myeloid leukaemia (AML)) than in other AML cells (Supplementary Fig. 15). As human acute monoblastic and monocytic leukaemia cells are often associated with rearrangement of mixed-lineage leukaemia (MLL; a histone methyltransferase deemed a positive global regulator of gene transcription), we used a retroviral MLL-AF9 transplantation mouse model<sup>22,23</sup> to further examine the role of PIRB in regulation of AML development. Wild-type or PIRBTM donor Lin<sup>-</sup> cells infected by retroviral MLL-AF9-internal ribosome entry site (IRES)-yellow fluorescent protein (YFP) were used to induce AML as previously described<sup>22,23</sup>. We examined PIRB expression in YFP<sup>+</sup> Mac-1<sup>+</sup> Kit<sup>+</sup> cells that may be enriched for AML-initiating activity<sup>22,23</sup>, and found that about 80% of YFP<sup>+</sup> Mac-1<sup>+</sup> Kit<sup>+</sup> cells were PIRB<sup>+</sup> (Fig. 4a). We next investigated whether PIRB was required for the induction of AML by MLL-AF9. Mice transplanted with MLL-AF9-transduced wild-type cells developed AML and died within approximately 5 weeks, whereas those transplanted with MLL-AF9-transduced PIRBTM cells were resistant to the induction of MLL-AF9 and developed AML much more slowly (Fig. 4b and Supplementary Fig. 16). The significantly delayed development of the PIRBTM leukaemia was correlated with about a 50% reduction in numbers of white blood cells in circulation and a much less severe infiltration of myeloid leukaemia cells into

the liver and spleen (Fig. 4c, d). Consistently, PIRB deficiency caused an approximately 50% reduction of YFP<sup>+</sup> Mac-1<sup>+</sup> Kit<sup>+</sup> cells in both bone marrow and peripheral blood (Fig. 4d). There were more CD3<sup>+</sup> or B220<sup>+</sup> cells in mice that received MLL-AF9-transduced PIRBTM donor cells than in those given wild-type cells (Fig. 4d). These results demonstrate that PIRB-mediated signalling is associated with faster AML development and greater numbers of YFP<sup>+</sup> Mac-1<sup>+</sup> Kit<sup>+</sup> AML cells *in vivo*.

We further assessed whether PIRB potentially regulates differentiation and self-renewal of AML cells. Colony-forming unit (c.f.u.) assays showed that extrinsic ANGPTL stimulation led to increased c.f.u. numbers in wild-type but not PIRBTM AML cells, again indicating that PIRB directly mediates the effects of ANGPTLs (Supplementary Fig. 16d). In addition, wild-type AML cells formed mostly compact colonies, whereas PIRBTM cells tended to form more diffuse ones (Fig. 4e). The formation of diffuse colonies indicates high differentiation potential<sup>24</sup>. The inhibition of differentiation of AML cells by PIRB is in accordance with previous reports that PIRB inhibits differentiation of myeloid-derived suppressive cells<sup>25</sup> and osteoclasts<sup>26</sup>, as well as our data showing that endogenous ANGPTLs inhibit differentiation and increase replating efficiency of haematopoietic progenitors (Supplementary Fig. 17). Moreover, PIRBTM primary colony-forming units were unable to form secondary colonies upon replating (Fig. 4f), indicating that PIRB supports self renewal of AML c.f.u. cells.

Finally, we analysed the molecular signalling triggered by the binding of ANGPTLs to PIRB in AML cells. PIRBTM AML cells had decreased phosphorylation of phosphatase SHP-2 (Supplementary Fig. 13d), which is known to be associated with LILRB2 receptors and is an oncogene that supports leukaemia development<sup>13,16,18,27</sup>. ANGPTLs also stimulated SHP-2 phosphorylation (Supplementary Fig. 13d). Similar to untransformed PIRBTM cells, PIRBTM AML cells had decreased CAMK4 activation (data not shown). Furthermore, wild-type Mac-1<sup>+</sup> Kit<sup>+</sup> cells had much greater expression of leukaemia initiation/maintenance genes<sup>22,23</sup>, but markedly decreased expression of myeloid-differentiation genes as determined by DNA microarray analyses (Fig. 4g). qRT-PCR confirmed the increased expression of several *HOXA* genes, *Meis1*, *Eya1*, *Myb* and *Mef2c* in wild-type Mac-1<sup>+</sup> Kit<sup>+</sup> cells than their PIRBTM counterparts (Supplementary Fig. 18); these genes are critical for initiation or maintenance of MLL-rearranged

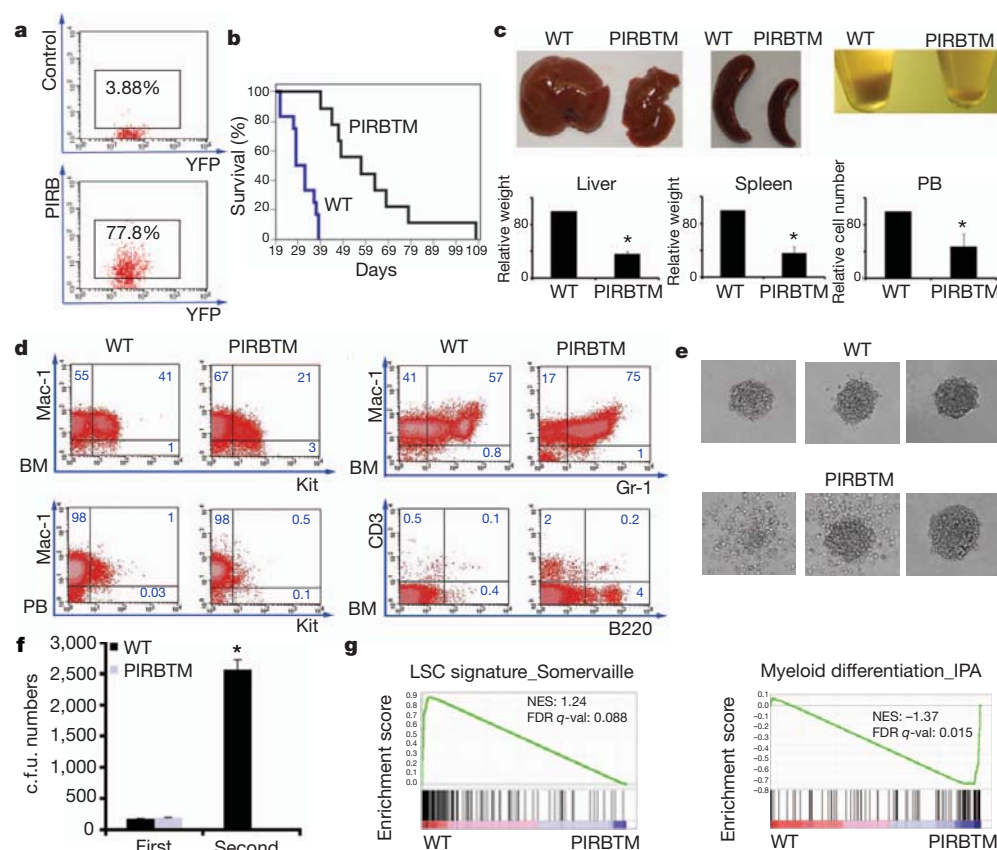


**Figure 4 | PIRB suppresses differentiation and enhances development of MLL-AF9 AML.** **a**, PIRB expression on YFP<sup>+</sup> Mac-1<sup>+</sup> Kit<sup>+</sup> AML cells as determined by flow cytometry. **b**, Survival curve of mice receiving MLL-AF9-infected WT or PIRBTM haematopoietic progenitors ( $n = 15$ );  $P < 0.05$ . **c**, Comparison of the sizes of spleen, liver and numbers of peripheral blood (PB) cells of the mice transplanted with wild-type (WT) MLL-AF9 cells and PIRBTM MLL-AF9 cells at 28 days after transplantation ( $n = 6$ ). **d**, Representative flow cytometry plots showing that PIRBTM AML mice have decreased Mac-1<sup>+</sup> Kit<sup>+</sup> cells and increased differentiated cells relative to mice transplanted with WT cells

AML (refs 22, 23). Similar to the MLL-AF9 model, the deficiency of PIRB in the AML1-ETO9a leukaemia model led to decreased numbers of leukaemia progenitors and increased numbers of differentiated cells (Supplementary Fig. 19). Collectively, these results indicate that the binding of ANGPTLs to PIRB promotes leukaemia development, probably through inhibiting differentiation of AML cells.

LILRB2 and PIRB are known to bind to other ligands, including various MHC class I molecules<sup>28</sup> and myelin inhibitors<sup>17</sup>. It will be important to investigate the *in vivo* context in which these different ligands bind LILRB and induce signalling. As ANGPTLs can be abundantly expressed by many types of cells, including those from endocrine organs<sup>11</sup> and potential bone marrow niche (endothelium and adipocytes<sup>9,11</sup>), and can be induced by hypoxia<sup>11</sup>, these secreted factors may have important direct and indirect effects on the activities of HSCs and leukaemia stem cells *in vivo*. Although the LILRB/PIRB receptors were reported to suppress activation of differentiated immune cells and inhibit neurite outgrowth of neural cells<sup>16,17</sup>, they support HSC repopulation and inhibit differentiation of AML cells. This result suggests the importance of these 'inhibitory receptors' in maintenance of stemness of normal stem cells and support of leukaemia development. In contrast to the 'stimulatory receptors' such as interferon receptors or Toll-like receptors that activate and induce differentiation of HSCs upon inflammation<sup>29</sup>, LILRB2 and PIRB may function as sensors of inflammation through binding to the inflammatory ANGPTLs<sup>12</sup> and protecting HSCs from excessive activation and exhaustion. Adult stem cells and cancer cells probably require

both stimulatory receptors and inhibitory receptors to maintain the balance of their cell fates.

**METHODS SUMMARY**

Plasmid cytomegalovirus (CMV)-Kozak human Angiopoietin-1 and ANGPTL 1, 2, 3, 4, 6 and 7 with Flag tags at the carboxy terminus were used for transfection. ANGPTL2-Flag was purified using M2 resin. Purified GST-ANGPTL5 was purchased from Abnova. Bacterially expressed Flag-ANGPTL2 (with Flag at the amino terminus) and ANGPTL2-Flag (with Flag at the C terminus) were constructed in pET-26b(+) vector, and GST-ANGPTLs-Flag in pGEX vector, and expressed and purified from bacteria. Murine stem cell virus (MSCV)-LILRB2-IRES-green fluorescent protein (GFP) or control retrovirus-infected Baf3 cells, CMV-driven LILRA-, LILRB-, PIRB-, or LAIR1-transfected 293T cells, or human mononuclear cord blood cells were used in binding assays. See the Methods for detailed experimental methods for flow cytometry, coimmunoprecipitation, SPR, liquid-phase binding, culture, transplantation, c.f.u. and gene set enrichment analysis (GSEA). Mice were maintained at the University of Texas Southwestern Medical Center animal facility. All animal experiments were performed with the approval of University of Texas Southwestern Committee on Animal Care.

both stimulatory receptors and inhibitory receptors to maintain the balance of their cell fates.

## METHODS SUMMARY

Plasmid cytomegalovirus (CMV)-Kozak human Angiopoietin-1 and ANGPTL 1, 2, 3, 4, 6 and 7 with Flag tags at the carboxy terminus were used for transfection. ANGPTL2-Flag was purified using M2 resin. Purified GST-ANGPTL5 was purchased from Abnova. Bacterially expressed Flag-ANGPTL2 (with Flag at the amino terminus) and ANGPTL2-Flag (with Flag at the C terminus) were constructed in pET-26b(+) vector, and GST-ANGPTLs-Flag in pGEX vector, and expressed and purified from bacteria. Murine stem cell virus (MSCV)-LILRB2-IRES-green fluorescent protein (GFP) or control retrovirus-infected Baf3 cells, CMV-driven LILRA-, LILRB-, PIRB-, or LAIR1-transfected 293T cells, or human mononuclear cord blood cells were used in binding assays. See the Methods for detailed experimental methods for flow cytometry, coimmunoprecipitation, SPR, liquid-phase binding, culture, transplantation, c.f.u. and gene set enrichment analysis (GSEA). Mice were maintained at the University of Texas Southwestern Medical Center animal facility. All animal experiments were performed with the approval of University of Texas Southwestern Committee on Animal Care.

**Full Methods** and any associated references are available in the online version of the paper at [www.nature.com/nature](http://www.nature.com/nature).

Received 15 July 2011; accepted 29 March 2012.

1. Zhang, C. C., Kaba, M., Iizuka, S., Huynh, H. & Lodish, H. F. Angiopoietin-like 5 and IGFBP2 stimulate *ex vivo* expansion of human cord blood hematopoietic stem cells as assayed by NOD/SCID transplantation. *Blood* **111**, 3415–3423 (2008).

2. Zhang, C. C. *et al.* Angiopoietin-like proteins stimulate *ex vivo* expansion of hematopoietic stem cells. *Nature Med.* **12**, 240–245 (2006).
3. Zhang, C. C. & Lodish, H. F. Cytokines regulating hematopoietic stem cell function. *Curr. Opin. Hematol.* **15**, 307–311 (2008).
4. Huynh, H. *et al.* IGFBP2 secreted by a tumorigenic cell line supports *ex vivo* expansion of mouse hematopoietic stem cells. *Stem Cells* **26**, 1628–1635 (2008).
5. Chou, S. & Lodish, H. F. Fetal liver hepatic progenitors are supportive stromal cells for hematopoietic stem cells. *Proc. Natl Acad. Sci. USA* **107**, 7799–7804 (2010).
6. Lin, M. & Zon, L. I. Genetic analyses in zebrafish reveal that angiopoietin-like proteins 1 and 2 are required for HSC development during embryogenesis. *Am. Soc. Hematol. 50th Ann. Meeting Abstract* 729 186 (2008).
7. Khoury, M. *et al.* Mesenchymal stem cells secreting angiopoietin-like-5 support efficient expansion of human hematopoietic stem cells without compromising their repopulating potential. *Stem Cells Dev.* **20**, 1371–1381 (2011).
8. Drake, A. C. *et al.* Human CD34<sup>+</sup> CD133<sup>+</sup> hematopoietic stem cells cultured with growth factors including Angptl5 efficiently engraft adult NOD-SCID Il2 $\gamma^{-/-}$  (NSG) mice. *PLoS ONE* **6**, e18382 (2011).
9. Zheng, J., Huynh, H., Umikawa, M., Silvany, R. & Zhang, C. C. Angiopoietin-like protein 3 supports the activity of hematopoietic stem cells in the bone marrow niche. *Blood* **117**, 470–479 (2011).
10. Zheng, J. *et al.* *Ex vivo* expanded hematopoietic stem cells overcome the MHC barrier in allogeneic transplantation. *Cell Stem Cell* **9**, 119–130 (2011).
11. Hato, T., Tabata, M. & Oike, Y. The role of angiopoietin-like proteins in angiogenesis and metabolism. *Trends Cardiovasc. Med.* **18**, 6–14 (2008).
12. Tabata, M. *et al.* Angiopoietin-like protein 2 promotes chronic adipose tissue inflammation and obesity-related systemic insulin resistance. *Cell Metab.* **10**, 178–188 (2009).
13. Barrow, A. D. & Trowsdale, J. The extended human leukocyte receptor complex: diverse ways of modulating immune responses. *Immunol. Rev.* **224**, 98–123 (2008).
14. Meyaard, L. LAIR and collagens in immune regulation. *Immunol. Lett.* **128**, 26–28 (2010).
15. Kitsos, C. M. *et al.* Calmodulin-dependent protein kinase IV regulates hematopoietic stem cell maintenance. *J. Biol. Chem.* **280**, 33101–33108 (2005).
16. Takai, T., Nakamura, A. & Endo, S. Role of PIR-B in autoimmune glomerulonephritis. *J. Biomed. Biotechnol.* **2011**, 275302 (2011).
17. Atwal, J. K. *et al.* PirB is a functional receptor for myelin inhibitors of axonal regeneration. *Science* **322**, 967–970 (2008).
18. Syken, J., Grandpre, T., Kanold, P. O. & Shatz, C. J. PirB restricts ocular-dominance plasticity in visual cortex. *Science* **313**, 1795–1800 (2006).
19. Chan, R. J. *et al.* Shp-2 heterozygous hematopoietic stem cells have deficient repopulating ability due to diminished self-renewal. *Exp. Hematol.* **34**, 1229–1238 (2006).
20. Si, J. & Collins, S. J. Activated Ca<sup>2+</sup>/calmodulin-dependent protein kinase II $\gamma$  is a critical regulator of myeloid leukemia cell proliferation. *Cancer Res.* **68**, 3733–3742 (2008).
21. Lukk, M. *et al.* A global map of human gene expression. *Nature Biotechnol.* **28**, 322–324 (2010).
22. Krivtsov, A. V. *et al.* Transformation from committed progenitor to leukaemia stem cell initiated by MLL-AF9. *Nature* **442**, 818–822 (2006).
23. Somerville, T. C. & Cleary, M. L. Identification and characterization of leukemia stem cells in murine MLL-AF9 acute myeloid leukemia. *Cancer Cell* **10**, 257–268 (2006).
24. Lavau, C., Szilvassy, S. J., Slany, R. & Cleary, M. L. Immortalization and leukemic transformation of a myelomonocytic precursor by retrovirally transduced HRX-ENL. *EMBO J.* **16**, 4226–4237 (1997).
25. Ma, G. *et al.* Paired immunoglobulin-like receptor-B regulates the suppressive function and fate of myeloid-derived suppressor cells. *Immunity* **34**, 385–395 (2011).
26. Mori, Y. *et al.* Inhibitory immunoglobulin-like receptors LILRB and PIR-B negatively regulate osteoclast development. *J. Immunol.* **181**, 4742–4751 (2008).
27. Chan, R. J. & Feng, G. S. PTPN11 is the first identified proto-oncogene that encodes a tyrosine phosphatase. *Blood* **109**, 862–867 (2007).
28. Shiroishi, M. *et al.* Human inhibitory receptors Ig-like transcript 2 (ILT2) and ILT4 compete with CD8 for MHC class I binding and bind preferentially to HLA-G. *Proc. Natl Acad. Sci. USA* **100**, 8856–8861 (2003).
29. Baldridge, M. T., King, K. Y. & Goodell, M. A. Inflammatory signals regulate hematopoietic stem cells. *Trends Immunol.* **32**, 57–65 (2011).

**Supplementary Information** is linked to the online version of the paper at [www.nature.com/nature](http://www.nature.com/nature).

**Acknowledgements** We thank S. Armstrong for the MSCV-MLL-AF9-IRES-YFP construct, H. Hobbs for the CMV-ANGPTL6-Flag plasmid, T. Takai for providing the PIRB knockout mice to S.-H.C., X.-J. Xie for binding analysis, and UTSW Genomics and Microarray Core facility for DNA array experiments. S.-H.C. thanks support from NIH. C.C.Z. was supported by NIH grant K01 CA 120099, American Society of Hematology Junior Faculty Award, March of Dimes Basil O'Connor Scholar Award, DOD PR093256, CPRIT RP100402, and the Gabrielle's Angel Foundation.

**Author Contributions** J.Z., M.U., C.C. and C.C.Z. were responsible for the study design, identification of receptors, binding, signalling and functional assays, data analysis and writing of the manuscript. J.L., X.C., C.Z., H.H., X.K., R.S. and X.W. were responsible for binding and signalling assays and data analysis. J.Y. and S.-H.C. carried out the ligand-binding assays, H.-Y.W. carried out AML characterization, and A.P.C. and E.S.W. carried out the SPR assay and data analysis.

**Author Information** DNA microarray data are available for download from the GEO under accession number GSE36329. Reprints and permissions information is available at [www.nature.com/reprints](http://www.nature.com/reprints). The authors declare no competing financial interests. Readers are welcome to comment on the online version of this article at [www.nature.com/nature](http://www.nature.com/nature). Correspondence and requests for materials should be addressed to C.C.Z. (Alec.Zhang@UTSouthwestern.edu).



## METHODS

**Mice.** C57BL/6 CD45.2 and CD45.1 mice, or NOD/SCID mice, were purchased from the University of Texas Southwestern Medical Center animal breeding core facility. The PIRBTM mice<sup>18</sup> were obtained from the MMRRC. The PIRB knockout mice<sup>20</sup> were a gift from T. Takai. Mice were maintained at the University of Texas Southwestern Medical Center animal facility. All animal experiments were performed with the approval of the University of Texas Southwestern Committee on Animal Care.

**Plasmids and proteins.** Plasmid CMV-Kozak human Ang1 and ANGPTLs 1, 2, 3, 4, 6 and 7 with Flag tags at the C terminus were transfected into 293T cells using Lipofectamine 2000, and the conditioned medium at 48 h was collected and different ANGPTL proteins were adjusted to the same level for flow cytometry-based binding experiments. ANGPTL2-Flag was purified using M2 resin. Purified GST-ANGPTL5 was purchased from Abnova. Bacterially expressed Flag-ANGPTL2 and ANGPTL2-Flag were constructed in pET-26b(+) vectors, and GST-ANGPTLs-Flag in pGEX vectors, and expressed and purified from bacteria. MSCV-LILRB2-IRES-GFP or control retrovirus-infected Baf3 cells, or CMV-driven LILRA-, LILRB-, PIRB- or LAIR1-transfected 293T cells collected at 48 h, or mononuclear human cord blood cells were incubated with Fc block and equal amounts of different Flag-tagged ANGPTLs at 4 °C for 60 min, followed by staining with anti-Flag- $\alpha$ -phycoerythrin (APC) and propidium iodide. Anti-LILRB2-phycoerythrin (PE) was used as indicated. Cells were analysed using either a FACSCalibur or FACSARIA instrument (Becton, Dickinson).

**Antibodies and shRNAs.** Flow cytometry antibodies anti-CD34-fluorescein isothiocyanate (FITC), anti-CD38-PE, anti-CD90-PE/Cy5.5, biotinylated lineage cocktail, anti-Kit-APC, anti-Sca-1-FITC, anti-Mac-1-APC, anti-Gr-1-PE, anti-CD3-APC and anti-B220-PE were purchased from BD Biosciences and used as described<sup>4,9,10,31</sup>. The manufacturers and catalogue numbers for other antibodies are as follows: anti-LILRB1, Biolegend (33707); anti-LILRB2, eBioscience (12-5149); anti-LILRB3, eBioscience (12-5159); anti-LILRB4, eBioscience (12-5139); anti-LILRB5, R&D Systems (AF3065); anti-PIRB-PE, R&D Systems (FAB2754P); anti-human LAIR1-PE, BD Pharmingen (550811); anti-mouse LAIR1-PE, eBioscience (12-3051); anti-Flag-APC, Prozyme (PJ255); anti-pCAMK2, Abcam (ab32678); anti-pCAMK4, Santa Cruz (sc-28443-R); anti-CAMK2, Cell Signaling (4436); anti-CAMK4, Cell Signaling (4032); anti-ANGPTL5, Abcam (ab57240); anti-PIRB, BD Pharmingen (550348) for coimmunoprecipitation of PIRB; anti-SHP-2, Cell Signaling (33975) for coimmunoprecipitation of SHP-2; and anti-Fc, Jackson ImmunoResearch (109-036-098). Combinations of multiple lentivirus-expressed shRNAs for inhibition of LILRB2 (hairpin sequences: TGCTGTTGACAGTGAGCGCCAGCTTGACCCTCAGACGGAATAGTGAAGCCACAGATGTATCCGCTCTGAGGGTCAAGCTGTTGCCTACTGCCTCGGA and TGCTGTTGACAGTGAGCGCAGCAGCAGCAGCTTGTGAAGAATAGTGAA TGCCAGATGTATCTCTCACAAAGCTCTGGTCTGATGCGCTACTGCCTCGGA); ANGPTL1 (TGCTGTTGACAGTGAGCGCCTCGTGTACTCAACTC TATATAGTGAAGCCACAGATGTATATAGAGTTGAGTAACACGAGATG CCTACTGCCTCGGA, TGCTGTTGACAGTGAGCGAAGAGCACTCGCCA ATTTAAATAGTGAAGCCACAGATGTATTTAAATTGGCGAGTGTCTCTC TGCCCTACTGCCTCGGA and TGCTGTTGACAGTGAGCGACCAATTTAAAT TGACACAGAACTAGTGAAGCCACAGATGTAGTTCTGTGTCATTTAAAT TGGCTGCTACTGCCTCGGA); ANGPTL2 (TGCTGTTGACAGTGAGCGC CACAGAGTTCTTGAATAAAATAGTGAAGCCACAGATGTATTTATTC CAAGAAGCTCTGTGATGCCTACTGCCTCGGA, TGCTGTTGACAGTGAGC GACACAGCAGCGGCAAGCTTATAGTGAAGCCACAGATGTATAAGC TTCTGCCGCTGCTGTGGTGCCTACTGCCTCGGA and TGCTGTTGACAG TGAGCGCCAGATGGAGGCTGGACAGTAATAGTGAAGCCACAGATGTA TTACTGTCCAGCCTCCATCTGATGCCTACTGCCTCGGA); ANGPTL3 (TG CTGTTGACAGTGAGCGACTCAGAAAGCACTAGTATTCAATAGTGAAGCC ACAGATGTATTGAATACTAGTCCTCTGAGCTGCCTACTGCCTCGGA, TGCTGTTGACAGTGAGCGCCAGCATAGTCAAATAAAAGAATAGTGAA GCCACAGATGTATTCTTTATTTGACTATGCTGTTGCCTACTGCCTCG GA and TGCTGTTGACAGTGAGCGCATACATATAAACAAGTCAAGTCAATA GTGAAGCCAGATGTATTGACTGTATGTTATGATGTAGTGCCTACTG CCTCGGA); ANGPTL4 (TGCTGTTGACAGTGAGCGCCACAGAGTTCTTG GAATAAAATAGTGAAGCCACAGATGTATTTTATCCAAGAACTCTGTG ATGCCTACTGCCTCGGA, TGCTGTTGACAGTGAGCGACACAGCAGCGG CAGAAGCTTATAGTGAAGCCACAGATGTATAAGCTTCTGCCGCTGCTG TGGTGCCTACTGCCTCGGA and TGCTGTTGACAGTGAGCGCCAGATGG AGGCTGGACAGTAATAGTGAAGCCACAGATGTATTACTGTCCAGCCTC CATCTGATGCCTACTGCCTCGGA); ANGPTL5 (TGCTGTTGACAGTGAG CGATAGAAGATGGATCTAATGCAATAGTGAAGCCACAGATGTATTGCA TTAGATCCATTCTACTGCTACTGCCTCGGA, TGCTGTTGACAGTGAGC GCGAATGGTTTATGATTGCACTGATATAGTGAAGCCACAGATGTATATC AGTGCAATCTAAACCATGTGCCTACTGCCTCGGA and TGCTGTTGACA

GTGAGCGATACGGACTCTTCAGTAGTTAATAGTGAAGCCACAGATGTA TTAAGTACTGAAGAGTCCGTAGTGCTACTGCCTCGGA); ANGPTL6 (TG CTGTTGACAGTGAGCGCCACTACCTGGCAGCACTAATAATAGTGAAGC CACAGATGTATTATAGTGTGCCAGGTAGTGCTACTGCCTCGGA, TGCTGTTGACAGTGAGCGGAGAGGCAAGATGGTTTCAGTCAATAGTGA GGCACAGATGTATTGACTGAACCATCTTGCCTCCTGCCTACTGCCTCG GA and TGCTGTTGACAGTGAGCGACCCAGAGAGACCAGACCCAGATA GTGAAGCCACAGATGTATCTGGGTCTGGTCTCTCTGGGTGCCTACTG CCTCGGA); and ANGPTL7 (TGCTGTTGACAGTGAGCGCCCGGACTGG AAGCAGTACAATAGTGAAGCCACAGATGTATTGTACTGCTTCCAGTC CCGGTTGCCTACTGCCTCGGA, TGCTGTTGACAGTGAGCGCCCGCATC TCTGGAGTGATATAATAGTGAAGCCACAGATGTATTATACACTCCAGAG ATGCGGTTGCCTACTGCCTCGGA and TGCTGTTGACAGTGAGCGCGG ACTGAGAAAACAGCCTATAATAGTGAAGCCACAGATGTATTATAGGCTG TTTCTCAGTCCTTGCCTACTGCCTCGGA) were purchased from Open Biosystems and used for knockdown experiments. The specificity of LILRB2 monoclonal antibody is confirmed by comparison of binding to all tested LILRA/Bs on transfected 293T cells. The specificities of other anti-LILRBs, anti-PIRB and anti-LAIR1 were confirmed by staining the respective complementary DNA-overexpressed 293T cells.

**Coimmunoprecipitation.** For *in vivo* coimmunoprecipitation, 293 cells were transiently co-transfected with plasmids encoding LILRB2-ECD-Fc, PIRB-ECD-Fc, or Tie-2-ECD-Fc and Flag-tagged ANGPTL2 or untagged ANGPTL5. Protein A beads were added to conditioned medium collected at 48 h after transfection, and proteins were detected by anti-Flag or anti-ANGPTL5 by western blot. For *in vitro* coimmunoprecipitation, purified ANGPTL2-Flag or GST-ANGPTL5 was incubated with purified LILRB2-ECD-Fc or Tie-2-ECD-Fc in PBS with 0.1% BSA and 0.1% NP-40 for 2 h followed by immunoprecipitation with protein A beads and western blotting.

**Liquid-phase binding assay.** Specific binding of radiolabelled GST-ANGPTL5 to Baf3 stably infected with MSCV-LILRB2-IRES-GFP (as LILRB2-Baf3 cells) was performed in a similar manner to before<sup>32</sup>. In brief,  $6 \times 10^6$  LILRB2-Baf3 cells were incubated with  $^{125}$ I-GST-ANGPTL5 (0.1–100 nM) in 200  $\mu$ l PBS/1% BSA for 3 h at 25 °C. Nonspecific binding on normal Baf3 cells was subtracted. In competition assay,  $2.5 \times 10^6$  LILRB2-Baf3 or Baf3 cells were incubated with unlabelled GST-ANGPTL5 (0.1–100 nM) in 200  $\mu$ l PBS/1% BSA for 1 h at 25 °C, followed by addition of 5 nM of  $^{125}$ I-GST-ANGPTL5 and incubation for 4 h. After incubation, the cells were washed twice by centrifugation, resuspended in ice-cold PBS with 1% BSA and then measured in a scintillation counter.

**Cell culture and infection.** Baf3 cells were grown in RPMI medium 1640 with 10% FBS and 10% Wehi conditioned cell medium. Human embryonic kidney 293T cells were grown in DMEM with 10% FBS.

For mouse HSC culture, indicated numbers of bone marrow Lin<sup>−</sup> Sca-1<sup>+</sup> Kit<sup>+</sup> CD34<sup>+</sup> Flk-2<sup>−</sup> cells or fetal liver Lin<sup>−</sup> Sca-1<sup>+</sup> Kit<sup>+</sup> cells isolated from 8–10-week-old C57BL/6 CD45.2 mice were plated in one well of a U-bottom 96-well plate (Corning) with 200  $\mu$ l of the indicated medium, essentially as we described previously<sup>4,9</sup>. Cells were cultured at 37 °C in 5% CO<sub>2</sub> and indicated levels of O<sub>2</sub>. For the purpose of competitive transplantation, we pooled cells from 12 culture wells and mixed them with competitor/supportive cells before the indicated numbers of cells were transplanted into each mouse. For western blotting, 3-week-old mouse spleen cells were cultured overnight in DME supplemented with 0.1% BSA, followed by treatment with indicated amount of ANGPTLs. Human mononuclear cord blood cells were cultured in DME containing 10% FBS overnight followed by starvation in serum-free DME for 4 h before ANGPTL stimulation.

The infection of Lin<sup>−</sup> cells by MSCV-MLL-AF9-IRES-YFP and MSCV-AML1-ETO9a-IRES-GFP was performed after procedures described in refs 22,23 and 33, respectively. In brief, we incubated Lin<sup>−</sup> cells overnight in medium with 10% FBS, 20 ng ml<sup>−1</sup> SCF, 20 ng ml<sup>−1</sup> IL-3 and 10 ng ml<sup>−1</sup> IL-6, followed by spin infection with retroviral supernatant in the presence of 4  $\mu$ g ml<sup>−1</sup> polybrene. Infected cells (300,000) were transplanted into lethally irradiated (1,000 rad) C57BL/6 mice by retro-orbital injection.

For human cell culture, fresh and cryopreserved human cord blood cells were obtained from University of Texas Southwestern Parkland Hospital through approved IRB protocol 042008-033. CD34<sup>+</sup> cells were isolated by AutoMACS and grown essentially as we described<sup>1,10</sup>. CD133<sup>+</sup> cells were purchased from AllCell. Lentiviral infection by shRNAs for LILRB2 or ANGPTLs was performed as recommended by Open Biosystems.

**Flow cytometry and reconstitution analysis.** Donor mouse bone marrow cells were isolated from 8–10-week-old C57BL/6 CD45.2 mice. Bone marrow Lin<sup>−</sup> Sca-1<sup>+</sup> Kit<sup>+</sup> CD34<sup>+</sup> Flk-2<sup>−</sup> cells were isolated by staining with a biotinylated lineage cocktail (anti-CD3, anti-CD5, anti-B220, anti-Mac-1, anti-Gr-1, anti-Ter119 and anti-7-4; Stem Cell Technologies) followed by streptavidin-PE/Cy5.5, anti-Sca-1-FITC, anti-Kit-APC, anti-CD34-PE, and anti-Flk-2-PE. The indicated numbers of mouse CD45.2 donor cells were mixed with  $1 \times 10^5$  freshly isolated CD45.1

competitor bone marrow cells, and the mixture injected intravenously through the retro-orbital route into each of a group of 6–9-week-old CD45.1 mice previously irradiated with a total dose of 10 Gy. To measure reconstitution of transplanted mice, peripheral blood was collected at the indicated times post-transplant and CD45.1<sup>+</sup> and CD45.2<sup>+</sup> cells in lymphoid and myeloid compartments were measured as we described<sup>4,9,10</sup>. The analyses of Mac-1, Kit, Gr-1, CD3 and B220 populations in AML blood or bone marrow were performed by using anti-Mac-1-APC, anti-Kit-PE, anti-Gr-1-PE, anti-CD3-APC and anti-B220-PE.

Uncultured or cultured progenies of human cells were pooled together and the indicated portions were injected intravenously through the retro-orbital route into sub-lethally irradiated (250 rad) 6–8-week-old NOD/SCID mice. 8 weeks after transplantation, bone marrow nucleated cells from transplanted animals were analysed by flow cytometry for the presence of human cells as we described<sup>11,10</sup>.

**c.f.u. assays.** 2,000 YFP<sup>+</sup> Mac-1<sup>+</sup> Kit<sup>+</sup> bone marrow cells from AML mice were plated in methylcellulose (M3534; Stem Cell Technologies) for c.f.u.–granulocyte macrophage assays, according to the manufacturer's protocols and our previously published protocol<sup>14</sup>. After 7 days, 2,000 cells from three dishes initially plated were used for secondary replating.

**Surface plasmon resonance.** Biacore 2000 and CM5 chips were used to analyse binding of purified ANGPTLs to the LILRB2 ECD fused to Fc, using a method similar to that previously described<sup>35</sup>. Recombinant protein A (Pierce) was pre-immobilized in two flow cells (~2,000 response units) using the amine-coupling kit from GE Healthcare. LILRB2-Fc was injected into one of the flow cells to be captured by the protein A to reach ~300 response units. GST-ANGPTL5 was injected over the immobilized LILRB2 in HBS-EP (GE Healthcare) containing 0.01 M HEPES (pH 7.4), 0.15 M NaCl and 0.005% polysorbate 20. Each binding sensorgram from the sample flow cell, containing a captured LILRB2-Fc, was corrected for the protein A-coupled cell control. After each injection of an antigen solution, which induced the binding reaction, and the dissociation period during which the running buffer was infused, the protein A surface was regenerated by the

injection of the regeneration solution containing 10 mM Na<sub>3</sub>PO<sub>4</sub> (pH 2.5) and 500 mM NaCl. All captured LILRB2-Fc, with and without ANGPTL5 bound, was completely removed, and another cycle begun. All measurements were performed at 25 °C with a flow rate of 30 µl min<sup>-1</sup>.

**GSEA.** GSEA<sup>36</sup> was performed using GSEA v2.0 software (<http://www.broadinstitute.org/gsea/index.jsp>) with 1,000 phenotype permutations, and normalized enrichment score and false-discovery rate *q*-value were calculated. Leukaemia-stem-cell and macrophage-development gene sets were obtained from the indicated publication<sup>37</sup>.

**Statistics.** A two-tailed Student's *t*-test was performed to evaluate the significance between experimental groups, unless otherwise indicated. The survival rates of the two groups were analysed using a log-rank test.

30. Ujike, A. *et al.* Impaired dendritic cell maturation and increased T<sub>H</sub>2 responses in PIR-B(−/−) mice. *Nature Immunol.* **3**, 542–548 (2002).
31. Simsek, T. *et al.* The distinct metabolic profile of hematopoietic stem cells reflects their location in a hypoxic niche. *Cell Stem Cell* **7**, 380–390 (2010).
32. Zhang, C. C., Krieg, S. & Shapiro, D. J. HMG-1 stimulates estrogen response element binding by estrogen receptor from stably transfected HeLa cells. *Mol. Endocrinol.* **13**, 632–643 (1999).
33. Yan, M. *et al.* A previously unidentified alternatively spliced isoform of t(8;21) transcript promotes leukemogenesis. *Nature Med.* **12**, 945–949 (2006).
34. Zhang, C. C., Steele, A. D., Lindquist, S. & Lodish, H. F. Prion protein is expressed on long-term repopulating hematopoietic stem cells and is important for their self-renewal. *Proc. Natl Acad. Sci. USA* **103**, 2184–2189 (2006).
35. Luo, Y., Lu, Z., Raso, S. W., Entrican, C. & Tangarone, B. Dimers and multimers of monoclonal IgG1 exhibit higher *in vitro* binding affinities to Fcγ receptors. *MAbs* **1**, 491–504 (2009).
36. Subramanian, A. *et al.* Gene set enrichment analysis: a knowledge-based approach for interpreting genome-wide expression profiles. *Proc. Natl Acad. Sci. USA* **102**, 15545–15550 (2005).
37. Zuber, J. *et al.* RNAi screen identifies Brd4 as a therapeutic target in acute myeloid leukaemia. *Nature* **478**, 524–528 (2011).

# AMPK regulates NADPH homeostasis to promote tumour cell survival during energy stress

Sang-Min Jeon<sup>1†</sup>, Navdeep S. Chandel<sup>2</sup> & Nissim Hay<sup>1</sup>

Overcoming metabolic stress is a critical step for solid tumour growth<sup>1,2</sup>. However, the underlying mechanisms of cell death and survival under metabolic stress are not well understood. A key signalling pathway involved in metabolic adaptation is the liver kinase B1 (LKB1)–AMP-activated protein kinase (AMPK) pathway<sup>2,3</sup>. Energy stress conditions that decrease intracellular ATP levels below a certain level promote AMPK activation by LKB1. Previous studies showed that LKB1-deficient or AMPK-deficient cells are resistant to oncogenic transformation and tumorigenesis<sup>4–6</sup>, possibly because of the function of AMPK in metabolic adaptation. However, the mechanisms by which AMPK promotes metabolic adaptation in tumour cells are not fully understood. Here we show that AMPK activation, during energy stress, prolongs cell survival by redox regulation. Under these conditions, NADPH generation by the pentose phosphate pathway is impaired, but AMPK induces alternative routes to maintain NADPH and inhibit cell death. The inhibition of the acetyl-CoA carboxylases ACC1 and ACC2 by AMPK maintains NADPH levels by decreasing NADPH consumption in fatty-acid synthesis and increasing NADPH generation by means of fatty-acid oxidation. Knockdown of either ACC1 or ACC2 compensates for AMPK activation and facilitates anchorage-independent growth and solid tumour formation *in vivo*, whereas the activation of ACC1 or ACC2 attenuates these processes. Thus AMPK, in addition to its function in ATP homeostasis, has a key function in NADPH maintenance, which is critical for cancer cell survival under energy stress conditions, such as glucose limitations, anchorage-independent growth and solid tumour formation *in vivo*.

The lack of LKB1 or AMPK activation rendered cancer cells more sensitive to cell death induced by glucose deprivation<sup>5,7–9</sup> (Supplementary Fig. 1). However, the mechanism by which the failure to activate AMPK accelerates cancer cell death during energy stress remains to be explained. Our results demonstrate that the effect of AMPK does not involve p53 or mTORC1, which were implicated in the LKB1–AMPK-mediated regulation of cell survival during glucose deprivation<sup>8,10</sup>. In both control A549 cells (A549-Vect) and dominant-negative p53 (p53DN)-expressing A549 cells (A549-p53DN), LKB1 reconstitution restored AMPK activation, as measured by ACC phosphorylation, and inhibited glucose-starvation-induced cell death to a similar extent (Fig. 1a, b). mTORC1 inhibition with rapamycin also did not affect the sensitivity of A549 cells to glucose deprivation (Fig. 1b).

Replacement of glucose with the non-metabolizable glucose analogues 2-deoxyglucose (2DG) or 5-thiogluconate (5TG) revealed that only 2DG protected LKB1-deficient cancer cells (A549 and HeLa) from glucose-starvation-induced cell death (Fig. 1b and Supplementary Fig. 2b). Unlike 5TG, 2DG strongly induced the activation of AMPK, even in LKB1-deficient cells (Fig. 1a and Supplementary Fig. 2a). This activation occurred by means of a poorly understood mechanism that is dependent on hexokinase (Supplementary Fig. 3). The results suggest that, by activating AMPK, 2DG inhibits cell death during glucose deprivation. However, LKB1 reconstitution in A549 cells induced higher AMPK activation than 2DG (Fig. 1a), yet 2DG

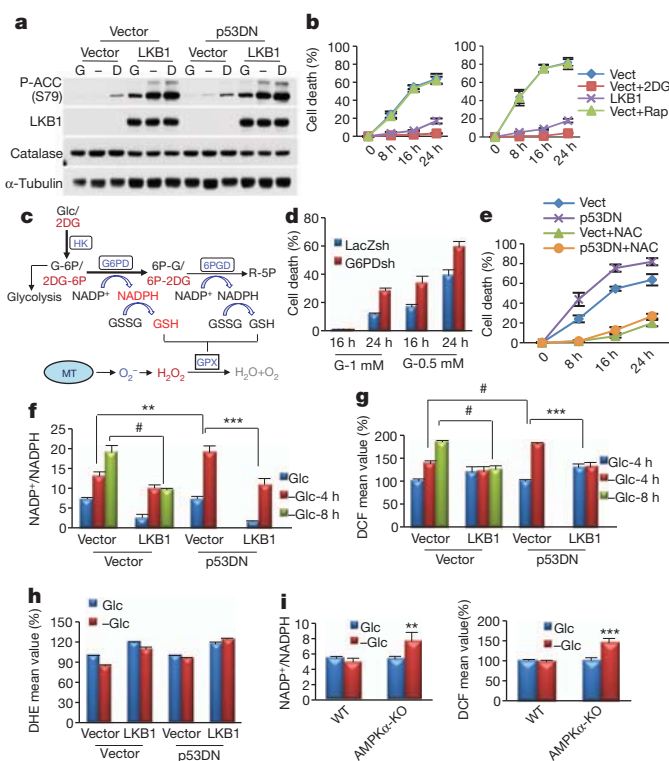


**Figure 1 | The failure to activate AMPK accelerates NADPH depletion, oxidative stress and cell death in the absence of glucose.** **a**, Immunoblotting analyses after incubating A549 cells expressing empty vector, LKB1, p53DN or both p53DN and LKB1 in the absence (–) or presence of 5 mM glucose (G) or 2DG (D) for 2 h. **b**, Cell death quantification after glucose starvation. For A549-Vect (left) and A549-p53DN (right) cells, 5 mM 2DG (Vect+2DG) or 100 nM rapamycin (Vect+Rap) were added to the medium. **c**, Illustration depicting partial metabolism of 2DG through the PPP, which could generate NADPH/GSH and eliminate  $H_2O_2$  generated from mitochondria (MT) (see the text for details). Glc, glucose; HK, hexokinase; G-6P, glucose 6-phosphate; 6PGD, 6-phosphogluconate dehydrogenase; 2DG-6P, 2-deoxyglucose 6-phosphate; 6P-G, 6-phosphogluconate; 6P-2DG, 6-phospho 2-deoxygluconate; R-5P, ribulose 5-phosphate. **d**, Quantification of cell death of A549 cells expressing LacZ-shRNA or G6PD-shRNA cultured in 1 mM or 0.5 mM glucose. **e**, Cell death quantification at different time points after glucose depletion in the presence or absence of 2 mM NAC. **f**, **g**,  $NADPH^+/NADPH$  ratio (**f**) and  $H_2O_2$  level (**g**) after incubation in the absence (–Glc) or presence of 5 mM glucose (Glc) for 4 or 8 h. **h**,  $O_2^-$  levels after incubation in the absence or presence of 5 mM glucose for 4 h. **i**,  $NADPH^+/NADPH$  ratio (left) and  $H_2O_2$  level (right) in wild-type (WT) or AMPK $\alpha$ -KO MEFs cultured in glucose-free medium in the absence (–Glc) or presence of 5 mM glucose (Glc) for 5 h. Results in **g**, **h** and **i** (right) are expressed as the percentage change in the mean DCF/DHE values relative to the glucose-treated control. Results are shown as means and s.e.m. for three independent (**b**, **d**, **f**, **h**, **i**) or four (**e**, **g**) experiments. Asterisk,  $P < 0.05$ ; two asterisks,  $P < 0.01$ ; three asterisks,  $P < 0.005$ ; hash,  $P < 0.001$  versus the glucose-treated control in each group.

<sup>1</sup>Department of Biochemistry and Molecular Genetics, College of Medicine, University of Illinois at Chicago, Chicago, Illinois 60607, USA. <sup>2</sup>Department of Medicine, Division of Pulmonary and Critical Care Medicine, Northwestern University Medical School, Chicago, Illinois 60611, USA. <sup>†</sup>Present address: Research Oncology, Genentech, South San Francisco, California 94080, USA.



protected the cells slightly better than LKB1 (Fig. 1b), implying that 2DG could protect cells by both AMPK-dependent and AMPK-independent mechanisms.

Glucose limitations could induce oxidative stress by decreasing NADPH generation in the pentose phosphate pathway (PPP) (Fig. 1c). NADPH is required for the regeneration of reduced glutathione (GSH), which is used by glutathione peroxidase (GPX) to eliminate  $H_2O_2$  (Fig. 1c). We therefore speculated as follows: first, that the failure to activate AMPK by glucose deprivation accelerates cell death through oxidative stress mediated by decreased PPP flux and NADPH/GSH generation; second, that AMPK activation under these conditions is required to inhibit cell death by decreasing oxidative stress; and third, that 2DG protects the cells by both AMPK activation and partial utilization in the PPP<sup>11</sup> (Fig. 1c).

We first established that decreased PPP flux and increased oxidative stress are the cause of the cell death. Glucose-6-phosphate dehydrogenase (G6PD) knockdown accelerated cell death in low glucose (Fig. 1d) and even in the absence of glucose (Supplementary Fig. 4a, b). Glucose deprivation rapidly depleted NADPH/GSH and elevated the  $H_2O_2$  level in control cells, which were further affected by G6PD knockdown (Supplementary Fig. 4c–e). Finally, the antioxidants *N*-acetylcysteine (NAC) and catalase inhibited cell death in LKB1-deficient or AMPK-deficient cells (Fig. 1e and Supplementary Figs 1c, 5 and 6).

We next examined the function of AMPK in redox regulation by using A549-Vect and A549-LKB1 cells. Unlike A549-Vect cells, A549-LKB1 cells maintained  $\text{NADP}^+/\text{NADPH}$  and  $\text{GSSG}/\text{GSH}$  ratios and prevented the increase in the  $\text{H}_2\text{O}_2$  level during glucose starvation (Fig. 1f, g and Supplementary Fig. 7). Expression of p53DN showed a faster depletion of NADPH and increase in  $\text{H}_2\text{O}_2$  level (Fig. 1f, g), explaining increased cell death (Fig. 1e). The superoxide ( $\text{O}_2^-$ ) level was not increased (Fig. 1h), suggesting that the increased  $\text{H}_2\text{O}_2$  level is due to NADPH depletion and impaired  $\text{H}_2\text{O}_2$  detoxification. LKB1 reconstitution neither decreased the  $\text{O}_2^-$  level (Fig. 1h) nor changed that of catalase (Fig. 1a), further suggesting that NADPH maintenance is the predominant mechanism by which AMPK prevents oxidative stress. Consistently, LKB1 or  $\text{AMPK}\alpha 1$  knockdown in MCF7 or H1703 cells significantly increased  $\text{H}_2\text{O}_2$  levels, but not those of  $\text{O}_2^-$ , during glucose deprivation (Supplementary Fig. 8). Similarly,  $\text{AMPK}\alpha$ -knockout ( $\text{AMPK}\alpha$ -KO) murine embryonic fibroblasts (MEFs) failed to maintain their  $\text{NADP}^+/\text{NADPH}$  ratio and low  $\text{H}_2\text{O}_2$  level after glucose starvation (Fig. 1i). Finally, as we had speculated, 2DG maintained NADPH, GSH and  $\text{H}_2\text{O}_2$  levels and protected from cell death largely by means of AMPK activation and to a smaller extent by

partial utilization in the PPP (Supplementary Fig. 4). This could explain why 2DG protects from cell death slightly better than LKB1 despite higher activation of AMPK by LKB1 (Fig. 1b). Thus, the combination of decreased NADPH generation by the PPP and impaired AMPK activation during glucose deprivation in LKB1-deficient or AMPK-deficient cells accelerates NADPH depletion and  $H_2O_2$  elevation, eventually causing cell death.

Next we investigated the mechanism by which AMPK maintains the NADPH level in the absence of glucose. The intracellular NADPH level is determined by the difference between its production and its consumption. NADPH is generated from the PPP and mitochondrial metabolism, and is consumed mainly during  $H_2O_2$  detoxification by GPX and peroxiredoxin (PRX) and fatty-acid synthesis (FAS) (Fig. 2a). Under limited glucose supply, the major NADPH source is mitochondrial metabolism, which is supported by fatty-acid oxidation (FAO). Metabolites provided by FAO to the tricarboxylic acid cycle generate malate and citrate, the substrates of NADPH-producing malic enzyme and isocitrate dehydrogenase, respectively. AMPK regulates fatty-acid metabolism through the phosphorylation and inhibition of ACC1 and ACC2, which in turn inhibit FAS and activates FAO, respectively<sup>12</sup>. Both ACC1 and ACC2 generate malonyl-CoA, the precursor of FAS and a potent inhibitor of carnitine palmitoyltransferase 1 (CPT1), the rate-limiting enzyme in FAO<sup>13</sup> (Fig. 2a). We therefore reasoned that AMPK might regulate NADPH homeostasis by inhibiting ACC1 and ACC2.

We first determined whether targeting ACC1 or ACC2 inhibits cell death, the accumulation of  $\text{H}_2\text{O}_2$  and the depletion of NADPH observed during glucose deprivation. Targeting either ACC1 or ACC2 in A549 cells by short interfering RNAs (siRNAs) demonstrated that only ACC2 knockdown significantly inhibited cell death and  $\text{H}_2\text{O}_2$  accumulation, without decreasing  $\text{O}_2^-$  (Supplementary Fig. 9). We therefore generated stable cell lines expressing ACC2-specific short hairpin RNA (shRNA) (Supplementary Fig. 10a). ACC2 knockdown in A549 cells maintained the  $\text{NADP}^+/\text{NADPH}$  ratio (Fig. 2b) and the GSSG/GSH ratio (Fig. 2c), inhibited the accumulation of  $\text{H}_2\text{O}_2$  (Fig. 2d) and prevented cell death (Fig. 2e). Similar results were obtained in HeLa, MCF7-LKB1sh and H1703-LKB1sh cells (Supplementary Fig. 10b–d). Targeting either ACC1 or ACC2 in AMPK $\alpha$ -KO MEFs significantly decreased the  $\text{H}_2\text{O}_2$  level during glucose starvation (Supplementary Fig. 11). The inability of ACC1 knockdown in A549 cells to decrease the  $\text{H}_2\text{O}_2$  level during glucose starvation was probably because FAS inhibition in these cells occurs to a similar extent regardless of LKB1 expression or ACC1 knockdown (Supplementary Fig. 12). In contrast, A549-LKB1 and A549-ACC2sh cells showed a

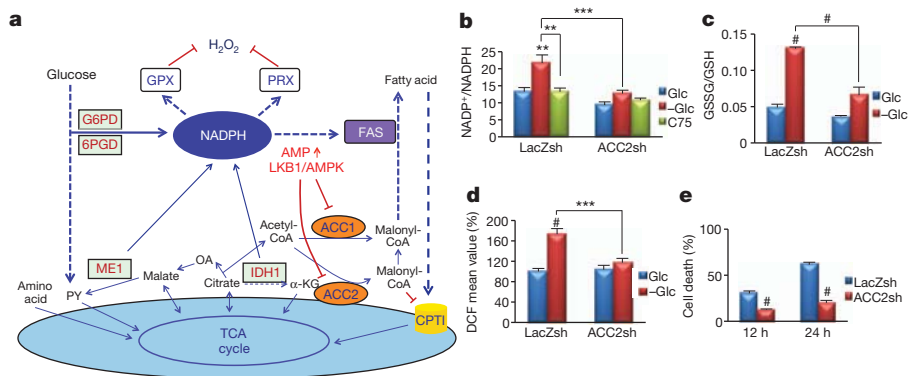


**Figure 2 | ACC2 ablation recapitulates AMPK activation, maintaining the NADPH level and decreasing the H<sub>2</sub>O<sub>2</sub> level during glucose deprivation.**

**a**, A schematic illustration depicting one potential mechanism by which AMPK regulates NADPH homeostasis (see the text for details). PY, pyruvate; OA, oxaloacetate;  $\alpha$ -KG,  $\alpha$ -oxoglutarate; ME, malic enzyme; IDH, isocitrate dehydrogenase; TCA, tricarboxylic acid. **b–d**, A549 cells expressing LacZ-shRNA or ACC2-shRNA 2 were incubated in glucose-free medium in the absence (–Glc) or presence of 5 mM glucose (Glc) or with 20  $\mu$ g ml<sup>−1</sup> C75.

After 6 h, the NADP<sup>+</sup>/NADPH ratio (**b**), GSSG/GSH ratio (**c**) and H<sub>2</sub>O<sub>2</sub> level (**d**) were measured. **e**, Quantification of cell death after glucose starvation for 10 and 24 h. Results in **d** are expressed as the percentage change in the mean DCF values relative to the glucose-treated control. Results are shown as means and s.e.m. for three independent experiments. Two asterisks,  $P < 0.01$ ; three asterisks,  $P < 0.005$ ; hash,  $P < 0.001$  versus the glucose-treated control in each group (**b–d**) or versus the LacZsh control (**e**) at each time point.

marked increase in FAO, explaining why ACC2 knockdown was able to decrease  $H_2O_2$  levels but ACC1 knockdown was not (Supplementary Fig. 12). Consistently, overexpression of the constitutively active ACC2(S212A) mutant significantly inhibited FAO and sensitized MCF7 cells to glucose-deprivation-mediated cell death, and partly blocked protection by 2DG in HeLa cells (Supplementary Fig. 13). Furthermore, short-term exposure to the FAS inhibitor C75, which also activates CPT1, mimicking the effects of AMPK on fatty-acid metabolism, lowered the  $NADP^+/NADPH$  ratio and protected A549 and HeLa cells during glucose deprivation (Fig. 2b and Supplementary Fig. 14a, b). However, because C75 inhibits FAS downstream of ACC1, long-term treatment with C75 leads to the cytotoxic accumulation of malonyl-CoA<sup>14</sup>. Indeed, etomoxir, a CPT1 inhibitor, abrogated the short-term effect of C75 without affecting the effect of NAC (Supplementary Fig. 14c). These results indicate that the short-term protective effect of C75 was largely due to the activation of CPT1 and the acceleration of FAO. Furthermore, treatment with the ACC inhibitor TOFA protected from cell death, whereas the malate supplement alone could not (Supplementary Fig. 15a). However, the combination of TOFA and malate further protected from cell death (Supplementary Fig. 15a). These results suggest that malate alone is not sufficient to induce NADPH accumulation, because NADPH could still be consumed by FAS. Thus, when FAS is inhibited by TOFA, malate can promote sufficient NADPH accumulation to inhibit cell death during glucose deprivation. Finally, the protective effect of ACC2 knockdown was abrogated by buthionine sulfoximine, which depletes GSH, but not by nicotinamide (NAM), which inhibits Sirt1, excluding a possible involvement of the  $NAD^+-Sirt1$  pathway<sup>15</sup> (Supplementary Fig. 15b).

Like glucose starvation, matrix detachment elicits energy stress followed by elevated  $H_2O_2$  levels and cell death<sup>16</sup>. Indeed, matrix detachment inhibited glucose uptake in A549 cells (Supplementary Fig. 16), and markedly activated AMPK in A549-LKB1 cells (Fig. 3a). AMPK was also activated in A549 cells but to a much smaller extent than in A549-LKB1 cells (Fig. 3a), which is dependent on calmodulin-dependent protein kinase kinase (CaMKK; Fig. 3b). We therefore tested whether AMPK activation is required for redox regulation during matrix detachment and anchorage-independent growth, which is a hallmark of cancer cells. Matrix detachment significantly increased the  $H_2O_2$  level in A549-Vect cells in comparison with A549-LKB1 cells, regardless of p53 status (Fig. 3c). CaMKK inhibition in A549 cells further elevated the  $H_2O_2$  level during matrix detachment (Fig. 3d), supporting a key function for AMPK in redox regulation during this

process. The results were confirmed in MCF7 cells with LKB1 knockdown or AMPK $\alpha$ 1 knockdown (Supplementary Fig. 17). The impaired AMPK activation and the higher  $H_2O_2$  level in matrix-detached A549 cells were correlated to the extent of NADPH depletion (Fig. 3e). The high  $NADP^+/NADPH$  ratio in A549 cells was further increased after matrix detachment, whereas the low  $NADP^+/NADPH$  ratio was maintained in A549-LKB1 cells (Fig. 3e).

We next investigated whether ACCs mediate the effect of AMPK during matrix detachment. Knockdown of ACC1 by siRNA, but not that of ACC2, blocked the increase in the  $H_2O_2$  level by matrix detachment (Supplementary Fig. 18). We therefore used A549 cells expressing ACC1-specific shRNA (Supplementary Fig. 19) and confirmed that ACC1 knockdown markedly decreased the  $NADP^+/NADPH$  ratio and  $H_2O_2$  level (Fig. 3f, g). Finally, the ACC inhibitor TOFA, but not the mTORC1 inhibitor rapamycin, decreased the  $H_2O_2$  level (Supplementary Fig. 20). LKB1 expression had a more pronounced effect on FAS inhibition than on FAO increase (Supplementary Fig. 21a). This effect was recapitulated by ACC1 knockdown (Supplementary Fig. 21b), explaining why ACC1 knockdown could decrease the  $H_2O_2$  level.

We then assessed whether redox regulation by ACCs has a function in anchorage-independent growth. Consistent with previous observations<sup>16</sup>, we found that treatment of A549 cells and AMPK $\alpha$ -KO-Ras<sup>V12</sup> MEFs with NAC substantially increased the number of colonies (Fig. 4a and Supplementary Fig. 22). Inhibition of CaMKK markedly inhibited anchorage-independent growth, which was rescued by NAC treatment (Fig. 4a and Supplementary Fig. 22a). Targeting either ACC1 or ACC2 substantially increased the number of colonies on soft agar and recapitulated the effect of NAC (Fig. 4b, c and Supplementary Fig. 23). However, the average colony size was increased only by ACC1 knockdown (Fig. 4b, c), which may reflect the predominant function of ACC1 in controlling the  $H_2O_2$  level after matrix detachment.

To assess further the function of ACCs in anchorage-independent growth, we overexpressed the ACC1(S79A) and ACC2(S212A) mutants in two LKB1-proficient cell lines, MCF7 and H1703. Both mutants increased FAS and the  $H_2O_2$  level after matrix detachment (Fig. 4d and Supplementary Fig. 24a), and potentially inhibited anchorage-independent growth, which was partly rescued by NAC (Fig. 4e and Supplementary Fig. 24b, c). These results indicate that the inhibition of either ACC1 or ACC2 by AMPK is required for anchorage-independent growth by means of redox regulation. In contrast, ACC1 knockdown or ACC2 knockdown in LKB1-reconstituted HeLa cells

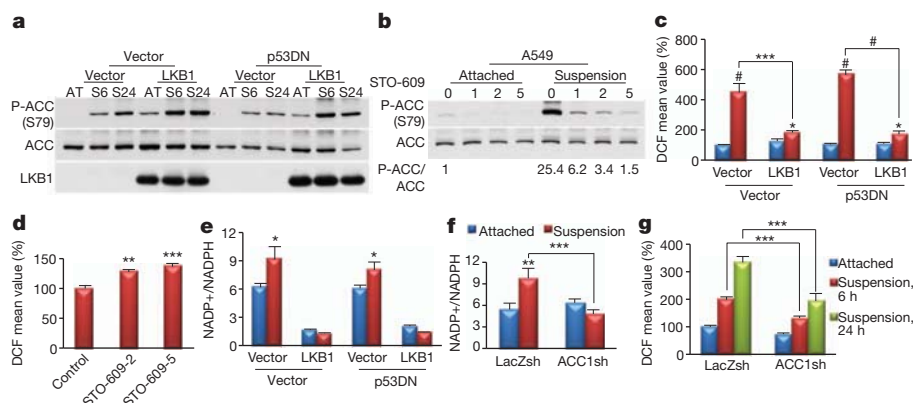


**Figure 3 | AMPK-mediated inhibition of ACC1 is required to maintain the NADPH and reactive oxygen species levels after matrix detachment.**

**a**, A549-Vect-Vect, A549-Vect-LKB1, A549-p53DN-Vect and A549-p53DN-LKB1 cells were grown attached (AT) or in suspension (S6, S24) and subjected to immunoblotting at the indicated time points (6 and 24 h). **b**, A549 cells were grown attached or in suspension in the presence or absence of STO-609 (1, 2 or 5  $\mu\text{g ml}^{-1}$ ) for 6 h and subjected to immunoblotting for quantification of phospho-ACC (P-ACC). **c**, **d**,  $H_2O_2$  levels after growth attached (blue columns) or in suspension (red columns) for 24 h (**c**) or for 6 h in the presence or absence

of 2 or 5  $\mu\text{g ml}^{-1}$  STO-609 (**d**). **e**,  $NADP^+/NADPH$  ratio after growth attached (blue columns) or in suspension (red columns) for 24 h. **f**, **g**, The effect of ACC knockdown on  $NADP^+/NADPH$  ratio (**f**) or  $H_2O_2$  level (**g**) after in suspension for 24 h (**f**) or for 6 and 24 h (**g**). Results in **c**, **d** and **g** are expressed as the percentage change in the mean DCF values over the values of the attached control. Results are shown as means and s.e.m. for three independent experiments. Asterisk,  $P < 0.05$ ; two asterisks,  $P < 0.01$ ; three asterisks,  $P < 0.005$ ; hash,  $P < 0.001$  versus the attached condition in each group (**c**, **e**–**g**) or versus the control (**d**).

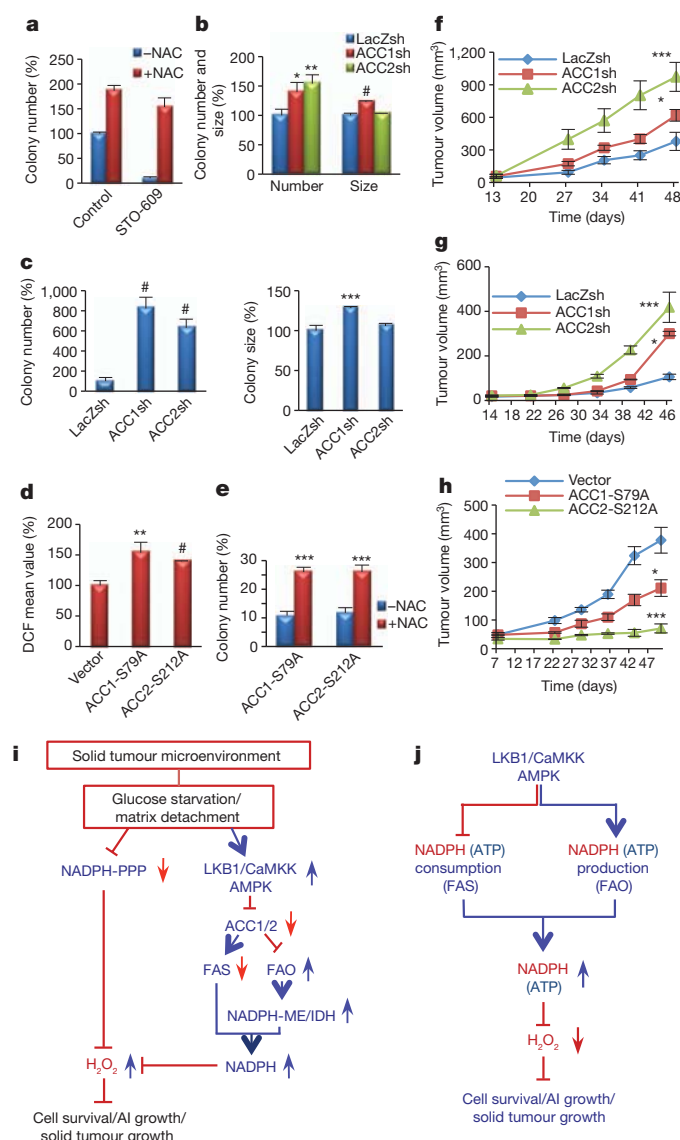


**Figure 4 | AMPK-mediated inhibition of ACC1 or ACC2 promotes anchorage-independent growth and solid tumour formation *in vivo*.** **a**, Quantification of soft agar colonies of A549 cells in the presence or absence of 5  $\mu\text{g ml}^{-1}$  STO-609, with or without 2 mM NAC. **b**, c, A549 cells (**b**) or AMPK $\alpha$ -KO-Ras<sup>V12</sup>-MEFs (**c**) expressing LacZ-shRNA, ACC1-shRNA, or ACC2-shRNA were plated on soft agar, and the number and size of the colonies were analysed. Results are expressed as the percentage change in the colony number and size relative to the -NAC control (**a**) or the LacZsh control (**b**, **c**). **d**, **e**, MCF7 cells expressing ACC1-S79A or ACC2-S212A were generated and grown in suspension for 6 h before quantification of the H<sub>2</sub>O<sub>2</sub> level (**d**) or were subjected to soft agar assay (with or without 2 mM NAC) (**e**). Results are expressed as the percentage change in the mean DCF values (**d**) or colony number (**e**) over the values of the vector control. Results are expressed as means and s.e.m. for three independent experiments. **f**, **g**, A549 cells (**f**), or AMPK $\alpha$ -KO-Ras<sup>V12</sup> cells (**g**) expressing LacZ-shRNA, ACC1-shRNA, or ACC2-shRNA were injected subcutaneously into nude mice. **h**, MCF7 cells expressing vector, ACC1-S79A or ACC2-S212A were mixed with Matrigel (10%) and injected orthotopically into the mammary fat pads of nude mice. Tumour growth was monitored and measured weekly. Results are shown as means and s.e.m. for four mice in each group. Asterisk,  $P < 0.05$ ; two asterisks,  $P < 0.01$ ; three asterisks,  $P < 0.005$ ; hash,  $P < 0.001$  versus LacZsh (**b**, **c**), vector (**d**) or -NAC in each group (**e**), and versus LacZ-shRNA (**f**, **g**) or vector (**h**) at each time point. **i**, Summary: under energy stress when PPP is impaired, AMPK activation attenuates cell death by maintaining NADPH level through FAO-induced NADPH production and by inhibiting NADPH consumption in FAS. AI growth, anchorage-independent growth. **j**, Proposed model: in addition to its function in ATP homeostasis, the LKB1/CaMKK-AMPK/ACC1/2 axis has a key function in NADPH homeostasis to decrease H<sub>2</sub>O<sub>2</sub> level and to promote cancer cell survival and metabolic adaptation.

*in vitro* results (Fig. 4e), ACC2(S212A) expression significantly inhibited solid tumour growth; ACC1(S79A) expression also inhibited tumour growth, although to a smaller extent, under two different experimental conditions (Fig. 4h and Supplementary Fig. 26b). Taken together, these results demonstrate that NADPH maintenance through AMPK-ACC1/ACC2 is critical for solid tumour growth *in vivo* (Fig. 4i). It was previously reported that ACC2 expression is significantly downregulated in papillary thyroid cancer<sup>18</sup>, supporting a tumour-suppressor function for ACC2 in certain contexts. Moreover, consistent with our results, it was shown that overexpression of CPT1 promotes solid tumour growth through the activation of FAO<sup>19</sup>.

Our results are not inconsistent with results showing that inhibition of FAS by the knockdown of fatty acid synthase (FASN) or ATP-citrate lyase (ACLY) inhibits tumorigenesis<sup>20,21</sup> because, unlike the inhibition of ACC, the inhibition of FASN or ACLY exerts additional cytotoxic effects. These cytotoxic effects seem to be through the accumulation of malonyl-CoA but not through the direct inhibition of FAS itself<sup>14,22,23</sup>, and through the inhibition of acetylation without decreasing lipid contents<sup>24,25</sup>. Our results seem paradoxical because of the tumour suppressor activity of LKB1-AMPK, partly through mTORC1 inhibition<sup>3</sup>. We propose that during glucose limitations or matrix depletion, AMPK activation, at physiological levels, is required for NADPH homeostasis, which surpasses the requirement for mTORC1 activity. Combating energy stress conditions by AMPK is particularly important in the early stages of solid tumour formation when cells migrate to the lumen, or during metastasis when cells migrate from the primary tumour to a different location. However, AMPK activation is probably occurring in a temporal manner, because FAO could also increase the ATP level (Supplementary Fig. 27), which would eventually inhibit AMPK. Our results therefore do not necessarily contradict the possibility that prolonged and robust AMPK activation inhibits cancer cell proliferation. In fact, they suggest that a combination of metabolic inhibitors, such as 2DG or metformin, and ACC activators could synergistically decrease cancer cell survival by concurrently inhibiting mTORC1 and the pro-survival activity of AMPK. This combination could be more effective in LKB1-null cancer cells.

Our findings could explain why AMPK-deficient cells are resistant to oncogenic transformation<sup>4,6</sup>. At the organismal level our results may explain why patients with Peutz-Jeghers syndrome, who have

inhibited anchorage-independent growth (Supplementary Fig. 25a). Thus, when AMPK is activated, further inhibition of ACC1 or ACC2 could not enhance tumorigenesis, instead attenuating it.

During the formation of a solid tumour, cells undergo metabolic stress including glucose deprivation and matrix detachment. Indeed, it has been shown that AMPK $\alpha$ -KO-Ras<sup>V12</sup> MEFs are severely impaired in their ability to form tumours *in vivo*<sup>6</sup> and that AMPK is activated during the early stages of solid tumour formation<sup>17</sup>. Thus, to determine whether ACCs have a function in solid tumour formation *in vivo*, we performed xenograft assays using A549 and AMPK $\alpha$ -KO-Ras<sup>V12</sup> MEFs expressing shRNAs targeting ACC1 or ACC2. Knockdown of ACC1 or ACC2 significantly enhanced tumour formation *in vivo* (Fig. 4f, g); the latter had a more pronounced effect on tumour growth than the former. However, neither ACC1 knockdown or ACC2 knockdown in A549-LKB1 cells had much effect on tumour growth (Supplementary Fig. 25b), further suggesting that physiological inhibition of ACC by AMPK, but not enhanced inhibition, is required to promote solid tumour growth. To assess these results further, we performed orthotopic transplantation using MCF7 cells. The knockdown of either LKB1 or AMPK $\alpha$ 1 in MCF7 cells significantly inhibited orthotopic tumour growth (Supplementary Fig. 26a). To test the function of ACC1 and ACC2 phosphorylation by AMPK in tumour growth, MCF7 cells expressing either ACC1(S79A) or ACC2(S212A) were subjected to orthotopic transplantation. Consistent with the



an inherited deficiency of LKB1, and most mouse models of LKB1 deficiency develop only benign tumours<sup>4</sup>. Although somatic mutations in LKB1 are rare in most cancers, the mutations are prevalent in certain cancers, such as non-small cell lung carcinoma and cervical carcinoma<sup>3</sup>. In mouse models, deficiency in LKB1 also promotes Ras-induced lung tumorigenesis<sup>26</sup>. One possible explanation is that certain microenvironmental factors may enable AMPK activation in the absence of LKB1 through other upstream activators, such as CaMKK, as shown in Fig. 3b. In addition, LKB1 deficiency may affect other multiple downstream effectors of LKB1 (ref. 26) that could circumvent the requirement for the LKB1–AMPK pathway during the early stages of solid tumour formation.

AMPK is known to maintain intracellular ATP level under conditions of energy stress. Consistently, we found that AMPK maintains ATP level in addition to NADPH level under these conditions (Supplementary Fig. 27a). However, NAC, which protected from cell death, did not restore ATP level during glucose starvation (Supplementary Fig. 27b), indicating that NADPH maintenance rather than ATP maintenance is the predominant mechanism by which AMPK promotes cell survival during metabolic stress (Fig. 4j).

Our study shows that under conditions of energy stress, when NADPH generation from the PPP is impaired, AMPK activation is required for the maintenance of NADPH level by inhibiting ACC1 and/or ACC2 (Fig. 4i, j). This function of AMPK is critical for cancer cell survival during metabolic stress, which can occur in the solid tumour microenvironment.

## METHODS SUMMARY

For glucose deprivation the cells were incubated in glucose-free DMEM medium containing 10% dialysed FBS; for matrix detachment the cells were plated on poly-HEMA-coated plates for the indicated periods. Cell death was measured by staining with 4',6-diamidino-2-phenylindole (DAPI) or with a trypan blue exclusion assay. The intracellular levels of H<sub>2</sub>O<sub>2</sub> and O<sub>2</sub><sup>•−</sup> were measured by flow cytometry with 2',7'-dichlorofluorescein diacetate (DCF-DA) and dihydroethidium (DHE), respectively. The NADPH and GSH assays were performed using enzymatic cycling methods, and ATP level was measured using the ATPlite assay (Perkin Elmer). Fatty-acid synthesis was measured by detecting <sup>3</sup>H-labelled lipids after incubation with [<sup>3</sup>H]acetate. Fatty-acid oxidation was measured by the detection of <sup>3</sup>H<sub>2</sub>O release after incubation with [9,10-<sup>3</sup>H]palmitate. Glucose uptake was measured with 2-deoxy[<sup>3</sup>H]glucose. The soft agar assays were performed in the presence or absence of 2 mM NAC for 3–4 weeks, and the colony number and size were analysed using ImageJ software. For the xenograft assays, A549 (2 × 10<sup>6</sup> cells) or MEFs (5 × 10<sup>6</sup> cells) were injected subcutaneously into the flanks, and MCF7 (5 × 10<sup>6</sup> cells) were orthotopically injected into the mammary fat pads in athymic nude mice. Tumour size was measured every week. Statistical analyses were performed with unpaired two-tailed Student's *t*-tests, and unless otherwise indicated all data are expressed as means and s.e.m. for three independent experiments.

**Full Methods** and any associated references are available in the online version of the paper at [www.nature.com/nature](http://www.nature.com/nature).

**Received 11 February 2011; accepted 21 March 2012.**

**Published online 9 May 2012.**

1. Folkman, J. Angiogenesis and apoptosis. *Semin. Cancer Biol.* **13**, 159–167 (2003).
2. Jones, R. G. & Thompson, C. B. Tumor suppressors and cell metabolism: a recipe for cancer growth. *Genes Dev.* **23**, 537–548 (2009).
3. Shackelford, D. B. & Shaw, R. J. The LKB1–AMPK pathway: metabolism and growth control in tumour suppression. *Nature Rev. Cancer* **9**, 563–575 (2009).
4. Bardeesy, N. *et al.* Loss of the Lkb1 tumour suppressor provokes intestinal polyposis but resistance to transformation. *Nature* **419**, 162–167 (2002).

5. Kato, K. *et al.* Critical roles of AMP-activated protein kinase in constitutive tolerance of cancer cells to nutrient deprivation and tumor formation. *Oncogene* **21**, 6082–6090 (2002).
6. Laderoute, K. R. *et al.* 5'-AMP-activated protein kinase (AMPK) is induced by low-oxygen and glucose deprivation conditions found in solid-tumor microenvironments. *Mol. Cell. Biol.* **26**, 5336–5347 (2006).
7. Chhipa, R. R., Wu, Y., Mohler, J. L. & Ip, C. Survival advantage of AMPK activation to androgen-independent prostate cancer cells during energy stress. *Cell. Signal.* **22**, 1554–1561 (2010).
8. Corradetti, M. N., Inoki, K., Bardeesy, N., DePinho, R. A. & Guan, K. L. Regulation of the TSC pathway by LKB1: evidence of a molecular link between tuberous sclerosis complex and Peutz–Jeghers syndrome. *Genes Dev.* **18**, 1533–1538 (2004).
9. Shaw, R. J. *et al.* The tumor suppressor LKB1 kinase directly activates AMP-activated kinase and regulates apoptosis in response to energy stress. *Proc. Natl Acad. Sci. USA* **101**, 3329–3335 (2004).
10. Jones, R. G. *et al.* AMP-activated protein kinase induces a p53-dependent metabolic checkpoint. *Mol. Cell* **18**, 283–293 (2005).
11. Le Goffe, C. *et al.* Metabolic control of resistance of human epithelial cells to H<sub>2</sub>O<sub>2</sub> and NO stresses. *Biochem. J.* **364**, 349–359 (2002).
12. Hardie, D. G. & Pan, D. A. Regulation of fatty acid synthesis and oxidation by the AMP-activated protein kinase. *Biochem. Soc. Trans.* **30**, 1064–1070 (2002).
13. Abu-Elheiga, L., Matzuk, M. M., Abo-Hashema, K. A. & Wakil, S. J. Continuous fatty acid oxidation and reduced fat storage in mice lacking acetyl-CoA carboxylase 2. *Science* **291**, 2613–2616 (2001).
14. Zhou, W. *et al.* Fatty acid synthase inhibition triggers apoptosis during S phase in human cancer cells. *Cancer Res.* **63**, 7330–7337 (2003).
15. Canto, C. *et al.* AMPK regulates energy expenditure by modulating NAD<sup>+</sup> metabolism and SIRT1 activity. *Nature* **458**, 1056–1060 (2009).
16. Schafer, Z. T. *et al.* Antioxidant and oncogene rescue of metabolic defects caused by loss of matrix attachment. *Nature* **461**, 109–113 (2009).
17. Jang, T. *et al.* 5'-AMP-activated protein kinase activity is elevated early during primary brain tumor development in the rat. *Int. J. Cancer* **128**, 2230–2239 (2011).
18. Kim, H. S. *et al.* Microarray analysis of papillary thyroid cancers in Korean. *Korean J. Intern. Med.* **25**, 399–407 (2010).
19. Zaugg, K. *et al.* Carnitine palmitoyltransferase 1C promotes cell survival and tumor growth under conditions of metabolic stress. *Genes Dev.* **25**, 1041–1051 (2011).
20. Hatzivassiliou, G. *et al.* ATP citrate lyase inhibition can suppress tumor cell growth. *Cancer Cell* **8**, 311–321 (2005).
21. Migita, T. *et al.* Fatty acid synthase: a metabolic enzyme and candidate oncogene in prostate cancer. *J. Natl. Cancer Inst.* **101**, 519–532 (2009).
22. Knowles, L. M., Yang, C., Osterman, A. & Smith, J. W. Inhibition of fatty-acid synthase induces caspase-8-mediated tumor cell apoptosis by up-regulating DDIT4. *J. Biol. Chem.* **283**, 31378–31384 (2008).
23. Bandyopadhyay, S. *et al.* Mechanism of apoptosis induced by the inhibition of fatty acid synthase in breast cancer cells. *Cancer Res.* **66**, 5934–5940 (2006).
24. Wellen, K. E. *et al.* ATP-citrate lyase links cellular metabolism to histone acetylation. *Science* **324**, 1076–1080 (2009).
25. Migita, T. *et al.* ATP citrate lyase: activation and therapeutic implications in non-small cell lung cancer. *Cancer Res.* **68**, 8547–8554 (2008).
26. Ji, H. *et al.* LKB1 modulates lung cancer differentiation and metastasis. *Nature* **448**, 807–810 (2007).

**Supplementary Information** is linked to the online version of the paper at [www.nature.com/nature](http://www.nature.com/nature).

**Acknowledgements** We thank B. Viollet for the AMPK-KO MEFs, M. R. Montminy for the ACC complementary DNA, and G. Hatzivassiliou for comments on the manuscript. This work was supported by grants CA090764, AG016927 and AG025953 from the National Institutes of Health, by the Chicago Biomedical Consortium with support from The Searle Funds at The Chicago Community, and by grant P60DK20595 to the Diabetes Research and Training Center, University of Chicago (to N.H.).

**Author Contributions** S.-M.J. and N.H. designed the experiments. S.-M.J. performed the experiments. N.S.C. provided advice. S.-M.J. and N.H. analysed the data and wrote the paper.

**Author Information** Reprints and permissions information is available at [www.nature.com/reprints](http://www.nature.com/reprints). The authors declare no competing financial interests. Readers are welcome to comment on the online version of this article at [www.nature.com/nature](http://www.nature.com/nature). Correspondence and requests for materials should be addressed to N.H. (nhay@uic.edu).

## METHODS

**Cell culture, transfection, transduction and western blotting.** MI5-4 CHO cells (a gift from J. Willson) were cultured in  $\alpha$ -MEM supplemented with 2 mM glutamine and 10% FBS (Gemini). All other cells were cultured in DMEM (Invitrogen) containing 10% FBS. For the glucose starvation experiments, the cells were washed with PBS and cultured in glucose-free DMEM (Invitrogen) containing 10% dialysed FBS (Gemini). For suspension culture, the cells were plated on poly-HEMA (2-hydroxyethyl methacrylate)-coated plates. For the transient transfection of the siRNAs,  $2 \times 10^5$  A549 cells or  $10^5$  AMPK $\alpha$ 1/ $\alpha$ 2-DKO MEFs immortalized with SV40 large T (ref. 6) (a gift from B. Viollet) were plated in 6-cm plates 1 day before transfection with 500 pmol of siRNA using Lipofectamine 2000 (Invitrogen). At 48 h after transfection, the cells were replated in six-well plates for western blot analysis or in 12-well plates for measurements of cell death and reactive oxygen species. The infections with lentiviruses and retroviruses were conducted overnight, and infected cells were selected with blasticidin, puromycin or hygromycin under the following conditions:  $25 \mu\text{g ml}^{-1}$  blasticidin for 6 days or  $0.5 \mu\text{g ml}^{-1}$  puromycin for 3 days for A549 cells;  $10 \mu\text{g ml}^{-1}$  blasticidin for 4 days for HeLa cells;  $15 \mu\text{g ml}^{-1}$  blasticidin for 4 days or  $1 \mu\text{g ml}^{-1}$  puromycin for 4 days for H1703 cells;  $10 \mu\text{g ml}^{-1}$  blasticidin for 4 days or  $1 \mu\text{g ml}^{-1}$  puromycin for 4 days for MCF7 cells;  $10 \mu\text{g ml}^{-1}$  blasticidin for 4 days or  $100 \mu\text{g ml}^{-1}$  hygromycin for 6 days for MEF-AMPK $\alpha$ -KO. For the western blot analyses, protein extracts were prepared in lysis buffer, as described previously<sup>27</sup>.

**Reagents and antibodies.** 5-Thio-D-glucose was purchased from ICN Biomedical. DCF and DHE were purchased from Molecular Probes. [ $^3\text{H}$ ]Acetate, [9,10- $^3\text{H}$ ]palmitate and 2-deoxy[ $^3\text{H}$ ]glucose were obtained from PerkinElmer. STO-609 and Ku-55933 were purchased from Calbiochem. All other chemicals were purchased from Sigma-Aldrich unless otherwise indicated. Antibodies against LKB1, AMPK $\alpha$ 1/2, ACC, P-ACC and HK2 were purchased from Cell Signaling, and antibodies specific for ACC2, catalase and  $\alpha$ -tubulin were purchased from Sigma-Aldrich. The G6PD antibody was purchased from Bethyl Lab, and the GSK3 antibody was from QCB.

**Plasmids, RNA-mediated interference (RNAi) and viruses.** The complementary DNAs encoding ACC1 and ACC2 were provided by M. R. Montminy. Site-directed mutagenesis of ACC1 (S79A) and ACC2 (S212) was performed with the QuickChange II XL Kit (Stratagene), as recommended by the manufacturer. The mutants were subcloned into the pLent6-D-TOPO vector (Invitrogen). SMART-pool siRNAs targeting human ACC1 and ACC2 and mouse ACC1 and ACC2 were purchased from Dharmacon (hACC1: 5'-gatgtgagcctgcggaata-3', 5'-ccatttgctg agcgattg-3', 5'-gcaattgattcgtgtga-3', 5'-gatcttagcgacccaat-3', hACC2: 5'-gatac atgacacggatat-3', 5'-gaagagaggtctacacatc-3', 5'-aggaagaggttgacagta-3', 5'-cctgt agatgtggaatta-3', mACC1: 5'-caagactgatggcgatatt-3', 5'-gaaatagactcacaaga-3', 5'-ggaagttaacagttatat-3', 5'-tcaatgtgatgaatggata-3', mACC2: 5'-gtggtgacggagc agcaa-3', 5'-gagattaagtccggaaga-3', 5'-tcaattactgaagcgga-3', 5'-gaagagaggtctac acgtc-3'). The constructs (pENTR-U6) expressing an shRNA targeting LacZ, G6PD, ACC1 or ACC2 were generated with the BLOCK-iT U6 RNAi Entry Vector Kit (Invitrogen). The shRNA sequences used were 5'-GCCTCAGTG CCACTTGACA-3' for hG6PD<sup>28</sup>, 5'-TACAAGGGATACAGGTATTTA-3' for hACC1.2, 5'-GTGGAGCTGATTGTGGACATT-3' for hACC2.1, 5'-GACGGC CTTAGACAATACAAA-3' for hACC2.2, 5'-GCAGATTGCCAATACCTA GA-3' for mouse ACC1, and 5'-GTGGTGACGGGACGAGCAA-3' for mouse ACC2. The shRNA expression cassettes were transferred to a lentiviral vector (plenti6) with the use of the BLOCK-iT Lentiviral RNAi Expression System (Invitrogen). The lentiviral constructs (pLKO.1) expressing shRNAs for a non-targeted control (5'-CAACAAGATGAAGAGCACCAA-3') and hLKB1 (5'-GCCAACGTGAAGAAGGAAATT-3') were purchased from Sigma-Aldrich. The lentiviral vector expressing the AMPK $\alpha$ 1-specific shRNA with the sequence 5'-CTATGCTGCACCAGAAGTA-3' was a gift from M. Karin, and was described previously<sup>29</sup>. All lentiviruses were produced with the BLOCK-iT Lentiviral RNAi Expression System (Invitrogen), as recommended by the manufacturer. To produce retroviruses expressing dominant-negative p53 (p53-DN) or constitutively active Ras (Ras<sup>V12</sup>), the pBabe-Puro-GSE56 plasmid or the pBabe-hygro-Ras<sup>V12</sup> plasmid was transfected into amphotropic or ecotropic Phoenix cells, respectively, as described previously<sup>30</sup>.

**Cell death assay.** In most of the experiments, apoptotic cell death was measured by using DAPI staining, as described previously<sup>27,31</sup>. Cells were plated at a low density ( $(0.7-1) \times 10^5$  cells per well in a 12-well plate); on the next day, the cells were washed with PBS and cultured in glucose-free medium supplemented with dialysed FBS. At each time point, the cells were fixed by the direct addition of formaldehyde (final concentration 12%) to the culture medium. After overnight fixation, the cells were stained for 5 min with DAPI ( $1 \mu\text{g ml}^{-1}$ ), and then left in PBS. The cells were detected with fluorescence microscopy, and cells with condensed and/or fragmented chromatin indicative of apoptosis were counted as dead

cells. For MCF7 cells, a trypan blue exclusion assay was performed to measure cell death.

**Assays of reactive oxygen species.** The intracellular levels of  $\text{H}_2\text{O}_2$  and  $\text{O}_2^-$  were measured with DCF and DHE, respectively. Cells ( $10^5$ ) were plated in a 12-well plate and treated with DCF or DHE for 30 min. The cells were then washed with PBS and collected as single-cell suspensions. Fluorescence was detected by flow cytometry.

**NADPH, GSH and ATP assays.** The intracellular levels of NADPH and total NADP (NADPH + NADP $^+$ ) were measured with previously described enzymatic cycling methods, with modifications<sup>32,33</sup>. In brief,  $1.8 \times 10^6$  cells were plated in 10-cm dishes; on the next day, the cells were lysed in 400  $\mu\text{l}$  of extraction buffer (20 mM nicotinamide, 20 mM  $\text{NaHCO}_3$ , 100 mM  $\text{Na}_2\text{CO}_3$ ) and centrifuged. For NADPH extraction, 150  $\mu\text{l}$  of the supernatant was incubated at  $60^\circ\text{C}$  for 30 min. Next, 160  $\mu\text{l}$  of NADP-cycling buffer (100 mM Tris-HCl pH 8.0, 0.5 mM thiazolyl blue, 2 mM phenazine ethosulfate, 5 mM EDTA) containing 1.3 U of G6PD was added to a 96-well plate containing 20  $\mu\text{l}$  of the cell extract. After a 1-min incubation in the dark at  $30^\circ\text{C}$ , 20  $\mu\text{l}$  of 10 mM glucose 6-phosphate (G6P) was added to the mixture, and the change in absorbance at 570 nm was measured every 30 s for 4 min at  $30^\circ\text{C}$  with a microplate reader. The concentration of NADP $^+$  was calculated by subtracting [NADPH] from [total NADP]. The intracellular levels of GSH and total glutathione (GSSG + GSH) were measured with the use of enzymatic cycling methods, as described previously<sup>34</sup>. The intracellular level of ATP was measured with an ATPlite assay kit (Perkin Elmer).

**Metabolism assays.** Fatty-acid synthesis and oxidation were measured as described previously<sup>35,36</sup>. In brief,  $10^5$  cells were seeded in a 12-well plate for 1 day. For the glucose starvation experiments, the cells were incubated in glucose-free medium for 2 h, and either [ $^3\text{H}$ ]acetate (for FAS) or [9,10- $^3\text{H}$ ]palmitate (for FAO) was added for a further 3 h. For matrix detachment,  $10^5$  cells were seeded on poly-HEMA-coated 12-well plates for 2 h, and either [ $^3\text{H}$ ]acetate or [9,10- $^3\text{H}$ ]palmitate was added for a further 3 h. For the measurement of FAS, total lipids were extracted from [ $^3\text{H}$ ]acetate-treated cells with chloroform/methanol. For the measurement of FAO, the medium from [9,10- $^3\text{H}$ ]palmitate-treated cells was collected to recover  $^3\text{H}_2\text{O}$  using Dowex 1X8-200 columns.  $^3\text{H}$ -labelled lipids and water were quantified by liquid scintillation counting. Glucose uptake was measured with 2-deoxy[ $^3\text{H}$ ]glucose.

**Soft-agar assay.** A total of  $3 \times 10^4$  cells were suspended in DMEM (10% FBS, 5 mM glucose) containing 0.35% agarose and layered on solidified medium containing 0.7% agarose in six-well plates. For MCF7 cells, 1 mM sodium pyruvate was added to the medium. After solidification, the top layer was covered with the medium. When necessary, 2 mM NAC or  $5 \mu\text{g ml}^{-1}$  STO-609 was added to each layer and the cover medium. The medium was replaced every week. Images were taken after 3–4 weeks and analysed with ImageJ software.

**Xenograft assay.** Male and female athymic nude mice (6–8 weeks old) were purchased from Charles River Laboratories. A549 cells ( $2 \times 10^6$  per 0.1 ml of PBS) or AMPK $\alpha$ -KO-MEFs-Ras<sup>V12</sup> cells ( $5 \times 10^6$  per 0.1 ml of PBS) expressing the LacZ-specific, ACC1-specific or ACC2-specific shRNA were injected subcutaneously into both the left and right flanks of each mouse. A xenograft assay using A549 cells was performed twice. MCF7 cells were injected orthotopically into the mammary fat pads (two positions per mouse) in two different conditions, namely the absence (Supplementary Fig. 25) and presence (Fig. 4g) of 10% Matrigel in cell suspensions. Before injection, 17 $\beta$ -oestradiol pellets (1.7 mg/pellet, 60-day release; Innovative Research of America) were implanted in each mouse. The tumour size was measured every week, and the tumour volume was calculated with the equation  $V (\text{in mm}^3) = a \times b^2/2$ , where  $a$  is the longest diameter and  $b$  is the shortest diameter. When the tumour size reached the end-point criterion (a diameter greater than 2 cm), the mouse was killed. All animal experiments were performed in accordance with the animal care policies of the University of Illinois at Chicago and were approved by the Animal Care Committee of the University of Illinois at Chicago.

**Statistical analysis.** All statistical analysis was performed with unpaired two-tailed Student's  $t$ -tests, and all data are expressed as means and s.e.m. for at least three independent experiments, unless otherwise indicated.

- Bhaskar, P. T. *et al.* mTORC1 hyperactivity inhibits serum deprivation-induced apoptosis via increased hexokinase II and GLUT1 expression, sustained Mcl-1 expression, and glycogen synthase kinase  $3\beta$  inhibition. *Mol. Cell. Biol.* **29**, 5136–5147 (2009).
- Li, D. *et al.* A new G6PD knockdown tumor-cell line with reduced proliferation and increased susceptibility to oxidative stress. *Cancer Biother. Radiopharm.* **24**, 81–90 (2009).
- Budanov, A. V. & Karin, M. p53 target genes sestrin1 and sestrin2 connect genotoxic stress and mTOR signaling. *Cell* **134**, 451–460 10.1016/j.cell.2008.06.028 (2008).

30. Skeen, J. E. *et al.* Akt deficiency impairs normal cell proliferation and suppresses oncogenesis in a p53-independent and mTORC1-dependent manner. *Cancer Cell* **10**, 269–280 (2006).
31. Kennedy, S. G. *et al.* The PI 3-kinase/Akt signaling pathway delivers an anti-apoptotic signal. *Genes Dev.* **11**, 701–713 (1997).
32. Wagner, T. C. & Scott, M. D. Single extraction method for the spectrophotometric quantification of oxidized and reduced pyridine nucleotides in erythrocytes. *Anal. Biochem.* **222**, 417–426 (1994).
33. Zerez, C. R., Lee, S. J. & Tanaka, K. R. Spectrophotometric determination of oxidized and reduced pyridine nucleotides in erythrocytes using a single extraction procedure. *Anal. Biochem.* **164**, 367–373 (1987).
34. Rahman, I., Kode, A. & Biswas, S. K. Assay for quantitative determination of glutathione and glutathione disulfide levels using enzymatic recycling method. *Nature Protocols* **1**, 3159–3165 (2006).
35. Buzzai, M. *et al.* The glucose dependence of Akt-transformed cells can be reversed by pharmacologic activation of fatty acid beta-oxidation. *Oncogene* **24**, 4165–4173 (2005).
36. Deberardinis, R. J., Lum, J. J. & Thompson, C. B. Phosphatidylinositol 3-kinase-dependent modulation of carnitine palmitoyltransferase 1A expression regulates lipid metabolism during hematopoietic cell growth. *J. Biol. Chem.* **281**, 37372–37380 (2006).



## ADDENDUM

doi:10.1038/nature11113

## Addendum: Verbal and non-verbal intelligence changes in the teenage brain

Sue Ramsden, Fiona M. Richardson, Goulven Josse, Michael S. C. Thomas, Caroline Ellis, Clare Shakeshaft, Mohamed L. Seghier & Cathy J. Price

*Nature* **479**, 113–116 (2011)

We measured<sup>1</sup> changes in intelligence quotient (IQ) between time 1 and time 2 in teenage subjects and searched their brains for regions where changes in IQ predicted changes in grey matter density (GMD). We found highly significant effects in two localized brain regions, after correcting for multiple comparisons across the whole brain. This provided an unbiased inference that longitudinal changes in IQ were meaningful rather than attributable to measurement error. In *post hoc* analyses, we quantified the (standardized) effect sizes<sup>2</sup> by reporting that 20% of the variance in verbal IQ (VIQ) at time 2 and 13% of the variance in performance IQ (PIQ) at time 2 could be explained by changes in GMD at the most significant voxel in the regions identified by the whole brain analyses. These (in-sample) effect sizes pertain to the sample studied and should not be confused with out-of-sample predictions<sup>3</sup>: that is, IQ predictability given new or independent subjects. Out-of-sample predictions finesse the inherent sampling bias of (in-sample) effect sizes—known in neuroimaging as ‘the non-independence problem’.

Here we report out-of-sample estimates of effect size using a split-half procedure (and take the opportunity to compare VIQ and PIQ effects by including both in the same model). This involved splitting our sample into two groups (group 1 with  $n = 17$  and group 2 with  $n = 16$ ). One group was used to select voxels in which IQ changes

predict GMD changes and the other group was used to predict IQ change from GMD change in these voxels. We found that GMD changes in group 2 (in voxels selected using group 1) predicted 16% of time-2 VIQ and 11% of time-2 PIQ. Conversely, GMD changes in group 1 (in voxels selected using group 2) predicted 16% of time-2 VIQ and 15% of time-2 PIQ (see Fig. 1 for details). These out-of-sample predictions are consistent with our original effect sizes. However, the split-half procedure is one of several procedures we could have used: an alternative approach—that minimizes type II (false negative) errors during voxel selection—is based on ‘leave one out’ procedures<sup>4</sup> and provides unbiased out-of-sample predictions of IQ change from GMD for each subject, in voxels identified in the other subjects. We will report this analysis elsewhere.

1. Ramsden, S. *et al.* Verbal and non-verbal intelligence changes in the teenage brain. *Nature* **479**, 113–116 (2011).
2. Wilkinson, L. APA task force on statistical inference statistical methods in psychology journals: guidelines and explanations. *Am. Psychol.* **54**, 594–604 (1999).
3. Leeb, H. Evaluation and selection of models for out-of-sample prediction when the sample size is small relative to the complexity of the data-generating process. *Bernoulli* **14**, 661–690 (2008).
4. Martens, H. A. & Dardenne, P. Validation and verification of regression in small data sets. *Chemom. Intell. Lab. Syst.* **44**, 99–121 (1998).

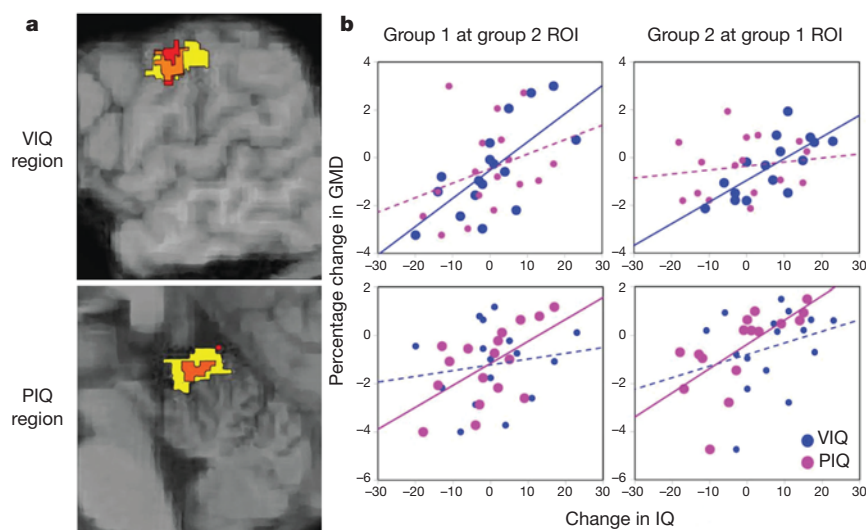


**Figure 1 | Results of the split-half analysis.** **a**, Brain images showing regions where IQ change predicted GMD change in group 1 (red) and group 2 (yellow)—in the left motor/premotor cortex for VIQ and in the anterior cerebellum for PIQ. Orange indicates an overlap of red and yellow. The criteria for selecting these voxels requires that 100 contiguous voxels (or more) survived an uncorrected threshold of  $P < 0.01$  (VIQ) or  $P < 0.05$  (PIQ) and a difference between VIQ and PIQ at  $P < 0.05$  (uncorrected). Using these criteria, the only overlapping voxels, in a whole-brain analysis, are shown in orange above. No other (non-overlapping) effects survived these criteria in the slices shown. **b**, Plots of GMD change against IQ change for group 1 averaged across all voxels in the group 2 region of interest (yellow and orange areas in the left-hand

panel) and for group 2 averaged across all voxels in the group 1 region of interest (red and orange areas in the left-hand panel). The solid line is the significant regression slope and the dashed line is the non-significant regression slope. The  $P$  values for the difference in regression slopes for VIQ and PIQ pooled over both groups (that is, after pooling the unbiased data points from the group 1 and group 2 regressions above) were  $P = 0.009$  ( $t = 2.5$ ; one-tailed) in the VIQ region (above) and  $P = 0.04$  ( $t = 1.9$ , one-tailed) in the PIQ region (below). The analyses used to identify voxels (left) and to quantify the data (right) were identical to those in the original paper<sup>1</sup> except that each step included only half the data (and we combined VIQ and PIQ in the same regression model).